EVALUATION OF THE RIBEYE DEFLECTION MEASUREMENT SYSTEM

Narayan Yoganandan and Frank A. Pintar
Medical College of Wisconsin
Milwaukee, WI USA
Paper number 09-0020

ABSTRACT

The objective of the present study is to evaluate the RibEye system used to obtain deflections in impact-related tests. A description of the system is presented based on the specifications of the manufacturer. Evaluations included chest compression tests under varying loading condition: mid-sternum, offset, and diagonal loading. Accuracy assessment tests included: sternum-mounted, and rib-mounted LEDs with and without initial chest rotation about the z-axis, and indenter-mounted LEDs. These quasi-static tests were followed by pure and oblique pendulum tests to the thorax at velocities of 4.8 and 6.6 m/s. LEDs on the sternum responded similar to the available internal chest potentiometer. The accuracy of the system depended on positioning of the LEDs on the rib, magnitude of rib deformation, and potential interference from devices such as the presence of the internal chest potentiometer. Signal drop out depended on the type of indenter, with diagonal loading producing more signal loss. The deflection response along the x-and y-directions were deemed to be reasonable in oblique loading tests. Results from dynamic tests indicated that light interference from the internal component(s) restricts the ability of the system to obtain accurate deflections including signal drop out. In oblique tests, the system captured the asymmetric motions of the chest by demonstrating greater deflections on all left side ribs than right side ribs, thus showing its potential under this loading condition. The current fundamental evaluations helps in understanding of the performance of the system as installed in the mid-size male Hybrid III dummy.

INTRODUCTION

crashworthiness assessments for frontal impact in the United States Federal Motor Vehicle Safety Standard (FMVSS) No. 208 used the Hybrid III dummy family [1]. As far as chest instrumentation is concerned, the dummy houses a triaxial accelerometer on the spine to record the chest acceleration, and an internal deflection potentiometer to measure the chest deflection. The chest force-deflection responses are applicable to blunt frontal impacts and are based on tests to the mid-sternum impacts using a 23.4 kg pendulum at velocities of 4.3 and 6.7 m/s [2-4]. The peak chest deflection is obtained from the internal potentiometer measuring the linear displacement of the sternum with respect to the thoracic spine, and the force is recorded from a load cell attached to the pendulum impactor. Data are gathered and processed according to the Society of Automotive Engineers SAE J211 specifications [5].

Chest deflection measurements at multiple points facilitate an assessment of non-uniform, asymmetric thorax loading. Occupant out-of-position effects may also contribute to asymmetrical chest deformations even in pure frontal impacts. Eppinger from the National Highway Traffic Safety Administration of the United States Department of Transportation developed a dedicated instrument, chestband, for measuring deformations [6]. It is a noninvasive device made of high carbon steel alloy strip with strain gauges bonded at 59 locations. During the early years of development, lesser gages were used. Deflections at multiple levels have been obtained using more than one chestband. This device has been used to compare chest deflections in simulated frontal impacts in a laboratory environment [7, 8].

Recognizing that deflections can be used for understanding injury mechanisms and might serve to define injury criteria, recently, an optically-based instrument, termed RibEye, has been developed by Robert A. Denton, Inc., to measure internal chest deflection of devices such as the Hybrid III dummy [9]. As a systematic evaluation have not been reported, this paper describes procedures to evaluate the RibEye system in the mid-size Hybrid III dummy with a focus on frontal impact applications.

DETAILS OF THE SYSTEM

The underlying concept is that an optically-based system, being not affixed to a specific mechanical linkage such as the internal chest potentiometer connecting the spine and sternum, can enhance the number of deflection measurements. Briefly, the

RibEye system is comprised of up to twelve light emitting diodes (LEDs) mounted to the ribs of the dummy internally, two incident light detectors (sensors) that receive light from the LEDs, a controller, and an interface box (Figures 1-7). The current version of the system is capable of obtaining deflection data along the x- and y-directions, fore-aft and side to side. The sensors are mounted laterally to each side of the thoracic spine of the dummy, and the controller is located within the spine box at its uppermost location. LEDs connect to the controller via a block mounted superior to the sensor heads. The interface box can be secured in the trunk of the test vehicle in full scale experiments.

LEDs can be mounted at various positions on the inside surface of the ribs or sternum. The default LED locations are placed one on each rib on either side. However, the RibEye allows the user to override the default condition and position multiple LEDs on the same rib or sternum as long as proper z-axis location is maintained. All LEDs are connected via a cable to the data acquisition system housed within the thoracic spine of the Hybrid III dummy. The user indicates the position of the LED in the "Location" field of the user-interface. Three LED case designs exist: with different back angles that direct light toward the RibEye sensors (Figure 4). The flat back LEDs are designed for positioning on ribs three and four, the 20-deg angled back LEDs are designed for positioning on ribs two and five, and the 35-deg angled back LEDs are designed for positioning on ribs one and six. Optionally, the 35-degree angled back LEDs may be positioned on the upper and lower sternum using the mounting plates (Figures 5-7).

Each LED is powered sequentially and sampled at 10,000 Hz during testing, while two sensors detect the angle of the LED with respect to frontal and lateral planes. The resulting digital data are stored in memory. This constitutes the "raw data" from the RibEye system. These data are then corrected for ambient light conditions and adjusted using calibration curves housed within the software of the data acquisition system. In other words, the light intensity data collected based on the incident angle is converted by an embedded microprocessor using optical triangulation techniques to compute deflection records at each LED position. These processed data are then stored in the RibEye flash memory. Data are downloaded to an external computer and saved as a text file using the RibEye interface within a web browser (Figure 7). Thus, it is possible to obtain fore-aft and side-side coordinates of deflection of the rib or sternum at the positioned LED location during loading. Using twelve sensors, deflections can be determined at twelve locations. The system allows the user to download "raw data" using the Hyperterminal software. However, processing of this "raw data" to provide LED deflections can be only be done by the manufacturer, Robert A. Denton, Inc.

The following multi-point deflection measurement system specifications were extracted from the User Manual. The measurement ranges in the x-y and x-z planes are demonstrated in Figures 8-9. For Figures 8 and 9, the x=0, y=0, z=0, i.e., origin, is the midpoint of the line segment connecting the two sensors. With respect to the dummy, this is approximately on the front surface of the spine mount box in the center of the chest. Thus, the absolute location of the midsternum is approximately x=87, y=0, z=0 mm. The system does not account for out-of-plane movements. Thus, any z-axis movement of an LED will produce measurement inaccuracies. Tables 1 and 2 list the system accuracy associated with z-direction deflection ranges.

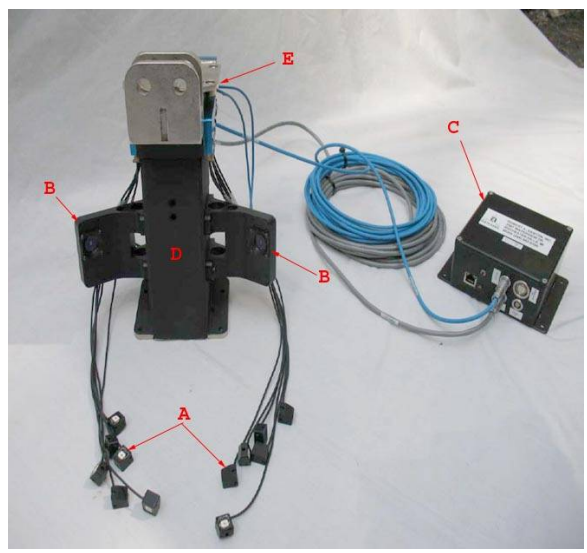

Figure 1. RibEye system: LEDs (A), two sensor heads located on both sided of the thoracic spine (B), interface box (C and E), dummy thoracic spine box (D), and LED connector block (F).

The power supply to the system should be 12 to 36 volts DC. Fuse protection is an internal self-resetting polymer fuse in the interface box. RibEye's self-contained data system has a sampling rate of 10,000

Hertz per LED and an acquisition time of 90 milliseconds pre-trigger, 910 milliseconds post-trigger (1 second total). All data are collected in RAM and stored post-test in the system memory.

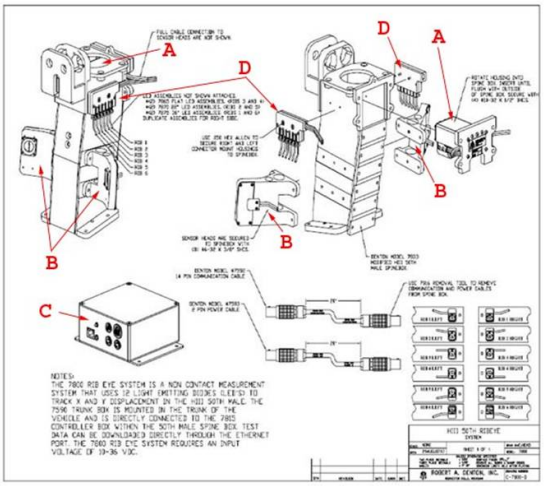

Figure 2. RibEye system components showing the controller (A), sensor heads (B), interface box (C), and LED connector block (D).

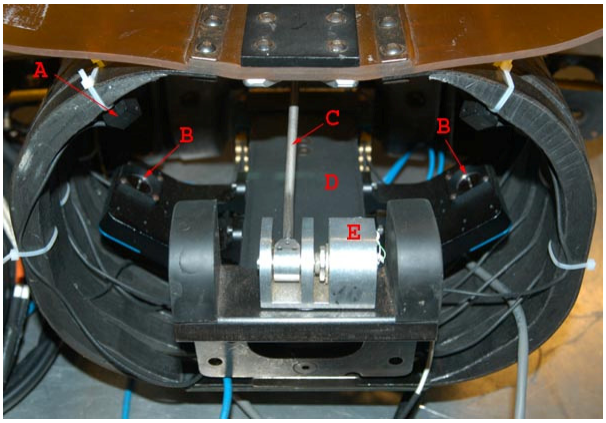

Figure 3. RibEye system shown installed in the mid-size Hybrid III dummy. The photo shows an LED fixed to right sixth rib (A), sensors (B). The standard Hybrid III sternum displacement slider arm (C), dummy thoracic spine box (D), and internal chest potentiometer assembly (E) are also shown.

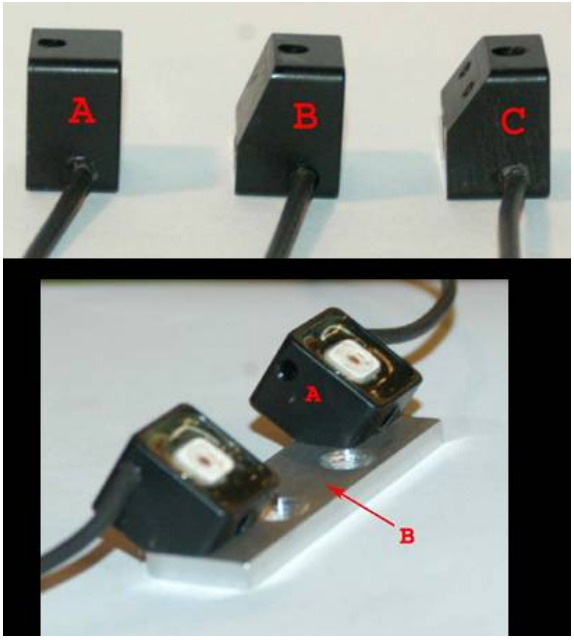

Figure 4. The top illustration shows the LED case design: flat back LED (A), 20-deg angled back LED (B), and 35-deg angled back LED (C). The bottom illustration shows the 35-deg angled back LED (A) and the sternum mounting plate (B).

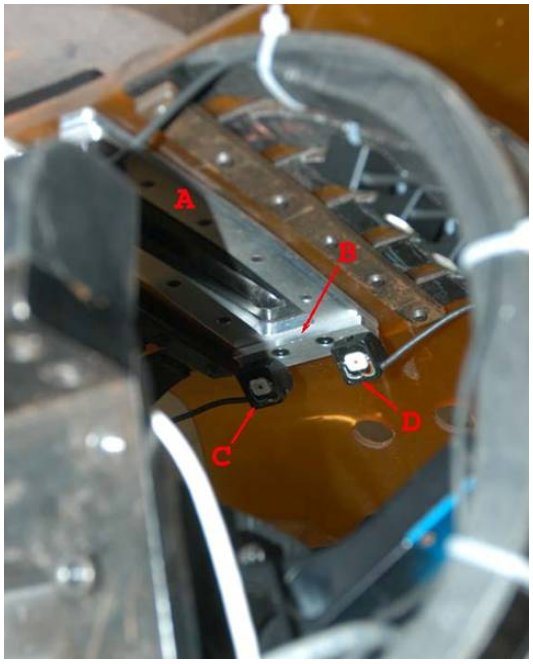

Figure 5. Mid-size Hybrid III dummy chest showing the sternum assembly (A), sternum mounting plate (B), upper right and left sternum LEDs (C and D).

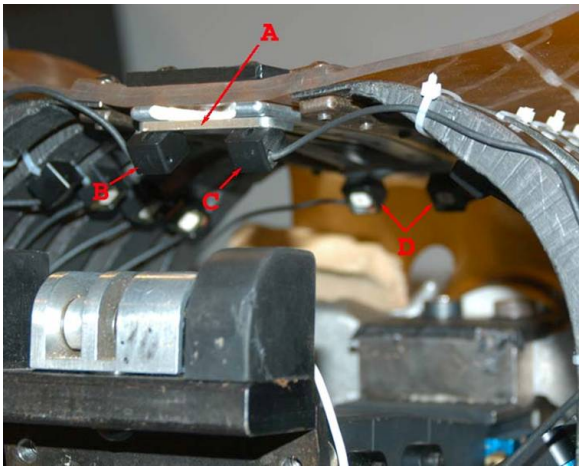

Figure 6. Inferior view of the sternum-mounted LED: sternum mounting plate (A), lower right and left sternum LEDs (B, C), and upper sternum LED (D).

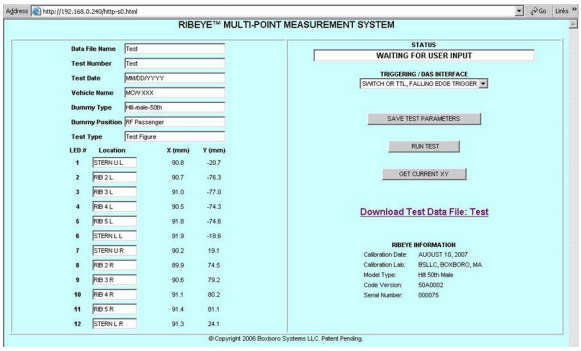

Figure 7. RibEye use interface.

Table 1.
RibEye accuracy with z-axis deviation

z-deviation mm	x-accuracy mm	y-accuracy mm
0	1.0	1.0
± 12.5	1.0	2.0
12.5 to 25.0	2.0	2.0
-12.5 to -25.0	2.0	2.0

Table 2.
Power requirements

Operating conditions	Interface box (W)	Controller and LEDs (W)	Total (W)
On or idle	3.3	2.0	5.3
Collecting data	3.3	5.0	8.3
Maximum*	3.3	9.0	12.3

*: when all LEDS are out of view of both sensors and driven to full power

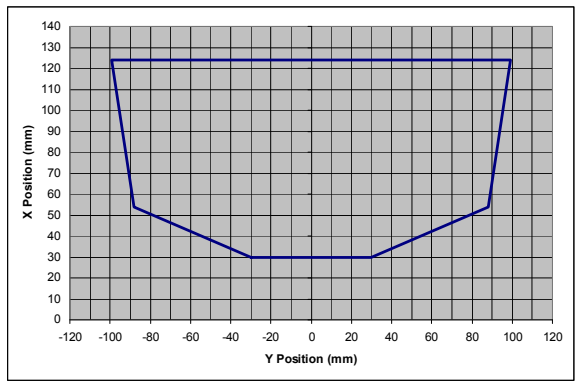

Figure 8. The specified range for LED x-y positions for the mid-size Hybrid III dummy.

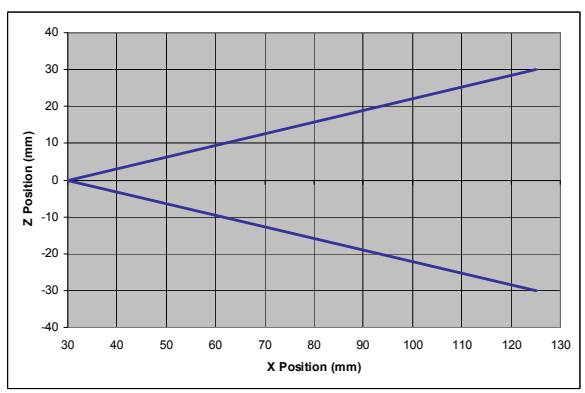

Figure 9: The specified range for LED x-z positions for the mid-size Hybrid III dummy.

QUASI-STATIC EVALUATIONS

LED Positioning

This was accomplished as follows. The thorax of the mid-size male Hybrid III dummy was mounted on a cross table and attached to a testing device. LEDs were positioned on the inside surface of the ribs and position measurements were obtained from the midline of the sternum along the outer surface of the ribs.

LED Signal Drop Out Assessment

In order for the RibEye system to optically track the position of the LEDs, there must be sufficient light projected from each LED onto the spine box-mounted sensors. If either or both sensors detect inadequate light intensity, data from that particular LED will be forced out of range and the system will not track the LED motion until the light intensity requirement is again satisfied. This light intensity requirement can also be affected by extraneous light such as those resulting from high intensity lighting systems, typically used in crashworthiness studies (example, sled tests) to obtain overall kinematics. However, the dummy chest jacket use minimizes extraneous light interference. When sensors detect inadequate light intensity, signal drop out occurs, resulting in gaps within the RibEye deflection records.

In the x-direction deflection plot, drop out appears an instantaneous negative change in the displacement of the LED followed by a horizontal interval (Figure 10). The displacement magnitude of the horizontal interval indicates the initial absolute position of the LED prior to compression, and any association with the indenter and chest potentiometer traces is coincidental. At the end of the drop out period, there is an instantaneous positive change in the displacement as normal LED tracking resumes. In the y-direction deflection plot, signal drop out pattern is similar to the x-direction, but in right-sided LEDs the deviation is negative and in left-sided LEDs it is positive (Figure 11).

The graphical appearance of signal drop out is therefore, a consequence of the RibEye system methodology in data processing under inadequate signal conditions. If inadequate light from a particular LED is provided to the left sensor, all data for that LED during the period of diminished optical signal is assigned an integer value, "1." On the other hand, if inadequate light is provided to the right sensor, all data for that particular LED is assigned an integer value, "2." However, if inadequate light is provided to both sensors, all data for that LED is assigned an integer value, "3." These values do not appear to be in the "raw data", but is most likely included in the output from the microprocessor which feeds into the flash memory.

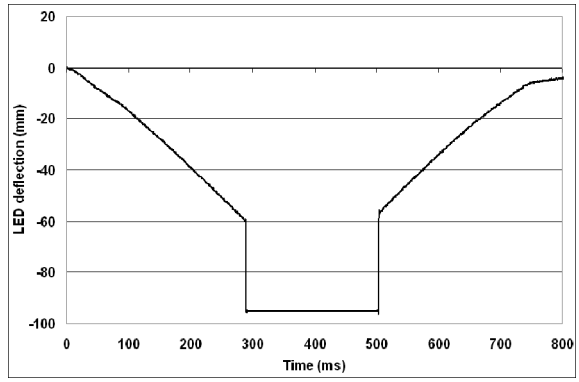

Figure 10. Deflection along the x-direction of the right fourth rib LED positioned at 6 cm. While the indenter continues to compress the chest, drop out occurs in the LED signal. The shape of the drop out pulse is similar regardless of the positioning of the LED.

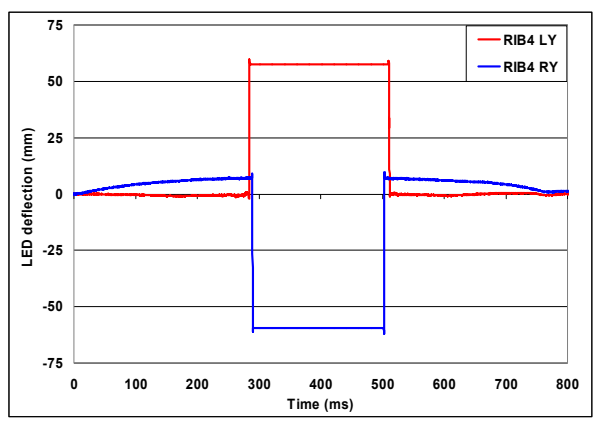

Figure 11: Deflections along the y-direction of the right and left fourth rib LEDs positioned at 6 cm. The drop out occurs in both LEDs. The polarity reversal between the left and rib LEDs are discussed in the text. The shape of the drop out pulse between the left and right LED is similar regardless of the positioning of the LED.

Appendix A contains a portion of the text output from the RibEye web interface software. The output provides absolute xy location information for each LED. Note that data demonstrating insufficient light detection by the left sensor from the LED affixed to left rib six (RIB6 LX and RIB6 LY) at 100.3 milliseconds are assigned the integer value, "1". The right sensor detected inadequate light projected from LEDs attached to right ribs one and two during the 99.3 – 100.9 millisecond interval shows the integer value, "2". In this example, at no time were the LED light signals undetectable by both sensors. In subsequent plots the absolute position data are filtered and converted to relative data such that all sensors begin at zero. In other words, the initial absolute position value is subtracted from all values to establish zero base line. This process results in converting integer values indicating drop out to relative deflection magnitudes.

LED signal drop out may occur from ribcage (rib or sternum) bending that directs the light beam away from the sensor(s), or, obstruction of the beam by another component of the mid-size III dummy such as the slider arm of the chest potentiometer. Signal drop out secondary to the bending path appears as a horizontal interval symmetric about the center of the indenter trace corresponding to maximal compression. In contrast, signal drop out due to the slider arm obstruction appears as two shorter intervals. The initial drop out interval occurs during compression while the second interval occurs symmetrically during release (Figure 12).

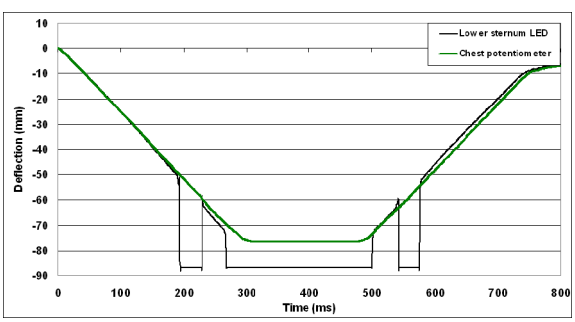

Figure 12. Plot showing drop out from the lower sternum LED on the right side (deflection shown is along the x-direction) due to light interference from the presence of the slider arm of the internal chest potentiometer. Displacement data from the potentiometer is included. Data corresponds to 3-in chest compression test.

Drop out assessment tests were conducted using a ramp waveform and indenter displacements ranged from 1-in to 3-in. It should be noted that the maximum sternum deflection specified FMVSS 208 is 2.5 inches [10]. Indenter velocities were 0.25 or 0.50 m/s. All tests, except with LEDs at the 11 cm position, were performed with and without the internal chest potentiometer slider arm. RibEye data were separated into individual channels and a CFC600 filter was used according to SAE J211-1 2003 specifications for filtration of thorax deflections.

In mid-Sternum compression loading, a wooden cylinder of diameter 15 cm attached to the actuator of the testing device was used to determine the drop out with varying LED positions and sternum compression parameters. The loading paralleled the mid-size Hybrid III dummy evaluation criterion. Quasi-static compression tests were performed with LEDs mounted to ribs one through six on each side in the following configurations: 6, 8, 9, 10, 11, or 13 cm from the sternum midline. The center of the indenter contacted the thorax at mid-sternum (Figure 13).

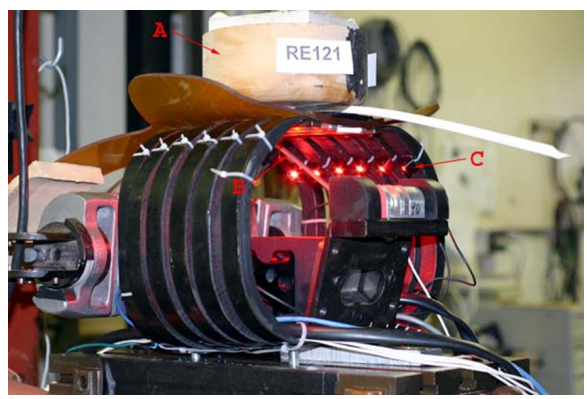

Figure 13. Photograph showing the test system with the wooden indenter (A) and LEDs positioned on the left sixth rib (C) at 11 cm. The dummy rights ribs are identified (B).

The sternum attachment option was evaluated with four LEDs mounted to the upper and lower corners of the sternum plate via screws. The remaining LEDs were mounted to ribs two through five at either 8 or 9 cm from the midline (Figure 14). The RibEye system was compressed using a 15 cm square aluminum plate indenter in these tests. A leveling

plate was used to compensate for the convexity of the sternum plate and provide level contact surface for loading the sternum.

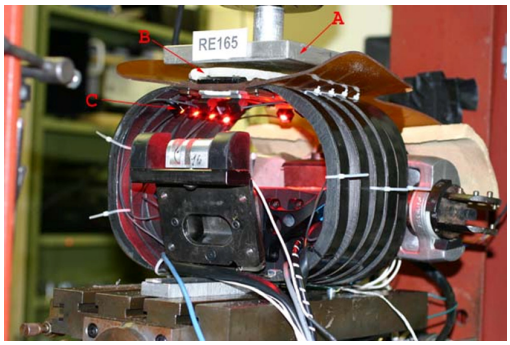

Figure 14. Photograph showing the test system with the aluminum indenter (A) and LEDs positioned at 8 cm on the right 2-5 ribs (C). The PMMA leveler is identified (B).

The presence of the linkage arm of the internal chest potentiometer in the mid-size Hybrid III dummy appeared to increase the likelihood of interference as the location of LEDs moved away (towards left or right) from the 9 cm position. As expected, increasing the magnitude of the chest compression increased the likelihood of drop out. The percentage of LED drop out was sensitive to positioning, the magnitude of sternum compression (1-in test), and the presence of the internal chest potentiometer. No drop out occurred in tests with 1-in sternum compression. This was independent of the presence or absence of the mid-size Hybrid III dummy the internal chest potentiometer. In the 2-in compression test without the presence of the potentiometer, the drop out occurred only at the 13 cm position. However, the presence of the potentiometer at this compression magnitude produced drop out at the following positions: 6 cm; 8 cm; 13 cm; and the sternum. The 3-in sternum test without the chest potentiometer produced dropout at all LED positions except the 9 cm position. Inclusion of the potentiometer in the 3-in compression test resulted in LED dropout in all configurations. These findings indicate that the mechanism of signal drop out can be influenced by obstruction within the light field (presence of internal chest potentiometer slider arm), initial position of the LED, and orientation of the LED deflection path of the ribcage.

Peak chest compressions before drop out depended on the position of the LED. The 9 cm position showed no drop out (the 3-in compression test) and increasing drop outs occurred with positions away from the 9 cm position. As shown in Figure 15, at the 6 cm LED position, the peak compression before drop out was 62 mm, followed by 70 mm at the 8 cm, 64 mm at the 10 cm, and 24 mm at the 13 cm LED positions. At the sternum, the peak chest compression occurred at 66 mm. These results suggest that 9 cm position is optimal. Because the peak sternum compression exceeded the injury assessment reference value (IARV) of 63 mm, according to FMVSS No. 208, (section S6.4, Code of Federal Regulations, 10/1/2006 edition) with LEDs positioned at 8 cm, 9 cm, and 10 cm, and on the sternum, it may be appropriate to use these positions when the symmetrical load is on the center of the sternum in the mid-size Hybrid III dummy.

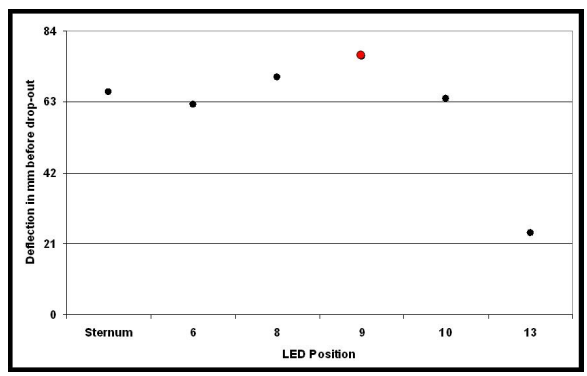

Figure 15. Peak chest compression before drop out from LEDs positioned at locations shown on the x-axis. The 9 cm positioned LED did not have any drop out and hence the maximum displacement achieved by the indenter was recorded. The sternum compression before drop out exceeded the IARV of 63 mm in LEDs positioned at 10, 9, and 8 cm and sternum. Note the decreasing peak deflections before drop out as LED positioning moves away from 9 cm position.

The purpose of offset tests was to determine the drop out characteristics with asymmetric loading to the ribcage in the mid-size Hybrid III dummy. In the left side offset tests, the longitudinal edge of the indenter, 51 mm x 102 mm, was aligned with the front end stiffener plate of the left side ribs two through five. The performance was evaluated in the 1-, 2-, and 2.5-in compression tests, with LEDs mounted at the 6

cm, 9 cm, and 13 cm positions, resulting in nine tests. The extreme case of the 3-in compression test was not considered because subjecting the mid-size Hybrid III dummy thorax to this magnitude may exceed its capacity. The purpose of the diagonal loading tests was to determine the drop out characteristics with asymmetric loading generated by a typical diagonal shoulder belt. Loading was accomplished using a 51 mm wide metal plate angled at approximately 45 deg in the frontal plane and positioned with its center at mid-sternum. LEDs were positioned at the 9 cm location, and the plate was displaced to compress the dummy chest to 1-in, 2-in, and 3-in. Two tests at each of the two lower compressions were conducted. These tests indicated that system is able to follow the offset loads. The upper- and lower-most LEDs appear to be sensitive to drop out in the diagonal loading, with no drop outs occurring in the middle ribs. Drop out only occurred in the 3-in compression test and the first LED dropped out at an indenter displacement exceeding the sternum compression IARV. Because drop outs occurred in multiple LEDs, the system may not fully capture the ribcage motion at this severe chest displacement in the mid-size Hybrid III dummy.

Accuracy Assessments

The purpose of these tests was to directly compare the deflection measuring capability of the RibEye system with the current deflection measuring standard (internal chest potentiometer) or with the indenter deflection. The potentiometer measures sternum compression via a transducer arm whose end travels in a midline track within the dummy sternum. The transducer arm induces rotation in a potentiometer during compression and the resulting electrical signal is converted to linear displacement. These tests were designed to evaluate the accuracy of deflection records along x- and y-directions (Table 3). Tests in this series consisted of four subseries. The first three subseries involved test configurations that maintained the integrity of the dummy thorax such that LEDs were mounted to the sternum, rib, or rib inter-space while the chest compression was induced by the indenter. The fourth subseries entailed mounting an LED directly to the actuator of the test device and tracking its displacement. Indenter displacement and velocity were varied with each subseries. Following each test the RibEye data was separated into individual channels and CFC60 filter was used. RibEye deflection data were compared to the displacement of the indenter and with the chest displacement potentiometer data in the sternum-mounted subseries of tests.

Table 3.
Accuracy description of tests

LED Location	Loading	Compare with	Accuracy
Sternum	central sternum	pot + Indenter	x
Right rib 4	over LED	Indenter	x (+/- z deviation)
Right rib 4 (rotated thorax)	over LED	Indenter	x and y
Indenter extension	None	Indenter	x

Sternum-mounted LED tests evaluated the accuracy of RibEye detection of four LEDs mounted on the upper and lower corners of the sternum (Figure 16). The remaining eight LEDs were considered secondary and mounted on the sternum or, onto ribs two through five at either 8 or 9 cm from the midline. It was expected that the deflections from the corner mounted LEDs will match the internal chest potentiometer deflection. However, because of bib flexibility in the mid-size Hybrid III dummy chest, mismatch can occur between the internal chest potentiometer and the indenter.

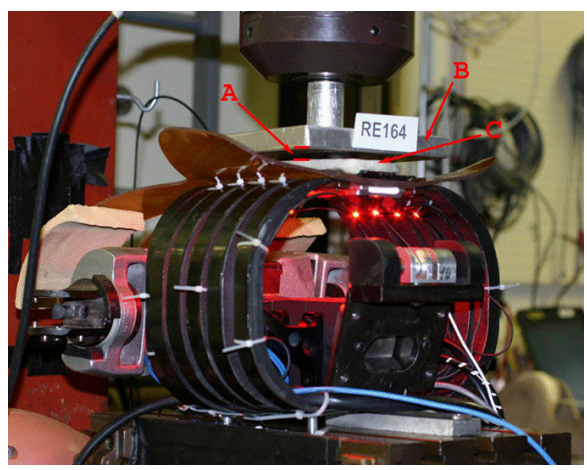

Figure 16. Test configuration for sternum-mounted loading. A: Offset for the trigger system, B: the Aluminum plate indenter, and C: PMMA leveler.

Rib-mounted LED tests were done using the standard z-location at the center of each rib and at a z-direction offset position of 1.5 cm from the center of each rib. The latter offset position corresponds to the interspace between adjacent ribs. An LED was mounted at the antero-medial rib margin of the right fourth rib (Figure 17).

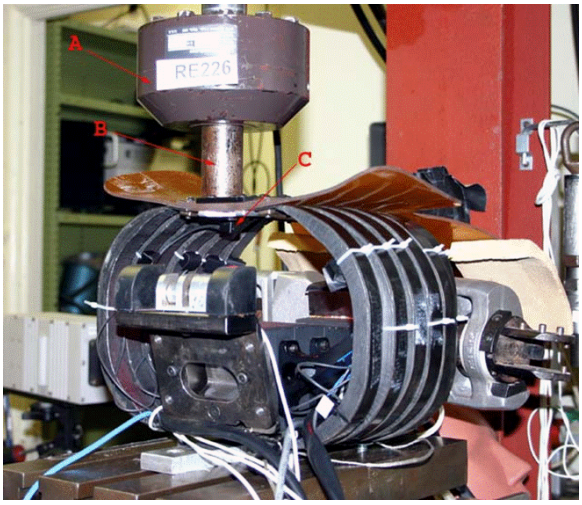

Figure 17. Test configuration for rib-mounted loading. A: indenter load cell, B: indenter, C: LED at right frontend stiffener plate at 4th rib.

Rib-mounted LED tests with rotated chest were conducted with the dummy chest rotated 13 degrees about its z-axis, as shown in Figure 18, and securely fixed to the cross table. The small circular indenter was placed directly over an LED attached to the right fourth rib at 8 cm from the sternum midline. and chest compression tests were performed.

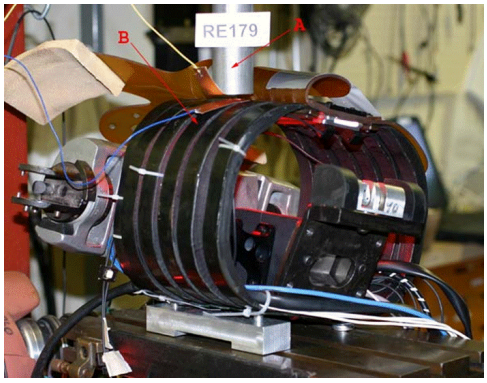

Figure 18. Photograph showing the setup for thorax rotated loading tests. A: indenter and B; right fourth rib.

Table 4 compares peak LED deflections with indenter displacements corrected for the initial rotation. In the subsequent subseries of indenter-mounted accuracy tests, an LED was mounted to an extension of the indenter that allowed for positioning of the LED directly under the rib of interest. The mid-size Hybrid III dummy sternum was modified to allow the indenter extension to pass between the ribs, but maintain the original thorax geometry (Figure 19). This configuration essentially produced an accuracy bench test that maintained integrity of both the mid-size Hybrid III dummy and RibEye system. Compression tests were performed at the left third and right sixth ribs. Velocities ranged from 0.08 m/s to 0.25 m/s with nominal deflections of 12 to 60 mm.

Table 4.
Right rib 4 LED deflections compared to indenter displacement in oblique thorax tests

Peak Indenter deflection (mm)	Peak Rib 4 deflection (mm)	Change (mm)	% Change
-15.8	-14.3	-1.5	-9.4
-21.9	-21.2	-0.7	-3.4
-28 5	-27.6	-0.9	-3.1
-40.8	-40.0	-0.8	-1.9

These tests indicated that the RibEye system is capable of capturing the ribcage deformations in the mid-size Hybrid III dummy. LEDs on the sternum respond similar to the available internal chest potentiometer. The accuracy of the system depends on where the LEDs are positioned on the rib, magnitude of rib deformation, and potential interference from devices such as the presence of the internal chest potentiometer. Optimum locations appear to be at a distance of 9 cm measured along the outer curvilinear path of the rib from mid-sternum on either side. At this positioning, the system showed no signal drop out at deflections representative of current frontal impact standards. However, it should be noted that eccentric z-axis placement of LEDs may result in loss of accuracy of deflection of measurements. The signal drop out depended on the type of indenter, with the diagonal indenter producing more signal loss and affecting accuracy. The deflections response along the x-and y-directions were deemed reasonable in oblique loading tests in these tests.

DYNAMIC EVALUATIONS

The RibEye system was also subjected to pendulum tests. Seven tests were conducted with the mid-size Hybrid III dummy in the neutral and two tests were conducted with the dummy in the 25-degree oblique position about the vertical (z) axis so that the pendulum impacted the right side of the thorax. The neutral positioning used in these tests followed specifications according to 49 CFR 572.34 [3].

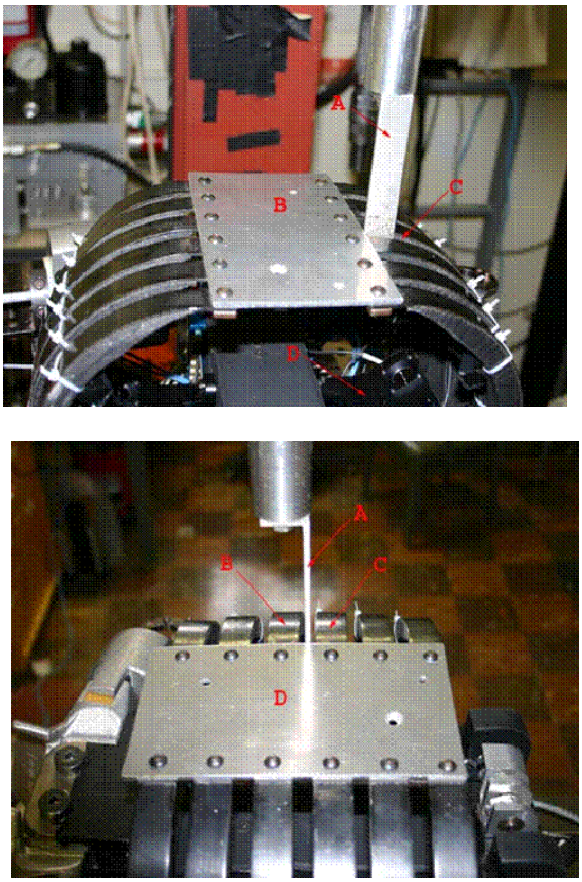

Figure 19. Setup used in indenter-mounted LED tests. Top: A: indenter extension, B: sternum modification, C: left 3-4 interspace, and D: RIbEye sensor head. Bottom: A: indenter extension, B and C: left third and fourth ribs, and D: sternum

Impact velocity measured with an optical system for Hybrid III thorax qualification tests ranged from 3.0 m/s to 6.6 m/s. The internal chest potentiometer was used in four of the neutral tests. It was not used in any oblique test. The initial test in this series (Test 1, probe velocity = 6.6 m/s) served as a thoracic impact calibration test. The maximum sternum deflection measured by the internal chest potentiometer, 67 mm, was within the qualification corridor in 49 CFR 572.34. Drop out did not occur in tests conducted at velocities ranging from 3.0 to 4.8 m/s, regardless of the presence or absence of the dummy internal chest potentiometer (Table 5). However, drop out occurred in three of twelve (25%) LEDs in the 6.6 m/s test in the neutral position with inclusion of the internal chest potentiometer. The analogous test without the potentiometer produced no drop out and implicated the chest pot slider arm as the source of sensor interference.

Table 5.
Summary of pendulum test data

ID	1	2	3	4	5
Position	N	N	N	N	N
Velocity (m/s)	6.6	4.1	3.0	4.1	4.1
Chest pot use	Y	Y	Y	Y	N
Pot def (mm)	66.8	39.5	27.0	41.1	-
LED drop out	3	0	0	0	0
% drop out	25.0	0.0	0.0	0.0	0.0

ID	6	7	8	9
Position	**N**	N	O	O
Velocity (m/s)	3.0	6.6	4.1	4.8
Chest pot use	N	N	N	N
Pot def (mm)	-	-	-	-
LED drop out	0	0	0	0
% drop out	0.0	0.0	0.0	0.0

Figures 20-22 include deflections along the x-direction from the upper, middle, and lower ribs with LED drop out associated with the lower rib output. The internal chest potentiometer data are also included in all plots. Rib deflection profiles closely followed the sternum deflection measured by the chest potentiometer in both timing and shape. The morphologies of these profiles were found to be similar. As expected, rib deflections were lower than the sternum deflection secondary to positioning of LEDs on the ribs and rib motion during compression. Because of the three-dimensional nature of the ribcage and off-central locations of the LEDs,

sternum-measured displacements were greater than the displacements recorded by the LEDs positioned on the ribs.

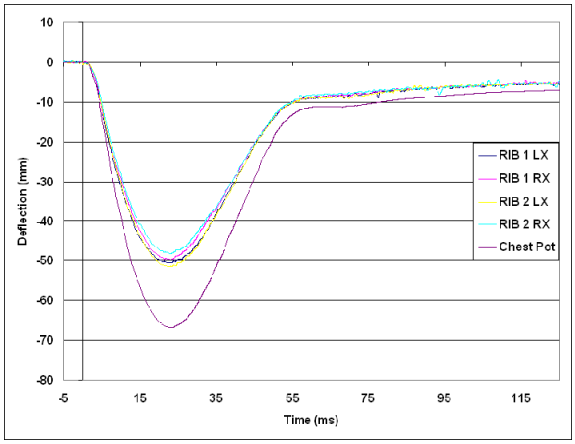

Figure 20. Comparison of deflections in the x-direction from the internal chest potentiometer and LED positioned at 9 cm on ribs one and two during 6.6 m/s pendulum test.

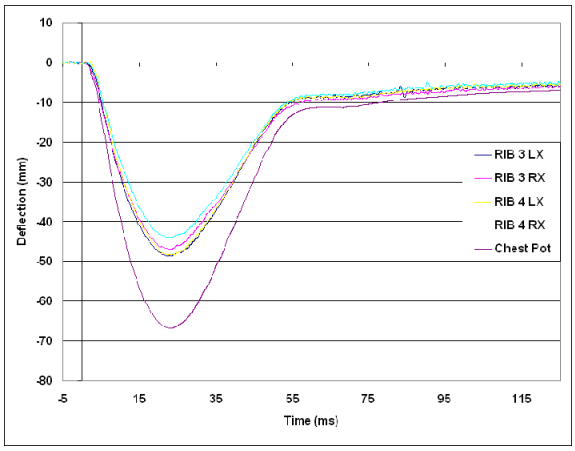

Figure 21. Comparison of deflections in the x-direction from the internal chest potentiometer and LED positioned at 9 cm on ribs three and four during 6.6 m/s pendulum test.

Figure 23 shows deflections along the y-direction. The ribs on the right side deflect along the positive y-direction while the opposite is true for the left side (hoop deformation). This expected response is reflective of central loading of the mid-size dummy chest during impact from the pendulum.

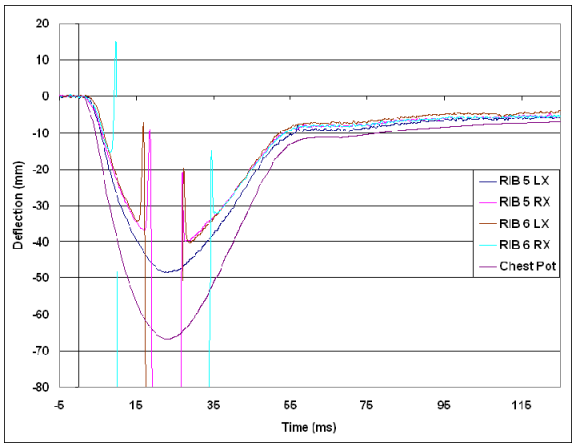

Figure 22. Comparison of deflections in the x-direction from the internal chest potentiometer and LEDs positioned at 9 cm on ribs five and six during 6.6 m/s pendulum test. Drop out occurred in three LEDs.

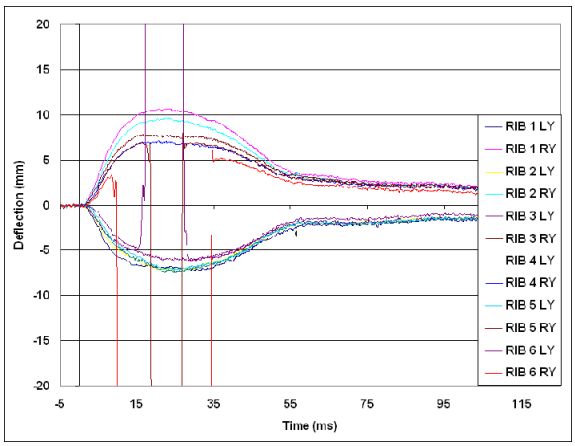

Figure 23. Deflections in the y-direction from LEDs positioned at 9 cm on all ribs during 6.6 m/s pendulum test. Drop out occurred in three LEDs.

Figures 24-26 include deflections along the x-direction from the upper, middle, and lower ribs for the test without the internal chest potentiometer. No signal drop out occurred in these evaluations. Figure 27 shows deflections along the y-direction for all LEDs demonstrating no drop out.

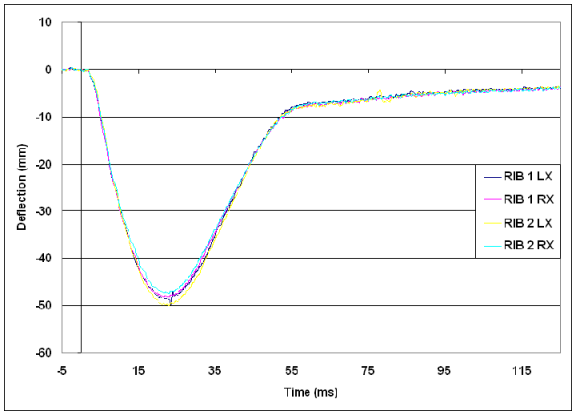

Figure 24. Deflections in the x-direction from LEDs positioned at 9 cm on ribs one and two during 6.6 m/s pendulum test.

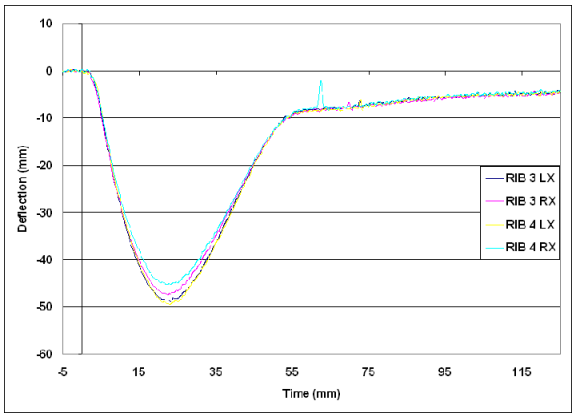

Figure 25. Deflections in the x-direction from LEDs positioned at 9 cm on ribs three and four during 6.6 m/s pendulum test.

Figures 28-30 include deflections along the x-direction from the upper, middle, and lower ribs for the oblique test. The right side ribs demonstrated greater deflection magnitudes in the x direction compared to the left side ribs. This is reflective of the right oblique chest loading imparted by the pendulum. No signal drop out occurred in these evaluations. Figure 31 shows deflections along the y-direction for all LEDs, again demonstrating no drop out. These deflections were approximately the same magnitude, which would be expected because the loading is from the right to the left side causing a deflection of all ribs toward the left side.

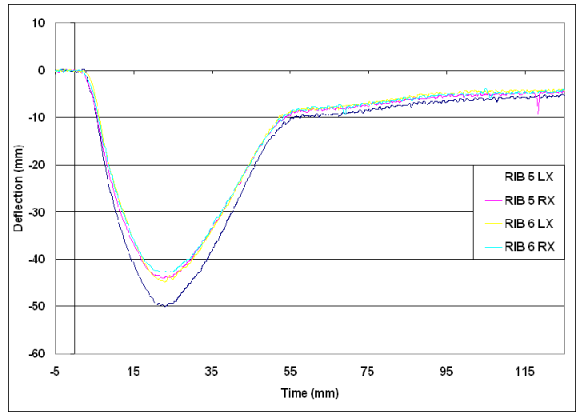

Figure 26. Deflections in the x-direction from LEDs positioned at 9 cm on ribs five and six during 6.6 m/s pendulum test.

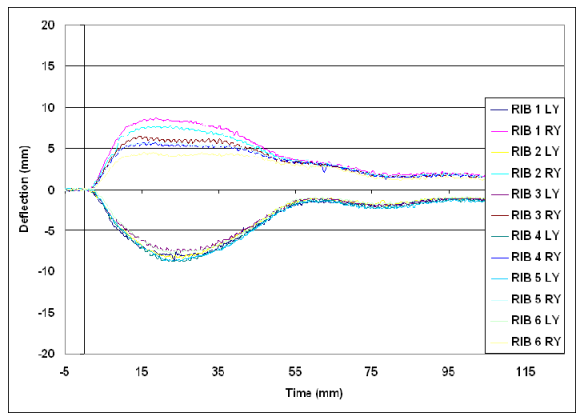

Figure 27. Deflections in the y-direction from LEDs positioned at 9 cm on all ribs during 6.6 m/s pendulum test.

The system evaluated is with specific reference to the mid-size Hybrid III dummy. As the construction of the dummies is different for different sizes even in the Hybrid III family, the same system cannot be incorporated into the other dummies. In the same vein, while a modified system has the potential to be incorporated into other types of dummies, the present evaluations should be considered only as a first step in the performance of such systems. It should be noted that the system is stand-alone and requires integration into standard data acquisition systems that are used in routine crashworthiness tests, and the sample frequency and recording time are fixed for the current version. In tests conducted in the present

evaluation study, occasional data download issues included browser and system re-boots in addition to data delimiters were missing in six tests. Thus additional studies may be needed to resolve such issues.

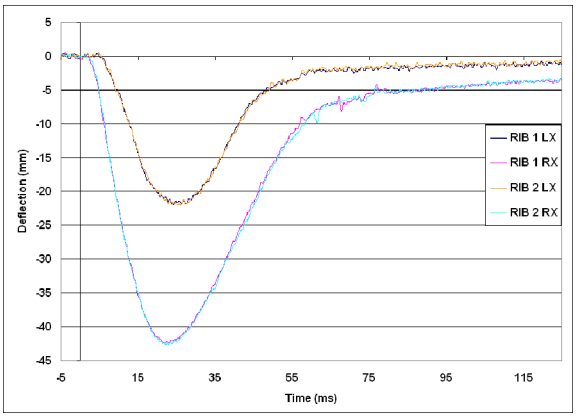

Figure 28. Deflections in the x-direction from LEDs positioned at 9 cm on ribs one and two during 4.8 m/s oblique pendulum test.

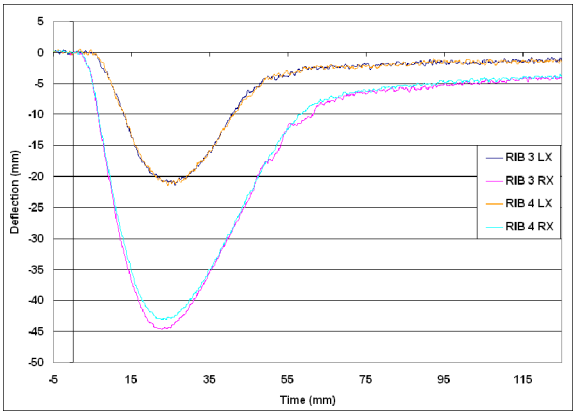

Figure 29. Deflections in the x-direction from LEDs positioned at 9 cm on ribs three and four during 4.8 m/s oblique pendulum test.

To summarize, the objective of the present study was to evaluate the RibEye system intended for obtaining deflections in impact-related tests. To achieve the objectives, signal drop out and accuracy assessment tests were conducted using quasi-static and dynamic loading conditions. The former series of experiments were conducted using a custom-designed testing device. In contrast, the latter dynamic tests were conducted using a pendulum impactor at velocities ranging from 3.0 to 6.6 m/s. Mid-size Hybrid III dummy internal chest potentiometer was used along with the testing device indenter records in the assessment processes.

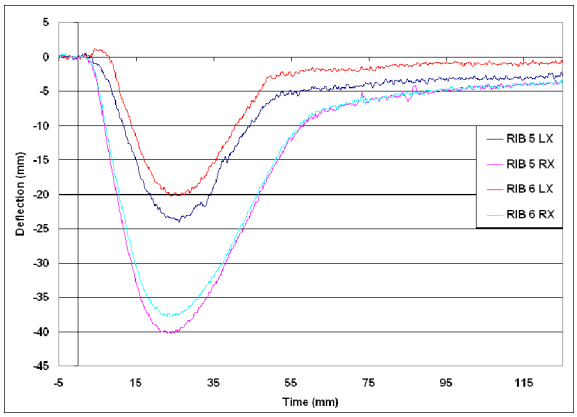

Figure 30. Deflections in the x-direction from LEDs positioned at 9 cm on ribs five and six during 4.8 m/s oblique pendulum test.

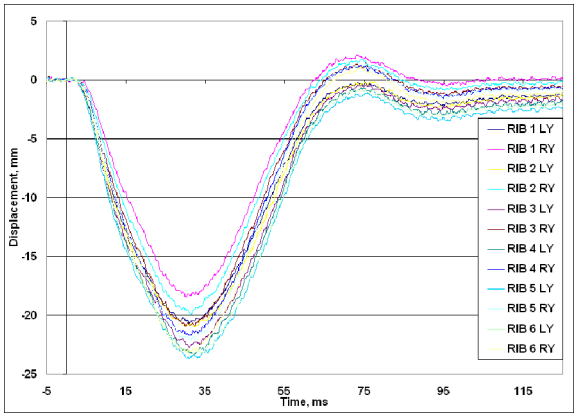

Figure 31. Deflections in the y-direction from LEDs positioned at 9 cm in all ribs during 4.8 m/s oblique pendulum test.

Signal drop out depended on the type of indenter, with the belt-type indenter producing more signal loss. The deflections response along the x-and y-directions were deemed reasonable in oblique loading tests. Results from dynamic tests indicated that light interference from internal components restricts the ability of the system to obtain deflections including signal drop out. In oblique tests, the

system captured the asymmetric motions of the chest by demonstrating greater deflections on all left side ribs than right side ribs, demonstrating its potential under this loading condition. These evaluations assist in understanding of the performance of the system as installed in the mid-size Hybrid III dummy.

ACKNOWLEDGMENTS

This study was supported in part by DTNH22-07-H-00173, DTNH22-05-X-01209, and VA Medical Research. The assistance of James Rinaldi and the Neuroscience research staff is gratefully acknowledged.

REFERENCES

1. 49-CFR, *Code of Federal Regulations, Part 572*. 2000, US Department of Transportation: Washington, DC.
2. Kroell, C.K., D.C. Schneider, and A.M. Nahum. *Impact tolerance and response to the human thorax*. in *Stapp Car Crash Conf.* 1971.
3. Kroell, C.K., D.C. Schneider, and A.M. Nahum. *Impact tolerance and response to the human thorax II*. in *Stapp Car Crash Conf.* 1974. Ann Arbor, MI: SAE, Warrendale, PA.
4. Neathery, R.F. *Analysis of chest impact response data and scaled performance recommendations*. in *Stapp Car Crash Conf.* 1974.
5. *Society of Automotive Engineers*, in *Human tolerance to impact conditions as related to motor vehicle design-J885*. 1980, SAE: Warrendale, PA.
6. Eppinger, R.H. *On the development of deformation measurement system and its application toward developing mechanically based indices*. in *Stapp Car Crash Conf.* 1989.
7. Yoganandan, N., et al. *Thoracic biomechanics with air bag restraint*. in *Stapp Car Crash Conf.* 1993. San Antonio, TX.
8. Yoganandan, N., et al. *Thoracic deformation contours in a frontal impact*. in *Stapp Car Crash Conf.* 1991.
9. Handman, D.F., *Multipoint position measuring and recording system for anthropomorphic test devices*. 2007, Boxboro systems, LLC, Newton, NA: USA.
10. 49-CFR, *Code of Federal Regulations, Part 571*. 2000, US Department of Transportation: Washington, DC.

Appendix A: RibEye data demonstrating drop out

Time (ms)	RIB5 LX	RIB5 LY	RIB6 LX	RIB6 LY	RIB1 RX	RIB1 RY	RIB2 RX	RIB2 RY
99.3	47.5	-118.6	46.3	-103.8	2	2	2	2
99.4	47.2	-118.5	47.1	-103.2	2	2	2	2
99.5	47.4	-119.0	46.7	-103.0	2	2	2	2
99.6	47.8	-119.2	46.6	-102.6	2	2	2	2
99.7	47.6	-119.2	46.1	-102.4	2	2	2	2
99.8	47.4	-119.3	45.8	-102.6	2	2	2	2
99.9	46.9	-119.4	45.5	-102.0	2	2	2	2
100	47.4	-118.8	46.2	-101.7	2	2	2	2
100.1	47.7	-118.9	45.9	-101.3	2	2	2	2
100.2	47.5	-119.4	46.0	-100.7	2	2	2	2
100.3	47.8	-119.4	1	1	2	2	2	2
100.4	47.0	-120.0	1	1	2	2	2	2
100.5	47.7	-119.0	1	1	2	2	2	2
100.6	47.8	-118.9	1	1	2	2	2	2
100.7	47.1	-119.7	1	1	2	2	2	2
100.8	47.0	-120.1	1	1	2	2	2	2
100.9	46.9	-120.4	1	1	2	2	2	2

Note: “1”: left sensor drop out; “2”: right sensor drop out; and “3”: would indicate drop out from both sensors.

EVALUATION OF AN ALTERNATIVE THORAX DEFLECTION DEVICE IN THE SID-IIs ATD

Jack Jensen
Jeff Berliner
Barbara Bunn
Hollie Pietsch
Occupant Safety Research Partnership
U.S.A.
Dan Handman
Boxboro Systems, Inc.
U.S.A.
Mike Salloum
Denton ATD, Inc.
U.S.A.
Dominique Charlebois
Suzanne Tylko
Transport Canada
Canada
Paper Number 09-0437

ABSTRACT

The use of a RibEye system in a SID-IIs crash dummy was evaluated. The SID-IIs is a small adult female side impact anthropomorphic test device. The RibEye is a non-contact optical system that uses triangulation to measure rib deflection.

This study quantified RibEye measurements using four evaluation environments. First, a SID-IIs thorax with an internal RibEye was impacted with a linear impactor and the measurements were compared to accelerometer and video measurements. Next, the RibEye was mounted in a vertical drop tower and impacted with a falling drop mass, simulating a purely lateral side impact. The RibEye measurements were compared to data from linear potentiometers, which are typically used in the SID-IIs. A similar drop tower test series was then conducted which included tests with the RibEye mounted at an angle to simulate oblique loading to a dummy during a side impact.

Lastly, a series of full vehicle crash tests were conducted to compare measurements from a SID-IIs dummy with a RibEye to a SID-IIs dummy with linear potentiometers.

The lateral drop tower tests indicated that peak deflections measured by the RibEye were generally within 1 mm of the linear potentiometer measurements. In the full vehicle crash tests, the RibEye and linear potentiometer measurements fell within the expected variability from crash test to crash test. User interface issues and the practicality of RibEye in the full vehicle tests are also discussed. In oblique loading tests, the RibEye revealed significant X-axis motions that cannot be measured by linear potentiometers as typically mounted in the SID-IIs thorax.

INTRODUCTION

The SID-IIs is a small adult female side impact Anthropomorphic Test Device (ATD). It was designed in the 1990s jointly by the three domestic U.S. auto manufacturers and First Technology Safety Systems working through the Occupant Safety Research Partnership (OSRP) of the United States Council for Automotive Research (USCAR). This ATD was designed to be a second-generation side impact dummy with improved biofidelity compared to existing side impact dummies. It was intended to be available for global harmonization of crash test regulations. The biofidelity of this ATD's beta version was reported by Scherer, et al. [1]

To simulate human anatomy, the SID-IIs uses a collection of steel bands called "ribs". The SID-IIs has one shoulder rib, three thoracic ribs, and two abdominal ribs, each made of Vascomax© steel with bonded dampening material. The dummy typically utilizes linear potentiometers (pots) (as specified in the Code of Federal Regulations – 49 CFR Part 572) to measure the amount of rib deflection for these six ribs during impact tests. The upper thoracic rib linear pot is shown in Figure 1 (with the shoulder rib pot removed).

The laboratories represented by the OSRP member companies as well as other laboratories have

experienced data quality issues with these pots in the crash testing environment. Frequently, electronic noise and data dropouts have resulted from damage to the resistive elements inside the pots. The pots are mounted using spherical bearings to reduce any off-axis loading; however, the noise may have been due to inertial effects. Sources of this noise were investigated by Arbelaez, et al. [2]. An example of erroneous crash data recorded with the pots is shown in Figure 2. Thus, there was a need to investigate alternative technologies for measuring the motion of the impacted side of the SID-IIs ribs relative to the spine box.

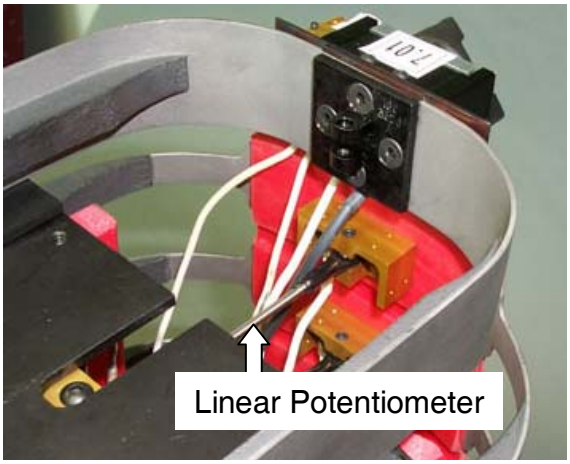

Figure 1. Linear pot mounted to thorax rib.

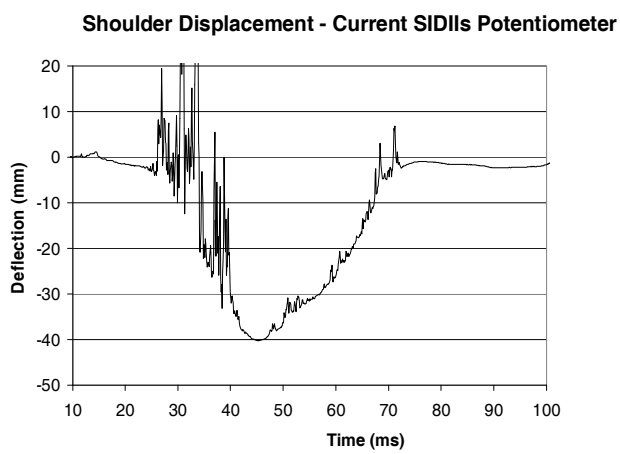

Figure 2. Sample crash data from a current SID-IIs linear pot.

RibEye Technology

RibEye is a new electro-optical technology that measures deformation of the ribcage in three dimensions at high speeds. The RibEye was designed to not affect the biofidelity of the dummy. RibEye uses light-emitting diodes (LEDs) placed at the desired measurement points, with three optical sensors mounted to the dummy spine. The sensors capture light from the LEDs and translate the light angle into a deflection measurement. Simple triangulation, as used in sailing and mapping, yields data on three-dimensional movement of all ribs. The RibEye sensor module is shown in Figure 3and the RibEye LEDs mounted on the SIDIIs ribs are shown in Figure 4.

Figure 3. RibEye sensor module.

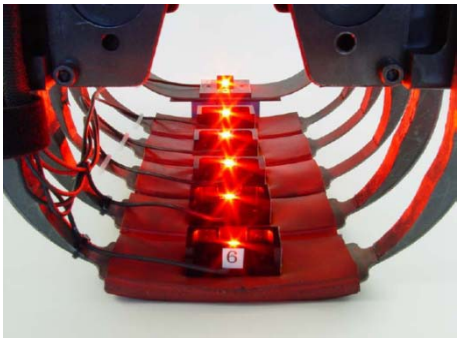

Figure 4. RibEye LEDs on SID-IIs ribs.

Unlike current methods, RibEye reports measurements with respect to the sensor location, as opposed to pots which simply report the stroke of its shaft. Also, RibEye constantly controls LED brightness to get accurate readings over a wide range of sensor-to-LED distances, which has not been done by previous optical methods.

LIMITATIONS

This evaluation was intended to quantify the accuracy of the RibEye measurements by exercising the system in several different loading conditions. This included linear impact tests, two series of drop tower tests and full vehicle crash tests. During each evaluation the RibEye measurements were compared to alternate measurements such as linear pots or video analysis.

For controlled laboratory tests such as drop tower and linear impact tests, differences in measured peak deflections between the alternate technologies of less than 1.5 mm were considered "good". This represents 2% of 75 mm, which was a typical displacement observed during these test evaluations. Those differences between 1.5 and 3.0 mm (2% - 4%) were considered "marginal".

This evaluation did not fully address all of the laboratory, user and durability issues associated with a new measurement technology. As an example, comments concerning the integration of RibEye to a data acquisition system are presented but a thorough analysis was not completed.

Previous testing had indicated the RibEye may susceptible to ambient light interference. Alternate dummy clothing had been proposed to address this issue by blocking ambient light from entering the dummy's chest cavity. However, this alternate clothing was not fully evaluated as part of this study.

For the purposes of this project, rib locations are referenced as Rib 1 through Rib 6. As an example, a reference to Rib 2 in this paper corresponds to thoracic rib 1 in the dummy (the second rib from the top in the dummy.)

LINEAR IMPACTOR TEST SERIES

A series of ten linear impactor tests was conducted to compare the response of the RibEye system in the thorax of the SID-IIs dummy with that of individual Y-axis mounted rib accelerometers and with high-speed video analysis. Most of these tests concentrated specifically on the in-line Y-axis motion of the ribcage.

Linear Impactor Test Methodology

The ribcage of a SID-IIs dummy was mounted to a reaction block via upper and lower mounting brackets as shown in Figure 5. The shoulder rib of the dummy was not included in these tests to improve photographic coverage, thus these tests concentrated on the remaining ribs of the thorax and abdomen. The mounting brackets were attached to the top and bottom of the dummy's spine box. The reaction block was bolted rigidly to the floor of the test facility. Ensolite foam pads for the thoracic and abdominal ribs were also included as part of the dummy's ribcage. Two or three high-speed video cameras were used during the testing (mounted off-board) to capture ribcage motion. Standard off-board lighting was used during the tests.

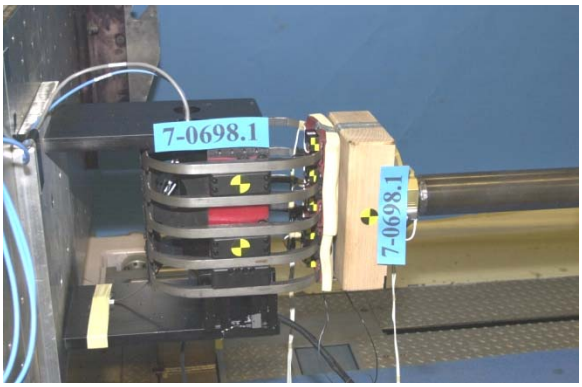

Figure 5. Targets on linear impactor.

The linear impactor machine was positioned to allow for pure in-line Y-axis loading. The intent was to exercise the RibEye system at a rib deflection rate similar to what is observed in typical side impact crash tests. This was estimated to be approximately 4.9 m/s (11 mph).

Test data was collected using three independent methods: 1) a RibEye system, 2) Endevco 7264C-2000 uniaxial accelerometers, and 3) TrackEye© video analysis using targets mounted to the spine box and ribcage. The accelerometers were mounted on each rib near the RibEye LEDs (5 total data channels). An accelerometer was also mounted to the loading ram to measure the input acceleration. The linear impactor face was a wood block. The spine box was assumed to be rigidly mounted to a non-moving fixture. The dummy's chest jacket and clothing were not used during the linear impactor testing so that the video cameras could adequately capture the ribcage motion.

Although RibEye measures deflections in all three axes, the primary focus of these tests was the Y-axis deflections. Each rib-mounted accelerometer was double-integrated to obtain the corresponding deflection of the individual rib. In addition, high-

speed motion analysis techniques were used to measure the Y-axis deflection of each rib. The accelerometer and RibEye data were filtered according to the Society of Automotive Engineers (SAE) standard J211/1 [3].

Linear Impactor Test Results

Figure 6 shows the deflection time-history plot for abdominal Rib 5 for one of the ten linear impactor tests. Rib 5 generally had the best correlation among the RibEye Y-displacement, motion analysis, and the accelerometer calculations. The raw RibEye data (Y-axis deflection) is shown in blue; RibEye data filtered at CFC600, CFC180, and CFC60 are shown in green, red, and light blue, respectively. One source of noise in the RibEye measurements may have been the ambient lighting in this test series as there was no dummy clothing on the thorax. The unfiltered uniaxial accelerometer mounted to Rib 5 was doubled-integrated by two independent software packages (purple and yellow curves).

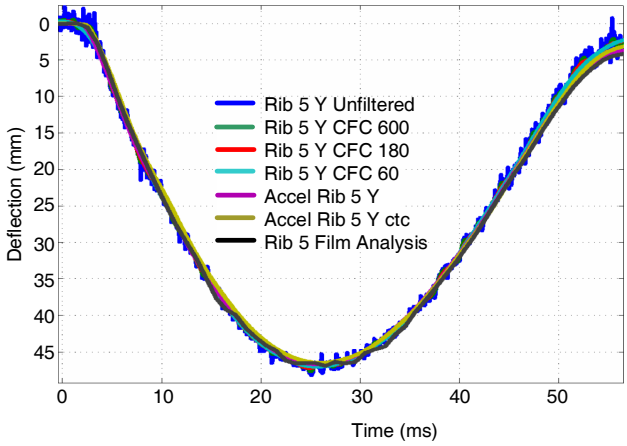

Figure 6. Sample linear impact test (Rib 5).

Figure 7 shows an enlargement of the peak deflections on Rib 5 during this test. The peaks for the filtered RibEye data were approximately 47 mm; accelerometer data peaks ranged from 46.5 to 46.7 mm; and the motion analysis peak was 46.7 mm. The effects of the various CFC filters on the RibEye raw data can clearly be observed.

The CFC filter of 180 appears to retain the useful waveform while reducing the noise in the signal. This is different than the recommended SAE filter class of 600 due to the additional noise in the RibEye signal for this test set-up. For the subsequent tests which did not use a dummy jacket, CFC class 180 was used for RibEye measurements, while the recommend SAE filter of 600 was used for tests using a dummy jacket (such as for the full vehicle crash tests.)

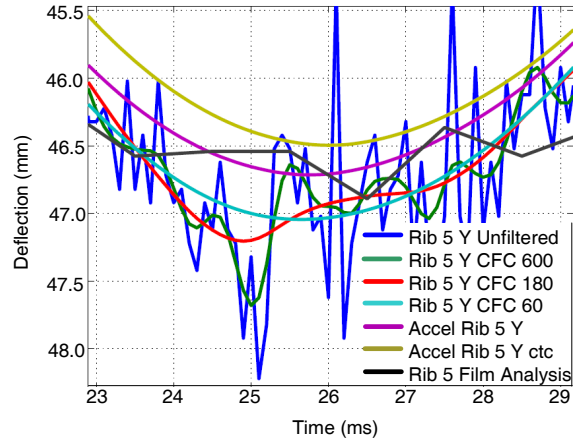

Figure 7. Peak deflections in sample linear impact.

Figure 8 shows an enlargement of the peak deflections on Rib 2 during one of the tests. Rib 2 generally had the lowest correlation among the RibEye Y-displacement, motion analysis, and the accelerometer calculations. The peaks for the filtered RibEye data were approximately 54 mm; accelerometer data peaks ranged from 50.2 to 51.0 mm; and the motion analysis peak was 52.3 mm. Again, the effects of the various CFC filters on the RibEye data are clear.

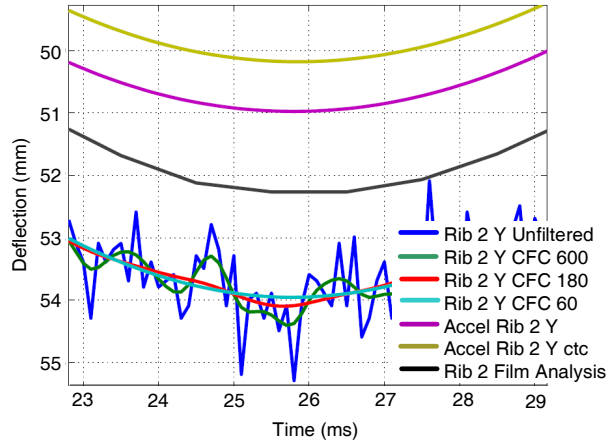

Figure 8. Sample linear impact test, Rib 2.

The difference in correlation between Rib 5 (with good correlation) and Rib 2 (with marginal correlation) prompted an investigation of the precision of the LED placement on the RibEye calibration fixture. Some inaccuracies in LED placement were found at all locations, which caused improper calibration of the RibEye system. This improper calibration resulted in the discrepancies between Rib 2 and Rib 5 in the linear impact test series.

A review of the film analysis of the targets mounted to the rigid spine box revealed motion in the Y-direction during the tests. As an example, approximately 2 mm of spine box motion was observed in one of the tests. Originally it was assumed that the spine box would be completely rigid, as it was attached to the reaction block. This motion contaminated the correlation of the RibEye data and video data (both of which were able to report relative displacement by compensating for spine box motion) to the accelerometer data (which could only report absolute displacement relative to the earth).

In addition, there were other suspect sources of inaccuracy in the linear impact testing. The rib targets were not fully visible for the duration of the film analysis, and the imager-to-target measurements were found to be suspect following the test series.

Linear Impactor Test Discussion and Limitations

This test series demonstrated that some ribs had good correlation between the RibEye and the alternative measurement techniques, while other ribs had marginal correlation. This was determined to be due to inadequacies of the test set-up and methodology. Thus the linear impact testing was most useful at identifying methodology issues that needed to be corrected for future testing to quantify the RibEye's precision more accurately. Specifically, the issues are:

- The placement of the RibEye LEDs on the calibration fixture was resolved, and the RibEye system was re-calibrated.
- Additional testing using film analysis requires 1) more accurate measurements of target-to-camera dimensions and 2) assurance that the targets remain visible for the duration of the test.
- The spine box needs to be completely rigid to compare displacements calculated from absolute measurements (such as data from the rib-mounted accelerometers, which record acceleration relative to the earth) to relative displacements (such as measured by RibEye).
- The RibEye signal is most appropriately filtered at class 180 rather than class 600 or 60 (for bench tests such as these that did not use a jacket.)

DROP TOWER TEST SERIES #1

The goal of this series of tests was to evaluate the accuracy of RibEye measurements under dynamic conditions that simulate high-speed rib motion during a side impact crash test. To achieve this goal, independent measurement instruments were needed for comparison.

Drop Tower Test Series 1 Methodology

This series of drop tower testing compared the RibEye to linear pots using the EuroSID rib drop test facility. A test fixture was designed that allowed for mounting the RibEye in multiple positions to measure either one axis or multiple axes of displacement. Although the SIDIIs ribs were not used, the fixture allowed for the mounting of the LEDs in locations representing their respective locations in the dummy (with respect to the sensors and to the other LEDs.)

The test fixture (Figure 9) consisted of upper and lower aluminum mounting plates, a RibEye system, four high-strength steel guideposts, three 6-inch linear pots, four brass bearings and two dampers. The guideposts (item 1) allowed the RibEye LEDs, which are attached to the underside of the upper aluminum plate, to glide up to 100 mm (about 65 mm free motion followed by 35 mm of restrained motion). The RibEye sensors (2) were affixed to the lower mounting plate. The stroke of the pots was aligned with the guideposts. The pot sample rate was set to 10 samples per ms.

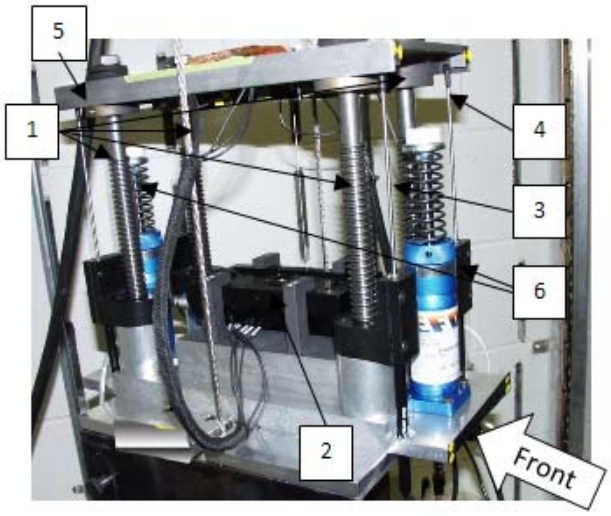

Figure 9. Drop tower fixture.

The three pots were located at the left front corner of the plate (3), the right front corner of the plate (4), and the left rear corner of the plate (5). The spacing between the front pots was 130 mm and the spacing between the front and rear pots was 330 mm. The brass bearings minimized friction and provided alignment between the guideposts and the RibEye LED mounting plate. The adjustable dampers (6) and

linear springs were mounted between the aluminum plates to cushion the LED plate, limit its movement, and absorb its energy. The initial position of the aluminum plate was about 60 mm above the dampening system and was held by spring loaded detents before impact. A block of expanded polystyrene foam was used between the impacting mass and the upper plate to minimize high frequency noise and inertial effects. Contact tape was used for the time zero signal for the RibEye, the pot data acquisition system, and the video imagers.

The EuroSID drop test fixture and 8-kg impact mass were used to accelerate the RibEye LED mounting plate. Four tests were conducted: one at 5 m/s, two at 7 m/s, and one at 10 m/s. These tests simulated pure lateral motion (Y-axis only). These tests are identified as test #s GT1 through GT4 (Table 1). The dampers were adjusted so that more restraining force was applied as the drop speed increased, preventing damage to the fixture. As a result of this adjustment, the maximum deflections did not necessarily increase with increasing drop speed.

High-speed imaging analysis was also conducted using TrackEye©. Originally the lighting set-up for the imagers interfered with the RibEye LED sensors. Thus, the imager speed was changed from 1000 frames per second (fps) to 500 fps to reduce the amount of light necessary. Also, the test fixture was surrounded by a light closeout to eliminate interference with the sensors. The closeout consisted of black opaque construction paper. Video analysis used four 16 mm (5/8 inch) targets over the length of travel. Resolution of the image was approximately 0.3 mm per pixel.

Drop Tower Test Series 1 Results

Data from pots at the front of the aluminum plate was averaged and compared to the closest RibEye LED, on Rib 1. (There were no actual dummy ribs used in these tests, however, the LEDs are referred to as Rib 1, Rib 2, to reference their positions on the plate.) Similarly, the pot displacement on the rear corner of the plate was compared to the RibEye LED at Rib 6. Table 1 reports the peak displacement and data analysis from this drop tower test series.

Table 1.
Peak Displacement for GT Test Series

	GT1, 5 m/s	GT2, 7 m/s	GT3, 7 m/s	GT4, 10 m/s
	mm			
Front pot avg.	81.3	79.2	79.0	69.6
Rib 1Y	81.3	79.3	79.4	70.1
Rib 2Y	81.8	79.5	79.5	70.1
Rib 3Y	81.7	79.5	79.7	71.2
Rib 4Y	82.1	79.9	80.1	71.2
Rib 5Y	82.5	80.0	80.4	71.2
Rib 6Y	82.7	80.0	80.7	71.0
Rear pot	82.1	79.9	79.8	70.6
Imaging Analysis	81.4	79.6	79.3	70.1
Mean	81.9	79.7	79.8	70.6
Std Dev	0.5	0.3	0.5	0.6
CV %	0.6	0.4	0.7	0.9

The first drop tower test, GT1, had good correlation between the RibEye system, linear pots, and imaging analysis. Figure 10 shows the peaks for the linear pots, imaging analysis, and RibEye measurements for Ribs 1 and 6. The difference between the maximum peak displacement of Rib 1 and the average of the front pots was 0.04 mm. (This difference is rounded to zero in Table 1.). The difference between the maximum peak displacement of Rib 6 and the rear pot was 0.6 mm. The standard deviation for the peak values in Figure 10 was 0.6 mm. Rib 6 and the front pots had the largest deviation, 1.4 mm. Rib 6 and the front pots were on opposite sides of the test fixture; thus this difference might have been caused by vibrations or tilting of the upper plate during impact.

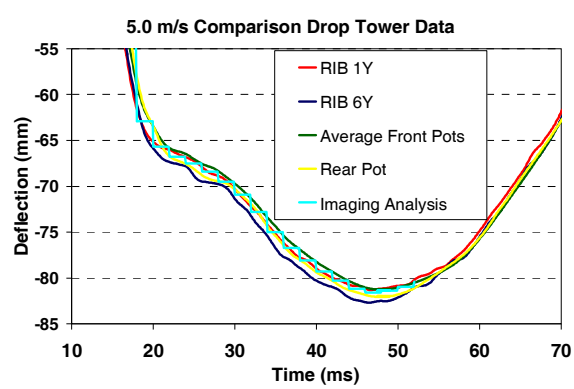

Figure 10. Drop tower Test GT1, 5 m/s.

Figure 11 shows the peak displacement measured from the RibEye LEDs (Ribs 1 through 6). The peak

displacement difference between Ribs 1 and 6 was 1.4 mm.

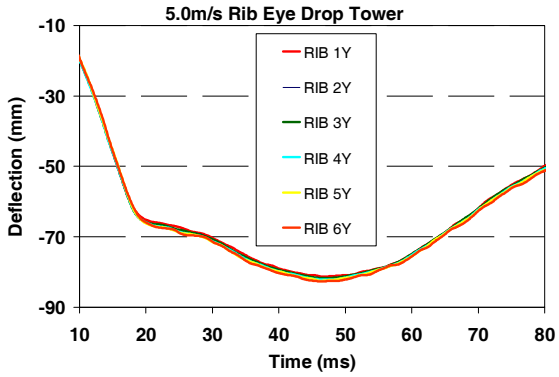

Figure 11. Drop tower Test GT1, 5 m/s.

For drop tower Test GT2, the impactor was raised to a height of about 2500 mm to increase speed to 7.0 m/s. The peak displacements between the RibEye system, corresponding linear pots, and imaging analysis is shown in Figure 12. The peak displacement difference between Rib 1 and the average of the front linear potentiometers was 0.1 mm. The peak displacement difference between Rib 6 and the rear potentiometer was 0.1 mm. The maximum displacement difference of 0.8 mm occurred between Rib 6 and the average of the front pots. The standard deviation for the measurements in Figure 12 was 0.3 mm. The maximum peak displacement difference of 0.7 mm occurred between Ribs 1 and 6 (Figure 13), which were on opposite sides of the RibEye plate.

.

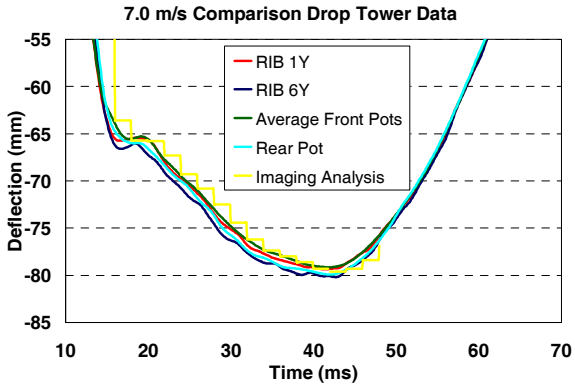

Figure 12. Drop tower Test GT2, 7 m/s.

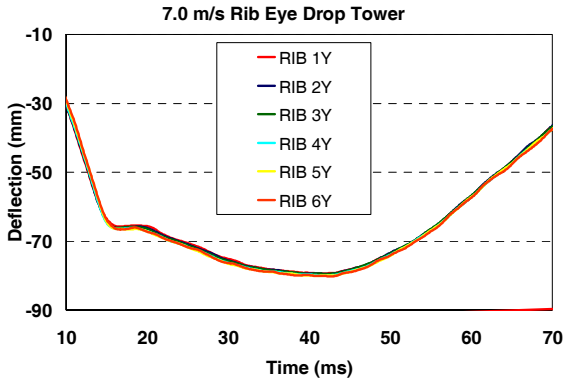

Figure 13. Drop tower Test GT2, 7 m/s.

The second 7.0 m/s test, GT3, confirmed that the transducers and/or sensors on the outer periphery of the test fixture had the greatest displacement differences.

Test GT4 was conducted at 10.0 m/s. The impactor was raised to approximately 4800 mm. Again, the maximum difference in peak deflection occurred between opposite sides of the fixture: 1.4 mm between Rib 6 and the average of the front linear pots (Figure 14). The maximum difference between the RibEye system and the high-speed imaging analysis was 1.1 mm. The maximum difference between the linear pots and the high speed imaging analysis was 0.5 mm. The imaging analysis peak displacement correlated better to the linear pots and RibEye measurements for Ribs 1 through 3, probably due to the proximity of the imaging targets being analyzed. Figure 15 shows just the RibEye data for all six ribs in Test GT4

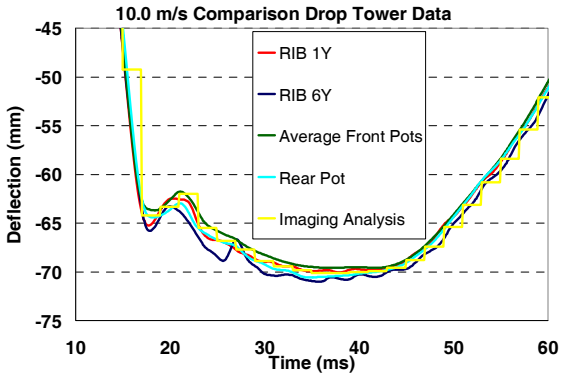

Figure 14. Drop tower Test GT4, 10 m/s.

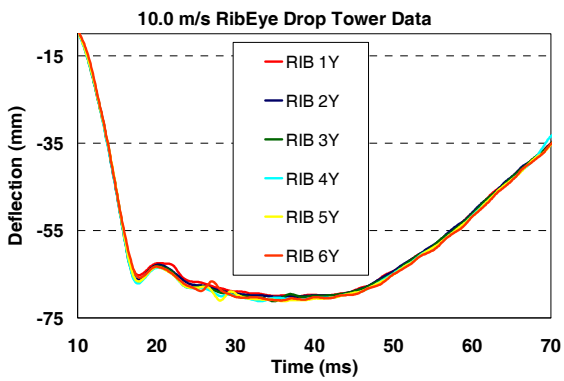

Figure 15. Drop tower Test GT4, 10 m/s.

Drop Tower Test Series 1 Discussion

This test series demonstrated that the RibEye, linear pots, and high-speed imaging had good correlation. The comparison of the pots and their closest rib LED indicated good correlation (within 0.6 mm.) The largest deviations between the front pots and Ribs 3 through 6 (1.4 mm to 1.6 mm) occurred during the 10 m/s test. This larger deviation was attributed to tilting of the plate during the impact. Comparison of the three data sets shows that as the LED plate moved along the Y-axis, the plate tilted rearward, so that the rear of the plate traveled further than the front of the plate.

As seen in Table 1, when the test speed increased, the deflection readings decreased. This was due to the higher setting on the adjustable dampers at higher speeds.

DROP TOWER TEST SERIES #2

This test series included single axis and multiple axes testing of the RibEye.

Single Axis Methodology

The set-up for this series of drop tower tests was similar to that used in the first drop tower series. Five tests were conducted to evaluate pure lateral motion: two at 5 m/s, two at 6 m/s, and one at 7 m/s. For this series, however, there was no film analysis conducted.

Single Axis Results and Discussion

The first drop tower test, DT1, suggested good correlation between those RibEye measurements and the measurement of the closest linear pots (Table 2). Rib 6 and the front pots had the largest deviation, 2.9 mm.

For these tests the accuracy of the system was comparable to the results of the first drop tower test series – that is, RibEye measurements between Ribs 1 and 6 were within 3 mm, and the difference was likely due to tilting of the plate as confirmed by the pot measurements. Comparing the LED that was closest to a pot, the difference was less than 0.5 mm.

Table 2.
Peak Displacement for Single Axis Test Series

	DT1, 5 m/s	DT2, 5 m/s	DT3, 6 m/s	DT4, 6 m/s	DT5, 7 m/s
	mm				
Front pot avg.	78.6	79.9	66.5	65.3	70.5
Rib 1Y	78.7	79.9	66.1	65.0	71.2
Rib 2Y	79.3	80.4	66.8	65.6	71.2
Rib 3Y	79.9	80.8	66.8	65.6	71.2
Rib 4Y	80.0	80.4	67.0	65.9	71.2
Rib 5Y	80.6	81.5	67.5	66.1	70.1
Rib 6Y	81.5	81.9	67.2	66.0	70.0
Rear pot	81.2	81.6	67.3	66.2	69.2
Mean	80.0	80.8	66.9	65.7	70.6
Std Dev	1.1	0.8	0.5	0.4	0.8
CV%	1.4	1.0	0.7	0.6	1.1

Multiple Axis Methodology

For the multiple axis drop tower tests, the test set-up was modified to simulate oblique loading in a SID-IIs dummy. This was done by tilting the RibEye sensors about the X-axis 10 degrees and about the Z-axis 20 degrees, exposing the RibEye to displacements in all three axes. The RibEye LEDs were not moved or tilted. Figure 16 is an illustration of the test fixture with the RibEye sensors (item 1) in an oblique position supported by the compound mounting block (2).

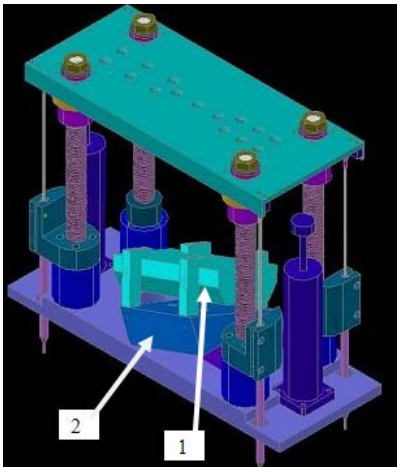

Figure 16. Test fixture illustration.

Only two pots were used in the multiple axis tests because the third pot failed and no replacement was available. The two pots were mounted on the front left and rear right of the fixture. The way the RibEye was mounted on the block, the Rib 1 LED was closest to the rear pot and Rib 6 LED closest to the front pot (the opposite of the first drop tower series).

Multiple Axis Results

Three tests were conducted, all at 5 m/s. The compound angle change of the sensors resulted in the pure Y displacements (with respect to the pots) being measured as X, Y, and Z displacements by the tilted RibEye sensors. Thus, the RibEye data were converted from its coordinate system to the potentiometer coordinate system, so that the pot data and the converted RibEye Y data could be compared.

Figure 17 shows Rib 1 LED data in the RibEye coordinate system (1X, 1Y, and 1Z) and the same data converted to the pot coordinate system (X~, Y~, and Z~). Data from other ribs showed similar results. Figure 18 shows all rib Y data (Ribs 1-6) in both the RibEye and the pot coordinate systems. Figure 19 is an enlarged view of all rib Y data. It was expected that there is two groupings of curves, one represents the Y deflection in the RibEye coordinate system the other is the same data converted to the pot coordinate system. Table 3 summarizes rib Y data converted to the pot coordinate system.

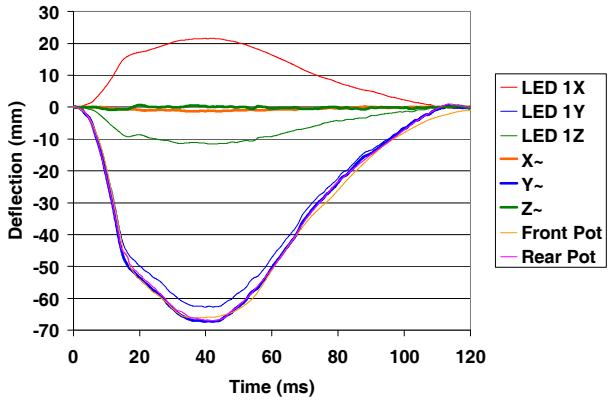

Figure 17. Rib 1 LED data.

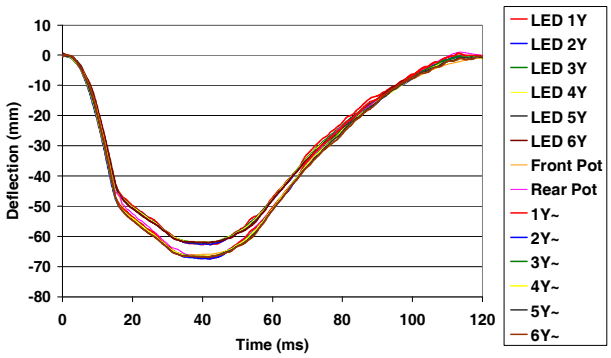

Figure 18. All rib Y data.

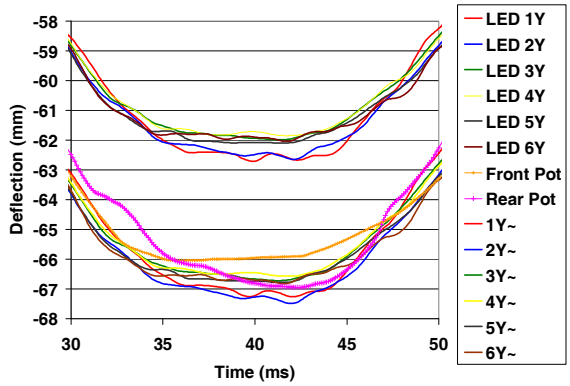

Figure 19. Enlargement of all rib Y data.

Table 3.
Peak Displacement for Multiple Axis Test Series

	CP1	CP2	CP3
	mm		
Rear pot	64.9	66.9	66.7
Rib 1Y~	65.7	67.3	67.0
Rib 2Y~	65.9	67.5	67.2
Rib 3Y~	65.0	66.7	66.5
Rib 4Y~	64.5	66.6	66.4
Rib 5Y~	64.7	66.8	66.6
Rib 6Y~	64.8	66.8	66.6
Front pot	63.3	66.0	65.9
Mean	64.9	66.8	66.6
Std Dev	0.8	0.5	0.4
CV%	1.2	0.7	0.6

Multiple Axis Discussion

The maximum difference between a RibEye converted Y measurement and the closest pot measurement was 1.5 mm (test CP1: the front pot and Rib 6Y~). However, the other tests demonstrated good correlation.

The RibEye X and Z data, converted to the pot coordinate system, showed differences in displacements of less than 1 mm. Because the RibEye sensors were rotated for this series, the LEDs are moving through the sensor's field of view at an oblique angle. The true displacement of the LEDs however, is in line with the linear pots. Thus the RibEye X and Z data, converted to the pot coordinate system, would theoretically be zero. The actual converted measurements of less than 1 mm suggest accurate RibEye measurements in multiple axes.

FULL VEHICLE CRASH TEST COMPARISON SERIES

Methodology

Full-vehicle paired crash tests were conducted to investigate the three-dimensional capability of the RibEye and to compare chest deflection measurements obtained with the RibEye to those obtained with linear pots.

The vehicle sample included 10 paired tests, which included a mix of crossover vehicles and passenger vehicles. The vehicles were all model year 2007-2008 and equipped with side curtain airbags and seat-mounted airbags for the driver position, with the exception of one vehicle model where only the curtain airbag was available for the driver. Comparisons were conducted in both the driver seat position and the rear struck side passenger seat position. There were three paired tests at the driver position and seven paired tests in the rear passenger position (Table 4).

Table 4.
Number of paired tests
by configuration and seat position

	IIHS	FMVSS 214 MDB	FMVSS214 Pole
Driver	2	--	1
Rear Passenger	2	5	--

Notes: IIHS tests: perpendicular impact at 50 km/h
FMVSS 214 tests: crabbed barrier, 27 degrees at 54 km/h
Pole test: 15 degrees angle at 32 km/h

One SID-IIs (Build Level D) dummy was instrumented with linear pots, while the second was modified to accommodate the RibEye measurement system. Both dummies underwent pendulum tests to verify that the rib sets had comparable responses. Other instrumentation included head, spine, and pelvis accelerometers, as well as acetabulum and pubic load cells. The data was acquired and filtered according to SAE J211-1 [3] standards and the film footage was recorded at 1000 fps.

The dummies were positioned as per the IIHS or FMVSS 214 seating procedure in the driver seat. No specific protocol was followed for the rear seat; however, an attempt was made to position the dummies similarly and their positions were verified using a Platinum Faro arm ©.

The impact velocity for the IIHS barrier was 50 km/h ± 0.4 km/h; FMVSS 214 and pole impact were 54 ± 0.13 km/h and 32 ± 0.9 km/h, respectively. The impact points for the IIHS barrier tests were within 2 mm of the target, the FMVSS 214 barrier impact points were within 28 mm, and the pole impacts were within 7 mm of the target.

These full vehicle tests utilized the standard jacket for the SID-IIs dummy. A prototype jacket was available to reduce ambient light interference. However, since the purpose of the study was to evaluate dummy measurement capability, it was thought inadvisable to conduct tests with different jackets. Furthermore, since the dummy was not

subject to direct light exposure in the test vehicle, measurement interference was not anticipated.

Calculations for Equivalency

Since the RibEye measures deflection in axes and the linear pots measure the compression of the pot shaft, some calculations were required to obtain comparable measurements. The initial position of the pots and the LEDs needed to be identified to make these calculations. The spatial relationship of the LED and the pot are shown in Figure 20, where the top dot represents the initial position of the LED on the rib.

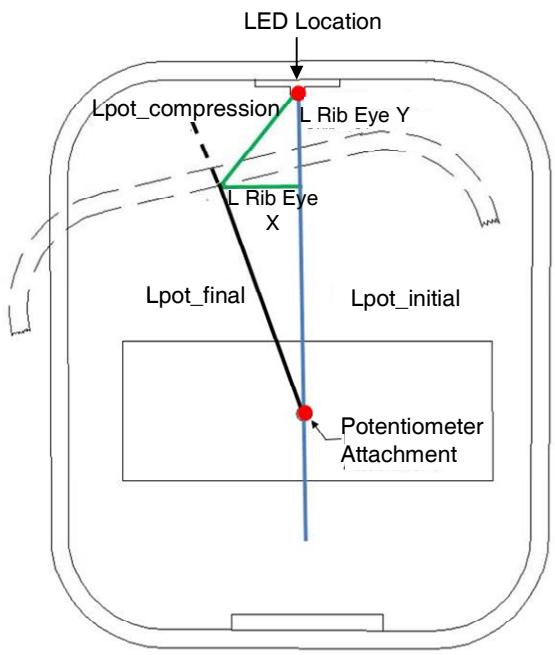

Figure 20. RibEye to pot conversion.

The mathematical relationship between the two instruments is defined by Equation 1, where $L_{pot_initial}$ is the distance between the attachment point of the pot on the rib and the corresponding attachment point on the spine box. This distance is on average 120 mm. $L_{pot_compression}$ represents the calculated RibEye equivalency to the linear pot. $L_{RibEyeX}$, $L_{RibEyeY}$, and $L_{RibEyeZ}$ are values recorded by the RibEye along the X-axis, Y-axis, and Z-axis, respectively.

(1.)

$$L_{pot_compression} = L_{pot_initial} - \text{sqrt}\left[(L_{pot_initial} - L_{RibEyeY})^2 + L_{RibEyeX}^2 + L_{RibEyeZ}^2 \right]$$

Results

Two principal deflection patterns were found in this study: 1) a uni-axial deflection, where the major contributor of the deflection was along the Y-axis and deflections in X-axis and Z-axis were insignificant; and 2) a multi-axial deflection, where the major contributor of the deflection was in the fore-aft direction with a less important lateral or vertical component.

Uni-axial deflection was most frequently observed in perpendicular or purely lateral loading environments such as the driver position in the IIHS configuration. Multi-axial deflections were observed in the oblique or combined loading environments such as rear passenger for IIHS tests and both rear and front occupants for FMVSS 214 barrier and pole test configurations.

As shown in Figures 21-23 the differences between the peak measurements of the RibEye dummy and the standard dummy for Ribs 2, 3, and 4 were 1.7 mm, 3.7 mm, and 0.3 mm respectively. Unlike the controlled drop tower tests where the linear pots and RibEye were measuring the same impact, these reported differences reflect different crash tests. Thus the differences noted not only reflect on the crash test to crash test repeatability but also repeatability between RibEye and linear pot measurements. The shapes of the curves suggest good test to test repeatability.

Figure 24 presents an example of the X, Y and Z components for the same rib (Rib 3) shown in Figures 22 as measured by the RibEye. As described, the principal direction of loading in this sample case was perpendicular or almost completely lateral. This was characterized by the peak deflection occurring in the lateral or Y-axis with negligible fore-aft or vertical contributions to deflection.

Multi-axial deflection was most frequently observed in oblique loading conditions. As an example, Figure 25 illustrates the time histories for the corrected RibEye deflection and the corresponding pot deflection for Rib 3. The peak deflection measurement of the pot was equivalent to the corrected RibEye measurement. There was greater difference in shapes of the traces as compared to the more lateral test conditions because the oblique loading of the ribs may have been causing greater variability in the rib motion. Differences may be more apparent because the overall magnitude of the

Y-deflection was significantly lower for the oblique conditions.

The corresponding three deflection components for Rib 3 as measured by the RibEye are shown in Figure 26. In this loading environment the RibEye indicated that a fore-aft deflection of 33.1 mm was present in addition to the 20.1 mm of lateral deflection.

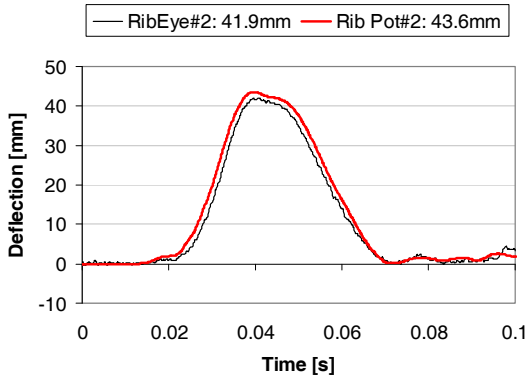

Figure 21. Rib 2 deflections measured for driver in an IIHS test.

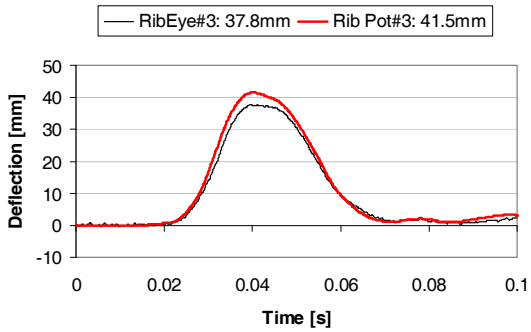

Figure 22. Rib 3 deflections measured for driver in an IIHS test.

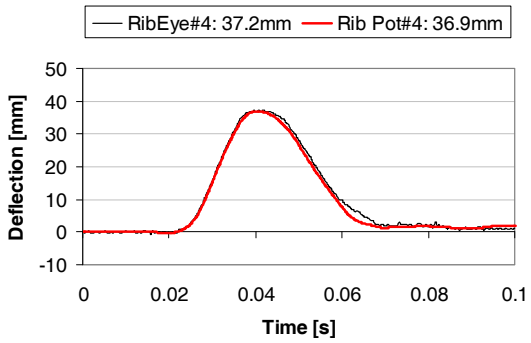

Figure 23. Rib 4 deflections measured for driver in an IIHS test.

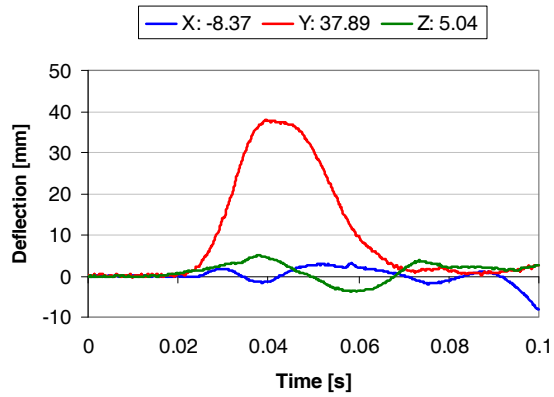

Figure 24. Deflection components as measured by the RibEye for driver in IIHS test.

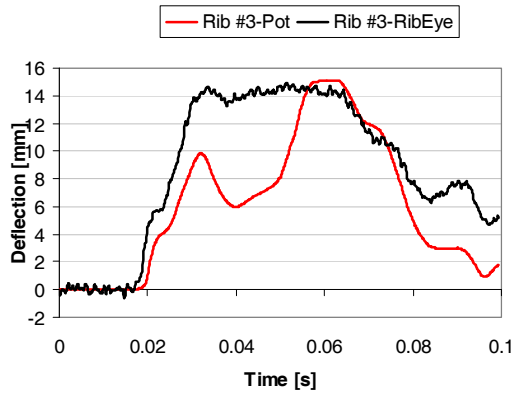

Figure 25. Deflection of rib 3 as measured with the linear pot and the RibEye for driver in FMVSS214 pole test.

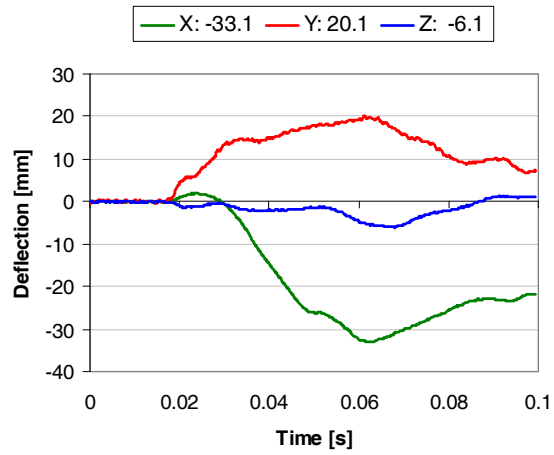

Figure 26. Three components of deflection for rib 3 as measured with the RibEye for driver in FMVSS214 pole test.

Discussion

The RibEye system was reliable and did not present any durability issues throughout the vehicle crash test series. In contrast, the significant loading associated with certain tests did cause damage to the linear pots both at the attachment point and in the wiring, resulting in noise and loss of data.

For the full vehicle crash tests, the proposed dummy clothing designed to block ambient light from entering the chest cavity was not used. Standard dummy clothing was used. However, of the ten full vehicle crash tests using RibEye, only one test had saturated signals and it occurred after 100 ms post impact (after the region of occupant interest.) Some laboratory testing had been completed to demonstrate the effectiveness of the new clothing, but that evaluation is not reported here.

Another possible limitation of the RibEye system is that the software application was not integrated with a data acquisition system. This required a parallel set-up to the central data acquisition system and was time consuming. Integrated software that interfaces with the standard data acquisition systems would greatly improve the usability of the RibEye in the laboratory environment.

Under controlled paired crash configurations, the RibEye demonstrated the ability to measure rib motion in three directions with respect to the spine box. The deflection as measured by the RibEye in the Y- direction was found to correlate well with that of the linear pots. It should be noted, however, that currently used thorax injury risk curves for side impact utilize lateral deflections only. Additional research may be necessary to fully understand the 3-dimensional aspects associated with thoracic and abdominal injury.

SUMMARY

The initial linear impactor test series was useful at identifying testing shortcomings that were corrected for the subsequent tests.

In the drop tower test series, which were conducted at different laboratories, the RibEye measurements, the linear pots, and high-speed imaging demonstrated good correlation (within 1.5 mm difference). The worst case difference between a peak RibEye measurement and the corresponding peak pot measurement was 1.5 mm, and occurred during an oblique test. Many of the other measurements demonstrated much better correlation (significantly less than 1.5 mm difference.)

The RibEye system is designed to measure deflections in all three dimensions. A limited amount of oblique tested demonstrated the ability to measure displacements in both the Y and X directions.

The full vehicle crash tests demonstrated similar peak value measurements between the RibEye dummy and the standard dummy. During FMVSS 214 and pole impact tests, the RibEye revealed significant X-axis deflection that cannot be measured by linear pots.

A full durability analysis was not completed on the RibEye, however in the limited amount of testing conducted there were no durability issues identified. The linear pots, however, did exhibit some damage during some of the full vehicle crash tests.

Although there were not significant ambient light interference issues with RibEye during the full vehicle crash tests, further analysis of the redesigned clothing may be necessary.

ACKNOWLEDGEMENTS

The authors wish to acknowledge John Athey, Daryl Black, Lynn Byers, Dawn Firth, Ryan Goocher, Lynn Byers, Kim Malone, Craig Morgan, and Marianna Sierra Ramerez.

REFERENCES

1. Scherer, R., Kirkish, L., McCleary J., Rouhana, S.W., Athey, J.B., Balser, J.S., Hultman, R.W., Mertz, H.J., Berliner, J.M., Xu, L., Kostyniuk, G.W. 1998. “SID-IIs Beta+ Prototype Dummy Biomechanical Responses”, SAE 983151, Warrendale, PA, Society of Automotive Engineers.
2. Arbelaez, R.A., Brumbelow, M., Wang, Z., Van Ratingen, M. 2006. “A New Calibration Specification for Linear Displacement Transducers”, SAE 2006-01-0719, Warrendale, PA, Society of Automotive Engineers.
3. Society of Automotive Engineers, “Instrumentation for Impact Test, Part 1, Electronic Instrumentation”, SAE J211/1, Warrendale, PA, July 2007.
4. National Highway Traffic Safety Administration, Reference No. 572.185, Subpart U.

WORLDSID SMALL FEMALE TWO-DIMENSIONAL CHEST DEFLECTION SENSORS AND SENSITIVITY TO OBLIQUE IMPACT

Bernard Been and Kees Waagmeester
First Technology Safety Systems
The Netherlands
Xavier Trosseille
LAB PSA Peugeot Citroën RENAULT
France
Jolyon Carroll and David Hynd
TRL Ltd
United Kingdom

Paper Number 09-0418

ABSTRACT

In the EC FP6 Integrated Project APROSYS, the first WorldSID small female prototype was developed and evaluated by BASt, FTSS, INRETS, TRL and UPM-INSIA. Results were presented at the ESV 2007 conference (Been *et al.*, 2007[1]). A concern was raised that the current chest deflection measurement system, IR-Traccs, registered flat top responses and sometimes may not register the peak deflection. This was believed to be related to forward deformation of the ribs relative to the spine and associated extension of the IR-Traccs. In the mean time an update version of the dummy, called Revision1, was developed to address the issues found in the first evaluation round.

To improve oblique thorax loading sensitivity, a two-dimensional chest deflection sensor, the 2D IR-Tracc was developed. Measuring the angle between the spine box and the IR-Tracc enables the displacement of the most lateral point on the rib rib to be calculated in the XY (transverse) plane.
To evaluate the new system, FTSS conducted single rib unit tests on a drop tower under pure lateral and oblique test conditions. The compression and rotation data were analysed to find the displacement of the most lateral part of the rib, and the rib deformation in the impact area. In addition, TRL subjected a complete Revision1 prototype dummy to oblique thorax pendulum tests and LAB conducted full dummy static deployment airbag tests under various impact angles and impact severities.

The 2D IR-Tracc proved to be very useful in understanding phenomena taking place under various lateral and oblique impact conditions that could not have been understood with the current (1D) compression sensor alone. The reduced sensitivity of the conventional IR-Tracc (Dy rib) to oblique impact was confirmed in this study.
The calculated lateral displacement Y offered a simple and straightforward parameter to improve the sensitivity to oblique impacts, as compared to the current single axis deflection sensor.

INTRODUCTION

It is generally accepted that the WorldSID dummy is superior in thorax biofidelity to other side impact dummies. There is information on human response in oblique conditions (Viano[2]), but until now oblique responses were not considered, because older dummies were designed to be sensitive in the lateral axis only. During service dummies may be loaded in directions other than pure lateral. To name a few, the US National Highway Traffic Safety Administration specified a 75 degrees oblique pole test (FMVSS 214 [3]), rear seat passengers could be loaded in frontal oblique direction and seatback mounted side airbags could load the dummy from the rear of lateral, with a significant forward component. Based on its design and construction it is expected that the WorldSID oblique biofidelity and sensitivity is better than other dummies, but the comparative dummy data doesn't exist to prove this. With the existing rib deflection sensor (the IR-Tracc) of the WorldSID, the dummies displayed a reduced sensitivity of the rib deflection measurement system to oblique impact in various studies [4, 5].

Figure 1 illustrates this problem. The basic WorldSID construction is presented schematically by an oval, with the spine box in the middle. The compression measurement system is represented by a telescope. The spine box and deflection measurement system base are mounted to the rear of the rib, giving anterior-posterior asymmetry. Under pure lateral deformation (b) the spine box moves rearward and the sternum moves forward. The lateral section of the rib, where the chest deflection system is connected moves forward with respect to the base of the deflection measurement device. The forward motion of the rib lateral section introduces extension in the chest deflection measurement system. Under rear oblique load (c) the extension effect is stronger because of the larger

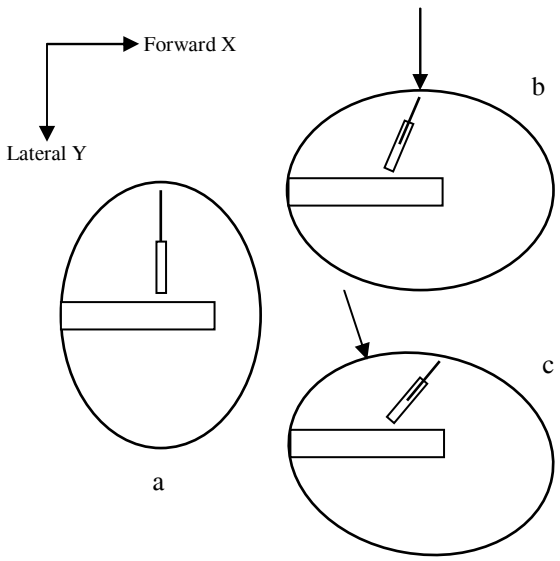

Figure 1 Schematic transverse section WorldSID chest, (a) uncompressed, (b) lateral compression, (c) rear oblique compression

forward component of rib displacement. The current chest deflection measurement device is suspected to be less sensitive to oblique load. Moreover the device does not provide information to quantify any effect of oblique load.

To address this issue and to improve oblique thorax loading sensitivity, a two-dimensional chest deflection sensor, the 2D IR-Tracc (*Infra-Red-Telescoping-Rod-for-Assessment-of-Chest-Compression*) was developed. Measuring the angle between the spine box and the IR-Tracc enables the displacement of the rib to be calculated in the transverse (X-Y) plane. The sensitivity to oblique load of the two-dimensional chest deflection measurement device was evaluated under three different test conditions. First, FTSS conducted single rib unit tests on a drop tower; then TRL subjected a complete WorldSID small female Revision1 prototype dummy equipped with 2D IR-Traccs to oblique thorax pendulum tests and finally LAB conducted full dummy static airbag deployment tests. This paper presents details of the 2D IR-Tracc and its displacement calculation method and test results under various loading conditions, impact angles and impact severities.

MATERIALS AND METHOD

2D IR-Tracc

Working principle

The 2D IR-Tracc, FTSS part IF-370, is based on the standard WorldSID small female IR-Tracc, FTSS part IF-369. The deflection sensor working principle is based on emission of Infra Red Light from a LED in the small end of the IR-Tracc and a photocell in the big end of the unit. The intensity of the infra red light on the photocell is inversely proportional to the square of the distance: the larger the distance, the smaller the light intensity. An electronic linearisation circuit is build into the unit, providing linear voltage output to the IR-Tracc compression. The separate rotation sensor works according the voltage division principle of a rotation potentiometer. The voltage output of the potentiometer central slider is linearly proportional to the input voltage and the position of the shaft.

The 2D IR-Tracc shares many components with the standard IR-Tracc. A potentiometer housing is mounted to the base of the IR-Tracc to measure its angle with respect to the interface to the spine box. To allow vertical motion of the rib, the housing of the potentiometer is pivoted about the anterior-posterior axis, see Figure 2.

Figure 2: 2D IR-Tracc

Built into the dummy the nominal length of the IR-Tracc from spine box to ball joint axis is 111.5mm; the compression range from nominal is 54mm; the extension range from nominal is 26mm. The spine box interface bracket allows over 60° of rotation of the IR-Tracc. In the first version 2D IR-Tracc, used in the drop tests and the pendulum tests, the rotation range was ±30°. As it was found that during compression the rib rotation is biased toward the front, an new interface bracket was developed. The forward range was made larger than the rearward rotation. The new interface allows forward rotation of >40° and the backward rotation of over -20°, see Figure 3 through Figure 6. The new brackets were installed in the dummy before the airbag tests.

Figure 3: Fully extended range from nominal +26mm

Figure 4: Fully compressed range from nominal -54mm

Figure 5: Fully forward rotation +40°

Figure 6: Fully rearward rotation -20°

Calculation method

Interpretation software was written in a spreadsheet (MS Excel) to calculate rib displacement in x- and y- direction in the dummy co-ordinate system and the resultant deformation of the rib in the x-y plane. The equations are given below and the symbols used are explained in Figure 7 (input in blue, output in red) and Table 1.

$$Xi = (L_0\text{-}dyi)*\sin(\varphi xyi) \quad (1)$$
$$Yi = L_0 - (L_0 - dyi)*\cos(\varphi xyi) \quad (2)$$
$$Ri = \sqrt{(Xi^2 + Yi^2)} \quad (3)$$

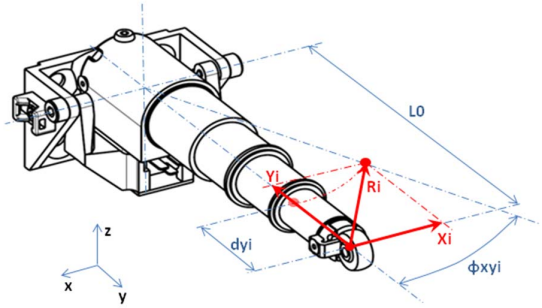

Figure 7: equations symbols

Table 1: equation symbols and description

Parameter	Description
t_0 [s]	Time zero
L_0 [mm]	Reference length at t_0.
dyi [mm]	IR-Tracc **compression dy** at time step i
ϕxyi [degrees]	IR-Tracc angle at time step i (positive angle forward)
Xi [mm]	Calculated x displacement at time step i
Yi [mm]	Calculated y displacement at time step i
Ri [mm]	Calculated Resultant displacement at time step i

Calculating the x and y co-ordinate for each time step allows to plot the rib displacement trajectory. This allows quantifying the amount of lateral (Yi) and anterior-posterior (Xi) motion of the lateral rib segment. It was expected that these parameters would be correlated with impact angle. The resultant displacement was also calculated as it seemed to be a useful output parameter to correlate with and assess impact severity, independent from impact direction. Five 2D IR-Traccs were installed in each of the two WorldSID small female revision1 prototypes. Figure 8 shows how the 2D IR-Traccs are integrated in the dummy (bottom view left thorax half, sternum at the top).

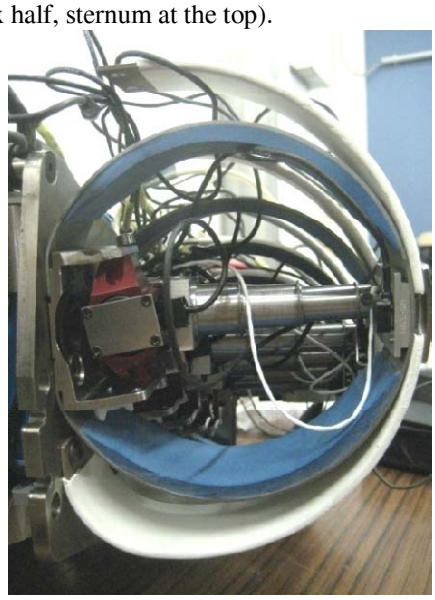

Figure 8: 2D IR-Tracc integrated in dummy

Drop tower test set up

The single rib sensitivity tests were performed on a EuroSID-1 / ES-2 drop rig. Details of the test set-up are given in Figure 9.

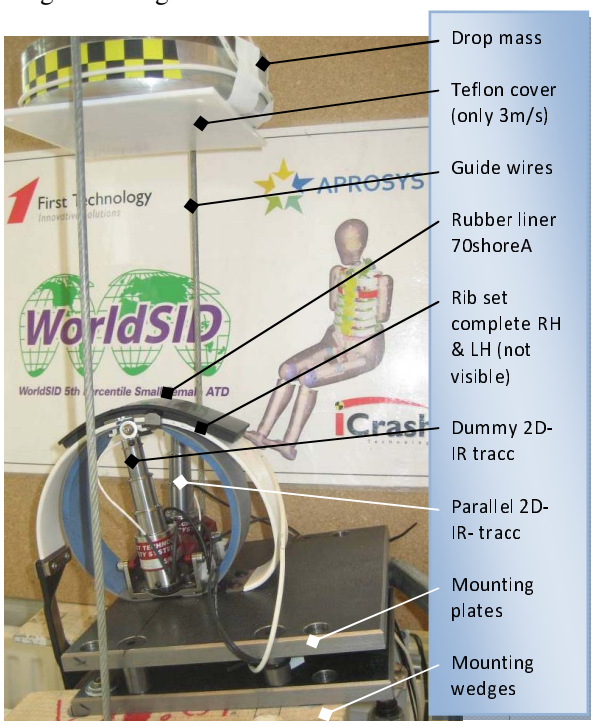

Figure 9 drop tower test set up single rib unit

Two 2D IR-Traccs were used, one is mounted in the original position in the dummy ('dummy IR-tracc'), an additional IR-Tracc is attached to the rib with a clamp in such position that the IR-Tracc centreline is in the impact plane ('parallel IR-tracc'). The

single rib unit tests are done at seven impact directions: ±30°, ±20°, ±10°, and 0° pure lateral at 3m/s, positive angle is forward oblique. Also a high speed (5m/s) test condition was done at +30°, +20° and ±10°, and 0°. The 5.0m/s -30° and -20° rearward oblique tests were not conducted due to the limitation of the forward range of motion of the rotation sensor. Each test condition was repeated at least three times. In total 54 tests were performed.

Full dummy pendulum impact test set up

The oblique sensitivity tests were conducted with a set-up similar to the biofidelity pendulum test series. The WorldSID small female Revision1 dummy was seated on a platform in order to give correct vertical alignment. A wooden block was fitted to the front of the impactor, measuring 34 x 120 x 60 mm. This block was aligned so as to strike the most lateral aspect of the top thoracic rib. The dummy was supported overhead with a leash released via an electromagnet prior to contact with the pendulum. The torso was reclined until the first thoracic rib was level (anterior to posterior).

To make it easier to observe the deformation of the ribs with an overhead mounted camera, the head and arms of the dummy were removed. The test setup is shown in Figure 10.

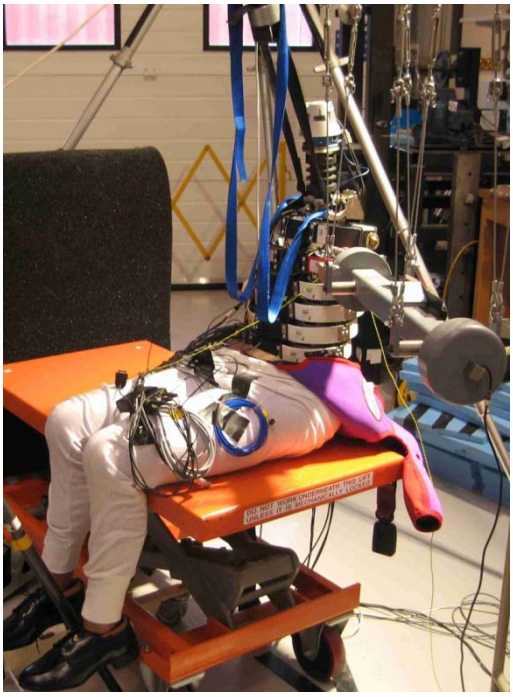

Figure 10: Full dummy oblique pendulum test

The impact velocity for the oblique sensitivity tests was 2.5m/s, the pendulum mass was 14kg. The angles of impact were +30°, ±15°, and 0°.

Static airbag deployment test set up

The testing device is shown in Figure 11. The WorldSID small female Revision1 dummy was positioned left side onto the unfolded airbag, in an upright sitting position. The pelvis was fixed to a metallic structure which only rotates about the dummy x axis immediately below the pelvis of the dummy. Prior to the test, nylon straps kept the thorax in a balanced position. At time to fire, the lifting strap was released using a controlled electromagnetic system. The pyrotechnic generator ignition inflated the airbag membrane which applied thoracic loads. The airbag-thorax distance was varied in order to modify the force magnitude. Forces applied to the thorax were measured by means of load cells mounted behind the airbag mounting plate. The dummy was instrumented with rib deflection sensors and thoracic accelerometers.

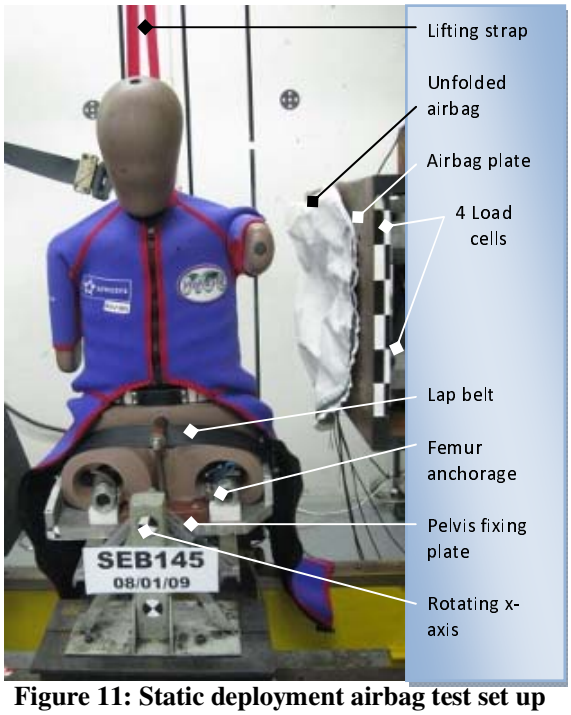

Figure 11: Static deployment airbag test set up

The WorldSID small female Revision1dummy was tested at two distances between the thorax and the airbag module (178mm and 108mm) and two angles (pure lateral and 30°forward).

RESULTS

Drop tower tests

Figure 12 - Figure 16 show the rib trajectories of the dummy 2D IR-Tracc (yellow) and the additional parallel 2D IR-Tracc (red), with a pictures of the test set-up in the background. The graph's orientations are aligned with the spine box co-ordinate system and show the actual motion trajectories of the rib relative to the background picture. The plots are arranged on the page, such that corresponding angles are plotted next to each other, placed on the left are forward oblique, and on the right are rearward oblique.

Figure 12: + 30 degrees forward impact

Figure 13: +10 degrees forward impact

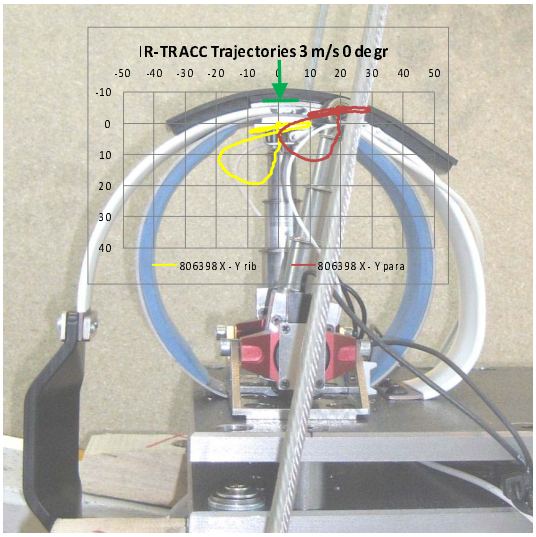

Figure 14: 0 degrees lateral impact (Note: Picture shows not actual set-up. For illustration a photo of -10 degrees set-up was rotated.)

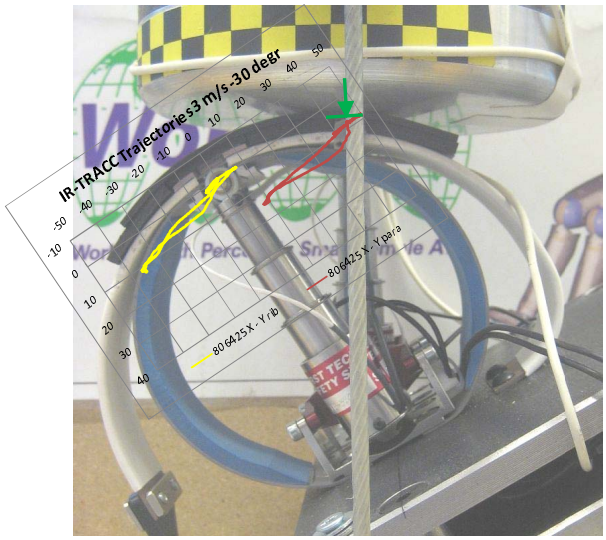

Figure 15: -30 degrees rearward impact

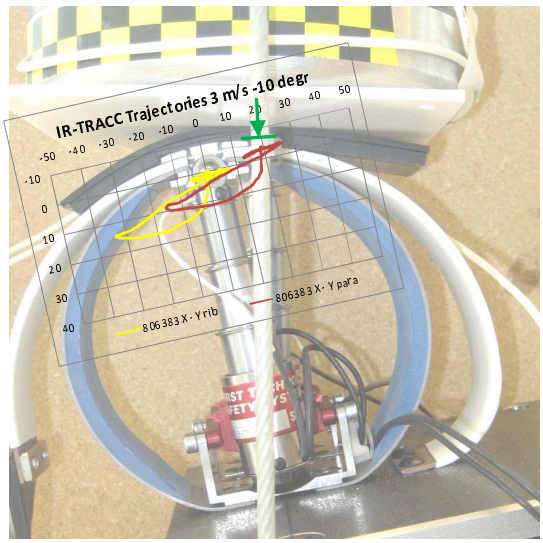

Figure 16: -10 degrees rearward impact

Note the considerable differences in response to rearward and forward oblique tests, by comparing adjacent images. The graphics show that trajectories of the rib measured with 'parallel' (red) and with 'dummy' (yellow) IR-Traccs are very similar. Also note that in all test conditions the rib deformation starts inline with the impact direction. The plots show 3.0m/s results.

Note that in the drop tower tests forward displacement has a negative sign, whereas in the pendulum and airbag tests forward displacement is positive.

Figure 17 and Figure 18 show the rib trajectories in all impact directions, at 3.0m/s and 5.0m/s impact velocity. Figure 17 also shows displacement parameters X (anterior-posterior), Y (lateral) and R (resultant X-Y). A schematic overhead view of a human is shown for orientation purpose.

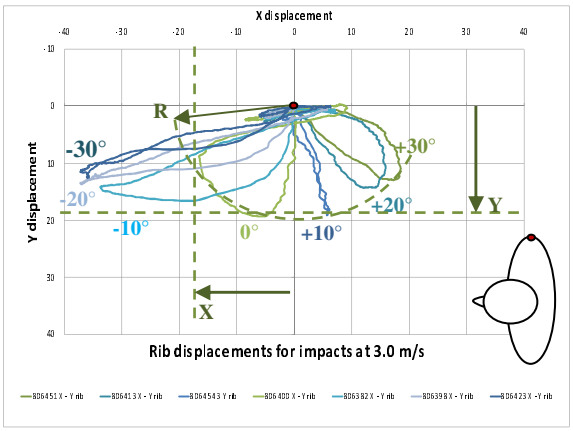

Figure 17: Rib trajectories all impact directions at 3.0m/s and human body overhead view

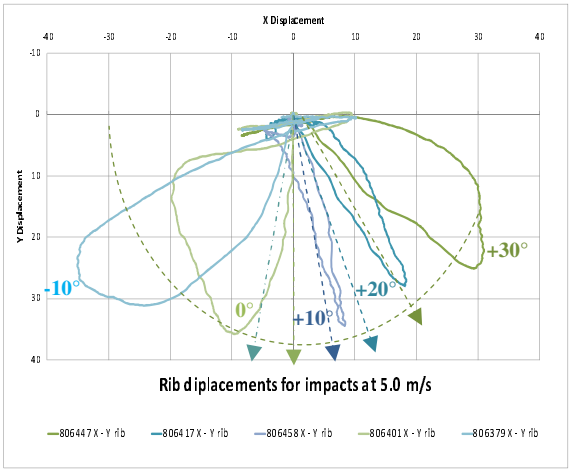

Figure 18: Rib trajectories all impact directions at 5.0m/s

Both figures clearly show there is large forward deformation even under pure lateral tests. In all rearward oblique tests, the forward motion exceeds the lateral deformation. Figure 17 also shows that the resultant displacement R remains relatively constant for pure lateral and forward oblique tests, but R is much larger for rearward oblique. The R parameter alone is therefore not a good indictor of impact severity or injury risk. All test results are summarised in Table 2, in a numerical format, giving averages of three tests and the coefficient of variation, which is the standard deviation divided by the average. In the table F_{imp} is the impactor force (N), Dy is the compression of the IR-Tracc alone, X, Y, and R are calculated parameters as explained in the 'Calculation Method' section (in mm). The coefficient of variation is well below 3% for most test conditions and parameters. Note that the parameters Dy, X and Y from dummy IR-Tracc and parallel IR-Tracc cannot be directly compared, as the results are given in the co-ordinate system aligned with the instrument. The resultant displacements (R) from the dummy IR-Tracc and parallel are independent from impact direction and can be compared directly. The R parameters are generally very similar. This makes sense, as these segments are coupled by the rib section between them. Some further observations: The impactor forces F_{imp} are more or less constant and appear to be not very dependent on impact direction, however the highest impact forces appear under 20° forward loading and the lowest under rearward oblique impact.

Table 2: Average peak results 3 tests each condition

			Dummy IR-Tracc				Parallel IR-Tracc			
		F_{imp}	Dy	X	Y	R	Dy	X	Y	R
3m/s	+30°	827	11.1	19.0	12.9	22.6	19.1	13.2	19.8	22.8
	+20°	846	13.6	15.4	14.5	20.0	19.2	11.3	19.5	20.9
	+10°	802	19.0	5.8	19.2	19.8	20.1	-3.0	20.1	20.2
	0°	795	19.0	-17.9	18.9	20.8	16.8	-13.3	16.8	18.1
	-10°	719	14.3	-33.3	16.4	36.2	16.7	-31.3	20.1	36.8
	-20°	702	9.0	-37.2	13.4	39.5	16.6	-30.8	22.8	38.2
	-30°	709	5.7	-36.7	12.2	38.3	18.3	-28.8	23.9	37.3
	CV	1.24	1.75	1.55	1.73	2.03		1.95	0.80	2.40
5m/s	+30°	1293	19.0	29.9	24.9	38.1	32.8	22.0	34.8	38.4
	+20°	1398	25.0	18.4	27.7	33.0	35.2	7.6	35.5	36.1
	+10°	1299	34.0	8.2	34.6	35.6	36.2	-5.9	36.2	36.2
	0°	1231	35.2	-18.5	35.9	36.9	32.4	-16.0	32.5	32.7
	-10°	1248	26.4	-36.0	31.1	44.7	31.4	-31.5	34.5	44.3
	CV	1.1	1.6	4.2	1.2	1.3			3.6	3.5

Full dummy pendulum impact test

Observations from the overhead camera view are shown in Figure 19 through Figure 22, starting with +30° and +15° forward impact followed by lateral and -15° rearward oblique tests. Rearward motion of the IR-Tracc is observed in the 30° forward oblique test; approximately pure lateral compression is visible in the 15° forward oblique test, which was also observed in the single rib unit drop tests at 10° forward oblique. In this test the end of the rotation range was reached at around 31° rotation, as can be observed in Figure 23 as a discontinuity.

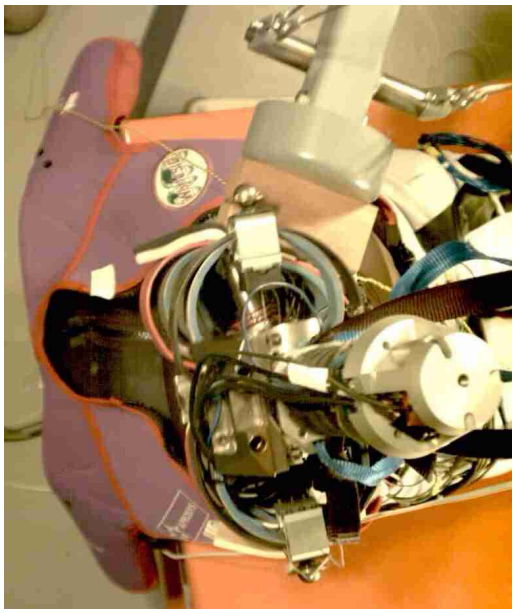

Figure 19: Overhead image + 30 degrees ~26 ms

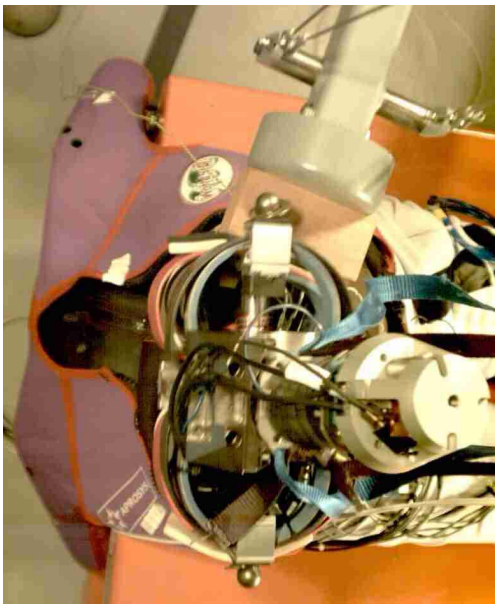

Figure 20: Overhead image +15 degrees ~26 ms

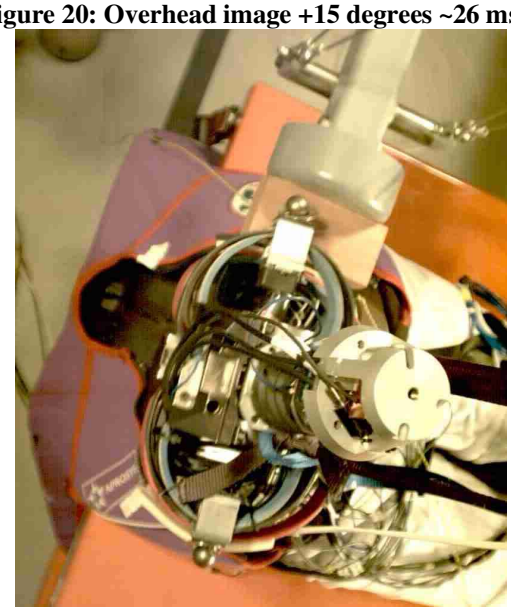

Figure 21: Overhead image lateral test ~26 ms

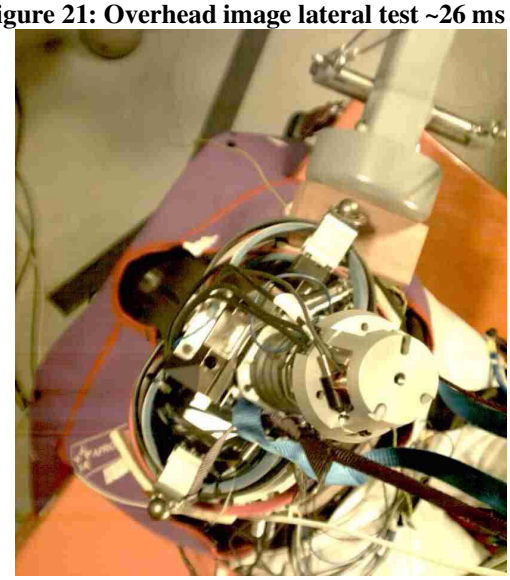

Figure 22: Overhead image - 15 degrees ~26 ms

The purple dotted line is an estimated reconstruction of the response without rotation bottoming out. As a result of this test, the 2D IR-Tracc mounting brackets were updated to shift the range of motion from ±30° to +40° – -20°.

Figure 24 shows the IR-Tracc compression. The output of the IR-Tracc is much lower for the +30° and -15° impact angle tests than the lateral and +15° forward oblique tests. Figure 25 shows the calculated Y lateral displacement. The -15° test (purple) clearly shows the bottoming out of the rotation, with its deviating waveform. Clearly the calculated Y is less dependent from the impact angle, however at +30 the output is still lower than pure lateral test.

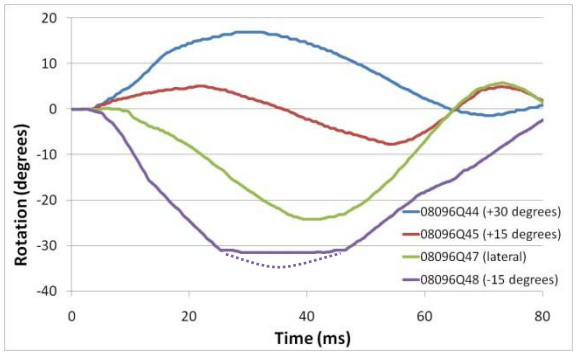

Figure 23: 2D IR-Tracc rotation oblique sensitivity tests

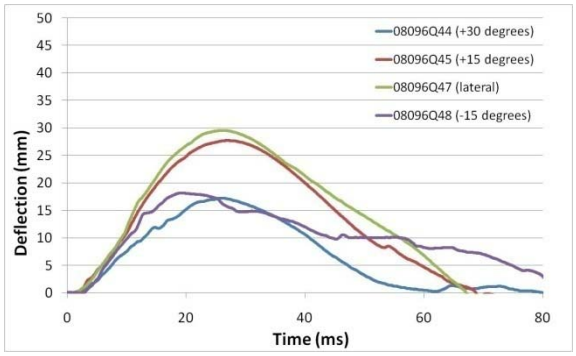

Figure 24: Dy IR-Tracc compression oblique sensitivity tests

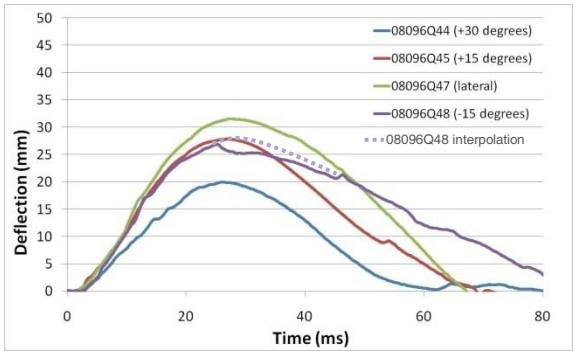

Figure 25: Calculated Rib Y displacement oblique sensitivity tests

The pendulum acceleration responses from the four oblique sensitivity tests are shown in Figure 26. It is evident from this figure that the + 30 degree and the -15 degree impacts had a slightly lower peak pendulum acceleration than the +15 degree and lateral impacts. This probably reflects the alignment of the pendulum being closer to the dummy centre of gravity in the +15 degree and lateral impacts. The responses from the 15 degrees forward of lateral and pure lateral tests are similar, with a difference of only 0.5 % between the peak values.

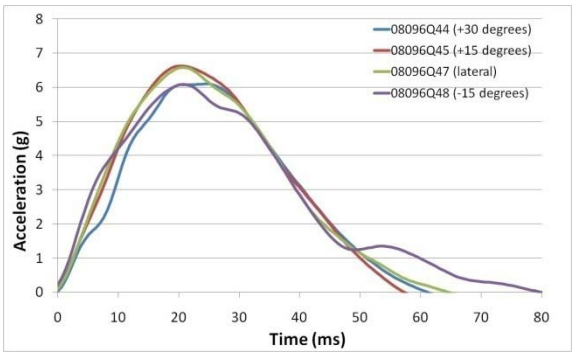

Figure 26: pendulum acceleration responses

The results of the pendulum test are presented in numerical format in Table 3. The table includes a comparison of the oblique test peak results with the peak result from the lateral test.

Table 3: Peak parameters pendulum tests

Direc-tion	F_{imp}	Dy	2D IR-Tracc calculated			Ratio oblique/lateral		
			X	Y	R	$Dy/Dy_{0°}$	$Y/Y_{0°}$	$R/R_{0°}$
+30°	838	17.2	20.5	20.0	28.1	0.58	0.64	0.74
+15°	909	27.8	-10.5	27.9	28.1	0.94	0.89	0.74
0°	904	29.5	-27.4	31.5	38.1	1	1	1
-15°	835	18.1	-39.4	26.9	45	0.61	0.85	1.18

Static airbag deployment test

The peak results of the static airbag tests are given in Table 4. In this table the average of two tests is given. For the ribs results are given for IR-Tracc compression Dy, 2D IR-Tracc rotation, X displacement, Y displacement and R resultant displacement. The bold figures highlight the highest of three thorax ribs and two abdomen ribs. The table shows that peak thoracic rib deflections occur either at thorax rib 2 or 3, and peak abdominal rib deflections always occur at the first abdominal rib. Figure 38 is illustrative for the reason behind this, as the airbag deploys in a spherical shape, putting more load on the centrally placed ribs. The parameters Dy and Y do not always agree on which of the thorax ribs is in highest deflection, however the difference between the thorax 2 and thorax 3 are generally low for both parameters. The results clearly show that the 30° forward tests gives much lower rib lateral deflections that the lateral tests. The output of the rotation sensor does provide insight of the loading direction of the dummy, with forward rib displacement under lateral and rearward rib displacement under forward load.

The largest rib rotations and X displacements occur at thoracic rib 2 in the lateral tests and at thoracic ribs in the oblique conditions.

Table 4: Test results airbag average of two tests

Condition		178mm, 0deg	108mm, 0deg	108mm, 30deg	178mm, 30deg
	F	3624	6232	5704	3757
Shoulder	Dy	16.9	21.0	9.6	5.6
Thorax 1	Dy	6.4	14.8	3.7	3.2
	Rot	9.3	19.8	**-17.4**	**-11.0**
	X	13.3	25.1	**-26.7**	**-16.8**
	Y	7.3	19.2	5.4	3.7
	R	14.8	31.4	26.9	16.9
Thorax 2	Dy	10.3	**18.8**	5.5	4.8
	Rot	**12.3**	**20.4**	-14.1	-9.1
	X	**17.2**	**25.1**	-20.6	-13.9
	Y	**11.6**	**22.9**	**6.2**	5.1
	R	19.9	33.2	20.8	14.0
Thorax 3	Dy	**10.6**	17.3	**5.7**	**5.2**
	Rot	10.9	18.9	-10.8	-7.4
	X	15.2	23.7	-16.3	-11.2
	Y	11.5	21.0	6.1	**5.5**
	R	18.2	31.0	16.5	11.4
Abdomen 1	Dy	**9.1**	**15.0**	**5.3**	**4.9**
	Rot	9.2	16.3	-7.0	-5.5
	X	12.9	21.1	-10.9	-8.5
	Y	**9.9**	**17.7**	**5.6**	**5.1**
	R	15.4	27.0	10.9	8.5
Abdomen 2	Dy	2.8	6.0	3.5	2.3
	Rot	4.9	11.5	-6.5	-0.4
	X	7.8	16.1	-10.1	-0.6
	Y	3.0	7.5	3.5	2.3
	R	8.1	17.7	10.1	7.7

Figure 27 shows the trajectories for pure lateral and 30 degree tests. It can be observed that the deflections are more due to the rotation than the compression of the IR-Tracc, confirming the necessity to measure both parameters.

The lateral displacement is almost absent in the 30° oblique test, and also in the pure lateral test, forward motion is larger than the lateral compression.

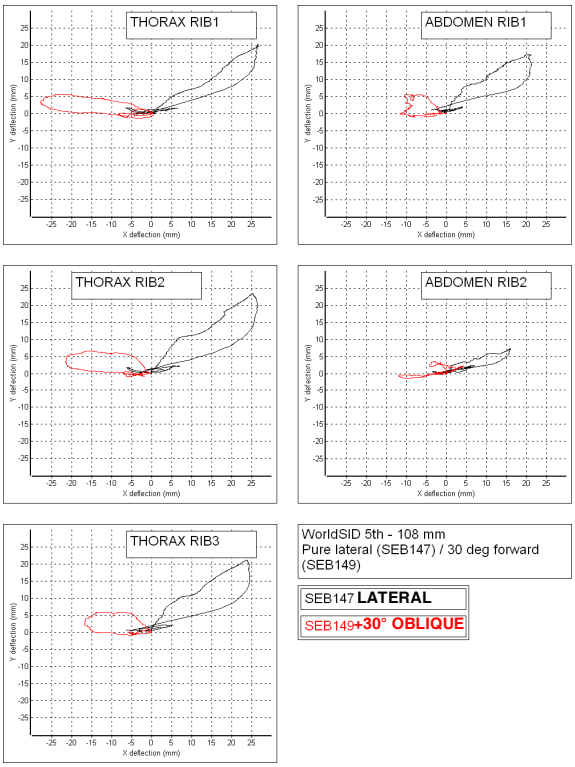

Figure 27: Rib trajectories for pure lateral and 30 deg forward tests at 108 mm

ANALYSIS, DISCUSSION AND SYNTHESIS

Drop tower tests

In Figure 28 the peak impact forces versus impact direction are shown both in absolute values as well as in percentages of peak lateral impact forces. For this analysis the average peak impact forces are calculated for each impact direction and impact speed.

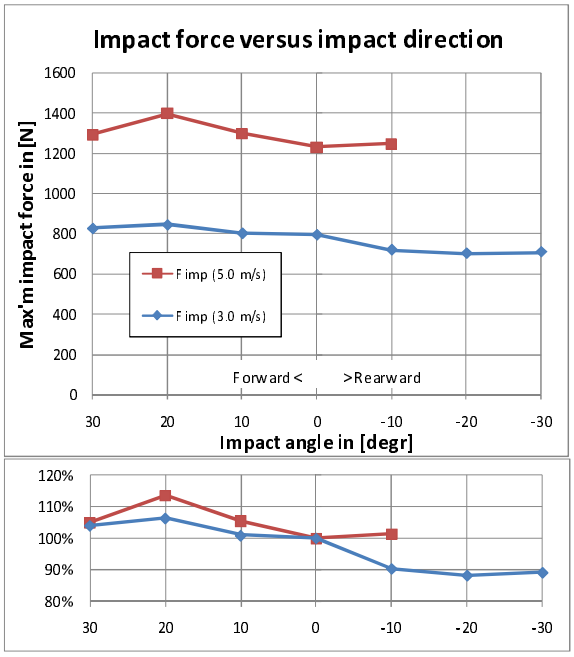

Figure 28: Impact force versus impact direction absolute and in percentages of pure lateral

It can be concluded that the impact force generated by the rib is not largely dependent on the impact direction and remains rather constant. For impacts at an impact speed of 3.0 m/s the deviations are between +6.3% and -11.8% and for impacts at an impact speed of 5.0 m/s the deviations are between +13.5% and 0%. At +20 degrees forward impact direction the ribs compressions are 6-14% lower than pure lateral and beyond 20 degrees rearward impact the ribs displacements are higher by 10%.

In Figure 29 the peak lateral displacements (Y rib) versus impact direction are shown both in absolute values as well as in percentages of the peak displacements at pure lateral impacts. For reference the compression of the IR-Tracc (Dy) is also given. The average rib displacements at lateral and +10 degrees impact angles are more or less constant at 19mm for 3m/s and around 35-36mm for 5m/s. The plots in Figure 29 show reduced Y rib compression under both rearward and forward impact, around 20% reduction of the average peak displacement at -10° and +20° impact angles increasing to 30% reduced average rib displacement at +30° and -20° to -30° impact directions.

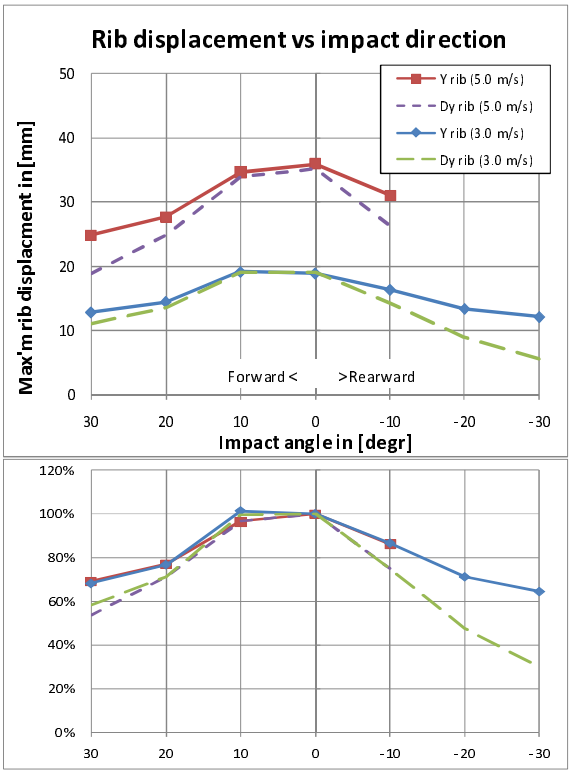

Figure 29: Rib displacement versus impact direction absolute and in percentages of pure lateral

Figure 29 reveals another important difference if we compare the output of the 'plain' IR-Tracc alone (green and purple dotted lines) with the lateral displacement Y rib calculated from the 2D IR-Tracc. The reduced sensitivity of 'plain' IR-Tracc is

clearly illustrated: at 30 degrees forward impact the IR-Tracc compression, Dy, is 54-58% of the pure lateral output and at 30 degrees rearward impact the output is reduced to 29% of the pure lateral output. Although reduced, the calculated parameter Y rib is much more sensitive under oblique impact direction: at 30 degrees forward impact the Y rib is 68% of the pure lateral Y rib and at 30 degrees rearward impact the Y rib is reduced to 63% of the pure lateral Y rib. It can be concluded that Y rib obtained from the 2D IR-Tracc provides a much better insight in the rib deformation under both lateral and oblique impacts, than the deformation recorded with the IR-Tracc alone (Dy). More over the parameter Y rib discriminates between the high severity and the low severity test conditions.

Figure 30 shows a comparison between Y para (compression aligned with impact direction) and Y rib, lateral compression in spine box co-ordinate system. Please note that these parameters are not in the same co-ordinate system. The figure shows that the deviation between the parameters becomes larger with larger deviation of the angle between the instrumentation, which is to be expected. The compression in impact direction remains more or less constant, between +30 and -10 degrees impact angle for both 3m/s and 5m/s impacts. The compression increases with rearward of lateral tests.

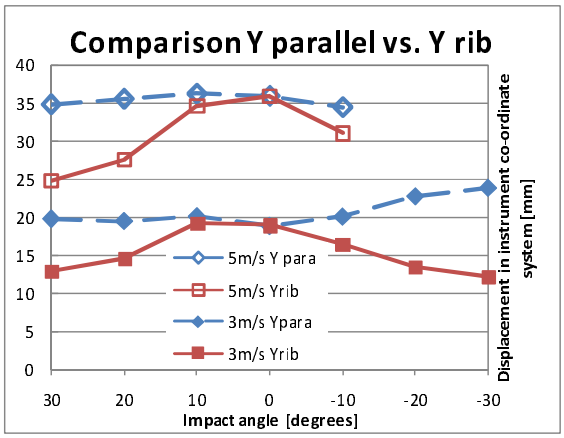

Figure 30: Comparison displacement Y para and Y rib in instrument co-ordinate system

Figure 31 shows the correlation between the calculated peak resultant displacement versus the impact angle in absolute values as well as percentage of the pure lateral impact value. The resultant displacements are relatively flat in the pure lateral and forward oblique tests. This means that the resultant displacement is not dependant on impact angle. However, under rearward oblique impacts, the resultant displacements of the 3m/s tests are as high as the lateral and forward oblique results of the 5m/s test. This parameter alone is not able to discriminate between a high severity lateral test and a rearward oblique impact of lower severity. Figure 31 also shows a comparison between the resultant displacements as measured by the parallel IR-Tracc and the dummy IR-Tracc. The results are clearly close together the dummy IR-Tracc, is reflecting the rib displacement in impact direction, independent form the impact direction.

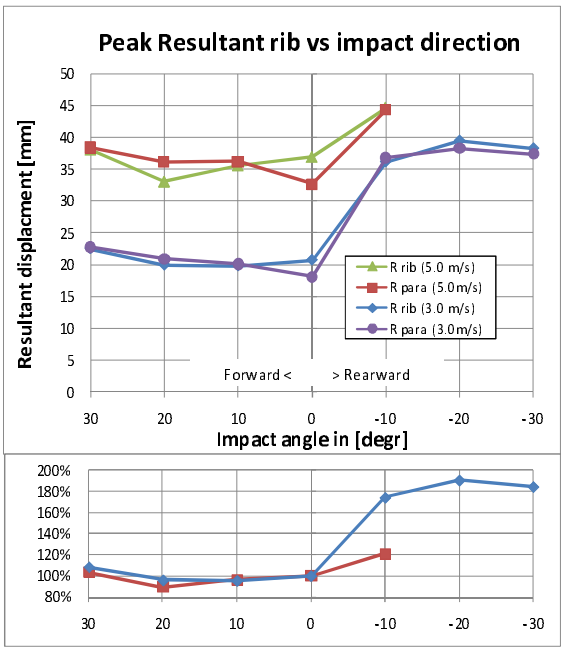

Figure 31: Peak resultant rib displacement versus impact angle drop tests

Larger forward than rearward motion of the rib can be explained from the construction of the ribs in the WorldSID dummy. The rib units are assembled from inner and outer ribs. The inner ribs are a cylindrical hoop attached symmetrically with respect the lateral axis to the spine box. The outer ribs are asymmetrically attached only to the rear of the spine box, similar to the human thorax construction. An asymmetric behaviour of the dummy and the human chest is to be expected.

Pendulum tests

The pendulum tests show similar results to the single rib unit drop tests (Figure 32). Rib displacements are similar for lateral and small angles frontal, with reduced output with increasing oblique test angles. Also in the pendulum test the Y displacement is less sensitive to impact angle than the Dy compression of the IR-Tracc alone. The R resultant displacement is higher under rearward oblique than forward oblique tests. The force response is hardly dependent from impact angle (Figure 26). Interestingly, at +15° impact all parameters are very close to one another around 28mm. This indicates that there is very little rotation in this test. Indeed around the time of peak displacement of the +15° test, the rotation angle is close to 0° (Figure 23 & Figure 24). This observation is illustrative of the valuable insight the

2D IR-Tracc offers in the behaviour of the rib deformation.

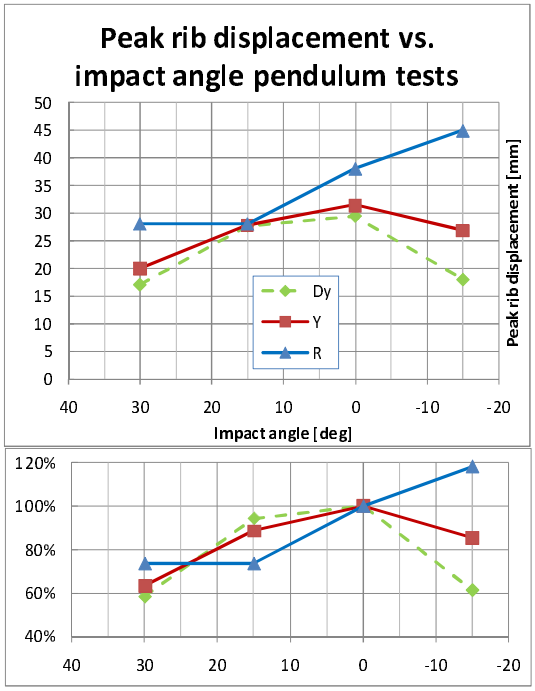

Figure 32: Pendulum tests rib displacements vs. impact angle

Airbag deployment tests

Figure 33 to Figure 37 show the effect of angle respectively on the plate force, the IR-Tracc compression Dy, the X deflection the Y deflection and the Resultant deflection. The compression Dy and the Y deflection demonstrate a large sensitivity on the loading angle, with reduced output under oblique load, while the resultant deflection is less affected. The X deflection parameter is also very sensitive for oblique load and clearly indicates the direction of load. Regardless of the sign, the peak X displacements are rather similar in amplitude in the pure lateral and 30° forward tests. This implies that the smallest forward and backward displacements (thus pure lateral displacement) could be expected around 15° forward impact. This is in line with the pendulum test result, see Figure 32.

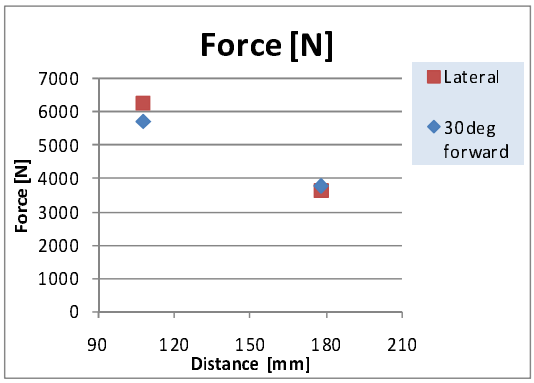

Figure 33: Plate force vs. airbag distance

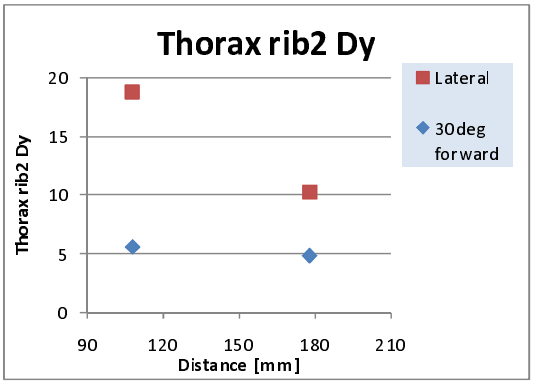

Figure 34: Thorax rib 2 IR-Tracc compression vs. airbag distance

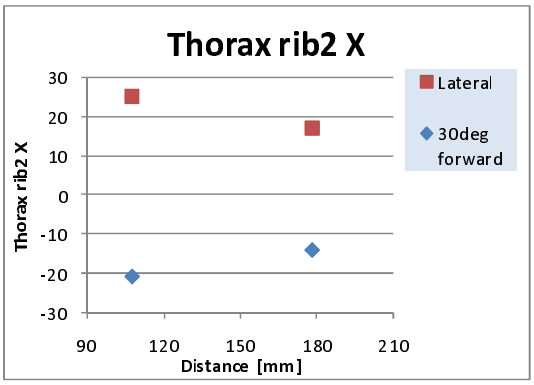

Figure 35: Thorax rib 2 X-displacement 2D IR-Tracc vs. airbag distance

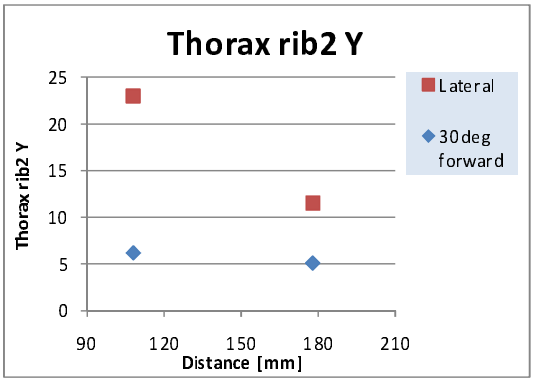

Figure 36: Thorax rib 2 Y-displacement 2D IR-Tracc vs. airbag distance

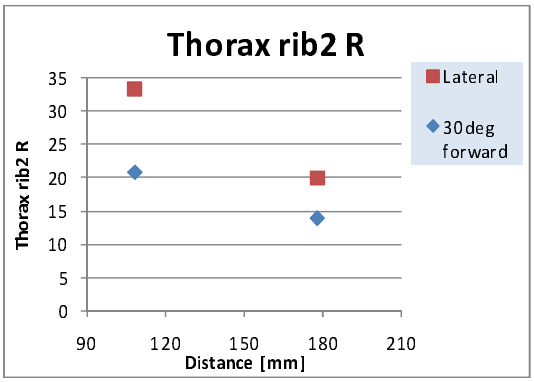

Figure 37: Thorax rib 2 Resultant displacement 2D IR-Tracc vs. airbag distance

Table 5 gives a summary of the test results in numerical format for the three thorax ribs. In this table the results are presented in the ratio of the oblique and the lateral parameter. A ratio of more than 1 indicates the parameter is higher in the oblique condition and below 1 indicates that the oblique parameter is lower. The lower severity test results are shown in the left column and the higher severity in the right column. For Dy and Y parameters, the oblique results are lower than the lateral results. For the force and thorax rib1 X- and resultant displacement the ratio is higher than 1, indicating the oblique results are higher. Further it is clear that generally the ratios of parameters are much lower in the high severity test, with ratios around 0.25-0.30. An exception is the X parameter, which changes its sign, but the absolute values are closer to 1.

Table 5: Ratio of parameters 30° and parameters lateral

		ratio +30° oblique/ lateral	
		178mm	108mm
	F	1.04	0.92
Thorax 1	Dy	0.50	0.25
	X	-1.26	-1.07
	Y	0.50	0.28
	R	1.14	0.86
Thorax 2	Dy	0.46	0.29
	X	-0.81	-0.82
	Y	0.44	0.27
	R	0.70	0.63
Thorax 3	Dy	0.49	0.33
	X	-0.73	-0.69
	Y	0.47	0.29
	R	0.63	0.53

To study further the reasons for the large difference between the outputs of two test condition, the high speed videos of the tests were analysed. Sequences of high speed videos of the lateral test (Figure 38) and oblique test (Figure 39) clearly show the different behaviour of the dummy in these test conditions. In the pure lateral test, the dummy's response is pure sideways motion; and in the 30° oblique the dummy's chest is rotating backward. Peak displacements were around 35ms in pure lateral and, much earlier, around 20ms in forward oblique tests. The chest rotation could explain a lower deflection in the oblique test; however, the rotation began after the deflection started to decrease, i.e. in the unloading phase.

A plausible explanation could be the following. In the lateral test the vector of force is directed towards the centre of gravity of the dummy. The inertia of the dummy provides a counter reactive force within the dummy against which the ribs (which are acting like springs/dampers) are deforming. In the forward oblique test however, the

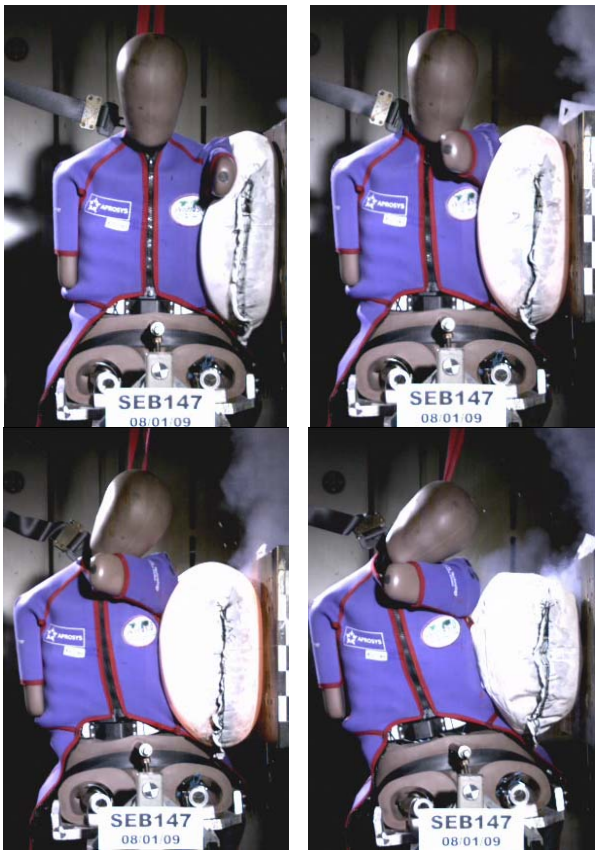

Figure 38: Sequence of high speed video stills 20, 30, 40 & 50ms lateral tests

Figure 39: Sequence of high speed video stills 20, 30, 40 & 50ms, 30° frontal oblique test

vector of force is not directed to the centre of gravity, causing rotation of the dummy's chest. It is believed that the counter reactive force within the dummy has a much larger forward-backward component, causing rearward rib rotation and highly reduced lateral compression. The rotation inertia does not provide the internal counter reactive force against which the ribs are compressing. The restriction in rotation around a vertical axis at the pelvis is not working for the dummy, as the lumbar spine is developed to allow human like shear motion and is not validated for moment about the vertical axis. The rotation of the chest is the 'easy way out' for the dummy and only restricted by the rotation inertia of the chest, neck and head. The rotation component is confirmed by the asymmetrical loading which is observed on the airbag plate forces: the forces at the back of the plate are higher than the forces at the front for the 30° forward loading, indicating a moment reaction. For pure lateral tests, the plate forces are almost equal between back and front, indicating pure lateral loading.

Synthesis drop & pendulum tests and airbag tests

Generally there is a good correlation between the Drop test and Pendulum test results. The IR-Tracc compression, Dy, and lateral deflection, Y, remain at the same level when the impact angle is varied between about lateral and 15° forward oblique. This means that when the dummy is loaded close to the lateral axis direction, there is no problem with the current deflection measurement system, the IR-Tracc.

With further deviation from the lateral, the output of the lateral deflection is reduced. The Y displacements remain at a higher level than the compression Dy of the IR-Tracc alone over a wider impact angle variation. The drop test and pendulum results indicate that the Y displacements remain within 80% of the lateral test output between impact angles ranging between 20° forward oblique and 15° rearward oblique, and about 70% between 30° forward and 25° rearward oblique impacts. The Y displacement appears to be a simple but efficient parameter to improve the sensitivity to oblique impacts.

The resultant displacement was also tested for oblique impact sensitivity. Due to the large forward displacements of the ribs in rearward oblique impacts, the resultant displacement becomes very large and comes into the range of resultant displacement of higher severity tests under lateral test conditions. The R parameter is not able to discriminate between a high severity lateral impact and mid severity rearward oblique test.

The situation for rearward oblique is different from forward oblique. This has to do with the construction of the WorldSID thorax, with outer ribs mounted to the rear of the spine-box and free floating connections between left and right ribs in the front. Forward rib motions in rear oblique impact are larger than rearward motion in forward oblique impacts. This results in forward rib displacements, even under pure lateral tests. The test results indicate that the turning point is at around 0° – +15° forward oblique, which impact angle leads to more or less pure lateral deflections. All of these observations were made possible by the addition of the rotation sensor and calculation of rib trajectories in the X-Y plane of the ribs.

A discrepancy was found between the Airbag tests on one hand and Pendulum and Drop tests on the other hand. The output of the deflections sensors under forward oblique tests, both from IR-Tracc and 2D IR-Tracc, were much further reduced in the Airbag tests (~25-30% from pure lateral) than the Pendulum and Drop tests (~60-70% from pure lateral). The differences in dummy response between the drop table and pendulum tests on hand, and airbag tests on the other hand can be explained from the difference between the test conditions. The pendulum and drop tests involve loading with high inertia loading devices, which will not easily deviate from their path of travel. The dummy ribs and the impactor mass are well coupled by the friction in the pendulum tests (to lesser extend in 3m/s drop tests by use of PTFE sheet), therefore, at impact, the rib displaces more or less in the direction of travel of the impactor.

The airbag on the contrary is a low mass loading device, with energy content in the form of lightweight expanding gasses and airbag fabric at high velocity. It appears that the expanding gasses can more easily deviate from the path of travel and can take the easy escape route, wherever the lowest restrictions are. This is reflected in the airbag response trajectories (Figure 27), where the displacement of the rib deviates from the impact direction right from the start.

No matter the difference between these test conditions, also in the airbag tests the 2D IR-Tracc results proved to be very helpful indeed to study the phenomena taking place. Still many questions remain from these tests, but in any case the 2D IR-Tracc offers a good tool to study them.

CONCLUSION AND RECOMMENDATIONS

Conclusions

The 2D IR-Tracc was assessed for oblique sensitivity in three test conditions: on a drop table with rib components, in full dummy pendulum tests

and static deployment airbag tests. The impact angle and impact severity was varied in the test conditions and the outputs of the two-dimensional chest deflection sensor were analysed.

The 2D IR-Tracc proved to be very useful indeed in understanding phenomena taking place under various lateral oblique impact conditions and could not have been understood with the current (1D) compression sensor. The reduced sensitivity of the conventional IR-Tracc compression (Dy) to oblique impact was confirmed in this study.

Three calculated displacement parameters from the 2D IR-Tracc were assessed and compared to the standard measurement parameter. The calculated lateral displacement Y offered a simple and straightforward parameter to improve the sensitivity to oblique impacts, as compared to the current single axis deflection sensor. The drop test and pendulum results indicate that the Y displacements remain within 80% of the lateral test output between impact angles ranging between 20° forward oblique and 15° rearward oblique, and about 70% between 30° forward and 25° rearward oblique impacts.

The forward-rearward displacement X parameter offers very good indication of the loading direction of the dummy. The smallest forward-rearward displacements were found under 10°-15° forward-oblique impacts. Large forward displacements were found under rearward-oblique impacts and these were generally larger than the lateral displacement from -10° impact angles and beyond.

The 2D IR-Tracc resultant displacement parameter, R, correlates well with the displacements found in impact direction in the drop table tests and provides information on the magnitude of the rib deformation in impact direction. However this parameter is not useful as injury assessment parameter, as it does not discriminate between impact severity under all impact conditions, especially rearward oblique impacts.

The objective of improving the oblique loading sensitivity has been met with the development of the 2D IR-Tracc. Further research is necessary to develop an injury criterion based on its output that correlates well with injury under lateral and lateral-oblique loading conditions.

In this study only test-to-test comparisons were done by variation of the test condition with one dummy. The important open item is, the comparison of the PMHS chest deflection in the X-Y plane with those of the dummy in the same test condition. So far, as far as the authors are aware, no two-dimensional deflection data have been derived. Maltese et.al. [6] used the chest band device to obtain deflections in the cross sections of PMHS chests in sled tests; however, only single parameters of lateral deflection were published. It could be useful to re-analyse this database for two-dimensional rib displacements. Yoganandan et.al. 2007 [7] expanded the Maltese test conditions with an oblique mounted force plate for the thorax, to obtain lateral-oblique human response data. It would be useful to install 2D IR-Traccs in the WorldSID 50the male dummy and subject it to the same test conditions.

The objective of improving the oblique loading sensitivity has been met with the development of the 2D IR-Tracc. Further research is necessary to develop an injury criterion based on its output that correlates well with injury under lateral and lateral-oblique loading conditions.

Some inconsistencies were identified when the dummy is loaded by an airbag. More investigations are needed to understand the inconsistencies.

Recommendations

It is recommended to validate further the dummy oblique thorax response with available human response data. It should be considered to develop the 2D IR-Tracc so as to be suitable for the WorldSID 50th percentile male dummy and explore its potential benefits for this dummy. Also application in other dummies, such as the Q3s and Q6s, the Q-dummy side impact family should be considered.

ACKNOWLEDGEMENTS

This work was supported through funding from: the European Commission, UK Department for Transport. Staff of test laboratories at FTSS, LAB and TRL.

REFERENCES

[1] Been B.W., Meijer R., Bermond F., Bortenschlager K., Hynd D., Martinez L. and Ferichola G. 2007. “WorldSID small female side impact dummy specifications and prototype evaluation.” Proceedings of the 20th Enhanced Safety of Vehicles (ESV) Conference, Lyon, France.

[2] Viano D. C. (1989), ‘Biomechanical Responses And Injuries In Blunt Lateral Impact’, Proceedings of the 30th Stapp Car Crash Conference (SAE paper number 892432, pp. 113-142), Warrendale, PA, U.S.A., Society of Automotive Engineers, Inc. (SAE).

[3] FMVSS214, 49 Code Federal Regulation paragraphs 571.214, Nat'l Highway Traffic Safety Admin. DOT, October 2008.

[4] Hynd D., Carrol J.A., Been B.W., Payne A.R. (2004), 'Evaluation of the Shoulder Thorax and Abdomen of the WorldSID Pre-Production Side Impact Dummy', IMechE Vehicle Safety Conference 2004.

[5] Lécuyer E. (2007) APROSYS Status report AP SP52 0070, 'Lateral and Oblique Static Deployment Airbag Tests on a WorldSID 50th %-ile Male Dummy'.

[6]Maltese R.M., Eppinger R.H., Rhule H.H., Donnely B.R., Pintar F.A., Yoganandan N.; 'Response Corridors of Human Subjects in Lateral Impacts'; Stapp Car Crash Journal vol 46, p. 321-351; Technical paper 2002-22-0017

[7] Yoganandan N., Pintar F.A., Gennarelly T.A., Martin P.G., Ridella S.A. (2007), 'Chest Injuries and Injury Mechanism in Oblique Lateral Impacts', Paper 07-311 Proceeding of the IRCOBI Conference, Maastricht, the Netherlands, 2007.

WORLDSID PRODUCTION DUMMY BIOMECHANICAL RESPONSES

Risa Scherer
Klaus Bortenschlager
Akihiko Akiyama
Suzanne Tylko
Markus Hartlieb
Takeshi Harigae
WorldSID Tri-Chair Committee
Members of the WorldSID Task Group, Design Team and Project Manager
Paper Number 09-0505

ABSTRACT

The results of biomechanical testing of the WorldSID production dummy are presented in this paper. The WorldSID dummy is a new, advanced **World**wide **S**ide **I**mpact **D**ummy that has the anthropometry of a mid-sized adult male. Based on previous testing the dummy design was frozen and developed into a production version of the WorldSID dummy. This dummy has been tested to determine that the biofidelity of the dummy has not degraded during its development and refinement.

The response corridors are defined in the International Organization of Standardization (ISO) Technical Report 9790. This dummy has been subjected to a rigorous program of testing to evaluate its biofidelity. The dummy's head, neck, thorax, abdomen and pelvis were evaluated against the ISO technical report requirements. Testing included drop tests, pendulum impacts, and sled tests. The biofidelity rating of the WorldSID was calculated using the weighted biomechanical test response procedure developed by ISO.

The WorldSID dummy has an overall ISO Biofidelity rating of 8.0, which corresponds to an ISO classification of "good". In addition the dummy shows good repeatability and good reproducibility. A comparison of the WorldSID dummy biofidelity compared to other existing side impact dummies biofidelity ratings will also be provided.

INTRODUCTION

In November 1997, the WorldSID Task Group was formed under the auspices of the International Organization for Standardization (ISO) TC22/SC12/WG5 - Anthropomorphic Test Devices Working Group [1]. The Task Group's purpose was to develop a unique, technologically advanced side impact dummy. This dummy is intended to be a more biofidelic side impact dummy and to replace the current side impact dummies in regulation and other testing.

Currently, six mid-sized male side impact dummies were available for regulatory, consumer information and development use. They are the USDOT-SID dummy [2]; the EuroSID-1 dummy [3]; the ES-2 dummy which is regulated in a European standard [4]; the ES-2re which is utilized in the United States side impact protection regulation [5]; the SID/H3 dummy which is utilized in the United States side impact protection regulation FMVSS-201 [6]; and the BioSID dummy [7]. All six dummies have different levels of biofidelity and none of these dummies has a "good" rating on its biofidelity using the ISO rating scale (Table 1). The six dummies are structurally different, have different instrumentation and associated injury assessment criteria. Partially because of these reasons, and the differences in the test procedures, these dummies typically provide different design direction to the vehicle development engineer.

Table 1.
ISO Biofidelity Classifications

Excellent	> 8.6 to 10.0
Good	> 6.5 to 8.6
Fair	> 4.4 to 6.5
Marginal	> 2.6 to 4.4
Unacceptable	0 to 2.6

The vision of ISO was to develop a harmonized dummy that would have technological buy-in from biomechanics, dummy and regulatory experts from around the world. To accomplish this, the Task Group was charged with developing the dummy's specifications, its design, and finally with fabricating and evaluating the dummy. The results of years of hard work by the WorldSID Task Group and Design Team will be presented in this paper.

The completed WorldSID dummy is shown in Figure 1.

Figure 1. WorldSID production dummy.

BIOFIDELITY RATINGS

The biofidelity rating method published in the International Standards Organization (ISO) Technical Report (TR) 9790 [8] was used for determining the WorldSID biofidelity rating.

Equation 1 is used to determine the overall biofidelity of the dummy.

$$B = \frac{\sum_{i=1,2,..6} U_i B_i}{\sum_{i=1,2,..6} U_i} \qquad (1)$$

where,

B - overall biofidelity rating which has a value between 0 (poorest) and 10 (best)
B_i - biofidelity rating for each of the body regions
U_i - weighting factor for each body region
i - subscript to represent each body region (i=1 Head, i=2 Neck, i=3 Shoulder, i=4 Thorax, i=5 Abdomen and i=6 Pelvis)

The equation used to calculate the biofidelity of a body region B_i is shown in Equation 2.

$$B_i = \frac{\sum_{j=1,2,...m} V_{i,j} T_{i,j}}{\sum_{j=1,2,..m} V_{i,j}} \qquad (2)$$

where,

V_{ij} - weighting factor for each test condition for a given body region

T_{ij} - test biofidelity for each test condition for a given body region

The equation used to calculate the test biofidelity is shown in Equation 3.

$$T_{i,j} = \sum_{k=1,2,...n} W_{i,j,k} R_{i,j,k} \Big/ \sum_{k=1,2,..n} W_{i,j,k} \qquad (3)$$

where,

W_{ijk} - weighting factor for each response measurement for which a requirement is given

R_{ijk} - the rating of how well a given response meets its requirement

Values for the response rating, R_{ijk}, are as follows:

R_{ijk} = 10 if the response meets its requirements

R_{ijk} = 5 if the response is outside of its requirement, but lies within one corridor width of requirement

R_{ijk} = 0 if response is outside of requirement by more than one corridor width of the requirement

Repeat runs were performed on the majority of the tests and response ratings were assigned to each run. The five ISO classifications were used to indicate the degree of biofidelity for each response target, test, body region and the overall biofidelity rating of the dummy. Tests that were not conducted are not included in the biofidelity rating.

BIOMECHANICAL TESTING

The WorldSID was tested in accordance with the ISO TR 9790 requirements. The dummies responses were compared with the response corridors that are defined in ISO TR 9790 for a 50th percentile adult male.

For the WorldSID, all the ISO TR 9790 biomechanical tests were conducted, with the following exceptions. Tests requiring APR and Wayne State University (WSU) padding were not conducted because of the unavailability of the padding or an acceptable alternative. The 2.0 m abdominal drop and the 8.9 m/s rigid wall sled test were considered too severe, so they were not

performed.

Head Test 1

This test consists of dropping the head from a 200 mm height onto a rigid surface (Figure 2). Targets are given for the head resultant acceleration.

Figure 2. Head drop configuration.

The peak head acceleration for the left side impact was 140.8 *g*. The peak acceleration for the right side of the head was 129.2 *g*. The left and right side of the head were within the response target range of 100 - 150 *g*. The results are in Table A1, Appendix A.

The Head Drop Test 1 biofidelity rating is 10, which corresponds to an ISO classification of "excellent".

Overall head biofidelity

The overall head biofidelity rating is 10, which corresponds to an ISO classification of "excellent".

Neck Test 1

This test consists of restraining the torso and pelvis of the dummy, with the arms down (Figure 3). The mean sled velocity was 6.9 m/s and average sled deceleration was 7.2 g, described in ISO TR 9790. Boundaries were given for lateral acceleration and displacement at T1, lateral and vertical head centre of gravity (CG) displacement relative to T1, the time of peak head excursion, lateral and vertical peak head acceleration, the peak lateral flexion angle and the peak twist angle.

Neck Test 1 results are in Tables A2, Appendix A.

The Neck Test 1 biofidelity rating is 7.4, which corresponds to an ISO classification of "good".

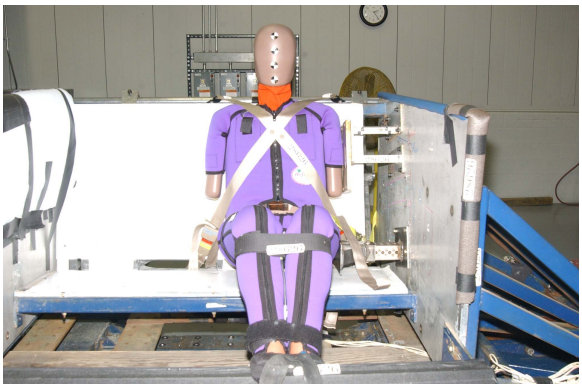

Figure 3. Neck Tests 1-3 configuration.

Neck Test 2

This test consists of restraining the torso and pelvis of the dummy, with the arms down (Figure 3). The sled velocity was 5.8 m/s and the constant deceleration level was 6.7 g. From this test, boundaries for peak flexion angle, peak forces and moments at the occipital condyles and peak head resultant acceleration were given.

Neck Test 2 results, are in Tables A3, Appendix A.

The Neck Test 2 biofidelity rating is 2.0, which corresponds to an ISO classification of "unacceptable".

Neck Test 3

This test consists of restraining the torso and pelvis of the dummy, with the arms down (Figure 3). An acceleration-type sled is accelerated to 12.2 *g* using the sled pulse described in ISO TR 9790. Boundaries are given for peak lateral T1 acceleration, peak lateral head CG acceleration, peak horizontal displacement of the head CG relative to the sled, peak flexion angle and peak twist angle.

Neck Test 3 results are in Table A4, Appendix A.

The Neck Test 3 biofidelity rating is 7.2, which corresponds to an ISO classification of "good".

Overall Neck Biofidelity

The overall neck biofidelity rating is 5.3, which corresponds to an ISO classification of "fair".

Shoulder Test 1

This test consists of impacting the shoulder, with the arm down, using a 23 kg, 150 mm diameter rigid pendulum impactor at 4.5 m/s. Targets are given for the pendulum force/time history and the maximum shoulder deflection.

The pendulum forces and peak shoulder deflections were within the response corridors. The peak shoulder deflections were 39, 37 and 40 mm, which are within the response target of 34-41 mm. The results are shown in Figure A1 and Table A5, Appendix A.

The Shoulder Test 1 biofidelity rating is 10, which corresponds to an ISO classification of "excellent".

Shoulder Test 2

This test consists of restraining the torso and pelvis of the dummy, with the arm down (Figure 3). The mean sled velocity was 6.9 m/s and average sled deceleration was 7.2 g, described in ISO TR 9790. Targets are given for peak horizontal T1 acceleration and peak horizontal T1 displacement.

The peak lateral T1 accelerations with respect to the sled were 16, 13, 13, 12, 12 and 12 *g* and the peak displacements with respect to the sled were 59.4, 53.6, 56.8, 53.9, 52.3 and 53.4 mm. These responses were within the response target corridors of 12-18 *g* and 46-63 mm, respectively. The results are in Tables A6, Appendix A.

The Shoulder Test 2 biofidelity rating is 10.0, which corresponds to an ISO classification of "excellent".

Shoulder Test 3

This test consists of restraining the torso and pelvis of the dummy, with the arms down (Figure 3). An acceleration-type sled is accelerated to 12.2 *g* using the sled pulse described in ISO TR 9790. Targets are given for T1 accelerations.

The peak T1 lateral accelerations with respect to the sled were 20.0, 17.9, 19.1, 17.2, 18.2 and 17.1 *g*. These responses were within the response target corridors of 17-23 *g*. The results are in Table A7, Appendix A.

The Shoulder Test 3 biofidelity rating is 10, which corresponds to an ISO classification of "excellent".

Overall Shoulder Biofidelity

The overall shoulder biofidelity rating is 10, which corresponds to an ISO classification of "excellent".

Thorax Test 1

This test consists of impacting the thoracic ribs, with the arm 90 degrees forward from vertical, using a 23.4 kg, 150 mm diameter rigid pendulum impactor at 4.3 m/s. Targets are given for the pendulum force and upper spine lateral acceleration.

The pendulum forces were within their respective response corridor and the upper spine lateral deflections were within one corridor width of their respective corridors. The results are shown in Figures A2-3 and Table A8, Appendix A.

The Thorax Test 1 biofidelity rating is 7.8, which corresponds to an ISO classification of "good".

Thorax Test 2

This test consists of impacting the thoracic ribs, with the arm 90 degrees forward from vertical, using a 23.4 kg, 150 mm diameter rigid pendulum impactor at 6.7 m/s. Targets are given for the pendulum force.

The pendulum forces were within the response corridor. The results are shown in Figure A4 and Table A9, Appendix A.

The Thorax Test 2 biofidelity rating is 10.0, which corresponds to an ISO classification of "excellent".

Thorax Test 3

This test consists of dropping the dummy laterally from a height of 1 m onto a continuous rigid plate, which spans the shoulder, thorax and abdomen regions with a separate plate for the pelvis region. The arm is rotated 20 degrees forward of the dummy's thoracic spine. Targets are given for the thoracic plate force and peak rib deflection.

All of the thoracic force plate loads were within the response corridors. The peak center thoracic rib displacements were 41, 42 and 30 mm. One of the rib displacements was within the response target corridor of 26-38 mm and two were within one corridor width. The results are shown in Figure A5 and Table A10, Appendix A.

The Thorax Test 3 biofidelity rating is 8.3, which

corresponds to an ISO classification of "good".

Thorax Test 5

This test requires a Heidelberg-type rigid wall sled impact at 6.8 m/s. Targets are given for the thorax plate force, peak lateral upper spine acceleration, peak lateral lower spine acceleration, and peak lateral acceleration of the impacted rib.

The thoracic region loading was within the thoracic force plate response corridors. One of the T1 accelerations was within one corridor width of the 82-122 g response target and twelve were greater than one corridor width. The peak T12 accelerations were within one corridor width of the response target of 71-107 g. The results are shown in Figure A6 and Table A11, Appendix A.

The Thorax Test 5 biofidelity rating is 6.4, which corresponds to an ISO classification of "fair".

Overall Thorax Biofidelity

The overall thorax biofidelity rating is 8.2, which corresponds to an ISO classification of "good".

Abdomen Test 1

This test consists of dropping the dummy laterally from a height of 1 m onto a simulated armrest, which protrudes 41 mm above a continuous rigid plate. The plate spans the shoulder, thorax and abdomen regions with a separate plate for the pelvis region. The arm is removed from the dummy to simulate the cadaver arm position. Targets are given for the armrest force, peak lower spine acceleration, peak impacted rib acceleration, and peak abdominal penetration.

The armrest force plate loads were within the response target corridor. The peak upper abdominal rib displacements were 50.9, 51.4 and 47.4 mm. The peak upper abdominal rib accelerations were 126.9, 130.9 and 193.3 *g*. The peak T12 accelerations were 32.0, 33.5 and 34.5 *g*. The abdominal rib displacements were within the response target of deflection greater than 41 mm. Two of the abdominal rib accelerations were within one corridor of the response corridor of 100-125 g and one was greater than one corridor width of the response corridor. All of the T12 accelerations were within the 29-35 *g* response corridor. The results are shown in Figure A7 and Table A12, Appendix A.

The Abdomen Test 1 biofidelity rating is 9.0, which corresponds to an ISO classification of "excellent".

Abdomen Test 3

This test consists of a WSU-type rigid wall, deceleration sled (Figure 4) accelerated to 6.8 m/s. The dummy is seated on the sled with the arm at 45 degrees forward from vertical. A target is given for the abdominal plate force.

The abdomen force plate loads, except for local oscillations, were within the response corridor. The results are shown in Figure A8 and Table A13, Appendix A.

The Abdomen Test 3 biofidelity rating is 10, which corresponds to an ISO classification of "excellent".

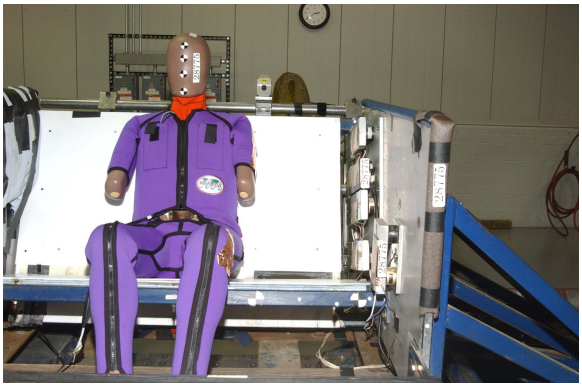

Figure 4. WSU-type sled test configuration.

Overall Abdomen Biofidelity

The overall abdomen biofidelity rating is 9.3, which corresponds to an ISO classification of "excellent".

Pelvis Test 1

This test consists of a rigid pendulum impact at 6 m/s. The impactor is defined as a 17.3 kg rigid impactor with a 600 mm radius of curvature and an outer diameter of 127 mm. A target is given for the pendulum force.

The peak forces were within the corresponding response corridors. The results are shown in Figure A9 and Table A14, Appendix A.

The Pelvis Test 1 biofidelity rating is 10.0, which corresponds to an ISO classification of "excellent".

Pelvis Test 2

This test consists of a rigid pendulum impact at 10 m/s. The impactor is defined as a 17.3 kg rigid impactor with a 600 mm radius of curvature and an outer diameter of 127 mm. A target is given for the pendulum force.

The peak force was within one corridor width of the corresponding response corridor. The results are shown in Figure A9 and Table A15, Appendix A.

The Pelvis Test 2 biofidelity rating is 5.0, which corresponds to an ISO classification of "fair".

Pelvis Test 3

This test consists of dropping the dummy laterally from a height of 0.5 m onto a continuous rigid plate, which spans the shoulder, thorax and abdomen regions with a separate plate for the pelvis region. The arm is rotated 20 degrees forward of the dummy's thoracic spine. A target is given for the peak pelvic acceleration.

The peak pelvic accelerations were 29.3, 31.2 and 30.2 *g*. All of the pelvic accelerations were within one corridor width of the 37-45 *g* response corridor. The results are shown in Table A16, Appendix A.

The Pelvis Test 3 biofidelity rating is 5.0, which corresponds to an ISO classification of "fair".

Pelvis Test 4

This test consists of dropping the dummy laterally from a height of 1 m onto a continuous rigid plate, which spans the shoulder, thorax and abdomen regions with a separate plate for the pelvis region. The arm is rotated 20 degrees forward of the dummy's thoracic spine. A target is given for the peak pelvic acceleration.

The peak pelvic accelerations were 45.6, 45.5 and 42.0 *g*. All of the peak pelvic accelerations were greater than one corridor width from the response corridor of 63-77 *g*. The results are shown in Table A17, Appendix D.

The Pelvis Test 4 biofidelity rating is 0, which corresponds to an ISO classification of "poor".

Pelvis Test 7

This test requires a Heidelberg-type rigid wall sled impact at 6.8 m/s. Targets are given for the peak pelvic force and the peak pelvic acceleration.

All of the peak pelvis force responses were greater than one corridor width of the 6.4-7.8 kN response corridors. Ten of the peak pelvic accelerations were within the 63-77 g response corridor and three accelerations were within one corridor width of the response corridor. The results are shown in Table A18, Appendix A.

The Pelvis Test 7 biofidelity rating is 3.9, which corresponds to an ISO classification of "marginal".

Pelvis Test 10

This test requires a WSU-type rigid wall sled impact at 6.8 m/s (Figure 4). Targets are given for the pelvic plate force and the peak lateral pelvic acceleration.

Six of the pelvis forces were greater than one corridor width of the response corridors. Three of the pelvis forces were within one corridor width of the response corridor. The pelvic accelerations were all within one corridor width of the 85-115 *g* corridor. The results are shown in Figure A10 and Table A19, Appendix A.

The Pelvis Test 10 biofidelity rating is 3.1, which corresponds to an ISO classification of "unacceptable".

Overall Pelvis Biofidelity

The overall pelvis biofidelity rating is 5.1, which corresponds to an ISO classification of "fair".

REPEATABILITY AND REPRODUCABILITY

A series of verification tests were performed for the purpose of assessing the repeatability of the WorldSID dummy. Tests were performed as per ISO 15830-2 and generally included a minimum sample of three trials. Analysis was performed using the coefficient of variation (CV) as a figure of merit. The CV is defined as the standard deviation of the samples divided by the sample mean, and is expressed as a percentage. Responses, which have a CV of 3% or less, are commonly considered as having an excellent level of repeatability whereas a value of 10% and above is considered to have a poor level of repeatability.

The WorldSID production dummy test results include a combination of repeat tests performed on the same

dummy (repeatability) and tests performed on different dummies (reproducibility). The CV values from these tests should be considered representative of the WorldSID repeatability and reproducibility. . Results are presented by body region in Tables 2- 8.

Table 2.
Head Repeatability and Reproducibility

Response Measurements	CV (%)
Lateral drop peak resultant CG acceleration	5.6
Frontal drop peak resultant CG acceleration	4.3

Table 3.
Neck Repeatability and Reproducibility

Response Measurements	CV (%)
Peak flexion angle	4.1
Peak M_x	4.7

Table 4.
Shoulder Repeatability and Reproducibility

Response Measurements	CV (%)
Pendulum force	4.2
Peak shoulder deflection	4.9

Table 5.
Thorax Repeatability and Reproducibility (with arm)

Response Measurements	CV (%)
Pendulum force	4.1
Upper spine T4 lateral acceleration	6.7
Lower spine T12 lateral acceleration	5.6
Thorax rib 1 deflection	7
Thorax rib 2 deflection	4.3
Thorax rib 3 deflection	4

Table 6.
Thorax Repeatability and Reproducibility (without arm)

Response Measurements	CV (%)
Pendulum force	4.7
Upper spine T4 lateral acceleration	8.1
Lower spine T12 lateral acceleration	10.7
Thorax rib 1 deflection	6.4
Thorax rib 2 deflection	4.6
Thorax rib 3 deflection	5.5

Table 7.
Abdomen Repeatability and Reproducibility

Response Measurements	CV (%)
Pendulum force	3.9
Peak acceleration of the lower spine T12	6.3
Abdomen rib 1 deflection	3.9
Abdomen rib 2 deflection	4.4

Table 8.
Pelvis Repeatability and Reproducibility

Response Measurements	CV (%)
Pendulum force	5.5
Pelvis acceleration	6.5

SIDE IMPACT DUMMY BIOFIDELITY COMPARISON

The biofidelity rating of the WorldSID is compared to the USDOT-SID, ES-2re, Eurosid-1, ES-2, and BioSID in Table 9. It should be noted that not all tests were conducted for each dummy. As previously mentioned, tests that are not conducted are not

included in the biofidelity rating. This may influence the body region and overall biofidelity ratings.

The overall biofidelity rating of the WorldSID dummy is 8.0, which corresponds to an ISO classification of "good". The biofidelity ratings of the WorldSID body regions are shown in Appendix B.

Table 9.
Mid Male Side Impact Dummy Biofidelity Comparison

	Biofidelity rating						
	Head	Neck	Shoulder	Thorax	Abdomen	Pelvis	Overall
WorldSID production version	10	5.3	10	8.2	9.3	5.1	8
BioSID	6.7	6.7	7.3	6.3	3.8	4	5.7
ES-2	5	4.4	5.3	5.2	2.6	5.3	4.6
EuroSID-1	5	7.8	7.3	5.4	0.9	1.5	4.4
ES-2RE	5	4.2	4.5	4	4.1	3.2	4.2
USDOT-SID	0	2.5	0	3.1	4.4	2.5	2.3

CONCLUSIONS

This paper presents the results of a biofidelity, repeatability and reproducibility evaluation of the WorldSID production dummy conducted by the WorldSID Task Group.

Based on the results presented in this paper the following observations have been made:

1) The WorldSID dummy has the highest ISO biofidelity rating (8.0) of the existing mid male side impact dummies.
2) The WorldSID demonstrates good repeatability and reproducibility. The majority of the measurements compared have a CV of 6% or less.

ACKNOWLEDGEMENTS

The Task Group would like to thank Transport Canada, Ford Motor Company and the National Highway Traffic Safety Administration for sponsoring biofidelity testing. We would also like to acknowledge PMG Technologies, Hollie Pietsch, and Jim Stricklin for their dedication to the WorldSID evaluation.

REFERENCES

1. ISO/TC22/SC12/WG5 N542, 36th Meeting, November 5-6, 1997, Orlando, Resolution 1.
2. Side Impact Dummy 50th Percentile Male, 49 Code of Federal Regulations, Part 572, Subpart F.
3. Roberts, A.K., M.C. Beusenberg, D. Cesari, K.-P. Glaeser "The Biofidelity of the Production Version of the European Side Impact Dummy EUROSID-1. Experimental Safety Vehicles, 1991.
4. Byrnes Katie; Abramczyk Joseph; Berliner Jeff; Irwin Annette; Jensen Jack; Kowsika Murthy; Mertz Harold J; Rouhana Stephen W; Scherer Risa; Shi Yibing; Sutterfield Aleta; Xu Lan; Tylko Suzanne; Dalmotas Dainius, "ES-2 Dummy Biomechanical Responses", Stapp Car Crash Journal, Volume 46, pp. 353-396, Paper #2002-22-0018, 2002.
5. ES-2re Side Impact Crash Test Dummy, 50th Percentile Adult Male, 49 Code of Federal Regulations, Part 572, Subpart U.
6. Side Impact Hybrid Dummy 50th Percentile Male, 49 Code of Federal Regulations, Part 572, Subpart M.
7. Michael S. Beebe, “What is Biosid?” SAE International Congress, 1990.
8. ISO/TC22/SC12/WG5, Technical Report 9790 – Road Vehicles – Anthropomorphic Side Impact Dummy – Lateral Impact Response Requirements to Assess the Biofidelity of the Dummy, 2000.
9. ISO15830-2, Road Vehicles – Design and Performance Specifications for the WorldSID 50th Percentile Male Side Impact Dummy – Part 2: Mechanical Subsystems, 2005.

APPENDIX A

Table A1.
Head test 1 - 200 mm rigid lateral test results

Measure	Lower bound	Upper bound	Run #1	Rating
Peak resultant acceleration (non-impacted side), left impact	100	150	141	10,0
Rating			10	
Peak resultant acceleration (non-impacted side), right impact	100	150	129	
Rating			10	

Table A2.
Neck test 1 – 7.2 g lateral sled test

Measure	Lower bound	Upper bound	Run #1	#2	#3	#4	#5	#6	Avg	Rating
Horizontal acceleration of T1 (G) CFC180	12	18	16	13	13	12	12	12	13	7,4
Rating			10	10	10	10	10	10	10	
Horizontal displacement of T1 relative to sled (mm)	46	63	59	54	57	54	52	57	55,5	
Rating			10	10	10	10	10	10	10	
Horizontal displacement of head CG T1 (mm)	130	162	124	121	124	131	125	134	126,5	
Rating			5	5	5	10	5	10	6,7	
Vertical displacement of head CG relative to T1 (mm)	64	94	66	57	63	61	52	65	60,7	
Rating			10	5	5	5	5	10	6,7	
Time of peak head excursion (sec)	0,159	0,175	0,122	0.113	0,120	0,120	0,113	0,120	0,118	
Rating			0	0	0	0	0	0	0	
Lateral acceleration of head CG (G) CFC1000	8	11	11	12	12	11	11	12	11,5	
Rating			10	5	5	10	10	5	7,5	
Vertical acceleration of head CG (G) CFC1000	8	10	9	10	9	9	9	9	9,2	
Rating			10	10	10	10	10	10	10	
Head flexion angle (degrees)	44	59	51	50	51	47	44	48	48,5	
Rating			10	10	10	10	10	10	10	
Head twist angle (degrees)	32	45	22	21	23	22	22	22	22,0	
Rating			5	5	5	5	5	5	5	

Table A3.
Neck test 2 – 6.7 g lateral sled test

Measure	Lower bound	Upper bound	Run #1	#2	#3	Avg	Rating
Head flexion angle (degrees)	40	50	Nm	Nm	Nm		2,0
Rating			0	0	0	0	
Peak moment A-P axis at OC, Mx (Nm)	40	50	13	13	15	13,7	
Rating			0	0	0	0	
Peak moment R-L axis OC, M y (Nm)	20	30	4	4	3	3,7	
Rating			0	0	0	0	
Peak twist moment, M z (Nm)	15	20	8	9	9	8,7	
Rating			0	0	0	0	
Peak shear force OC, F y (N)	750	850	427	428	428	427,7	
Rating			0	0	0	0,0	
Peak tension force OC, F z (N)	350	400	384	363	397	381,3	
Rating			10	10	10	10	
Peak A-P shear force, F x (N)	325	375	63	55	63	60,3	
Rating			0	0	0	0,0	
Peak resultant head acceleration (G)	18	24	14	15	15	14,7	
Rating			5	5	5	5,0	

Table A4.
Neck test 3 – 12.2 g lateral sled test

Measure	Lower bound	Upper bound	Run #1	#2	#3	#4	#5	#6	Avg	Rating
Peak lateral acceleration of T1 (G)	17	23	20	18	19	17	18	17	18,2	7,2
Rating			10	10	10	10	10	10	10,0	
Peak lateral acceleration of head CG (G)	25	47	14	14	14	13	13	13	13,5	
Rating			5	5	5	5	5	5	5,0	
Peak horizontal displacement of head CG relative to sled (G)	185	226	213	202	207	211	214	210	209,5	
Rating			10	10	10	10	10	10	10,0	
Peak flexion angle (degrees)	62	75	64	63	64	58	59	58	61,0	
Rating			10	10	10	5	5	5	7,5	
Peak twist angle (degrees)	62	75	28	26	27	25	25	26	26,2	
Rating			0	0	0	0	0	0	0,0	

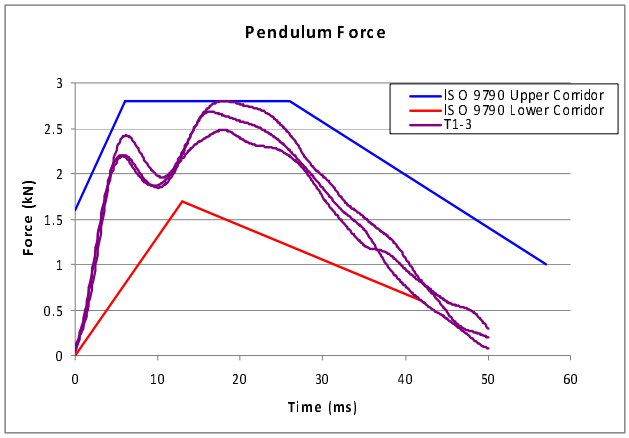

Figure A1 - Shoulder test 1 - pendulum force.

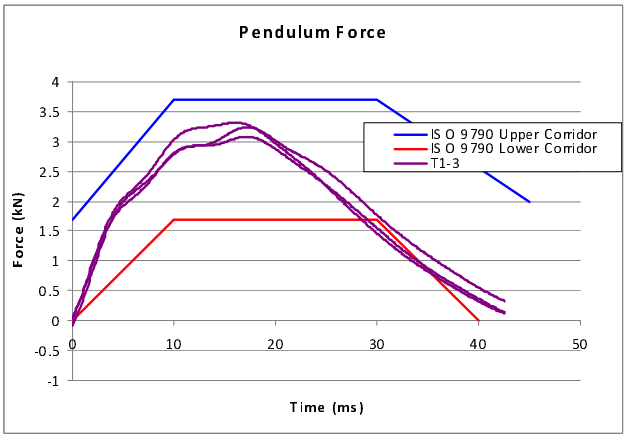

Figure A2 - Thorax test 1 - pendulum force.

Table A5.
Shoulder test 1 – 4.5 m/s pendulum test results

Measure	Lower bound	Upper bound	Run #1	Run #2	Run #3	Run Avg	Rating
Shoulder pendulum force (N)	Plot	Plot	Plot	Plot	Plot	Plot	10
Rating			10	10	10	10	
Peak shoulder deflection (mm)	34	41	39	37	40	39	
Rating			10	10	10	10,0	

Table A6.
Shoulder test 2 – 7.2 G sled test results

Measure	Lower bound	Upper bound	Run #1	Run #2	Run #3	Run #4	Run #5	Run #6	Run Avg	Rating
Horizontal acceleration T1 (g)	12	18	16	13	13	12	12	12	13,0	10,0
Rating			10	10	10	10	10	10	10	
Horizontal displacement T1 relative to sled (mm)	46	63	59	54	57	54	52	53	54,8	
Rating			10	10	10	10	10	10	10	

Table A7.
Shoulder test D3 - 12,2 G sled test results

Measure	Lower bound	Upper bound	Run #1	Run #2	Run #3	Run #4	Run #5	Run #6	Run Avg	Rating
Peak lateral acceleration T1 (G)	17	23	20	18	19	17	18	17	18,2	10,0
Rating			10	10	10	10	10	10	10,0	

Table A8.
Thorax test 1 - test results

Measure	Lower bound	Upper bound	Run #1	Run #2	Run #3	Run Avg	Rating
Pendulum force (kN)	Plot	Plot	Plot	Plot	Plot	Plot	7,8
Rating			10	10	10	10,0	
T1 lateral acceleration (G)	Plot	Plot	Plot	Plot	Plot	Plot	
Rating			5	5	5	5	

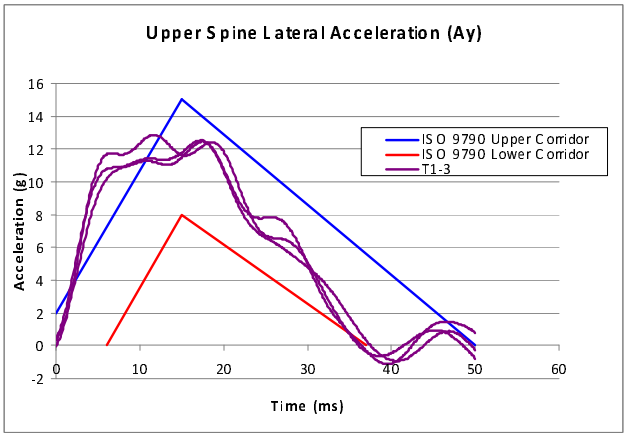

Figure A3 - Thorax test 1 - T1 lateral acceleration.

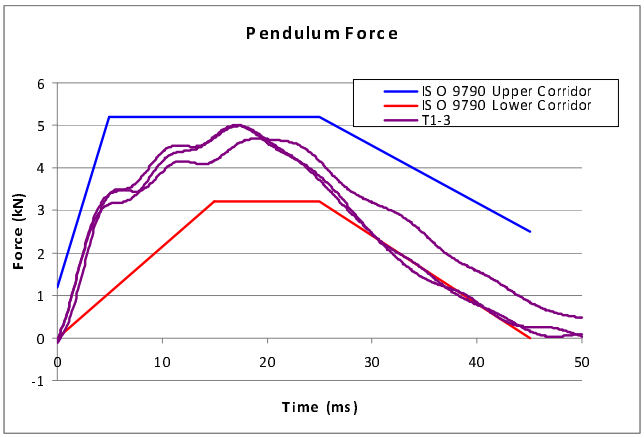

Figure A4 - Thorax test 2 - pendulum force.

Table A9.
Thorax test 2 – 6.7 m/s test results

Measure	Lower bound	Upper bound	Run				Rating
			#1	#2	#3	Avg	
Pendulum force (kN)	Plot	Plot	Plot	Plot	Plot	Plot	10,0
Rating			10	10	10	10,0	

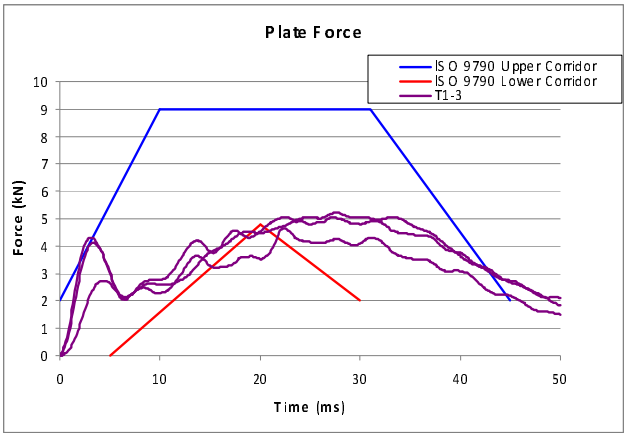

Figure A5 - Thorax test 3 - plate force.

Table A10.
Thorax test 3 – 1 m drop test results

Measure	Lower bound	Upper bound	Run				Rating
			#1	#2	#3	Avg	
Thorax plate force (kN)	Plot	Plot	Plot	Plot	Plot	Plot	8,3
Rating			10	10	10	10,0	
Peak deflection impacted rib (mm)	26	38	41	42	30	37	
Rating			5	5	10	6,7	

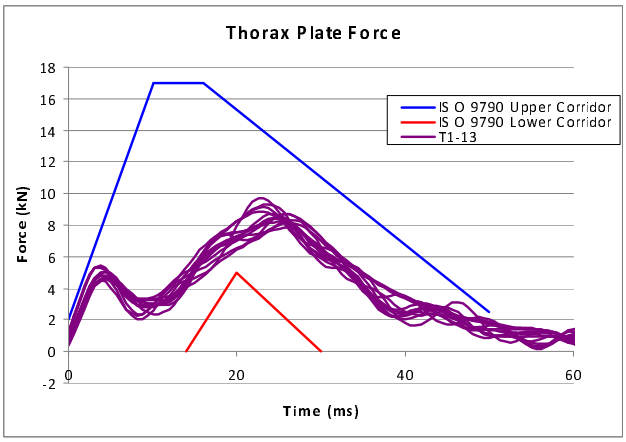

Figure A6 - Thorax test 5 – plate force.

Table A11.
Thorax test 5 – 6.8 m/s sled test results

Measure	Lower bound	Upper bound	Run		Rating
			1 to 13	Avg	
Thorax plate force (kN)	Plot	Plot	Plot	Plot	6,4
Rating			All tests 10	10,0	
Peak upper spine lateral acceleration (G)	82	122		39	
Rating			2 tests 5, 11 tests 0	0,8	
Peak lower spine lateral acceleration (G)	71	107		52,0	
Rating			All tests 5	5,0	
Peak lateral acceleration impacted rib (G)	64	100		86	
Rating			All tests 10	10	

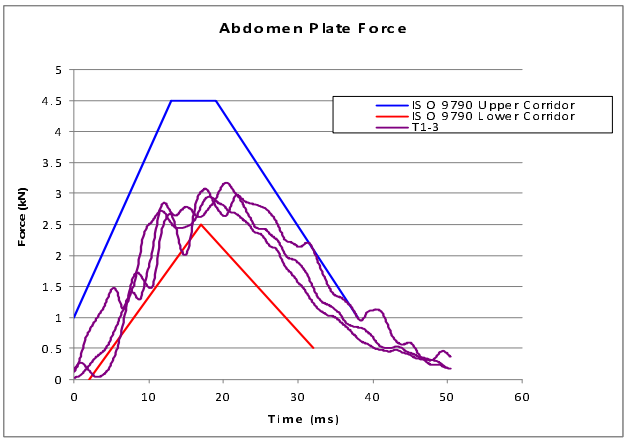

Figure A7 - Abdomen test 1 – armrest force.

Table A12.
Abdomen test 1 - 1 m rigid armrest test results

Measure	Lower bound	Upper bound	Run				Rating
			#1	#2	#3	Avg	
Armrest force (kN)			See plot	See plot	See plot		9,0
Rating			10	10	10	10,0	
T12 lateral acceleration (G)	29	35	32	34	35	34	
Rating			10	10	10	10,0	
Peak acceleration of impacted rib (mm)	100	125	127	193	130	150	
Rating			5	0	5	3,3	
Abdomen penetration (mm)	41		51	51	47	50	
Rating			10	10	10	10,0	

Figure A8 - Abdomen test 3 - plate force.

Table A13.
Abdomen test 3 – 6.8 m/s plate force sled test results

Measure	Lower bound	Upper bound	Run		Rating
			1 to 9	Avg	
Abdomen plate force (kN)			See plot		10,0
Rating			10	10,0	

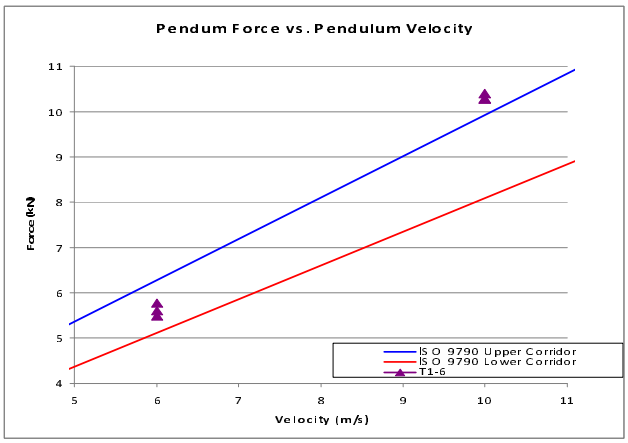

Figure A9 - Pelvis test 1 and 2 - pendulum force.

Table A14.
Pelvis test 1 – 6.0 m/s pendulum test results

Measure	Lower bound	Upper bound	Run				Rating
			#1	#2	#3	Avg	
Pendulum force (kN)	Plot	Plot	Plot	Plot	Plot	Plot	10,0
Rating			10	10	10	10,0	

Table A15.
Pelvis test 2 – 10.0 m/s pendulum test results

Measure	Lower bound	Upper bound	Run				Rating
			#1	#2	#3	Avg	
Pendulum force (kN)	Plot	Plot	Plot	Plot	Plot	Plot	5,0
Rating			5	5	5	5,0	

Table A16.
Pelvis test 3 – 0.5 m acceleration drop test results

Measure	Lower bound	Upper bound	Run				Rating
			#1	#2	#3	Avg	
Peak pelvis acceleration (G)	37	45	30	31	30	30	5,0
Rating			5	5	5	5,0	

Table A17.
Pelvis test 4 – 1.0 m rigid drop test results

Measure	Lower bound	Upper bound	Run				Rating
			#1	#2	#3	Avg	
Peak pelvis acceleration (G)	63	77	46	45	42	44	0,0
Rating			0	0	0	0	

Table A18.
Pelvis test 7 – 6.8 m/s rigid sled test results

Measure	Lower bound	Upper bound	Run		Rating
			1 to 13	Avg	
Pelvis plate force (kN)	6,4	7,8		12,1	3,9
Rating			0 all tests	0,0	
Peak pelvis acceleration (G)	63	77		66,1	
Rating			5 three tests, 10 ten tests	8,4	

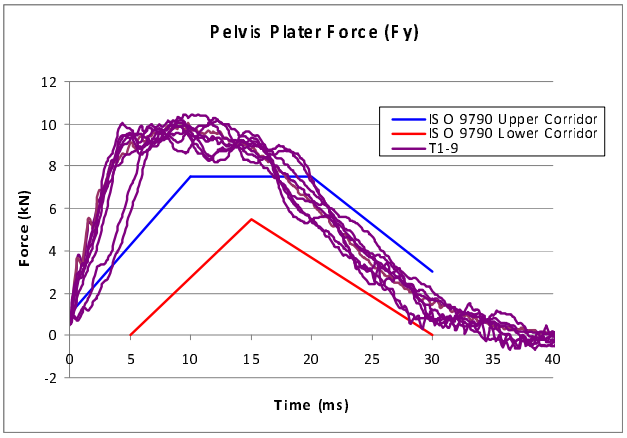

Figure A10 - Pelvis test 10 - pelvis plate force.

Table A19.
Pelvis test 10 – 6.8 m/s Wayne State rigid sled test results

Measure	Lower bound	Upper bound	Run		Rating
			1 to 9	Avg	
Pelvis plate force (kN)	Plot	Plot	Plot	Plot	3,1
Rating			4 tests 5, 5 tests 0	1,7	
Peak pelvis acceleration (G)	85	115		50,0	
Rating			All tests 5	5,0	

APPENDIX B

Table B1.
WorldSID Biofidelity Ratings by Test and Body Region

Body Test No. & Test Description	Test Weighting, $V_{i,j}$	Test Biofidelity
Head Test 1 200 mm Rigid Drop	8	10.0
Head Test 2 1200 mm Padded Drop	4	N. M.
	Head Biofidelity, B1	**10.0**
Neck Test 1 7.2 G Sled Impact	7	7.4
Neck Test 2 6.7 G Sled Impact	6	2.0
Neck Test 3 12.2 G Sled Impact	3	7.2
	Neck Biofidelity, B2	**5.3**
Shoulder Test 1 4.5 m/s Pendulum	6	10.0
Shoulder Test 2 7.2 G Sled Impact	5	10.0
Shoulder Test 3 12.2 G Sled Impact	3	10.0
Shoulder Test 4 8.9 m/s Padded Sled	7	N. M.
	Shoulder Biofidelity, B3	**10.0**
Thorax Test 1 4.3 m/s Pendulum	9	7.8
Thorax Test 2 6.7 m/s Pendulum	9	10.0
Thorax Test 3 1.0 m Rigid Drop	6	8.3
Thorax Test 4 2.0 m Padded Drop	5	N. M.
Thorax Test 5 6.8 m/s Rigid Sled	7	6.4
Thorax Test 6 8.9 m/s Padded Sled	7	N. M.
	Thorax Biofidelity, B4	**8.2**
Abdomen Test 1 1.0 m Rigid Drop	7	9.0
Abdomen Test 2 2.0 m Rigid Drop	6	N. M.
Abdomen Test 3 6.8 m/s Rigid Sled	3	10.0
Abdomen Test 4 8.9 m/s Rigid Sled	3	N. M.
Abdomen Test 5 8.9 m/s Padded Sled	7	N. M.
	Abdomen Biofidelity, B5	**9.3**
Pelvis Test 1 6.0 m/s Pendulum Impact	8	10.0
Pelvis Test 2 10.0 m/s Pendulum Impact	9	5.0
Pelvis Test 3 0.5 m Rigid Drop	4	5.0
Pelvis Test 4 1.0 m Rigid Drop	4	0.0
Pelvis Test 5 2.0 m Padded Drop	3	N. M.
Pelvis Test 6 3.0 m Padded Drop	5	N. M.
Pelvis Test 7 6.8 m/s Rigid Sled	8	3.9
Pelvis Test 8 8.9 m/s Rigid Sled	7	N. M.
Pelvis Test 9 8.9 m/s Padded Sled	8	N. M.
Pelvis Test 10 6.8 m/s Rigid Sled	3	3.1
Pelvis Test 11 8.9 m/s Rigid Sled	3	N. M.
Pelvis Test 12 8.9 m/s 15 psi Padded Sled	3	N. M.
Pelvis Test 13 8.9 m/s 23 psi Padded Sled	7	N. M.
	Pelvis Biofidelity, B6	**5.1**
N.M. = Not Measured		
	WorldSID With Blue Ribs Overall Biofidelity	**8.0**

COMPARISON OF WORLDSID AND ES-2RE BIOFIDELITY USING AN UPDATED BIOFIDELITY RANKING SYSTEM

Heather Rhule
Kevin Moorhouse
Bruce Donnelly
National Highway Traffic Safety Administration
United States
Jim Stricklin
Transportation Research Center Inc.
United States
Paper Number 09-0563

ABSTRACT

In 2002 the biofidelity of the SID-HIII, ES-2 and prototype WorldSID side impact dummies were compared using a new Biofidelity Ranking System (BRS or BioRank) [Rhule, 2002]. The current study introduces updates made to the BRS and assesses the biofidelity of the ES-2re and the latest WorldSID side impact dummies. Approximately twelve drop tests, ninety pendulum tests and forty sled tests with a dual-occupant buck were performed with the ES-2re and WorldSID dummies, including lateral and oblique shoulder impactor tests [Bolte, 2003]; lateral and oblique thorax impactor tests [Shaw, 2006]; five Maltese sled tests [Maltese, 2002]; and several drop, pendulum and sled tests from ISO 9790 [ISO, 1999]. Test condition weight factors used previously have been eliminated in the updated BRS, giving all test conditions equal value. A scale for quality of the biofidelity ranking value, B, is demonstrated by comparing individual human subject responses to response targets and generating individual cadaver B values for both External and Internal Biofidelity. Having a scale of B values for the subject responses used to create the target response will give the user a metric for understanding the quality of a dummy's biofidelity. Finally, the sensitivity of the biofidelity ranking value, B, is illustrated using data from repeated tests on multiple WorldSID dummies. The sensitivity analysis will help the user understand if the biofidelity of two (or more) dummies is similar or different. This recent data and updated BRS show that the WorldSID dummy exhibits improved overall biofidelity over the ES-2re. Results of the updated BRS show that the WorldSID and ES-2re demonstrated Internal Biofidelity values of 1.2 and 1.7, respectively; the WorldSID demonstrated an External Biofidelity score of 2.2 while the ES-2re demonstrated an External Biofidelity score of 2.8.

INTRODUCTION

In 2002 a new Biofidelity Ranking System (BRS) was introduced and used to compare the biofidelity of the SID-HIII, ES-2 and prototype WorldSID side impact dummies [Rhule, 2002]. Since then the BRS has been used to evaluate several side impact dummies and has received constructive critique from the biomechanics community [Irwin, 2003]. Criticisms included use of less biofidelic dummies for evaluation of the relevance of test conditions and assignment of test condition weights, a desire for further explanation of the meaning of the biofidelity "B" values, and lack of analysis of the sensitivity of the B values. This paper addresses each of these concerns by eliminating test condition weights from the updated BRS, providing further analysis of the statistical meaning of the B values and a scale for interpreting the quality of biofidelity from the B values, as well as providing analysis of the significant difference between two B values. This paper discusses the updates that have been made to the Biofidelity Ranking System and presents results of its application to recent test data from two side impact dummies, the ES-2re and the current production WorldSID dummy.

The evaluation and modification of the WorldSID dummy has been accomplished with the collaboration and support of the WorldSID Organization. Recent changes to the dummy include relocating the pelvis data acquisition docking station, a change in rib damping material and a change in IRTRACC mounting range-of-motion.

BACKGROUND

The purpose of the Biofidelity Ranking System is to objectively quantify response differences between human subjects and crash test dummies to evaluate how well a dummy replicates the behavior and response of a human. In order to evaluate a dummy's

biofidelity, it must be subjected to a set of tests that have associated human subject response targets (also referred to as biofidelity corridors). The set of tests and response measurements (and associated human response targets) to be used for evaluating biofidelity are selected by the analyst prior to utilizing the objective BRS and will affect results.

The fundamental nature of the Biofidelity Ranking System lies in the comparison of each dummy response to its corresponding mean human subject response. The Response Measurement Comparison Value (R) for each required measurement is calculated as a ratio of the cumulative variance of the dummy response relative to the mean cadaver response (DCV) over the cumulative variance of the mean cadaver response relative to the mean plus one standard deviation (CCV), as described in Rhule et al, 2002. A lower DCV/CCV ratio indicates a closer dummy response relative to that of the mean cadaver, and better dummy biofidelity.

The BRS calculates ranks for External Biofidelity and Internal Biofidelity by first calculating the DCV/CCV ratio (R) for each response measurement and then taking its square root; then those values are averaged for various test conditions and then for various body regions. External Biofidelity describes the ability of a dummy to replicate human loading of a test environment. Signals which measure the response of the test environment due to its interaction with the dummy (or human subject) are used to calculate External Biofidelity ranks. Internal Biofidelity describes the ability of a dummy to duplicate the responses of human subjects. Signals which measure the response of the dummy (or human subject) due to its interaction with the test environment are used to calculate Internal Biofidelity ranks.

UPDATES TO THE BIOFIDELITY RANKING SYSTEM

Over the last several years the Biofidelity Ranking System has been used to evaluate the biofidelity of many dummies. As with any state of the art system evolution is inevitable. As a result of its development, the following updates have been incorporated into the evaluation of side impact dummy biofidelity using the BRS.

Test Condition Weights Removed

The Test Condition Weights included in the original BRS were based on a combination of 1) the number of subjects used to create the human subject response target (Subject Score) and 2) how well the biofidelity test represented the intended crash environment (Test Relevance Score). The equation to calculate the Test Condition Weights subjectively added one-third of the Subject Score to two-thirds of the Test Relevance Score.

The Test Relevance Score indicates how well each biofidelity test represents regulatory-type crash tests. The biofidelity tests whose dummy responses are equal to or less than the dummy response in crash tests receive higher Test Relevance Scores. Some in the biomechanics community argued that the dummies used (SID-HIII and ES-2) to evaluate the relevance of the biofidelity tests were not very biofidelic, which invalidated the Test Condition Weights.

The assessment of subject sample size and test relevance in this paper was performed during the data selection process and is not part of the completely objective BRS. The Test Condition Weights have been eliminated from the BRS. All tests used for evaluating dummy biofidelity are now of equal value.

Biofidelity Rank Calculation

Without the Test Condition Weights, the equation for calculating the biofidelity ranks is different from that presented in 2002. In the updated BRS, External and Internal Biofidelity ranks are calculated according to Equation 1. The External and Internal Biofidelity ranks are each made up of an average of ranks from each body region (i in Equation 1). The body regions include the head, neck, shoulder, thorax, abdomen and pelvis. Each body region rank is made up of an average of ranks from each corresponding test condition (j in Equation 1). Each test condition rank (for a given body region) is made up of an average of the square root of the response measurement comparison values (R in Equation 1) for each measurement required (k in Equation 1) for that test condition. Figure 1 illustrates the sequence of averages that result in the External (or Internal) Biofidelity ranks.

INTERPRETING THE BIOFIDELITY VALUES

What do the biofidelity values (B-values) mean? Albeit a lower value of B indicates better biofidelity, but what do the numbers represent? How different do the numbers have to be to indicate a significant difference in biofidelity?

$$B = \frac{\sum_{i=1}^{l} \left(\frac{\sum_{j=1}^{m} \left(\frac{\sum_{k=1}^{n} \sqrt{R_{i,j,k}}}{n} \right)}{m} \right)}{l} \qquad (1).$$

where

B= biofidelity rank, either External or Internal
R = Response Measurement Comparison Value
i = body region
j = test condition
k = response measurement
l = number of body regions
m = number of test conditions
n = number of response measurements per test condition

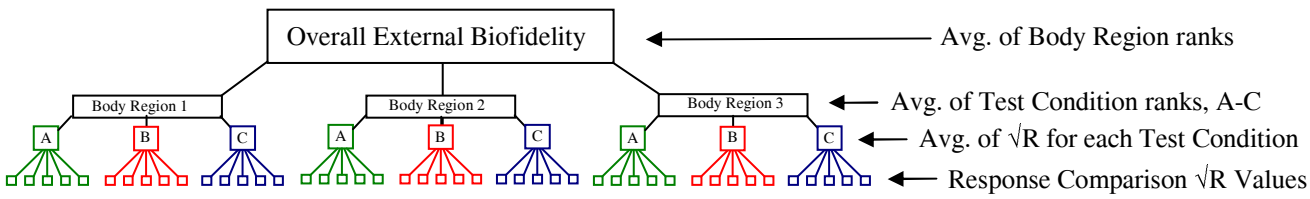

Figure 1. Schematic showing the sequence for averaging √R values.

B-value Scale

It is important to understand what a BioRank score actually means. For any given response measurement in a biofidelity test, a DCV/CCV ratio, or R value, is calculated and its square root is taken so that it represents multiples of a cumulative standard deviation. A value of $\sqrt{R} < 1$ would indicate that the dummy response is less than one cumulative standard deviation different from the cadaver mean response for that set of cadaver test data. Similarly, a value of $\sqrt{R} < 2$ would indicate that the dummy response is within two cumulative standard deviations of the cadaver mean and a value of $\sqrt{R} < 3$ indicates the dummy is within three cumulative standard deviations of the cadaver mean response. This assumes that the cadaver data set is a representative sample of the cadaver population and is normally distributed. Because cadaver sample size is usually rather small and the variation in the cadaver data set is due to both natural human variation as well as test-to-test variation, there is no guarantee that this assumption is valid.

A methodology for developing a scale for the BioRank was developed by Rhule [Rhule 2002]. In that study a set of external cadaver responses was analyzed by comparing one cadaver from the set of cadavers to the mean and standard deviation of the remaining cadavers in the set. This approach is analogous to comparing a dummy response to a cadaver mean and standard deviation but calculates a $\sqrt{R}$ value for each cadaver in the data set and allows for the assessment of the distribution statistics for the sample of cadaver responses. If the cadaver data is normally distributed then it is reasonable to use values of $\sqrt{R}$ = 1, 2 and 3, etc., as measures of dummy similarity to the cadaver mean response. For a value of $\sqrt{R} < 1$ the dummy would be as similar to the mean response as 68% of cadavers, $1 < \sqrt{R} \leq 2$ would be as similar to the mean response as the next 27% of cadavers, $2 < \sqrt{R} \leq 3$ would be as similar as the next 4% of cadavers, and $\sqrt{R} > 3$ would only be as similar as 1% of cadavers. This basic approach was used again to evaluate the distribution of cadaver responses for additional channels of both external and internal responses for the Maltese data [Maltese, 2002] and the Shaw data [Shaw, 2006].

This more extensive analysis has a few differences from the analysis presented in Rhule's 2002 study. In both studies the Maltese data for the padded high-speed flat wall sled tests (PHF) were used because there were seven subjects tested under that condition and this provided a reasonably large sample size. After the publication of the 2002 paper, Maltese re-analyzed his data and made it available on the NHTSA website. This re-analysis included phase shifting of the data to minimize the cumulative variance with the idea of eliminating time shifts due to subject "fatness" and "thinness". This phase-shift corrected data was used in the analysis presented here. In addition to analyzing external data for thorax, abdomen and pelvis load force, the internal responses for chest-band deflection and lower spine acceleration were also analyzed. In this study the Shaw pendulum test data was also analyzed which included seven subjects (Note: the force data was re-

analyzed for this paper due to an error in the inertial mass of the impactor). For this data the external pendulum force in both lateral and oblique tests were analyzed as well as the internal chest-band deflection.

The results for the analysis of the $\sqrt{R}$ values for the selected test data from Maltese and Shaw are shown in Table 1. Note that the subject identification numbers for the subjects are also presented in the table. The Maltese sled data for padded high-speed flat wall tests was analyzed for the thorax, abdomen and pelvis load forces, for the upper and middle chest-band deflection and the lower spine y acceleration. The results of Table 1 show that although the $\sqrt{R}$ values vary, the average values for each channel are approximately 1.0 and a dummy with a *B*-value of ≤1.0 has a response that is less than or equal to one cumulative standard deviation different from the mean cadaver response. This is true for both external measures and internal measures. The Shaw data from lower energy pendulum tests in lateral and oblique impacts was analyzed for external force and for internal chest-band deflection. The results of Table 1 show that, similar to the Maltese data, the Shaw data has values of $\sqrt{R}$ that average approximately 1.0 and that a dummy with a *B*-value of ≤1.0 has a response that is less than or equal to one cumulative standard deviation different from the mean cadaver response. A set of χ^2 goodness-of-fit tests on the channels shown in Table 1 indicate that eight of the twelve channels do not reject the hypothesis that they are from a normal distribution at the $\alpha = 0.05$ level [Mathworks, 2008]. Although there are only seven subjects, this provides some limited confidence that the cadaver data is normally distributed.

This analysis provides support for a biofidelity ranking metric as shown in Table 2. This scoring metric is continuous and directly related to the normal distribution statistics of multiples of standard deviation. This metric can also be used to compare and contrast the responses of different dummies to a cadaver data set and, without too much risk, to compare different dummies and different cadaver data sets so long as the assumption of a normal distribution within the cadaver populations is valid.

Table 1.
$\sqrt{R}$ values for selected cadaver to cadaver mean response data

	Maltese Data							
	3320	3321	3323	3580	3581	3586	3589	Channel Average
PHF Thorax Force-external	1.16	1.03	1.97	0.55	0.92	1.21	0.55	1.06
PHF Abdomen Force-external	0.75	0.75	1.27	0.77	1.39	0.84	1.67	1.06
PHF Pelvis Force-external	0.75	1.19	1.07	1.03	1.05	0.79	1.61	1.07
Total External Average								1.06
PHF Lower Spine-internal	0.63	2.29	1.14	0.68	0.93	0.63	1.13	1.06
PHF Upper Chest Half Deflection-internal	2.67	0.43	0.41	1.45	1.26	0.44	0.55	1.03
PHF Lower Chest Half Deflection-internal	1.19	1.14	0.36	1.27	1.11	1.55	0.74	1.05
Total Internal Average								1.05
	Shaw Data							
	503	504	505	506	507	601	602	
Lateral Force-external	1.41	0.80	1.01	1.16	0.47	0.80	1.75	1.06
Oblique Force-external	0.98	1.21	1.92	0.42	1.37	0.95	0.43	1.04
Total External Average								1.05
Lateral Deflection-internal	0.43	0.31	0.33	1.23	1.02	1.34	2.46	1.02
Oblique Deflection-internal	0.72	1.92	2.53	0.47	0.50	0.63	0.44	1.03
Total Internal Average								1.02

Table 2.
Biofidelity Scale

$B \leq 1$	within one standard deviation of the mean cadaver response
$1 < B \leq 2$	between one and two standard deviations of the mean cadaver response
$2 < B \leq 3$	between two and three standard deviations of the mean cadaver response
$B > 3$	more than three standard deviations from the mean cadaver response

B-value Sensitivity

It is important to know the sensitivity of the B-value with respect to the response of the post-mortem human subjects (PMHS) to which it is being compared. This is especially important if two different dummies, such as the WorldSID and the ES-2re, are being compared to the same PMHS data set and the resulting B-values for the two dummies are similar but not exactly the same – is the difference significant? Stated a different way, if two dummies have B-values separated by a small amount, such as $\Delta B = 0.2$ for example, is one actually more biofidelic than the other?

The sensitivity of the B-values can be assessed by studying the B-values calculated separately for two of the same dummy type, i.e., reproducible dummies, compared to the same PMHS data set. In this study two different WorldSID dummies that have been assessed for reproducibility and found not to be significantly different in response were subjected to multiple identical sled tests in several different configurations. The dummy responses from the repeat sled tests were used to calculate mean $\sqrt{R}$ values for each dummy in each response. In Table 3, Dummy Responses 1-22 show the mean $\sqrt{R}$ values for Dummies 1 and 2 for internal and external thorax, abdomen and pelvis measurements. A set of paired differences were then created from the mean $\sqrt{R}$ values from each configuration, and the mean and standard deviation were calculated. A critical value of difference in $\sqrt{R}$ value was calculated using the two-tailed t-statistic for the means of paired differences and a value of $p = 0.05$. The standard deviation for paired differences is

$$S_d^2 = \frac{\sum (d_i - \bar{d})^2}{n-1}$$

where S_d = standard deviation of paired differences
n = sample size
d_i = differences between paired values
$\bar{d}$ = the mean of the differences.

The critical value is found by manipulating the equation for the t-statistic for paired observations,

$$d_0 = \bar{d} - t \cdot S_d / \sqrt{n}$$

where d_0 = critical value of difference
t = the t-statistic for p=0.05 and (n-1) DOF

From this analysis we can infer that a difference larger than this critical value indicates that the biofidelity of the two dummies is not the same. Therefore, the critical difference in the B value of two dummy responses is given by:

$$\Delta B = \bar{d} - d_0$$

For the two WorldSID dummies being used as an example, Table 3 shows the means of the paired differences for each body region, the standard deviations of the paired differences, the resulting critical values of difference, d_0, and the critical values for ΔB.

The ΔB values in the last row of Table 3 range from 0.13 to 0.27 with an average value of 0.20. The internal ΔB values range from 0.13 to 0.18 with an average of 0.15 and the external ΔB values range from 0.19 to 0.27 with an average of 0.24. This indicates that for the two WorldSID dummies exposed to a set of sled tests, the sensitivity of the B-value is approximately 0.15 for internal biofidelity and 0.24 for external biofidelity with an overall average sensitivity of 0.20.

This exercise indicates that B-values that are less than or equal to 0.2 different, $\Delta B \leq 0.2$, are not significantly different and the biofidelity of two dummies or body regions being compared is essentially the same. This analysis is not a rigorous proof and to be accurate, this analysis would have to be repeated for each case; however, it serves as a general guideline for evaluating the biofidelity results for two dummies or two body regions.

Table 3.
Sensitivity results for mean √R and corresponding ΔB

Region	Thorax						Abdomen						Pelvis						
	Internal			External			Internal			External			Internal			External			
Dummy	1	2	Diff	1	2	Diff	1	2	Diff	1	2	Diff	1	2	Diff	1	2	Diff	
Response Measurements																			
1	6.200	5.857	0.343	1.300	1.200	0.100	2.673	2.817	0.143	0.657	0.543	0.113	1.560	1.490	0.070	6.971	6.543	0.429	
2	3.844	4.178	0.333	3.260	3.220	0.040	1.577	1.697	0.120	1.890	1.330	0.560	2.273	1.897	0.377	1.807	1.717	0.090	
3	0.388	1.000	0.612	4.550	3.870	0.680	1.550	2.000	0.450	0.860	1.020	0.160	1.240	1.080	0.160	2.473	1.790	0.683	
4	2.277	2.360	0.083	3.640	3.970	0.330	2.830	2.750	0.080	3.600	3.820	0.220	1.890	1.990	0.100	4.050	4.070	0.020	
5	1.623	1.687	0.063	5.620	5.560	0.060	2.810	2.960	0.150	3.000	2.660	0.340	1.340	1.180	0.160	1.480	1.720	0.240	
6	1.477	1.743	0.267	2.800	2.330	0.470				1.683	1.747	0.063				3.950	3.590	0.360	
7	1.903	2.033	0.130																
8	1.307	1.243	0.063																
9	1.357	1.313	0.043																
10	0.703	0.727	0.023																
11	0.687	0.917	0.230																
12	1.820	3.140	1.320																
13	1.260	1.570	0.310																
14	0.790	0.540	0.250																
15	1.790	1.800	0.010																
16	4.500	4.270	0.230																
17	2.760	2.670	0.090																
18	4.610	4.590	0.020																
19	0.880	0.750	0.130																
20	0.900	0.940	0.040																
21	0.430	0.530	0.100																
22	0.440	0.480	0.040																
Mean			0.215			0.280			0.189			0.243			0.173			0.304	
S			0.288			0.260			0.149			0.182			0.120			0.242	
do			0.088			0.008			0.004			0.051			0.024			0.050	Mean
Delta B			0.13			0.27			0.18			0.19			0.15			0.25	0.197

DUMMY BIOFIDELITY COMPARISON

Several drop, pendulum and sled tests were conducted with the ES-2re and production WorldSID dummies in order to assess and compare their biofidelity utilizing the updated Biofidelity Ranking System.

Selected Tests and Response Measurements

The tests selected for biofidelity evaluation, as well as which response measurements are to be used, are entirely up to the user and should be considered carefully because they will have a significant impact on the biofidelity results.

Ideally, the more response measurements and test conditions utilized for biofidelity evaluation, the better and more well-rounded the evaluation will be. However, sometimes including all possible response measurements and test conditions is not feasible. In addition, if only one body region is to be assessed, only those associated response measurements and test conditions are necessary for evaluation.

When assessing a dummy's whole-body biofidelity, rather than just one body region, each body region would ideally have the same number of test conditions and response measurements so that each body region has equal representation in the overall biofidelity rank, which is an average of the body region ranks. It is important to recognize the effect of various measurements, test conditions and body regions on biofidelity ranks since some body regions may have more test conditions than others and some test conditions may have more response measurements than others. In addition, it is possible for a body region of one dummy to have better biofidelity than that of another dummy, but have a worse overall biofidelity rank. For this reason, body region ranks should be considered carefully along with the overall biofidelity ranks.

Some of the tests used to compare dummy biofidelity in the 2002 paper were removed for the current study and other tests have been added. Tests that were removed include ISO 9790 Shoulder Test 1 and Maltese's High Speed Rigid Flat Wall sled test. ISO's Shoulder Test 1 was removed because a definition of time zero could not be obtained and the response

corridor was generated from both oblique and lateral data rather than just lateral or just oblique. The Maltese test was removed because the test condition was deemed too severe.

Tests that were added include 15° and 30° oblique shoulder [Bolte] and 30° oblique thorax [Shaw] pendulum tests so that responses in the oblique direction could be evaluated. However, displacement in the oblique shoulder tests was not used because appropriate measurements were difficult to obtain using video. In addition, Shaw's lateral thorax pendulum test was included in order to add the thorax force and deflection measurements in a lower speed pendulum test to the array of response measurements. ISO's Pelvis Test 1 was added to include a localized impact to the pelvis region. ISO's 6.8 m/s Heidelberg and 6.8 m/s Wayne State sled tests were added to include additional full-body sled tests.

Additional tests were considered for use in the current study but were not selected due to unavailability of test materials that replicate those of the original human subject studies.

In the original BRS presented in 2002, the internal ranks were calculated only from signals used in injury criteria. Internal ranks are calculated here using as many internal responses for which there are matching human subject response targets. Additional signals are used for biofidelity evaluation because ideally, a dummy would respond in every way like a human.

The set of tests and response measurements selected for comparing the ES-2re and WorldSID biofidelity in this paper (Table 4.) is quite comprehensive considering the fact that human subject data for this particular application is not vast.

Adjusted Targets

In order for the Biofidelity Ranking System to result in meaningful, quantitative comparisons, it is important that the human response targets for the measurements and tests selected for comparison consist of a common statistical definition. In the BRS, the denominator of the DCV/CCV ratio is the cumulative squared difference of the cadaver mean to the cadaver mean plus one standard deviation. For the tests selected for inclusion in this study that had some other definition for the human response target, an adjusted human response target was established.

Table 5 and Table 6 list the tests and response measurements, the reference response corridor, the method for establishing the adjusted target shown, the size assumption of the reference corridor, and the starting and ending points for the DCV/CCV calculation. It is recognized that these adjustments will have an effect on the results of the BRS ranks.

Table 4.
Test conditions and response measurements for biofidelity evaluation of the ES-2re and WorldSID dummies

Test Type	Reference	Test Description	Measurement
Pendulum	Bolte	4.4 m/s Lateral Pendulum Impact	Pendulum Force
			Shoulder Y-axis Displacement
		4.4 m/s 15º Pendulum Impact	Pendulum Y-axis Force
			Pendulum X-axis Force
		4.4 m/s 30º Pendulum Impact	Pendulum Y-axis Force
			Pendulum X-axis Force
	Shaw	2.5 m/s Lateral Pendulum Impact	Pendulum Force
			Thorax Displacement
		2.5 m/s 30º Pendulum Impact	Pendulum Force
			Thorax Displacement
Drop	ISO 9790	Head Test 1: 200 mm Rigid Lateral Head Drop	Peak Resultant Head Acceleration on opposite side of head*
Pendulum		Thorax Test 1: 4.3 m/s Pendulum Impact	T-1 Lateral Acceleration
			Pendulum Force
		Pelvis Test 1: 6 m/s Lateral Pendulum Impact	Peak Pendulum Force
Sled		Neck Test 1: 7.2 g Sled Test	Peak Horizontal Displacement of Head cg Relative to T-1
			Peak Vert. Displacement of Head cg Relative to T-1
			Peak Flexion Angle
		Neck Test 3: 12.2 g Sled Test	Peak Horizontal Displacement of Head cg Relative to Sled
			Peak Flexion Angle
		Shoulder Test 2: 7.2 g Sled Test	Peak Horizontal Displacement of T-1 Relative to Sled
		Thorax Test 5 & Pelvis Test 7: 6.8 m/s Heidelberg Sled	Thorax Plate Force
			Peak Lateral Acceleration of T-1
			Peak Lateral Acceleration of T-12
			Peak Lateral Acceleration of the Impacted Rib
			Peak Pelvis Plate Force
			Peak Pelvis Lateral Acceleration
		Abdomen Test 3 & Pelvis Test 10: 6.8 m/s Wayne State Sled	Abdomen Plate Force
			Pelvis Plate Force
			Peak Pelvis Lateral Acceleration
	Maltese	6.7 m/s Padded Flat Wall 6.7 m/s Rigid Flat Wall 6.7 m/s Rigid Abdomen Offset 6.7 m/s Rigid Pelvis Offset 8.9 m/s Padded Flat Wall	Thorax Plate Force
			T-1 Lateral Acceleration
			T-12 Lateral Acceleration
			Upper Thoracic Lateral Deflection
			Lower Thoracic Lateral Deflection
			Abdomen Plate Force
			Mid-Abdominal Deflection
			Pelvis Plate Force
			Pelvis Lateral Acceleration

*Dummy measurements were located at the center of gravity location in the head

Table 5.
Adjusted time series response targets

ISO 9790 Test Name	Thorax Test 1		Thorax Test 5	Abdomen Test 3	Pelvis Test 10
Channel Name	T1 Lateral Acceleration vs. Time	Pendulum Force vs. Time	Thorax Plate Force vs. Time	Abdomen Plate Force vs. Time	Pelvis Plate Force vs. Time
Reference PMHS Corridor Used	Irwin's [Irwin, 2008] draft proposed corridor	Irwin's [Irwin, 2008]draft proposed corridor	Petitjean's [Petitjean, 2008] draft corridor	ISO 9790	ISO 9790
Steps to Follow To Generate Mean and Standard. Deviation Targets	Extend lower corridor line from 8 ms to 0 ms. Extend lower corridor from 35 to 50 ms matching slope of upper corridor.	Remove 700 N from plateau of upper and lower corridors. Extend lower corridor line from 5 ms to 0 ms. Extend lower corridor from 30 ms to 45 ms matching slope of upper corridor.	Extend lower corridor line from 10 ms to 0 ms. Extend lower corridor from 38 to 55 ms matching slope of upper corridor.	Leave ISO corridor as-is, except extend lower corridor from 38 to 45 ms, matching slope of upper corridor.	Leave ISO corridor as-is.
Assumption of Reference Corridor Size	mean +/- 2 SD	mean +/- 2 SD	mean +/- 3 SD	mean +/- 1 SD	mean +/- 1 SD
DCV/CCV Calculation Start Point	Time zero	Time zero	Time zero	Time zero	Time zero
DCV/CCV Calculation End Point	When corridor mean reaches 10% of its max (1.24 g)	45 ms; doesn't go down to 10% of mean	When corridor mean reaches 10% of its max (0.931 kN)	45 ms; doesn't go down to 10% of mean	30 ms; doesn't go down to 10% of mean

Table 6.
Adjusted peak value response targets

ISO 9790 Test Name	Channel Name	ISO 9790 Lower Bound	ISO 9790 Upper Bound	Size Assumption of Reference Corridor	BRS Lower Bound	BRS Upper Bound
Thorax Test 5	Peak lateral acceleration of the upper spine	82 g	122 g	mean +/- 2 SD	92 g	113 g
	Peak lateral acceleration of the lower spine	71 g	107 g		80 g	98 g
	Peak lateral acceleration of the impacted rib	64 g	100 g		74 g	91 g
Pelvis Test 1	Peak pendulum force	5.11 kN	6.27 kN	mean +/- 1 SD	5.11 kN	6.27 kN
Pelvis Test 7	Peak pelvic plate force	6.4 kN	7.8 kN	mean +/- 1 SD	6.4 kN	7.8 kN
	Peak lateral pelvic acceleration	63 g	77 g	mean +/- 1 SD	63 g	77 g
Pelvis Test 10	Peak lateral pelvic acceleration	85 g	115 g	mean +/- 2 SD	93 g	108 g

Time Zero

In order to properly evaluate dummy biofidelity, it is important to define time zero, or the start of the event. If the condition of the test is such that it results in a steep increase in response over a short amount of time, but time zero is undefined, assessing whether a dummy responds similarly in time to the human will be difficult. In the case that time zero is not defined by the author of the human subject response data, a time zero definition must be established so that the dummy and human subject response target data can be located in time consistently.

Table 7 indicates the definition of time zero for each response measurement and test condition selected, as well as how the time zero definition was established.

Table 7.
Filter classes and time zero definitions

Test Description	Data Channel	Filter	Time Zero Definition
ISO 9790 Head Test 1	Peak Head Resultant Acceleration	CFC 1000	n/a
ISO 9790 Neck Test 1	All Data	Video	n/a
ISO 9790 Shoulder Test 2			n/a
ISO 9790 Neck Test 3	All Data	Video	n/a
NHTSA (Bolte) Shoulder Tests	Pendulum Force	CFC 180	Time of contact between pendulum and subject
	Shoulder Displacement	Video	
ISO 9790 Thorax Test 1	Pendulum Force	FIR 100	Last zero crossing before maximum*
	T-1 Lateral Acceleration	FIR 100	
NHTSA (Shaw) Thorax Tests	Pendulum Force	CFC 600	Time of contact between pendulum and subject
	Thorax Deflection	CFC 1000	
ISO 9790 Thorax Test 5	Thorax Plate Force	CFC 1000	5% of peak of thorax plate force is time zero (assuming thorax plate is first contact)
	Peak T-1 Lateral Acceleration	FIR 100	n/a
	Peak T-12 Lateral Acceleration	FIR 100	n/a
	Peak Impacted Rib Lateral Acceleration	FIR 100	n/a
ISO 9790 Pelvis Test 7	Peak Pelvis Plate Force	FIR 100	n/a
	Peak Pelvis Lateral Acceleration	FIR 100	n/a
ISO 9790 Abdomen Test 3	Abdomen Plate Force	CFC 1000	Last zero crossing before maximum*
ISO 9790 Pelvis Test 10	Pelvis Plate Force	CFC 1000	Last zero crossing before maximum*
	Peak Pelvis Lateral Acceleration	CFC 1000	n/a
ISO 9790 Pelvis Test 1	Peak Pendulum Force	CFC 1000	n/a
NHTSA (Maltese) Sled Tests	Thorax, Abdomen and Pelvis Plate Forces	CFC 1000	See Note
	T-1 Lateral Acceleration	CFC 180	
	T-12 Lateral Acceleration	CFC 180	
	Upper Thoracic Lateral Deflection	CFC 600	
	Lower Thoracic Lateral Deflection	CFC 600	

* Indicates that no time zero definition was given in the original work, and an assumption was made here based on figures shown in ISO 9790.

Note: For flat wall tests, time-zero is determined by initiation of arm contact on the thoracic load plate. In pelvic and abdominal offset tests, time-zero is coincident with specimen contact with the offset load plate. Contact with the load plate is determined by finding the first point in time on the load wall force-time history where the load exceeds 200 N and then incrementing backward to find the point in time where the force-time history crosses zero load (zero-crossing load). The time of occurrence of the zero-crossing load is taken to be the start of the impact event for **all** recorded signals.

Data Processing

Another vital element of evaluating dummy biofidelity is processing the dummy data identically to that of the human subjects, including setting time zero and filtering. In order to duplicate an exact biofidelity ranking number using the BRS, updated or not, the sequence of steps taken is also important. In the updated BRS, all of the transducer data from the dummy tests were recorded according to the digital data sampling requirements of SAE J211-1 [SAE, 2003]. For the data that was determined using video analysis, digital video cameras with a recording rate of 1000 frames-per-second were used. Following acquisition, all transducer data were processed in software as follows:

1. Any pre-test data channel bias was removed.
2. Sled wall body region force plate (e.g. Thorax Plate, Pelvis Plate) loads were calculated by summing the individual load cells used at each force plate location. Since the force plate load cells are recorded at SAE J211 Channel Filter Class (CFC) 1000 by the sled data acquisition system, the load cell channels were summed at CFC 1000.
3. The data channels were digitally filtered using the same filter specification used for the human subject biofidelity corridor data. The filter specifications are shown in Table 7.
4. Time zero was set as defined for the human subject data, also shown in Table 7.
5. Since all of the biofidelity corridors are positive polarity, negative polarity data channels were inverted to be positive.
6. The data channels were sub-sampled to match the sample rate of the human subject response target data.
7. The data channels were truncated to match the length of the response targets, shown in Table 5.
8. The √R values were calculated.

RESULTS

Table 8 shows the External and Internal Biofidelity ranks achieved when the updated BRS is applied to recent test data with the two dummies. Table 8 includes External and Internal ranks for each dummy for each body region as well as overall ranks. In addition, Table 8 shows overall Internal biofidelity ranks without the abdomen body region.

Table 8.
External and internal biofidelity ranks for WorldSID and ES-2re

Body Region	External Biofidelity		Internal Biofidelity	
	WorldSID	ES-2re	WorldSID	ES-2re
Head			0.3	1.0
Neck			0.8	2.2
Shoulder	1.0	2.1	0.9	1.3
Thorax	3.2	3.1	2.0	2.4
Abdomen	1.9	2.7	2.4	n/a
Pelvis	2.7	3.5	1.8	1.5
Overall (with Abdomen)	2.2	2.8	1.4	-
Overall (without Abdomen)	-	-	1.2	1.7

DISCUSSION

External Biofidelity of WorldSID vs. ES-2re

As shown in Table 8, the WorldSID dummy received an overall external BioRank score of 2.2 versus the ES-2re's overall score of 2.8. The WorldSID ranked better than the ES-2re in all body regions except the thorax where both dummies received equivalent ranks with scores of 3.2 and 3.1, respectively. The external thorax assessment consists of thorax plate force responses from the NHTSA [Maltese, 2002] and Heidelberg [ISO 1999] sled test conditions and pendulum force responses from the ISO 9790 Thorax Test 1 and the NHTSA [Shaw, 2006] 2.5 m/s lateral and oblique thorax test conditions. As shown in Figure 2, both dummies performed well in the Heidelberg sled test, which would be expected since this test was used as a performance criterion for the development of both dummies. Neither dummy performed as well in the NHTSA [Maltese, 2002] sled test conditions as shown in the plots of Figure 3, Figure 4, and Figure 5. Figure 5 shows how the vertical linkage of human body regions is important, especially the phasing among them. Specifically, as shown in Figure 5, the thorax load wall is loaded

earlier by the dummies than by the human subjects. Both the ES-2re and WorldSID need improvement regarding the timing of the thorax response in such a loading condition; however, the magnitude of the ES-2re response is much closer to the mean human response than is that of the WorldSID.

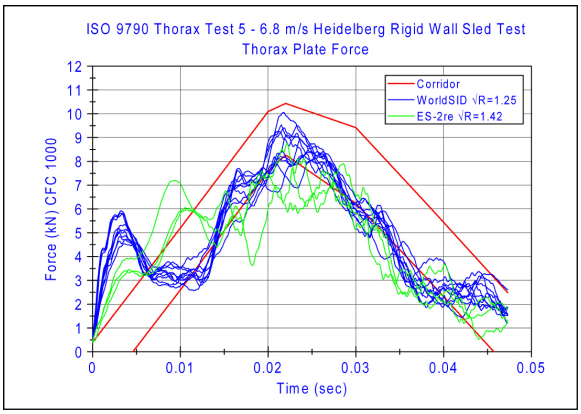

Figure 2. Thorax plate force from ISO 9790 Thorax Test 5.

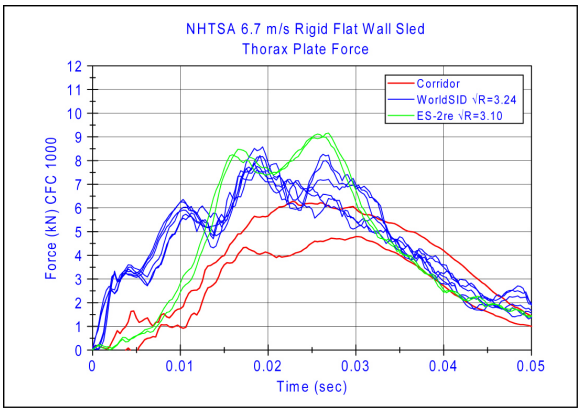

Figure 3. Thorax plate force from Maltese Rigid Low-Speed Flat Wall Sled Test.

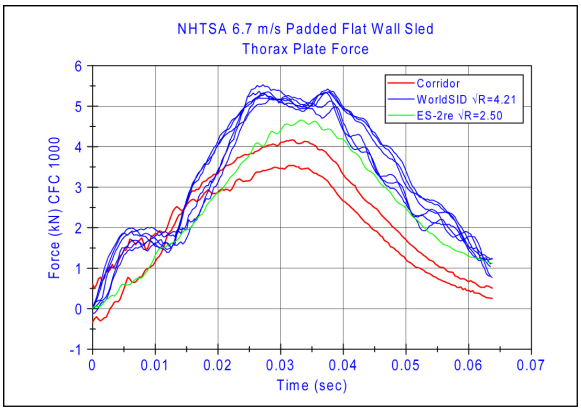

Figure 4. Thorax plate force from Maltese Padded Low-Speed Flat Wall Sled Test.

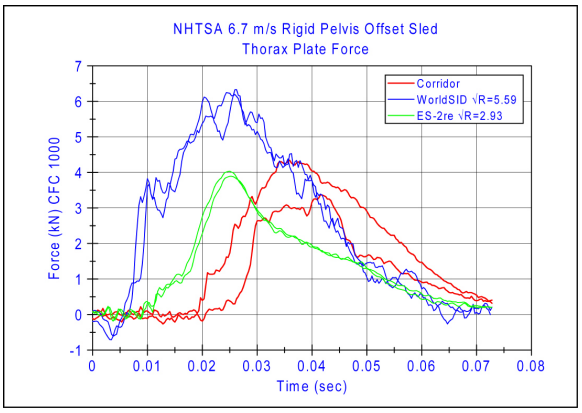

Figure 5. Thorax plate force from Maltese Rigid Low-Speed Pelvis Offset Sled Test.

Internal Biofidelity of WorldSID vs. ES-2re

As shown in Table 8, excluding the abdominal ranking for a direct and fair comparison, the WorldSID dummy received an overall internal BioRank score of 1.2 versus the ES-2re's overall score of 1.7. When the abdominal rank is included, the WorldSID receives a BioRank score of 1.4. The WorldSID dummy ranked well in all body regions except the abdominal region which received a score of 2.4. Since internal abdomen biofidelity is based on abdominal deflection response targets, the ES-2re is not ranked in this category. The ES-2re ranked well in all body regions except for the neck and thorax regions where it received scores of 2.2 and 2.4, respectively. Figure 6 shows data for the lower thoracic rib deflection from the NHTSA [Maltese, 2002] Rigid Abdomen Offset test where the WorldSID had a √R of 0.7 and the ES-2re, 1.9. The difference in responses is suspected to be a result of the offset abdomen plate engaging the lower thoracic region of the human subject and WorldSID dummy while engaging below the thoracic region of the ES-2re dummy due to its higher seated stature.

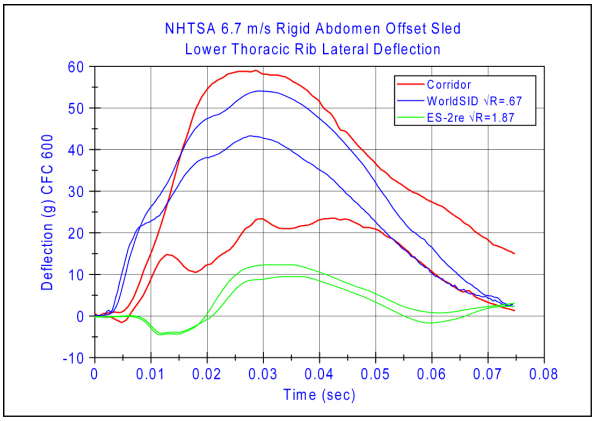

Figure 6. Lower thoracic rib deflection from Maltese Rigid Low-Speed Abdomen Offset Sled Test.

Design Differences Between the WorldSID and ES-2re

Head - The ES-2re head is based on the Hybrid III 50th percentile head and consists of a cast aluminum skull covered with a removable vinyl skin. The WorldSID head assembly uses a molded polyurethane skull with a bonded vinyl skin. Although the head assemblies are significantly different in design, the ES-2re and WorldSID dummies received similar internal head BioRank scores of 1.0 and 0.3, respectively.

Neck - With the exception of fore/aft tuning buffers in the WorldSID neck, which were modified to better tune the WorldSID's flexion /extension response, the ES-2re and WorldSID dummies use the same neck design. Although the neck designs are similar, the dummies ranked differently with the WorldSID receiving an internal score of 0.8 and the ES-2re receiving a score of 2.2. There are other factors that may account for the difference in neck biofidelity scores. The necks are ranked using ISO 9790 Neck Test 1 and Neck Test 3 which are restrained occupant sled tests. Since the dummies are restrained against a wall in these tests, differences in shoulder and thorax responses could influence the results. Also, the WorldSID head has a slightly higher mass than the ES-2re head which could have some effect on head translation. Another unknown but potential difference is in the methodologies used to perform the video data acquisition and analysis.

Shoulder - There are significant differences between ES-2re and WorldSID shoulder designs. The ES-2re shoulder consists of two pivoting clavicles guided between two shoulder plates that limit their movement to one plane. The clavicles are held in their neutral position by elastic cords. Shoulder deflection occurs by pivoting the clavicle from the neutral position forward in an arcing motion, resulting in both anterior and medial shoulder deflection. The ES-2re shoulder cannot deflect in the purely lateral direction or pivot rearward. The WorldSID torso, including the shoulder, consists of six rib assemblies: one shoulder, three thoracic and two abdominal. Each rib assembly consists of two inner rib bands (one on each side of the thorax) and an outer rib band that defines the torso's shape. Each outer rib band is fastened to the spine box at the rear and to a plastic sternum at the front. The inner rib bands have a bonded damping material to tune the rib response for each specific body region. The design of the WorldSID ribs allows a purely lateral deflection as well as some capability of forward and rearward deflection under oblique loading.

The ES-2re has no instrumentation for measuring shoulder deflection while each of the WorldSID ribs is instrumented with an IRTRACC on the impact side of the dummy for measuring lateral deflection only.

The 4.4 m/s lateral and oblique pendulum impact tests resulted in unrealistic shoulder deflections in both the ES-2re and WorldSID dummies. The human subject shoulders deflected medially in pure lateral impacts and posteriorly and medially, with decreased stiffness, during anterolateral impacts [Bolte 2000, Bolte 2003]. The WorldSID force response was similar to that of the human subjects resulting in an external shoulder biofidelity score of 1.0. Due to the location of pendulum impact on the WorldSID's shoulder, the pendulum tended to deflect upward, pushing the shoulder rib downward. Although this motion is not consistent with that of the human subjects the WorldSID rank for shoulder internal biofidelity, based on only the lateral deflection, is 0.9. The inability of the ES-2re clavicle to deflect posteriorly resulted in the shoulder response becoming stiffer when the loading moved from the lateral to the anterolateral direction resulting in an external biofidelity score of 2.1. The ES-2re clavicle exhibited a tendency for forward rotation, even during anterolateral impacts. Although this motion is also not consistent with that of the human subjects the ES-2re dummy rank for shoulder internal biofidelity is 1.3. The reasonably good ranks for dummy shoulder kinematics that do not simulate the human kinematics result from incomplete displacement data from the human subjects, allowing limited comparison with the dummies.

Thorax - The ES-2re thoracic region consists of three rib modules. Each of the three rib modules is comprised of a steel rib bow covered with flesh-simulating foam. A linear guide assembly attaches between the impact and non-impact side of the rib and limits the deflection to purely lateral. In parallel with the linear guide assembly is a hydraulic damper. A spring inside the linear guide assembly is used to tune the performance of the modules. A potentiometer is installed in each rib module to measure deflection. The WorldSID thoracic region consists of three rib band assemblies as described in the shoulder section, having the same lateral and oblique deflection capabilities. The thoracic biofidelity of the WorldSID and ES-2re are nearly the same with external ranks of 3.2 and 3.1 and internal ranks of 2.0 and 2.4, respectively. With the exception of the NHTSA [Shaw, 2006] 2.5 m/s 30° pendulum impact test, all of the thorax biofidelity tests provide only lateral inputs to the dummy. Therefore, differences in oblique thorax response capabilities between the two dummies are not highlighted. Both dummies demonstrated scores indicative of needing improvement for the pendulum force response measurement of the oblique pendulum impact test (WorldSID 4.1, ES-2re 5.7). In the lateral impacts, both dummies achieve lower (i.e., better) scores for the ISO tests, but higher (i.e., worse) scores for the Shaw and Maltese tests. This is likely due to the fact that the Shaw and Maltese data is relatively new and the ISO data was used as design criteria for both dummies.

Abdomen – The WorldSID abdomen is represented by "rib" structures as discussed previously and measures abdominal deflection with IRTRACCs. The ES-2re abdominal region consists of a foam-covered cast aluminum drum positioned around the lumbar spine. There are three load cells attached to the drum to measure the force between the drum and the foam covering. There is no instrumentation for measuring abdominal deflection. Since the internal abdominal biofidelity response targets are based on abdomen deflection, the ES-2re could not be rated for internal abdomen biofidelity; however, the WorldSID only scored a 2.4. External biofidelity scores were 1.9 and 2.7 for the WorldSID and ES-2re, respectively.

Pelvis - The ES-2re and WorldSID dummies have pelvis structures consisting of a central sacrum block and two polyurethane iliac wings that are joined at the pubic symphysis by a load cell. The WorldSID pubic symphysis load cell is coupled to the iliac wings using rubber bushings while the ES-2re uses aluminum bushings. The WorldSID pelvis design exhibited a less rigid response than the ES-2re pelvis resulting in external pelvis biofidelity scores of 2.7 and 3.5, respectively. In spite of the stiffer ES-2re pelvis the internal biofidelity score of 1.5 was slightly better than the WorldSID at 1.8.

CONCLUSIONS

The Biofidelity Ranking System (BRS) has been updated and used to assess the biofidelity of the WorldSID and the ES-2re side impact dummies.

- The subjective decision as to what test data are included in the biofidelity ranking of a dummy is made before the application of the objective BRS.
- The various tests selected for use in the BRS are no longer weighted – each test condition receives the same weight if it is included by the analyst in the BRS. Care should be taken to assure that the tests selected represent an appropriate assessment of the dummy biofidelity based on test severity, body region distribution and data reliability.
- A scale of biofidelity has been established for B values based on the number of standard deviations from the mean cadaver responses.
- A sensitivity analysis of $\sqrt{R}$ values indicates that two B value ranks with a difference of 0.2 or less are not significantly different.
- The WorldSID received an overall internal biofidelity rank of 1.2 and the ES-2re received an overall internal biofidelity rank of 1.7.
- The WorldSID received an overall external biofidelity rank of 2.2 and the ES-2re received an overall external biofidelity rank of 2.8.
- This biofidelity evaluation using the updated BRS indicates good biofidelity for this improved version of the WorldSID dummy.

REFERENCES

Bolte, IV,J.H., Hines, M.H., McFadden, J.D., and Saul, R.A. (2000) Shoulder Response Characteristics and Injury Due to Lateral Glenohumeral Joint Impacts. Stapp Car Crash Journal 44: 261-280. Society of Automotive Engineers, Warrendale, PA.

Bolte, IV,J.H., Hines, M.H., Herriott, R.G., McFadden, J.D., and Donnelly, B.R. (2003) Shoulder Impact Response and Injury Due to Lateral and Oblique Loading . Stapp Car Crash Journal 47: 35-53. Society of Automotive Engineers, Warrendale, PA.

Hodgson, V.R. and Thomas, L.M. (1975) Head Impact Response. Vehicle Research Institute Report – VRI 7.2. Society of Automotive Engineers.

Irwin, A., Sutterfield, A., Hsu, T., Kim, A., Mertz, H., Rouhana, S., Scherer, R. (2005) Side Impact Response Corridors for the Rigid Flat-Wall and Offset-Wall Side Impact Tests of NHTSA Using the ISO Method of Corridor Development. Stapp Car Crash Journal. 49:423-456.

Irwin, A. (June 2008) Personal communication.

ISO (1999) Technical Report 9790: Road Vehicles – Anthropomorphic Side Impact Dummy – Lateral Impact Response Requirements to Assess the Biofidelity of the Dummy.

Maltese, M.R., Eppinger, R.H., Rhule, H.H., Donnelly, B., Pintar, F.A. and Yoganandan, N. (2002) Response Corridors of Human Surrogates In Lateral Impacts. Stapp Car Crash Journal 46: 321-351.

Mathworks, Inc. Matlab version 7.7.0.471 (R2008b), September 17, 2008.

Morgan, R.M., Marcus, J.H., and Eppinger, R.H. (1986) Side Impact – The Biofidelity of NHTSA's Proposed ATD and Efficacy of TTI. Proc. 30th Stapp Car Crash Conference, pp. 27-40. Society of Automotive Engineers, Warrendale, PA.

Petitjean, A. (June 2008) Personal communication.

Rhule, H.H., Maltese, M.R., Donnelly, B.R., Eppinger, R.H., Brunner, J.K., and Bolte, J.H.IV. (2002) Development of a New Biofidelity Ranking System for Anthropomorphic Test Devices. Stapp Car Crash Journal 46: 477-512.

SAE. (2003) Surface Vehicle Recommended Practice, SAE J211-1, Rev. Dec. 2003. Society of Automotive Engineers, Warrendale, PA.

Shaw, J.M., Herriott, R.G., McFadden, J.D., Donnelly, B.R., Bolte, IV,J.H. (2006) Oblique and Lateral Impact Response of the PMHS Thorax. Stapp Car Crash Journal 50: 147-167.

APPENDIX A. SQUARE ROOT OF R VALUES FOR EACH RESPONSE MEASUREMENT USED TO EVALUATE THE BIOFIDELITY OF THE ES-2re AND WORLDSID DUMMIES USING THE UPDATED BRS

	Test Type	DROP	SLED			PENDULUM							SLED						
Measurement	Dummy	ISO 9790 Head Test 1	ISO 9790 Neck Test 1	ISO 9790 Neck Test 3	ISO 9790 Shoulder Test 2	Bolte Lateral Shoulder	Bolte 15º Shoulder	Bolte 30º Shoulder	ISO 9790 Thorax Test 1	Shaw Lateral Thorax	Shaw 30º Thorax	ISO 9790 Pelvis Test 1	ISO 9790 6.8 m/s Heidelberg	ISO 9790 6.8 m/s Wayne State	Maltese 6.7 m/s Rigid Flat Wall	Maltese 6.7 m/s Padded Flat Wall	Maltese 6.7 m/s Rigid Abdomen Offset	Maltese 6.7 m/s Rigid Pelvis Offset	Maltese 8.9 m/s Padded Flat Wall
Peak Resultant Head Acceleration	WSID	0.33																	
	ES-2re	1.02																	
Peak Horiz. Disp. of Head cg Relative to T-1	WSID		1.22																
	ES-2re		3.25																
Peak Vert. Disp. of Head cg Relative to T-1	WSID		1.22																
	ES-2re		2.49																
Peak Flexion Angle	WSID		0.40	1.15															
	ES-2re		1.00	2.85															
Peak Horiz. Disp. of Head cg Relative to Sled	WSID			0.25															
	ES-2re			1.59															
Pendulum Force	WSID					0.87			1.27	2.94	4.13								
	ES-2re					1.10			2.29	2.52	5.71								
Pendulum Y-axis Force	WSID						1.26	0.54											
	ES-2re						2.96	3.44											
Pendulum X-axis Force	WSID						0.84	1.59											
	ES-2re						1.96	1.83											
Peak Horiz. Disp. of T-1 Relative to Sled	WSID				0.24														
	ES-2re				1.47														
Shoulder Y-axis Displacement	WSID					1.55													
	ES-2re					1.11													
Thorax Plate Force	WSID												1.25		3.24	4.21	3.81	5.59	2.57
	ES-2re												1.42		3.10	2.50	4.22	2.93	2.83
T-1 Lateral Acceleration	WSID								1.66						2.32	1.28	2.48	1.80	0.82
	ES-2re								2.64						1.50	1.31	3.30	1.59	1.23
Thorax Displacement	WSID									1.54	3.17								
	ES-2re									1.22	3.32								
Peak T-1 Lateral Acceleration	WSID												6.03						
	ES-2re												6.86						
Peak T-12 Lateral Acceleration	WSID												4.01						
	ES-2re												4.22						
Peak Lateral Accel. of Impacted Rib	WSID												0.70						
	ES-2re												2.95						
T-12 Lateral Acceleration	WSID														1.66	1.34	1.42	4.39	0.92
	ES-2re														1.54	1.27	3.15	4.03	0.94
Upper Thoracic Lateral Deflection	WSID														1.61	0.72		2.72	0.48
	ES-2re														2.34	0.90		2.18	0.93
Lower Thoracic Lateral Deflection	WSID														1.97	0.81	0.67	4.60	0.46
	ES-2re														2.00	1.01	1.87	4.73	0.77
Abdomen Plate Force	WSID													1.72	0.60	1.61	0.94	3.71	2.83
	ES-2re													2.08	0.58	1.05	5.28	3.95	3.24
Mid-Abdominal Deflection	WSID														2.75	1.64	1.78	2.79	2.89
	ES-2re														n/a	n/a	n/a	n/a	n/a
Peak Pendulum Force	WSID											0.23							
	ES-2re											5.39							
Peak Pelvis Plate Force	WSID												6.76						
	ES-2re												7.89						
Pelvis Plate Force	WSID													1.61	1.77	2.13	4.06	1.60	3.77
	ES-2re													1.63	2.44	2.13	2.14	1.49	4.82
Peak Pelvis Lateral Acceleration	WSID												0.35	3.98					
	ES-2re												1.50	1.00					
Pelvis Lateral Acceleration	WSID														1.53	2.09	1.16	1.94	1.26
	ES-2re														1.72	1.69	1.09	2.62	1.09

Internal Head Values; Internal Neck Values; External Shoulder Values; Internal Shoulder Values; External Thorax Values; Internal Thorax Values; Ext Abdomen Values; Int Abdomen Values; External Pelvis Values; Internal Pelvis Values

Final Ranks:		**Head**	**Neck**	**Shoulder**	**Thorax**	**Abdomen**	**Pelvis**				
EXTERNAL	**WSID**			**1.0**	**3.2**	**1.9**	**2.7**	**Overall**	**2.2**		
	ES-2re			**2.1**	**3.1**	**2.7**	**3.5**		**2.8**		
INTERNAL	**WSID**	**0.3**	**0.8**	**0.9**	**2.0**	**2.4**	**1.8**	**Overall**	**1.4**	**Overall**	**1.2**
	ES-2re	**1.0**	**2.2**	**1.3**	**2.4**	**N/A**	**1.5**	**w/abd**	**n/a**	**w/o abd**	**1.7**

HEAD AND SPINAL TRAJECTORIES IN CHILDREN AND ADULTS EXPOSED TO LOW SPEED FRONTAL ACCELERATION

Sriram Balasubramanian, PhD
Thomas Seacrist, MS
Matthew R. Maltese, MS
Kristy B. Arbogast, PhD
Center for Injury Research and Prevention
The Children's Hospital of Philadelphia
USA
Terrance Hopely, BS
Eric Constans, PhD
Department of Mechanical Engineering
Rowan University
USA
Robert Sterner, PhD
Department of Health and Exercise Science
Rowan University
USA
Hiromasa Tanji
Kazuo Higuchi
Takata Corporation
Japan
Paper Number 09-0263

ABSTRACT

Head injuries are the most common injuries sustained by children in motor vehicle crashes. Prevention of these injuries through advances in vehicles and restraint systems requires a biofidelic anthropomorphic test device (ATD). Pediatric ATDs are primarily developed from scaling down adult volunteer and cadaver impact test data. Limited experimental data exist on pediatric head and neck kinematics in order to evaluate the biofidelity of the ATDs. The aim of the current study was to evaluate the head and spinal kinematics of pediatric and adult volunteers in response to a dynamic low-speed frontal sled test. Low speed volunteer testing of five male subjects in each of two specific age groups (9-12, and 18-30 years) were performed using a pneumatically actuated – hydraulically controlled sled. Safe limits were established from measurement of bumper car accelerations at an amusement park ride (4.9 *g*, 55.7 msec rise time, 110 msec duration), which we believed to be sub-injurious to the adult and child amusement park population. We subsequently recreated the bumper car environment in the laboratory, by developing a low-speed hydro-pneumatic sled. As an added measure of safety, our average maximum cart acceleration was 3.59 *g* for children and 3.78 *g* for adults, thus producing occupant loads that are approximately 25% less than the bumper car amusement park ride. Spherical reflective markers were placed on the head, neck, torso, upper and lower extremities and tracked using a 3D motion analysis system. An angular rate sensor was mounted to a bite plate of an athletic mouth guard to measure the head rotational velocity. Electromyography sensors were attached to key muscle groups to measure the muscle response of the subjects to the loading environment. Each subject was subjected to six sled runs. Head and neck trajectories were compared between the adult and pediatric subjects. In addition, the effect of habituation on kinematic response was examined by comparing within subject changes in kinematics throughout the series of six sled runs.

INTRODUCTION

Traumatic brain and skull injuries are the most common serious injuries sustained by children in motor vehicle crashes regardless of age group, crash direction, or restraint type (Arbogast et al. 2005; Arbogast et al. 2002; Durbin et al. 2003; Howard et al. 2003; Orzechowski et al. 2003; Arbogast et al. 2004). Head injuries are responsible for one-third of all pediatric injury deaths (Adekoya et al. 2002; Thompson and Irby 2003) and are particularly relevant clinically as the developing brain is difficult to evaluate and treat. Prevention of these injuries through effective motor vehicle safety systems requires a biofidelic anthropomorphic test device (ATD) to ensure safety systems mitigate injuries in real children. The extent to which the pediatric ATD

accurately predicts the dynamics and kinematics of the occupant's head and spine in particular restraint and crash conditions directly influences safety system design and thus injury potential.

A growing body of evidence points to critical differences in spinal kinematics between humans and ATDs in the same restraint system. Compliance in the thoracic and cervical spine is a primary cause of this difference. The human spine is a relatively mobile, multi-segmented system, while the Hybrid III dummy's thoracic spine is essentially rigid. This difference in spinal compliance can generate differences in the head trajectory of the dummy relative to a human. Studies have shown that crash environments that would be defined as non-injurious based on a dummy's response can actually generate substantial injuries to the head, neck, and thorax of a cadaver since increased compliance in the spine creates an entirely different head trajectory and results in severe head contact with interior vehicle structures. (Shaw et al. 2001)

The same phenomenon has been demonstrated in the pediatric literature where the thoracic spine of the pediatric ATD has been shown to be much stiffer than that of a real child (Sherwood et al. 2003). This sled-based data compared pediatric post mortem human subjects (PMHS) data from the 1970s (Kallieris et al. 1978) with Hybrid III 6 year old ATD response and demonstrated the inaccurate predictions of a child's head trajectory and total forward excursion as well as the development of unrealistically high moments at the OC-C1 junction. As pediatric PMHS data is extremely limited, additional evidence on kinematic differences between pediatric ATDs and live humans comes from comparison of laboratory findings to field accident data. In many sled and vehicle frontal crash tests using pediatric ATDs, the published thresholds for the cervical spine injury metrics, Nij and neck tension, as well as the Head Injury Criterion (HIC) are often exceeded (Menon et al. 2003; Sherwood et al. 2003; Malott et al. 2004). Experience in incorporating pediatric ATD's in the rear seat of NHTSA's frontal NCAP tests and in development of enhancements to FMVSS 213 resulted in the ATD's inability to meet the proposed head and neck tolerance criteria. (Kuppa 2005) These results are at odds with several reports on the rarity of cervical spine injuries in child restraints and booster seats in the field and the overall effective protection of these restraints (Durbin 2002; Arbogast et al. 2002; Zuckerman et al. 2004).

These biofidelic inaccuracies are due in part to the pediatric ATD's spinal construction as a single steel beam rather than the multi-segmented, multi-degree-of-freedom complex structure characteristic of real children. As a result, the actual injury risk to a human child exposed to a similar collision environment may be overstated potentially providing misdirected guidance for restraint design. To further confound the issue, the effects of the non-biofidelic spine of the ATD's are restraint system dependent (Shaw et al. 2001). Thus, comparisons of alternative design concepts may be skewed due to poor predictions of head trajectory and thus inaccurate assessment of head injury risk.

Traditionally, improvements in ATD biofidelity are achieved through rigorous evaluation of PMHS impact testing. Although this approach is an accepted method for obtaining adult ATD design specifications, child PMHS data is limited and thus current pediatric ATD's are based on adult biomechanical test data scaled to account for geometric and material differences between adults and children, to the extent such data is available. However, during the human developmental process, local and regional anatomical structures change in ways that are not quantitatively considered in the scaling processes. Thus, to address this limitation and improve the ability of the current pediatric ATDs to mimic the interaction of real children with a restraint system, novel methods for determining pediatric dynamic response are required.

Human volunteer experiments have a long established history in biomechanics research. Early researchers used themselves as test specimens (Stapp 1949) or enrolled adult human volunteers to define the dynamic response of the head and neck to trauma (Ewing et al. 1968; Mertz and Patrick 1971; Wismans et al. 1987). To our knowledge, no data exists on the dynamic response of the head and neck of children relative to the automotive environment. Therefore the objective of this research was to develop a methodology to safely study the sub-injurious kinematics of child volunteers in dynamic automotive-like events and through testing of adult volunteers in a similar loading environment, evaluate the effect of age on the kinematic response. This paper describes the methodologic development of the test protocol and provides exemplary data from both the child and adult test subjects.

METHODS

This study protocol was reviewed and approved by the Institutional Review Boards at The Children's

Hospital of Philadelphia, Philadelphia, PA and Rowan University, Glassboro, NJ.

Test device

A pneumatically actuated – hydraulically controlled 'low-speed acceleration seating buck' (LASB) shown in Figure 1, was designed to subject restrained human volunteers to a sub-injurious, low-speed frontal crash pulse.

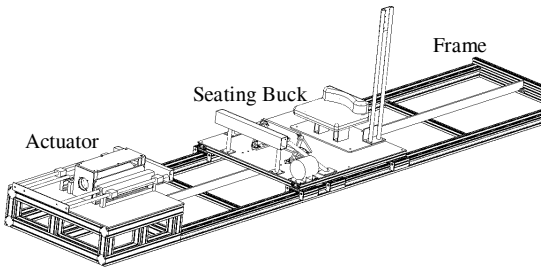

Figure 1. Schematic of the low-speed acceleration seating buck (LASB).

The LASB is primarily comprised of three sub-assemblies, namely frame, actuator and seating buck. The frame for the LASB was constructed of extruded aluminum tubing (MiniTec Framing Systems LLC, Victor, NY). The structural framework included a platform (for the actuator assembly) which was rigidly connected to two 18 feet long parallel support rails with equally spaced cross members for rigidity. A steel bar between the two support rails served to slow the sled to a stop following the primary acceleration pulse. The actuator assembly was comprised of a pneumatic actuator (Mc Master-Carr, Robbinsville, NJ) (diameter – 4 inches, stroke length – 20 inches, operating pressure – 200 psi) connected to an opposing dual hydraulic piston-cylinder (Model TZ22, Vickers Cylinders, Eaton Corporation, Cleveland, OH) arrangement using a rigid frame. A 2-way high dynamics proportional throttle cartridge valve (Model LIQZO-LE, Atos, Italy) was used in the custom-designed hydraulic circuit to control the displacement profile of the pneumatic actuator. When the pneumatic actuator was fired, it delivered the impact force to the seating buck.

The seating buck assembly (Figure 2) framework was also constructed using extruded aluminum tubing (MiniTec Framing Systems LLC, Victor, NY). It was comprised of a moving platform mounted on the two support rails by means of six low friction linear bearings. A custom-built impact fixture was mounted on the platform to transfer the force from the pneumatic actuator to the moving platform. A rigid low-back padded seat, an adjustable height shoulder belt anchor post (similar to a B-pillar in an automobile), lap belt anchors and an adjustable footrest were mounted on the platform. The low-back seat allowed for the motion analysis markers along the spine to be visible to the cameras. A standard automotive three-point belt system was attached to the lap belt and shoulder belt anchor points. An onboard pneumatic braking system was provided to interact with the braking rail to decelerate the moving platform. In order to limit the excursion of the subject during rebound associated with braking, a nylon strap was attached to two vertical bars behind the seat (at the location of T4).

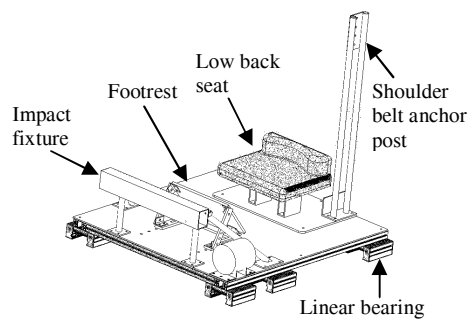

Figure 2. Schematic of the seating buck assembly.

Safe volunteer crash pulse

An amusement park bumper car ride was studied to provide a benchmark of a crash-like situation commonly and safely used by children for recreation and enjoyment. Safe limits on the volunteer crash pulse were defined from measuring a bumper car-to-wall impact in an amusement park (Six Flags Great Adventure, Jackson, NJ). An accelerometer was secured to the rigid cross-member of the steering assembly of a bumper car. The car was used in its typical usage patterns, impacting the wall of the arena, another vehicle head to head, and another vehicle in a T-type configuration. This process was repeated with two different bumper car vehicles. The maximum pulse obtained was 4.9 *g* in 55.7 msec (Figure 3). This was defined as the envelope of safety for the human volunteers.

Design considerations for safety

Additional safety evaluations were performed during the design and operation of the LASB to ensure safety, comfort and protection of the human subjects. Firstly, the restraints of the amusement park bumper car were studied and the LASB restraints were designed to provide more custom-fit protection. The amusement park bumper cars provided restraint through two load paths – 1) a loop of belt across the torso, and 2) a footrest that restrained the lower extremities. The bumper car restraints were not

adjustable for different size occupants. The LASB, in contrast, features a customizable restraint system to distribute test forces over three load paths: 1) torso loads are carried by a shoulder belt that rests on the clavicle, 2) pelvic loads by a lap belt, and 3) lower extremity loads by the foot rest. The LASB belt and foot rest are fully adjustable to maximize occupant comfort, ensuring that that shoulder belt passes over the clavicle and sternum, that the lap belt engages the iliac wings, and that the leg restraints are adjustable to allow a bent knee. Thus, because the LASB restraints distribute forces through more load paths than the traditional bumper car restraint, and provide adjustability for optimal fit, we expect that the pressure applied by the restraints to the test subjects to be lower in magnitude and more optimally placed than a typical bumper car.

As further confirmation of the safety of this event, a literature review on sub-injurious loading to human volunteers was performed. All of this literature uses adult human subjects, as there is no data on children, however we believe the findings are relevant to our study and support the safety of our test environment. First in the amusement environment, the top 7 roller coaster rides by *g*-loading in the United States in 2001 exposed occupants to accelerations of 5 to 6.5 *g* (Braksiek and Roberts, 2002). Roller coaster loading likely differs in loading direction, duration and onset rate and thus limit our ability to directly compare roller coaster data to the volunteer sled. More direct comparisons can be obtained from Ewing et al. (1968) who measured the dynamic response of the head and neck by exposing seated and restrained adult human volunteers to a frontal peak sled acceleration of 2.8 *g*. Mertz and Patrick (1971) subjected a human volunteer to frontal sled plateau accelerations ranging from 2 to 9.6 *g*. Although low levels of acceleration (<8 *g*) were well tolerated by the volunteer, he experienced neck pain beyond 8 *g*. This review further confirms that the acceleration levels at which the LASB is designed have previously been tolerated safely by human volunteers.

Lastly, the design of the LASB itself had several safety mechanisms through which the application of the low-speed acceleration was controlled. The hydraulically controlled – pneumatic powered actuator system was designed to deliver an acceleration pulse with a maximum acceleration of less than 4.5 *g* with a rise time of 50-70 msec – within the defined safety envelope. However, the subjects received a slightly lower pulse (shown in the results section). Other safety system redundancies included:

1. Well documented countdown procedure, safety check list and testing protocol
2. Manual pressure checks at the pneumatic and hydraulic accumulators equipped with pressure relief valves
3. Synchronized trigger circuit with key operated 'arm' switch and push button 'fire' switch to operate all systems simultaneously
4. Warning light on control box when system is 'armed' and ready to be fired
5. On board pneumatic system activated braking calipers on the front and back of the moving platform
6. Emergency braking system consisting of two hydraulic dampers mounted at the end of the rails
7. Multiple abort switches for each system
8. Fail safe volunteer-controlled abort contact-switch

These safety checks ensured that the LASB delivered the appropriate pulse and could only be triggered and actuated when the test area of the LASB was cleared by personnel and the subject was appropriately restrained and ready for testing. Dynamic proof testing of the LASB and all components was also completed prior to human volunteer testing.

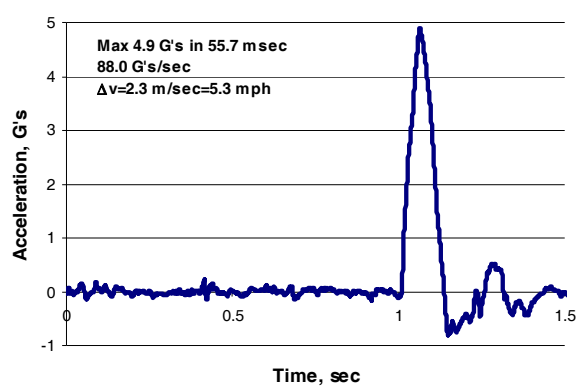

Figure 3. Bumper car to wall acceleration pulse.

Human Subjects

<u>Inclusion criteria</u> – Specific inclusion criteria were male subjects aged between 6 and 40 years whose height, weight and BMI were within 5th and 95th percentile for the subject's age (based upon CDC growth charts for children (CDC Growth Charts, 2000) and CDC NHANES data for subjects 18+ years (NHANES data, 1994)). Subjects with existing neurologic, orthopedic, genetic, or neuromuscular conditions, any previous injury or abnormal pathology relating to the head, neck or spine were excluded from the study. Subjects were recruited

from flyers placed in the community and throughout CHOP and Rowan sites. Prior to the testing dates, telephone interviews were conducted with the adult subjects and parent / guardian of child subjects to confirm eligibility.

For the analyses presented herein, a total of 10 male subjects – five subjects in each of the two age groups (9-12 years and 18-30 years) were tested. Upon arrival at the test site, the study was explained in detail to all subjects including a demonstration of how the LASB functions by firing the sled without an occupant. The adult subjects were given a self-consent letter and the parent / guardian of the child subjects were given a parental consent letter with a child subject assent. After the subjects had been consented, height and weight were measured to verify that their height, weight and body mass index (BMI) were consistent with the inclusion criteria.

The subjects were asked to remove their shirt(s) to facilitate placement of the instrumentation and the following anthropometric measurements:

1. Head medial-lateral width at the level of nasion
2. Head anterior-posterior depth at the level of opisthocranion
3. Head girth at the level of opisthocranion
4. Head length from head top to mandible
5. Neck medial-lateral width at the level of C3-C4
6. Neck anterior-posterior depth at the level of C3-C4
7. Neck length (Opisthocranion to C7)
8. Neck girth at the level of C3-C4
9. Chest medial-lateral width at Xyphoid process
10. Chest anterior-posterior depth at Xyphoid process
11. Shoulder width (distance between left and right acromion processes)
12. Distance between Suprasternal notch to Xyphoid process
13. Seated height measured from head top to seat top
14. Waist girth at umbilicus
15. Hip width at Iliac crests
16. Buttock to Popliteal length
17. Knee to foot distance measured from lateral femoral condyle to floor

Instrumentation

Subject – Spherical reflective markers (10 mm diameter) were placed on the head, neck, torso, upper and lower extremities and tracked using a 3D motion analysis system (Model Eagle 4, Motion Analysis Corporation, Santa Rosa, CA). Specifically, the photoreflective targets were attached to the following anatomical landmarks:

1. Head – On a tight-fitting elastic cap (Left and right temple, top and front of head in two places along the mid-sagittal plane, and on the occiput posteriorly), nasion and anterior to the left and right external auditory meatus.
2. Spine – Spinous processes of C4, T1, T4, T8, and L1.
3. Upper Extremity – Lateral humeral epicondyle, and ulnar styloid, all bilaterally
4. Torso – Acromion process (bilaterally), suprasternal notch, and Xiphoid process
5. Pelvis and Lower Extremity – Anterior superior iliac spine, lateral femoral epicondyle, lateral malleolus all bilaterally.

A comprehensive list of all the markers is provided in the Appendix – Table A1. An angular rate sensor – ARS (Model ARS-300, DTS Inc, Seal Beach, CA) was mounted via a custom fixture to a subject-specific athletic mouth guard to measure the head rotational velocity. Surface Electromyography (EMG) sensors were attached bilaterally to key muscle groups of the neck (Sternocleidomastoid, Paraspinous and Trapezius), lower torso (Erector Spinae), and lower extremities (Rectus femoris) to measure the muscle response of the subjects to the loading environment. A grounding electrode was centered over the right mastoidale. A telemetric Surface EMG system, Noraxon – TeleMyo 2400T V2 (Noraxon USA Inc, Scottsdale, AZ) was used to record the EMG signals. For each subject, their maximum isometric contraction for these muscles was measured prior to sled testing.

LASB – Spherical reflective markers were also placed on various locations on the seating buck and tracked using a 3D motion analysis system (Model Eagle 4, Motion Analysis Corporation, Santa Rosa, CA). A piezoresistive accelerometer (Model 7264-200, Endevco, San Juan, CA) was mounted to the moving platform frame to record the acceleration of the LASB. Lightweight belt webbing load cells (Model 6200FL-41-30, Denton ATD Inc, Rochester Hills, MI) were attached five inches from the D-ring location on the shoulder belt and on the inboard and outboard locations on the lap belt, respectively. Six-axis load cells was placed under the seat pan (Model IF-217, FTSS, Plymouth, MI) and footrest (Model IF-234, FTSS, Plymouth, MI), respectively to measure the reaction forces exerted by the subjects.
A high-speed video camera (MotionXtra HGTH, Redlake, San Diego, CA) was placed sagittally to record the event at a rate of 1,000 frames per second (fps). In addition, two standard video camcorders (Model DC20, Canon Inc., Japan) were used to capture the frontal and sagittal views at 30 fps. The

hydraulic controller, Motion Analysis, T-DAS, EMG and high speed camera systems were triggered synchronously using a custom made circuit.

Testing

After the instrumentation setup was completed, the subjects were seated in the LASB as shown in Figure 4. The torso and knee angles were maintained at 110 degrees by adjusting the position of the footrest and nylon strap to mimic the posture of a seated occupant in an automobile (Reed et al. 2005). The shoulder belt angle at the D-Ring (defined as the angle the shoulder belt makes with the horizontal) and lap belt buckle angle (defined as the angle the lap belt buckle makes with the horizontal) were set at 70 degrees at initial position for all the subjects. In order to minimize the effect of initial head position, the subjects were asked to focus at a point placed directly in front of them at the level of their nasion. The lap and shoulder belts were then adjusted and secured to fit optimally for the subject's size.

The experimental procedure with the LASB is a series of six tests, with each successive test designed to encourage the occupant to relax their muscles and allow the restraints to support their weight during the acceleration event, thus simulating the condition of an unbraced occupant in a frontal vehicle crash whose inertial forces are supported by the restraint system in the vehicle. Subjects received a countdown in each test prior to firing of the actuator. Each subject was given the option to either continue or withdraw from further testing at the completion of each test run. All the tests were conducted identically with a rest period of approximately 10 minutes between subsequent tests.

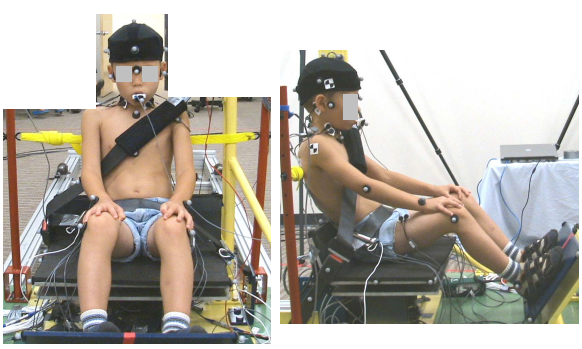

Figure 4: Child subject seated in LASB.

Data acquisition and analyses

Signals from the ARS, accelerometer and load cells were sampled at 10,000 Hz using a T-DAS data acquisition system (Diversified Technical Systems Inc., Seal Beach, CA) with a built-in anti-aliasing filter (4,300 Hz). The Motion Analysis data were acquired at 100 Hz and analyzed using EVaRT5 software (Motion Analysis Corporation, Santa Rosa, CA). MyoResearch XP software was used to export the EMG data into ASCII format. The T-DAS, Motion Analysis and EMG data processing were automated using MATLAB 8.0 (The Mathworks Inc, Natick, MA). The high-speed video data were analyzed with Falcon software (Falkner Consulting for Measuring Technology GmbH, Gräfelfing-Lochham, Germany).

For the analyses presented herein, only the Motion Analysis data and the sled acceleration data will be discussed. The sled acceleration data were filtered at SAE channel frequency class (CFC) 60, as recommended by the SAE J211 standards.

RESULTS

The age, height, weight and BMI for the subjects whose data are presented herein are listed in Table 1.

Table 1.
Height, Weight and BMI for subjects

Subject #	Age years	Height cm	Height Percentile	Weight kg	Weight Percentile	BMI kg/m^2	BMI Percentile
11	9	124	5	25.1	17	16.3	51
8	10	136	31	28.5	22	15.4	23
18	10	144	68	33.1	47	16	32
16	12	165	92	50.3	74	18.5	54
19	12	155	68	40.3	41	16.8	29
21	22	172	38	64.8	14	21.7	31
23	22	176	51	86.6	65	28	66
24	22	180	69	106.6	94	32.8	93
22	24	169	22	73.4	37	25.8	47
27	30	180	69	80.7	53	24.8	39

For Child subjects, ages 6-18 years: Height, Weight and BMI percentiles were calculated using the CDC growth charts (2000)

For Adult subjects, ages 20+ years: Height, Weight and BMI percentiles were calculated using the NHANES data (1994)

The individual and averaged sled acceleration pulse for a set of six trials on a single subject is shown on Figure 5. The activation of the synchronous trigger (henceforth called 'time zero') was followed by a time delay before the movement of the sled (event). The time delay (approximately 100 msec) was attributed to the response lag associated with the LASB hydraulic system. Event onset (vertical line in Figure 5) was defined as the time at which the sled acceleration reached 5% of its peak value.

The five phases of the event are outlined below:

1. Acceleration – This is the first phase of the event that immediately follows event onset and corresponds to the pre-programmed acceleration pulse of the sled.

2. Restraint loading – The subject loads the seatbelt restraints.
3. Rebound – After maximum excursion, the subject rebounds back and interacts with the nylon strap behind the seat.
4. Coasting – During this phase, the sled coasts on the rails.
5. Braking – The pneumatic brakes are applied during this phase causing the gradual deceleration of the sled.

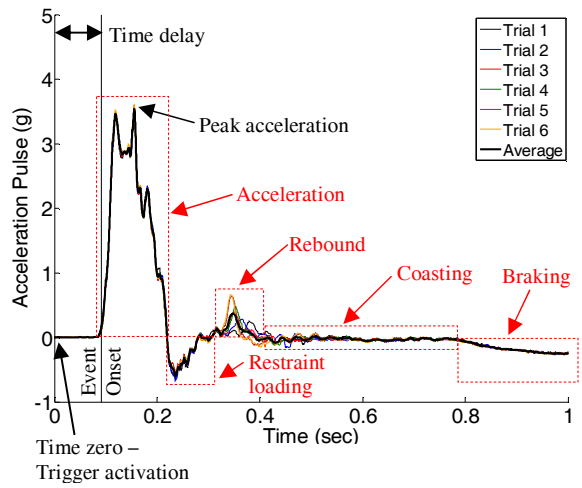

Figure 5. Sled acceleration pulse of six individual trials and their average for a single human volunteer. Various phases of the event are shown in red – dashed boxes.

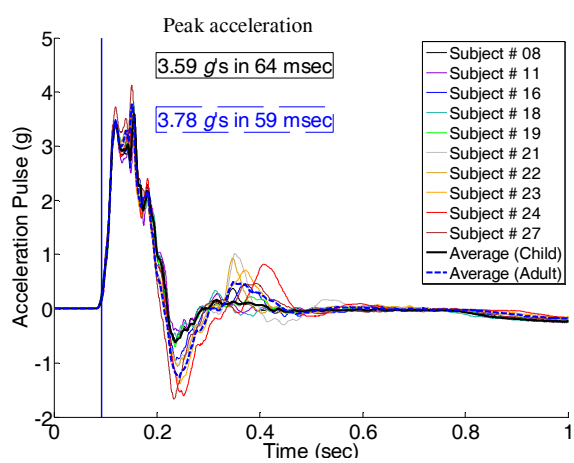

Figure 6. Average sled acceleration pulse with peak values for child and adult subjects.

The sled acceleration pulse from the six trials for each subject were averaged and plotted for the two age groups – child and adult (Figure 6). The children had slightly lower average peak acceleration (3.59 *g*) with slightly longer rise time (64 msec) compared to adults (3.78 *g* in 59 msec).

The marker on the right rear of the cart ('Cart back right – CBR #32') was chosen as the reference point (origin) for the local coordinate axes shown in Figures A1a and A1b (Appendix). All marker trajectories were plotted with respect to this reference point. As an example, the head top marker trajectories were plotted along the sagittal plane (X-Z plane) for each of the six trials and averaged in time. An exemplar head top trajectory for a child and adult subject is shown in Figures 7a and 7b, respectively. Standard deviation bars in X and Z, indicating the variability among the six trials, were plotted at 100 msec intervals for a total duration of 600 msec.

The start point for each trajectory coincides with time zero. The average head top trajectories for the child and adult groups are shown in Figures 8a and 8b, respectively. The variation in the initial position of the trajectory start point between subjects can be attributed to the difference in seated height (Z-axis) and initial fore-aft head position (X-axis). The range of total displacement for the head top marker in the pediatric population was 298 – 371 mm (X-axis) and 38 – 109 mm (Z-axis). Similarly, the total displacement ranges for head top marker in the adult population were 297 – 463 mm (X-axis) and 35 – 79 mm (Z-axis).

The average trajectories for the C4 marker are shown on Figures 9a and 9b. The range of total displacement for the C4 marker in the pediatric population was 180 – 260 mm (X-axis) and 41 – 90 mm (Z-axis). Similarly, the total displacement ranges for C4 marker in the adult population were 211 – 294 mm (X-axis) and 40 – 77 mm (Z-axis). The average left iliac crest (pelvis) marker trajectories are shown on Figures 10a and 10b. The range of total displacement for the pelvis marker in the pediatric population was 81 – 128 mm (X-axis) and 15 – 36 mm (Z-axis). Similarly, the total displacement ranges for pelvis marker in the adult population were 138 – 167 mm (X-axis) and 18 – 38 mm (Z-axis).

The average trajectories for the left and right acromion markers were plotted in the transverse plane (X-Y plane) along with the schematic of a subject in the initial position (Figures 11a and 11b). Both the left and right marker trajectories remained almost perpendicular to this plane throughout the test. This is indicative of a lack of rotation of subjects about their Z-axis during the acceleration, restraint loading and rebound phases.

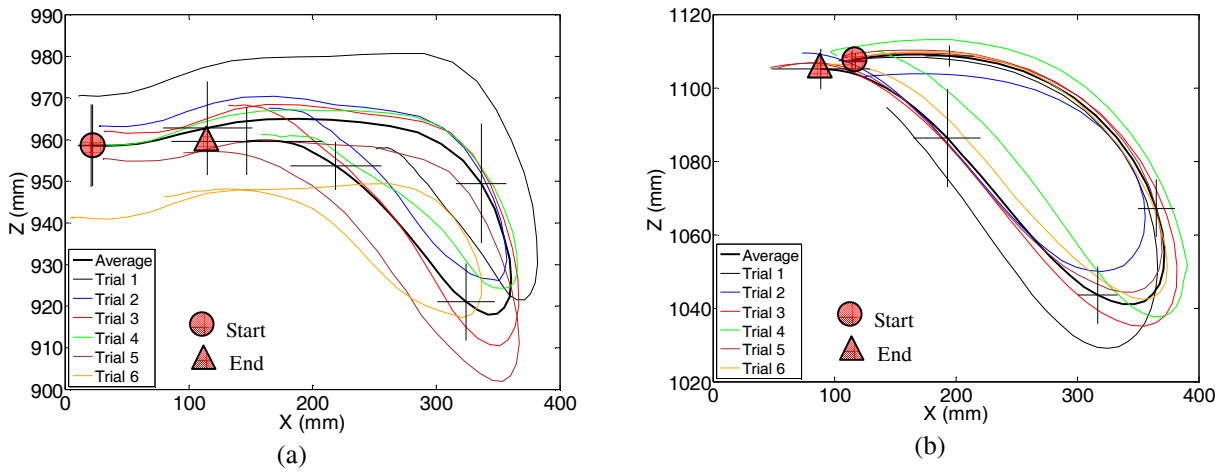

Figure 7. Individual and average (with standard deviation bars in X and Z) head top marker trajectories in the sagittal plane for an exemplar (a) child and (b) adult subject.

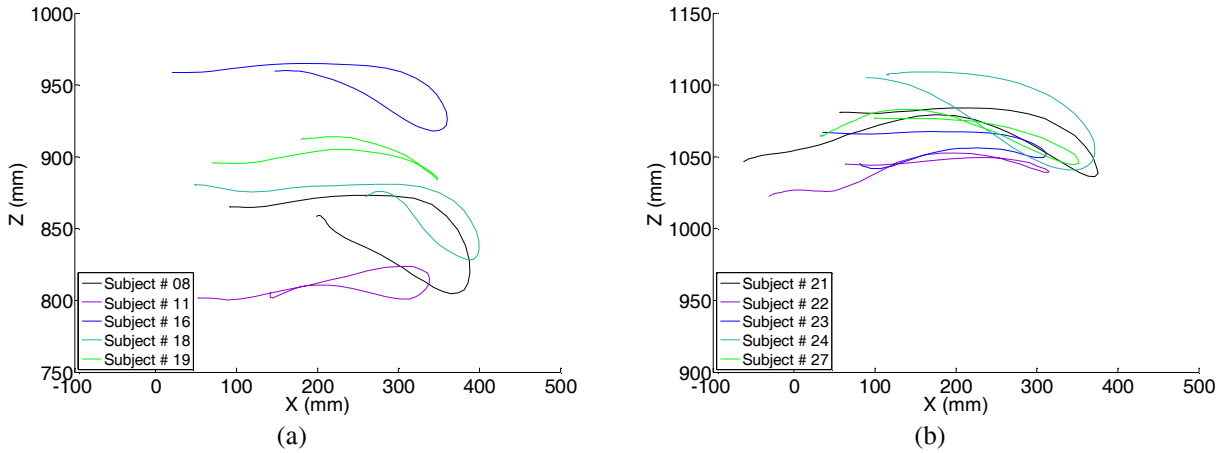

Figure 8. Subject-Average head top marker trajectories in the sagittal plane for the (a) child and (b) adult group.

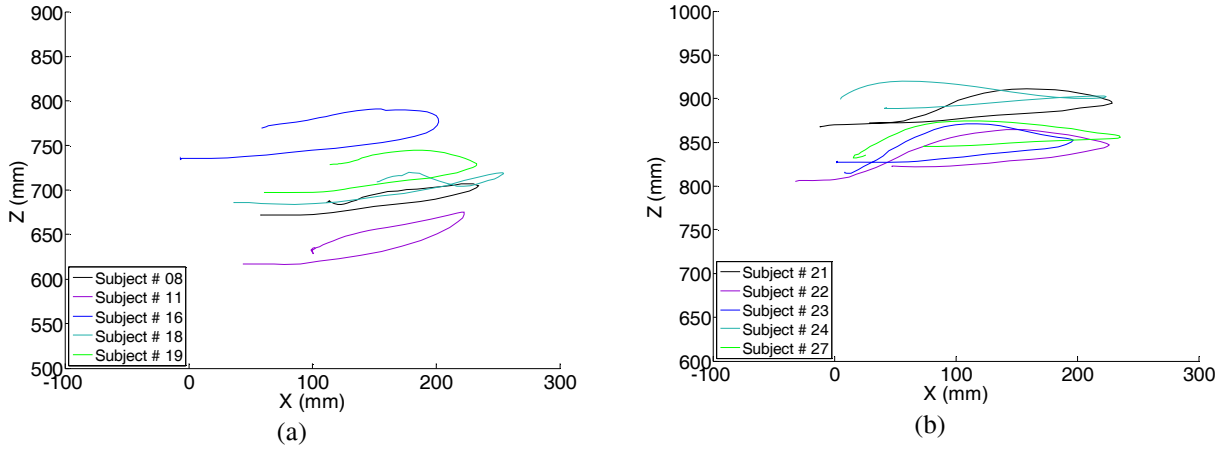

Figure 9. Subject-Average C4 marker trajectories in the sagittal plane for the (a) child and (b) adult group.

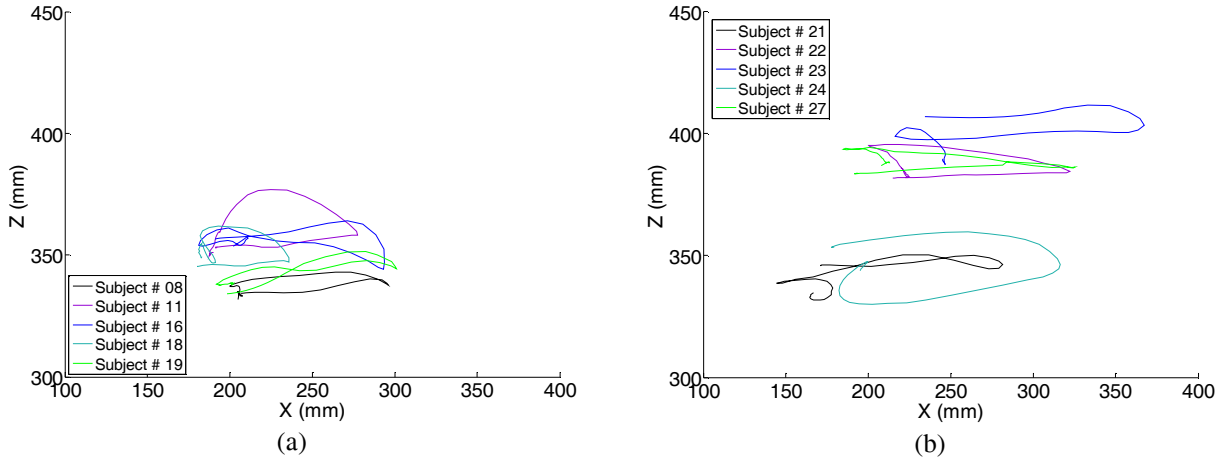

Figure 10. Subject-Average left iliac crest marker trajectories in the sagittal plane for the (a) child and (b) adult group.

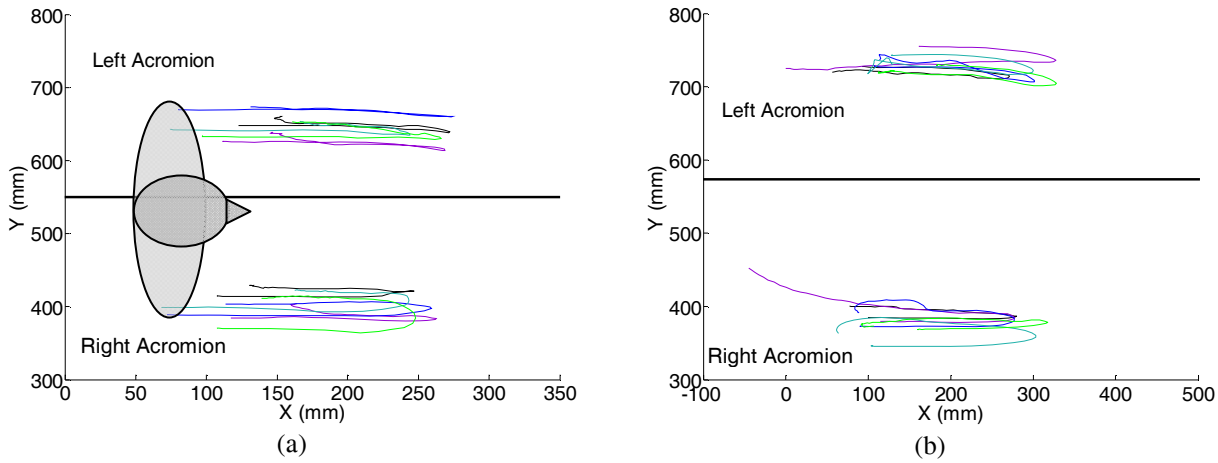

Figure 11. Subject-Average left and right acromion marker trajectories in the transverse plane for the (a) child (superimposed by a schematic of a subject) and (b) adult group.

DISCUSSION AND CONCLUSIONS

This paper describes the development of method and device capable of providing a safe frontal pulse to restrained pediatric and adult human volunteers. While adult volunteers have previously been used in impact biomechanics, this effort represents the first to use child subjects in this manner. The envelope for a safe volunteer crash pulse was derived using a novel approach – determining the "pulse" associated with a bumper car to wall impact in an amusement park setting. From this envelope, a custom designed sled was constructed that allowed for the safe conduct of low speed frontal sled tests for the volunteers. Across the six trials for a single subject, the acceleration pulse is very repeatable. Both adult and child volunteers experience similar accelerations however the mass differences between the subject groups lead to slightly greater restraint loading and rebound phases for the adults.

From the preliminary analyses of the head top marker trajectories, the adult subjects displayed a greater maximum displacement in the X-axis when compared to pediatric subjects. However, in the Z-axis, the pediatric group had a higher maximum displacement when compared to the adult group. This is indicative of a greater angular head rotation in children. Anatomic differences in the pediatric cervical spine – including more horizontal facets, ligaments with increased laxity, and a higher fulcrum of rotation – likely lead to these differences. It is important to note that these results demonstrate differences between adults and those 9-12 years – an age group which is not universally considered "pediatric" from a biomechanical perspective.

Future studies will combine data from the angular rate sensor with the head trajectories to understand the nature and timing of these differences in head rotation. Normalization schemes using anthropometric measures will shed insight into whether this variability is truly age dependent or can be explained by differences in size. .

Previous rear impact studies of adult human volunteers exposed to repeated acceleration of similar magnitude demonstrated a habituation response of the neck muscles, thereby leading to muscle relaxation with subsequent exposure (Blouin et al., 2003). In this study the pediatric and adult volunteers were subjected to a series of six frontal impacts of equal magnitude. If there is attenuation in neck muscle response with repeated exposure, one would expect increased head excursion in subsequent trials. But, no such trends were observed in these tests. Future work will correlate the dynamic EMG activity to the head and neck kinematics.

Several limitations of this approach need to be discussed. First, the head and neck trajectories were measured using a 'state of the art' 3D motion capture system utilizing markers affixed to the skin. Some error exists in assuming these skin markers exactly match the movement of the skeletal structures they represent. The magnitude of this error can be assessed by examining the time change of the distance between markers affixed to points on the same rigid body. For the head and neck, these differences are less than 2%. Second, examination of the acromion trajectories in the transverse plane revealed little movement perpendicular to this plane. Subjects primarily moved in the sagittal plane. For this reason, in this manuscript, although, three dimensional data were recorded, only two dimensional analyses were performed. The 2D plots of the marker trajectories were projections of the 3D trajectories on the sagittal plane. This approach may lead to slight under estimation of marker displacements.

In the absence of traditional efforts to define biomechanical response for children using pediatric PMHS, this approach represents a novel means by which to obtain important data that is needed for the design of biofidelic ATDs. By subjecting living child volunteers to sub-injurious dynamic loading, we gain a quantitative understanding of how real children move compared to adults. The human volunteer work described herein is part of a larger project in collaboration with University of Virginia and Takata Corporation in which adult PMHS will be subjected to crashes similar to those experienced by the volunteers and then those same PMHS will be loaded at crash relevant speeds. The synthesis of the volunteer data with the adult PMHS data using either traditional scaling methods and/or computational models will greatly increase our knowledge of the biomechanics of child occupants, leading to better tools for optimizing protection of these occupants in motor vehicle crashes.

ACKNOWLEDGEMENTS

The authors would like to thank all the human volunteers who participated in this study for their patience and willingness to take part in this research, Richard Kent, PhD (University of Virginia) for his assistance in design of the LASB and Ewout van der Laan, MSc (Technical University of Eindhoven, The Netherlands) for helping design the sled control system. The authors would like to acknowledge Takata Corporation, Japan for their collaboration and financial support for this study. The results presented in this report are the interpretation solely of the author(s) and are not necessarily the views of Takata Corporation.

REFERENCES

Adekoya, N., D. Thurman, D. White and K. Webb (2002) "Surveillance for traumatic brain injury deaths – United States, 1989-1998." MMWR Surveill Summ. 51(10): 1-14.

Arbogast K.B., J.S. Jermakian, Y. Ghati, R .Smith, R.A. Menon and M.R. Maltese (2005) "Patterns and predictors of pediatric head injury." Proceedings of the International Research Conference on the Biomechanics of Impact, Prague, Czech Republic.

Arbogast, K. B., I. Chen, D. Durbin and F. K. Winston (2004). "Injury risks for children in child restraint systems in side impact crashes." Proceedings of the International Research Conference on the Biomechanics of Impact, Graz, Austria.

Arbogast, K. B., R. A. Cornejo, M. J. Kallan, F. K. Winston and D. R. Durbin (2002) "Injuries to children in forward-facing child restraints." Annu Proc Assoc Adv Automot Med 46: 213-30.

Blouin J.S., M. Descarreaux, A. Blanger-Gravel, M. Simoneau and N. Teasdale (2003) "Attenuation of human neck muscle activity following repeated imposed trunk-forward linear acceleration." Experimental Brain Research. 150:458-464

Braksiek R.J and D. Roberts (2002) "Amusement Park Injuries and Deaths." Annals of Emergency Medicine. 39:1

CDC growth charts (2000) Center for Disease Control and Prevention Growth Charts – Published May 30, 2000. http://www.cdc.gov/GrowthCharts/

Durbin, D. R., M. R. Elliott and F. K. Winston (2003) "Belt-positioning booster seats and reduction in risk of injury among children in vehicle crashes." JAMA 289(21): 2835-40.

Ewing C.L., D.J. Thomas, G.W. Beeler, L.M. Patrick and D.B Gillis (1968) "Dynamic response of head and neck of living human to gravity impact acceleration." Proceedings of the twelfth Stapp Car Crash Conference. P-26. Paper 680792. Society of Automotive Engineers Inc.,

Howard, A., L. Rothman, A. McKeag et al (2003) "Children in side impact motor vehicle crashes: seating positions and injury mechanisms." Journal of Trauma 56: 1276-1285.

Kallieris, D., G. Schmidt, J. Barz, R. Mattern and F. Schulz (1978) "Response and Vulnerability of the Human Body at Different Impact Velocities in Simulated Three-Point Belted Cadaver Tests." Proc. IRCOBI, pp.105-209

Malott, A., C. Parenteau, S. Marigowda and K. Arbogast (2004) "Sled test results using the Hybrid III 6 year olds: an evaluation of various restraints and crash configurations." SAE World Congress, Detroit, MI, Society of Automotive Engineers.

Menon, R., Y. S. Ghati, S. Ridella, S. Roberts and F. K. Winston (2003) "Evaluation of restraint type and performance tested with 3- and 6-year-old Hybrid III dummies at a range of speeds." SAE 2003 World Congress.

Mertz H.J and L.M. Patrick (1971) "Strength and response of the human neck." Proceedings of the fifteenth Stapp Car Crash Conference. P-39. Paper 710855. Society of Automotive Engineers Inc.,

NHANES data (1994) Center for Disease Control and Prevention Anthropometric reference data (1988 - 1994) http://www.cdc.gov/nchs/about/major/nhanes/anthropometric_measures.htm

Orzechowski, K., E. Edgerton, D. Bulas et al (2003) "Patterns of injury to restrained children in side impact motor vehicle crashes: the side impact syndrome." Journal of Trauma 54: 1094-1101.

Reed M.P., S.M. Ebert-Hamilton and L.W. Schneider (2005) "Development of ATD Installation Procedures Based on Rear-Seat Occupant Postures." Proceedings of the 49th Stapp Car Crash Conference. P-394. Paper 2005-22-0018. Society of Automotive Engineers Inc.,

Shaw, C, R. Kent, E. Sieveka and J. Crandall (2001) "Spinal kinematics of restrained occupants in frontal impacts." IRCOBI Conference on the Biomechanics of Impact, Isle of Man.

Sherwood, C., C. Shaw, L. V. Rooij, R. Kent, J. Crandall, K. Orzechowski, M. Eichelberger and D. Kallieris (2003) "Prediction of cervical spine injury risk for the 6-year-old child in frontal crashes." Traffic Inj Prev **4**(3): 206-213.

Stapp, J. (1949). "Human response to linear deceleration." AF Technical Report 5915

Thompson, M. and J. Irby (2003) "Recovery from mild head injury in pediatric populations." Seminars in Pediatric Neurology 10(2): 130-139.

Wismans, J., M. Phillippens, E. van Oorschot, D. Kallieris and R. Mattern (1987) "Comparison of human volunteer and cadaver head-neck response in frontal flexion." Stapp Car Crash Conference.

Zuckerbraun, BS, K. Morrison, B. Gaines, H.R. Ford, D.J. Hackam (2004) "Effect of Age on Cervical Spine Injuries in Children After Motor Vehicle Collisions: Effectiveness of Restraint Devices." J Pediatr Surg 39:483-486.

APPENDIX

Table A1.
List of motion analysis marker locations on the subject and seating buck

Marker #	Name	Abbreviation	Marker #	Name	Abbreviation
1	Head Top	HT	28	Buckle Bottom	BB
2	Head Front	HF	29	Buckle Top	BT
3	Head Left	HL	30	Angular Rate Sensor	ARS
4	Head Right	HR	31	Cart Back-Left	CBL
5	Opisthocranion	OP	32	Cart Back-Right	CBR
6	EAM Left	EAML	33	Cart Front-Left	CFL
7	Nasion	NAS	34	Cart Front-Right **Reference**	CFR
8	EAM Right	EAMR	35	Foot Rest Back Left	FRBL
9	C4	C4	36	Foot Rest Back Right	FRBR
10	T1	T1	37	Foot Rest Front Left	FRFL
11	T4	T4	38	Foot Rest Front Right	FRFR
12	T8	T8	39	Seatback 1	SB1
13	T12	T12	40	Seatback 2	SB2
14	Acromion Left	ACL	41	Seatback 3	SB3
15	Acromion Right	ACR	42	Seatback 4	SB4
16	Humeral Epicondyle Left	HEL	43	Seatpan Back-Left	SPBL
17	Humeral Epicondyle Right	HER	44	Seatpan Back-Right	SPBR
18	Ulnar Styloid Process Left	USPL	45	Seatpan Front-Left	SPFL
19	Ulnar Styloid Process Right	USPR	46	Seatpan Front-Right	SPFR
20	Supra-Sternal Notch	SSN	47	Tower Bottom-Front	TWBF
21	Xiphoid Process	XP	48	Tower Bottom-Rear	TWBR
22	Iliac Crest Left	ICL	49	Tower Top-Front	TWTF
23	Iliac Crest Right	ICR	50	Tower Top-Rear	TWTR
24	Femoral Epicondyle Left	FEL	51	Belt	BLT
25	Femoral Epicondyle Right	FER	52	D-Ring Front	DRF
26	Lateral Malleolus Left	LML	53	D-Ring Rear	DRR
27	Lateral Malleolus Right	LMR			

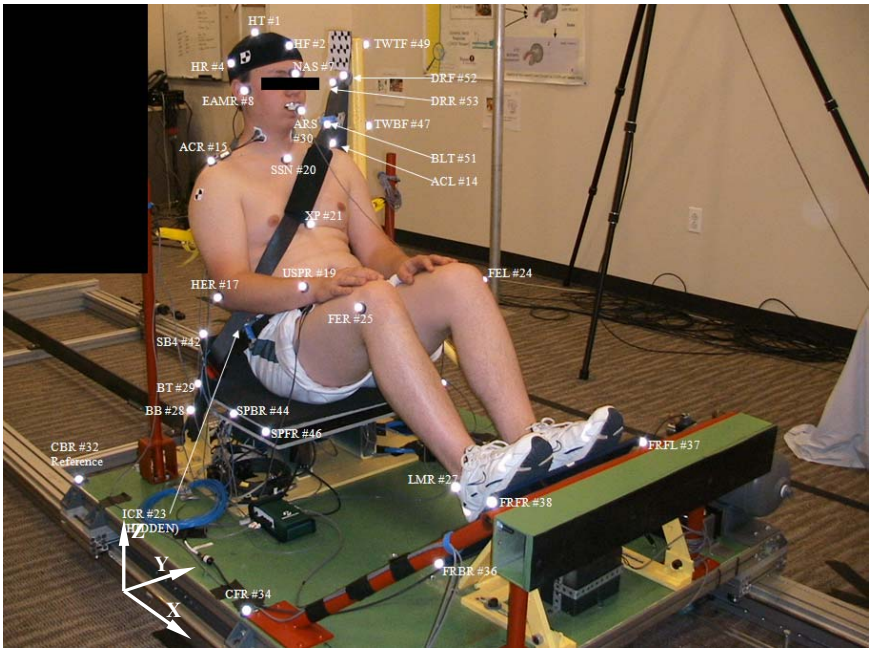

(a)

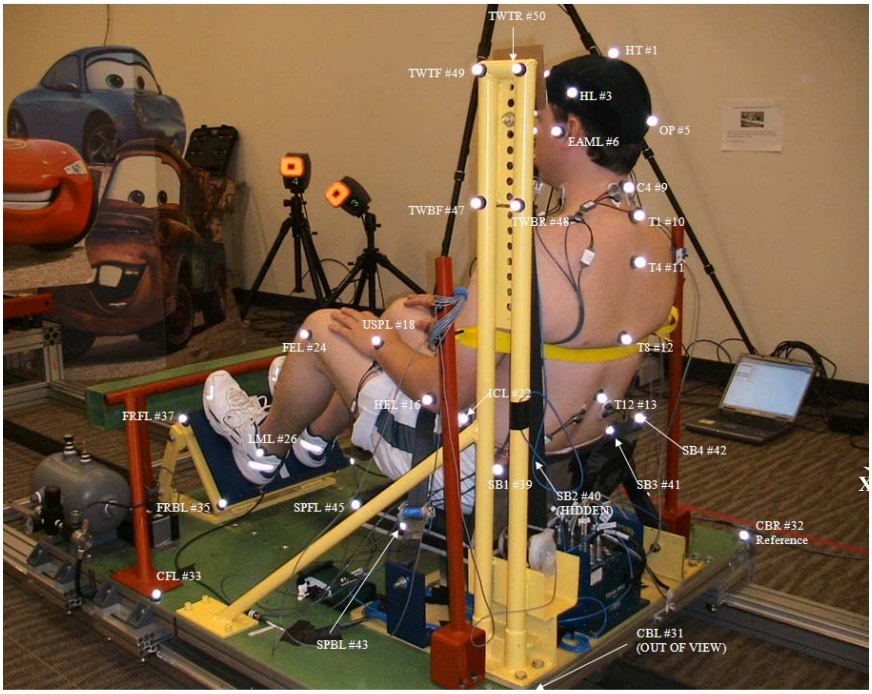

(b)

Figure A1. (a) Frontal view and (b) rear view of an adult subject seated in LASB with all motion analysis markers labeled. The local coordinate axes along with the reference marker is shown.

COMPARISON OF PASSIVE CERVICAL SPINE FLEXION IN CHILDREN AND ADULTS

Thomas Seacrist, MBE
Matthew R. Maltese, MS
Sriram Balasubramanian, PhD
J. Felipe Garcia-Espana, PhD
Kristy B. Arbogast, PhD
Center for Injury Research and Prevention
The Children's Hospital of Philadelphia
USA
Robert Sterner, PhD
Department of Health and Exercise Science
Rowan University
USA
Jami Saffioti, MS
Jennifer Kadlowec, PhD
Department of Mechanical Engineering
Rowan University
USA
Paper Number 09-0142

ABSTRACT

Head trauma is the most frequent injury sustained by children in car crashes, and the neck plays a key role in governing head kinematics during the crash. Pediatric anthropomorphic test devices (ATDs) are used to assess the risk of head injury, yet the pediatric ATD neck is a size-scaled model of the adult ATD neck, with no consideration for the tissue properties and morphological changes during human development. To help understand the effects of maturation on the changes in neck flexion biomechanics, this study compared the passive cervical spine flexion of children to adults in specific age groups (6-8, 9-12, 20-29, 30-40 years). Subjects with restrained torsos and lower extremities were exposed to a 1g inertial load in the posterior-to-anterior direction, such that the head-neck complex flexed when the subject relaxed their neck musculature. Surface electromyography with audio feedback was used to coach the subjects to relax their neck musculature. A multicamera 3-D target tracking system was employed to capture the motion of specific landmarks on the head (Frankfort Plane) and thoracic spine (T1 and T4). Neck flexion angle with muscles relaxed was calculated for each subject. Neck flexion angle significantly decreased with age, with changes in head-to-neck girth ratio partially explaining the decrease. A statistically significant increase in cervical spine flexion was found in adult females compared to adult males. Data also illustrate this trend in children, but it was not statistically significant. In summary, these results demonstrate an increased passive cervical spine flexion in children compared to adults, and females compared to males. These data will help guide the development and validation of pediatric ATDs.

INTRODUCTION

Head trauma is the most frequent injury sustained by children in car crashes (Durbin et al., 2003) and the neck plays a key role in governing head kinematics during the crash. Designing effective motor vehicle safety systems to mitigate such injuries requires the use of a humanlike (biofidelic) anthropomorphic test device (ATD). In the case of head injury assessment, it is essential that the ATD accurately predict the likelihood of an interior head impact and, given an impact, the velocity and orientation of the head immediately prior to impact.

The ATD neck is of particular importance when predicting head kinematics as it is the primary structure through which restraint loads are transferred from the torso to the head. The biofidelity requirement for the adult ATD neck is specified as a relationship between the bending moment at the head/neck junction and the angle between the head and the torso (Mertz et al., 1989). This relationship has been quantified for adults via experimental studies of the cervical spine in post-mortem human subjects (PMHS), post-mortem animal subjects (PMAS), and live human volunteers (Mertz and Patrick, 1967; Mertz and Patrick, 1971; Ewing and Thomas, 1973; Mertz and Patrick, 1973; Melvin et al., 1973; Ewing et al., 1975; Ewing et al., 1976; Patrick and Chou, 1976; Ewing et al., 1977; Ewing et al., 1978; Begeman et al., 1983; Wismans and Spenny, 1984; Wismans et al., 1986; Ma et al., 1995;

Thunnissen et al., 1995; Deng et al., 1998, Ching et al., 2001; Hilker et al., 2002; Nightingale et al, 2002; Nuckley and Ching, 2006; Nightingale et al., 2007). However, owing to the paucity of pediatric cadaver biomechanical data, the 3 and 6 year old pediatric ATD necks have been based on size-scaled models of adult data with little consideration for the tissue and morphological changes during human development (Irwin and Mertz, 1997).

A growing body of literature suggests that, biomechanically, children are not simply size-scaled versions of adults. From year 1 to 2, C1 consists of three boney masses that fuse to form the ring structure of C1 at age 4 to 6 years. Similarly, at birth C2 is comprised of 4 pieces, and fuses completely by age 6 years. Vertebrae C3 through C7 are each represented by 3 separate boney masses at birth, which fuse by age 4 years. The uncovertebral joints present in C3-C7 do not form until age 6 years (Schuer and Black, 2000). In the child, the ligaments are lax as compared to the adult, and the facets are predominantly horizontal, thus providing limited restriction of anterior-posterior shear (subluxation) at the facets (Bailey, 1952; Townsend and Rowe, 1952; Sullivan et al., 1958; Cattell and Filtzer, 1965; Kewalramani and Tori, 1980; Walsh et al., 1983; Menezes, 1987; Hadley et al., 1988; Pollack et al., 1988; Fuchs et al, 1989; Osenbach and Menezes, 1989; Janssen et al., 1991; Kriss and Kriss, 1996; Schuer and Black, 2000; Weber, 2002; Yoganandan et al., 2002). The current pediatric neck scaling procedures (Irwin and Mertz, 1997) do not consider age-dependent differences beyond size. Consequently, the biofidelity of current pediatric ATD necks are called into question.

Recent studies have examined the differences in biomechanical response of the cervical spine across the age range using PMHS, PMAS and human volunteers. Using a baboon model, Ching et al. (2001) measured the tensile stiffness of different functional spinal units (FSU). The results illustrated an average 75% increase in tensile stiffness of the C7-T1 FSU compared to the Oc-C2 FSU in 3 year old specimens, versus a 6% decrease in 12 year old specimens. A second baboon model by Nuckley and Ching (2006) showed a significant correlation between maturation and increasing tensile and compressive stiffness of the cervical spine. Hilker et al. (2002) demonstrated that the bending stiffness of 6 and 12 year old human age-equivalent caprine specimens were 40% and 60% of adult caprine specimens, respectively. Increased tensile stiffness with age has also been demonstrated in pediatric PMHS tests. Nuckley et al. (2005) found increased compressive stiffness at the C3-C5 joint while assessing 11 PMHS spines from 2 to 28 years of age. Similarly, Ouyang et al. (2005) examined 10 pediatric PMHS head-neck complexes with intact ligamentous cervical spines and found a 46% increase in tensile failure in older pediatric subjects (6-12 years) versus younger subjects (2-4 years).

Perhaps most relevant to the current study, Arbogast et al. (2007) measured the active cervical spine range of motion in 67 pediatric volunteers from ages 3 to 12 years. In this study, subjects with restrained torsos were asked to flex, extend, laterally bend, and rotate to their maximum range under active muscle control. The study concluded that, in children 3-12 years, active cervical spine flexion and horizontal rotation increased with age. Overall flexion in children was found to be greater than adults. This previous study characterized the active range of motion which is governed in part by forces generating by active firing of the muscles. As a complement to this work, we sought to characterize cervical flexion under *passive* muscle forces in pediatric and adult volunteers. Based on previous literature, we hypothesized that passive cervical spine flexion of pediatric volunteers will be greater than that of adults.

METHODS

Participants

Children 6-12 years and adults 20-40 years were enrolled into one of four age groups (6-8, 9-12, 20-29, and 30-40 years). Subjects were prescreened for prior injuries, physical limitations, or medical conditions involving the head, neck, or spine and to ensure their body mass index (BMI) fell within the 10th to 90th percentile.

Anthropomorphic Data

Subjects' height and weight were measured prior to setup and their BMI was calculated. The following anthropometric data were gathered using a flexible tape ruler: head girth, neck height (opisthocranion to C7), neck girth, seated height, and sternum height (distance from Xyphoid Process to the Manubrium).

Instrumentation

Subjects were asked to remove their shirt(s) and don a tight fitting, sleeveless shirt with cutouts along the thoracic spine and on the shoulders to accommodate photoreflective markers and EMG electrodes on the skin. Prior to electrode placement, each subject's

skin was cleaned by applying NUPREP Skin Prepping Gel (Weaver and Co., Aurora, CO). Disposable, self-adhesive dual surface electrodes (Noraxon, Inc., Scottsdale, AZ) were placed bilaterally on the sternocleidomastoid (SCM), paraspinous (PS), and trapezious (TR) muscles (See Figure 1). A grounding electrode was centered over the left mastoidale. Electrodes were connected to the TeleMyo 2400T V2 telemetry system (Noraxon, Inc., Scottsdale, AZ) and electromyography (EMG) data were recorded throughout each trial at 1000 Hz per channel.

To collect our primary data measure, cervical spine flexion, the Eagle 1 Digital RealTime motion capture system (Motion Analysis, Inc., Santa Rosa, CA) was used. The Eagle 1 system consists of 8 cameras capable of tracking photoreflective markers in 3D space. To detect movement of the head, spine, torso and testing apparatus, 10mm diameter reflective markers were placed in the following locations (See Figure 2):

- Acromion Processes
- External Auditory Meatus (1.5 cm anterior)
- Head (on cap) front, left, right, top
- Midpoint between Xyphoid Process and Supra Sternal Notch
- Nasion
- Seatback top and bottom
- Sternoclavicular joints (~3 mm lateral to the sternoclavicular joint)
- T1
- T4

Motion analysis data were collected for each trial at a sampling rate of 60 Hz.

After EMG and motion analysis setup was complete, subjects were escorted to the testing apparatus. (See Figure 3) The device consisted of a rigid seatback, four point belt system, and thigh and lower leg restraints. The seat was attached to a motor capable of rotating subjects slowly through an angle of 90

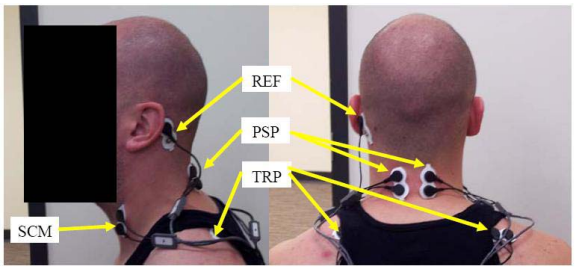

Figure 1. Electromography (EMG) electrodes were attached to the sternocleidomastoid (SCM), trapezious (TRP), paraspinous (PSP), and a reference (REF).

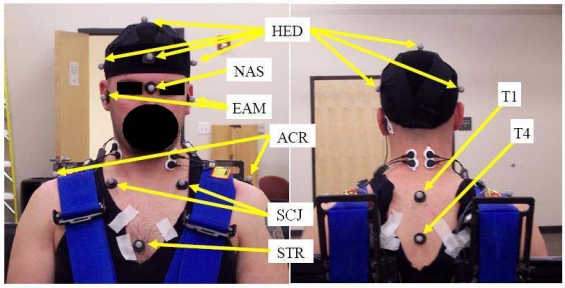

Figure 2. Anterior (left) and Posterior (right) Motion Analysis Marker Placement. Markers were attached to the acromion processes (ACR), four positions on the head (HED), external auditory meatus (EAM), nasion (NAS), sternoclavicular joints (SCJ), mid-sternum (STR), T1, T4, and the seatback top and bottom (not shown).

degrees. The subject was asked to sit in the test apparatus and don the restraints provided. With assistance from a member of the research team, the restraints were adjusted to restrict the motion of the torso, pelvis and lower extremities. An EZ-TILT-2000 rev-2 gravity-based tilt sensor (Advanced Orientation Systems, Inc., Linden, NJ) was placed on the subject's skin between the T1 and T4 markers. This tilt sensor provided real-time measure of the angle of the upper torso with respect to ground, and allowed the researchers to rotate seat of the test apparatus such that the subject's spine reached specific, predetermined angles with respect to ground.

Neck Muscle Relaxation Criteria

The Resting-to-Active Transition Voltage (RATV) was established for each subject as follows to provide an objective assessment of muscle activity. Once secured in the test apparatus with EMG electrodes attached, the subjects were instructed to relax their neck musculature, allowing the neck to flex forward under the influence of gravity. Subjects were coached to relax their neck muscles using the phrase "relax your neck muscles, as if you were asleep" and

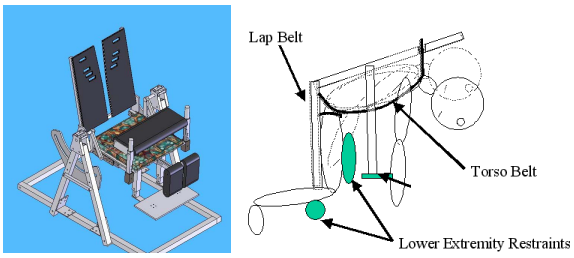

Figure 3. Test Apparatus Design (left) and Function with Occupant (right).

"allow your head to fall forward." The RATV was initially set as the maximum voltage measured from any of the measured muscle groups in this relaxed state. The subjects were then instructed to voluntarily raise their head up, and the maximum voltage from any of the measured neck muscle groups was noted and the RATV adjusted to this value. This process was repeated iteratively until the all neck muscle voltages were a) just below the RATV value in the relaxed state, and b) just above the RATV as the subjects raised their head from the relaxed state. A smoothing window of 500 ms was used to analyze the data.

Testing Protocol

With the subjects seated and restrained in the test apparatus, before the test began, the subjects were instructed to relax their shoulder muscles during the test, allowing their arms to rest freely in their lap. Subjects were given a countdown after which they were instructed allow their neck to flex while seated upright. Subjects were coached via automated EMG audio feedback to relax their muscles to a state at or below the RATV. Once EMG levels were below the RATV, subjects were instructed to remain relaxed for approximately ten seconds. Throughout the experiment EMG and the target tracking system were continuously recording data. (Note: In the data analysis phase, neck muscle relaxation during the test was reviewed; and if the subject's muscle activation did not meet certain criteria with respect to the RATV, that subject's trial was removed from the analysis. This is described further in the Data Reduction section.) Immediately following, the chair portion of the test apparatus was rotated forward until the subject's spine (vector from T1 to T4) was at 45° relative to ground. Subjects were again coached to relax their neck musculature and allow their necks to flex forward and relax for ten seconds, all while EMG and target tracking data were collected. Subjects were rotated further until their spine (vector from T1 to T4) was parallel to the ground, and coached to relax their musculature, and held in position for ten seconds while EMG and target tracking data were collected. At the conclusion of the three rotations, subjects were returned to the starting position and given a short break, approximately one minute, before beginning the next trial. To acclimate the subject to the test environment, several iterations of the protocol described above were conducted before data were collected. Then, for data collection the previous test sequence was repeated for a total of three trials.

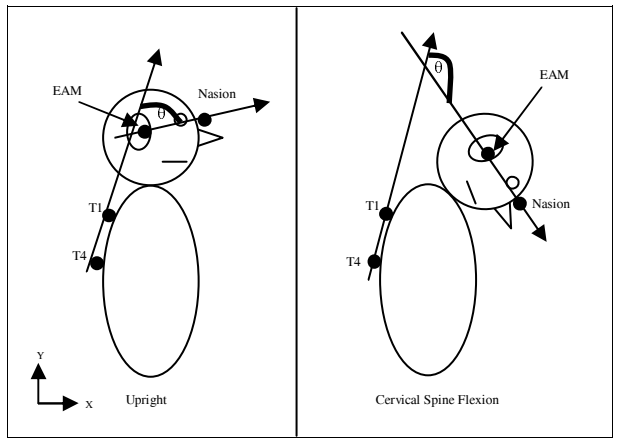

Figure 4. Head vs. Spine Angle Calculation

Data Reduction

The time series motion analysis data for each trial of all subjects were imported into MATLAB (Mathworks, Inc., Natick, MA) for data analysis using a custom written program. A head vector was generated from the midpoint of the left and right EAM markers and the nasion, the seat vector from the upper and lower markers placed on the seatback and the spine vector from the T4 to the T1 marker. The resulting head, seat and spine vectors were projected onto the sagittal plane. The head vs. spine angle was computed as the angle between the head and spine vectors shown in Figure 4. Average angle values were computed during the portions of the trial where the test apparatus was stationary and the subject's muscle activity remained below his/her RATV for one or more seconds. Conditions and/or trials where the subjects' paraspinous or SCM muscle activity remained above their RATV, leaving less than one second of relaxation, were eliminated from the head vs. spine angle analysis. Head vs. spine angles were averaged across age groups for comparison.

We postulated that a patient with a disproportionately large head compared to their neck would have greater mass and thus greater forces acting to flex the neck, and thus we calculated the head-to-neck girth (Equation 1) and incorporated this into our analyses.

$$Head-to-Neck\ Girth = \frac{Head\ Girth}{Neck\ Girth} \qquad (1).$$

Similarly, we postulated that the slenderness of the neck would also influence its flexibility under load, and thus we calculated the neck slenderness (Equation 2).

$$Neck\ Slenderness = \frac{Neck\ Length}{Neck\ Girth} \qquad (2).$$

Statistical Analysis

Anthropometry ratios were imported into SPSS 14.0 (SPSS, Inc., Chicago, Illinois) and SAS 9.2 (SAS Institute Inc., Cary, NC) for statistical analysis. The experiment-wise error rate was held at the 0.05 level. Data were analyzed using both descriptive and inferential statistical techniques. Analysis occurred in three distinct phases. In phase I, descriptive statistics such as frequency distributions, histograms and measures of central tendency, variability, and association were computed for all relevant variables in the dataset. In order to use appropriate statistical methods, variables were tested for normality. In phase II, bivariate plots were generated in which age and head-to-neck girth ratio were plotted against angle for each subject and gender. In phase III, inferential statistical techniques were applied.

A one-way Analysis of Variance (ANOVA) with a Post-Hoc Tukey's Honestly Significant Difference test was used to compare the head-to-neck girth and neck slenderness ratios between the 6-8, 9-12, 20-29, and 30-40 year old groups.

Generalized estimating equations (GEE), with an unstructured correlation matrix, were used to assess the association between age, gender, and head-to-neck girth with passive cervical spine flexion. GEE modeling was used because the design of the study included repeated measures (i.e. multiple trials) for every angle tested (multiple conditions) leading to correlated outcome data. To distinguish between adult and pediatric age groups, analyses were stratified by age (6-12 years old and 20+) for the GEE analyses.

RESULTS

Overall, 38 subjects were enrolled. Sample data including mean age, gender distribution and anthropomorphic ratios for each age group are listed in Table 1.

Table 1.
Age-Based Sample Data

Subjects	Age	Gender	BMI	Head Girth	Neck		Head-to-Neck Girth Ratio	Neck Slenderness Ratio
					Height	Girth		
	yrs	M/F	kg/m^2	cm	cm	cm		
6-8 Year Old	6	M	15	52	12.7	26.3	1.98	0.48
	6	M	14	52	14.5	27	1.93	0.54
	6	F	16	51	14	26	1.96	0.54
	7	F	16	49.9	14	29	1.72	0.48
	7	F	20	49	14	30	1.63	0.47
	7	M	14	53	14	27.5	1.93	0.51
	8	F	14	49	13	24	2.04	0.54
	8	M	17	54.9	15	30.5	1.80	0.49
	8	F	16	53	17	26	2.04	0.65
Average	7.0	M=4 F=5	16	51.5	14.2	27.4	1.89	0.52
Std Dev	0.9		2	2.0	1.2	2.1	0.05	0.02
9-12 Year Old	9	M	14	53.7	11.5	25.5	2.11	0.45
	9	M	15	51.5	11.6	27.5	1.87	0.42
	10	F	21	55	16.5	28.5	1.93	0.58
	10	M	15	52.5	15	28	1.88	0.54
	10	F	17	53.6	17.3	28	1.91	0.62
	11	F	17	53.5	17	28.3	1.89	0.60
	11	M	20	56	17	32	1.75	0.53
	11	F	20	54.5	16.5	29	1.88	0.57
	12	F	23	55.1	16.5	31.5	1.75	0.52
	12	M	18	55.5	15.5	31	1.79	0.50
Average	10.5	M=5 F=5	18	54.1	15.4	28.9	1.88	0.53
Std Dev	1.1		3	1.4	2.2	2.0	0.03	0.02
20-29 Year Old	20	M	25	58	19.5	39.5	1.47	0.49
	20	M	22	58.2	15.5	36.5	1.59	0.42
	21	M	19	54.5	17.5	35	1.56	0.50
	21	F	25	57	16.5	32	1.78	0.52
	22	M	24	55.5	15.5	36	1.54	0.43
	22	F	20	57.5	20	31.5	1.83	0.63
	22	F	20	55.5	17	31.5	1.76	0.54
	22	M	27	58.5	16.5	41.5	1.41	0.40
	24	F	23	57	12.3	31	1.84	0.40
	26	M	22	58	20.5	36.9	1.57	0.56
Average	22.0	M=6 F=4	23	57.0	17.1	35.1	1.64	0.49
Std Dev	1.8		3	1.4	2.5	3.6	0.05	0.02
30-40 Year Old	31	F	23	56	15	32.5	1.72	0.46
	32	M	28	62	16	41	1.51	0.39
	33	F	23	57.5	18	33.5	1.72	0.54
	34	M	23	56.8	17	37	1.54	0.46
	36	M	26	58.5	21	39	1.50	0.54
	37	F	23	56	13.5	32	1.75	0.42
	37	F	27	59	16	35	1.69	0.46
	40	F	22	56.5	16	34.5	1.64	0.46
	40	F	35	52.5	19	40	1.31	0.48
Average	35.6	M=3 F=6	26	57.2	16.8	36.1	1.60	0.47
Std Dev	3.3		4	2.6	2.2	3.3	0.05	0.02

Age- and Gender-Based Differences in Anthropometry

Results revealed significantly larger head-to-neck girth ratio in 6-8 year olds when compared to 20-30 year old group ($p<0.01$) and the 30-40 year old group ($p<0.01$). Similarly, 9-12 year olds exhibited significantly larger head-to-neck girth ratios compared to the 20-30 year old group ($p<0.01$) and the 30-40 year old group ($p<0.01$). No significant differences were found between the 6-8 year old group and the 9-12 year old group ($p=0.99$). No significant differences were found between the 20-29 and 30-40 year old groups ($p=0.94$). No significant differences were found in neck slenderness ($p\geq0.13$).

To detect gender related differences, the 38 subjects were organized into four gender-age groups. Since no significant differences in head-to-neck girth were found between the 6-8 and 9-12 year age groups or between the 20-29 and 30-40, the 6-12 year olds and the 20-40 year olds were combined into single

Table 2.
Gender-Based Sample Data

Subjects	Age	Gender	BMI	Head Girth	Neck		Head-to-Neck Girth Ratio	Neck Slenderness Ratio
					Height	Girth		
	yrs	M/F	kg/m^2	cm	cm	cm		
Female Pediatric	6	F	16	51	14	26	1.96	0.54
	7	F	16	49.9	14	29	1.72	0.48
	7	F	20	49	14	30	1.63	0.47
	8	F	14	49	13	24	2.04	0.54
	8	F	16	53	17	26	2.04	0.65
	10	F	21	55	16.5	28.5	1.93	0.58
	10	F	17	53.6	17.3	28	1.91	0.62
	11	F	17	53.5	17	28.3	1.89	0.60
	11	F	20	54.5	16.5	29	1.88	0.57
	12	F	23	55.1	16.5	31.5	1.75	0.52
Average	9.0	F=10	18.1	52.4	15.6	28.0	1.9	0.6
Std Dev	2.1		3.0	2.4	1.6	2.2	0.1	0.1
Female Adult	21	F	25	57	16.5	32	1.78	0.52
	22	F	20	57.5	20	31.5	1.83	0.63
	22	F	20	55.5	17	31.5	1.76	0.54
	24	F	23	57	12.3	31	1.84	0.40
	31	F	23	56	15	32.5	1.72	0.46
	33	F	23	57.5	18	33.5	1.72	0.54
	37	F	23	56	13.5	32	1.75	0.42
	37	F	27	59	16	35	1.69	0.46
	40	F	22	56.5	16	34.5	1.64	0.46
	40	F	35	52.5	19	40	1.31	0.48
Average	30.7	F=10	24.2	56.5	16.3	33.4	1.7	0.5
Std Dev	7.8		4.5	1.7	2.4	2.7	0.2	0.1
Male Pediatric	6	M	15	52	12.7	26.3	1.98	0.48
	6	M	14	52	14.5	27	1.93	0.54
	7	M	14	53	14	27.5	1.93	0.51
	8	M	17	54.9	15	30.5	1.80	0.49
	9	M	14	53.7	11.5	25.5	2.11	0.45
	9	M	15	51.5	11.6	27.5	1.87	0.42
	10	M	15	52.5	15	28	1.88	0.54
	11	M	20	56	17	32	1.75	0.53
	12	M	18	55.5	15.5	31	1.79	0.50
Average	8.7	M=9	15.9	53.5	14.1	28.4	1.9	0.5
Std Dev	2.1		2.1	1.7	1.8	2.3	0.1	0.0
Male Adult	20	M	25	58	19.5	39.5	1.47	0.49
	20	M	22	58.2	15.5	36.5	1.59	0.42
	21	M	19	54.5	17.5	35	1.56	0.50
	22	M	24	55.5	15.5	36	1.54	0.43
	22	M	27	58.5	16.5	41.5	1.41	0.40
	26	M	22	58	20.5	36.9	1.57	0.56
	32	M	28	62	16	41	1.51	0.39
	34	M	23	56.8	17	37	1.54	0.46
	36	M	26	58.5	21	39	1.50	0.54
Average	25.9	M=9	24.0	57.8	17.7	38.0	1.5	0.5
Std Dev	6.4		2.8	2.1	2.1	2.3	0.1	0.1

pediatric and adult age groups, respectively, and then separated by gender. Gender-based sample data including mean age, gender distribution and anthropomorphic ratios for each age group are listed in Table 2.

Results revealed significantly larger head-to-neck girth ratio in pediatric males when compared to adult males ($p<0.01$). Similarly, pediatric females exhibited a significantly larger head-to-neck girth ratio ($p=0.02$) compared to adult females. Statistically significant differences were found in head-to-neck girth ($p=0.01$) between adult males and adult females. Significant differences were found between pediatric females and adult males ($p<0.01$)

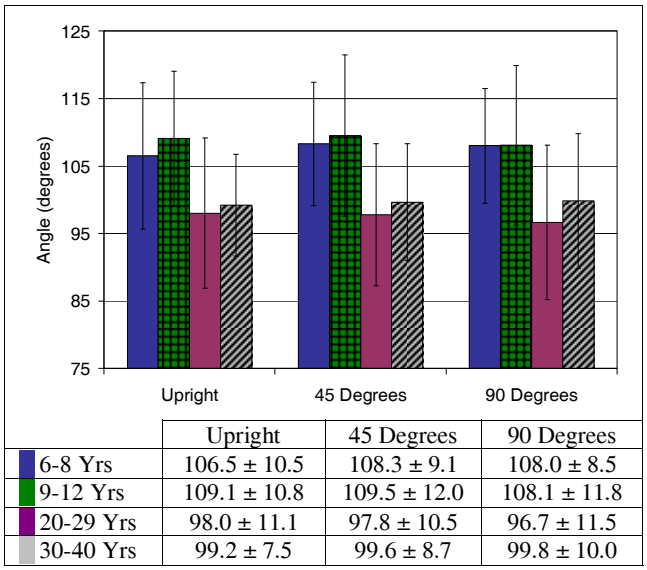

Figure 5. Age-based angle comparison.

and between pediatric males and adult females ($p<0.01$). No significant differences were found between pediatric females and pediatric males ($p=0.99$).

No significant differences were found in neck slenderness between pediatric females and males ($p=0.12$), adult females and males ($p=0.78$), pediatric and adult females ($p=0.07$), pediatric and adult males ($p=0.70$) or pediatric male and adult female ($p>0.99$). A statistically larger neck slenderness ratio was found in pediatric females compared to adult males ($p<0.01$).

Age- and Gender-Based Differences in Cervical Flexion

The head vs. spine flexion angle means and standard deviations for each age group are illustrated in Figure 5. Combining 38 subjects with three trials and three conditions yielded the potential for 342 total data points (81 in the 6-8 yr olds, 90 in the 9-12 yr olds, 90 in the 20-29 yr olds and 81 in the 30-40 yr old group). Conditions and/or trials that violated the relaxation criteria were eliminated, reducing the number of data points to 295 (55 in the 6-8 yr olds and to 69 in the 9-12 yr olds). No data were eliminated from the adult groups.

The head vs. spine flexion angle means and standard deviations for the gender-age groups are illustrated in Figure 6. Eliminating data points that violated the relaxation criteria yielded 76 in the female pediatric group, 90 in the female adult group, 48 in the male pediatric group, and 81 in the male adult group for a total of 295 data points.

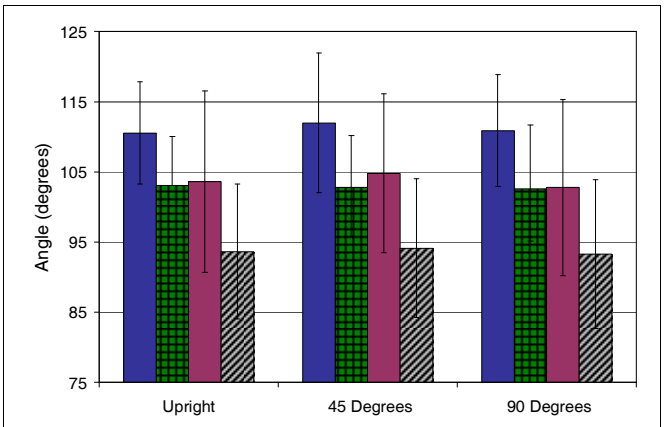

	Upright	45 Degrees	90 Degrees
Fem. Ped.	110.6 ± 7.3	112.0 ± 9.9	110.9 ± 8.0
Fem. Adult	103.0 ± 7.0	102.8 ± 7.4	102.5 ± 9.1
Male Ped.	103.6 ± 12.9	104.8 ± 11.3	102.8 ± 12.6
Male Adult	93.6 ± 9.6	94.1 ± 9.9	93.3 ± 10.6

Figure 6. Gender-base angle comparison.

Differences in cervical flexion angle were demonstrated for both gender and age; females exhibited larger neck flexion angle than males ($p = 0.013$) and flexion angle decreased with age ($p = 0.006$). There was no significant interaction between age and gender ($p = 0.76$). Head-to-neck girth ratio in part explained these differences. Adding this to the model yielded a significant effect ($p = 0.004$), and eliminated both the effect of age ($p = 0.39$) and gender ($p = 0.13$). Of note, condition (upright, 45°, 90°) and trial number had no effect on flexion angle ($p = 0.45$ and $p = 0.72$, respectively).

To illustrate the change in head vs. spine angle across age, all trials and conditions meeting the relaxation criteria were plotted across age for males and females in Figure 7.

Stratifying the analyses by age groups revealed that the gender effect remained significant only in the adult group ($p = 0.04$); no gender effect was seen ($p = 0.18$) among the 6-12 year olds. Within the pediatric age group, an increased head-to-neck ratio resulted in significantly more cervical flexion ($p = 0.024$).

DISCUSSION/CONCLUSION

This study utilized pediatric and adult human volunteers and demonstrated significant decreases in passive cervical spine flexion with age for both males and females. Gender differences were present among adults - adult females exhibited significantly greater flexion than males. This trend was present in pediatric data, but was not statistically significant. The age and gender differences were explained in

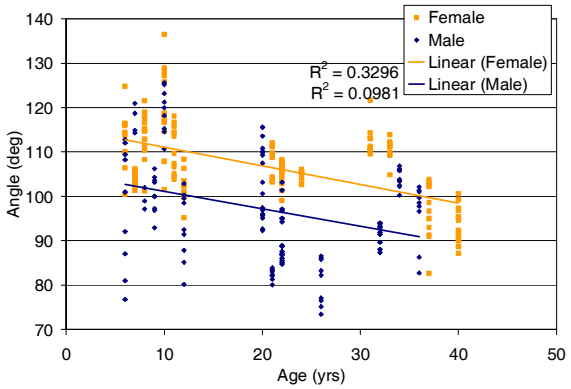

Figure 7. Head vs. Spine Angle vs. Age

part by differences in the head-to-neck girth ratio. This parameter which decreased with age and was greater in females versus males was the most significant contributor to the decrease in cervical spine flexion.

Previous PMHS and PMAS studies have shown that tensile strength increased with age (Ching et al., 2001; Hilker et al., 2002; Nuckley et al., 2005; Ouyang et al., 2005; Nuckley and Ching, 2006). While our study was an external measurement of cervical spine flexion, these internal findings may help explain our results. Increased tensile stiffness in the adult population could result in reduced strain of the cervical spine ligaments and passive musculature, decreasing overall flexion angle. Contrarily, reduced tensile stiffness in the pediatric age range would lead to greater strain and greater neck flexion. Greater neck flexion in children is also likely due to their increased head-to-neck ratio as compared to adults which would yield greater neck loads and increased tension on the passive neck musculature. Further biomechanical analysis is required to detect correlations between neck loads, neck flexion, and head-to-neck dimensions.

Unlike Arbogast et al (2007) we found no significant differences between the 6-8 year old group and 9-12 year old group. This difference may be attributed to the addition of active musculature, as motor control improves with maturation.

Previous studies have reported no gender based differences in pediatric cervical spine range of motion (Feipel et al., 1999; Lewandowski and Szulc, 2003; Arbogast et al., 2007). This study showed a trend towards increased flexion in pediatric females compared to pediatric males, however these differences were not statistically significant. The lack of statistical significance may be due to an insufficient sample size as a total of 47 data points

were removed from the possible 171 in the pediatric age range due to exceeding the relaxation criteria. Of interest, if the relaxation criteria is waived and all trials of all pediatric subjects are included, gender has a significant effect on cervical spine flexion among children (p=0.02). This may suggest differences in muscular control between the genders that may have an influence on neck kinematics. Future studies are needed to fully understand gender based differences in neck flexion among pediatric subjects.

The paucity of pediatric post-mortem human subjects for biomechanical research necessitates other methods for obtaining pediatric data. Sub-injurious human volunteer studies like those described herein compliment the rare PMHS data and animal studies. These data quantify the changes in passive cervical spine flexion across maturation and act as a validation data set for computational cervical spine models. Ultimately, these data will contribute to the development of an improved pediatric ATD biofidelity requirement.

ACKNOWLDEGEMENTS

Funding for this analysis has been provided by the Center for Child Injury Prevention Studies and its member companies: Britax Child Safety, Inc., Nissan Technical Center North America, TK Holdings Inc., Toyota Motor, Inc. NA, State Farm Insurance Companies, Dorel Juvenile Products and Volkswagen of America. The views expressed herein are those of the authors and do not represent the views of the Center for Child Injury Prevention Studies or its member companies.

REFERENCES

Arbogast, K.B. Cholve, P.A. Friedman, J.E. Maltese, M.R. Tomasello, M.F. Dormans, J.P., 2005. Normal cervical spine range of motion in children 3-12 years old. Spine 32 (10), E309-315.

Bailey, D.K., 1952. The normal cervical spine in infants and children. Radiology 59, 712–719.

Begeman, P.C. Levine, R.S., King, A.I., 1983. Belt slip measurements on human volunteers and the part 572 dummy in low -gx impact acceleration. In Proceedings of the 27th Stapp Car Crash Conference, SAE 831635.

Cattell, H., Filtzer, D., 1965. Pseudosubluxation and other normal variations in the cervical spine in children. A study of one hundred and sixty children. Journal of Bone and Joint Surgery (Am) 47, 1295–1309.

Ching, R.P. Nuckley, D.J. Hersted, S.M. Eck, M.P. Mann, F.A., 2001. Tensile mechanics of the developing cervical spine. In Proceedings of the 45th Stapp Car Crash Conference.

Deng, B. Melvin, J.W. Rouhana, S.W., 1998. Head-neck kinematics in dynamic forward flexion. In Proceedings of the 42nd Stapp Car Crash Conference. Society of Automotive Engineers, Warrendale, PA.

Durbin, D. Elliot, M. Winston, F., 2003. Belt positioning booster seats and reduction in risk of injury in motor vehicle crashes. JAMA 289 (21), 2835-2840.

Ewing, C.L. Thomas, D.J., 1973. Torque versus angular displacement response of human head to -gx impact acceleration. In Proceedings of the 17th Stapp Car Crash Conference, SAE 730976.

Ewing, C. Thomas, D. Lustick, L. Muzzy, W. Willems, G., Becker, E., 1975. The effects of the initial position of the head and neck on the dynamic response of human head and neck to -gx impact acceleration. In Proceedings of the 19th Stapp Car Crash Conference.

Ewing, C. Thomas, D. Lustick, L. Muzzy, W. Willems, G. Majewski, P., 1976. The effects of duration, rate of onset, and peak sled accelerationon the dynamic response of the human head and neck. In Proceedings of the 20th Stapp Car Crash Conference.

Ewing, C. Thomas, D. Lustick, L. Muzzy, W. Willems, G. Majewski, P., 1977. Dynamic response of human head and neck to +gy impact Acceleration. In Proceedings of the 21st Stapp Car Crash Conference.

Ewing, C. Thomas, D. Lustick, L. Muzzy, W. Willems, G. Majewski, P., 1978. Effect of initial position on the human head and neck response to +y impact acceleration. Society of Automotive Engineers Transactions, (SAE Paper No. 780888), 101-138.

Feipel, V. Rondelet, B. Pallec, J.L. Rooze, M., 1999. Normal global motion of the cervical spine: An electrogoniometric study. Clinical Biomechanics 14 (7), 462-470.

Fuchs, S. Barthel, M.J. Flannery, A.M. Christoffel, K. K., 1989. Cervical spine fractures sustained by young children in forward-facing car seats. Pediatrics 84 (2), 348-354.

Hadley, M.N., Zabramski, J.M., Browner, C.M., Rekate, H., Sonntag, V.K., 1988. Pediatric spinal trauma. Review of 122 cases of spinal cord and vertebral column injuries. Journal of Neurosurgery 68 (1), 18–24.

Hilker C.E., Yoganandan, N. Pintar, F.A., 2002. Experimental determination of Adult and pediatric neck scale factors. In Proceedings of the 46th Stapp Car Crash Conference.

Irwin, A. Mertz, H. J., 1997. Biomechanical basis for the CRABI and Hybrid III child dummies. Society of Automotive Engineers Transactions (SAE Paper No. 973317), 261-272.

Janssen, E. G. Nieboer, J. J. Verschut, R. Huijskens, C. G., 1991. Cervical spine loads induced in restrained child dummies. In Proceedings of the 35th Stapp Car Crash Conference, San Diego, CA.

Kewalramani, L.S., Tori, J.A., 1980. Spinal cord trauma in children. Neurologic patterns, radiologic features, and pathomechanics of injury. Spine 5 (1), 11–18.

Kriss, V.M., Kriss, T.C., 1996. SCIWORA (spinal cord injury withoutradiographic abnormality) in infants and children. Clinical Pediatrics 35 (3), 119–124.

Lewandowski J, Szulc P., 2003. The range of motion of the cervical spine in children aged from 3 to 7 years–An electrogoniometric study. Folia Morphol (Warsz) 62, 459–461.

Ma, D. Obergefell, L.A. Rizer, A.L., 1995. Development of human articulating joint parameters for crash dynamics simulations. In Proceedings of the 39th Stapp Car Crash Conference, SAE 952726.

Melvin, J.W. McElhaney, J.H., Roberts, V.L., 1973. Evaluation of dummy neck performance. In: King, W.F., Mertz H.J.Human Impact Response: Measurement and Simulation, Plenum, New York, pp. 247-261.

Menezes, A., 1987. Traumatic lesions of the craniovertebral junction. In: VanGilder, J., Menezes, A., Dolan, K. (Eds.), Textbook of Craniovertebral Junction Abnormalities. Futura Publishing, Mount Kisco.

Mertz, H.J. Patrick, L.M., 1967. Investigation of the kinematic and kinetics of whiplash. In Proceedings of the 11th Stapp Car Crash Conference, SAE 670919.

Mertz, H.J. Patrick, L.M., 1971. Strength and response of the human neck. In Proceedings of the 15th Stapp Car Crash Conference, SAE 710855.

Mertz, H.J., Neathery, R.F. Culver, C.C., 1973. Performance requirements and characteristics of mechanical necks. In: King, W.F., Mertz H.J.Human Impact Response: Measurement and Simulation, Plenum, New York, pp. 263-288.

Mertz, H.J. Irwin, A.L. Melvin, J.W. Stalnaker, R.L. Beebe, M.S., 1989. Size, weight and biomechanical impact response requirements for adult size small female and large male dummies. Society of Automotive Engineers Paper No 890756.

Nightingale, R.W. Winkelstein, B.A. Knaub, K.E. Richardson, W.J. Luck, J.F. Myers, B.S., 2002. Comparative strengths and structural properties of the upper and lower cervical spine in flexion and extension. Journal of Biomechanics 35, 725-732

Nightingale, R.W., Chancey, V.C. Ottaviano, D. Luck, J.F., Tran, L. Prange, M. Myers, B.S., 2007. Flexion and extension structural properties and strengths for male cervical spine segments. Journal of Biomechanics 40, 535-542.

Nuckley, D.J. Yliniemi, E.M. Cohen, A.M. Harrington, R.M. Ching, R.P., 2005. Compressive mechanics of the maturing human spine. In Proceedings of the ISB XXth Congress - ASB 29th Annual Meeting, Cleveland, Ohio.

Nukley, D.J. Ching, R.P., 2006. Developmental biomechanics of the cervical spine: tension and compression. Journal of Biomechanics 39, 3045-3054.

Osenbach, R.K., Menezes, A.H., 1989. Spinal cord injury without radiographic abnormality in children. Pediatric Neuroscience 15(4), 168–174.

Ouyang, J. Zhao, Q. Xu, Y. Chen, W. Zhong, S., 2005. Biomechanical assessment of the pediatric cervical spine under bending and tensile loading. Spine 30 (24), E716-E723.

Patrick, L.M. Chou, C.C., 1976. Response of the human neck in flexion, extension and lateral flexion. Vehicle Institute Report No. VRI-7.3. Society of Automotive Engineers, Warrendale, PA.

Pollack, I.F., Pang, D., Sclabassi, R., 1988. Recurrent spinal cord injury without radiographic abnormalities in children. Journal of Neurosurgery 69 (2), 177–182.

Schuer, L. Black, S., 2000. Developmental Juvenile Osteology. Academic Press, London.

Sullivan, C.R., Bruwer, A.J., Harris, L.E., 1958. Hypermobility of the cervical spine in children: a pitfall in the diagnosis of cervical dislocation. American Journal of Surgery 95, 636–640.

Thunnissen, J. Wismans J., Ewing C.L., Thomas, D.J., 1995. Human volunteer head-neck response in frontal flexion: A new analysis. In Proceedings of the 39th Stapp Car Crash Conference, SAE 952721.

Townsend, E.J., Rowe, M., 1952. Mobility of the upper cervical spine in health and disease. Pediatrics 10, 567–574.

Walsh, J.W. Stevens, D.B. Young, A.B., 1983. Traumatic paraplegia in children without contiguous spinal fracture or dislocation. Neurosurgery 12 (4), 439–445.

Weber, K., 2002. Child passenger protection. In: Nahum, A. Melvin, J. (Eds), .Accidental Injury: Biomechanics and Prevention. Springer, New York, pp. 523-549.

Wismans, J. Spenny, C.H., 1984. Head-neck response in frontal flexion. In Proceedings of the 28th Stapp Car Crash Conference, SAE 841666.

Wismans, J. van Oorschot, H. Woltring H., 1986. Omni-directional human head-neck response. In Proceedings of the 30th Stapp Car Crash Conference.

Yoganandan, N. Kumaresan, S. Pintar, F. Gennarelli, T., 2002. Pediatric biomechanics.
In: Nahum, A. Melvin, J. (Eds.), .Accidental Injury: Biomechanics and Prevention. Springer, New York, pp. 550-587.

INVESTIGATION OF FACET JOINT RESPONSE UNDER REAR IMPACT CONDITIONS USING FE MODEL OF THE CERVICAL SPINE

Jason B. Fice
Duane S. Cronin
University of Waterloo
Canada
Matthew B. Panzer
Duke University
United States of America
Paper Number 09-0154

ABSTRACT

Whiplash injury resulting from rear impact is a significant issue in terms of societal cost, and the resulting pain and reduction in quality of life. The facet joints in the cervical spine have been identified as a source of pain in whiplash injuries; however, the responses of these joints are difficult to measure in vivo or in vitro. In this study, a detailed explicit FE model of the cervical spine was used to investigate facet joint response under rear impact loading conditions. The model represents a mid-size male with detailed vertebrae, discs, ligaments and Hill-type active muscles. This model was previously validated extensively at the segment level and validated for frontal impact scenarios. In this study, the cervical spine model was validated against rear impact volunteer and cadaver tests (13 volunteers exposed to 28 rear impacts at speeds of 5 to 7kph; 26 cadavers exposed to rear impacts at speeds of 5 to 15.5kph) using experimental acceleration, displacement and rotation traces of the T1. Capsular ligament (CL) strains were measured in the model and compared to values presented in the literature to identify pain or sub-catastrophic failure. Simulation of 4, 7, and 10g rear impacts showed good agreement with the experimental data. The predicted CL strains were below or near the approximate threshold for pain and sub-catastrophic damage (35% strain), and exceeded this value for a 12g rear impact case. This study included muscle activation, and provides a link between published strain limits for facet joint capsules evaluated in controlled lab conditions and strains predicted under rear impact loadings.

INTRODUCTION

Whiplash, or cervical spine injury resulting from low speed rear impact, is a significant issue with the annual societal costs in the United States estimated to be between 4.5 and 29 billion dollars (Keinberger 2000, Freeman 1997). Whiplash can reduce the victim's quality of life for a significant amount of time, as up to 33% of patients continued to seek treatment for whiplash 33 months after sustaining the injury (Freeman 1997). With respect to sources of pain, one focus of whiplash research has been on capsular ligament (CL) strain with several clinical and biomechanical studies implicating this anatomical site as a likely source of injury (Lord, et al. 1996, Barnsley, et al. 1995, Lu, et al. 2005, Lee, Davis, et al. 2004, Lee, Franklin, et al. 2006, Ivancic, et al. 2008, Quinn, et al. 2007, Panjabi, et al. 1998, Pearson, et al. 2004, Deng 1999a). Clinical studies using double-blind anesthetic blocks have shown that 54% to 60% of whiplash patients have CL pain (Barnsley, et al. 1995, Lord, et al. 1996). By measuring behavioral sensitivities or nerve discharge, in-vivo animal models of the goat and rat have shown that tensile force applied across the facet joint led to pain (Lu, et al. 2005, Lee, Davis, et al. 2004). In the rat model, it was shown that in-vitro sub-catastrophic failure of the CL occurred at a distraction magnitude of 0.57mm that led to pain for up to 14 days in-vivo (Lee, Davis, et al. 2004, Lee, Franklin, et al. 2006, Quinn, et al. 2007). Authors have shown that CL strain in cadavers and cadaveric cervical spine sections peak values range from 28.5% to 39.9% during low speed rear impact, which exceeds physiologic strain of this structure (Panjabi, et al. 1998, Pearson, et al. 2004, Deng 1999a). The stiffness of CLs exposed to rear impact was less than the control CLs, which showed that some damage had occurred in the ligaments despite a lack of visual indication (Ivancic, et al. 2008).

Four types of studies have been undertaken to measure or predict the level of strain in the CL during rear impact scenarios: full-body cadaver sled tests, full cervical spine bench-top sled tests, quasi-static cervical spine motion segment tests, and finally, computational models. These different approaches have provided important information and understanding, but with some limitations. Deng et al. (1999a) performed a series of 26 rear-impact sled tests on six post-mortem human subjects and

measured capsular strain using a pair of lead spheres in each vertebra, which were tracked by high-speed x-ray. However, one of the challenges with cadaver studies is the lack of active musculature, which affects the kinematics of the neck (Thunnissen, et al. 1995, van der Horst, et al. 1997). Studies that use a bench-top sled to impose rear-impact loads on cervical spine sections (Panjabi, et al. 1998, Pearson, et al. 2004), typically do not include the upward motion and extension of the T1 caused by straightening of the spine and the torso ramping up the seat (Deng 1999a). Winkelstein et al. (1999) and Seigmund et al. (2000) applied bending and shear loads to isolated motion segments, and measured the capsular strains. However, this type of study did not include dynamic effects, such as changes to the axis of rotation of each vertebra during rear-impact (Ono, et al. 1997). Current computational models that have been used to calculate CL strain under rear impact include the TNO model (Stemper, Yoganandan and Pintar 2005) and THUMS model (Kitagawa, Yasuki and Hasegawa 2008), but these studies did not incorporate active musculature or detailed facet joints.

This current study is based on a detailed validated finite element model of the cervical spine (Panzer 2006, Panzer and Cronin 2009) and the prediction of capsular ligament strains during rear impact. These strains were compared to published limits for sub-catastrophic failure and pain. The CL strains were measured at every cervical level at the anterior and posterior position of each facet joint. The results of this study are unique in that active musculature and realistic loadings were included.

METHODS

The finite element model used in this study represents a mid-size male and was developed at the University of Waterloo (UW); a full description is available in Panzer (2006) (Figure 1). The model was developed with the focus on accurate geometric and material representation at the local tissue level. The vertebrae geometry was based on the model developed by Y. C. Deng et al. (1999b) and the vertebrae were modeled as rigid for computational efficiency. The intervertebral discs were constructed with solid elements for the annulus fibrosus ground substance and layers of shell elements representing the fibre lamina, and solid elements to model the nucleus pulposus. The facet joints were modeled with a superior and inferior layer of solid elements for the articular cartilage with a squeeze-film model to simulate the synovial fluid (Figure 2). Ligaments were represented using multiple 1D non-linear spring elements. In total, 90 pairs of active Hill-type 1D elements were used to model 27 muscle pairs in the cervical spine. Both the flexors and extensors were activated 74ms after impact (Siegmund, Sanderson, et al. 2003). Studies have found that flexor and extensor muscles activate at the same time and that EMG muscle signals start at 60 to 79ms after impact (Siegmund, Sanderson, et al. 2003, Ono, et al. 1997, Roberts, et al. 2002, Szabo and Welcher 1996). It is possible that the actual muscle activation scheme for rear impact is more complex, but no conclusive information is available at this time. The material models for all the components were based on studies in the literature. Viscoelasticity and anisotropy were incorporated where applicable.

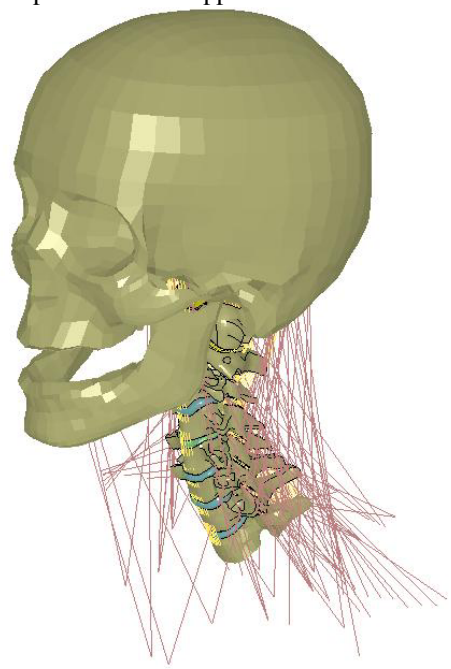

Figure 1. FE model of the cervical spine. Pink lines represent muscle elements, and yellow lines represent ligaments.

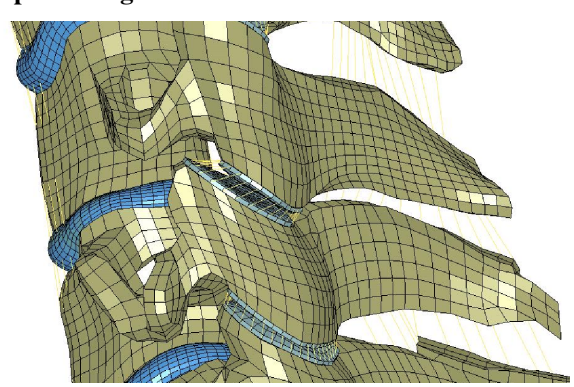

Figure 2. Facet joint detail, showing the CL and articular cartilage.

The cervical spine model used in this study was previously validated at the segment level in flexion, extension, lateral bending, axial rotation, tension, compression, and anterior, posterior, and lateral shear (Panzer 2006). Panzer found generally excellent correlation (within one standard deviation) with the quasi-static loadings. This model was validated against volunteer frontal impacts up to 15g (Panzer 2006).

For the model to be used to predict CL strains during rear-impact, the model must first be validated for this type of loading. Davidsson et al. (1998) and Deng (1999a) were found the most suitable based on the severity of impact, number of test samples, and full data of the T1 motion in the sagittal plane. The head kinematic response corridors and T1 inputs for Davidsson's experiments came from Hynd et al. (2007).

Davidsson et al. (1998) performed 28 rear impacts on thirteen human volunteers at speeds between 5 and 7kph with an average peak acceleration of 3.6g. The test involved the collision of a bullet sled with a stationary target sled, which seated a volunteer on a laboratory seat with a headrest. To model these rear impacts, the average T1 X-acceleration (fore-aft), Z-displacement (superior-inferior), and Y-rotation (flexion-extension) were input into the cervical spine model T1 as prescribed motion constraints (Figure 3). The model's T1 was constrained in all other directions, and the head was not constrained. The headrest for the test was described as a stiff backing plate covered with 4cm of foam, attached to a rigid frame with four coil springs of a specified preload and stiffness. The mass of the headrest and dimensions were also specified. To model the headrest, the average sled x-acceleration was input as prescribed motion to the frame attachment points of the springs (Figure 3). The headrest material properties were non-linear viscoelastic based on automotive seat cushion material tested at UW and the stiff backing was assumed to be pine with orthotropic elastic material properties (Green, Winandy and Kretschmann 1999, Cambell and Cronin 2007). Muscle activation was included for validation against Davidsson et al. (1998) to mimic the behavior of volunteers.

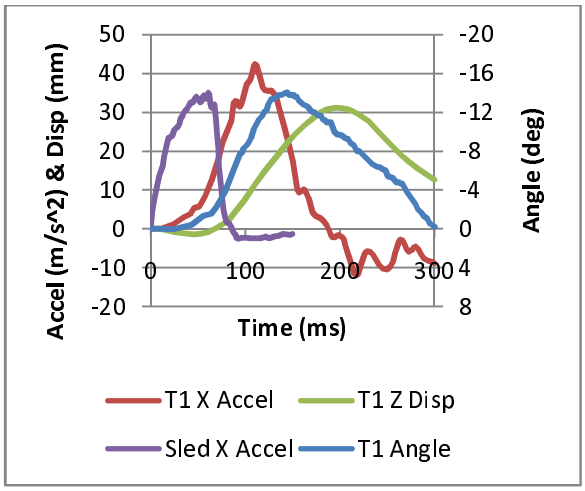

Figure 3. Davidsson et al. (1998) T1 Inputs for a 4g loading case, X direction is positive forward, Z direction is positive upwards, and T1 rotation is positive in extension. Inputs are in a fixed global coordinate system.

Deng (1999a) performed a series of 26 rear impacts on 6 whole body cadavers at delta velocities ranging from 5 to 15.5kph, and accelerations from 5 to 9.9g. These experiments involved a cadaver seated in a custom seat, with or without a headrest, and being accelerated from rest using a pneumatic cylinder. When modeling these tests the headrest was not included, because in the experiments the headrest was initially positioned at least 100mm away from the cadavers head and did not influence kinematics until late in the simulation, and the author found all peak CL strains occurred before headrest contact (Deng 1999a). Two specific runs were chosen to simulate based on the impact severity and available data. The experimental T1 X-acceleration, Z-acceleration, and Y-rotation were input into the model as prescribed motion (Figure 4). The T1 was constrained from moving in any other direction and everything else was free in all directions. Muscle activation was not included in the validation against Deng (1999a) to mimic the behavior of cadavers. More aggressive rear impacts were undertaken by scaling the 10g simulation to 11 to 20g to identify the threshold for CL strain injury in the model.

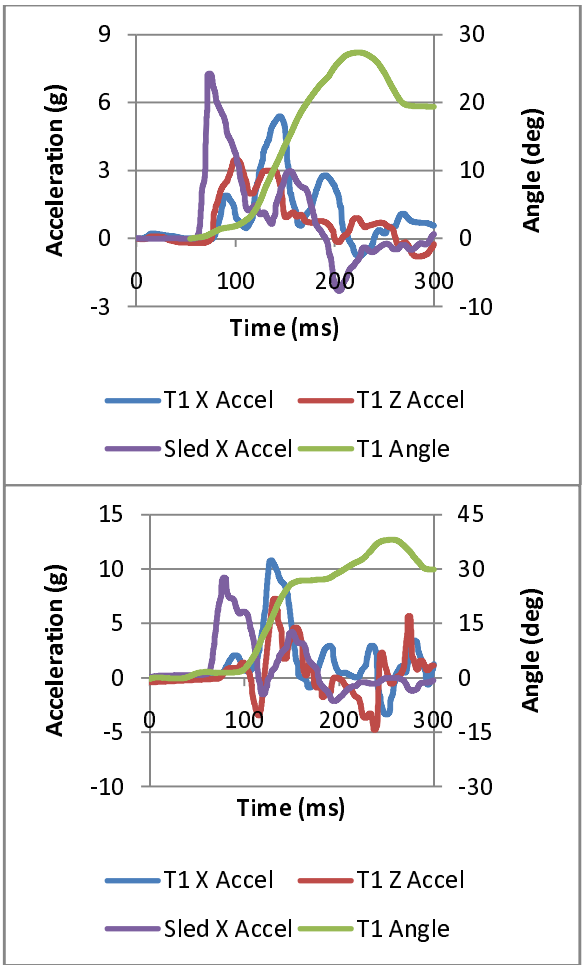

Figure 4. Deng (1999a) T1 Inputs for 7g (above) and 10g (below) loading cases, X direction is positive forward, Z direction is positive upwards, and T1 rotation is positive in extension. The sled acceleration was not used in the simulation. Inputs given in a rotating anatomical coordinate system.

The CL strains in the model were calculated by measuring the change in length of 1D discrete elements representing the CL and dividing by CL ligament lengths measured on cadavers (Panjabi, et al. 1998). The strains were calculated at the anterior most position and posterior most position of the facet joint for each cervical level. These positions were chosen, because the CL strain should be the most extreme at these locations.

RESULTS

The model was able to reproduce the kinematics of volunteers in Davidsson's (1998) experiment (Figures 5 to 9). The head centre of gravity (CG) motion in the fore-aft (X) direction was in excellent agreement with the data for both with respect to the first thoracic vertebrae (T1) and with respect to the sled (Figures 5 & 6). Head rotation in the sagittal plane with respect to the T1 was in good agreement with the volunteer data (Figure 7). The occipital condoyle (OC) superior-inferior (Z) direction movement was also in good agreement with the data, when measured with respect to the sled and with respect to the T1 (Figures 8 & 9).

The model's response to a 7g rear impact was in reasonable agreement to the cadaver tests performed by Deng (1999a) (Figures 10 to 13). The rotations of the model's upper cervical spine joints (C1-C2 and C2-C3) did not exhibit enough relative flexion, and the middle cervical spine joint (C4-C5) did not exhibit enough relative extension (Figure 10). The combination of relative vertebral rotations lead a head rotation that was a good fit to Deng's data (Figure 11). The model's head CG X-acceleration has a similar double peak shape to the cadaver results, but the peaks were on the lower end of the measured data (Figure 12). In the Z-direction the model's acceleration did have similar peaks or shape compared to the cadaver data (Figure 13).

At 10g, the model's responses were a reasonable fit to a limited data set from Deng (1999a) (Figures 14, 15, & 16). The angle of the model's head was a good fit to cadaver head angles at similar impact accelerations (Figure 14). The X-acceleration of the head CG was of similar shape, and the peak accelerations lie mostly in the data spread of cadaver results (Figure 15). As was the case for the 7g impact, the head's CG Z-acceleration was neither a similar shape nor did it have similar peak values when compared to the cadaver data (Figure 16).

When considering the CL strains in the different load cases, the CL strain on the anterior portion of the C5-C6 facet joint was always greater than the posterior portion, because the motion segments were loaded in extension and posterior shear (Figures 17 to 20). The model predicted a peak CL strain of 22.6% at the C4-C5 level during the 4g rear impact (Table 1). The next highest strains were 28.6% and 32.4% at the C5-C6 and C2-C3 levels respectively during a 10g impact with passive muscles (Table 1). When including active muscles, the CL strain reduced at every level except for C4-C5. A CL strain of 35.4% was measured in the C2-C3 during a 12g rear impact, which exceeded the sub-catastrophic strain of the CL ligament reported by Seigmund et al. (2001) (Table 1).

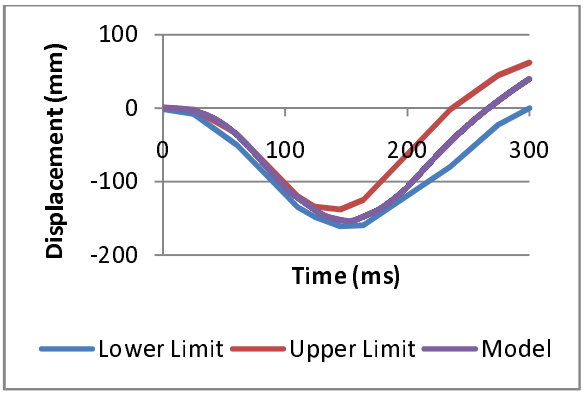

Figure 5. 4g - Head CG X-Displacement w.r.t. the Sled (Davidsson, et al. 1998).

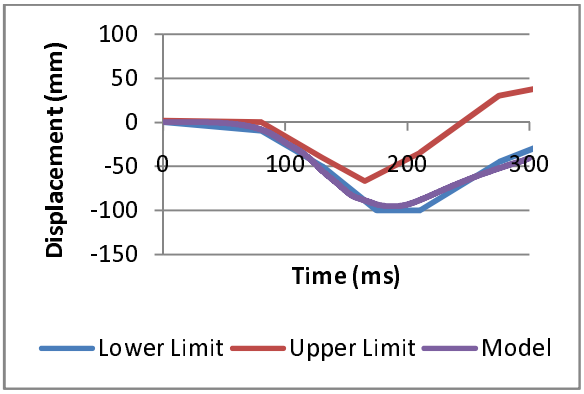

Figure 6. 4g - Head CG X-Displacement w.r.t. the T1 (Davidsson, et al. 1998).

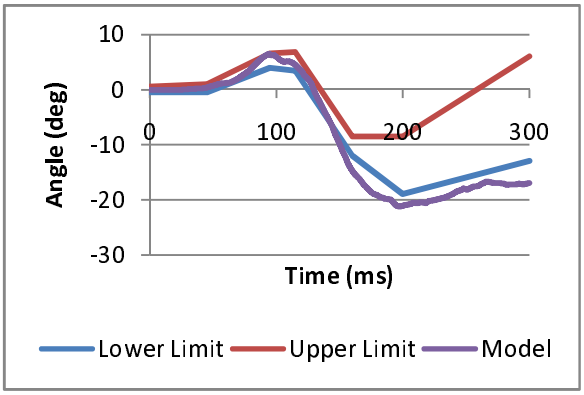

Figure 7. 4g - Head rotation w.r.t. the T1 (Davidsson, et al. 1998).

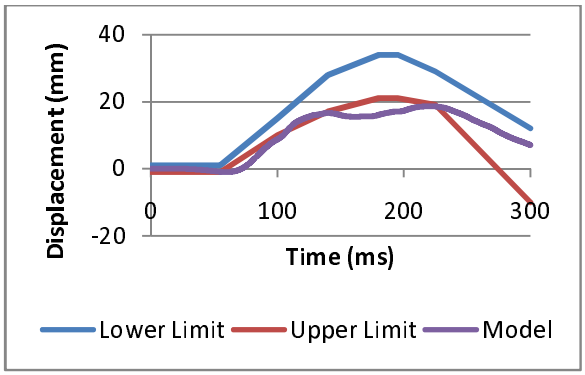

Figure 8. 4g - O.C. Z-Displacement w.r.t. the Sled (Davidsson, et al. 1998).

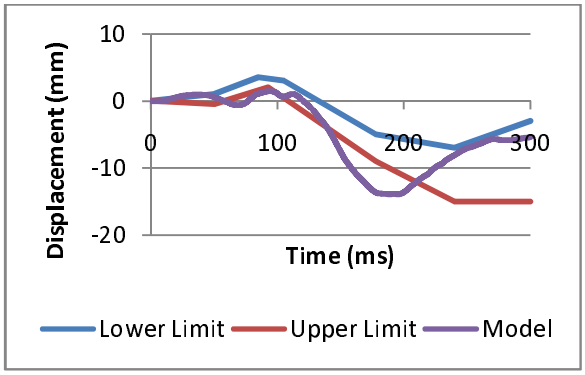

Figure 9. 4g - O.C. Z-Displacement w.r.t. the T1 (Davidsson, et al. 1998).

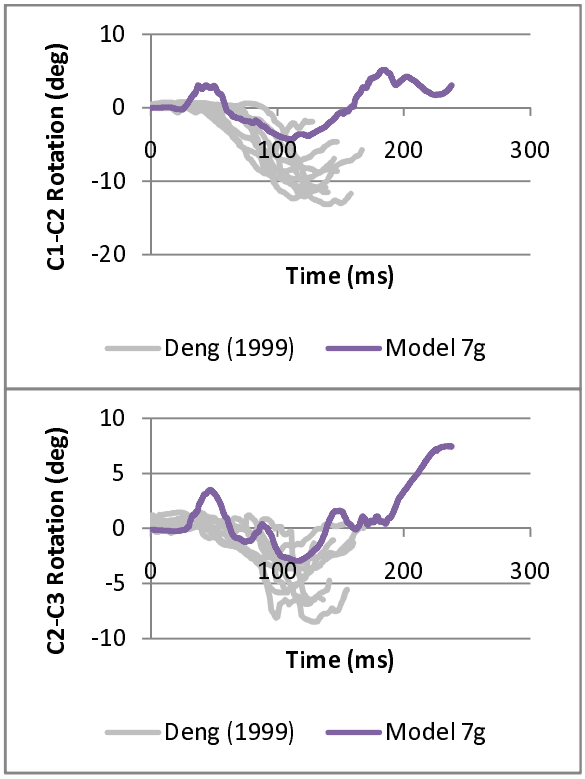

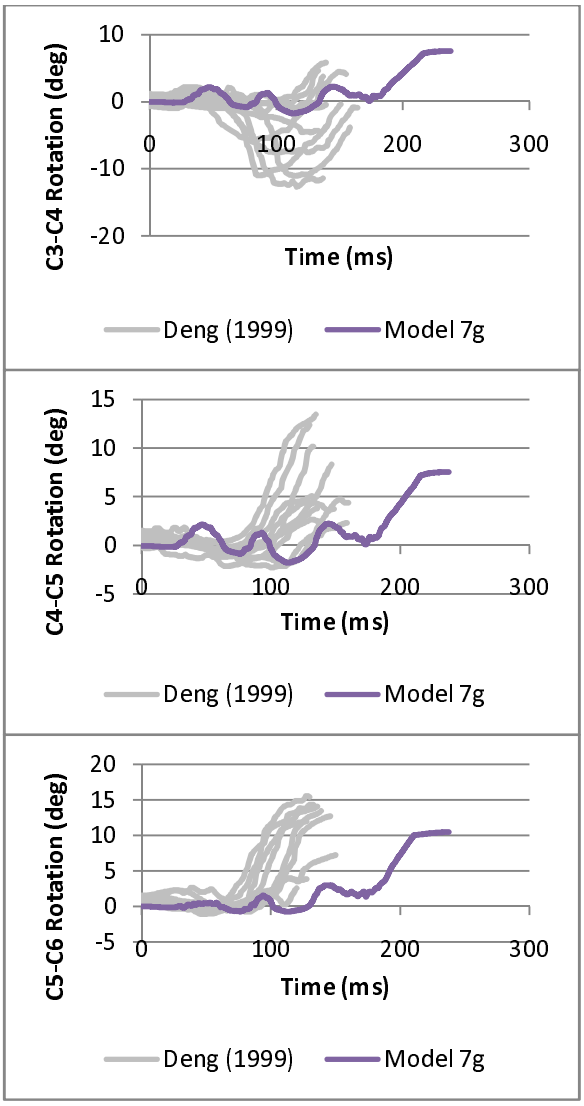

Figure 10. Spine segment relative rotations in the sagittal plane. Positive angles for extension.

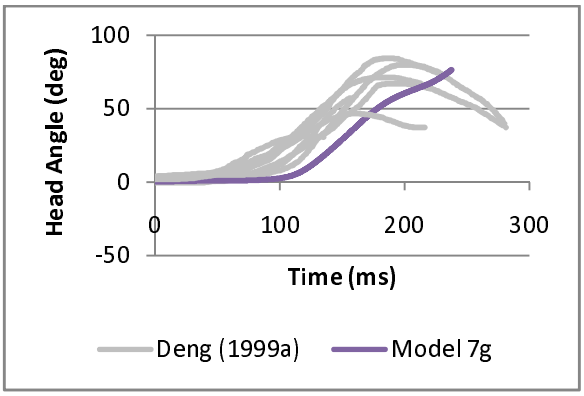

Figure 11. Cadaver head rotations for loadings between 6 to 8g compared to the model's response at 7g. Positive angles for extension.

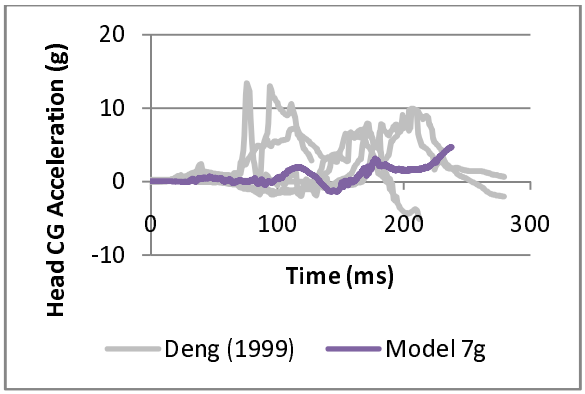

Figure 12. Cadaver head CG X-acceleration for loadings between 6 to 8g compared to the model's response at 7g. Positive g's in the forward direction.

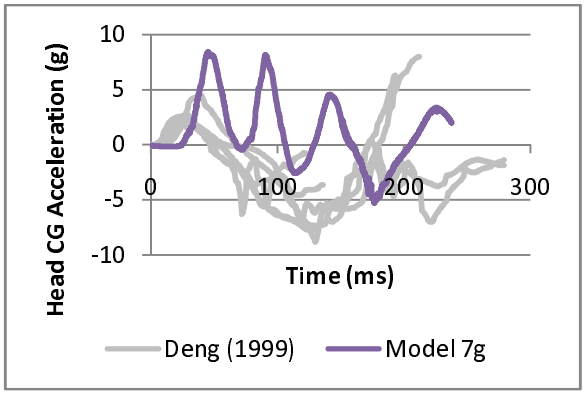

Figure 13. Cadaver head CG Z-acceleration for loadings between 6 to 8g compared to the model's response at 7g. Positive g's in the upward direction.

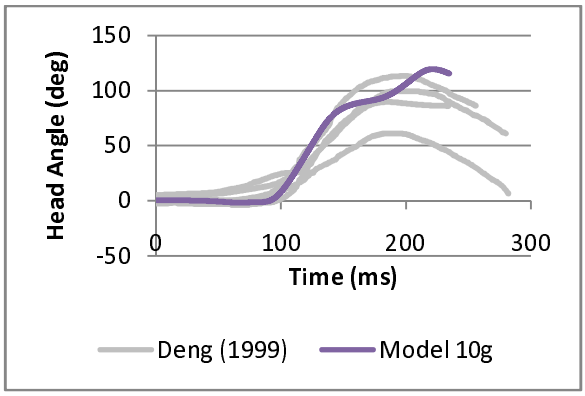

Figure 14. Cadaver head rotations for loadings between 8 to 10g compared to the model's response at 10g. Positive angles for extension.

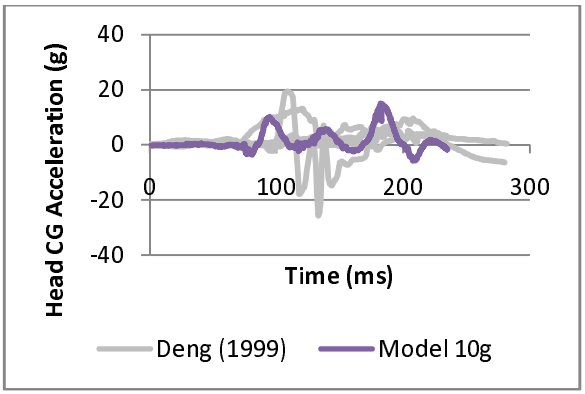

Figure 15. Cadaver head CG X-acceleration for loadings between 8 to 10g compared to the model's response at 10g. Positive g's in the forward direction.

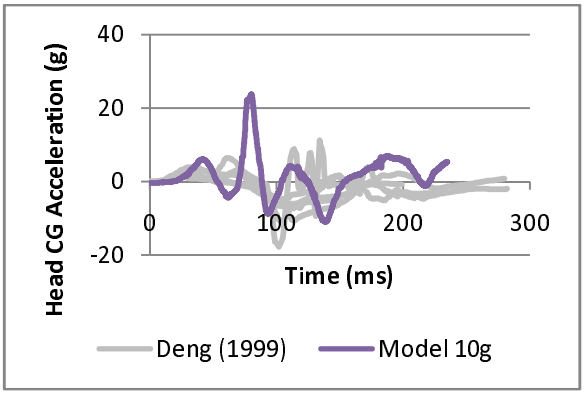

Figure 16. Cadaver head CG z-acceleration for loadings between 8 to 10g compared to the model's response at 10g. Positive g's in the upward direction.

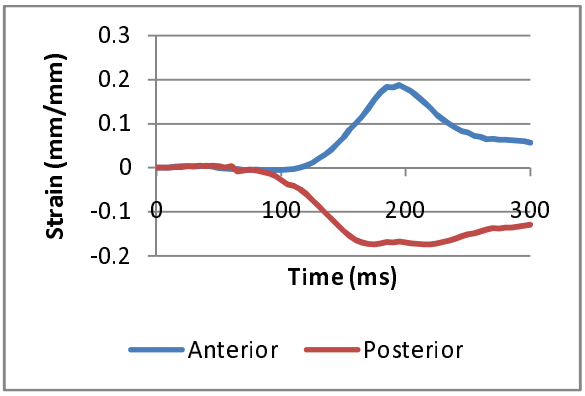

Figure 17. Predicted C5-C6 CL strain for a 4g impact.

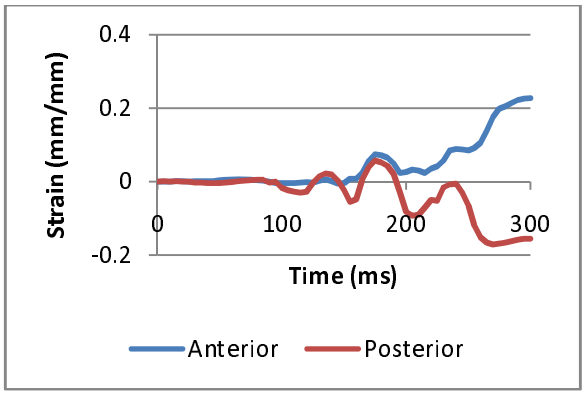

Figure 18. Predicted C5-C6 CL strain for a 7g impact with passive muscles.

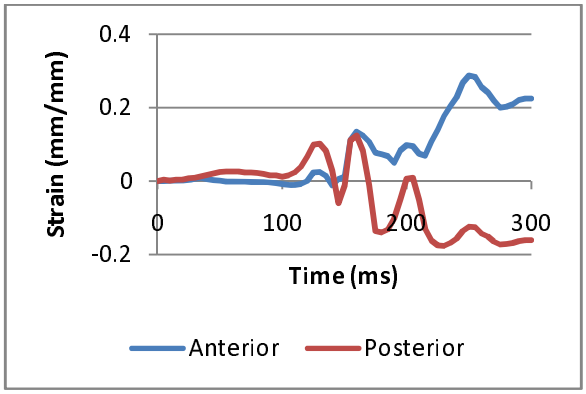

Figure 19. Predicted C5-C6 CL strain for a 10g impact with passive muscles.

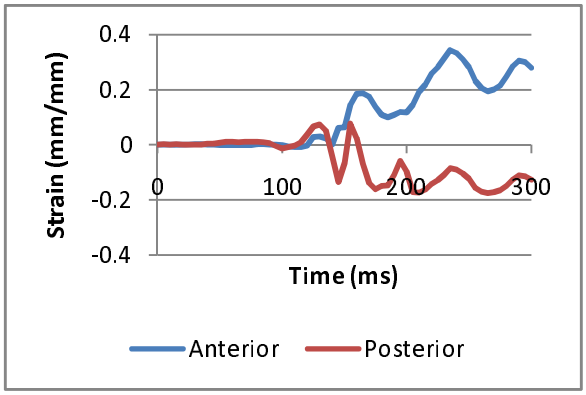

Figure 20. Predicted C5-C6 CL strain for a 12g impact with passive muscles.

Table 1.
Maximum CL strains in the model for different impact loads

	4g [2]	7g [1]	7g [2]	10g [1]	10g [2]	12g [1]
C2-C3	11.9	17.4	16.3	32.4	21.7	35.4
C3-C4	10.4	10.8	16.5	23.7	21.3	24.5
C4-C5	22.6	21.4	26.6	23.1	26.4	30.2
C5-C6	18.7	22.7	22.0	28.6	25.0	34.3
C6-C7	1.5	8.8	0.82	13.6	2.0	13.2
Maximum	22.6	22.7	26.6	32.4	26.4	35.4

1 Passive muscles
2 Active muscles

Table 2.
Model CL strains at various impact accelerations compared to published data (average (SD) in %)

	Model			Deng (1999a)		Panjabi et al. (1998)			Pearson et al. (2004)		
	4g	7g[1]	10g[1]	5g	6g	4.5g	6.5g	10.5g	3.5g	6.5g	8g
C2-C3	11.9	17.4	32.4	9.7	8.5	9.6 (13.7)	24.3 (26.3)	20.4 (5.3)	13.4 (9.3)	15.8 (13.5)	16.7 (6.3)
C3-C4	10.4	10.8	23.7	22.2	23.9	12.1 (4.0)	17.8 (13.6)	6.9 (0.3)	17.4 (15.2)	30.8 (25.1)	29.9 (17.8)
C4-C5	22.6	21.4	23.1	14.8	10.9	11.1 (15.8)	16.9 (10.5)	18.9 (13.8)	22.3 (20.6)	31.1 (22.5)	26.5 (18.7)
C5-C6	18.7	22.7	28.6	28.5	25.8	11.7 (5.1)	5.8 (7.5)	22.1 (15.1)	26.8 (17.9)	35.9 (21.9)	38.5 (24.6)
C6-C7	1.5	8.8	13.6			12.7 (N/A)	29.5 (25.7)	35.4 (N/A)	18.9 (14.2)	28.8 (20.0)	39.9 (26.3)

1 Passive muscles where used.

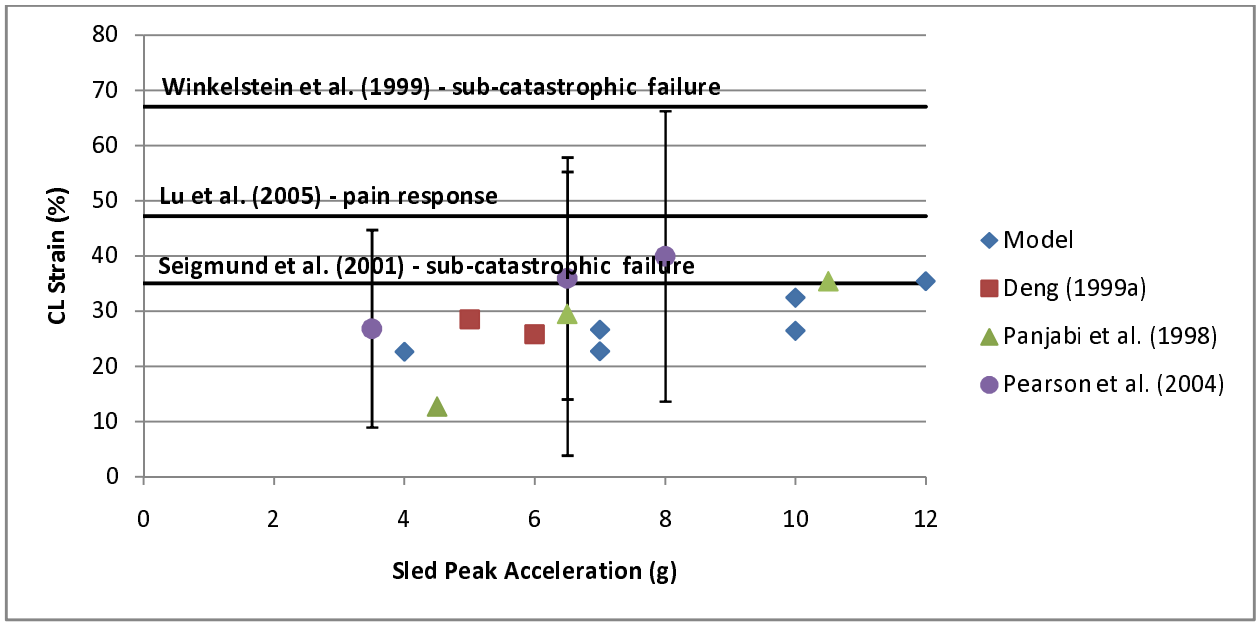

Figure 21. Maximum CL strain vs. peak sled acceleration for experimental results and the model. Standard deviation shown when available. Includes thresholds for injury.

DISCUSSION

Strain in the capsular ligament has been proposed as a possible source of neck pain for victims of rear impact and several clinical and biomechanical studies support this theory (Lord, et al. 1996, Barnsley, et al. 1995, Lu, et al. 2005, Lee, Davis, et al. 2004, Lee, Franklin, et al. 2006, Ivancic, et al. 2008, Quinn, et al. 2007, Panjabi, et al. 1998, Pearson, et al. 2004, Deng 1999a). A FE model of the cervical spine was used to measure capsular strains for rear impacts of 4, 7, 10g, and 12g. The results are unique from previous studies that have reported CL strain because the simulation included detailed facet joint modeling, active neck musculature, and full dynamic motion of the T1 in the sagittal plane.

The model was constructed accurately at the tissue level with the best available material properties, and was validated at the motion segment level and the whole cervical spine level for different frontal and rear impact scenarios. It should be emphasized that the model was not calibrated to any test conditions or data in order to preserve the accuracy at the tissue level, with the assumption that the CL strains measured during these simulations will be representative. The average CL strain was calculated by dividing joint distraction by ligament length and assumed a uniform strain state. Local CL strain could be predicted if shell elements were used for the ligament; however there is little literature available on local CL strain to justify this increase in model complexity. Another assumption made was that all the muscles contract at a given time, which was supported by EMG measurements of volunteers in rear impacts (Siegmund, Sanderson, et al. 2003, Ono, et al. 1997, Roberts, et al. 2002, Szabo and Welcher 1996). Further investigation into the effect of activate musculature on the CL strain during rear impact is required.

A possible limitation to the model was that the model was not calibrated to any of the impact tests. As a result, the model was in poor agreement with some of the experimental measures. The disagreement with the experimental impact data was more likely a limitation of the available tissue data used to develop the full spine model. In particular, some soft tissue characteristics such as viscoelasticity, nonlinearity, and anisotropy are not implemented in the model due to the lack of literature, and/or appropriate material models. The study and incorporation of these characteristics is a focus for model improvement in the future. Finally, it should be stated that the model is limited to the range of loads for which it has been validated.

The strains predicted in the CLs of the model have been compared to research performed by Deng (1999a), Panjabi et al. (1998), and Pearson et al. (2004) (Table 2). Deng used 6 cadavers in a series of 26 rear impacts, and measured the motion of each vertebra using a high speed X-ray to track implanted spheres and inferred a facet joint distraction. It should be noted that the strain results reported in Table 2 from Deng come from two tests, and have been scaled by a factor of Deng's initial gage length divided by CL lengths reported by Panjabi et al. (1998) for comparison to the current study. Panjabi et al (1998) used a specially designed spinal ligament transducer affixed across the facet joint to track joint distraction during rear impacts of four T1 to occipital cadaveric spines and divided that by anatomical ligament lengths to get strain Pearson et al. (2004). used a bench top sled with active muscle replication to impose rear impact loads on six occipital to T1 spine sections and measured vertebral motion by tracking marker flags using high speed cameras, and then inferred facet joint distraction that was divided by anatomical ligament lengths to get strain. The results in Table 2 show that for spinal levels C4-C5, and C5-C6 the predicted strains from the finite element model were within the quoted experimental range (Table 2). At the C6-C7 level the model predicted strains that were below the experimental range for all impact severities tested (Table 2). The model was in good agreement with the published data for the 10g case, but predicted a higher strain value at the C2-C3 level (Table 2).

In quasi-static spinal segment testing authors have found CL strains ranging from 11.6% to 17.8%, which are significantly lower than strains measured in dynamic tests (Table 2), demonstrating the importance of dynamic effects (Winkelstein, et al. 1999, Siegmund, Myers, et al. 2001). In an in-vivo study of goat facet joint distraction, Lu et al (2005) found what they hypothesized to be nociceptive (pain) receptors fire at a maximum principle strain of 47.2%. Testing of isolated facet joints from cadaver cervical spines have found sub-catastrophic damage to the CL at strains ranging from 35% to 66.8% in quasi-static testing, and 67% at 100mm/s (Winkelstein, et al. 1999, Siegmund, Myers, et al. 2001). At 10g the model predicted CL strain of 32.4% and 28.6% at the C2-C3 and C3-C4 levels respectively, which was just below the 35% threshold for sub-traumatic damage, and was well below the 47.2% threshold for pain. When the model was exposed to a 12g rear impact, the CL strain exceeded the 35% threshold reported by Seigmund et al. (2001). The model predicted CL strains have been

compared to experimental results, and published thresholds for injury (Figure 21). In a study of 28 instrumented real life accidents with 38 occupants, twenty occupants had short-term consequences at less than 10g, and two had long term consequences at 13g and 15g (Krafft, et al. 2000). In another study of 66 real life accidents, 13 of the 15 people that sustained neck injuries for longer than a month experienced a rear impact of greater than 9g (Krafft, et al. 2002). The 7g impact presented in this paper corresponds to an impact velocity of 7.5mph (Deng 1999a), and volunteer tests have been performed up to 6.8mph without mild symptoms, defined as lasting longer than 4days (McConnell, et al. 1995).

Future development of the cervical spine model will focus on improving the accuracy of the tissue models with the expectation that improved tissue models will improve the agreement between the full spine model and the experimental literature. This also includes a thorough investigation of the effect of active neck musculature on the response of the cervical spine in rear impact. The goal of this work is to better identify injury thresholds in rear impact scenarios, and to investigate out of position effects which has been suggested to increase strains (Winkelstein, et al. 1999).

CONCLUSIONS

The finite element cervical spine model used in this study, constructed from accurate geometry and the best available material properties, was previously validated at the segment level and for frontal impact scenarios. In this study, the model validated against volunteer and cadaver tests in rear impact scenarios and shown to be in good agreement. Capsular ligament strains predicted by the model approach thresholds for pain and sub-traumatic injury, but did not exceed them under 10 g rear impact loads which is consistent with the data in the literature. However, application of a 12g rear impact case did show higher strains that would be expected to result in pain or injury.

REFERENCES

Barnsley, Leslie, Susan M Lord, Barbara J Wallis, and Nikolai Bogduk. "The prevalence of chronic cervical zygapophysial joint pain after whiplash." *Spine* 20, no. 1 (1995): 20-26.

Cambell, Brett, and Duane S Cronin. "High rate characterization of automotive seat foams." *Proceedings of SEM 2007.* Springfield, MA: Society for Experimental Mechanics, 2007.

Davidsson, Johan, Christian Deutscher, Wlfram Hell, Astrid Linder, Per Lovsund, and Mats Svensson. "Human volunteer kinematics in rear-end sled collisions." *IRCOBI.* Goteborg, 1998. 289-301.

Deng, Bing. *Kinematics of human cadaver cervical spine during low speed rear-end impacts.* PhD Thesis, Detroit: UMI, 1999a.

Deng, Y. C, X Li, and Y Liu. "Modeling of the Human Cervical Spine Using Finite Element." *43rd Stapp Car Crash Conference Proceedings.* SAE International, 1999b.

Freeman, Michael D. *A Stduy of Chronic Neck Pain Folloing Whiplash Injury.* Ann Arbor, MI: UMI Dissertation Services, 1997.

Green, David W, Jerrold E Winandy, and David E Kretschmann. *Mechanical Properties of Wood.* Madison, WI: U.S, 1999.

Hynd, David, Mats Svensson, Xavier Trosseille, Michiel van Ratingen, and Johan Davidsson. *Dummy requirements and injury criteria for a low-speed rear impact whiplash dummy.* EEVC, 2007.

Ivancic, Paul C, et al. "Whiplash causes increased laxity of cervical capsular ligament." *Clinical Biomechanics* 23 (2008): 159-165.

Keinberger, M. "Importance of head restraint position on whiplash injury." In *Frontiers in Whiplash Trauma: Clinical & Biomechanical*, by N Yoganandan, FA Pintar and (Eds.), 477-490. Amsterdam, The Neterlands: ISO Press, 2000.

Kitagawa, Yuichi, Tsuyoshi Yasuki, and Junji Hasegawa. "Research study on neck injury lesseing with active head restraint using human body FE model." *IRCOBI.* Bern, 2008. 382-396.

Krafft, M, A Kullgren, C Tingvall, O Bostro, and R Fredriksson. "How crash severity in rear impacts influences short- and long-term consequences to the neck." *Accident Analysis and Prevention* 32 (2000): 187–195.

Krafft, Maria, Anders Kullgren, Anders Ydenius, and Claes Tingvall. "Influence of crash pulse characteristics on whiplash associated disorders in rear impacts - crash recording in real life crashes." *Traffic Injury Prevention* 3, no. 2 (2002): 141 — 149.

Lee, Kathryn E, Andrew N Franklin, Martin B Davis, and Beth A Winkelstein. "Tensile cervical facet capsule ligament mechanics: Failure and subfailure responses in the rat." *J. of Biomechanics* 39 (2006): 1256-1264.

Lee, Kathryn E, Martin B Davis, Roanne M Mejilla, and Beth A Winkelstein. "In vivo cervical facet capsule distraction: mechanical implications for whiplash and neck pain." *Stapp Car Crash Journal.* Nashville: SAE International, 2004. 373-395.

Lord, Susan M, Les Barnsley, Barbara J Wallis, and Nikolai Bogduk. "Chronic Cervical Zygapophysial Joint Pain After Whiplash: A Placebo-Controlled Prevalence Study." *Spine*, 1996: 1737-1744.

Lu, Ying, Chaoyang Chen, Srinivasu Kallakuri, Ajit Patwardhan, and John M Cavanaugh. "Neural response of cervical facet joint capsule to stretch: a study of whiplash pain mechanism." *Stapp Car Crash Journal.* Washington: SAE International, 2005. 49-65.

McConnell, Whiman E, et al. "Human head and neck kinematics after low velocity rear-end impacts - understanding "whiplash"." *Stapp Car Crash Conference Proceedings.* SAE International, 1995.

Ono, Koshiro, Koji Kaneoka, Adam Wittek, and Janusz Kajzer. "Cervical injury mechanism based on the analysis of human cervical vertebral motion and head-neck-torso kinematics during low speed rear impacts." *Stapp Car Crash Conference Proceedings.* SAE International, 1997.

Panjabi, Manohar M, Jacek Cholewicki, Kimio Nibu, Jonathan Grauer, and Michael Vahldiek. "Capsular ligament stretches during in vitro whiplash simulations." *J. of Spinal Disorders* 11, no. 3 (1998): 227-232.

Panzer, Matthew B. "Numerical modelling of the human cervical spine in frontal impact." MASc Thesis, Waterloo, 2006.

Panzer, Matthew B, and Duane S Cronin. "C4–C5 segment finite element model development, validation, and load-sharing investigation." *Journal of Biomechanics* 42 (2009): 480-490.

Pearson, Adam M, Paul C Ivancic, Shigeki Ito, and Manohar Panjabi. "Facet joint kinematics and injury mechanisms during simulated whiplash." *Spine* 29, no. 4 (2004): 390-397.

Quinn, Kyle P, Kathryn E Lee, Chukwunyere C Ahaghotu, and Beth A Winkelstein. "Structural changes in the cervical facet capsular ligament: potential contributions to pain following subfailure loading." *Stapp Car Crash Journal.* San Diego: SAE International, 2007. 169-187.

Roberts, A. K, D Hynd, P. R Dixon, O Murphy, M. Magnusson, and M. H Pope. "Kinematics of the human spine in rear impact and the biofidelity of current dummies." *IMechE Conference Proceedings.* Professional Engineering Publishing, 2002. 227-246.

Siegmund, Gunter P, Barry S Myers, Martin B Davis, Herbert F Bohnet, and Beth A Winkelstein. "Mechanical evidence of cervical facet capsule injury during whiplash: a cadaveric study using combined shear, compression, and extension loading." *Spine* 26, no. 19 (2001): 2095-2101.

Siegmund, Gunter P, David J Sanderson, Barry S Myers, and J Timothy Inglis. "Awareness Affects the Response of Human Subjects Exposed to a Single Whiplash-Like." *Spine* 28, no. 7 (2003): 671-679.

Stemper, Brian D, Narayan Yoganandan, and Frank A Pintar. "Effects of abnormal posture on capsular ligament elongations in a computational model subjected to whiplash loading." *J. of Biomechanics* 38 (2005): 1313-1323.

Szabo, Thomas J, and Judson B. Welcher. "Human subject kinematics and electromyographic activity during low speed rear impacts." *Stapp Car Crash Conference Proceedings.* SAE International, 1996.

Thunnissen, J, J Wismans, C. L Ewing, and D. J Thomas. "Human volunteer head-neck responses in frontal flexion: a new analysis." *Stapp Car Conference Proceedings.* SAE International, 1995.

van der Horst, M. J, J. G. M Thunnissen, R Happee, R. M. H. P van Haaster, and J. S. H. M Wismans. "The influence of muscle activity on head-neck response during impact." *Stapp Car Crash Conference Proceedings.* SAE International, 1997.

Winkelstein, Beth A, Roger W Nightingale, William J Richardson, and Barry S Myers. "Cervical facet joint mechanics: its application to whiplash injury." *43rd Stapp Car Crash Conference Proceedings.* San Diego: SAE International, 1999.

A GLOBAL HEAD NECK TORSO MODEL FOR WHIPLASH INJURY CRITERIA INVESTIGATION

Nicolas Bourdet
IMFS, University of Strasbourg
France
Rémy Willinger
IMFS, University of Strasbourg
France
Paper Number 09-0412

ABSTRACT

The development of new protective systems must be performed on tools reliable and representative of alive human. In an earlier study, a simplified but realistic modeling of the head-neck-torso system under moderate rear impact was performed. This model of minimum complexity (MC-HNT model) but able to reproduce the 5 first experimental vibration modes was validated in the frequency domain in terms of natural frequencies and damping as well as mode shapes. The human model was then coupled to a car seat-head rest complex on Madymo Code in order to give real body behaviors and accurate T1 accelerations. The hypothesis of linear behavior was used for the torso being subjected to small deformations. The present study shows in detail the methodology carried out for real-world rear impact accident reonstruction in order to establish more accurate neck injury criteria as well as associated tolerance limits. In order to proceed to that, 87 accident cases were simulated using our MC-HNT human body model coupled to 3 Toyota seats under Madymo code. Several injury criteria, such as Neck Fx, Neck Fz, T1 acceleration, NIC_{max}, N_{km} and NDC, were calculated in order to correlate the risk of AIS1 neck injury using MC-HNT. A similar work has then been done with the BioRID II model. Then a comparison between the predictive risk curves obtained by analyzing the MC-HNT model and the BioRID II model has been performed. This comparison was expressed in terms of Nagelkerke *R-square* values obtained with these analyses. It appears that the MC-HNT model gives a higher correlation than the BioRID II one for all parameter, and that the lower neck axial force is shown as the best candidate to correlate with the neck injury.

INTRODUCTION

Despite advances in safety devices, neck injuries in traffic accidents, especially non-severe rear impact accidents, are still a serious and costly social problem. The high cost of whiplash injury has been extensively documented in several countries [1,2]. In order to decrease the incidence of whiplash injuries, development of safety measures requires reliability and fidelity of human body surrogates. Most injury prevention strategies are based on impact analysis using anthropomorphic crash test dummies or mathematical models. Improvement of injury prevention techniques needs agreement between both experimental and computational models on the one hand and experimental *in vivo* human body mechanical responses on the other. Unfortunately the spine is one of the most complex structures in the human skeletal system and its behavior during impact is still poorly understood.

Today no less than three crash test dummies are used in experimental rear impact analysis: The Hybrid III dummy, developed by Foster et al [3], the BioRID II reported by Davidsson [4] and the RID dummy proposed by Cappon et al [5]. Several validation studies on neck responses have been carried out on these dummies against volunteers and post mortem subjects [4,5,6,7,8,9]. They demonstrated several limitations of this human body surrogate under low speed rear impact in terms of biofidelity. It is unclear if this lack of biofidelity is due to the torso behavior or the neck characteristics or a combination of both.

Modeling of the human trunk began in the middle of the last century and existing models can be divided into two categories i.e. continuous models [10] and lumped parameters models [11]. However, most of these models do not have a realistic behavior compared to the human body. On the one hand, models are often too detailed and involve a high number of parameters that are not easily identified with existing experimental data. On the other hand, they represent only one particular dynamic behavior of the trunk and can therefore not be used for other applications such as the simulations of rear impacts. Finally, most of the studies concerning the torso aim at characterizing the global dynamic behavior of the trunk-head system under seat ejection for military applications. In addition, none of them has studied the kinematic behavior of the first thoracic vertebra (T1) under rear impact, an essential aspect for neck injury investigation.

In previous studies undertaken by Willinger and Bourdet [12], the experimental in vivo modal analysis of the human head-neck system has

provided us with natural frequencies and deformed mode shapes of this structure. Later, based on Kitazaki [13], the previous authors developed a whole human body model including the identification on five deformed mode shapes of the spine. In 2005, Bourdet *et al* [14] studied the influence of the trunk mobility.

In the first section the general methodology is presented including the use of existing experimental modal analysis for the identification of a torso lumped parameter model and its coupling to both the head neck and the car seat for rear impact applications. In the result section, the influence of trunk mobility is analyzed through comparison between responses of a rigid versus a flexible trunk under a standard rear impact pulse. Finally a parametric study is performed in order to evaluate the effect of mechanical parameters of the seat on the human neck response.

MATERIAL AND METHOD

Real-world data

In the present study the crash pulse acceleration of 87 real-life rear-end impact from Folksam database have been reconstructed. The acceleration-time history was measured during a crash by a crash pulse recorder fixed up on three car models of the same make. The recording and the analyzing have been described by [15,16,17]. The sampling rate of the crash pulse recorder is 1000 Hz during the impact phase of the crash. The acceleration data recorded were filtered at approximately 60 Hz. The occupant injury severity was divided into three categories regarding duration of symptoms; no neck injury, initial symptoms and symptoms more than one month. Examples of symptoms are neck pain, headache, dizziness and neck stiffness. The numbers of victims are presented in Table 2 for the various injury categories, car model and occupant location.

Table 1. Gender and average age for occupants with various injury categories.

	Average age	Gender (%) Male	Female
No neck injury	46	52	48
Initial symptoms	44	33	67
Symptoms > 1 month	48	47	53
Total	46	47	53

The age distribution and gender for the injury categories can be seen in Table 1. It was a similar proportion of males and females for occupants with symptoms more than one month and for all occupants. Also average age was similar for those groups.

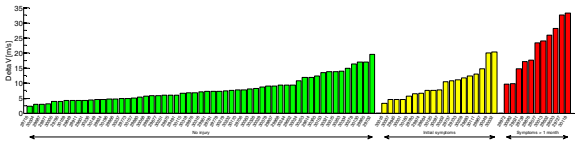

Figure 1. Representation of the Delta V of pulses versus injury severity.

Figure 1 represents the ΔV of the pulses extracted from the accident cases according to the level of injury obtained on the victim. It is interesting to observe that it appears a correlation between ΔV and injury.

Minimal complexity multi body torso model

In a previous study [12], an experimental and theoretical modal analysis of the human head-neck system in the sagittal plane have been carried out. The method has allowed to identify the mechanical properties of the head-neck system and to validate a mathematical model in the frequency domain. The extracted modal characteristics consist of a first natural frequency at 1.3 ± 0.1 Hz associated with head flexion-extension motion and a second mode at 8 ± 0.7 Hz associated with antero-posterior translation of the head, also called retraction motion, as illustrated in Figure 2.

Table 2. Number of occupants in various car models (D = Driver, FSP = Front Seat Passenger)

	Total	Total D	Total FSP	Car model 1 D	Car model 1 FSP	Car model 2 D	Car model 2 FSP	Car model 3 D	Car model 3 FSP
No neck injury	77	57	20	18	4	23	11	16	5
Initial symptoms	30	19	11	2	3	13	8	4	0
Symptoms > 1 month	15	11	4	4	1	3	2	4	1
Total	122	87	35	24	8	39	21	24	6

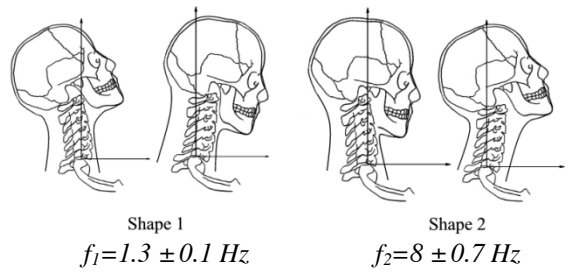

Figure 2. Representation of the two deformed mode shapes of the head neck system.

In order to address this issue, an original lumped model of the human torso was developed and coupled to a car seat-head rest complex. The hypothesis of linear behavior was used for the torso being subjected to small deformations. In a second study, the modal analysis of the human torso in a seating position conduced by Kitazaki [13] was used for both masses and mechanical properties identification [14].

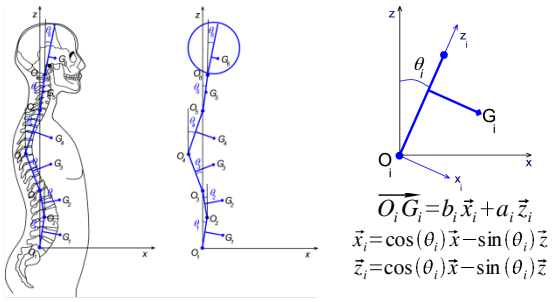

Figure 3. Representation of the lumped parameters model of the trunk, where $\theta_i=\theta_{i0}+\psi_i$ où θ_{i0} is the initial angle and ψ_i is a time dependent parameter.

In order to reproduce the four mode shapes identified experimentally the torso was divided in six segments to obtain the five degrees of freedom with the head neck system, as illustrated in Figure 3. This model of minimum complexity but able to reproduce the 5 first experimental vibration modes was validated in the frequency domain in terms of natural frequencies and damping as well as mode shapes.

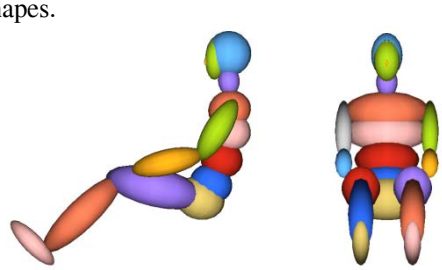

(a) (b)

Figure 4. Representation of the Minimal Complexity Head Neck Torso model (MC-HNT) : (a) side view and (b) front view.

BioRID II model

To compare the MC-HNT model, the BioRID II model is used. It is the production version of a rear impact dummy developed by Chalmers University of Technology, and manufactured by Denton ATD Inc., that has been produced to meet the need for more biofidelic dummy response to rear impact events than can be obtained using a standard Hybrid III dummy. While largely based on the Hybrid III 50th percentile dummy, the BioRID II has a hinged-segment spine design, with each of the 24 vertebrae explicitly represented. Stiffening springs and dampers are fitted to model the effect of the neck muscles, and the thoracic spine and torso are more flexible than that of the Hybrid III.

Car seat models

Both models are coupled to the models of three car seats used by Kullgren *et al* [17]. In order to carry out the accident simulations, it was necessary to set the three impact configurations, i.e. to position the dummies in three seats with a torso angle of 25°. Moreover, the distance between head and headrest is defined for two configurations (50 mm and 90 mm), without modify the torso angle, in order to take account the influence of the initial seatback inclination. Figure 5 shows the setting of the dummies in various seats configurations. Moreover it shows that the initial conditions are very close between for both models.

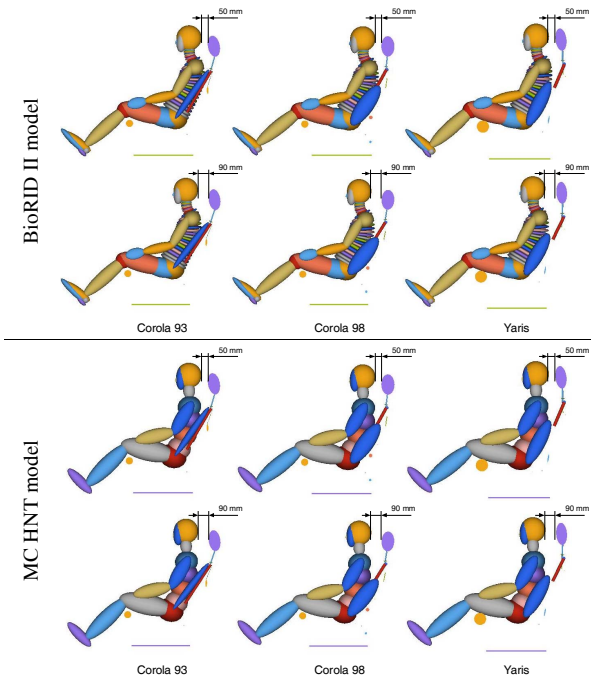

Figure 5. Position of the BioRID II and MC-HNT models in the three seats with two head-headrest distances.

87 real accidents have been reconstructed under both distance configurations and with both models. Thus, 348 simulations have been carried out. A

logistic regression has been conducted giving the Nagelkerke R^2 for the risk of initial symptom and symptoms over than one month for each model.

Accident simulations

The 87 real rear impacts accidents were simulated with both BioRID II and Minimal Complexity Head-Neck-Torso models seated on three car seats modeled in a previous study [17]. These reconstructions aim at analyzing the model behavior in order to investigate the correlation between the output parameters, as Neck Fx, Neck Fz and neck My at lower and upper neck as well as head and T1 acceleration, and three criteria as NIC_{max} [18], N_{km} [19] and NDC [20], with the injury severity.

Statistic correlation analysis

Injury correlation was evaluated by calculating the correlation coefficient, of logistic regression for each mechanical candidate parameter. The correlation coefficient R^2 proposed by Nagelkerke in 1991 [21] was used. This coefficient permits it to evaluate the quality of the regression. For that, a sample $(x_i,y_i)_{i=1,\dots,N}$ was introduced, where the x_i are the observed values of the explicative variable x and y_i are the random variable of y taking 0 for no injured and 1 for injured at case i. The logistic regression model used is a logistic function written in equation (1) which defines the probability of injury for various x.

$$p(y=1|x) = \frac{e^{\alpha+\beta x}}{1+e^{\alpha+\beta x}} \qquad (1)$$

The maximum of likelihood is calculated to identify the α and β constants. The likelihood is defined as equation (2).

$$L(\alpha,\beta) = \prod_{i=1}^{n} p(x_i)^{y_i}\,(1-p(x_i))^{1-y_i} \qquad (2)$$

$$\ell(\alpha,\beta) = -\ln\big(L(\alpha,\beta)\big) \qquad (3)$$

The maximum of likelihood criterion defines the α and β values that give a maximum likelihood. For this purpose, it must be considered the opposite of its logarithm: the *log-likelihood* function defined in equation (3). This function is minimized by using the Newton Raphson's algorithm.

The correlation coefficient is well established in classical regression analysis [22]. It is defined as the proportion of variance explained by the regression model. It is used as a measure of success of predicting the dependent variable from the independent variable. In order to generalized the concept to models without easily residual variance and where the maximum of likelihood is its criterion of fit, in 1989, Cox and Snell [23] proposed a R^2 as defined in equation (4). This correlation coefficient was modified by Nagelkerke in 1991 [21], in order to "normalize" the result, expressed in equation (5), where N_k is the population number of responses in category k, i.e. 0 or 1.

$$R^2_{RC} = 1 - \left(\frac{L(\alpha_0,0)}{L(\alpha,\beta)}\right)^{2/N} \qquad (4)$$

$$R^2_N = \frac{R^2_{RC}}{1-L(\alpha_0,0)^{2/N}} \qquad (5)$$

$$\text{With } \alpha_0 = \ln\left(\frac{N_1}{N_0}\right) \qquad (6)$$

For each parameter, two logistic regressions are calculated: the risk of initial symptoms and the risk of symptoms over one month. The total number of occupants is 122. Concerning the risk of initial symptoms, the occupants with initial symptoms and the occupants with symptoms over one month were merged. Thus the logistic regression was calculated for 77 no-injured cases and 45 injured cases. In the same way, for the risk of symptoms over one month, the occupants with initial symptoms were regrouped with the no injured occupants. Thus the logistic regression was calculated for 107 cases having at most initial symptoms and 15 cases with long-term symptoms.

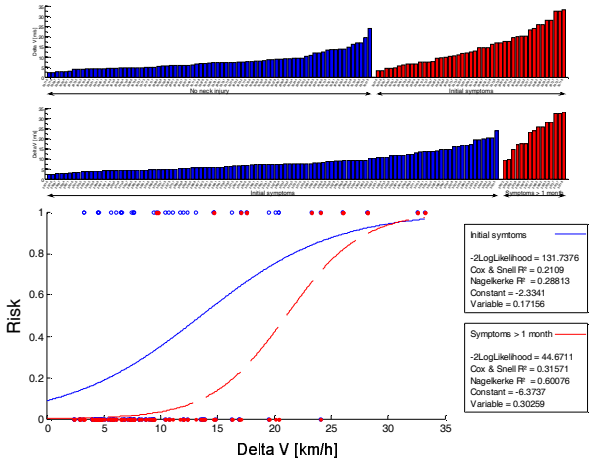

Figure 6. Histograms of Delta-V used for the two logistic regressions, and Delta-V risk curves of initial symptoms and symptoms > 1 month.

As an example, Figure 6 represents the Delta-V histogram and risk curves of initial symptoms and long term symptoms versus Delta-V for the two logistic regressions. It can be observed that Delta-V correlates well the long-term symptoms with a R^2_N of 0.6. For a 50% risk of initial symptoms, the Delta-V is of 21 km/h and for 20% risk of symptoms over one month is of 15 km/h. In 2005, Krafft *et al* [24] found 18 km/h for the same risk.

RESULTS

Comparative results on one case

An example of a comparative accident reconstruction is shown in detail in Figure 7, for a distance between head and headrest of 50 mm. It illustrates the behavior differences of the head-neck system between the BioRID II Madymo model and the MC-HNT model. Indeed, BioRID II has a light translation movement of the head followed at 150 milliseconds by an extension movement, while the MC-HNT model continues its retraction motion until 200 milliseconds.

Figure 8 and Figure 9 represent T_1 linear accelerations according to X and Z axis. In spite of prevalent oscillations on MC-HNT model, the behavior is coarsely identical. The behavior difference is especially illustrated in Figure 10 which represents the rotation of the first thoracic vertebrae (T1). Indeed, while the BioRID II upper thorax rotates forward (positive rotation), the MC-HNT model's ones undergoes an extension. Figure 11 shows relative rotation between the head and the neck for both models. It can be observed that BioRID II does not present any retraction until 120 milliseconds (positive relative rotation), while the MC-HNT model presents this movement clearly at approximately 110 milliseconds.

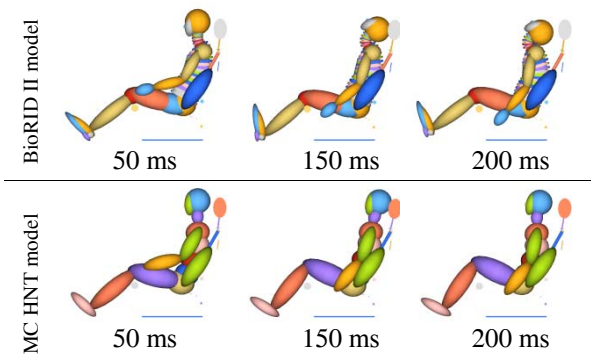

Figure 7. Pictures extracted from a simulation of case for the BioRID II and MC-HNT models.

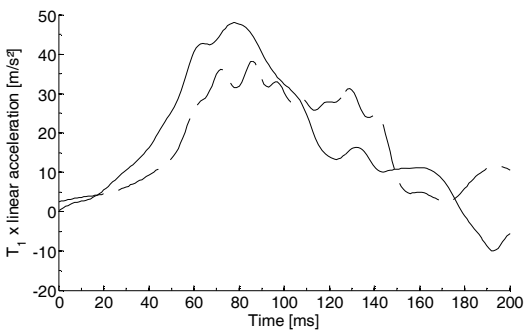

Figure 8. Superimposition of T_1 x linear acceleration for both models (— BioRID II model, – – MC-HNT model)

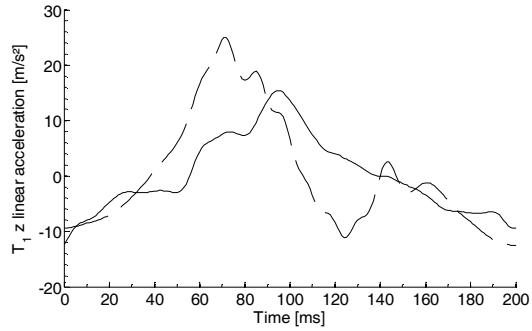

Figure 9. Superimposition of T_1 z linear acceleration for both models (— BioRID II model, – – MC-HNT model)

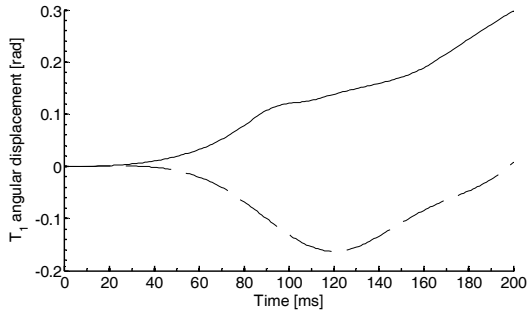

Figure 10. Superimposition of T1 angular displacement for both models (— BioRID II model, – – MC-HNT model)

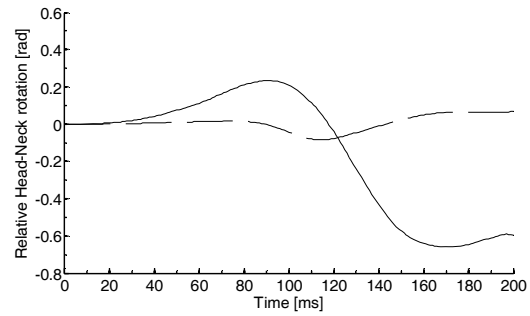

Figure 11. Superimposition of Head angular displacement both models (— BioRID II model, – – MC-HNT model)

Global statistic correlation

Figure 13 to Figure 14 represent the Nagelkerke's *R-squared* of each parameter under the two configurations for each model. It is clear that the results from the BioRID II models give different regressions according the distance between head and headrest. Indeed, concerning the risk of initial symptom, on one configuration the best candidates are T1 acceleration and the upper neck axial force as well as the lower neck shear force with R_N^2 of 0.26, R_N^2 of 0.25 and R_N^2 of 0.25 respectively. On the other configuration the best correlation is obtained with the upper neck axial force with R_N^2 of 0.10. In contrast, for the MC-HNT model, the best candidates tied are the lower neck moment, shear

and axial forces as well as the upper neck axial force with a Nagelkerke *R-squared* of 0.3 under the shorter distance head-headrest configuration, and 0.32 under the higher distance configuration, adding the upper neck shear force and N_{km} criterion.

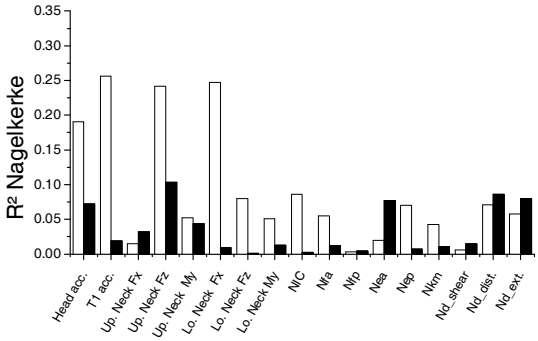

Figure 12. BioRID II model R^2_N for the risk of initial symptom (□ $d_{headrest}$=50 mm, ■ $d_{headrest}$=90 mm).

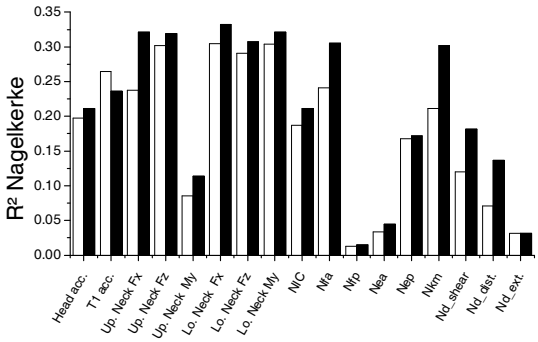

Figure 13. MC-HNT model R^2_N for the risk of initial symptom (□ $d_{headrest}$=50 mm, ■ $d_{headrest}$=90 mm).

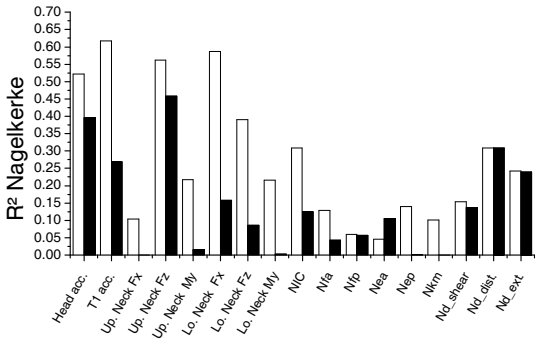

Figure 14. BioRID II model R^2_N for the risk of symptom > 1 month (□ $d_{headrest}$ = 50 mm, ■ $d_{headrest}$ = 90 mm).

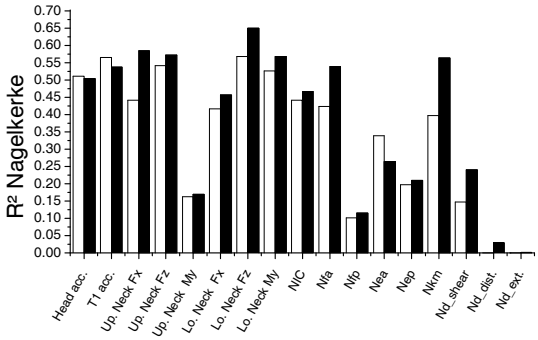

Figure 15. MC-HNT model R^2_N for the risk of symptom > 1 month (□ $d_{headrest}$ = 50 mm, ■ $d_{headrest}$ = 90 mm).

Concerning the risk of symptoms over one month, the BioRID II model shows various best candidate parameters according to the configuration. For instance, the best candidates for the first configuration are the T1 acceleration, the lower neck shear force and the upper neck axial force with $R^2_N = 0.62$ $R^2_N = 0.59$ and $R^2_N = 0.56$ respectively, and for the other configuration the best ones are the upper neck axial force and the head acceleration with $R^2_N = 0.46$ and $R^2_N = 0.40$ respectively. On the contrary, the MC-HNT model is better correlated by the lower and upper neck axial force ($R^2_N = 0.57$ and $R^2_N = 0.54$ respectively) as well as T1 acceleration with $R^2_N = 0.56$ in the first configuration case. The lower neck axial force is clearly the best candidate in case of distance head-headrest of 90 mm with $R^2_N = 0.65$.

No clear correlation between the common injury criteria and the injury outcome could be found for BioRID II model, as shown in Figure 12 and Figure 14. The best scores is given by the NIC with $R^2_N = 0.09$ concerning the risk of initial symptoms and $R^2_N = 0.31$ for the risk of symptoms over one month in case of shorter distance configuration, and $Nd_{distraction}$ in case of higher distance configuration with $R^2_N = 0.09$ and $R^2_N = 0.31$ respectively.

Candidate parameters to injury correlation

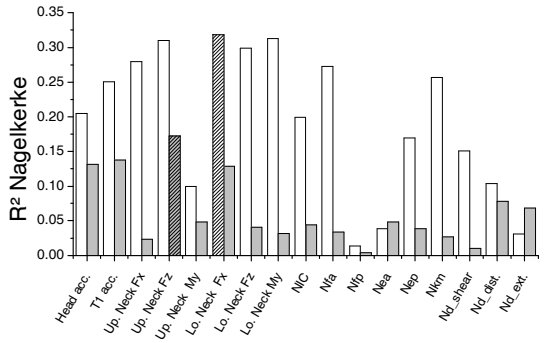

Figure 16. Representation of the mean R^2_N obtained with both model and the maximum value in black, for initial symptom (□ MC-HNT, ▢ BioRID II, ▨ Maximum value).

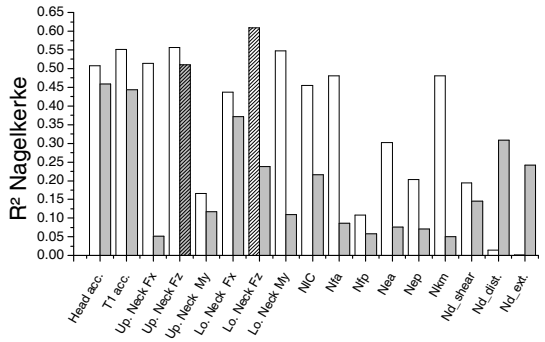

Figure 17. Representation of the mean R^2_N obtained with both and the maximum value in black model for symptom > 1 month (□ MC-HNT, ▢ BioRID II, ▨ Maximum value).

In order to extract the parameter which seems to present the correlation with neck symptoms, a mean value of R^2_N was calculated from the two configurations values. Thus, Figure 16 and Figure 17 gather the MC-HNT and the BioRID scores highlighting the best candidate represented by hatched histograms.

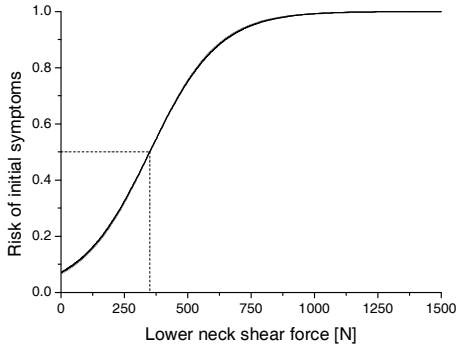

Figure 18. Lower neck shear force risk curve of initial symptoms. Grey area represents risks limited by the minimum and the maximum criterion values for both distance configuration and black line is the median (MC-HNT model).

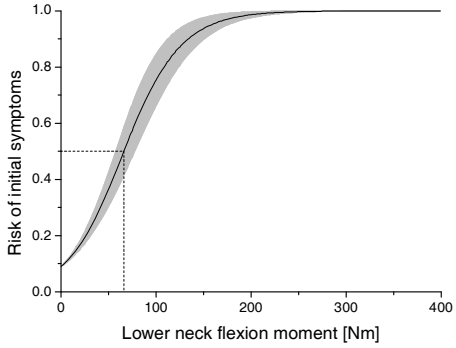

Figure 19. Lower neck moment risk curve of initial symptoms. Grey area represents risks limited by the minimum and the maximum criterion values for both distance configuration and black line is the median (MC-HNT model).

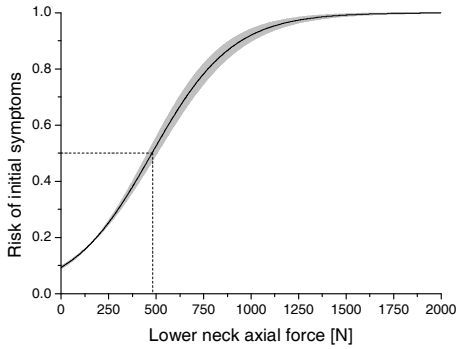

Figure 20. Lower neck axial force risk curve of initial symptoms. Grey area represents risks limited by the minimum and the maximum criterion values for both distance configuration and black line is the median (MC-HNT model).

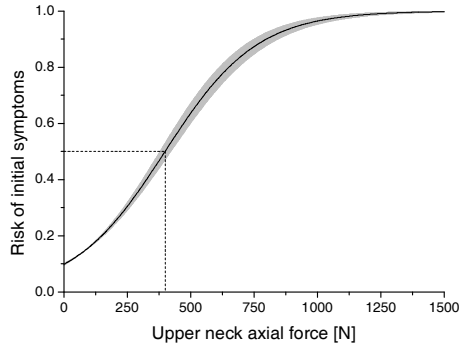

Figure 21. Upper neck axial force risk curve of initial symptoms. Grey area represents risks limited by the minimum and the maximum criterion values for both distance configuration and black line is the median (MC-HNT model).

For MC-HNT model, the lower neck shear force seems to be the parameter which give a best regression to evaluate the risk of initial symptoms with R^2_{Nmean}= 0.31. We can observe that, the lower neck moment and axial force as well as the upper axial force give R^2_{Nmean} very close to the maximum. For BioRID II model, the best parameter candidate is the upper neck axial force with R^2_{Nmean} = 0.17. Figure 18 to Figure 21 represent the risk curve of the four best candidate parameters. The limit at 50% risk of initial symptoms is about 68 ± 9 Nm for the lower neck flexion moment, 480 ± 24 N for the lower neck axial force, 350 ± 0.01 N for the lower neck shear force and 400 ± 20 N for the upper neck axial force. The risk curves obtained from both distance configurations are very close themselves. Except for the lower neck moment, the deviations of the limit at 50% risk don't exceed 10%.

In contrast, for the BioRID II model, the four best candidate parameters are the upper neck axial force, T1 and Head acceleration and the lower neck shear force with R^2_{Nmean}= 0.17, R^2_{Nmean}= 0.14, R^2_{Nmean} = 0.13 and R^2_{Nmean}= 0.13 respectively.

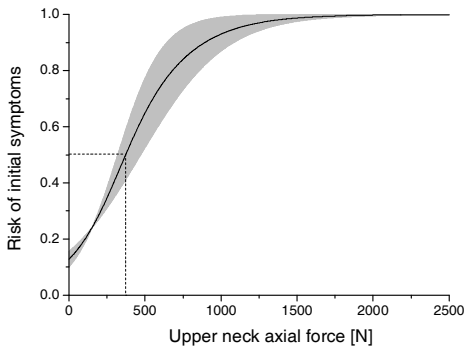

Figure 22. Upper neck axial force risk curve of initial symptoms. Grey area represents risks limited by the minimum and the maximum criterion values for both distance configuration and black line is the median (BioRID II model).

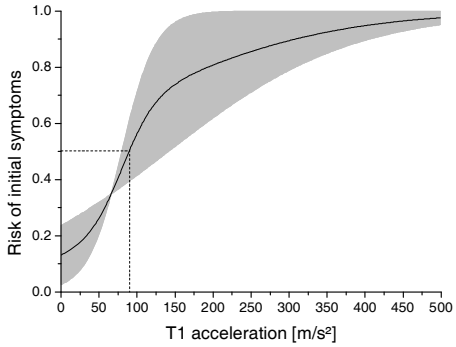

Figure 23. T1 acceleration risk curve of initial symptoms. Grey area represents risks limited by the minimum and the maximum criterion values for both distance configuration and black line is the median (BioRID II model).

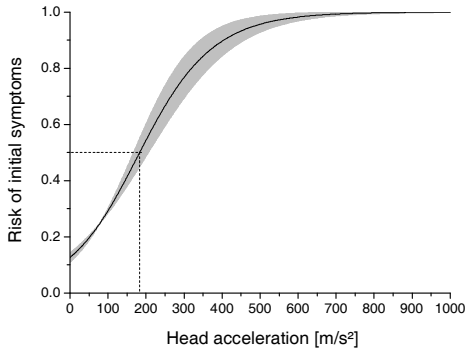

Figure 24. Head acceleration risk curve of initial symptoms. Grey area represents risks limited by the minimum and the maximum criterion values for both distance configuration and black line is the median (BioRID II model).

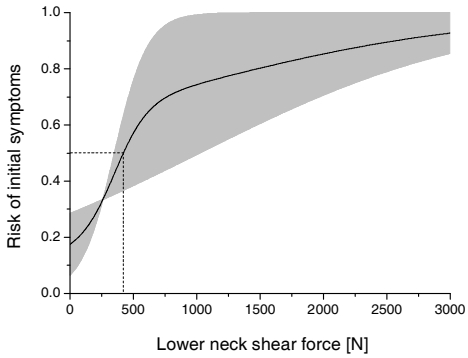

Figure 25. Lower neck shear force risk curve of initial symptoms. Grey area represents risks limited by the minimum and the maximum criterion values for both distance configuration and black line is the median (BioRID II model).

The BioRID II model risk curves of the best regressions define large corridors. The limit values at 50% risk of initial symptoms are 373 ± 75 N for the upper neck axial force, 9 ± 3 g for T1 acceleration, 18.4 ± 2 g for Head acceleration and 422 ± 336 N for the lower neck shear force. The deviations of the limits exceed 40%, as illustrated in Figure 23 to Figure 25.

Regarding the risk of symptoms over one month, Figure 26 represents the risk curves for the lower neck axial force obtained from MC-HNT model. As for the initial symptoms, the curves are very close giving a 50% risk of 703 ± 28 N.

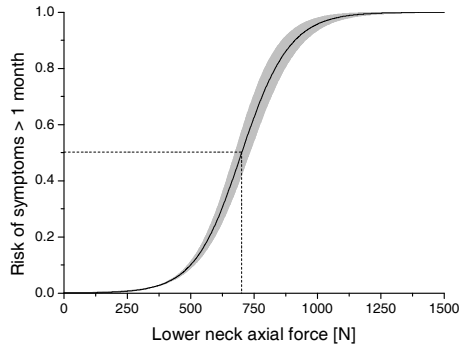

Figure 26. Lower neck axial force risk curve of initial symptoms. Grey area represents risks limited by the minimum and the maximum criterion values for both distance configuration and black line is the median (MC-HNT model).

For BioRID II, the risk at 50% of symptoms over than one month for the upper neck axial force is 516 ± 38 N, as shown in Figure 27. The deviation is smaller than for initial symptoms risk (15% against 40 % for initial symptoms risk).

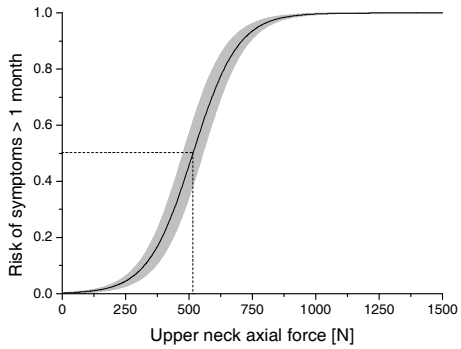

Figure 27. Upper neck axial force risk curve of initial symptoms. Grey area represents risks limited by the minimum and the maximum criterion values for both distance configuration and black line is the median (BioRID II model).

DISCUSSION

Since over ten years many investigation on new neck injury criteria for rear end impact have been carried out. Bolström *et al* [25] proposed the NIC (Neck injury Criterion) as a value to correlate the head-neck movement with the ganglia caused by transient pressures changes in spinal canal. It addresses the relative acceleration between head and torso in the head translational motion. The

threshold proposed is of 15 m²/s². In 2002, Schmitt *et al* [19] proposed the N_{km} criterion based on the linear combination of shear force and bending moment at the occipital condyle.

In 2006, Eriksson and Kullgren [26] simulated 79 real accident cases from the same database used on our study under 100 posture of BioRID II and proposed a NIC risk curve for symptoms > 1 month. It estimates that a NIC of 24.5 ± 10 m²/s² corresponds to risk of 50 %, as illustrated in Figure 28. As for the NIC_{max}, they established a N_{km} risk curve for symptoms > 1 month. It estimates that a N_{km} of 0.5 ± 0.3 corresponding to risk of 50 %, as illustrated in Figure 29.

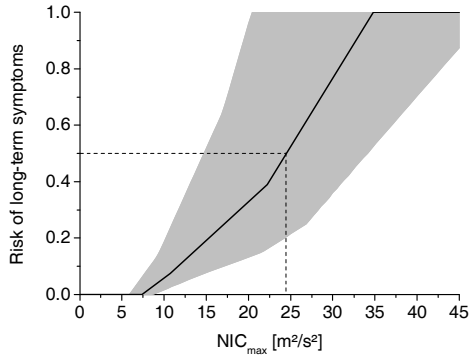

Figure 28. NIC_{max} Risk curve for symptoms > 1 month from Eriksson and Kullgren [26].

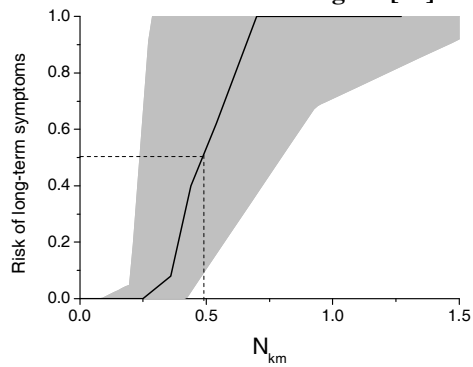

Figure 29. Risk curve of symptoms > 1 month versus lower neck axial force for both models.

Moreover, several multi body human models have been developed for rear-end impacts. A two-dimensional human model has been proposed by Jernström *et al* [27] and the computed head-torso relative angle was compared to the one recorded on a volunteer undergoing a velocity change of 8 km/h. In Jakobsson *et al* [28] it was then shown that neither the upper thoracic spine curvature of the model nor the calculated duration of the contact between the head and the headrest were in accordance with experimental data. These numerical and physical spine models are usually validated against experiments on volunteers or post-mortem human subjects (PMHS) in the time domain by superimposing model and human response parameters as a function of time. This methodology is limited as it is very difficult to characterize a multiple degrees of freedom system under impact in the time domain. The mentioned limitation illustrates the need for further torso experimental and theoretical analysis.

The present paper is to refer on in vivo human trunk characterization available in the literature using modal analysis techniques and to develop a lumped parameters model of this segment in the sagittal plane to be validated in the frequency domain. This model was seated in three car seats and 87 real accidents have been simulated. The same work has been carried out with BioRID II model in order to compare the prediction of neck damages. The simulations showed different behaviors about the head-neck-trunk system. Indeed, the MC-HNT model translation phase is longer period of time than the BioRID II model. This can be explained by the fact that the MC-HNT model presents a lower stiffness at the head-neck-trunk system. This behavior softer leads the model to be more sensitive. Indeed, during the deceleration phases, the trunk is pushed by the backseat leaving the head. The loading at the head-neck and neck-thorax junctions increases considerably if the head is pulled by the rest of the body before it contacts the headrest. This force can be projected either to axial force or to shear force according the head-thorax angle.

One of main limitations of this study is not to know the initial posture of the occupants. Indeed, the posture has a drastic influence on the behavior, leading to different logistic regressions. A first evaluation of this influence has been carried out but it should be interesting to make in deep a parameter study to extract the best candidate parameters which correlate the injury severity. Nevertheless, it highlighted the difference behavior between the two models, and the homogeneous results in terms of parameter criteria, for the MC-HNT model.

CONCLUSION

Performing 87 real accident cases from Folksam database on three seats under two configuration of distance between head and headrest using a minimum complexity model (MC-HNT model) based on the reproducibility of the 5 first experimental vibration modes of the vertebrae column revealed several parameters with higher correlation coefficient values in the logistic regression against the lesion severity. The lower neck axial force is shown as the best value of Nagelkerke R-square for both initial symptoms risk and symptoms over than one month risk.

The 87 accident cases were also simulated using BioRID II model. Then we performed a comparison between the predictive risk curves obtained by

analyzing the MC-HNT model and the BioRID II model. In addition we compared the Nagelkerke R-square values obtained with these analyses. It appears that the MC-HNT model gives a better regression than the BioRID II one for all parameter.

ACKNOLEDGEMENTS

Thanks go to Anders Kullgren from Folksam Research and Karolinska Institutet of Stockholm and to Ola Boström from AUTOLIV Research.

REFERENCES

1 Szabo T.J., and Welcher J.B., Human Subject kinematics and electromyographic activity during low speed rear impacts. Proc. of the 40th Stapp Car Crash Conference, 1 Vol. SAE 962432, Albuquerque (USA), 1996, pp. 339-356.

2 Szabo T. J., Voss D. P., and Welcher J. B., Influence of seat foam and geometrical properties on BioRID P3 kinematic response to rear impacts, Proc. IRCOBI Conference, Munich (Germany), 1 Vol. pp. 87-101., 2002.

3 Foster, J.K., Kortge, J.O., and Wolanin, M.J., Hybrid III-a biomechanically-based crash test dummy, Proc. of the 21st Stapp Car Crash Conference, 1 Vol. SAE 770938, pp.975-1014, New York (USA), 1977.

4 Davidsson J., BioRID II final report, Crash Safety Division, Departement of Machine and Vehicle Design, Chalmers University of Technology, Göteborg, Sweden, 1999.

5 Cappon H., Philippens M., Ratingen v., and Wismans J. Development and evaluation of a new rear-impact crash dummy: the RID2, Proc. of the 45th Stapp Car Crash Conference, 1 Vol. SAE 2001-22-0010, pp. 225-238, San Antonio (USA), 2001.

6 Seemann M. R., Muzzy W. H., and Lustick L. S., Comparison of human and Hybrid III head and neck response, Proc. of the 30th Stapp Car Crash Conference, 1 Vol. SAE 861892, pp. 291-312, USA, 1986.

7 Prasad P., Kim A., and Weerappuli D. P. V., Biofidelity of anthropomorphic test devices for rear impact, Proc. of the 41th Stapp Car Crash Conference, 1 Vol. SAE 973342, pp. 387-415, USA, 1997.

8 Davidsson, J., Lövsund, P., Ono, K., Svensson, M., and Inami, S., A comparison between volunteer, BioRID P3 and Hybrid III performance in rear impact., Proc. IRCOBI Conference, Sitges (Spain), 1 Vol. pp. 165-190, 1999.

9 Siegmund G. P., Heinrichs B. E., Lawrence J. M., and Philippens M., Kinetic and kinematic responses of the RID2a, Hybrid III and Human Volunteers in low-speed rear-end collisions, Proc. of the 45th Stapp Car Crash Conference, 1 Vol. SAE 2001-22-0011, pp. 239-256, San Antonio (USA), 2001.

10 Hess, J.L., and Lombard, C.F., Theoretical investigations of dynamic response of man to high vertical acceleration. Aviat. Med. 29, 1958.

11 Vulcan, A.P., King, A.I., and Nakamura, G.S., Effects of bending on the vertebral column during +Gz acceleration. Aerosp. Med. 41: 294, 1970.

12 Willinger R., Bourdet N., Fischer R., Le Gall F., New method for biofidelity evaluation of dummy necks. 18th ESV Conf., 18ESV-000343, Nagoya (Japon), 2003

13 Kitazaki Satoshi, 1992, Application of experimental modal analysis to the human whole-bodyvibration. Proceedings of the United Kingdom Informal Group Meeting on Human Response to Vibration, held at The University of Southampton, Southampton, Hampshire, 28-30 September, 1992, 17-39.

14 Bourdet N., Willinger R. Human body-car seat coupling under rear impact. 19th ESV Conf., 19ESV-05-261,Washingthon (United States),2005

15 Aldman, B., Kullgren, A., Lie, A., Tingvall, C., 1991. Crash pulse recorder (CPR)-development and evaluation of a low cost device for measuring crash pulse and delta-V in real life accidents. Proc. of the 13th ESV Conf., Paris. Paper, 91-S1-W- 26, 188–192.

16 Kullgren, A., Lie, A., Tingvall, C., 1995. Crash Pulse Recorder (CPR)-validation in full scale crash tests. Accident Analysis Prevention 27, 717–727.

17 Kullgren A, Eriksson L, Boström O, Krafft M (2003) Validation of neck injury criteria usingreconstructed real-life rear-end crashes with recorded crash pulses. Proc. of the 18thTechn. Conf. on ESV, Paper No. 344, Tokyo.

18 Boström O.; Fredriksson R.; Håland Y.; Jakobsson L.; Krafft M.; Lövsund P.; Muser M.H.; Svensson M.Y.(2000) Comparison of Car Seats in low Speed Rear-End Impacts Using the BioRID Dummy and the new Neck Injury Criterion (NIC). Accident Analysis & Prevention, Volume 32, No. 2

19 Schmitt K-U, Muser M H, Walz F H, and Niederer P, Nkm— a proposal for a neck protection criterion for low speed rear-end impacts 2002, Traffic Injury Prevention, Vol. 3(2), pp. 117-126

20 Viano D, Davidsson J (2002) Neck displacements of volunteers, BioRID P3 and Hybrid III in rear impacts: implications to whiplash assessment by a neck displacement criterion (NDC), Traffic injury prevention, Vol. 3, No. 2

21 Nagelkerke N. J. D., A note on a general definition of the coefficient of determination, Biometrika, 78 (3), p. 691-692, 1991

22 Rao C.R., Linear statistical inference and its application, 2nd ed. New York, Wiley, 1973

23 Cox D.R. and Snell E.J., The analysis of binary data, 2nd ed. London, Chapman and Hall, 1989.

24 Maria Krafft, Anders Kullgren, Sigrun Malm, Anders Ydenius, Influence of crash severity on various whiplash injury symptoms: a study based on real-life rear-end crashes with recorded crash pulses, 19th ESV Conf., 19ESV-05-363,Washingthon (United States),2005

25 Boström O., Svensson M. Y., Aldman B., Hansson H., Håland Y., Lövsund P., Seeman T., Suneson A., Säljö A. and Örtengren T, (1996) "A new neck injury criterion candidate based on injury findings in the cervical spine ganglia after experimental neck extension trauma". International IRCOBI conference on the Biomechanics of Impacts, Dublin, Ireland.

26 Eriksson Linda; Kullgren Anders, Influence of Seat Geometry and Seating Posture on NIC_{max} Long-Term AIS 1 Neck Injury Predictability, Traffic Injury Prevention, Volume 7, Issue 1 March 2006 , pages 61-69.

27 Jernström C., Nilsson G. And Svensson M. Y., A first approach to an implementation in MADYMO of a human body model for rear impact modeling. Proc of the 4th International Madymo User's Meeting, september 6-7, Eindhoven (The Netherlands), 1993.

28 Jakobsson, L., Norin, H., Jernström, C., Svensson, S.-E., Johnsén, P., Isaksson-Hellman, I., and Svensson, M.Y., Analysis of Different Head and Neck Responses in Rear-End Car Collisions Using a New Humanlike Mathematical Model. Proc. of the IRCOBI Conference, Lyon (France), pp. 109-126, 1994.

COUPLING OF STRASBOURG UNIVERSITY HEAD MODEL TO THUMS HUMAN BODY FE MODEL: VALIDATION AND APPLICATION TO AUTOMOTIVE SAFETY

IPEK H.
MAYER C.
Daimler AG
Germany

DECK C.
LUCE H.
DE GUESELLE P.
WILLINGER R.
University of Strasbourg, IMFS-CNRS
France

Paper Number 09-0384

ABSTRACT

Human body segments and whole body models are more and more used in automotive safety research. Detailed in deep validated segmental models exist and are used for the definition of improved injury criteria, transforming the models into injury prediction tools. The present collaborative work's objective is to couple and to validate the Strasbourg University Head FE Model (SUFEHM) with the THUMS human body model under Ls-Dyna code before applying the new tool under accidental environment.

In a first effort, Strasbourg University Head Model and related injury criteria developed in earlier studies under RADIOSS code had to be transferred under Ls-Dyna code, both at constitutive laws and injury criteria definition level. For this, a validation of the SUFEHM against Nahum and Yoganandan's experiments in order to validate brain and skull behavior respectively under Ls-Dyna has been done. After these validations the reconstruction of 59 real world head trauma has been conducted in order to propose head tolerance limits to specific injuries under Ls-Dyna code.

After this, the SUFEHM was coupled to the THUMS neck in order to create a hybrid "THUMS-Strasbourg head" model. At geometrical level the coupling was performed by creating interfaces at bone contact level and connecting ligaments and soft tissue elements to the head model. At mechanical level the coupled FEMs was validated under front, lateral and oblique impact regarding head-neck kinematics superimposed to experimental data.

This coupled model constitutes an original research tool for further investigation on the importance of human head boundary condition in case of head impact, whatever the accident condition are, car occupant, pedestrian or even motorcyclists.

INTRODUCTION

Since several years human body models became a useful tool for the simulation of the human body under impact conditions. Human body models are directly modelled like the human body. In comparison the common dummy simulation models are modelled like the anthropomorphic test device which they are representing.

Generally the results which can be obtained by a simulation model of the dummy are limited to the measurements which are delivered by the anthropomorphic test device.

The results which human body simulations deliver have of course also limitations. But compared to an anthropomorphic test device human body models are able to represent the kinematics of the human body in a more realistic way. A human body model can be loaded from different directions. For instance the same model is able to simulate the frontal and the side impact loading of an occupant. In fact the same model should be able to simulate a pedestrian accident situation if positioned in a standing posture.

All over the world several human body models are available. Additionally detailed models of body regions are also available. Body region models can be used for special impacts like a leg model impacting a front end model of a car. Regarding the body regions under the aspects of crash and impact the head is one of the most vulnerable body regions despite of having a strong bone structure. Therefore models of the head have been developed to simulate the impact and the possible injury caused by these impacts.

A typical human body model for the whole human body is the THUMS model used with Ls-Dyna code [Iwamoto2002, Oshita 2002]. Due to the fact, that the basic version of the THUMS model has a rigid skull modelling, the head impact of this whole body human model cannot be evaluated for possible head or brain injuries.

A typical state of the art head model is the Strasbourg University Head FE Model (SUFEHM), which is able to predict head injuries caused by impacts. This model is available under Radioss code. The aim of this study is first to transfer SUFEHM under Ls-Dyna code, validate it and propose some tolerance limits to specific injuries by reconstructing real world head trauma under Ls-dyna code, second to couple SUFEHM with the THUMS and validate the head-neck kinematics.

STRASBOURG UNIVERSITY FINITE ELEMENT HEAD MODEL UNDER L-DYNA CODE

Meshing presentation

Kang et al., in 1997, has developed the Strasbourg University Finite Element Head Model. The geometry of inner and outer surfaces of the skull was digitised from a human adult male skull. The main anatomical features modelled were the skull, falx, tentorium, subarachnoid space, scalp, cerebrum, cerebellum, and the brainstem. The finite element mesh is continuous and represents an adult human head. Globally, SUFEHM model consists of 13208 elements. Its total mass is 4.7 kg, a representation is given in Figure 1.

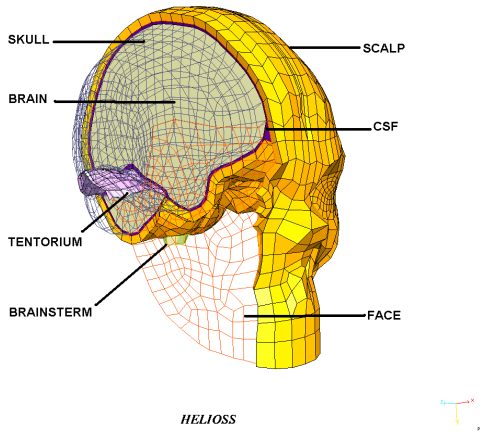

Figure 1. Section through the Strasbourg University Finite Element Head Model (SUFEHM).

Mechanical properties under Ls-dyna software

Introduction - The source model is available under Radioss code; the aim here is to implement mechanical properties under Ls-Dyna code before SUFEHM's validation. Material properties of the cerebral spinal fluid, scalp, facial bones, tentorium and falx are all isotropic, homogenous and elastic, with mechanical properties similar than those used under Radioss code (*MAT_ELASTIC law) (Willinger et al., 1995).

Brain material law choice – The brain is assumed to be visco-elastic. The visco-elastic law used under Ls-Dyna code is Material Type 6 (MAT_VISCOELASTIC). This model allows the modeling of visco-elastic behavior for beams, shells and solids. The shear relaxation behavior is described by:

$$G(t) = G_\infty + (G_0 - G_\infty)Exp(-\beta t)$$

With G_0 short-time shear modulus, G_∞ Long-time shear modulus and β Decay constant. Values of the parameters are the same than for Radioss code i.e. G_0=4.9E^{-02} MPa, G_∞=1.62E^{-02} MPa and β=145s^{-1}.

Skull material law choice - The skull was modelled by a three layered composite shell representing the inner table, the diplöe and the external table of human cranial bone. For this an INTEGRATION_SHELL card has been implemented in order to define the three skull layers (cortical bone and diploe) as layers' thicknesses. The material model 55, which is available under a single label "*mat_enhanced composite_damage*", in LS-DYNA was used to represent the mechanical behavior of the skull bones The material model 55 has three failure criteria expressions for four different types of in-plane damage mechanisms. Each of them predicts failure of one or more plies in a laminate. The expressions accommodate four in-plane failure modes: matrix cracking, matrix compression, fiber–matrix shearing and fiber breakage. Skull mechanical parameters are presented in Table 1.

Table 1. Skull mechanical parameters under Ls-Dyna code

	Cortical bone	*Diploe bone*
Mass density [Kg/m3]	1900	1500
Young modulus [MPa]	15000	4665
Poisson's ratio	0.21	0.05
Shear stress parameter	-0.5	-0.5
Longitudinal and transverse compressive strength [MPa]	145	24.8
Longitudinal and transverse tensile strength [MPa]	90	34.8

Validation

After Strasbourg University Head FE meshing transfer under Ls-Dyna code and after the identification of the material laws, the SUFEHM validation under this code for Nahum's impact (in order to validate brain response) and for Yoganandan's impact (in order to validate the skull behaviour and bones failure) is proposed.

Nahum's validation - The experimental data used in order to validate brain behaviour were published by Nahum et al.(1977) for a frontal blow to the head of a seated human cadaver. For this

impact configuration, a 5.6 kg rigid cylindrical impactor launched freely with an initial velocity of 6.3 ms-1 generates an interaction force and a head acceleration characterised by their peak values which are respectively 6900 N and 1900 ms-2 over a duration of 6 10-3 s. Intracranial pressures were also recorded in this test, at five well defined locations : behind the frontal bone, adjacent to the impact area, immediately posterior and superior to the coronal and squamosal suture, respectively in the parietal area, inferior to the lambdoidal suture in the occipital bone (one in each side), and at the posterior fossa in the occipital area.
Since the neck was not included in this model, a free boundary condition was used to simulate Nahum's impact. This hypothesis is based on the justification that the time duration of the impact is too short (6 ms) for the neck to influence the kinematics head response during pulse duration.
In order to reproduce the experimental impact conditions, the anatomical plane of the SUFEHM was inclined about 45°, as shown in Figure 2, like in the Nahum's experiment. For modelling a direct head impact, the model was frontally impacted by a 5.6 kg rigid cylindrical impactor (with an elastic padding, E= 13.6MPa, Poisson's ration=0.16) launched freely with an initial velocity of 6.3 m/s.

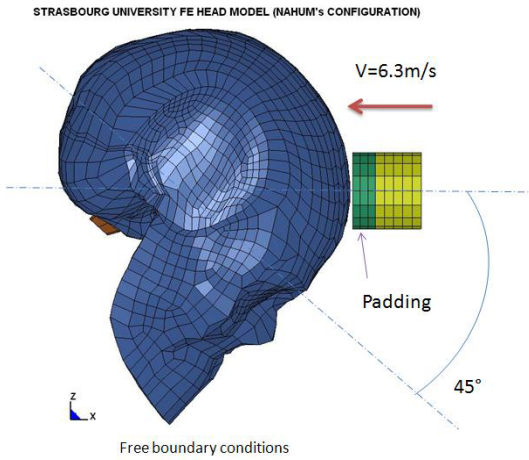

Figure 2. Nahum's configuration

<u>Yoganandan's validation</u> - Experimental tests carried out by Yoganandan et al. in 1994 has been used in order to validate the ability of the human head finite element model to predict a skull fracture. The impact configuration is shown in Figure 3. The surface of the impactor was modelled by a 96mm diameter rigid sphere. Initial conditions were similar to the experimental ones i.e. a mass of 1.213kg with an initial speed of 7.1 m/s. The base of the skull was embedded as in the experiment. For the model validation, the contact force and the deflection of the skull at the impact site, were calculated.

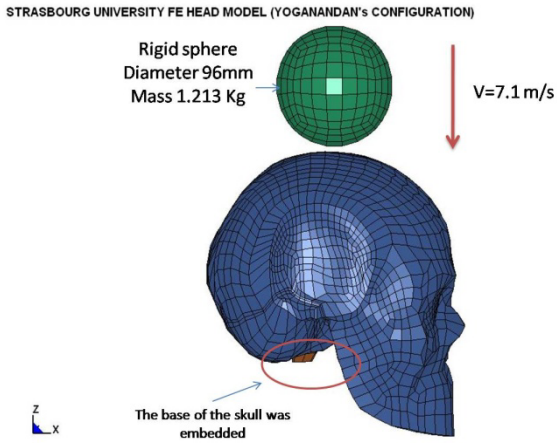

Figure 3. Yoganandan's configuration

Tolerance limits to specific injury mechanisms

SUFEHM tolerance limits to specific injury mechanisms are available under Radioss code and published by Deck et al. (2008). The objective here is to propose tolerance limits under Ls-dyna code. For this, 59 head impact conditions that occurred in motorcyclist, American football and pedestrian accidents were reconstructed with the SUFEHM under Ls-Dyna code. A summary of the type and number of accident reconstructions is given through Table 2.
The reconstructions involved applying the motion of the head from the accidents to the rigid skull of the SUFEHM. Same methodology (statistical analysis) than methodology used by Deck et al. (2008) has been undertaken.
For the statistical analysis the injuries for the accident data were categorised into the following types and levels based on the details of the medical report from each accident case:

- <u>Diffuse axonal injuries (DAI)</u>: DAI cases covered all incidences in which neurological injuries occurred and covered concussion, unconsciousness and coma. Incidences of DAI were broken down into mild and severe levels according to coma duration (<24H for moderate DAI and >24H for severe DAI)
- <u>Subdural Haematomas (SDH)</u>: This category of injuries covered all incidences in which vascular injuries with bleeding were observed between the brain and the skull of which there were six cases.

Table 2. Summary of the type and number of accident reconstructions

Accident Type	Number of cases
Motorcycle accidents	11
American football accidents	20
Pedestrian accidents	28

THUMS SUFEHM COUPLING

THUMS presentation

The Total Human Model for Safety (THUMS) was originally developed in the late nineties by the Biomechanics Laboratory from Toyota, with the help of a part of the model developed by the Wayne State University […]. The geometry of the model represents a 50th percentile American adult male body with 175 cm height and weighting 77 kg. This initial version of the model, composed of about 80,000 elements, is presented in Figure 4. Several projects performed at Daimler have led to an advanced model (165,127 elements) that is shown in Figure 5. This later model was used in the present study. Figure 6 gives an overview of the resulting global THUMS with the implemented SUFEHM (174,058 elements).

Figure 4. Basic THUMS model

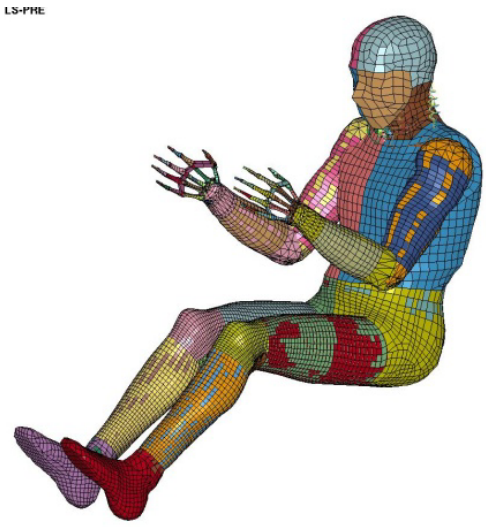

Figure 5. Advanced THUMS model

Figure 6. Advanced THUMS model with Strasbourg University Head FE Model (SUFEHM)

Coupling

The coupling of the SUFEHM head with the advanced THUMS model has been done manually by using a FE pre processor. The original head of the THUMS models has been replaced completely. The mesh of the THUMS neck has been changed in the connection area between the SUFEHM head and the THUMS neck. The connection methods are the same like in the original THUMS model. Between head and neck elements the same nodes are shared. The mesh is continuously without any tied contacts or boundary conditions. The Figure 7 shows the new generated head-neck complex.

Due to the changed head model it is necessary to verify the validation of the new generated head neck complex.

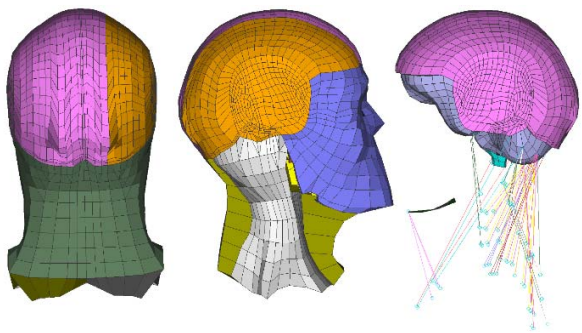

Figure 7. Head neck complex with SUFEHM head and modified THUMS neck.

Validation

After implementation of the SUFEHM on the THUMS model, a validation of the head-neck coupling was carried out according to data from studies on the human volunteer experiments conducted by Ewing et al. (1968, 1977) at the Naval Biodynamics Laboratory (NBDL).

In the experiments of Ewing et al. very healthy volunteers, from U.S. Army Air Defense Command, were put in seated position on a chair rigidly attached to a sled consisting of a horizontal accelerator that is shown in Figure 8. They were equipped with pelvic and torso restraint systems while allowing the head and neck to move freely as illustrated in Figure 9.

The subjects were then submitted to impact accelerations in frontal, lateral and oblique directions.

Two redundant systems were used to monitor the kinematics of the head-neck coupling. The first one is composed of transducers positioned over the posterior spinous process of the first thoracic vertebra (T1), over the posterior superior aspect of the head and at the mouth level as shown in Figure 10. The second system consists of high-speed cameras mounted to the sled.

Results of these tests give access to the dynamic responses (linear and angular accelerations and displacements) of the head with respect to the input accelerations, velocities and accelerations which have been recorded at T1.

Table 3 summarizes the conditions of the experiments for the different impact configurations.

Figure 8. Human volunteer positioned in the sled for a lateral impact (NBDL website)

Figure 9. Restraint systems (NBDL website)

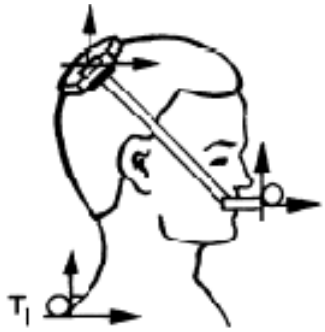

Figure 10. Anatomical locations for the transducer systems on volunteer head (Ewing et al. 1968)

Table 3. Summary of the set-up of the experiments for the three impact configurations (adapted from van der Vorst, PhD. Thesis, 2002)

Parameters	Frontal impact	Lateral Impact	Oblique Impact
Subject	Human volunteer	Human volunteer	Human volunteer
Total number of subjects	5	9	
Total number of tests	9	9	9
Average mass	68.6kg	76kg	
Average height	1.69m	1.77m	
Seat type	Rigid (90° to the floor)	Rigid (90° to the floor)	Rigid (90° to the floor)
Max sled pulse	15g	7g	>7g

In the validation procedure the THUMS model with the SUFEHM head model has to be loaded with the same accelerations like the volunteers in the tests of Ewing et al. To achieve the same loading conditions it is necessary to either model the same environment like in the test set up including the belt system or a simplification which allows validating the head-neck complex has to be done. A simplification of an existing deformable finite element model can be achieved by reducing the elements degrees of freedom for a part of the model. In this study the head-neck complex has been left deformable. The rest of the body has been defined as a rigid body. The rigid area includes the T1 bone (Figure 11).

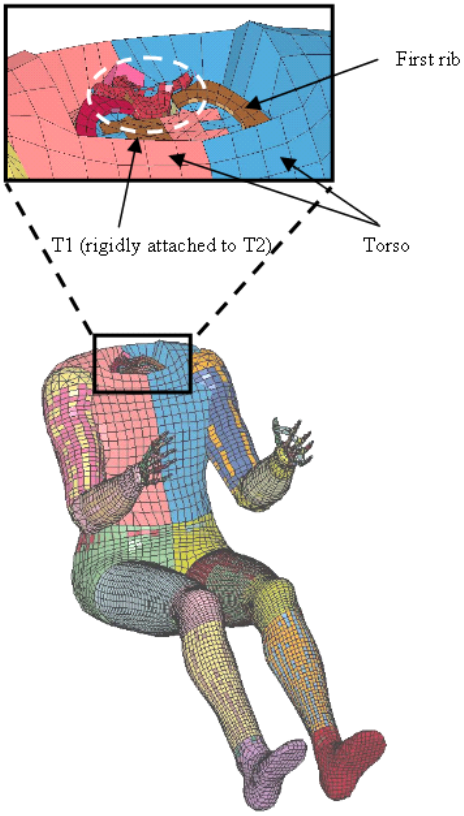

Figure 11. THUMS model rigid parts including T1 bone for validation procedure.

The velocities in the sled tests measured kinematics at the T1 bone can now be applied to the rigid part of the model. This approach saves computation time and allows validating the head-neck complex as an independent system in the first step.

From the tests of Ewing et al. average velocity curves are available for the three different loading directions. Figures 12 to 14 show the measured average speed.

For the validation of the model a change of any material property of the model has to be simulated and compared for all three loading directions (latatefrontal and oblique).

Tests with human volunteers deliver of course different results for each person despite of having similar body sizes and weights. Plotting the results in one diagram delivers usually a corridor of possible results. The aim in the validation is to achieve results for all three loading directions which are in the corridor.

The new created head-neck complex did not deliver simulation results which fit in the corridor of the test results with the original material properties of the THUMS neck model. It was necessary to change material properties for the neck in this validation procedure.

For realistic global kinematics of the head-neck complex it is necessary to define a contact between the head and the torso. Impact loadings of this severity can cause contacts of the head to the torso.

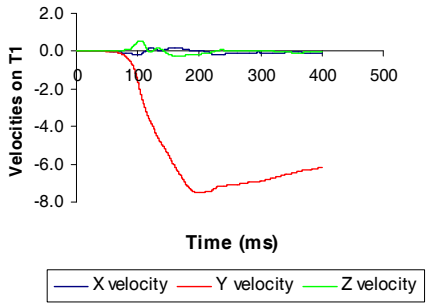

Figure 12 Velocities imposed on T1versus time for the lateral impact.

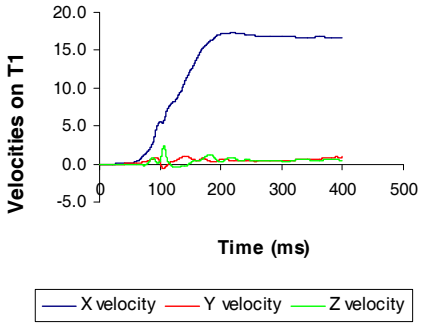

Figure 13. Velocities imposed on T1versus time for the frontal impact.

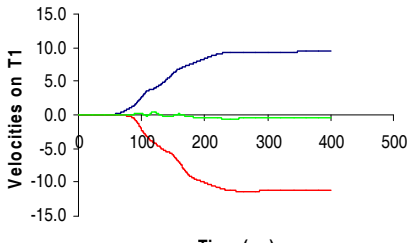

Figure 14. Velocities imposed on T1versus time for the oblique impact.

RESULTS

SUFEHM Results

Nahum's validation results – In order to validate brain mechanical properties under Ls-Dyna code, a Nahum's experiment has been numerically replicated. The comparison of numerical and experimental forces is shown in Figure 15a for the Nahum's impact. A good agreement for the impact force was found as the time duration of impact and the amplitudes were well respected. The comparison of pressure time histories between numerical and experimental data is presented in Figure 15b, c, d, e for the Nahum's impact simulation. As shown in these figures, five intracranial pressures from the model matched the experimental data very well. The maximum difference of pressure peak is under 10 %.

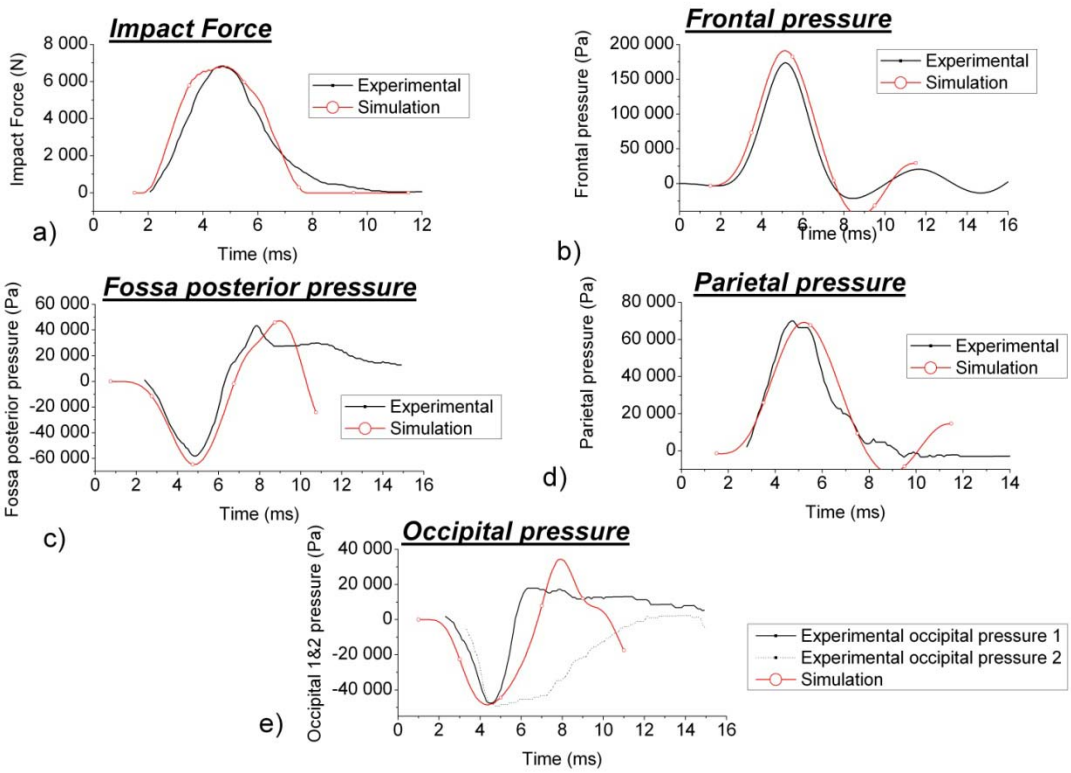

Figure 15. Experimental and numerical results comparison obtained for a Nahum's impact in terms of interaction force (a), frontal pressure (b), Fossa posterior pressure (c), parietal pressure (d) and occipital pressure (e) under Ls-Dyna code.

<u>Yoganandan's validation</u> - In order to validate material and section definition of the skull under Ls-Dyna software, Yoganandan's experiment was simulated. The numerical force-deflection curves are compared to the average dynamical response of experimental data (Figure 17). The dynamical model responses agree well with the experimental results, both the fracture force and the stiffness level.

When a layer fails, a parameter, called damage parameter, which is zero by default is set to one. Figure 16 illustrates damaged layer(s) in the simulation. The blue color indicates that at least one layer of the element failed. The model indicates fracture located around the impact point which complies with pathological observations.

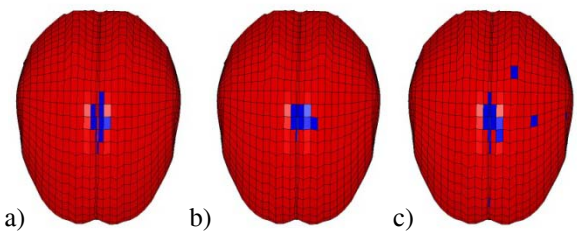

Figure 16. Skull failure description in terms of a) tensile fiber break, b) compressive fiber break and c) compressive matrix break

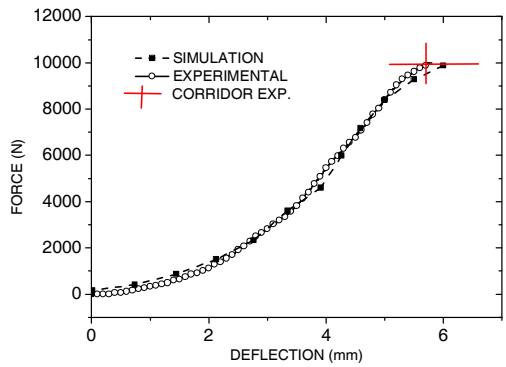

Figure 17. Experimental versus simulated force deflection curves until fracture (+ gives the corridor of Yoganandan's experimental results).

<u>SUFEHM Tolerance limits under Ls-dyna code</u>

Results computed with the SUFEHM under Ls-Dyna code are reported in terms of correlation coefficients (Nagelkerke R-Squared values) in order to express their injury prediction capability.

Based on SPSS method it appears that DAI are well correlated with intra-cerebral Von Mises

stress. Maximal principal strain as well as Von Mises strain presents also an acceptable correlation. Coming to maximum R^2 values, the maximum Von Mises stress conducts to 0.6 and 0.39 for respectively moderate and severe neurological injury.

The threshold for this parameter are of the order of 28 and 53 kPa respectively for moderate and severe neurological injuries as it appears in the injury risk curves reported in Figure 18.

Concerning the SDH injuries two mechanical parameters, i.e. CSF minimum pressure and CSF strain energy were considered.

With the SUFEHM it was shown (Table 4) that the best correlation with SDH was the maximum strain energy within the CSF, with a R^2 value of 0.465 and a threshold value of about 4950 mJ.

After the analysis of regression correlation method Figure 18 and figure 19 report the injury risk curves obtained with the SUFEHM for each of the injury types and the corresponding equations which permit to draw the S-curves. Finally Table 5 and Table 6 provide the tolerance limits for each injury mechanisms with an injury risk of 50%.

Table 4. Nagelkerke R-Squared value for the logistical regressions between the injury predictors computed with SUFEHM and the injury data.

Injury Predictors	Mild DAI	Severe DAI	SDH
CSF minimum pressure			0.367
CSF strain energy			**0.465**
Peak brain Von Mises stress	**0.6**	**0.39**	
Peak brain first principal strain	0.43	0.355	
Peak brain Von Mises strain	0.43	0.35	

Table 5. Tolerance limits calculated for DAI injuries (mild and severe) with the ULP FE head model and LS-DYNA software.

	Mild DAI	Severe DAI
Brain Von Mises stress [kPa]	28	53
Brain Von Mises strain [%]	30	57
Brain First principal strain [%]	33	67

Table 6. Tolerance limits calculated SDH injury with the ULP FE head model and LS-DYNA software.

	SDH
Minimum of CSF pressure [kPa]	290
CSF strain energy [mJ]	4950

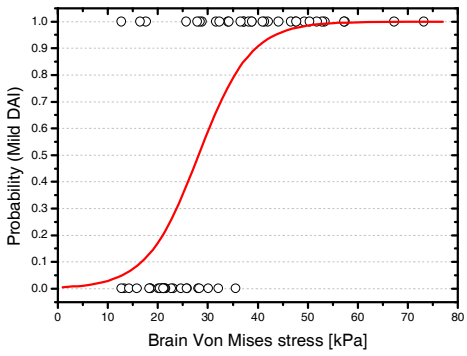

Regression: log(p/(1-p)) = -5.438 + 0.193X
where X is the maximum brain Von Mises Stress

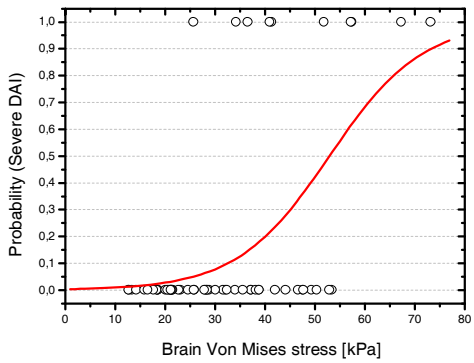

Regression: log(p/(1-p)) = -5.718 + 0.108X
where X is the maximum brain Von Mises Stress

Figure 18. Best fit regression models for DAI injury (moderate up and severe down) investigated for the SUFEHM considering brain Von Mises stress.

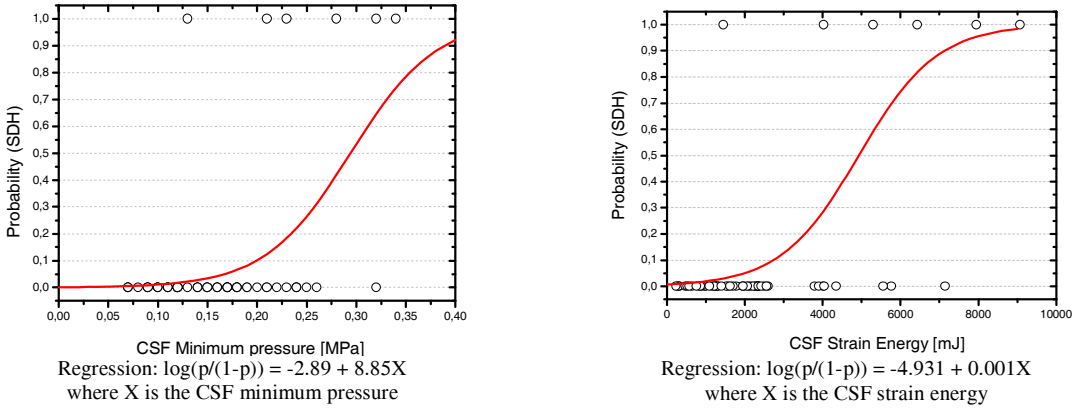

Figure 19. Best fit regression models for SDH/SAH injury investigated for the ULP head model considering CSF pressure (up) and CSF strain energy (down).

THUMS Validation Results

For the validation the simulation results can be compared for the head centre of gravity accelerations and displacements. In the tests of Ewing et al. the accelerations of the head centre of gravity have been calculated by considering the accelerometer positions which the occupants of the sled had fastened on their heads.

The centre of gravity for the SUFEHM model has been calculated by pre processing software tools. For the comparison of the results the closest node of the calculated head centre of gravity has been used (Figure 20).

The validation results for the impact loading are strongly dependent from the contact between torso and head. Therefore both curves with and without head contact to the torso are plotted in the result plots (Figures 21, 23 and 25 for frontal, lateral and oblique impact respectively).

Motions for a frontal, lateral and oblique impact of the finite element model deprived of the contact definition are given in figures 22, 24 and 26 respectively.

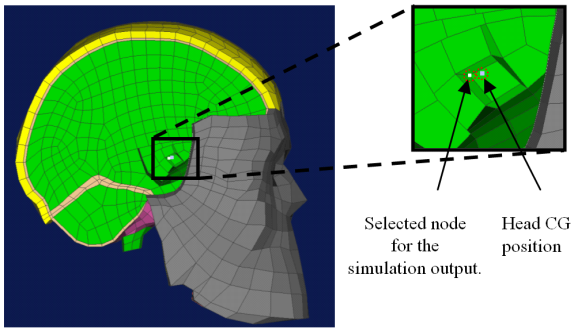

Figure 20. SUFEHM centre of gravity and closest node for comparison with simulation results.

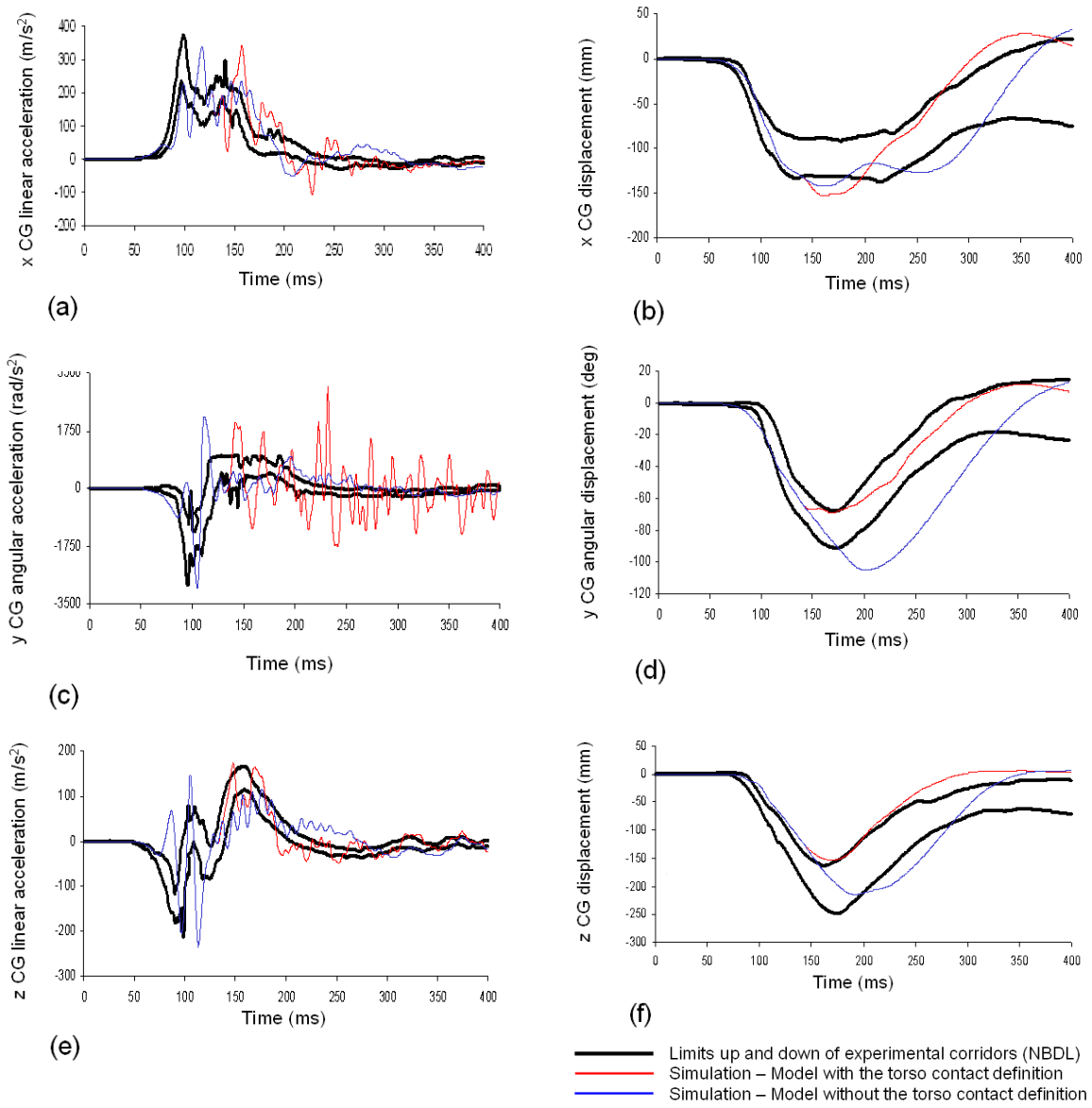

Figure 21. Simulation results of a frontal impact. Kinematics responses of the anatomical centre of the head: (a) x- angular acceleration; (b) y- linear displacement; (c) y- angular acceleration; (d) y- rotation; (e) z- linear acceleration; (f) z- linear displacement; Corridors and inputs for simulations follow experiments from Ewing et al. (1968, 1977)

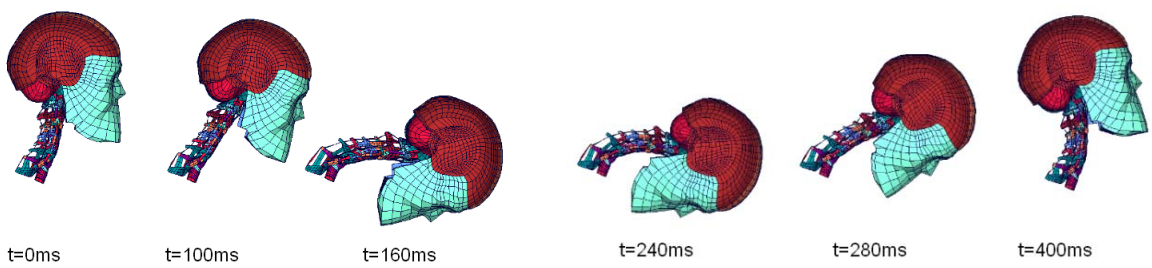

Figure 22. Motion for a frontal impact of the finite element model deprived of the contact definition (head and spine up to T1).

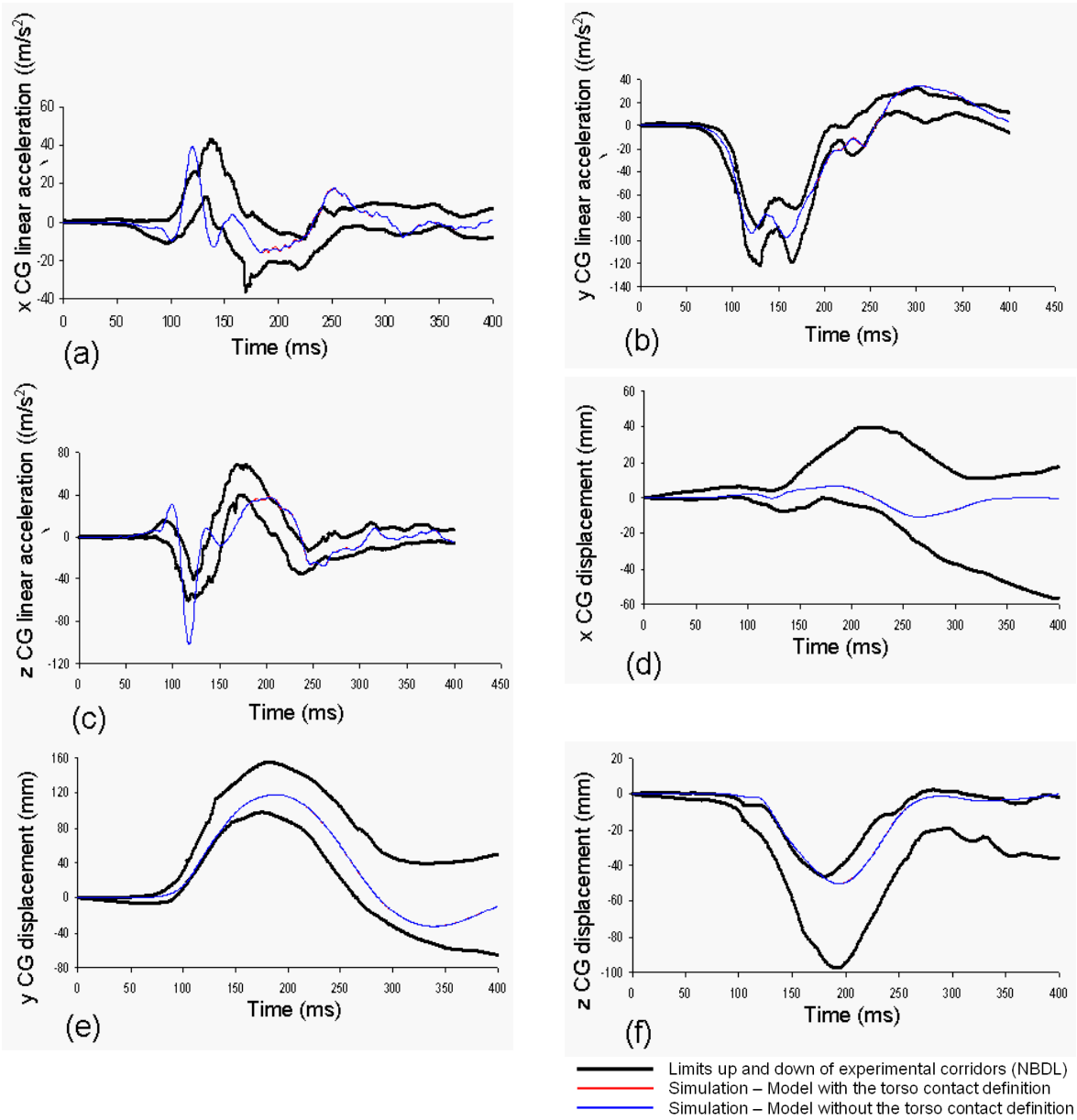

Figure 23. Simulation results of a lateral impact. Kinematics responses of the anatomical centre of the head: (a) x- (b) y- and (c) z- linear accelerations; (d) x- (e) y- and (f) z- linear displacements; (g) Motion of the finite element model deprived of the contact definition (head and spine up to T1). Corridors and inputs for simulations follow experiments from Ewing et al. (1968, 1977)

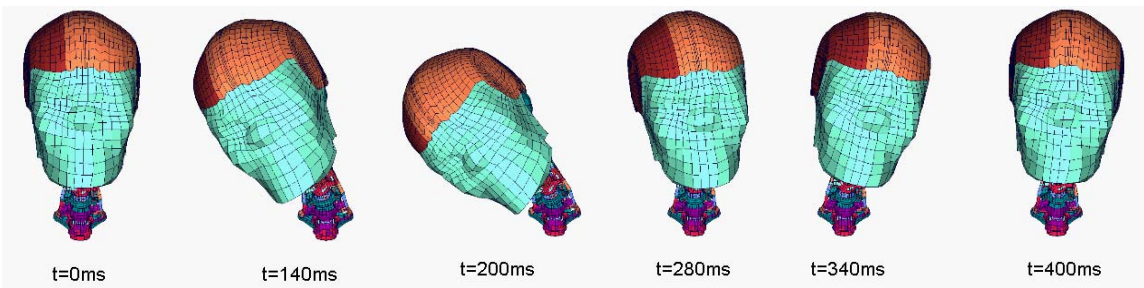

Figure 24. Motion for a lateral impact of the finite element model deprived of the contact definition (head and spine up to T1).

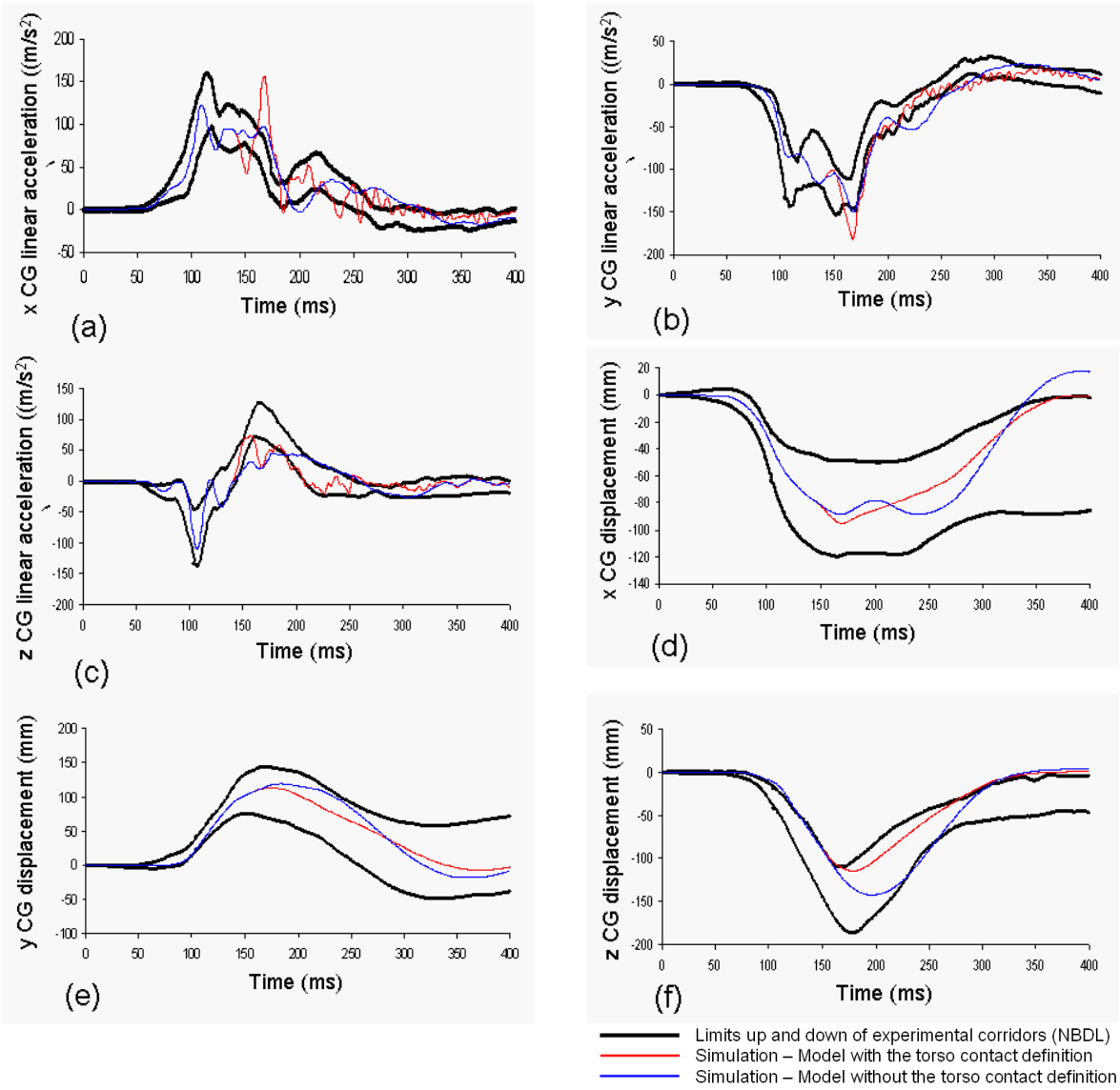

Figure 25. Simulation results of an oblique impact. Kinematics responses of the anatomical centre of the head: (a) x- (b) y- and (c) z- linear accelerations, (d) x- (e) y- and (f) z- displacements; Corridors and inputs for simulations follow experiments from Ewing et al. (1968, 1977)

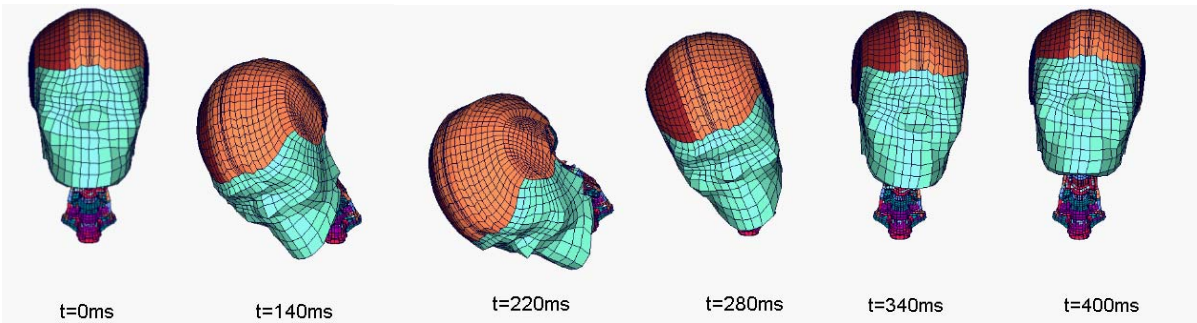

Figure 26. Motion for an oblique impact of the finite element model deprived of the contact definition (head and spine up to T1)

CONCLUSIONS AND DISCUSSION

In this study the Strasbourg University Finite Element Head Model (SUFEHM) has been transferred under LS-DYNA code, and mechanical properties have been implemented. Two experimental impacts have been replicated numerically, a Nahum's impact in order to validate the brain behaviour and a Yoganandan's shock to validate the skull stiffness and fracture.

In an attempt to develop improved head injury criteria under Ls-Dyna code, 59 real world head trauma that occurred in motorcyclist, American football and pedestrian accidents were reconstructed with SUFEHM. Statistical analysis was then carried out on intra cerebral parameters computed in order to determine which of the investigated metrics provided the most accurate predictor of the head injuries sustained in the accidents. Two tolerance limits to specific injury (for a 50% risk of injuries) have been computed:

- A maximum Von Mises stress value: 28 kPa for moderate DAI and 53 kPa for severe DAI.
- A maximum CSF strain energy: 4950 mJ for SDH

The original head model of the THUMS model has been replaced by the Strasbourg University Finite Element Head Model (SUFEHM). The Validation of the new head-neck complex has been done against the volunteer tests of Ewing et al. The results show a good fit for the linear accelerations and linear displacements of the head centre of gravity for all three impact directions.

The coupled model can now be used for further studies in which the whole body kinematics is important before the head suffers any impact. Compared with the real accident situations the whole body simulation is more realistic than a head impact model alone. The complete deformable finite element model can be used directly for simulations with other finite element models, without any pre simulations like with multi body models.

In car accidents the new model can be used for the analysis of pedestrian accidents and for occupants the oblique or multi directional loading can be simulated.

Another interesting study would be the accident analysis of motor cyclists. Especially the whole body kinematics with a helmet model can deliver new information.

REFERENCES

Deck C., Willinger R., (2008) Improved head injury criteria based on head FE model, International Journal of Crashworthiness, Vol 13, No 6, pp. 667-678.

Ewing, C., Thomas, D., Patrick, L., Beeler, G. and Smith, M. (1968) Dynamic response of the head and neck of the living human to -Gx impact acceleration. Proc. 12th Stapp Car Crash Conference, pp. 424-439. Society of Automotive Engineers, Warrendale, PA. Paper 680792.

Ewing, C., Thomas, D., Lustick, L., Muzzy, III W., Willems, G. and Majewski, P. (1977) Dynamic response of the human head and neck to +Gy impact acceleration. Proc. 21st Stapp Car Crash Conference, pp. 549-586. Society of Automotive Engineers, Warrendale, PA. Paper 770928

Iwamoto, M., Kisanuki, Y., Watanabe, I., Furusu, K., Miki, K., Hasegawa, J., 2002. "Development of a Finite Element Model of the Total Human Model for Safety (THUMS) and Application to injury reconstruction", 2002 International IRCOBI Conference, pp.31-42.

Kang, H.S., Willinger, R., Diaw, B., Chinn, B. (1997) Validation of a 3D anatomic human head model and replication of head impact in motorcycle accident by finite element modelling, Proc. of the 41th STAPP Car Crash Conf., pp. 329-338.

Nahum, A.M., Smith, R., Ward, C.C. (1977) Intracranial pressure dynamics during head impact, Proc. of the 21th STAPP Car Crash Conf., pp. 339-366.

NBDL website (URL: http://www.nbdl.org/NCSDB3/index.htm)

Oshita, F., Omori, K., Nakahira, Y., Miki, K., 2002. "Development of a finite element model of the human body". In Proceedings of the 7th International LS-DYNA Users Conference, Livermore Software Technology, Livermore, California, USA, 2002, pp. (3-37)-(3-48).

Van der Horst, M. J., 2002. Human head neck response in frontal, lateral and rear end impact loading -modeling and validation. Ph.D; thesis, Technical University of Eindhoven, Eindhoven, The Netherlands

Willinger R., Taleb L., Pradoura P., Head biomechanics from the finite element model to the physical model. Proceed. IRCOBI, pp 245-260, BRUNNEN, 1995.

Yoganandan, N., Biomechanics of Skull Fracture (1994). Proceed. of Head Injury 94 Symposium, Washington DC.

DEVELOPMENT OF NEXT GENERATION HUMAN FE MODEL CAPABLE OF ORGAN INJURY PREDICTION

Kenji Shigeta
Yuichi Kitagawa
Tsuyoshi Yasuki
Toyota Motor Corporation
Japan
Paper Number 09-0111

ABSTRACT

Although internal organ injury in car crashes occurs at a relatively lower frequency compared to bone fracture, it tends to be ranked higher in terms of injury severity. A generalized injury risk can be assessed in car crash tests by evaluating abdominal force and viscous criterion (VC) using a crash test dummy, but the injury risk to each organ cannot be estimated with current dummies due to a lack of parts representing the internal organs. Recently, human body modeling research has been conducted introducing organ parts. It is still a challenge to simulate the impact behavior of organ parts and their injury, based on an understanding of the differences in structure and material properties among the organs.

In this study, a next generation human body FE model has been developed to predict internal organ injury. The model represents the geometry of organ parts, their location in a living human body and their connections to surrounding tissues. The features of each organ part were taken into account in modeling, so that compressive material was assumed for hollow organs while incompressive material was applied to solid organs. Besides the major organ parts, other soft tissues such as membranes and fatty tissues were also incorporated in order to simulate relative motions among organs. The entire model was examined comparing its mechanical response to that in the literature. The study confirmed that the force-deformation response of the torso against anterior loading showed a good correlation with that of tested subjects.

INTRODUCTION

Computer simulation has attracted attention in recent years as a way of predicting occupant behavior and injury criteria in vehicle collisions. In fact, research and development efforts in this field date back to the 1960s. The most common modeling method in this period, called multibody simulation, recreated vehicle occupants using rigid body elements with links (McHenry, 1963) [1]. In a multibody model, major body parts such as the head, torso, and extremities are expressed by ellipsoids, with joints defined from among them. A multibody model could simulate impact behavior of a human body by adjusting the dimensions, mass, and inertia moment of the ellipsoids to those of the relevant body parts, and setting the rotational direction and angle of each joint with the same restrictions as human joints. It is also possible to predict mechanical response of the occupant after contact with interior parts or restraint devices by replacing the rigid ellipsoids with deformable elements. Other benefits of using multibody models in impact behavior simulations include short calculation times and simple parameter studies. However, such models are not well suited for recreating injuries such as bone fracture or soft tissue damage. In contrast, finite element (FE) models began to be used for analyzing vehicle body deformation in the 1980s. By representing structures of vehicle body panels in a FE model, it became possible to simulate deformation modes and force responses accurately. Moreover, it was also possible to predict whether metal sheets would rupture under given impact conditions by assuming the stress-strain property up to the rupture point. Despite the fact that FE simulation generally requires longer calculation times than multibody simulation, research using human FE models is an advanced method of predicting impact behavior and mechanical response. The development of human FE models started with component models, such as of the head or thorax. Such models are generated based on commercial databases of human anatomy and anatomical or sectional drawings of the body, and their material properties are input based on the mechanical properties of body tissues reported in the literature. The validity of a completed model can be verified by comparing impact response with that of post mortem human subjects (PMHS). FE models of the entire body have been built by combining component models from the head to the lower extremities. Several such models have already been developed, as reported by Choi et al. (1999) [2], Iwamoto et al. (2002) [3], Vezin et al. (2005) [4], and Ruan et al. (2003) [5].

One of these models is the Total Human Model for Safety (THUMS), which was jointly developed by Toyota Motor Corporation and Toyota Central R & D Labs., Inc., and has been used in a number of published studies attempting to reproduce injuries in vehicle collisions. THUMS includes a standing

pedestrian model and a sitting model of a vehicle occupant, both of which simulate an adult male of average physique. Iwamoto et al. (2002) used THUMS to simulate an actual traffic accident scenario (a vehicle colliding with a utility pole) and reproduced the injuries suffered by the occupants. Kitagawa et al. (2005) [6] used a human FE model to predict occupant behavior in a frontal collision to study knee joint deformation when the knees strike the instrument panel and the effect of airbags in helping to reduce such deformation. Hayashi et al. (2006) [7] and Kuwahara et al. (2008) [8] simulated vehicle side impact collisions to investigate the mechanism of rib fractures and the force-reduction effect of side airbags. In addition, Kitagawa et al. (2006 [9], 2007 [10], and 2008 [11]) simulated low-velocity rear-end collisions to analyze occupant head and cervical behavior and examine the mechanism of cervical whiplash injury. Yasuki et al. (2005) [12] also used a human FE model to predict pedestrian behavior in a vehicle collision and compare the results with the impact behavior of the TRL impactor used in lower extremity injury assessment tests.

Since injuries to the brain and internal organs generally tend to be more severe than bone fractures or ligament rupture, attempts have also been made to reproduce such injuries using human FE models. Tamura et al. (2006) [13] simulated vehicle collisions using a pedestrian model featuring a brain. This study indicated a high level of strain within the brain immediately before and directly after impact between the pedestrian's head and the vehicle's hood. In contrast, although several case studies have attempted to reproduce injuries by simulating impactor tests on PMHS, relatively few have attempted to predict organ injury under conditions equivalent to a vehicle collision. Hayashi et al. (2008) [14] demonstrated that internal lung pressure on the side facing the impact increases due to contact between the upper arm of a vehicle occupant and the side of the thorax in a side impact collision. This is a valuable piece of research that discusses internal organ injury risk under vehicle collision conditions, but it does not provide a quantifiable assessment of injury occurrence. Organs in the thoracic and abdominal areas tend to suffer greater deformation in an impact than the brain, which is encased in a highly rigid skull. However, it is not easy to accurately reproduce the mechanical response of internal organs, which are much softer than the skeleton or ligaments, or to predict their injury criteria. This research developed the next generation of the human FE model THUMS (THUMS ver.4.0). Featuring both standing and seated postures, THUMS ver.4.0 simulates the internal organ structures within the torso in detail. High-resolution CT scans were used to digitize the interior of the body and generate precise geometrical data for the internal organs. As a result, it was possible to accurately reproduce the layout of organs within the body and their connecting structures. Moreover, the modeling reflected the anatomical features of each organ, and by inputting data on the physical properties of organ tissue reported in the latest research, it is possible to simulate injury at a tissue level. The validity of the completed model was verified by comparing its mechanical response with impact test data from PMHS. The impact simulations with the human FE model used the finite element analysis (FEA) code LS-DYNA ™.

MODEL DEVELOPMENT

Torso Model

To predict organ injury accurately in a vehicle impact, it is necessary to simulate the structure inside the torso in detail. The developed model not only reproduces the geometry of the individual organs within the torso, but also their layout and connecting structures.

Acquisition of Anatomical Data - The internal torso structure was digitized in cooperation with the University of Michigan, which holds large quantities of data obtained using high-resolution CT scans. The CT scan measurement was performed for medical purposes and permission to use the data as a reference for developing the human FE model was obtained from the Michigan Institutional Review Board. Data groups of males in their 30s of average height and weight close to that of a 50th percentile American male (AM50: 175 cm, 77 kg) were extracted from the available data (approximately 558,000 people), and checked to eliminate samples with visible pathological abnormalities in the torso. The data of a 39-year old male with a height of 173 cm, a weight of 77.3 kg, and a BMI of 25.8 was selected. The CT scan data was measured at a pitch of 0.625 mm for the thorax, and 5 mm for the abdomen. Figure 1 shows images of the skin, skeleton, and soft tissue included in the scanned data. The scanned data was converted into Standard Triangulated Language (STL) format polygons for each body and tissue part using the 3D image conversion tool MIMICS ™. The skeletal structure was identified by applying a masking process to the CT scan images at a threshold value of 130 Hounsfield units (HU). The soft tissue was identified by a conversion process using a different HU level for each organ. The process was performed while verifying any partial omissions in the created polygon data. The following organs were converted into polygon data: heart, lungs, liver, kidneys, spleen, pancreas, gall bladder, bladder, esophagus, stomach,

duodenum, small intestine, and large intestine. However, due to the thinness of its walls, it was difficult to generate polygon data that reproduced the path of the small intestine. Compression of the abdomen not only causes compressive deformation in the small intestine itself, but also generates movement together with the neighboring area. Therefore, this model does not reproduce the exact path of the small intestine, but instead expresses the whole of the small intestine as a single element. In contrast, the paths of each artery and vein, and their connections to each organ were reproduced in polygon data. The end diameters of the blood vessels connected to each organ are expressed to a detail of approximately 5 mm. In addition, geometry for membranes surrounding the organs, such as the diaphragm, pleurae, peritoneum, and fascia, was also extracted. Thus, organs such as the pancreas, kidneys, bladder, small intestine, and large intestine are expressed as shapes included within the peritoneum. Separate polygon data was also generated for visceral fat. Subcutaneous fat, muscle, and the microscopic blood vessels between the skin and skeleton and between the skin and peritoneum were treated as belonging to the same group. The spinal cord was expressed within the spinal canal as a separate polygon data group from the vertebral body.

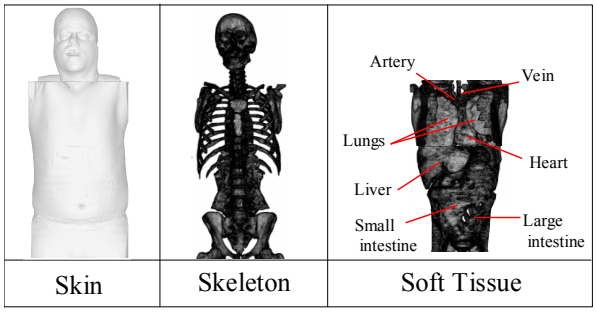

Figure 1. CT scan data.

Creation of FE Model - Surfaces were created by feeding the polygon data into the HyperMesh ™ mesh generator. Geometrical features with unnatural disconnections in the generated surfaces (such as bends or projections) were repaired in reference to anatomical drawings and the like. Interference between surfaces created for separate parts (particularly adjacent curved surfaces and so on) was handled by receding the surface geometry of the interfering portion without disturbing the shape of the parts. Guidelines were established before generating the FE mesh. The mesh density was adjusted so that the element length became 3 to 5 mm, which divided the sternum, a relatively small bony part in the thorax, into two sections in the anterior-posterior direction. In addition, the aorta, also a small organ part, was divided into eight elements in the circumference direction. The reference values for the quality of element geometry were set as follows: warpage = 50 degrees or less, aspect ratio = 5 or less, skew = 60 degrees or less, Jacobian = 0.3 or more. Solid elements were used wherever possible for FE mesh generation. However, since many cortical bones within the torso skeletal structure have a thickness of around 1 mm, these bones were modeled using shell elements and cancellous bones with solid elements. For soft tissue, solid organs and thick hollow tissue were modeled with solid elements, and thin tissue such as blood vessels and membranes were modeled with shell elements. In addition, cortical bones and soft tissue with little curvature were divided into quadrilateral shell elements and hexahedral solid elements. The appropriate hourglass control logic was applied to each type of element, using full integration for the shell elements and 1-point integration for solid elements. In addition, skin and subcutaneous fat adjacent to joints were modeled using quadrilateral elements to facilitate FE mesh regeneration after changes in posture.

Nodes at boundary surfaces between connective tissue were shared. For example, each of the following tissues are defined as separate parts, but include elements with shared nodes at their adjacent boundary surfaces: cortical and cancellous bones; rib cartilage and costal bones; the aorta/vena cava and the heart/lungs; and the digestive system (stomach/duodenum/small and large intestines) from the esophagus. Parts of various organs join with other tissue, for example, the superior portion of the liver joins with the diaphragm, and a portion of the rear of the large intestine joins with the peritoneum. These joints were also expressed with shared nodes at the corresponding parts. Other boundary surfaces, for example between different organs or between non-connecting organs and membranes, were defined to perform contact processing. It was assumed that no friction occurs between contact surfaces. Figure 2 shows the skeletal structure and internal organs of the torso model.

Skeletal parts were assumed to have elasto-plastic properties capable of expressing tissue injury. Membrane material was applied to ligaments and organ membranes, whereas incompressive material was assumed for the solid parts of organs. Compressive material was assumed for hollow organs such as the small and large intestines. The structure of the lungs includes air within the pulmonary alveoli. Membrane material was applied to the organ surface and their interior portions were expressed with elastic material simulating gas. Blood vessels were given the same structure. The physical properties input into each material model were selected from data obtained by Yamada (1970) [15] and Abe et al. (1996) [16].

Figure 2. Skeletal structure and internal organs of torso model.

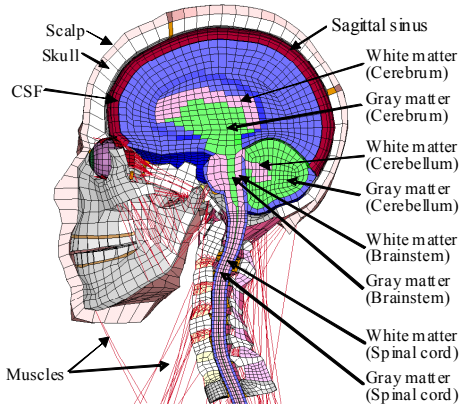

Figure 3. Head model (THUMS ver. 3.0).

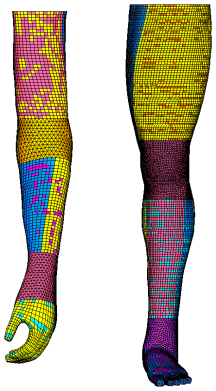

Figure 4. Outline of extremity models.

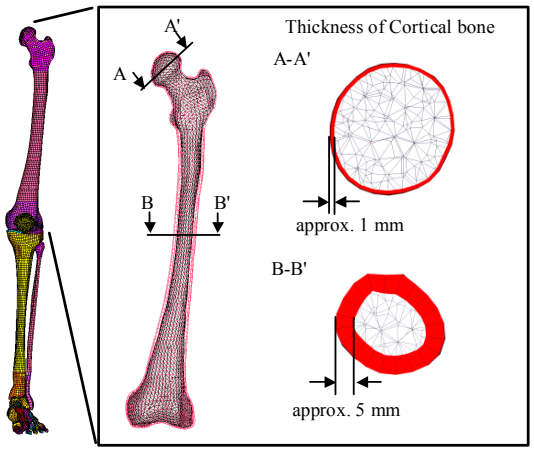

Figure 5. Section of bone along length of leg.

Head Model

THUMS ver.3.0 was used for the head model (Figure 3). This model was developed by Kimpara et al. (2006) [17] and its accuracy was validated against mechanical response results of impact tests in the literature. The elements in the FE mesh have a length of approximately 10 mm for the epidermis but 3 to 7 mm for the brain part that is essential for injury prediction, and matches well with the developed torso model. The merging positions of the models are as follows: the lower extremity of the cervix for the skin and subcutaneous fat, and the upper extremity of the cervix for the spine and spinal cord. The spinal cord is provided within the spinal canal using solid elements simulating the surrounding cerebrospinal fluid (CSF) and fatty layer. Its surface contacts that of the vertebral body without sharing nodes. Material properties equivalent to water are assumed for the CSF part. The cervical muscles are modeled in 1D elements in the same way as in THUMS ver.3.0, and recreate only resistance force when forcibly elongated. Table 1 lists the physical properties of the head model.

Extremity Models

Excluding the pelvis, the FE meshes of the extremities were modeled in reference to ViewPointTM geometrical data (Figure 4). The element division guidelines were the same as for the torso model. Since the extremity models are mostly used for assessing bone fractures, each leg model used solid elements to express the cortical bones as well as the femur, patella, tibia, and fibula (Figure 5).

Knee joint ligament injury risk is estimated to evaluate pedestrian protection performance. The cruciform and collateral ligaments were modeled using solid elements (Figure 6). Solid elements were also used for the tendon of the quadriceps femoris muscle, the patellar ligaments, and the Achilles

tendon. The integration points and material properties of the elements were set along the same lines as the torso model. Table 1 also lists the material properties defined in the extremity models. The extremities contain abundant musculature, which has a major effect on behavior and mechanical response in an impact. This study divided the muscles of the extremities into the major muscle groups. The upper extremity and tibia portions were divided into flexing and extending muscle groups. Adductor muscles were also provided for the femur portion in addition to the above two groups. The dividing positions for the muscle groups were determined based on anatomical reference books and visual data from the Visible Human Project. Shared nodes were provided for the parts at the boundaries between each muscle group and the skeletal structure, and between the muscles groups and the skin. Contact processing was applied between the muscle groups so that compression causes both movement and sectional deformation of each group. A friction coefficient of zero was assumed for the surface of the fascia. The extremity models were joined to the torso model at the shoulder and hip joints. The merging portions were modeled using shell elements equivalent to joint ligaments. The humerus was connected to the scapula and clavicle, and the femur was connected to the pelvis. The articular capsules were also modeled using shell elements. The FE mesh for the skin and muscles of the torso and extremity models was made consistent.

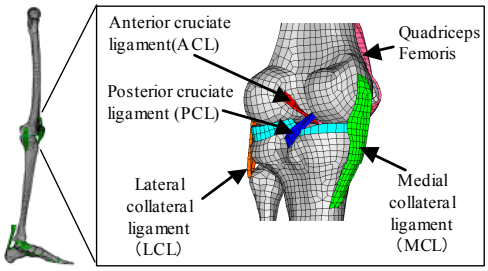

Figure 6. Knee joint ligaments.

Whole Body Models

The whole body models were assembled by fusing the torso, head, and extremity models. Since the CT scan torso geometry data was obtained while the subject was recumbent on the device looking upward, the standing model was created first. This model simulates a person standing in an upright position with their legs open at shoulder width. Both arms are hanging straight down to the sides of the torso. The seated model, simulating a vehicle occupant, was then created based on the standing model. The model was modified to position the lumbar vertebrae in a natural seating posture. The arms and legs of the seated model are both slightly extended in front of the torso. Figure 7 shows an outline of both models. Each contains approximately 630,000 nodes and 1.8 million elements. The model has a height of 178.6 cm and a weight of 63.0 kg, which is close to the person used as the basis for the torso model.

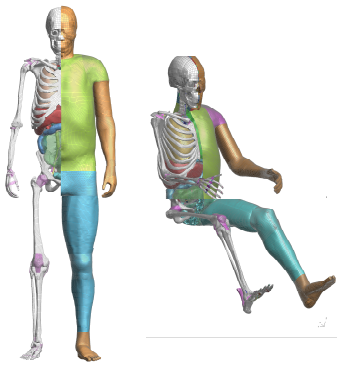

Figure 7. Outline of whole body models (standing and seated).

MODEL VALIDATION

The validity of the completed model was verified by comparing its mechanical response with the results of PMHS impact tests in the literature [20]-[25]. For verification, the conditions of the actual tests had to be reproduced using the FE model. For this reason, the selected test cases were those with detailed information on the impact conditions such as impactor geometry and velocity and the PMHS injury results. In addition, the posture of the assembled standing model was modified in accordance with the test conditions. Table 2 lists the literature data used for the validation. It is common for thoracic and abdominal impact tests to use an impactor, but the results of tests involving the application of a belt-shaped compressive force were also used to simulate a vehicle occupant wearing a seatbelt. Since the extremity models are mostly used to evaluate bone fracture and ligament injury, 3-point bending tests were selected for the bones in the upper and lower extremities and impactor tests were selected for the knees. The head and neck models have already been verified by Kimpara et al. (2006), but the literature data for these cases is also included in Table 2 for reference.

Table 1. Material characteristics of model body parts and tissues

				Density (kg/m^3)	Young's modulus E (MPa)	Poisson ratio	Yield stress (MPa)	Ultimate stress (MPa)	Reference
Bone	Skull	Frontal bone	Cortical	2,120	11,000	0.22	48		Yamada (1970) Wood (1971) Abe et al. (1996)
			Trabecular	1,000	100	0.22	0.35		
		Parietal, temporal,	Cortical	2,120	11,000	0.22	48		
			Trabecular	1,000	1,000	0.22	4.8		
		Facial bones	Cortical	2,120	11,000	0.22	48		
			Trabecular	1,000	200	0.22	0.7		
		Skull suture		2,120	13,000	0.22	12		Naruse (1993)
	Vertebrae		Cortical	2,000	12,000	0.3	100		Yamada(1970) Abe et al.(1996)
			Trabecular	1,000	1,000	0.3	8.3		
	Thorax	Rib / Sternum	Cortical	2,000	9,860	0.3	66.7		Kimpara (2005)
			Trabecular	1,000	40	0.45	1.8		Yamada(1970) Abe et al.(1996)
		Costal		1,000	49	0.4	4.9		
	Upper extremity		Cortical	2,000	11,000	0.3	110		Yamada (1970)
			Trabecular	1,000	1,100	0.3	7.7		
	Lower extremity	Fibula	Cortical		18,500	0.3		146	
			Trabecular		145.6	0.45		30.6	
		Talus	Cortical		15,000	0.3		140	
			Trabecular		145.6	0.45		30.6	
		Calcaneus	Cortical		15,000	0.3		140	
			Trabecular		145.6	0.45		30.6	
		Femur	Cortical		17,000	0.3		150	Iwamoto et al. (2005)
			Trabecular		145.6	0.45		30.6	
		Tibia	Cortical		18,000	0.3		150	
			Trabecular		145.6	0.45		30.6	
Soft tissue	Diaphragm			1,000	2	0.4	2		Shah et al. (2001)
		Cervical		2,000	1	0.4	2		
	Pleural, Mediastinum, Peritoneum, Fascia			1,000	13	0.4	1		
	Skin			900	31.5	0.45	0.1		Shah et al. (2001)
	Aorta			4,000	4	0.4	3		
	Ligaments			1,100	9 - 100	0.22	1 - 3		Yamada(1970) Abe et al.(1996)
	Fat			900	0.5				Lee and Yang (2001)
	Mascle			900	0.5				
		Intercostal		1,000	1	0.3			Yamada (1970)
Brain	CSF			1,000	1.60E-04	0.49			Galford and McElhaney (1970)
	Saggital sinus			1,000	1	0.49			
	Pia mater			1,000	1.1	0.4		0.4	McElhaney et al.(1973)
	Arachnoid			1,000	1.1	0.4		0.4	
	Meninx			1,000	31.5	0.45		0.2	Al-Bsharat et al.(1999)
	Tentrium			1,133	31.5	0.45		1	Willinger(2003)
	Dura mater			1,133	31.5	0.45		1	Zhang et al.(2002)
	Falx cerebri			1,133	31.5	0.45		1	Tokhounts et al.(2003)
				Density (kg/m3)	Modulus K (Mpa)	Shear Modulus G_0(Mpa)	Shear Modulus G_∞(Mpa)		Reference
	Cerebrum		White	1,000	2,160	0.0125	0.0061		Galford and McElhaney (1970)
			Gray	1,000	2,190	0.010	0.005		
	Cerebellum		White	1,000	2,160	0.0125	0.0061		McElhaney et al.(1973) Nakamichi et al.(2001)
			Gray	1,000	2,190	0.010	0.005		
	Brainstem		White	1,000	2,190	0.023	0.0045		Zhang et al.(2002) Tokhounts et al.(2003)
			Gray	1,000	2,190	0.010	0.005		

			Density (kg/m^3)	Young's Modulus E(Mpa)	Poisson ratio	Yield stress (Mpa)	Thickness (mm)	Reference
Neck	Cervical bone	Cortical	2,000	12,000	0.3	100		Yamada(1970) Abe et al.(1996)
		Trabecular	1,000	1,000	0.3	8.3		
	Cervical dura mater	Anterior	1,100	44.1	0.3		0.33	Yamada(1970)
		Posterior	1,100	43.35	0.3		0.68	
	Anterior Longitudinal Ligame			43.8		5.65		Yoganandan et al. (1989a and 1998)
	Posterior Longitudinal Ligame			40.9		4.54		
	Interspinous Ligament(ISL)			4.9		1.28		
	Ligament Flavum(LF)			3.1		1.26		
	Transvers Ligament(TL)			3.1		1.26		
	Capsular Ligament(CL)			5		2.84		

		Property data					
		Nominal strain 【%】					
		10	20	30	50		Preference
Internal organ	Heart	5.4	12.4	28	374.9		Yamada (1970)
	Lung	7.9	14.1	20.1	31.7		Hayamizu (2003)
	Liver	2.5	14.7	58.9	380.2		Tamura (2002)
	Spleen	1.5	2.5	3.7	9.8		Ishikawa (2000)
	Kidney	4.9	36.3	134.4			Yamada (1970)
	Small intestine	17.7	38.2	94.1	778.6		
	Large intestine	16.3	29.4	40.9	163.4		
	Blood vessel	14.9	29.7	66.9	193.2		
	Stomach	4.5	12.7	28.1	93.2		

Nominal stress 【KPa】

Table 2. PMHS test data used in validation

	Test conditon	Referance
Thorax	Thoracic frontal impact	Kroell et al. (1974)
	Thoracic dynamic belt compression	Cesari et al. (1990)
Abdomen	Abdomen frontal impact	Cavanaugh et al. (1986)
	Abdomen dynamic belt compression	Foster et al. (2006)
Upper extremities	Humerus static three point bending	Kemper et al. (2005)
	Humerus dynamic compression	
Lower extremities	Femur static three point bending	Yamada et al. (1970)
	Knee joint lateral loading	Kajzer et al. (1997, 1999)
Head and brain	Head impact	Nahum et al. (1977) Troseille et al. (1992) Hardy et al. (2001)
Head and neck	Neck flexion and cervical axial compression	Pintar et al. (1995) Thunnissen et al. (1995)

Cases of described injury conditions in the literature were compared with prediction results using the FE model. The FE model predicted injury based on the reference values shown in Table 3. Bone fracture was assumed to have occurred when the strain of the elements included in a cortical bone exceeded 3% [24]. Evaluation indices and reference values were assumed for each internal organ. Pulmonary contusion, i.e., injury to the alveolar tissue when the pressure inside the lungs increases due to blunt external force, is the most frequent lung injury mode. For this reason, a pressure index was applied to the elements inside the lungs. Karl et al. (1958) reported that there is a risk of alveolar tissue injury when the internal pressure of the lungs exceeds ±10 kPa [25]. Strain indices were applied to the other organs. A typical heart injury mode is myocardial laceration. Although the rupture threshold of the myocardiac muscle differs depending on the direction of force to the muscle fiber, Yamada (1970) states that tissue damage begins to occur with strain of 30% or above. Melvin et al. (1973) reported that the strain threshold for liver and kidney injury is approximately 30%, depending on the compression velocity. The reference value for the spleen is assumed to be 30%, the same as for the liver. Yamada (1970) also states that the rupture strain for the intestines is approximately 120%, and approximately 100% for thoracic and abdominal blood vessels. It should be noted, however, that the validity of these indices and reference values requires further investigation and verification. This study does not to debate the absolute accuracy of the organ pressures or strain levels predicted by the FE model, but simply compares the organ injuries predicted by the FE model with the conditions of PMHS injury assuming the reference values for injury criteria in Table 3.

Table 3. Reference values for injury criteria

		Index	Threshold	Reference
Bone		Strain	3.06%	Kemper et al.(2005)
Internal Organ	Heart	Strain	30%	Yamada et al.(1970)
	Lung	Pressure	±10kPa	Karl et al.(1958)
	Liver	Strain	30%	Melvin et al. (1973)
	Spleen	Strain	30%	-
	Intestine	Strain	120%	Yamada et al. (1970)
	Blood vessel	Strain	100%	

Verification of Thorax Model

Thoracic Impactor Response - Figure 8 shows the thoracic impactor test performed by Kroell et al. (1971, 1974). In this test, cylindrical impactors simulating a steering wheel hub (diameter: 152 mm, mass: 7.92 to 23.6 kg) were collided with the anterior surface of the thorax of a PMHS at an initial velocity of 6.3 to 14 m/s. Each test was synchronized on high-speed film and the displacement and acceleration of the impactor were measured to calculate force-deflection curves. This impactor test was performed on 38 PMHS to create a force response corridor for each impactor mass and initial velocity. Verification of the force response of the FE model referred to a corridor created under typical conditions (mass: 23.1 kg, initial velocity: 7.2 m/s). The state of injury after each test was reported for each PMHS. Verification of FE model injury prediction used 20 cases close to the force conditions (mass: 19.5 to 23.6 kg, initial velocity: 6.3 to 10.19 m/s). The posture of the PMHS in the tests is not described in the literature in detail but the FE model adopted an upright seated posture on the test device with both arms forward of the body, based on assumptions from photographs and images in the reports. The impactor force was output as a contact load between the impactor head and the anterior surface of the thorax. Impactor displacement was calculated from model node displacement, and thoracic deflection was calculated from changes in the distance between nodes on the anterior and posterior surfaces of the thorax.

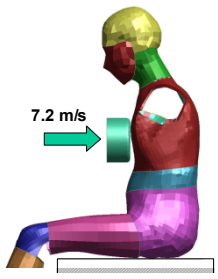

Figure 8. Thoracic impactor test.

Figure 9 shows the observed state of the thoracic geometry after impactor contact. The sectional diagrams are viewed from the left side of the body's median sagittal plane, and show thoracic deflection

of 0 mm, 15 mm, 30 mm, and 78 mm. In this case, maximum thoracic deflection was 78 mm. Up to an thoracic deflection of 15 mm, the skin and subcutaneous tissue (fat and muscle) were compressed. Deformation of the inferior portion of the sternum and the rib cartilage began at an thoracic deflection of 30 mm, initiating compression of the underlying heart and lungs. Rib deformation had progressed at an thoracic deflection of 78 mm, increasing the compressive deformation on the heart and lungs. After this point, since the posterior surface of the torso was not supported in the test, the spine at the height of the impactor displaced to the rear and the whole spine curved. Figure 10 shows the superior view of the horizontal section of the thorax at the height of the impactor center. It compares the states at thoracic deflection of 0 mm (initial state) and 78 mm. This section includes the sternum, ribs, spine, heart, and lungs. The contact area of the impactor includes the heart and a part of the lungs. The sectional deformation at an thoracic deflection of 78 mm shows that the heart was compressed in the anterior-posterior (AP) direction between the sternum and the spine, and that the heart elongated in the lateral direction. Additionally, the anterior surface of the thorax including the sternum and the ribs deformed into a flat shape along the contact surface with the impactor. The anterior portion of the lungs then deformed accordingly.

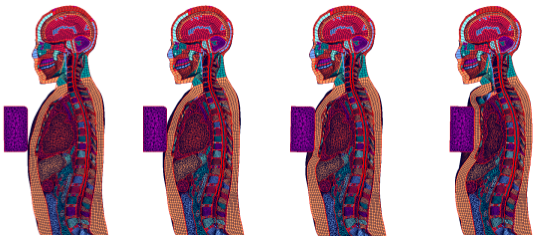

Figure 9. Thoracic deformation after impactor contact.

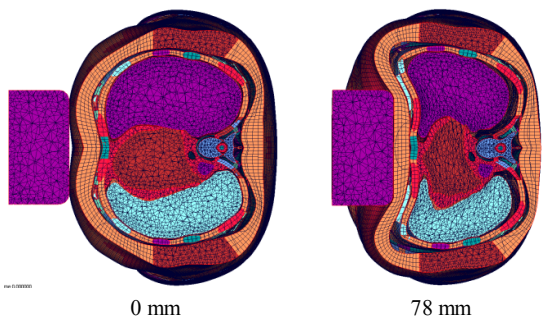

Figure 10. Sectional deformation of thorax (at height of impactor center).

Figure 11 compares the thoracic force response of the PMHS and FE model, with thoracic deflection on the horizontal axis and impactor force on the vertical axis. The force response of the PMHS is shown in the grey corridor and that of the FE model by the black solid line. Force initially peaked in both the PMHS and FE model at a thoracic deflection of 10 to 20 mm, before reaching a maximum peak at approximately 80 mm. The initial peak force with the PMHS was in a range from 2.5 to 4 kN, and the FE model recorded 3.5 kN. The maximum peak force with the PMHS was in the range from 3 to 4.5 kN, and was 4.5 for the FE model. Therefore, the peak force calculated by the FE model roughly corresponded to the range of the PMHS, but its force response curve partially fell outside the PMHS corridor. At around 20 mm, after the first peak force calculated by the FE model, the force fell to 1.5 kN, clearly below the PMHS corridor. However, several of the force response curves described in the literature also describe the force decreasing to a range of 1.5 to 3 kN after the initial peak. Thus, the 1.5 kN calculated by the FE model here was judged to be within the appropriate range.

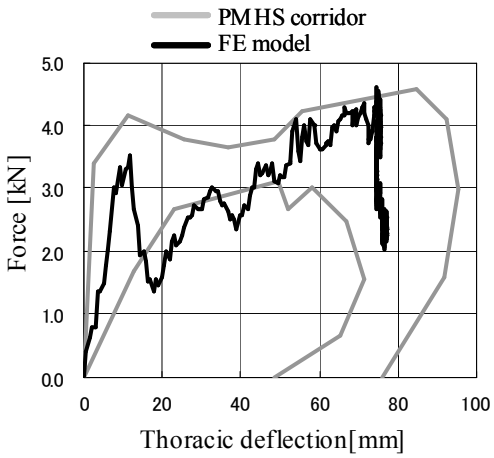

Figure 11. Comparison of thoracic force-deflection response.

Table 4 compares PMHS autopsy results and FE model predictions with respect to injury to the skeletal structure and the organs in the thorax. Kroell at al. (1971, 1974) reported that 18 of the 20 PMHS cases relevant to the model verification in this study incurred some kind of injury. All of these injury cases involved sternum or rib fracture, and 15 suffered soft tissue injury. Rib fractures occurred in an average of 11 locations from the first to the seventh ribs. With respect to organ injury, cases of heart and liver injury were most frequent (5), followed by the lungs (4). Cases of membrane injury were also frequent (9). The FE model predicted that cortical bones in the

sternum and ribs would have exceeded the 3% reference value for fracture strain in 8 locations. Two of these were located at the inferior portion of the sternum, and the other six occurred at either the left or right ribs. Figure 12 shows the corresponding locations. Figure 13 shows the state of occurrence for maximum principal strain and pressure in the FE model heart. Strain exceeded 0.3 in the heart and liver. Strain in the liver concentrated in the position at the center of the body corresponding with the contact position of the impactor. High levels of strain were also detected in an area of the stomach, but this was below the reference value of 1.2. Strain did not exceed the reference value in any of the other organs. Additionally, lung pressure exceeded 10 kPa. The state of organ injuries predicted by the FE model correlated well with the PMHS autopsy results.

Table 4. Injury cases and predicted results

Subject		Impact Condition		Bony Fractures		Soft Tissue Injuries				
Age	Gender	Mass	Velocity	Sternum	Ribs	Heart	Lung	Liver	Aorta	Others
60	F	19.5	6.3	0	11					
67	F	22.9	7.2	2	22		Y			
81	M	22.9	7.4	0	21	Y				
76	F	22.9	7.2	2	7	Y			Y	
80	M	23.6	6.9	0	13		Y			
78	M	23.6	6.7	2	14					Y
19	M	23.6	6.7	1	0					
29	M	23.6	6.7	0	0					
45	F	23.6	6.8	1	18					
72	M	23.6	6.7	0	17			Y		Y
58	F	19.5	7.7	0	23		Y			Y
65	M	22.9	9.7	2	M		Y	Y		Y
51	M	23.04	10.19	1	14					Y
75	M	22.86	9.92	1	20	Y				Y
64	M	18.96	8.23	0	13					Y
52	M	18.96	7.2	0	7			Y		
48	M	22.86	9.83	1	9			Y	Y	Y
46	M	19.28	7.33	0	0					
49	F	19.55	6.71	0	7	Y		Y		
46	F	19.55	9.92	0	8	Y				Y
				Average of Fractures		**Numbers of Soft Tissue Injuries**				
				Sternum	**Ribs**	**Heart**	**Lung**	**Liver**	**Aorta**	**Others**
				0.65	11.2	**5**	**4**	**5**	**2**	**9**
FE model		**23.0**	**7.2**	**2**	**6**	**Y**	**Y**	**Y**		

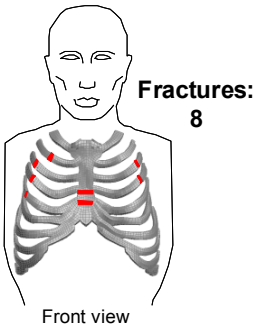

Figure 12. Bony fracture prediction in thoracic impactor test.

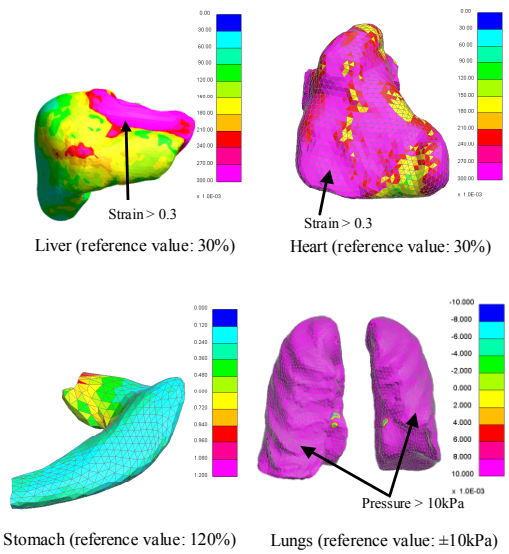

Figure 13. Strain and pressure distribution in thoracic organs (liver, heart, stomach: strain distribution; lungs: pressure distribution).

Thoracic Belt Compression Response - Figure 14 shows the thoracic belt compression test performed by Cesari et al. (1990). The test involved placing a belt-shaped impactor (width: approximately 50 mm) diagonally across the anterior surface of the thorax of a PMHS lying face upward on a test bench to simulate a seatbelt, and pulling both ends of the belt toward the posterior surface of the torso. The ends of the belt were connected by wires to a pressure receiver, and pulled the belt dynamically to simulate impactor contact. Displacement was recorded at multiple points on the thorax and measured on bar-shaped deflection meters suspended from the top of the test bench. The test was performed using 13 PMHS, and their injuries were recorded in post-test autopsies. The FE model was also placed face upward on a rigid flat plane simulating the test bench. The geometry of the spine was adjusted to that of the table by applying gravitational acceleration. The time history of the amount of belt pulling force in the PMHS test was input into the FE model belt ends. An impactor mass of 22.4 kg and an initial velocity of 7.78 m/s were selected from the various test conditions. The displacement measurement points were selected by referring to diagrams showing the test conditions. If the belt moved during compression, the node closest to the initial position on the plane was re-selected. Injury was predicted based on the reference values in Table 3.

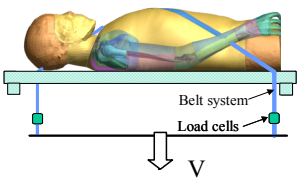

Figure 14. Thoracic belt compression test.

Figure 15 shows sectional views of thoracic deformation under belt compression from the left side of the median sagittal plane. The deformation is shown with thoracic deflection of 0 mm (0 ms), 20 mm (14 ms), and 70 mm (26 ms). As with the impactor test, compressive deformation of the subcutaneous tissue occurred before rib cage deformation. At a thoracic deflection of 30 mm, the sternum was pushed in the posterior direction, causing compressive deformation of the heart and lungs. When this occurred, the heart elongated in the inferior direction, also pressing the liver in the same direction. At a thoracic deflection of 70 mm, the sternum was pushed even further inward, advancing the deformation of the heart and lungs, and forcing the liver even further in the inferior direction. Since the posterior surface of the model was positioned against a flat plate under these test conditions, little motion was generated in the spine. The rib cage and organs incurred compressive deformation only in the areas where the belt force was applied.

Figure 16 shows the superior view of the horizontal section of the thorax at the height of the sternum center. It compares the deformation at thoracic deflections of 0 mm and approximately 70 mm (maximum deflection). This section includes the sternum, ribs, spine, heart, and lungs. The belt contacted the anterior surface of the thorax close to the sternum. The sectional deformation at the maximum deflection shows that the heart was compressed in the AP direction between the sternum and the spine, and that the body elongated in the lateral direction. Maximum deformation of the anterior surface of the thorax occurred at the belt contact position close to the sternum, and the surrounding ribs deformed dragged by the sternum. Although lungs deformation was seen close to the sternum, no significant deformation occurred in any other location.

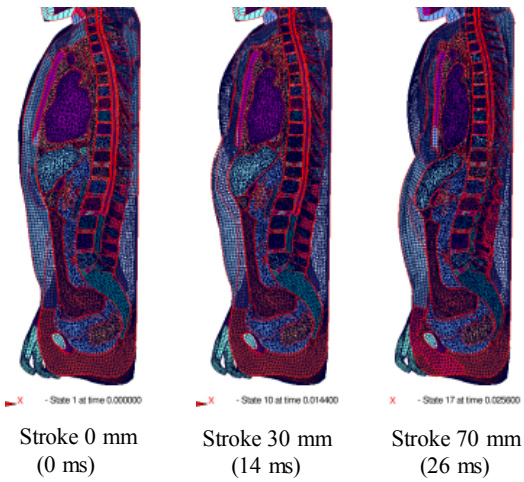

Figure 15. Thoracic belt compression behavior.

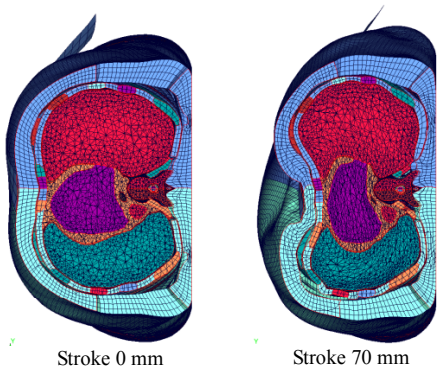

Figure 16. Sectional deformation of thorax (at height of sternum center).

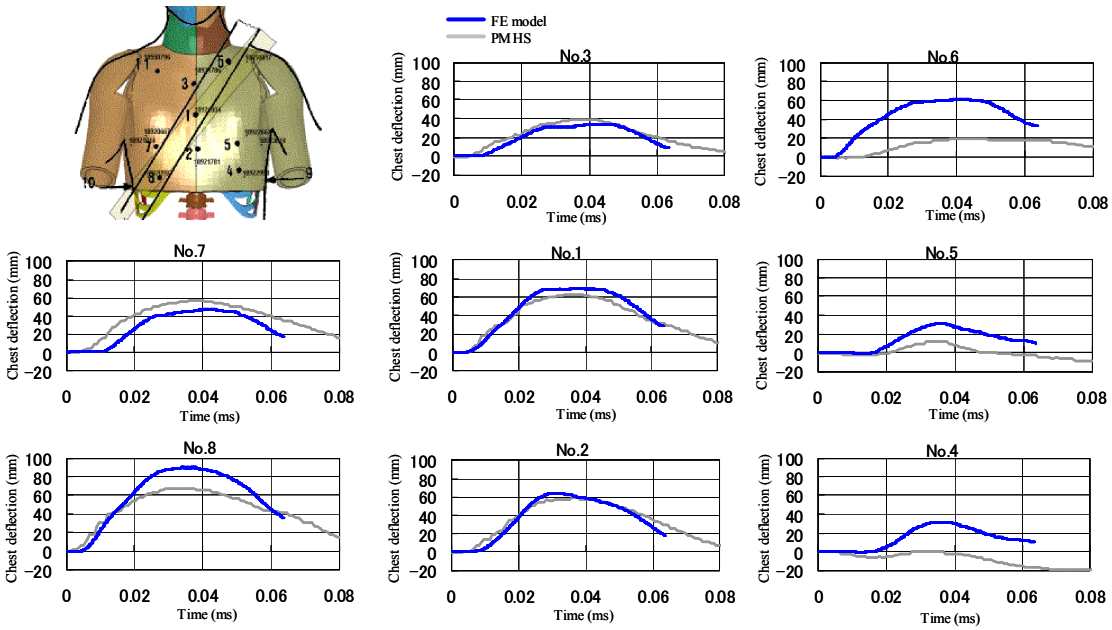

Figure 17. Displacement under thoracic belt compression.

Figure 17 shows the time history curves of displacement at each measurement point. The grey lines show the PMHS test results and the black lines show the results measured by the FE model. The same increasing trend for sternum displacement was achieved by both the PMHS and the FE model. Maximum deflection of the superior portion of the sternum was 10 mm larger with the PMHS and deflection in the center and inferior portions was 5 mm larger with the FE model. Maximum deflection measured at the rib cartilage showed a difference of 10 to 30 mm. Displacement at the left clavicle was 40 mm larger with the FE model.

Because no information on organ injury is available from the study by Cesari at al. (1990), the validity of the organ pressure and strain predicted by the FE model cannot be examined for these belt loading conditions.

Abdominal Impactor Response - Figure 18 shows the abdominal impactor test performed by Cavanaugh et al. (1986). This test impacted an aluminum bar (diameter: 25 mm, mass: 32 or 64 kg) against the abdomen of PMHS horizontally at an initial velocity of 5 to 10 m/s. The test was performed using 12 PMHS. Five of the tests used an average initial velocity of 6.1 m/s, and the remaining seven tests used an average initial velocity of 10.4 m/s. Each test recorded the abdominal deflection with respect to the impactor force, and the injury state of the PMHS was investigated after the test. Model verification referred to a force-deflection corridor created from the results of the five tests that used low initial impactor velocities. Since the posture of the PMHS in the tests is not described in detail in the literature, an upright seated posture was assumed in the same way as the thoracic impactor test. However, both arms were positioned hanging downward. The impactor force was output as a contact load between the impactor and the anterior surface of the abdomen. Impactor displacement was calculated from model node displacement, and abdominal deflection was calculated from changes in the distance between nodes on the anterior and posterior surfaces of the abdomen.

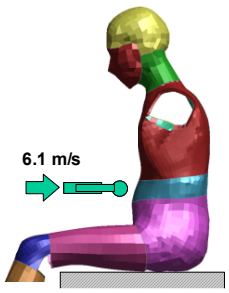

Figure 18. Outline of abdominal impactor test.

Figure 19 shows sectional views from the left side of the median sagittal plane of the FE model torso. The figure shows the states of the model at impactor strokes of 0 mm, 36 mm, 82 mm, and 100 mm. Up to 36 mm, compressive deformation was limited to the subcutaneous tissue, before subsequently spreading to the organs in the abdominal cavity such as the intestines. The compression ratio of the small intestine exceeded 90% at a stroke of 82 mm and the abdominal soft tissue impacted by the impactor

almost contacted the spine. After this point, since the posterior surface of the torso was not supported, the whole spine curved. No major changes in intestinal compression occurred in the impactor stroke range of 82 to 100 mm.

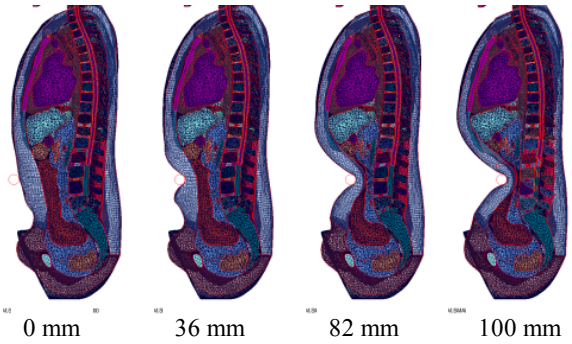

Figure 19. Abdominal impactor test behavior.

Figure 20 compares the deformation of the horizontal section of the abdomen at the height of the impactor center in its initial state and at an impactor stroke of 100 mm. The abdominal sections are viewed from the superior view and include the spine, the large intestine, the visceral fat near these organs, and the musculature at the posterior portion of the torso. The final contact range of the impactor covered the whole width of the abdomen. The sectional deformation at an impactor displacement of 100 mm shows that the anterior portion of the abdomen flattened in accordance with the shape of the impactor. The abdomen depth was compressed in the AP direction, but was elongated in the lateral direction. The small intestine was compressed in the AP direction between the subcutaneous tissue at the anterior surface of the abdomen and the spine. In contrast, compression of the large intestine was smaller and there was no major compressive deformation of the musculature at the posterior portion of the torso.

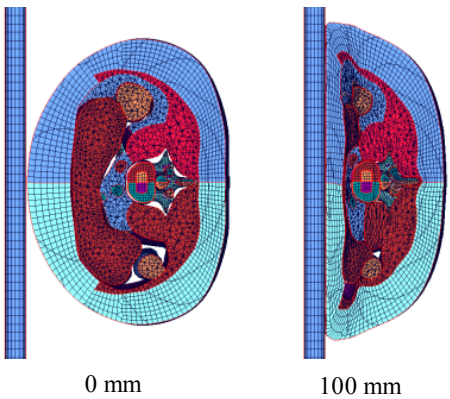

Figure 20. Sectional deformation of abdomen (at height of impactor center).

Figure 21 shows the time history curve of the impactor force with respect to its stroke. The grey lines show the force corridor calculated from the PMHS abdominal response, and the black line shows the response of the FE model. Impactor force at a stroke of 50 mm was between 0.8 and 1.9 kN with the PMHS and 1.5 kN with the FE model. In addition, at a stroke of 100 mm, the force was between 1.5 and 3 kN with the PMHS and 2.4 kN with the FE model. These results verify that the force curve of the FE model was appropriately within the PMHS corridor.

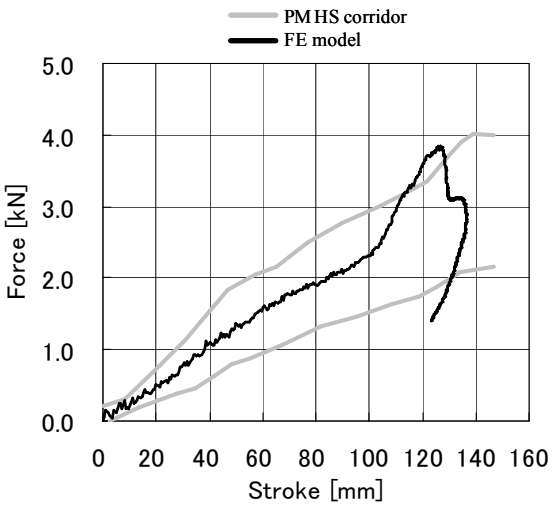

Figure 21. Abdominal impactor test F-s.

Cavanaugh et al. (1986) reported organ injury in one of the five test cases at the low initial velocity. Autopsy results show that AIS 4 liver injury occurred, but no mention is given of the small intestine. Figure 22 shows the strain distribution of the abdominal organs in the FE model. It indicates that strain in the liver exceeded the reference value of 0.3. A portion of the small intestine also exceeded the strain reference value of 1.2. The predictions of the FE model matched the test results with respect to liver injury, but close comparison was not possible due to a lack of data for other organs.

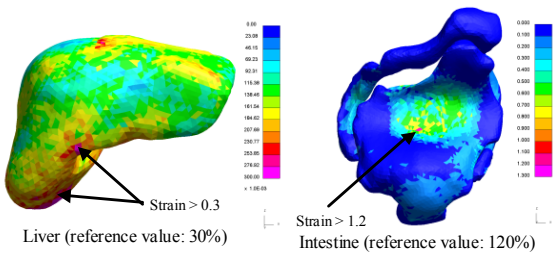

Figure 22. Strain distribution in abdominal organs.

Abdominal Belt Compression Response - Figure 23 shows the abdominal belt compression test performed by Foster et al. (2006). The test involved placing a lap belt (width: 50 mm) across the anterior surface of the abdomen of a PMHS and using a pyrotechnic pretensioner to pull the wound end toward the posterior surface of the PMHS in the horizontal direction. The posterior surface of the PMHS was supported by a rigid plate. The pretensioner had three settings for adjusting the pulling force to provide belt velocities of 4.0 to 5.4 m/s, 6.1 to 7.5 m/s, and 6.9 to 13.3 m/s. Belt force was measured by a load cell and abdominal deflection was measured by a laser deflection meter. The injuries of the PMHS were investigated after the tests. The FE model was set to reproduce the PMHS posture described in the literature, and a rigid plate was simulated at its posterior surface. Shell elements to simulate the belt were fitted to the torso around the abdomen, and the belt was pulled toward the posterior surface of the model. The comparison used the case with a belt pulling velocity of 6.9 m/s to recreate the time history of the pulling force of the belt end. Belt force was output from the sectional force of the shell elements, and abdominal deflection was calculated from changes in the distance between nodes on the anterior and posterior surfaces of the abdomen.

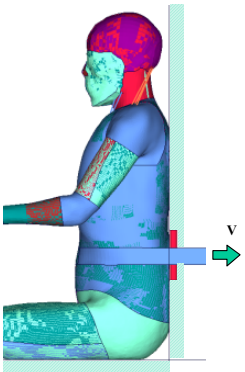

Figure 23. Outline of abdominal belt compression test.

Figure 24 shows sectional views from the left side of the median sagittal plane of the FE model torso. Abdominal deflection is shown at impactor strokes of 0 mm, 30 mm, 60 mm, and 120 mm. Up to 30 mm, compressive deformation was limited to the subcutaneous tissue, before subsequently spreading to the soft tissue in the abdominal cavity such as the small intestine. Compressive deformation of the small intestine progressed at an impactor stroke of 60 mm, and at 120 mm, the compression ratio exceeded 90%.

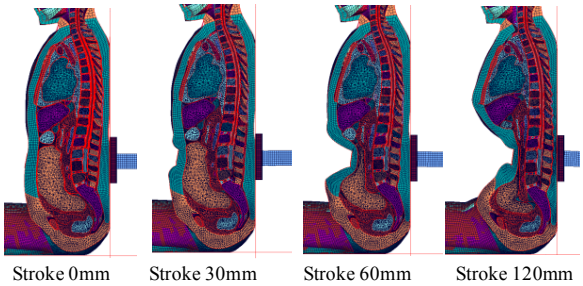

Figure 24. Behavior in abdominal belt test.

Figure 25 compares the deformation of the horizontal section of the abdomen at the height of the belt in its initial state and at a belt deflection of 120 mm. The abdominal sections are shown from the superior view and include the spine, the small and large intestines, the visceral fat near these organs, and the musculature at the posterior portion of the torso. Over the period of time from the initial to the final states, the belt becomes wrapped around the anterior half of the abdomen. The sectional deformation at an abdominal deflection of 120 mm shows that the anterior portion of the abdomen was deformed into a rounded state and the internal portions were compressed toward the spine. The posterior portion was flattened in accordance with the rigid plate. Unlike the impactor case, the body did not elongate in the lateral direction in accordance with AP direction compression. Mostly the small intestine was compressed in the AP direction between the subcutaneous tissue at the anterior surface of the abdomen and the spine. The large intestine was deformed between the subcutaneous tissue at the anterior surface of the abdomen and the musculature at the posterior portion of the torso.

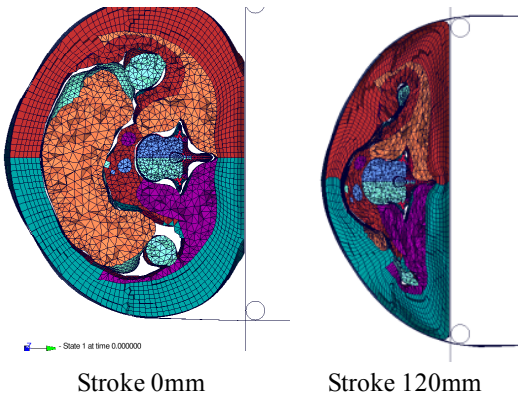

Figure 25. Sectional deformation of abdomen (at height of belt).

Figure 26 shows the time history curves of belt force with respect to abdominal deflection. The grey lines show the force corridor calculated from the PMHS abdominal response, and the black line shows the

response of the FE model. Belt force at a stroke of 20 mm was between 7.5 and 10 kN with the PMHS and 8.0 kN with the FE model. In addition, at a stroke of 75 mm, the force was between 0.4 and 8.0 kN with the PMHS and 5.3 kN with the FE model.

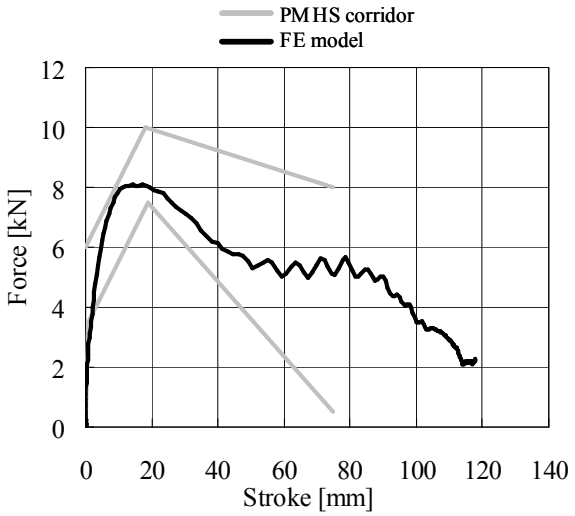

Figure 26. Abdominal belt test F-s.

Foster et al. (2006) tested four PMHS at belt pulling velocities between 6.9 and 13.3 m/s, of which three suffered organ injury. These injuries were to the liver, spleen, and kidneys, but all three injured PMHS were found to have sustained liver laceration. The case used for model verification did not suffer organ injury. Figure 27 shows the strain distribution in the abdominal organs of the FE model. Although the small intestine was compressed by 90% in the AP direction, the maximum strain in the small and large intestines did not exceed the reference value of 1.2. Strain in the intestines exceeded 0.3 close to the 10th rib on the right side, but no other organ exceeded its reference value for strain. These results indicate that the FE model successfully simulated the organ injury conditions of the PMHS for liver injury after abdominal compression. The FE model did not predict injury to any other organ. Its predictive accuracy cannot be discussed for the other organs because the injury results in the PMHS tests varied among the cases.

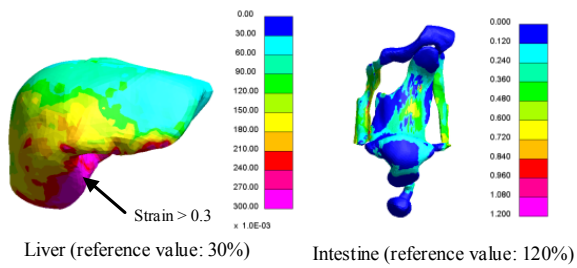

Figure 27. Strain distribution in abdominal organs.

Verification of Extremity Model

<u>Static Bending Response of Humerus</u> - Figure 28 shows the static 3-point bending test performed on the humerus by Kemper at al. (2005). In this test, the humerus was removed from the PMHS, both ends inserted into cylindrical aluminum jigs, and fixed using a hardened resin. One of the jigs was supported using a pin joint allowing rotation in the bending direction only, and the other was supported using a roller allowing the same rotation and displacement in the axial direction of the bone. The center of the humerus was then loaded using an impactor (diameter: 20 mm) at a velocity of 10 mm/s. The test was performed on three humerus bones, and the reaction force with respect to the impactor displacement was recorded. The FE model omitted the jigs and expressed the fixed portions using rigid elements. Nodes were set at the positions equivalent to the jig rotation centers, and defined with conditions for pin and roller support. Forcible displacement was applied by a model impactor on to the model humerus. The displacement of the impactor was output as model node displacement and the reaction force was output as the contact force with the humerus.

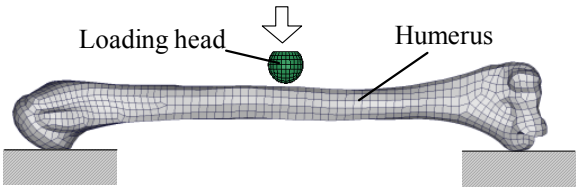

Figure 28. Static 3-point bending of humerus.

Figure 29 compares the force-displacement curves obtained in the three tests with that calculated by the FE model. The reaction force at a displacement of 5 mm was between 1.5 to 3.7 kN with the PMHS and 2.3 kN with the FE model. Additionally, the reaction force at a displacement of 10 mm was between 2.9 to 4.1 kN with the PMHS and 4.2 kN with the FE model. Although the reaction force of the FE model slightly exceeded that of the PMHS range at 10 mm, the curve history to that point fitted within the PMHS reaction force corridor.

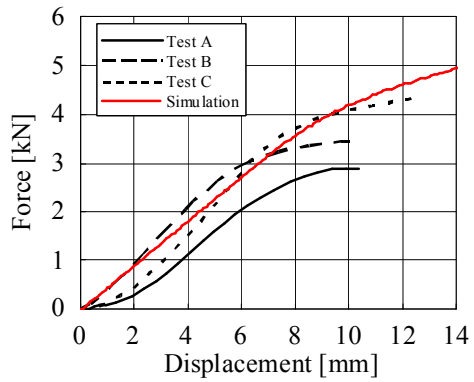

Figure 29. Relationship between impactor displacement and reaction force.

Dynamic Compression Response of Humerus - Figure 30 shows the dynamic test performed on the humerus by Kemper et al. (2005). In this test, the humerus was extracted from the PMHS including the flesh. The humerus was placed on a circular table with a diameter of 152 mm, and compressed by a circular impactor of the same dimensions applied in the downward direction at a velocity of 4 m/s. The test was performed on two humerus bones and the compressive displacement and compressive force were recorded. The same portion was extracted for the FE model, and placed between models of the circular jigs. The lower jig was fixed in space while the upper jig applied forcible displacement to compress the humerus model. The compressive displacement was output as displacement of the nodes in the upper jig, and the compressive force was output as the contact force between the humerus and the jigs.

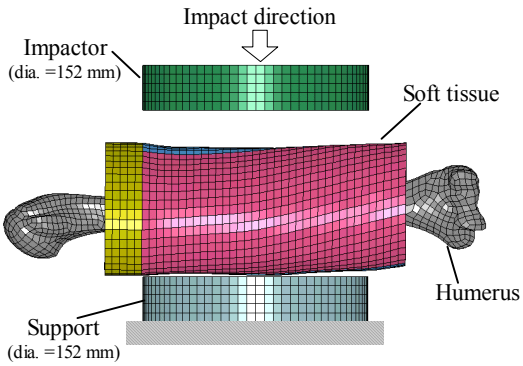

Figure 30. Humerus dynamic compression test.

Figure 31 compares the force-displacement curve obtained in the two tests with that calculated by the FE model. The force at a displacement of 15 mm was between 2 to 4 kN with the PMHS, and 2.5 kN with the FE model. Additionally, the force at a displacement of 25 mm was between 5 to 12 kN with the PMHS and 6.2 kN with the FE model. The force curve of the FE model was within the force range of the PMHS.

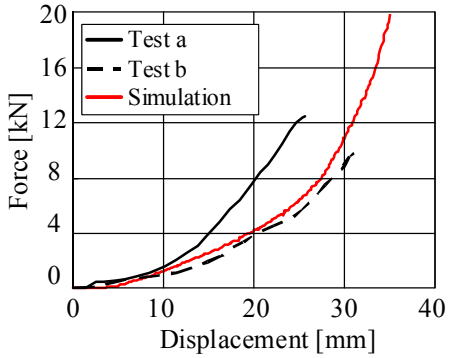

Figure 31. Relationship between impactor displacement and reaction force.

Static Bending Response of Femur - Figure 32 shows the static bending test performed on the femur by Yamada et al. (1970). In this test, the femur was removed from the PMHS, and both ends supported in a rotatable state. An impactor (diameter: 20 mm) was used to apply force at a velocity of 20 mm/s to the center of the femur. In the FE model, the same portions were also extracted and supported in a rotatable state at both ends. Forcible displacement was applied to the center of the femur in a manner equivalent to the test by a model of a rigid rod impactor. The displacement of the impactor was output as model node displacement and the reaction force was output as the contact force with the femur.

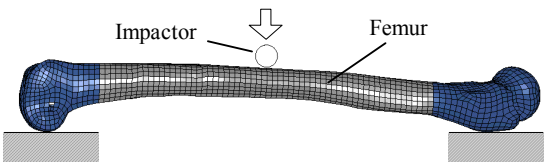

Figure 32. Static 3-point bending of femur.

Figure 33 compares the force-displacement curve obtained in the test with that calculated by the FE model. There is only one set of comparison data. The force at a displacement of 5 mm was 1.7 kN with the PMHS and 1.4 kN with the FE model. Additionally, the force at a displacement of 10 mm was 2.5 with the PMHS and 2.4 kN with the FE model. The force curve of the FE model was close to that of the PMHS.

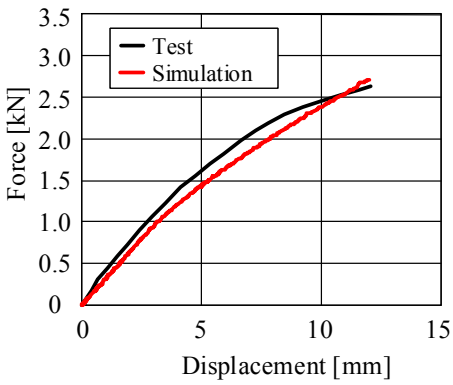

Figure 33. Relationship between impactor displacement and reaction force.

Impact Response of Knee - Figure 34 shows the impact test performed on the knee by Kajzer et al. (1997). This test used the lower extremity of a PMHS. The femur was fixed and an impactor (mass: 6.25 kg) was applied to the knee from the side at a velocity of 40 km/h, while force of 400 K was applied from under the foot. The diameter of the impactor was 100 mm, and a pad (thickness: 50 mm) was attached to its front surface. The test was performed on two lower extremity specimens, and the acceleration on impact was recorded by an accelerometer provided at the superior portion of the tibia. The same portion was extracted for the FE model, which also simulated the tibia support initial force under the foot. An impactor model was created and applied to the side of the knee at a velocity of 40 km/h. The acceleration was output from a node at an equivalent position to the accelerometer in the PMHS test.

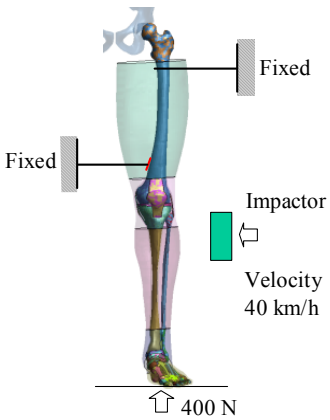

Figure 34. Knee impact test.

Figure 35 compares the acceleration time history obtained in the two tests with the acceleration curve calculated by the FE model. In all cases, acceleration peaked at approximately 4 ms after the impact, and then decreased. Peak acceleration with the PMHS was between 930 and 1020 m/s^2, and 1060 m/s^2 with the FE model. With the FE model, acceleration declined gradually immediately after the peak, but it re-produced the plateau in the acceleration curve at approximately 10 ms. Overall, the acceleration response of the FE model was higher than that of the PMHS, but their acceleration waveforms correlated well.

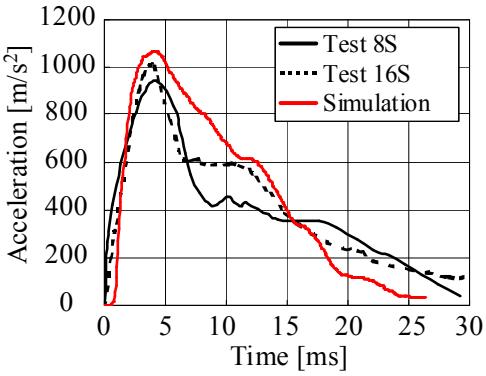

Figure 35. Impactor acceleration time history.

DISCUSSION

The predicted mechanical response of the thorax, abdomen, and extremities in the FE model correlated well with PMHS test data under the equivalent conditions. Although there is only limited data available to compare abdominal organ injury, the injuries predicted by the FE model based on assumed reference values correlated well with the PMHS test results. It is difficult to observe organ behavior during impact in PMHS tests, but FE model simulations visualized the internal behavior. Additionally, PMHS tests require precise techniques for attaching sensors such as load cells and potentiometers. FE models are capable of outputting force and displacement at any point of interest. It was useful to consider the mechanism of injuries incurred by thoracic and abdominal organs by analyzing the results of the model validation simulations, as follows.

Injury Mechanism of Thoracic Organs

According to the test results of Kroell et al. (1971) used to verify thoracic impactor response, multiple (seven or more) rib fractures occurred in all cases of organ injury. In contrast, in cases without rib fracture, no organ injury occurred. As shown in Figure 10, the anterior surface of the FE model thorax was flattened by the impactor. As a result, the lungs suffered compressive deformation as well as the heart located in the center of the thorax. At a thoracic deflection of approximately 70 mm, the thorax sectional area decreased by a ratio of approximately 21%. Figure 36 shows the time history of thoracic deflection

calculated at the sternum of the FE model overlaid with the time histories of strain in the heart, liver and lung pressure. Thoracic deflection increased immediately after impactor contact and reached a maximum value of 75 mm at approximately 14 ms. However, before that, the sternum and 4th rib fractured at 8 ms (thoracic deflection: 58 mm), and rib fractures occurred in six locations before the maximum thoracic deflection was reached. Strain in the heart and liver both increased in accordance with the thoracic deflection. Since the heart is located in the center of the thorax, it was caught between the sternum and the spine when the thorax was compressed in the AP direction. As a result, strain in the heart increased at the same time as the thoracic deflection. The left end of the liver was elongated up to a position close to the center of the body, but this area is located inferior to the bottom of the sternum. Under these conditions, since the liver was located slightly inferior to the impactor contact point, the increase in strain occurred a little later than for the heart. Therefore, it is considered that the organ strain timing differed depending on the position of the organ with respect to the pressure application area. The pressure in the lungs, which along with the heart were also immediately below the impactor, increased drastically from approximately 8 ms. This indicates that lung deformation was advanced by the start of the sternum and rib fractures.

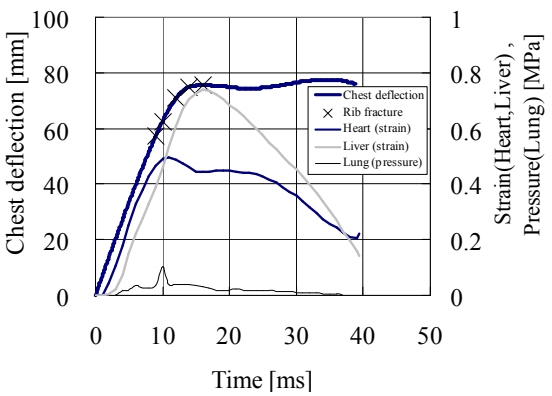

Figure 36. Thoracic deflection and organ force on impactor contact.

In contrast, although the heart was also compressed in the AP direction under the belt compression conditions in the same way as with the impactor contact, compressive deformation of the lungs was relatively small (Figure 16). In these sections, the belt mostly loaded the sternum. The surrounding ribs were not deformed a great deal, but were bent slightly inward dragged by the sternum. At a thoracic deflection of approximately 70 mm, the thorax sectional area decreased by a ratio of approximately 15%. Figure 37 shows the time history of thoracic deflection calculated by the FE model overlaid with the time histories of strain in the heart and liver and lung pressure. Under these conditions, strain in the heart and liver and lung pressure all increased in accordance with the increase in thoracic deflection. The sections in Figure 16 show the belt was positioned at the sternum, but multiple organs were compressed since the belt was actually placed diagonally across the anterior surface of the thorax. However, it is assumed that the deformation of the compressed organs was low because the ratio of sectional area decrease was less than with the impactor in these sections. In fact, the strain in the heart and liver shown in Figure 37 was smaller than at the same thoracic deflection in Figure 36. Strain in the liver was smaller because it was outside the area compressed by the belt. The amount of compressive deformation of these organs may have been small since the belt may have loaded multiple organs simultaneously. Deformation had a higher trend for the organs underneath the contact surface of the impactor. In other words, the thoracic organ injury risk may also be affected by the compression area and not only the amount of thoracic deflection. Since the study performed by Cesari et al. (1990) does not describe organ injury, the validity of the organ injury predictions under belt loading using the FE model needs to be verified in future study. The liver is located in the abdominal area, but it is covered by the inferior ribs. In the thoracic impactor test, strain was generated in the superior part of the liver by deformation of the right ribs. Although the liver was located away from the belt path in the reference test case, it would be compressed if the belt were worn over the other shoulder.

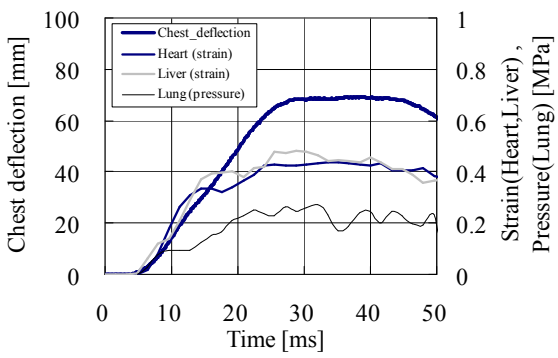

Figure 37. Thoracic deflection and organ force on belt compression.

Injury Mechanism of Abdominal Organs

A similar trend was observed for the abdomen. However, no large differences were found in the size of the abdomen compression area between the impactor and belt test. Comparing the abdominal

deformation in the sections in Figures 20 and 25, the former shows that the impactor flattened the anterior surface of the abdomen, whereas in the latter, the belt became wrapped around the anterior half of the abdomen and caused deformation by restraining the body toward the center. In other words, with impactor contact, large compression occurred above the impactor center, but the belt force applied large compression over the whole range of contact. At an abdominal deflection of approximately 60 mm, the abdominal sectional area decreased by approximately 13% with the impactor, and approximately 39% with the belt. That is, organ deformation and movement were larger under the belt conditions. Figures 38 and 39 show the time history of abdominal deflection calculated by the FE model overlaid with the time histories of strain for the small and large intestines and the liver, under both the abdominal impactor and belt compression conditions. Strain was output at the elements of the small and large intestines positioned at the height of the impactor. Elements close to the impactor were selected for the liver. In both cases, strain of the small intestine increased at the same time as the increase in abdominal deflection. Strain in the liver began to increase as compressive deformation of the abdomen progressed to a certain level, and increased again after abdominal deflection and strain in the small intestine peaked. This is probably because a portion of the liver is connected with the diaphragm, which causes compressive or tensile deformation when pulled by other organs under abdominal compression. The strain value in the liver was smaller than that in the small intestine. It should be noted, however, that the reference strain value for the liver is relatively small. In both cases, strain in the large intestine increased temporarily when abdominal compression reached a certain point, but eventually decreased. Although the large intestine is connected to the peritoneum, its long path gives it a larger tolerance for movement than organs such as the liver.

Limitations and Suggestion for Future Work

The human FE model developed in this research demonstrated a good correlation with the mechanical response of PMHS tests selected from the literature. However, there are limitations in the selected force conditions and cases that be used for comparison. Therefore, the validation results cannot confirm the validity of the model under various force conditions. Further research is needed for human injury prediction in vehicle collisions using this model.

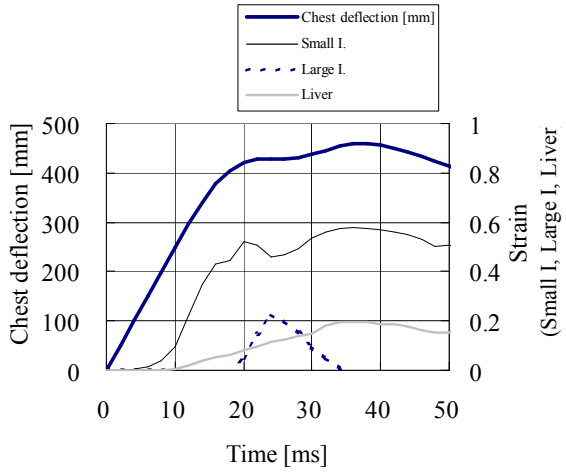

Figure 38. Abdominal deflection and organ force on impactor contact.

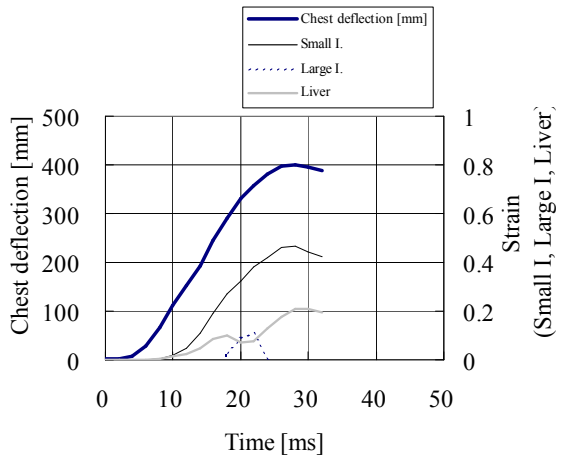

Figure 39. Abdominal deflection and organ force on belt compression.

CONCLUSION

A precise FE model of a torso was developed based on internal geometrical data digitized using high-resolution CT scans. The model was generated taking into account the properties of each organ and their connections with neighboring tissues. FE models were also created for the extremities with the same precision as the torso based on commercially available geometrical databases. THUMS ver.3.0 was used for the head model. These models were combined to complete a whole human body FE model (THUMS ver.4.0) comprising approximately 2 million elements simulating an adult male of average physique. The validity of the mechanical response of the developed human FE model was verified by comparison with PMHS impact test data. FE models simulated impactor and belt compression tests on the thorax and abdomen, 3-point bending tests on the extremities, and impactor tests on the knees to verify

correlation with PMHS force response. The mechanism of organ injuries in the thorax and abdomen was also discussed based on the validation results. Strain in heart and lung pressure increased in accordance with thoracic deflection, but the magnitude of them was affected by the compression area of the loading device. Strain in the small intestine increased in accordance with abdominal deflection, while strain in the liver increased locally as compressive deformation of the abdominal progressed. The absolute values for pressure and strain indicated by the FE model require further verification, but the developed FE model was shown to be useful for predicting trends of organ injuries in vehicle collisions.

ACKNOWLEDGMENTS

The human body geometry data was obtained with a high resolution CT-scan system developed by the University of Michigan. The authors wish to thank Dr. Stewart Wang for providing the digitized geometry data. Many of the techniques used for modeling were based on experience from using the THUMS model. THUMS was developed in collaboration with Toyota Central R & D Labs., Inc. The authors would also like to thank Toyota Technical Development Corporation for its assistance in the modeling and simulation work.

REFERENCES

[1] McHenry, R. R. 1963. "Analysis of the dynamic of automobile passenger restraint systems." Proc. 7th Stapp Car Crash Conference, pp. 207-249.

[2] Choi, H. Y., Lee, I. H. and Haug, E. 1999. "Advanced finite element modeling of the human body for occupant safety; H-Model for the next millennium." Proceeding of 5th HanPam, Seoul, Korea.

[3]Iwamoto, M.; Kisanuki, Y.; Watanabe, I.; Furusu, K.; Miki, K.; Hasegawa, J. 2002. "Development of a finite element model of the total human model for safety (THUMS) and application to injury reconstruction." Proc. International Conference on the Biomechanics of Impacts, pp. 31-42.

[4] Vezin, P., Verriest, J. P. 2005. "Development of a Set of Numerical Human Models for Safety." Proc. 19th ESV Conference, 05-0163.

[5] Ruan, J. S., El-Jawahri, R., Chai, L., Barbat, S., Prasad, P. 2003. "Prediction and Analysis of Human Thoracic Impact Response and Injuries in Cadaver Impacts using a full human Body Finite Element Model." Stapp Car Crash Journal, 47:299-321.

[6] Kitagawa, Y., Hasegawa, J., Yasuki, T. 2005. "A Study of Knee Joint Kinematics and Mechanics using a Human FE Model." Stapp Car Crash Journal, 49:117-131.

[7] Hayashi, S., Yasuki, T., Yamamae, Y., Takahira, Y. 2006. "A Study of Side Airbag Effectiveness in Reducing Chest Injury in Car to Car Side Impacts Using a Human FE Model." Proc. 2006 International Research Council on the Biomechanics of Impacts (IRCOBI), pp. 397-400.

[8] Kuwahara, M., Yasuki, T., Kitagawa, Y., Hayashi, S., Masuda, T. 2008. "A Study of SRS Side Airbag Performance in Chest Protection in a Pole Side Impact using a Human FE Model." Proc. 2008 FISITA, F2008-08-015.

[9] Kitagawa, Y., T. Yasuki and J. Hasegawa. 2006. "A Study of Cervical Spine Kinematics and Joint Capsule Strain in Rear Impacts Using a Human FE Model." Stapp Car Crash Journal 50: 545-566.

[10] Kitagawa, Y., T. Yasuki and J. Hasegawa. 2007. "Consideration of Possible Indicators for Whiplash Injury Assessment and Examination of Seat Design Parameters using Human FE Model." Proc. 20th ESV Conference, 07-0093.

[11] Kitagawa, Y., Yasuki, T., Hasegawa, J. 2008. "Research Study on Whiplash Injury Lessening with Active Head Restraint using a Human FE Model." Proc. 2008 International Research Council on the Biomechanics of Impacts (IRCOBI), pp. 381-396.

[12] Yasuki, T. 2005. "A Survey on the Biofidelity of the Knee Bending Angle of the TRL Lower Leg Impactor." Proc. 19th ESV Conference, 05-0101.

[13] Tamura, A., Nakahira, Y., Iwamoto, M., Watanabe, I., Miki, K., Hayashi, S., Yasuki, T. 2006. "The Influence of the Traction Force Due to Inertia of the Brain Mass on Traumatic Brain Injury during SUV-to-Pedestrian Impact." International Research Council on the Biomechanics of Impacts (IRCOBI), pp. 361-364.

[14] Hayashi, S., Yasuki, T., Kitagawa, Y. 2008. "Occupant Kinematics and Estimated Effectiveness of Side Airbags in Pole Side Impacts Using a Human FE Model with Internal Organs." Stapp Car Crash Journal, 52: 363-377.

[15] Yamada, H. 1970. "Strength of Biological Materials." FG. Evean, Ed., The Williams & Wilkins Company, Baltimore.

[16] Abe, H., Hayashi, K., Sato, M. 1996. “Data Book on Mechanical Properties of Living Cells, Tissues and Organs.” Springer-Verlag Tokyo.

[17] Kimpara, H., Nakahira, Y., Iwamoto, M., Miki, K. Ichihara, K., Kawano, S., Taguchi, T. 2006. “Investigation of Anteroposterior Head-Neck Responses during Severe Frontal Impact Using a Brain-Spinal Cord Complex FE Model.” Stapp Car Crash Journal, Vol.50, pp. 27-51.

[18] Shah, J.S., Yang, K.H., Hardy, W.N., Wang, H.K. and King, A.I. 2001. “Development of a computer model to predict aortic rupture due to impact loading.” Stapp Car Crash Journal, Vol.45, pp.161-182.

[19] Lee, J.B., and Yang, K.H., 2001. “Development of a finite element model of the human abdomen.” Stapp Car Crash Journal, Vol.45, pp. 79-100

[20] Kroell, C., Schneider, D., Nahum, A. 1971. “Impact Tolerance and Response of the Human Thorax.” Proc. 15th Stapp Car Crash Conference, pp. 84-134.

[21] Kroell, C., Schneider, D., Nahum, A. 1974. “Impact Tolerance and Response of the Human Thorax II.” Proc. 18th Stapp Car Crash Conference, pp. 383-457.

[22] Cesari, D., Bouquet, R. 1990. “Behaviour of Human Surrogates Thorax under Belt Loading.” SAE902310.

[23] Cavanaugh, J., Nyquist, G., Goldberg, S., King, A. 1986. “Lower Abdominal Tolerance and Response”. SAE861878.

[24] Foster, C., Hardy, W., Yang, K., King, A., Hashimoto, S. 2006. “High-Speed Seatbelt Pretensioner Loading of the Abdomen.” Stapp Car Crash Journal, Vol.50, pp. 27-51.

[25] Kemper, A., Duma, S., Matsuoka, F., Masuda, M. 2005. “Biofidelity of the SID-IIs and a Modified SID-IIs Upper Extremity: Biomechanical Properties of the Human Humerus.” Proc. 19th ESV Conference, 05-0123

[24] Kemper, A., McNally, C., Kennedy, E., Rath, A., Manoogian, S., Stitzel, J., and Duma, S. 2005. “Material Properties of Human Rib Cortical Bone from Dynamic Tension Coupon Testing.” Stapp Car Crash Journal, Vol.49, pp. 199-230.

[25] Karl, E.S., Wilbur, P.M, Jr., Charles, C.C., Averill, A.L. 1958. “Mechanisms in Development of Interstitial Emphysema and Air Embolism on Decompression From Depth.” Journal of Applied Physiology, Vol.13, pp. 15-29.

Load Transfer and Deformation Characteristics of the Pelvis in Non-destructive Side Impact Testing

Andrew Kemper, Craig McNally, and Stefan Duma
Virginia Tech – Wake Forest, Center for Injury Biomechanics
United States of America
Paper Number 09-0508

ABSTRACT

Although finite element models of the human body are becoming an integral tool in the reduction of automobile related injuries, these models must be locally and globally validated to be considered accurate. Therefore, the purpose of this study was to quantify the load transfer and deformation characteristics of the pelvis in side impact loading. A total of ten non-destructive side impact tests were performed on two human male cadavers. Three impact areas and two impacting surfaces were evaluated using a 16 kg pneumatic impactor at approximately 3 m/s: rigid-impact to the ilium, rigid-impact to the greater trochanter, rigid-impact to the ilium and greater trochanter, and foam-impact to the ilum and greater trochanter. Additional rigid-impacts to the ilum and greater trochanter were performed on one cadaver at 4 m/s and 5 m/s to evaluate the effect of loading rate. Load transfer through the pelvis was quantified by implanting custom *in situ* pelvic load cells in the ilio-sacral joint and pubic symphysis joint. In addition, strain gages were applied to the iliac wing, superior pubic ramus, ischium, and femur. The results showed that for all test conditions, except the rigid-impact to the iliac crest, a larger percentage of impactor force was transferred through the pubic symphysis joint than the ilio-sacral joint. The strain gage data showed that for all test conditions except one, ilium only impact, the superior pubic ramus and ischium were placed in compression. Conversely, the primary loading mode for the ilium 1st principle strain was tension for all test conditions. Impact speed was not found to have a considerable affect on the distribution of load through the pelvis. It is anticipated that this research will further the understanding of the biomechanical response of the human pelvis in side impact loading, and aid in the development and validation of computational models.

INTRODUCTION

The incidence of pelvic fractures in the United States is estimated to be more than 100,000 per year [9]. Motor vehicle collisions account for 44–64% of pelvic fractures, which are a major cause of death and residual disability in blunt trauma [6]. In addition, studies have shown that frontal occupants involved in lateral motor vehicle collisions have a significantly higher risk of sustaining a pelvic fracture versus those involved in a frontal collision [12, 13]. Understanding the biomechanical response of the pelvis to various loading conditions is the first step in reducing the number of incidences and severity of pelvic fractures. There have been a number studies which have investigated the biomechanical response and tolerance of the pelvis in lateral impact loading representative of that seen in motor vehicle side impact collisions [1, 2, 3, 4, 5, 11]. However, the injury criteria based on the results of these studies rely primarily on censored fracture data. Although finite element models of the human body are becoming an integral tool in the reduction of automobile related injuries, these models must be locally and globally validated in order to accurately predict injury. Therefore, the purpose of this study was to quantify the load transfer and deformation characteristics of the pelvis in side impact loading.

METHODS

A total of 10 non-destructive side impact tests were performed on two fresh previously frozen human male cadavers. Subject information and pelvic anthropometric measurements from each cadaver were recorded (Table 1).

Table 1: Subject information.

Test Measurement		Cadaver ID	
		1	**2**
Age	(yr)	75	57
Weight	(kg)	65	84
Height	(cm)	165	177
Pelvis Length (anterior-posterior)	(mm)	165	172
Pelvis Width (medial-lateral)	(mm)	285	320
Pelvis Height (superior-inferior)	(mm)	190	220

***In Situ* Pelvic Load Cells**

In order to quantify the load transfer through the pelvis, *in situ* pelvis loads cell were implanted in the ilio-sacral joint (Robert A. Denton, Inc. 7458FL, 8896 N, Rochester Hills, MI) and the pubic symphysis joint (Robert A. Denton, Inc. 7457FL, 8896 N, Rochester Hills, MI) (Figure 1). The appropriate size and shape of the *in situ* pelvis load cells and mating plates used to attached the potting cups were based on anthropometric measurements from 6 human pelvi (Figures 2 and 3). The load cells were attached to the mating plates with a dove-tail design. The dove-tail fixed the load cell in the medial-lateral direction, and set screws fixed the load cell in the anterior-posterior direction. The mating plates were designed to allow the load cell to be inserted from the anterior or posterior side of the post mortem human subject to allow for easy insertion and removal. This design provided a relatively simple attachment, while rigid enough to maintain the proper orientation.

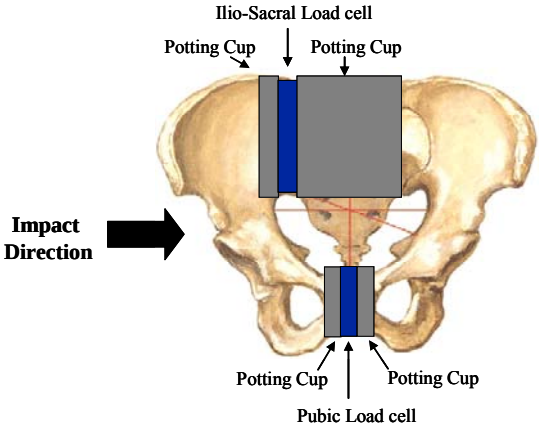

Figure 1: *In-situ* pelvic load cell locations.

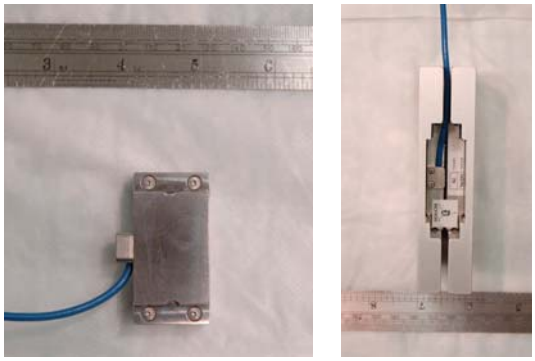

Load Cell | Load Cell & Matting Plates

Figure 2: Pubic symphysis load cell.

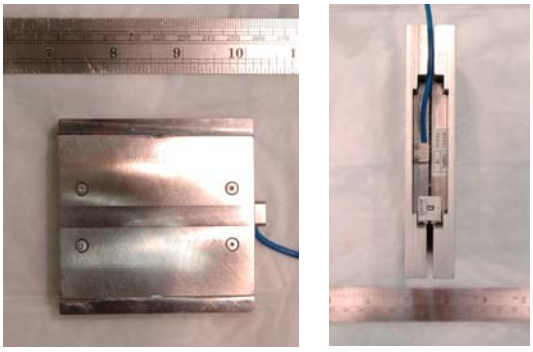

Load Cell | Load Cell & Matting Plates

Figure 3: Ilio-sacral load cell.

The load cells were attached to the pelvis through a number of detailed steps. In order to preserve the normal orientation of the pelvis, the load cells were implanted one at a time. The ilio-sacral load cell was implanted first (Figure 4). This was done by first measuring the width of the pelvis, and then rigidly securing the pelvis to prevent movement during the process. Second, a section of bone was removed from the site insertion site, and a bone screw was placed through the ilium to provide a more rigid attachment when using the bonding compound. Third, potting cups and load cell were placed in the pelvis and positioned properly. Special care was taken to ensure that the measuring axis of the load cell was perpendicular to the sagital plane. Then, the set screws where tightened to secure the load cell to the mating plates. The potting cups were then filled with a bonding compound (Bondo Corporation, Atlanta, GA), and bone screws were placed through the sacrum and L5. Finally, the pelvis width measurements were checked to ensure that they had not changed do the implantation of the ilio-sacral load cell.

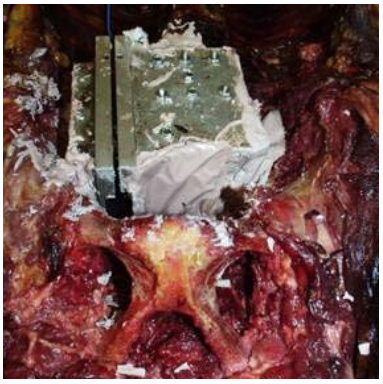

Figure 4: Ilio-sacral load cell implantation.

Once the bonding compound for the ilio-sacral load cell fully cured, the pubic load cell was implanted (Figure 5). A section of bone was removed from the insertion site. Care was taken to leave the enough bone to maintain the connection between the upper and lower ramus. Third, the potting cups and load cell were placed in the pelvis and positioned properly. Again, special care was taken to ensure that the measuring axis of the load cell was perpendicular to the sagital plane. Then, the set screws were tightened to secure the load cell to the mating plates. The potting cups were then filled with a bonding compound (Bondo Corporation, Atlanta, GA) and allowed to cure. Finally, the pelvis width measurements were rechecked to ensure that they had not changed do the implantation of the pubic load cell.

Figure 5: Pubic load cell implantation.

Pelvic and Femur Strain Gages

Each cadaver was instrumented with 6 strain gages (Figure 6, Table 2). Single axis strain gages were applied along the main axis of the anterior portion of the superior pubic ramus and ischium. A strain gage rosette was placed on the interior portion of the ilium and was oriented towards the superior portion of the pelvis (Figure 7). The strain output from the three gages that composed each rosette was used to calculate the first and second principle strains. The first and second principle strains are calculated with the following equation (Equation 1). A single axis strain gage was applied to the lateral portion of the femur, aligned with the long axis, at the midpoint between the knee and hip. All strain gages were applied to the impacted side of the body.

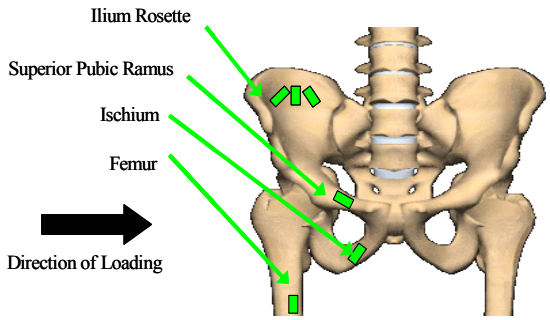

Figure 6: Strain gage locations for non-destructive side impact testing.

Table 2: Locations of strain gages and femur accelerometer.

Test Measurement Location		Cadaver ID	
		1	2
Ilium Rosette (to anterior superior iliac spine)	(mm)	57	50
Ilium Rosette (to posterior superior iliac spine)	(mm)	51	40
Pubic Ramus Gage (to pubic symphysis)	(mm)	52	50
Ischium Gage (to pubic symphysis)	(mm)	54	60
Right Femur Gage- (to center to patella)	(mm)	185	170

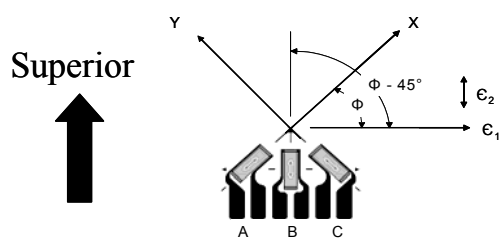

Figure 7: Ilium strain gage rosette labeling and orientation.

$$\varepsilon_{1,2} = \frac{\varepsilon_A + \varepsilon_C}{2} \pm \frac{1}{\sqrt{2}}\sqrt{(\varepsilon_A - \varepsilon_B)^2 + (\varepsilon_B - \varepsilon_C)^2} \quad \text{Eqn (1)}$$

Where:

ϵ_A = Strain output from gage A of the rosette

ϵ_B = Strain output from gage B of the rosette

ϵ_C = Strain output from gage C of the rosette

Experimental Setup

The primary component of the side impact experimental setup was a custom pneumatic impactor, which accelerates an impacting cart constrained by rails, to the desired speed via a piston (Figure 8). Prior to impact the piston loses contact with the cart, due to a limited piston stroke, resulting in an impact with finite energy. The displacement of the impacting cart, i.e. impactor stroke, was limited via a steel cable with a set length. The impactor was instrumented with a five-axis load cell (Robert A. Denton, Inc. 1968, 22,240 N, Rochester Hills, MI) and a single-axis accelerometer (Endevco 7264B, 2000 G, San Juan Capistrano, CA).

A custom test seat was designed and fabricated to allow a cadaver to be placed in a seated position (Figure 9). The use of an adjustable back support bar allowed for a clear line of sight to the posterior side of the cadaver, while maintaining an automotive-like seated posture and upper body load on the pelvis and spine. The head was held upright with the use of masking tape placed around the forehead and attached to the bar on the right and left side of the cadaver. This tape was cut approximately half way though on both sides in order to ensure the tape would break once the cadaver was impacted. A Teflon ® sheet was placed between the cadaver and the seat pan to minimize friction [2].

During the impact, the impactor plate contacted a trigger strip that was secured to the outermost portion of the pelvis to activate the data acquisition system for each test. Data from the load cell and strain gages were recorded at a sampling frequency of 15 kHz with an Analog-to-Digital conversion resolution of 16 bits using an Iotech Wavebook with WBK16 strain gage modules (Iotech WBK16, Cleveland, OH). Two high speed video cameras recorded the event from different angles (front and back view) at 1000 fps. All channels except for the strain gages were filtered to Channel Filter Class (CFC) 180. The inertially compensated impactor force was calculated by summing the measured impactor force and inertial force. The inertial force was calculated by taking the product of the impactor acceleration and effective impactor mass, i.e. the impacting plate mass plus ½ the load cell mass.

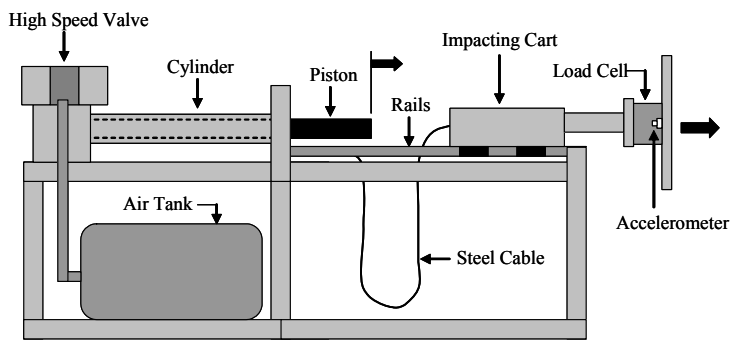

Figure 8: Custom pneumatic impactor.

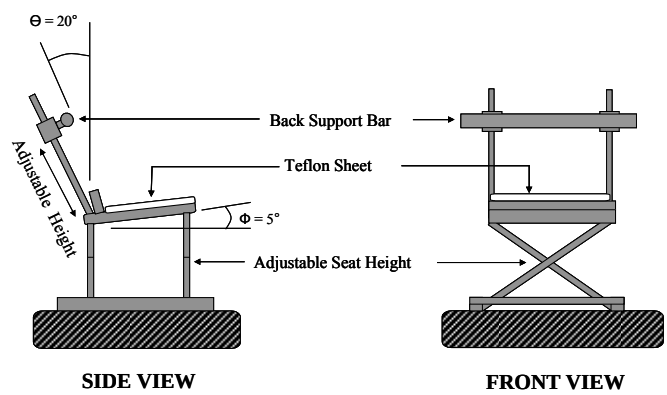

Figure 9: Custom side impact test seat.

Impact Conditions

A total of 10 non-destructive side impact tests were performed on two human male cadavers with a pneumatic impactor. Three impact locations and two impacting surfaces, rigid or foam, were evaluated (Table 3 and Figure 10). The combined ilium and femur impacts were performed with a 250 x 250 square impacting surface. In order to avoid contacting the testing seat, the square impactor was oriented at 22 degrees from horizontal. The ilium only impact and the trochanter only impact were performed using a rigid 127 mm diameter circular impacting surface. The majority of the testing was conducted at an impact speed of 3 m/s. However, two tests were performed on subject 2 higher impact velocities, 4 m/s and 5 m/s, to investigate the effects of loading rate. The impactor mass was 16 kg for all tests.

Table 3: Non-destructive pelvic side impact test summary.

Cadaver ID	Impact Surface	Impact Location	Speed
1	Foam	Ilium/ Femur	3 m/s
1	Rigid	Ilium/ Femur	3 m/s
1	Rigid	Ilium	3 m/s
1	Rigid	Trochanter	3 m/s
2	Foam	Ilium/ Femur	3 m/s
2	Rigid	Ilium/ Femur	3 m/s
2	Rigid	Ilium	3 m/s
2	Rigid	Trochanter	3 m/s
2	Rigid	Ilium/ Femur	4 m/s
2	Rigid	Ilium/ Femur	5 m/s

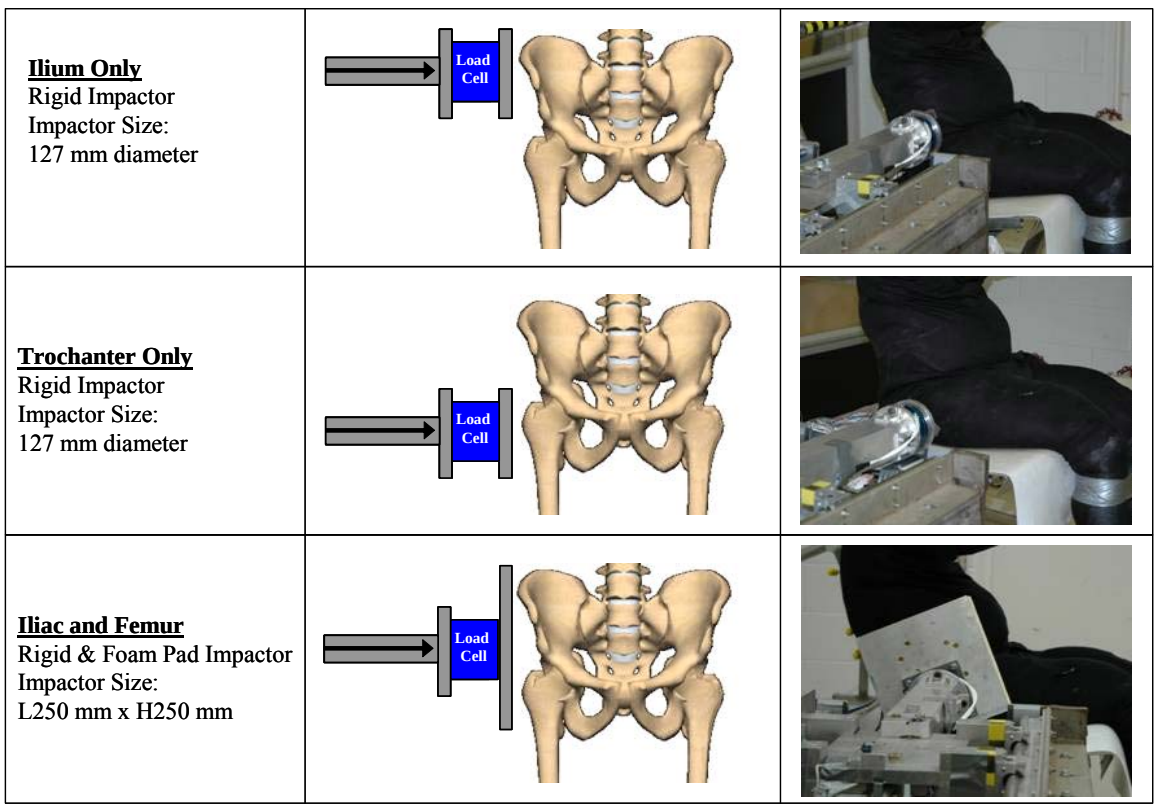

Figure 10: Impact locations and impactor surfaces.

RESULTS

The results of the *in situ* pelvic load cells as well as the pelvic and femur strain gages are presented in this section. It should be noted that no pelvic or femoral fractures where observed as a result of these tests.

Impactor Force and Pelvic Load Distribution

Each of the 10 non-destructive pelvic impact tests resulted in force time history for the impactor load cell, ilio-sacral load cell, and pubic load cell (Figure 11). The force time histories for each test are presented in the Appendix (Figures A1-A10). The reported impactor force is the inertially compensated impactor force. In order to directly compare the load distribution through the pelvis for the different test conditions, the peak ilio-sacral load and peak pubic load are shown as a percentage of the peak impactor force (Figures 12-14). The peak impactor force, peak ilio-sacral force, and peak pubic force for each test are reported in Table 4.

Pelvic Strain Distribution

The peak superior pubic ramus strain, ischium strain, femur strain, ilium 1st principle strain, and ilium 2nd principle strain in the primary mode of loading were plotted by test condition (Figures 15-17). The strain time histories for each test are presented in the Appendix (Figures A11-A20).

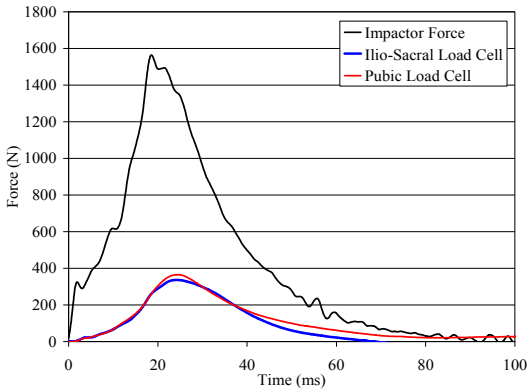

Figure 11: Typical force vs. time trace. (Cadaver 1- Ilium and femur - foam pad - 3m/s)

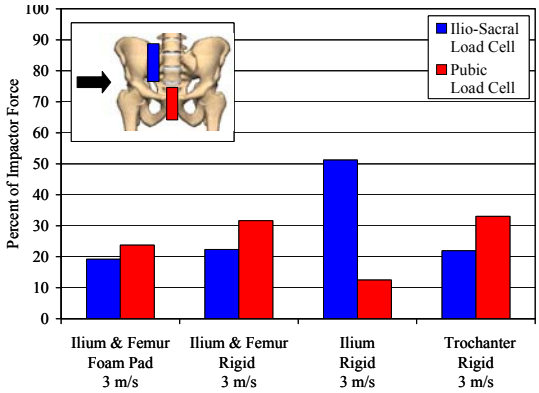

Figure 13: Cadaver 2 peak pelvic loads by test condition.

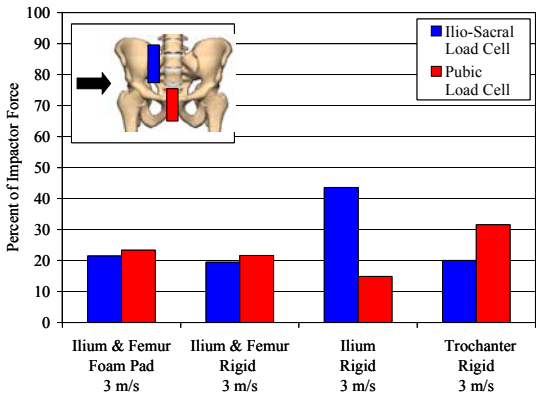

Figure 12: Cadaver 1 peak pelvic loads by test condition.

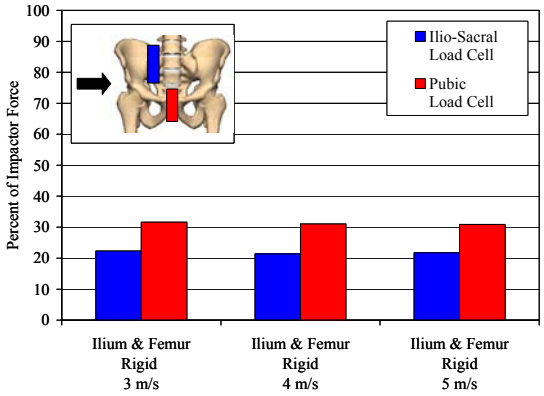

Figure 14: Cadaver 2 peak pelvic loads by loading rate.

Table 4: Peak impactor, ilio-sacral, and pubic forces.

Cadaver ID	Impact Location	Impactor Surface	Impact Speed	Peak Impactor Force	Peak Ilio-Sacral Force	Peak Pubic Force
				N	N	N
1	Ilium & Femur	Foam	3 m/s	1564	336	365
1	Ilium & Femur	Rigid	3 m/s	1654	322	358
1	Ilium	Rigid	3 m/s	1627	708	242
1	Trochanter	Rigid	3 m/s	1590	318	501
2	Ilium & Femur	Foam	3 m/s	1450	278	344
2	Ilium & Femur	Rigid	3 m/s	3100	693	980
2	Ilium	Rigid	3 m/s	2910	1490	363
2	Trochanter	Rigid	3 m/s	2982	654	986
2	Ilium & Femur	Rigid	4 m/s	4211	900	1307
2	Ilium & Femur	Rigid	5 m/s	6162	1340	1903

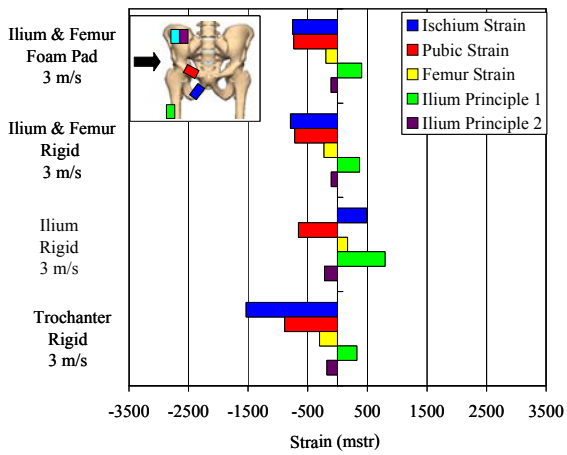

Figure 15: Cadaver 1 peak strain measurements. (primary mode of loading)

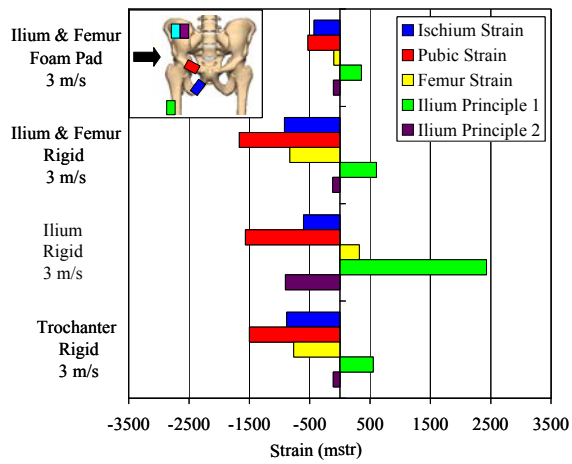

Figure 16: Cadaver 2 peak strain measurements. (primary mode of loading)

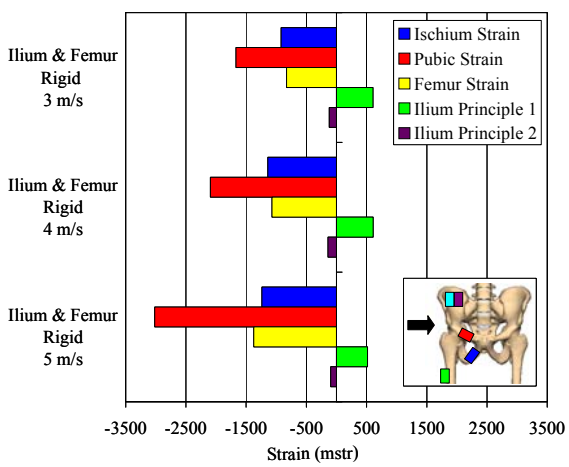

Figure 17: Cadaver 2 peak strain measurements by loading rates. (primary mode of loading)

DSCUSSION

The *in situ* load cell data showed that the only test condition that resulted in a larger percentage of the impactor load through the ilio-sacral joint than the pubic symphysis joint was when only the ilium was impacted. In all other test conditions, the pubic symphysis joint received a larger percentage of the impactor load than the ilio-sacral joint. In addition, the force time histories show that for all tests except the ilum only impact the pubic symphysis and ilio-sacral joints are essentially loaded simultaneously. The higher velocity tests performed on Cadaver 2 showed that impact speed did not have any considerable affect on the load distribution through the pelvis. Finally, the results show that for every test a considerable amount of the impactor force was lost; i.e. not transmitted though the pelvis, due to the inertia of the body.

In the current study, the strain distribution of the pelvis was quantified with the use of *in situ* strain gages. The strain gage data showed that for all test conditions both the superior pubic ramus and ischium were placed in compression. Although the primary mode of loading for the ischium during the ilum only impact was tension, the ischium was initially placed in compression (Figure A13). In addition, the strain time histories show that for all tests except the cadaver 1 ilum only impact the superior pubic ramus was loaded before the ischium. This is due to the fact that the superior pubic ramus is directly attached to the acetabulum and the main axis of the superior pubic ramus is relatively close to orientation of the applied load. Therefore, the geometry of the pelvis relative to the loading axis resulted in a lag in the loading of the inferior pubic ramus. The primary loading mode for the ilium 1st principle strain was tension for all test conditions, while primary loading mode for the ilium 2nd principle strain was compression for all test conditions. The only test condition which resulted in a tension load on the lateral side of the femur was when only the ilium was impacted. In all other test conditions, the femur was in compression. The higher velocity tests performed on Cadaver 2 showed that all stain measurements except the ilium 1st and 2nd principle strains increased with increasing impact speed.

CONCLUSIONS

In the current study the load transfer and deformation characteristics of the pelvis in side impact loading was quantified through 10 non-destructive tests performed on two human male cadavers. The results show that the only test condition which resulted in a larger percentage of the impactor load through the ilio-sacral joint than the pubic joint was when only the ilium was impacted. In all other test conditions, the pubic symphysis joint received a larger percentage of the impactor load than the ilio-sacral joint. The higher velocity tests performed on Cadaver 2 showed that impact speed did not have any considerable affect on the load distribution through the pelvis. For all tests a considerable amount of the impactor force was lost; i.e. not transmitted though the pelvis, due to the inertia of the body. With respect to pelvic strain, the results show that for all test conditions the superior pubic ramus and ilium 2nd principle strain were in compression. For all tests except one, a compressive load was placed on the ischium. Conversely, primary loading mode for the ilium 1st principle strain was tension for all test conditions. The only test condition which resulted in a tension load on the lateral side of the femur was when only the ilium was impacted. In all other test conditions, the lateral side of femur was placed in compression. The higher velocity tests performed on Cadaver 2 showed that ischium strain, superior pubic ramus strain, and femur strain increased with increasing impact speed. It is anticipated that this research will further the understanding of the biomechanical response of the human pelvis in side impact loading, and aid in the development and validation of computational models.

ACKNOWLEDGEMENTS

The authors would like to thank Toyota Motor Corporation for providing the funding for this research.

REFERENCES

[1] D. Beason, G. Dakin, R. Lopez, , J. Alonso, F. Bandak, and A. Eberhardt, “Bone mineral density correlations with fracture load in experimental side impacts of the pelvis,” *J. Biomechanics*, Vol. 36, pp. 219-217. 2003.

[2] R. Bouquet, and M. Ramet, “Thoracic and pelvis human responses to impact,” *Proc.*

14th International Conference on Enhanced Safety of Vehicles, Munich, Germany, 1994.

[3] R. Bouquet, M. Ramet, F. Bermond, Y. Caire, Y. Talantikite, S. Robin, and E. Voiglio, "Pelvis human responses to lateral impact," *Proc. 16th International Conference on Enhanced Safety of Vehicles*, Windsor, Ontario, Canada, 1998.

[4] J. Cavanaugh, Y. Haung, Y. Zhu, and A. King, "Regional tolerance of the shoulder, thorax, abdomen and pelvis to padding in side impact," Society of Automotive Engineers Transactions, Paper Number 930435, 1993.

[5] D. Césari, and M. Ramet, "Pelvic tolerance and protection criteria in side impact," *Proc. 26th Annu. Stapp Car Crash Conference*, SAE 1982.

[6] K. Inaba, P. Sharkey, D. Stephen, D. Redelmeier, F. Brenneman, "The increasing incidence of severe pelvic injury in motor vehicle collisions," *Injury*, vol. 35(8), pp. 759-765. 2004.

[7] A. Kemper, C. McNally, E. Kennedy, A. Rath, S. Manoogian, J. Stitzel, S. and Duma, , "Material properties of human rib cortical bone from dynamic tension coupon testing," *Stapp Car Crash Journal*, vol. 49, pp. 199-230. 2005.

[8] A. Kemper, C. McNally, C. Pullins, L. Freeman, and S. Duma, "The biomechanics of human ribs: Material and structural properties from dynamic tension and bending tests," *Stapp Car Crash Journal*, vol. 51, pp. 235-273. 2007.

[9] P. Rice, and R. Rudolph, "Pelvic Fractures," *Emergency Medicine Clinics of North America*, vol. 25(3), pp. 795-802. 2007.

[10] S. Rouhana, P. Bedewi, S. Kankanala, P. Prasad, J. Zwolinski, A. Meduvsky, J. Rupp, T. Jeffreys and L. Schneider, "Biomechanics of 4-p seat belt systems in frontal impacts," *Stapp Car Crash Journal*, vol. 47, pp. 367-399. 2003.

[11] D. Viano, I. Lau, and C. Asbury, "Biomechanics of the human chest, abdomen, and pelvis in lateral impact," *Accid. Anl. & Prev.*, vol. 21(6), pp. 553-574. 1989.

[12] D. Stein, J. O'Connor, J. Kufera, S. Ho, P. Dischinger, C. Copeland, , and T. Scalea, "Risk factors associated with pelvic fractures sustained in motor vehicle collisions involving newer vehicles," *J. Trauma,* vol. 61(1), pp. 21-30. 2006.

[13] E. Gokcen, A. Burgess, J. Siegel, S. Mason-Gonzalez, P. Dischinger, and S. Ho, "Pelvic fracture mechanism of injury in vehicular trauma patients," *J. Trauma*., vol. 36(6), pp.789-95. 1994.

Appendix

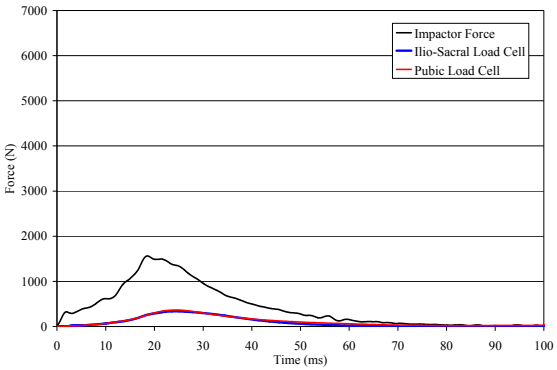

Figure A1: Cadaver 1 force vs. time (ilium and femur - foam pad - 3m/s)

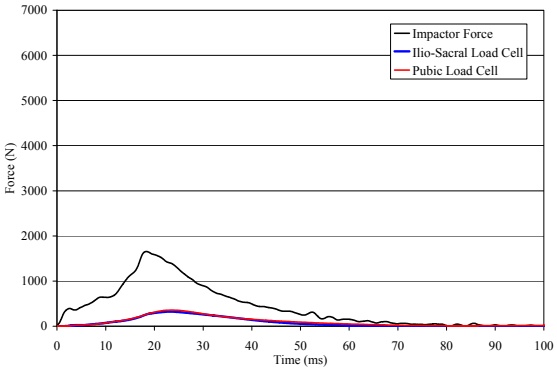

Figure A2: Cadaver 1 force vs. time (ilium and femur - rigid - 3m/s)

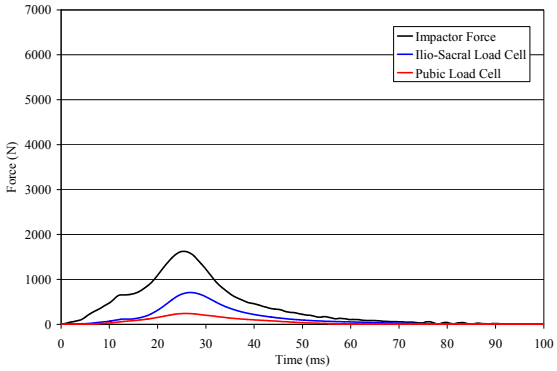

Figure A3: Cadaver 1 force vs. time (ilium- rigid - 3m/s)

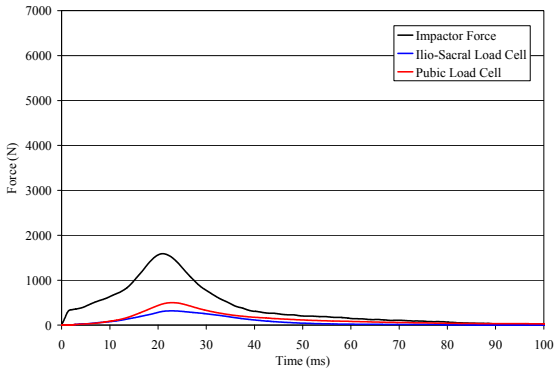

Figure A4: Cadaver 1 force vs. time (trochanter - rigid - 3m/s)

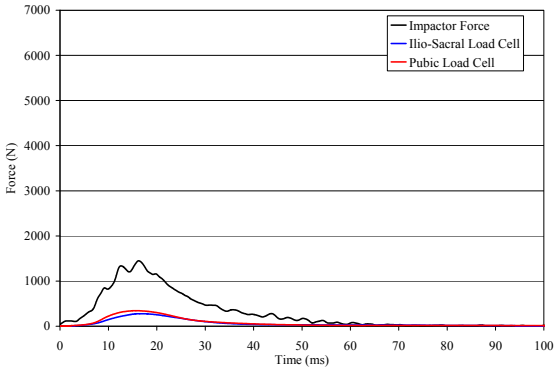

Figure A5: Cadaver 2 force vs. time (ilium and femur - foam pad - 3m/s)

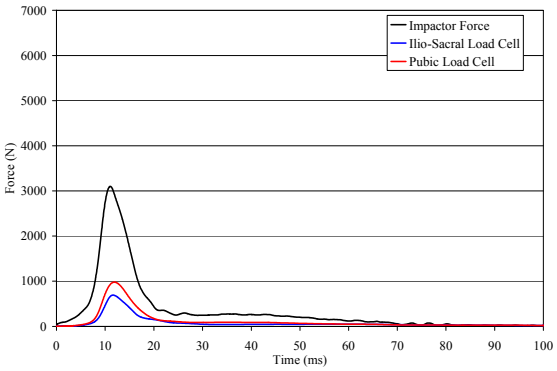

Figure A6: Cadaver 2 force vs. time (ilium and femur - rigid - 3m/s)

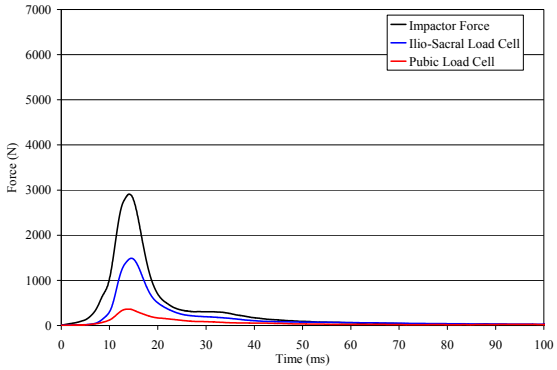

Figure A7: Cadaver 2 force vs. time (ilium - rigid - 3m/s)

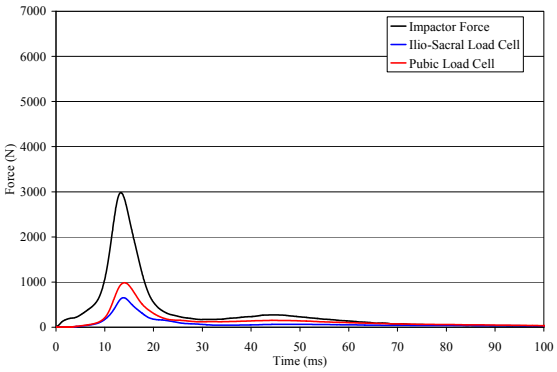

Figure A8: Cadaver 2 force vs. time (trochanter - rigid - 3m/s)

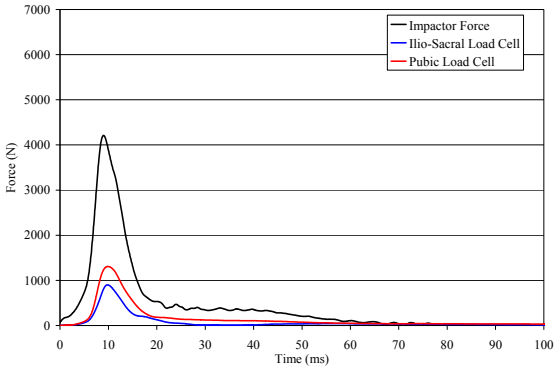

Figure A9: Cadaver 2 force vs. time (ilium and femur - rigid - 4m/s)

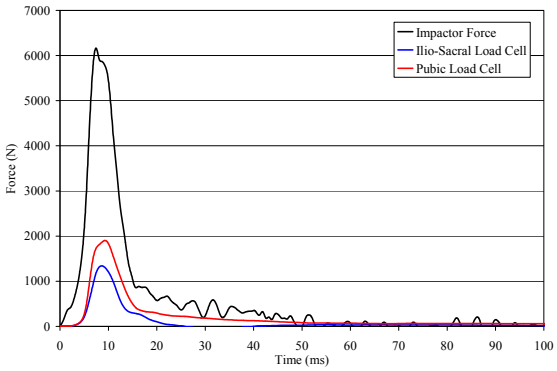

Figure A10: Cadaver 2 force vs. time (ilium and femur - rigid - 5m/s)

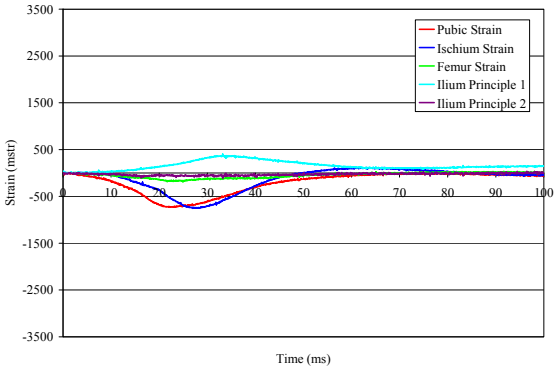

Figure A11: Cadaver 1 strain vs. time (ilium and femur - foam pad - 3m/s)

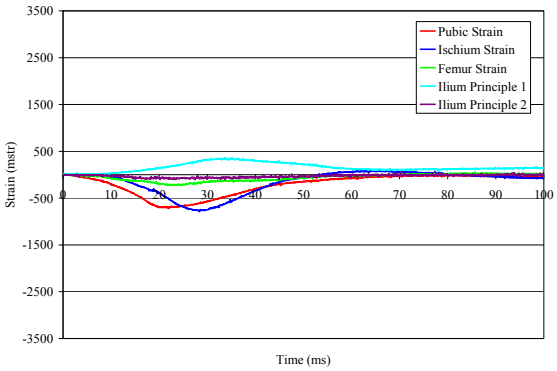

Figure A12: Cadaver 1 strain vs. time (ilium and femur - rigid - 3m/s)

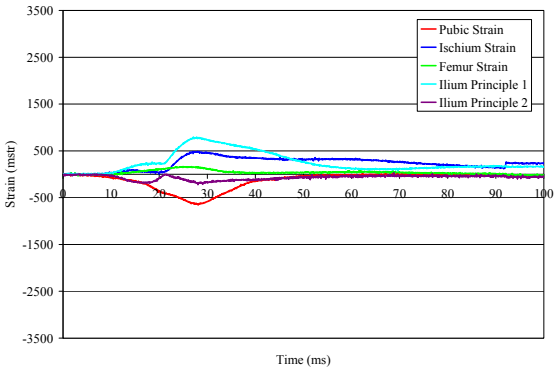

Figure A13: Cadaver 1 strain vs. time (ilium - rigid - 3m/s)

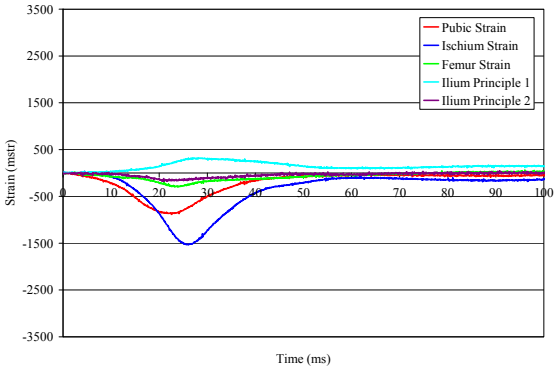

Figure A14: Cadaver 1 strain vs. time (trochanter - rigid - 3m/s)

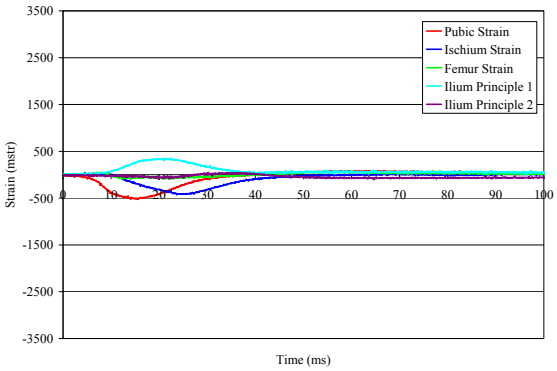

Figure A15: Cadaver 2 strain vs. time (ilium and femur - foam pad - 3m/s)

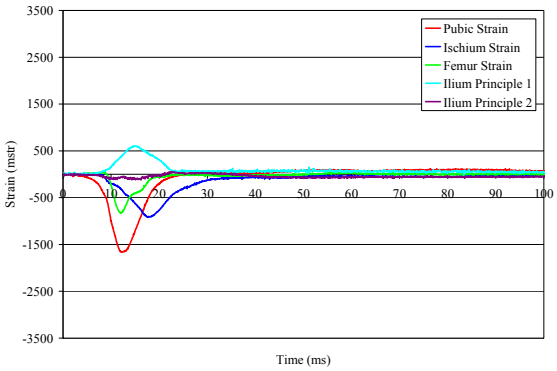

Figure A16: Cadaver 2 strain vs. time (ilium and femur - rigid - 3m/s)

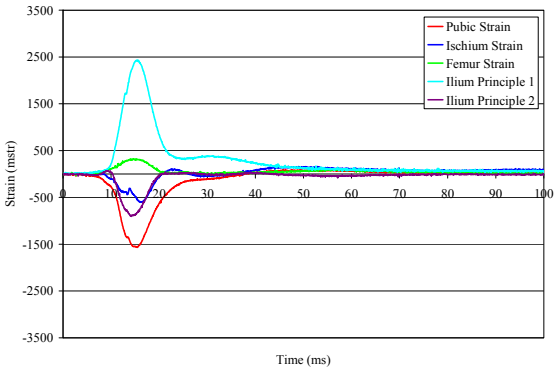

Figure A17: Cadaver 2 strain vs. time (ilium- rigid - 3m/s)

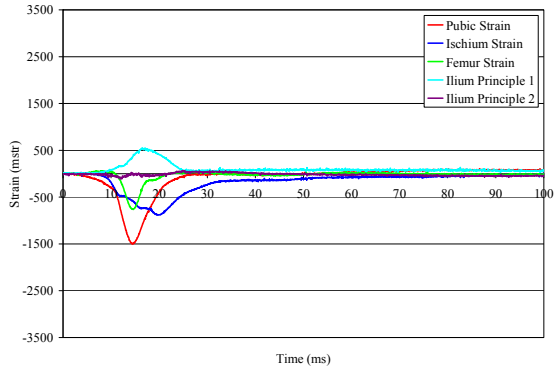

Figure A18: Cadaver 2 strain vs. time (trochanter - rigid - 3m/s)

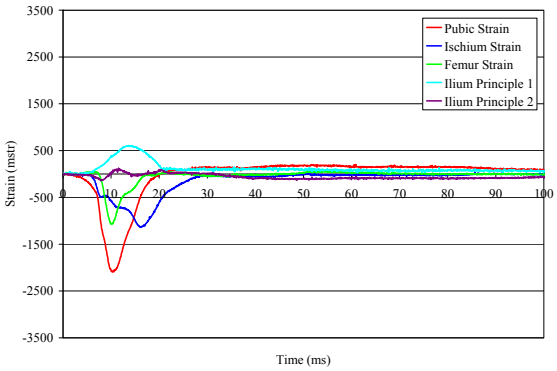

Figure A19: Cadaver 2 strain vs. time (ilium and femur - rigid - 4m/s)

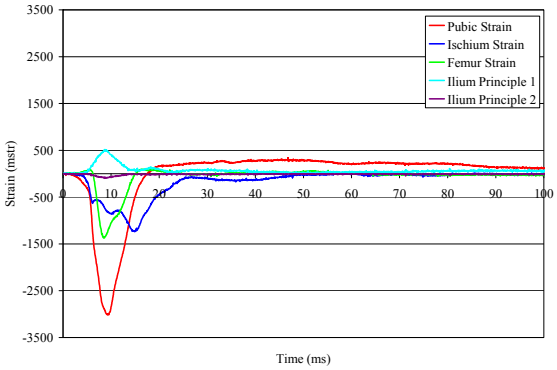

Figure A20: Cadaver 2 strain vs. time (ilium and femur - rigid - 5m/s)

DEVELOPMENT OF NEW CRITERIA FOR ASSESSING THE RISK OF KNEE-THIGH-HIP INJURY IN FRONTAL IMPACTS USING HYBRID III FEMUR FORCE MEASUREMENTS

Jonathan D. Rupp[1,2], Matthew P. Reed[1,4], Carl S. Miller[1], Nathaniel H. Madura[1], Kathleen D. Klinich, Shashi M. Kuppa[5], and Lawrence W. Schneider[1,3]

[1]University of Michigan Transportation Research Institute (UMTRI)

[2]The University of Michigan, Department of Emergency Medicine

[3]The University Michigan, Department of Biomedical Engineering

[4]The University Michigan, Department of Industrial and Operations Engineering

[5]National Highway Traffic Safety Administration

United States

Paper 09-0306

ABSTRACT

Injury patterns in real-world frontal crashes and the forces predicted in computational simulations of knee impacts suggest that the risk of hip injury is higher than the risk of knee/distal femur injury in most frontal crashes that are similar in severity to those used in FMVSS 208 and NCAP. However, the knee-thigh-hip (KTH) injury criterion that is currently used with Hybrid III femur forces in FMVSS 208 and NCAP only assesses the risk of knee/distal femur injury.

As a first step to developing new KTH injury assessment criteria that apply to hip and knee/distal femur injury, a one-dimensional lumped-parameter model of the Hybrid III ATD was developed and validated. Simulations were performed with this model and a previously validated lumped-parameter model of the cadaver to explore relationships between peak force at the Hybrid III femur load cell and peak force at the cadaver hip over the range of knee-loading conditions that occur in FMVSS 208 and NCAP crash tests. Results of these simulations indicate that there is not a singular relationship between peak Hybrid III femur force and peak force at the cadaver hip or at the knee/distal femur.

Because of the complex relationship between femur force measured in the Hybrid III femur load cells and forces and injury risks in the human KTH, a new injury assessment criterion has been developed for the KTH that uses peak force and impulse calculated from force histories measured by the Hybrid III load cell to determine if the probability of KTH injury exceeds a specified value. The use of impulse allows the new injury assessment criterion to identify the high-rate, short duration loading conditions that are likely to produce knee/distal femur fractures and the slower loading rates and longer durations that are more likely to produce hip fracture/dislocation.

INTRODUCTION

Fractures and dislocations (i.e., AIS 2+ injuries) to the knee-thigh-hip (KTH) complex occur in 2% to 3% of all tow-away frontal crashes of airbag-equipped vehicles (Kirk and Kuppa, 2009) and occur at a rate of approximately 30,000 per year in the US. (Rupp et al. 2002). Of these injuries, approximately 60% are to the shaft of the femur and hip (Kuppa and Kirk, 2009). Although a high proportion of KTH injuries are to the hip and femoral shaft, the risk curve used to establish the current 10-kN maximum femur force injury assessment reference value (IARV) used in FMVSS 208 and NCAP is based on a risk curve that was developed from fracture force data that are almost exclusively associated with knee and distal femur injuries (Rupp et al. 2002, Rupp 2006).

As part of a research program aimed at addressing this shortcoming, previous studies measured the force required to produce fracture of the human cadaver hip under knee-bolster-like loading conditions (Rupp et al. 2002 and 2003, Rupp 2006). Hip fracture force data from these tests were statistically analyzed to develop a new risk curve that expresses the probability of hip fracture as a function of force transmitted to the hip while accounting for stature and lower-extremity posture (Rupp 2008, Rupp et al. 2009). An earlier version of this risk curve was used along with the knee/distal femur injury risk curve reported by Kuppa et al. (2001) in a series of simulations with lumped parameter and finite element models of the KTH complex (Rupp et al., 2008, Chang et al. 2008). Results of these simulations predict that the hip is the part of the KTH complex that is most likely to be injured in a frontal crash for symmetric knee loading and in the absence of muscle tension.

Development of improved IARVs from these KTH injury risk curves is challenging because risk curves are based on fracture forces measured in testing of cadavers, while IARVs must apply to femur forces measured by the Hybrid III family of crash-test dummies. Specifically, results of previous studies demonstrate that the Hybrid III can produce

substantially higher knee impact forces than a similar sized cadaver and that forces at the femur load cell location (or anywhere else in the Hybrid III KTH complex) are different from the forces at corresponding locations in the cadaver (Donnelly and Roberts 1986, Masson and Cavallero 2003, Rupp et al. 2005). This suggests that either the response biofidelity of the Hybrid III dummy needs to be improved so that it produces similar KTH forces as the human, or that the KTH injury criteria need to be adjusted before the current Hybrid III ATD can be used to assess KTH injury risk in frontal crashes.

Typically, this adjustment would be developed empirically, using data from studies in which the knees of cadavers and ATDs are loaded using similar loading conditions, such as those by Donnelly and Roberts (1986) and Rupp et al. (2005). However, the empirical approach to adjusting injury criteria is only valid if the experimental knee-loading conditions span those that occur in crashes, which those reported in previous studies do not. In particular, the force-deflection characteristics of the surfaces used to load the knees in previous studies were either linear elastic or hyperelastic, and therefore do not represent current real-world knee bolsters, many of which are likely exhibit a force-limiting behavior. As a result, the relationships between forces measured by ATD femur load cells and force in the cadaver KTH developed from existing experimental data would not apply to many of the knee-loading conditions that are likely to occur in real-world crashes.

Figure 1 illustrates how knee bolsters with different force-deflection characteristics can produce different relationships between force applied to the dummy and human knee under similar loading conditions. For the linear elastic (constant stiffness) and hyperelastic knee bolsters, force applied to the knee is higher for the Hybrid III than for the similar-sized cadaver because the Hybrid III KTH is stiffer and has more tightly coupled mass than the cadaver KTH complex and therefore penetrates further into the knee bolster. For a force-limiting knee bolster, the Hybrid III knees still penetrate further into the knee bolster than the cadaver, but the peak forces applied to both the Hybrid III and cadaver knees are the same if the knees of both the Hybrid III and cadaver penetrate into the force-limiting region.

As a consequence of the differences in force applied to the knees of the cadaver and Hybrid III by each type of knee bolster, the relationships between force measured by the Hybrid III femur load cell and the risk of KTH injury (which is a function of force produced at the cadaver knee and hip) will vary with the force-deflection characteristics of the surface loading the knee. Because of this, and because previous research demonstrates that the knee-impact response of the cadaver varies with loading rate and loading duration (Atkinson et al. 1997, Yoganandan et al. 2001, Rupp 2006), an unreasonably large number of cadaver and Hybrid III knee-impact tests would need to be conducted to empirically define the relationships between forces in the human KTH and Hybrid III femur force measurements.

GENERAL APPROACH

Because a purely experimental approach is not feasible, this study used a computational approach to define relationships between forces measured by Hybrid III femur load cells and the risk of human KTH injury. This approach involved (1) developing and validating a lumped-parameter model of the Hybrid III midsize male ATD and then (2) performing simulations in which this model and the lumped parameter midsize male cadaver model (Rupp et al. 2008) were loaded by knee bolsters with a wide range of force-deflection characteristics. Results of these simulations were used to establish relationships between the risk of injury to the human cadaver KTH complex and forces measured by Hybrid III midsize male femur load cells. These relationships were then scaled using established techniques to develop new injury criteria for the Hybrid III small-female ATD.

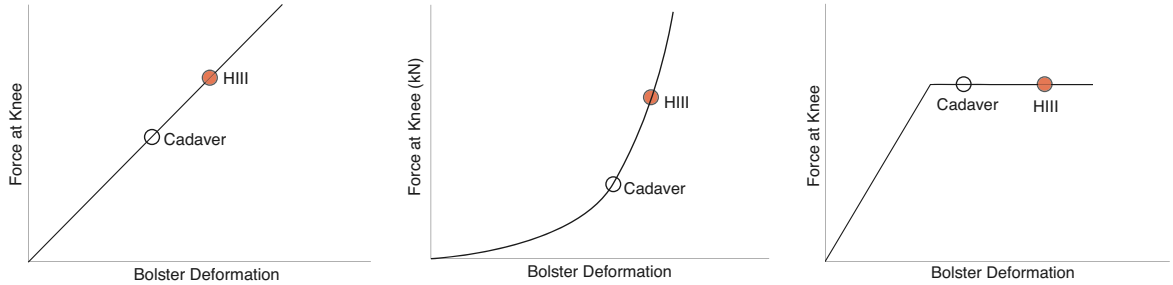

Figure 1. Force-deflection characteristics from linear-elastic (left), hyperelastic (middle), and force-limiting knee bolsters (right) illustrating peak applied force levels at the knee for midsize-male cadavers and the midsize-male Hybrid III.

DEVELOPMENT OF A HYBRID III LUMPED PARAMETER MODEL

The one-dimensional lumped parameter model that was developed to simulate the response of the Hybrid III midsize male ATD to symmetric knee loading is shown in Figure 2. This model represents the response of one side of the Hybrid III and is identical in form to the lumped parameter model that Rupp et al. (2008) used to describe the human cadaver knee impact response and to predict the drop in force between the knee and the hip. The methods used to develop the model involved defining known parameters from physical measurements of ATD components and identifying unknown parameters by simulating physical tests in which the knees of the a Hybrid III ATD were loaded and varying unknown model parameters were varied until predicted responses matched experimental results.

Model Formulation

There are 21 parameters in the Hybrid III model, including 7 masses, 6 springs, 6 damping coefficients, and two forces. Most of these parameters are known or can be inferred from the results of a series of physical tests in which the knees of a seated Hybrid III midsize male ATD were symmetrically loaded using the 1.2 m/s, 3.5 m/s, and 4.9 m/s loading conditions described by Rupp et al. (2008).

Table 1 summarizes the values for masses in the Hybrid III model. The static masses of the dummy knee, femur load cell, femur, and hip casting combine to form mA. Similarly, mB is also made up of the static masses of the dummy pelvis and thigh flesh. The stiffness and damping coefficients describing the coupling between the knee, femur, pelvis, and pelvis flesh were set so that the masses of the knee/femur (mA), the mass of the pelvis (mB), and the mass of the pelvis flesh (mC) were tightly coupled. Support for this is provided by the similarity in the magnitude and the phasing of femur and pelvis acceleration histories measured in symmetric knee impact tests performed on the Hybrid III ATD (Rupp et al. 2005). Because pelvis flesh is tightly coupled to the pelvis, it was not necessary to describe the mass of the pelvis flesh independently of that of the pelvic bone. Therefore, mB was set to the one half of the entire mass of the Hybrid III pelvis plus pelvis flesh and mC was set to a low value (0.001 kg).

Coupling between masses was described using linear springs and dampers in parallel, as shown in Figure 2, because this arrangement is thought to represent the simplest combination of elements that can appropriately describe the coupling of body segments across a wide range of knee impact conditions. Further, this arrangement was able to describe the response of the human cadaver to knee impact loading over a wide range of loading conditions and was therefore thought to be capable of modeling ATD response.

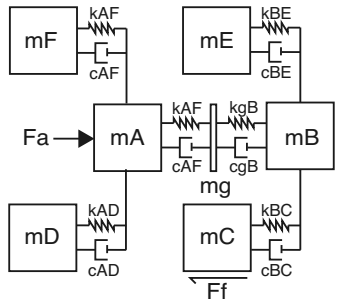

Figure 2. Lumped-parameter model.

Table 1. Descriptions of Masses in Hybrid III Midsize Male Lumped-Parameter Model

Mass	Descriptions
mA	Mass of knee, knee flesh, femur load cell, femur, and hip casting
mB	Mass of pelvis and flesh that is coupled to the pelvis
mC	Mass of the pelvis flesh
mD	Mass of leg below knee that is effectively coupled to the KTH
mE	Mass of torso that is effectively coupled to the pelvis
mF	Mass of thigh flesh that is coupled to femur
mg	Mass between femur and pelvis (set to 0.001 kg for all tests, needed so that femur force-deflection characteristics could be specified separately from those of the hip joint)

ATD Tests Used for Model Development

The ATD tests that were simulated to establish unknown parameters in the model are reported in the NHTSA biomechanics database (Test series ID NBED0607, Test Numbers 9346-9385). The methods for these tests are described by Rupp et al. (2005) and Rupp et al. (2008) and are therefore only summarized here.

The apparatus used in the Hybrid III tests is illustrated in Figures 2a and 2b. The apparatus functions by pneumatically accelerating a weighted platform into the knees of a stationary test subject. The velocity of the platform was set to be 1.2 m/s, 3.5 m/s, or 4.9 m/s just prior to impact. These velocities were used along with padding on the knee impact surfaces to produce knee loading rates and peak femur forces that were close to the 5th, 50th, and 95th percentiles of peak femur forces and loading

rates produced in FMVSS 208 and NCAP tests conducted between 1998 and 2004 (Rupp et al. 2008). For all tests, the ATD was seated in an upright posture with the knees at a 90˚ angle. The feet were supported by a platform whose height was adjusted to maintain this angle. The pelvis was supported by a force plate that measured the friction force produced by the pelvis flesh interacting with the platform. The ATD's feet were also supported by a different platform, the height of which was set so that the centerline of the impactor was aligned with the most forward surface on the knee. The Hybrid III midsize male ATD used in these tests was instrumented with a 6-axis femur load cell and triaxial accelerometer blocks were attached to the shaft of the femur, the pelvis, and the spine box. Prior to all tests, the knee response was verified by repeating the knee calibration test (SAE Dummy Testing and Equipment Subcommittee, 1998).

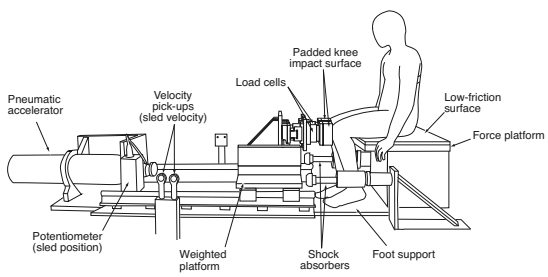

Figure 2a. Side-view (top) illustration of apparatus used to characterize ATD response.

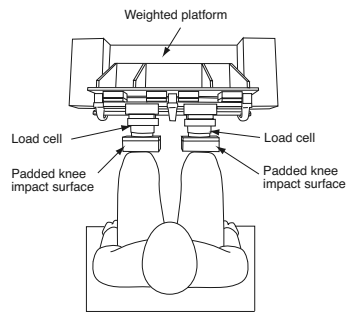

Figure 2b. Top-view (bottom) illustration of apparatus used to characterize ATD response.

Establishing Values for Unknown Model Parameters

Of the 21 model parameters (7 masses, 6 springs, 6 damping coefficients, and 2 forces), 15 are known and 6 are unknown, although reasonable bounds on all unknown parameters can be established. Table 2 lists values and data sources for the known parameters and bounds on the unknown parameters, which include the amounts of leg and torso mass that can couple to the KTH complex and the spring stiffnesses and damping coefficients that describe this coupling. Rows containing these unknown parameters are highlighted in Table 2.

Table 2. Parameters and Bounds on Parameter Values Used in Hybrid III Model

Element	Source	Value/Constraints
Fa	Test data	NA (from test data)
Ff	0.5*(Friction force applied to pelvis flesh)	NA (from test data)
mA	Static mass of Hybrid III knee + femur load cell + femur + hip casting mass	6.68 kg
mB	0.5*(Static mass of Hybrid III pelvis)	7.11 kg
mC	mC is rigidly coupled to mB and the mass of the pelvis flesh is treated as part of the pelvis.	0.001 kg
mD	Determined from optimization	0.1 < mD < 4.5 kg
mE	0.5*(Static mass of Hybrid III torso).	0.1 < mE < 20.8 kg
mF	Static mass of Hybrid III thigh flesh.	0.9 kg
mg	Set to near zero so that it has no effect on simulation results.	0.001 kg
k_{Ag}, c_{Ag}	Set to high values so that knee/femur/hip casting are effectively rigid.	k_{Ag} = 1,000 kN/m c_{Ag} = 25,000 Ns/m
k_{gB}, c_{gB}	Set to high values the coupling between the femur and pelvis is effectively rigid.	k_{gB} = 1,000 kN/m c_{gB} = 25,000 Ns/m
k_{BC}, c_{BC}	Set to high values the coupling between the femur and pelvis is effectively rigid.	k_{BC} = 1,000 kN/m c_{BC} = 25,000 Ns/m
k_{AD}, c_{AD}	Determined from optimization.	100 < k_{AD}< 50000 N/m 10 < c_{AD}< 5000 Ns/m
k_{BE}, c_{BE}	Determined from optimization.	0.01 < k_{BE} < 20 kN/m 10 < c_{BE} < 5000 Ns/m
k_{AF}, c_{AF}	Set to high values the coupling between the leg and knee is effectively rigid.	k_{BC} = 1,000 kN/m c_{BC} = 25,000 Ns/m

Bounds on the leg and torso masses were set so that the masses were varied between 0.1 kg and their static mass. Bounds on the coefficients describing the coupling of the masses to the KTH were set so that the coupling varied from loose (little effect on forces and accelerations predicted by the model) to stiff (effectively rigidly coupled).

The masses of the leg and torso that are effectively coupled to the KTH complex and the parameters describing the coupling between these masses and the KTH complex were determined using optimization techniques that are similar to those to define unknown parameters in the cadaver model by Rupp et al. (2008). In brief, the knee impact force histories from the 4.9 m/s test described above were applied to the knee of the Hybrid III model (mA). Unknown model parameters were then varied using a simulated annealing algorithm in Mathematica 6.0 (Wolfram Inc., Chicago, IL) until the until the sum of the areas between predicted and experimentally measured femur force and acceleration histories, and pelvis-acceleration histories in the direction of impact loading (x axis for pelvis and z-axis for femur) were minimized. For all model development simulations, half of the friction force measured by the force platform on which the ATD was seated was applied to the pelvis flesh (mC). Predicted femur force was calculated by inertially adjusting the predicted force at the connection between mA and mg using femur acceleration and the mass between mg and the femur load cell location (3.9 kg).

Table 3 shows the model parameters that produced the best fit of the experimental femur force, femur acceleration, and pelvis acceleration histories from the 4.9 m/s impact velocity. Figure 3 compares the femur force history predicted by the Hybrid III model to femur forces measured in repeated symmetric knee impacts performed using the Hybrid III midsize male ATD using the 4.9 m/s loading condition. Figures 4 and 5 make similar comparisons for femur and pelvis accelerations, respectively. All model predictions are within the range of experimentally measured responses from repeated tests on the same ATD.

Table 3. Parameters Used in Hybrid III Model

Param	Description	Final Value
mA	Static mass of Hybrid III knee, femur lc, femur, and hip casting	6.68 kg
mB	0.5*(Static mass of Hybrid III pelvis)	7.11 kg
mC	Mass of pelvis flesh (assumed to be tightly coupled to the pelvis)	0.001 kg
mD	Mass of leg from optimization	0.5 kg
mE	Coupled torso mass of, from optimization	5.4 kg
mF	Static mass of Hybrid III thigh flesh	0.9 kg
mg	Set to near zero so that it has no effect on simulation results	0.001 kg
k_{Ag}, c_{Ag}	Stiffness and damping coefficient between knee/femur and hip	k_{Ag} = 3,000 kN/m c_{Ag} = 25 kNs/m
k_{gB}, c_{gB}	Stiffness and damping coefficient of hip	k_{gB} = 3,000 kN/m c_{gB} = 30 kNs/m
k_{BC}, c_{BC}	Stiffness and damping coefficient between pelvis and pelvis flesh	k_{BC} = 1,000 kN/m c_{BC} = 25 kNs/m
k_{AD}, c_{AD}	Stiffness and damping coefficient between leg and knee/femur	k_{AD}= 13.52 kN/m c_{AD}= 1 kNs/m
k_{BE}, c_{BE}	Stiffness and damping coefficient between pelvis and torso	k_{BE}= 0.5 kN/m c_{BE}= 1.5 kNs/m
k_{AF}, C_{AF}	Stiffness and damping coefficient between thigh flesh and femur	k_{BC} = 100 kN/m c_{BC} = 25 kNs/m

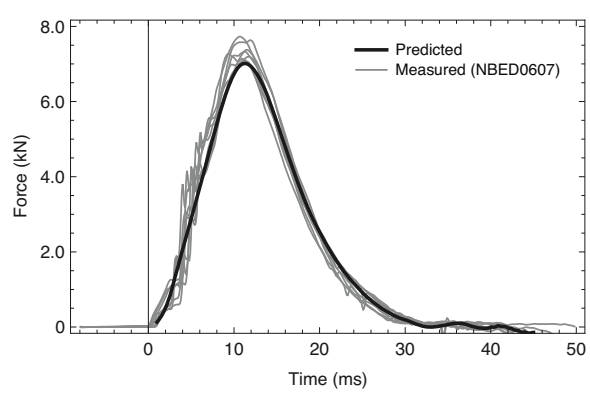

Figure 3. Predicted and experimentally measured femur force from 4.9 m/s tests.

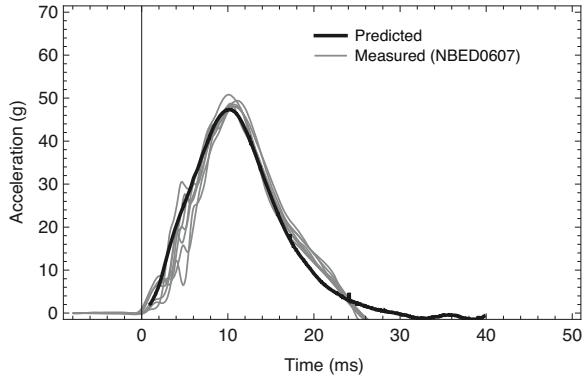

Figure 4 Predicted and experimentally measured femur Z-axis accelerations from 4.9 m/s tests.

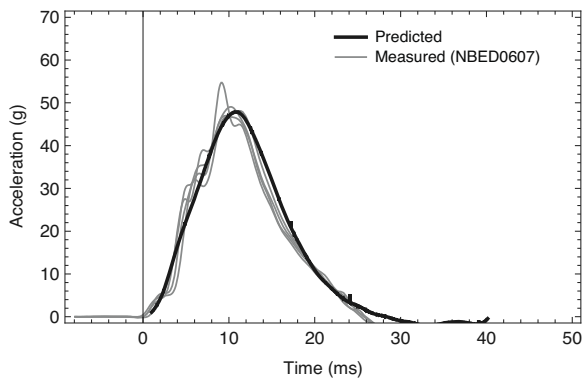

Figure 5. Predicted and experimentally measured pelvis X-axis accelerations from 4.9 m/s tests.

Model Validation

Model validation was performed by applying the average force histories applied to the Hybrid III ATD knees in repeated tests at the 3.5 m/s and 1.2 m/s impact velocities to the knee of the Hybrid III model and then comparing experimentally measured and predicted femur force, femur acceleration, and pelvis acceleration histories. To further verify that the parameters describing masses and the coupling of masses were appropriate, knee impacts in which the torso and thigh flesh had been removed from a Hybrid III midsize male ATD were also simulated. These tests were conducted using the 1.2 m/s, 3.5 m/s, and 4.9 m/s impact conditions described above. Predicted and measured femur force and acceleration, and pelvis acceleration, were compared. To simulate tests in which the dummy torso and the dummy thigh flesh were removed, the masses of these components in the lumped parameter model were set to 0.001 kg, so as to be close to zero but still high enough so that model predictions were stable.

Model validation results are shown in Figures 6 through 11. Figures 6 through 8 show that model predictions for femur force, femur z-axis acceleration, and pelvis x-axis acceleration from whole ATD tests at 3.5 m/s, respectively, are within the range of experimental results. Although not shown in this paper, a similar finding held for simulations of whole-dummy tests at 1.2 m/s.

Figures 8 through 11 demonstrate that model predictions of femur force, femur acceleration, and pelvis acceleration are within the ranges of experimentally measured values for simulations of tests in which thigh flesh and torso were removed at the 3.5 m/s impact condition. Simulations of the tests in which only the torso was removed (not shown here) indicate similar agreement with experimental results.

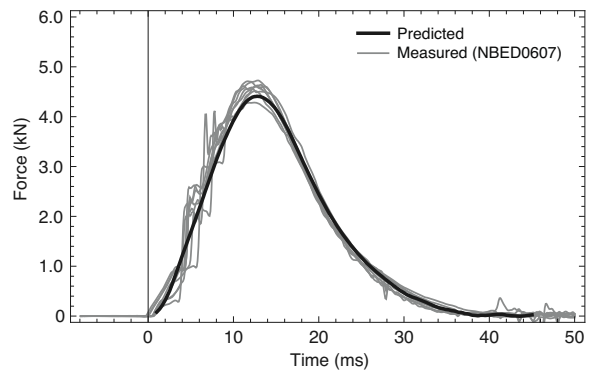

Figure 6. Predicted and experimentally measured femur forces from tests at 3.5 m/s with the whole Hybrid III midsize male ATD.

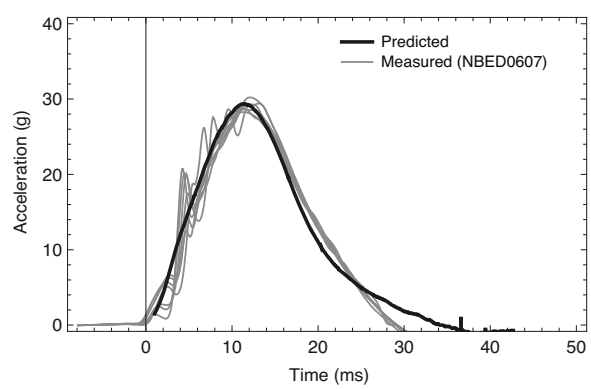

Figure 7. Predicted and experimentally measured femur z-axis accelerations from tests at 3.5 m/s with the whole Hybrid III midsize male ATD.

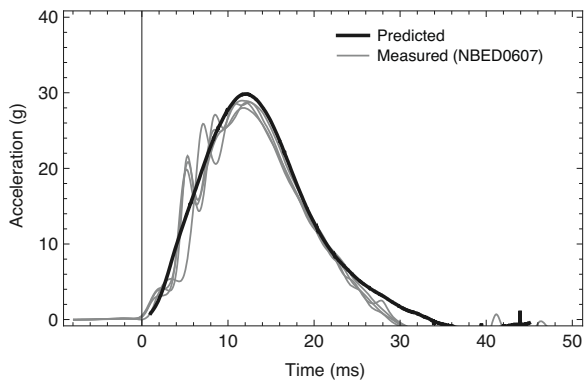

Figure 8. Predicted and experimentally measured pelvis x-axis accelerations from tests at 3.5 m/s with the whole Hybrid III midsize male ATD.

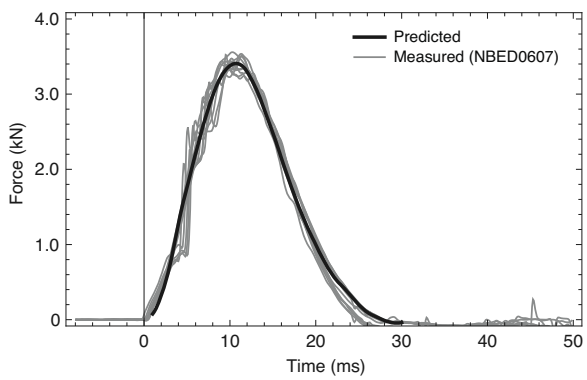

Figure 9. Predicted and experimentally measured femur forces from 3.5 m/s tests with the dummy torso and thigh flesh removed.

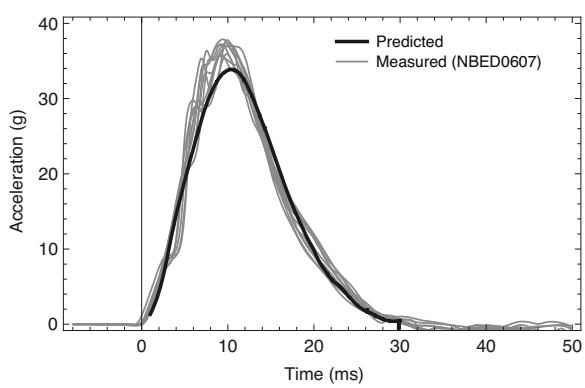

Figure 10. Predicted and experimentally measured femur z-axis accelerations from 3.5 m/s with the dummy torso and thigh flesh removed.

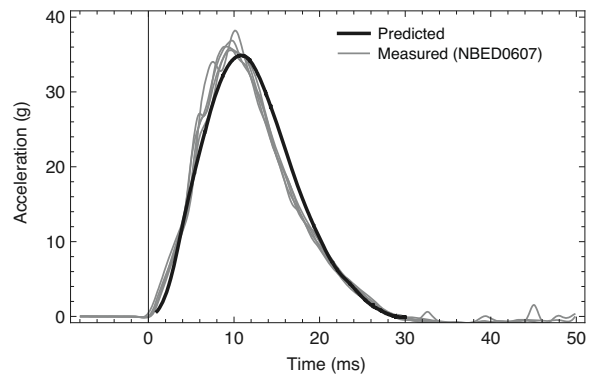

Figure 11. Predicted and experimentally measured pelvis x-axis accelerations from 3.5 m/s tests with the dummy torso and thigh flesh removed.

SIMULATIONS TO ESTABLISH INJURY ASSESSMENT CRITERIA

Simulations to Explore Relationships Between Peak Force at the Femur Load Cell and Peak Force at the Cadaver Hip

The relationship between Hybrid III peak femur force and risk of knee/distal femur injury is specified by existing injury criteria (i.e., the knee/distal femur risk curves reported by Kuppa et al. 2001 and Rupp et al. 2009). However, the relationship between peak force at the Hybrid III femur load cell and peak force at the human hip under similar knee-loading conditions is not known. Therefore, as a first step in developing new IARVs for the KTH complex, a series of simulations was performed to explore the relationships between peak forces in the cadaver and Hybrid III midsize male KTH complexes produced by similar knee-loading conditions.

In this series of simulations, the cadaver and Hybrid III models were loaded by simulated knee bolsters with three different types of force-deflection characteristics, including linear force-deflection (constant stiffness), bilinear force-deflection, and force-limiting. Figure 12 illustrates these force-deflection characteristics and shows how they were parameterized.

These three types of knee bolsters were selected because they span the range of force-deflection characteristics expected to occur in current production knee bolsters. In particular, a force-limiting knee bolster represents an ideal knee bolster design for a particular size of occupant because it limits the force applied to the knee while maximizing the amount of energy absorbed over the least amount of knee bolster compression. In contrast, for a

constant-stiffness knee bolster, the force applied to the knees increases linearly with compression of the bolster until the knees are completely stopped. A knee bolster with a bilinear force-deflection characteristic represents the scenarios where the stiffness of the knee bolster either suddenly decreases from yielding of components or suddenly increases because the occupant's knees bottom out the bolster.

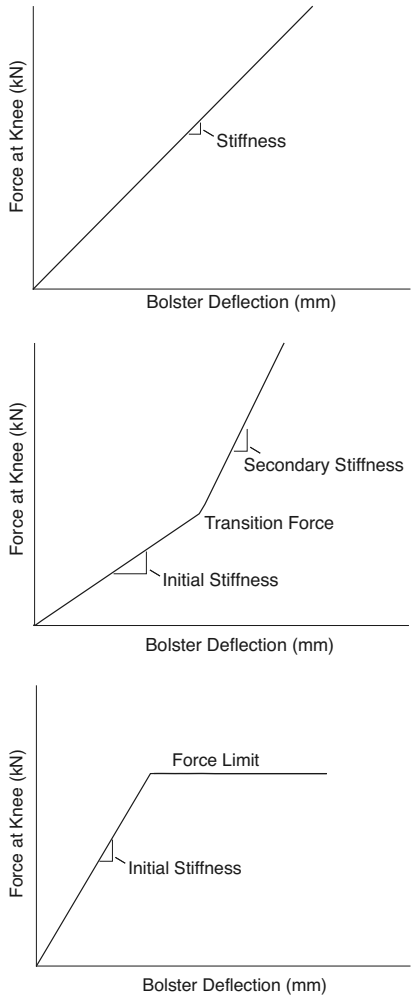

Figure 12. Illustrations of knee bolster force-deflection characteristics used in simulations: constant stiffness (top), bilinear force-deflection (middle), and force-limiting (bottom).

Table 4 lists the ranges of knee bolster force-deflection characteristics and impact velocities used in the simulations. These ranges were selected so that the simulated knee-loading conditions produced peak Hybrid III femur forces and loading rates that span the upper portion of the ranges of those that occur in FMVSS 208 and US NCAP tests. Knee bolster stiffness in these simulations was varied from 50 N/mm to 450 N/mm. The lower bound on knee bolster stiffness is based on data reported by Rupp et al. (2007), who loaded isolated production knee bolsters with cadaver knees. The upper bound on knee bolster stiffness is based on simulation results reported by Rupp et al. (2008), which indicated that a bolster stiffness above 450 N/mm produces knee-loading rates in excess of 2 kN/ms, which previous studies have associated with knee loading by a rigid (non-knee-bolster like) surface (Rupp et al. 2002, Rupp et al. 2007).

Table 4. Ranges of Parameters Used in Simulations

Bolster Type	Parameter Ranges
Force Limiting	Initial Stiffness: 200 to 450 N/mm Force Limit: 4 kN to 18 kN, Velocity: 3 to 8 m/s
Linear Force-Deflection	Stiffness: 50 to 450 N/mm Impact velocity: 2 to 8 m/s
Bilinear Force-Deflection	Initial stiffness: 50 to 450 N/mm Transition force: 2 to 8 kN Secondary stiffness: 50 to 250 N/mm Impact velocity: 2 to 8 m/s

To simulate knee-to-knee bolster loading, the lumped-parameter model was modified so that the force-based driving function was replaced by a 500-kg impactor mass, mI, which was connected to the knee by a spring. The stiffness of this spring, kIA, represents the combined stiffness of the impactor and the knee surface. The modified model is shown in Figure 13.

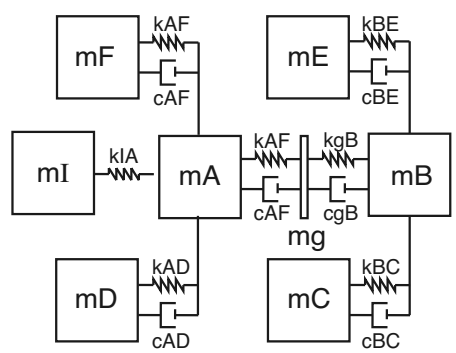

Figure 13. Lumped-parameter model with knee-bolster mass (mI).

Figure 14 compares the range (shaded area) of peak femur forces and loading rates produced in the simulations with the Hybrid III lumped-parameter model using the combinations of loading conditions listed in Table 4, to peak femur forces and loading rates from FMVSS 208 and NCAP tests from 1998-2004. To generate the data points in Figure 14, loading rate was calculated by taking the slope of the force history from the Hybrid III femur load cell

between 15% and 85% of peak force. Figure 14 shows that the knee-loading conditions used in the simulations span the upper portion of loading rates that occur in staged frontal crashes. As a result, these simulations represent knee-impact forces that are likely to produce significant risks of KTH fractures and are therefore relevant to exploring the relationship between Hybrid III femur force and force at the cadaver hip as it pertains to KTH injury assessment

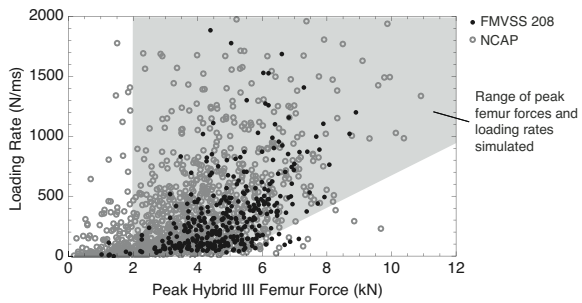

Figure 14. Comparison of peak Hybrid III femur forces and loading rates from FMVSS 208 and NCAP tests to combinations of similar parameters produced in all simulations.

Figures 15 and 16 illustrate the relationships between forces at different locations in the Hybrid III and cadaver KTH complexes that were produced by simulations with the Hybrid III and cadaver lumped-parameter models. Figure 15 shows forces at the knee, femur load-cell of the Hybrid III ATD, and hip that have been normalized by dividing the peak applied force at the knee. As illustrated by Figure15, the percentage of peak force at the Hybrid III knee that is transmitted to the femur load cell and the percentage of peak force applied to the cadaver knee that is transmitted to the hip are approximately 77% and 55%, respectively. Importantly, these values are relatively constant over the range of simulated knee-loading conditions. This finding indicates that knee loading by a surface that applies the same force to the knees of the cadaver and the Hybrid III (i.e., a force-limiting knee bolster) will produce a ratio of peak force at the femur load cell to peak force at the cadaver hip of 1.4 (0.77/0.55).

Because a singular relationship exists between peak force at the Hybrid III femur load cell and peak force at the cadaver hip for knee loading by a force-limiting knee bolster when both the cadaver and the Hybrid III load the bolster to the force limit, peak femur force can be used to predict the risks of both knee/distal femur injury and hip injury. For example, as illustrated by the thick black and gray lines in Figure 16, knee loading by a force-limiting knee bolster that applies a force of 8.3 kN to both the Hybrid III and cadaver knees will produce a peak Hybrid III femur force of ~6.4 kN and force at the cadaver hip of ~4.6 kN (6.4/1.4). Using the knee/distal femur and hip injury risk curves reported in Equations 1 and 2 in the following section of this paper, 6.4 kN at the Hybrid III femur load cell corresponds to an ~8% risk of knee/distal femur fracture and a ~25% risk of hip fracture/dislocation.

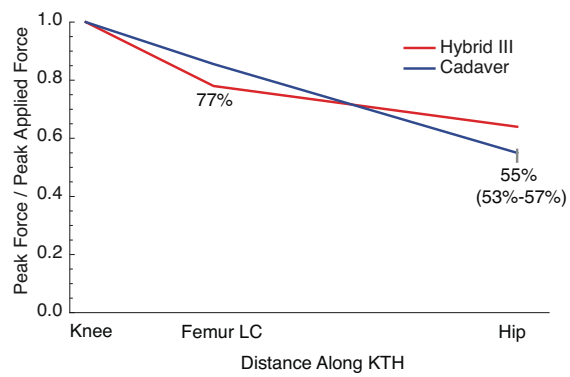

Figure 15. Percentages of force transmitted from the knee to the cadaver hip and from the knee to the Hybrid III femur load cell produce in all simulations.

For knee loading by knee bolsters that are not-force limiting (or loading by a force-limiting knee bolster that is not impacted at a velocity sufficient to generate a force in excess of its force limit), the peak force applied to the Hybrid III knee will always be greater than the peak force applied to the cadaver knee. This is because the Hybrid III has greater effective mass and stiffness than the cadaver and will therefore penetrate further into the knee bolster, regardless of bolster force-deflection characteristics.

Figure 16 illustrates the implications of the differences in knee impact force produced by different types of knee bolsters on the relationships between peak forces at in the Hybrid III and cadaver KTH complexes for all loading conditions that produce a 25% risk of hip fracture. Since all forces in Figure 16 are associated with the same risk of injury to the cadaver hip, they are associated with the same force at the cadaver hip (4.56 kN). As discussed earlier, the thick gray and black lines in Figure 16 represent the Hybrid III and cadaver responses produced by knee loading by a force-limiting knee bolster. The gray shaded area in Figure 16 illustrates how, for knee loading by a knee bolster that is not force-limiting (e.g., a constant-stiffness bolster) a higher peak force will be applied to the

Hybrid III knee and that this produces greater differences between peak Hybrid III femur force and force at the cadaver hip. As a result, knee loading by a force-limiting knee bolster will always produce the smallest possible difference between peak force at the Hybrid III femur load cell and peak force at the cadaver hip.

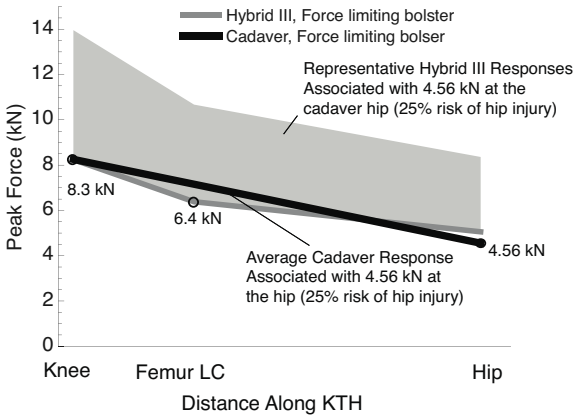

Figure 16. Relationships between peak forces at different locations in the cadaver and Hybrid III KTH complexes associated with a 25% risk of KTH injury (i.e., a force of 4.56 kN at the cadaver hip).

In summary, Figure 16 illustrates that there is no singular relationship between peak force at the Hybrid III femur load cell and peak force at the cadaver hip that is valid over the full range of knee bolster force-deflection characteristics that are thought to occur in production vehicles. As a result, it is not reasonable to base IARVs for the entire KTH complex on peak Hybrid III force alone. However, as discussed below, it is possible to develop injury assessment criteria for the hip that define the set of femur force histories that can be associated with a risk hip injury in excess of a target value.

Development of KTH Injury Assessment Criteria for the Hybrid III Midsize Male ATD

Simulations with the cadaver model reported by Rupp et al. (2008) demonstrate that the risk of hip injury is higher than the risk of knee or distal femur injury over most of the range of loading conditions that occur in frontal crashes. However, these simulations also demonstrate that the likelihood of knee/distal femur injury is higher than the likelihood of hip injury for high-rate, short-duration knee loading. This is because under these conditions, the femur has not displaced enough to recruit sufficient pelvis mass to produce a force at the hip that corresponds to a risk of hip injury that is greater than the risk of knee/distal femur injury associated with the force applied to the knee.

These observations suggest that injury criteria for the entire KTH should assess the risk of knee/distal femur injury for high-rate and short-duration loading, and should assess the risk of hip injury for the lower-rate, longer-duration loading conditions that are more typical of those produced in frontal crashes. Since a comprehensive KTH injury assessment criterion must determine whether to assess hip or knee/distal femur injury risk, such a criterion will need to incorporate a parameter that relates to femur displacement that can be measured by the Hybrid III femur load cell. For the injury assessment criteria development effort described below, this parameter was impulse (the integral of the femur force history between two points in time).

When plotted, the combination of the Hybrid III femur forces associated with a specified level (e.g., 25%) of knee/distal femur injury risk and hip injury risk along with the transition impulse that defines the transition between the two methods of injury assessment takes the form illustrated in Figure 17. Since the generalized injury assessment criterion shown in Figure 17 is a boundary and not a single value, or set of values, it has been termed an "injury assessment reference boundary." The three parts of the injury assessment reference boundary are called the lower- force limit (or hip-injury risk-based limit), the transition impulse, and the upper-force limit (or knee/distal-femur risk-based limit).

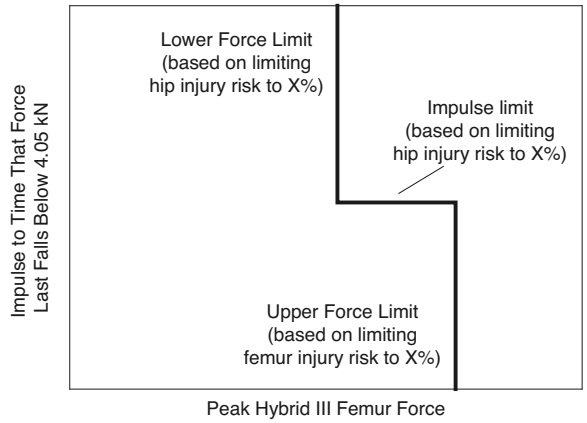

Figure 17. Generalized form of the KTH injury assessment reference boundary.

For all injury assessment reference boundaries, the transition impulse was determined by integrating Hybrid III femur force from the start of loading to the time that force last fell below 4.05 kN, as illustrated

in Figure 19. This value was chosen because it is the Hybrid III femur force that corresponds to the lowest hip fracture force of 2.89 kN reported by Rupp et al. (2003) – i.e., 4.05 = 1.4 times 2.78.

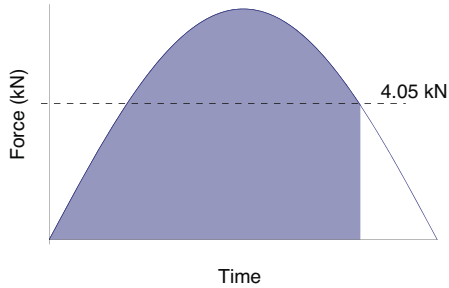

Figure 18. Impulse calculation.

Upper-force limit – The forces associated with the upper-force limit for a given level of knee/distal femur injury risk and hip injury risk were established using the injury risk curve in Equation 1.

$$Risk_{Knee/DistalFemurFX} = 1 - Exp\left[Exp\left[\frac{\ln[F] - 2.514}{0.2611}\right]\right] \quad [1]$$

where F is the peak compressive force measured by the Hybrid III femur load cell in kN and risk lies between zero and one.

Equation 1 is a slightly modified version of the risk curve that underlies the current FMVSS 208 maximum femur force criterion (Kuppa et al. 2001) that accounts for censoring in the knee impact fracture force data that were used to develop the current FMVSS 208 KTH injury risk curve (Rupp et al. 2009). This risk curve defines the risk of knee/distal femur injury in terms of peak force at the Hybrid III femur load cell.

Lower-force limit – Equation 2 defines the relationship between hip injury risk and force at the human hip as a function of occupant stature and hip posture (Rupp et al. 2009):

$$Risk_{HipFX} = \Phi\left[\frac{\ln[F] - (0.2141 + 0.0114s)*(1-(f-a)/100)}{0.1991}\right] \quad [2]$$

where, Φ is the cumulative distribution function of the standard normal distribution,
F is peak force transmitted to the hip in kN,
s is the stature of the target population for the risk curve (178 cm for midsize males),
f is the hip flexion angle in degrees, and
a is the hip abduction angle in degrees.

For developing midsize male injury assessment criteria, a stature of 178 cm was used and hip posture was set to 15˚ hip abduction and 30˚ flexion, which has been estimated to represent the typical hip posture at the time of peak femur force in full frontal crashes (Rupp et al. 2008). For reference, Figure 19 compares hip and femur injury risk curves.

Once the force at the human hip associated with a given level of hip injury risk was calculated, the lower-force limit was determined by multiplying this value by 1.4. As discussed above, this value represents the ratio of peak femur force at the Hybrid III femur load cell to peak force at the cadaver hip for knee loading by a force-limiting knee bolster, which, by virtue of applying the same force to the Hybrid III ATD and cadaver knees, produces the smallest possible difference between peak Hybrid III femur force and force at the cadaver hip.

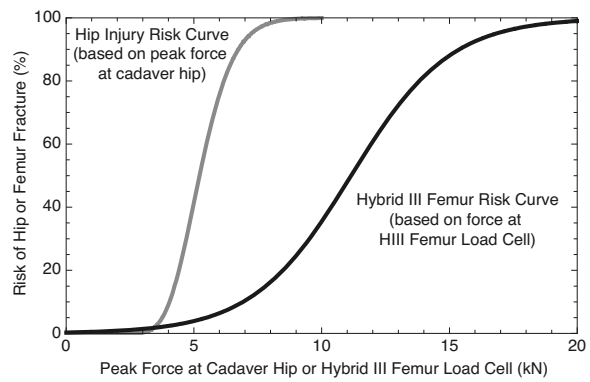

Figure 19. Femur injury risk curve and hip injury risk curve developed using with a stature of 178 cm and 15˚ abducted and 30˚ flexed hip posture.

Transition impulse–For a given level of KTH injury risk, the transition impulse was established by performing simulations with the Hybrid III and cadaver models to identify the smallest value of impulse that can be associated with a risk of hip injury above a specified percentage for peak femur forces between the upper and lower-force limits. Because the goal of these simulations was to establish the minimum impulse value associated with a given risk of hip injury, all of the transition impulse development simulations were performed using the highest knee bolster stiffness that was reasonable, which, for reasons previously noted, was 450 N/mm. The rationale for this approach was that the highest possible knee-loading rate produces the shortest duration of applied force, and therefore the smallest impulse, necessary to generate a specific force at the hip (and a specific level of hip injury risk).

When the knees of the cadaver model were loaded using a knee bolster with a stiffness of 450 N/mm, there was only a single knee impact velocity that produced a force at the cadaver hip associated with the target level of hip injury risk. However, this combination of impact velocity and bolster stiffness always produced a peak Hybrid III femur force that was greater than the value associated with the upper-force limit. Since the transition impulse does not apply to this loading condition, the force-deflection characteristics of the knee bolster were modified so that the knee bolster was force-limiting and had a force limit that produced a peak femur force that corresponded to the level of risk associated with the transition impulse. The impulse of the femur force produced by this knee bolster stiffness and impact velocity, calculated in the manner described above, represents the minimum impulse that can be associated with a given level of hip injury risk. This finding was confirmed by an alternate approach to transition impulse development in which knee bolster force-deflection characteristics and impact velocity were varied until the minimum impulse necessary to produce a given risk of hip injury was determined for forces between the upper and lower-force limits.

Example Development of 25% Risk Boundary–A more detailed example of how the injury assessment reference boundaries were developed is provided below and in Figure 20 for the injury assessment reference boundary corresponding to a 25% risk of KTH injury. Based on Equation 2, peak force at the cadaver hip associated with a 25% risk of hip injury is 4.56 kN. Multiplying this value by 1.4 indicates that the lower-force limit is 6.38 kN. As illustrated in the left column of Figure 20, the lower-force limit is produced through knee loading by a force limiting knee bolster with a force limit of 8.25 kN, which produces 4.56 kN at the cadaver hip and 6.38 kN at the Hybrid III femur load cell. As discussed above, this is because a force limiting knee bolster produces the smallest possible Hybrid III femur force that can be associated with a 25% risk of hip injury. To produce the responses shown in the left column of Figure 20, an impact velocity of 6.25 m/s was used. This velocity was selected because it is large enough so that the cadaver model knee sufficiently compresses the knee bolster to exceed its force limit.

The middle part of Figure 20 shows the loading condition and simulation results that define the transition impulse for the 25% risk boundary. For reasons discussed above, this loading condition was determined by loading the knees of the cadaver and Hybrid III models with a force limiting knee bolster with an initial stiffness of 450 N/mm. The force limit for this knee bolster was set to 11.56 kN, which produces a peak Hybrid III femur force of 8.93 kN, which Equation 1 associates with a 25% risk of knee/distal femur injury.

Simulations with the cadaver model using these loading characteristics indicated that an impact velocity of 5.2 m/s produced peak force at the hip of 4.56 kN (i.e., a 25% risk of hip injury). Since a 5.2 m/s impact velocity produces a force at the cadaver knee that is below the bolster force limit, the cadaver knee does not penetrate far enough into the knee bolster to reach the limiting force, as shown in the top and bottom cells in the middle column of Figure 20. However, as is also shown in Figure 20, at this impact velocity, force at the Hybrid III knee reaches the force limit. The impulse of the Hybrid III femur force, calculated using the procedure shown in Figure 18, associated with this loading condition is 137.1 Ns. This value is the smallest impulse capable of producing a force at the hip in excess of the value associated with 25% KTH injury risk, provided that knee bolster stiffness is not greater than 450 N/mm and that peak Hybrid III femur force is less than the upper-force limit for knee/distal femur injury.

The right side of Figure 20 shows the results of a simulation that was performed to check the transition impulse of the 25% injury risk boundary. This simulation used the same knee-bolster force-deflection characteristics as those used to establish the lower-force limit (8.25 kN force limit with a 450 N/mm initial stiffness), and a knee-impact velocity that resulted in an impulse of 137.1 Ns at the Hybrid III femur load cell. As shown in the bottom right part of Figure 20, at this impact velocity, there is not a sufficient amount of impact energy to cause the force at the knee to exceed the knee bolster force limit for a duration that is long enough for force at the hip to exceed the value associated with a 25% risk of hip injury.

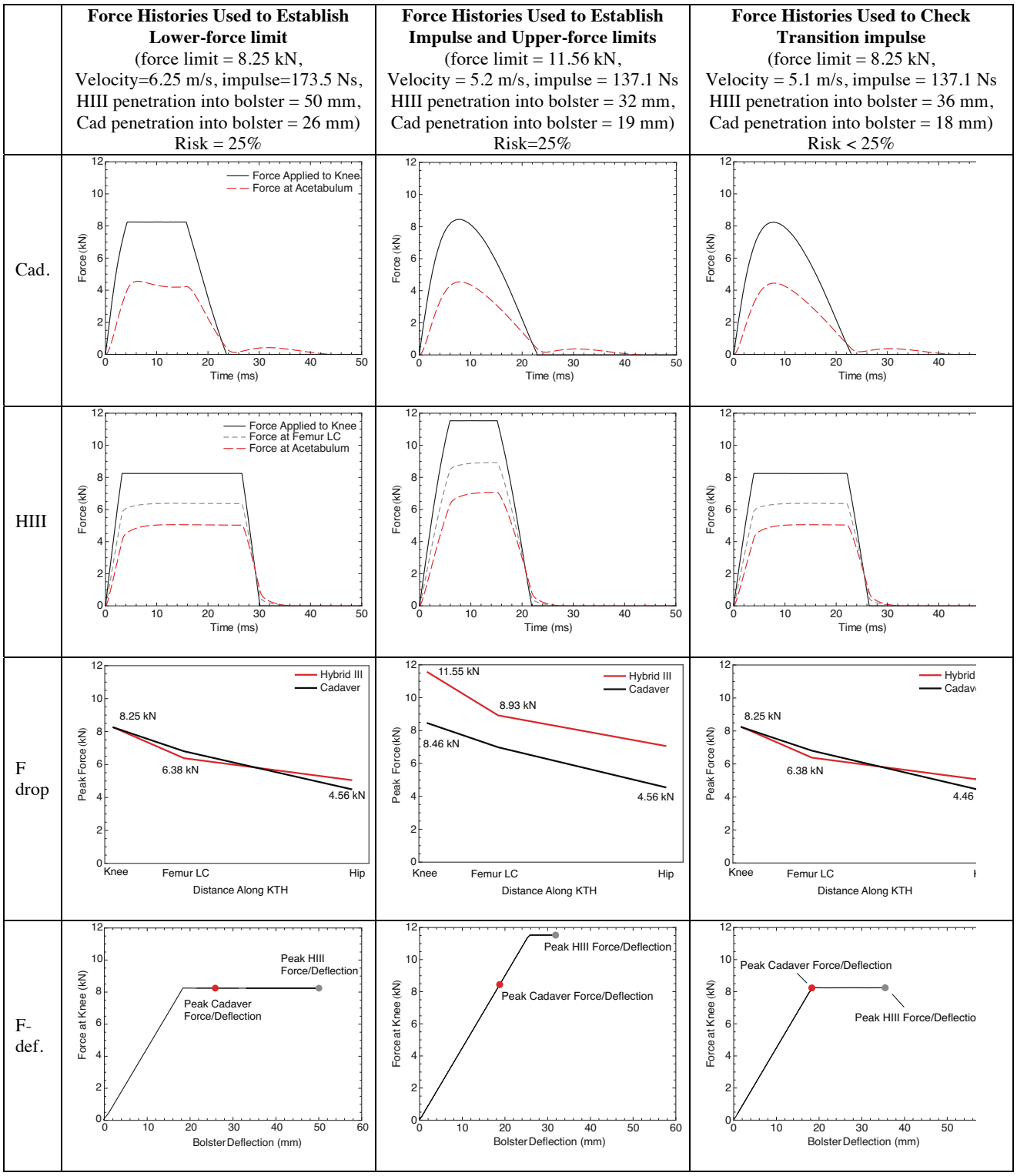

Figure 20. Force histories, plots of the decrease in force along the KTH, and knee bolster force penetration responses produced in simulations used to develop and check the upper and lower-force limits and the transition impulse associated with the 25% risk injury assessment reference boundaries.

Injury Assessment Risk Boundaries for Multiple Levels of KTH Injury Risk–Table 5 lists the lower-force limit, the transition impulse, and the upper-force limit associated with injury assessment reference boundaries for 3%, 5%, 10%, 15%, 20%, 25%, 30%, 35%, 40%, 45%, 50%, and 75% risk of KTH injury at a hip posture that is 30˚ flexed and 15˚ abducted (i.e., the typical posture at the time of peak femur force in an FMVSS 208 or NCAP test). The differences in the slopes of the femur and hip injury risk curves explain why the difference between the upper and, shown in Figure 17, the lower-force limits increases with the level of risk associated with each boundary. These same differences also explain why the upper and lower-force limits are equal at the 3% risk level. For reference, Figure 21 plots some of these injury assessment reference boundaries for each level of injury risk and Figure 22 plots each of the reference boundaries as a function of injury risk.

Table 5. Injury Assessment Reference Boundaries For 3% to 75% Risks of KTH Injury

Risk	Lower-force limit (kN) †	Transition impulse (Ns) †	Upper-force limit (kN)††
3	4.97	NA*	4.97
5	5.22	113.5	5.69
10	5.63	121.8	6.87
15	5.92	127.7	7.69
20	6.16	132.7	8.35
25	6.38	137.1	8.92
30	6.59	141.3	9.44
35	6.79	145.5	9.92
40	6.98	149.4	10.37
45	7.18	153.3	10.80
50	7.35	157.2	11.23
75	8.40	180.7	13.45

*Not applicable because the upper and lower-force limits are equal.

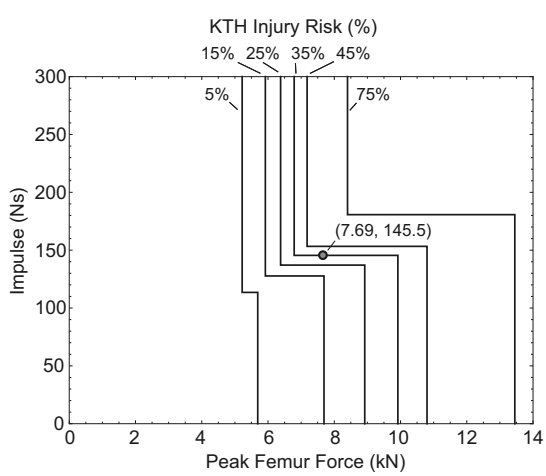

Figure 21. Select injury assessment reference boundaries.

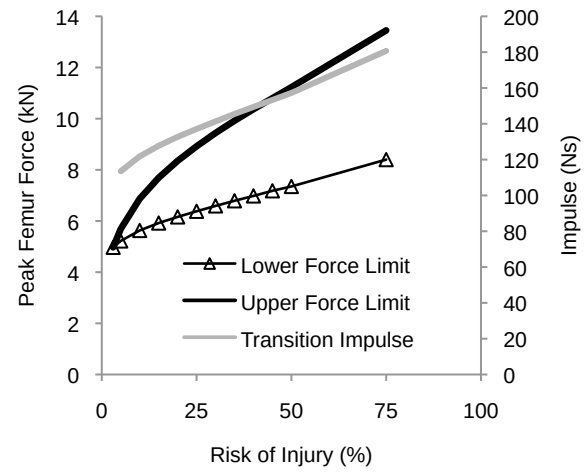

Figure 22. Lower force limit, upper force limit and transition impulse as functions of the associated level of injury risk.

Using the Injury Assessment Reference Boundaries to Estimate Hip and Knee/Distal Femur Injury Risk

The previous section described the development of injury assessment reference boundaries associated with specific levels of KTH injury risk. While each of these boundaries defines a pass/fail injury assessment criterion, like the current 10-kN maximum femur force criterion, no single boundary provides sufficient information to estimate the risks knee/distal femur and hip injury associated with a specified femur force history. However, when combined, multiple injury assessment risk boundaries can be used to estimate the risk of knee/distal femur injury and the maximum possible risk of hip injury associated with a Hybrid III femur force history. For example, based on the upper-force limit, a Hybrid III femur force history that is has a peak of 7.69 kN and an impulse of 145.5 Ns is associated with a 15% risk of knee/distal femur fracture based on Equation 1. The risk of hip fracture for this combination is the smaller of the risks of hip injury determined by comparing peak femur force to the lower force limit and impulse to the transition impulse. This approach is identical to determining which boundary passes through a particular combination of peak force and impulse. For example, as illustrated in Figure 21, a peak force of 7.69 kN and an impulse of 145.5 Ns are on the 35% risk boundary and are therefore associated with no more than a 35% risk of hip injury.

Checks on the Injury Assessment Reference Boundaries–As a check on the injury assessment reference boundaries listed in Table 5, peak Hybrid III femur force, impulse at the Hybrid III femur load

cell, and KTH injury risk were calculated from the set of Hybrid III and cadaver model predictions produced when the loading conditions in Table 4 were simulated. Combinations of peak femur force and impulse associated with KTH injury risks greater than the level of risk associated with each injury assessment boundary were then compared. For these comparisons, KTH injury risk was the maximum of the risk of injury to the hip predicted by the cadaver model and risk of injury to the knee/distal femur predicted by the Hybrid III model. Figure 23 shows that the 25% risk boundary defines all combinations of peak femur force and impulse that were associated risks of KTH injury greater than 25%. A similar finding held for all of injury assessment reference boundaries listed in Table 5.

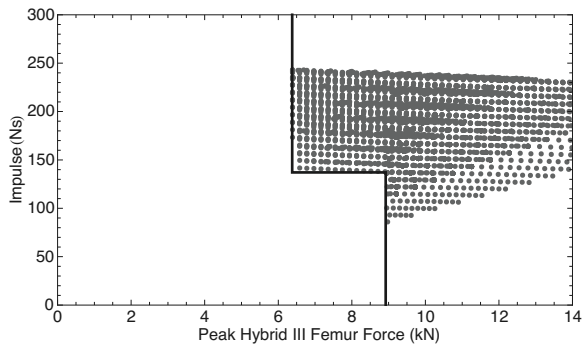

Figure 23. Comparison of 25% injury assessment reference boundary to combinations of peak femur force and impulse that produced risks of KTH injury greater than 25%.

Development of Injury Assessment Reference Boundaries for the Hybrid III Small-female ATD

The injury assessment reference boundaries listed in Table 5 only apply to the midsize male ATD. Development of injury assessment reference boundaries for the small-female ATD in the same manner that was used to develop the midsize male IARVs is currently not feasible, since it would require knee impact response data for similar-size female cadavers, which are not available. Consequently, injury assessment reference boundaries for the small-female ATD were developed using scaling techniques.

Mertz et al. (2003) used a factor of 0.679 to scale femur force in the Hybrid III midsize male to femur force in the Hybrid III small female based anthropometric and dimensional analysis considerations, so this factor was applied to scale the upper-force limit. An appropriate lower-force limit was established using Equation 2 with a posture of 15˚ abduction and 30˚ flexion and the small female stature (150 cm) to determine the force associated with each level of hip injury risk. The lower-force limit was then determined by multiplying this factor by 1.4 (the scale factor between peak force at the human hip and peak force at the Hybrid III femur load cell for the midsize male for knee loading by a force-limiting knee bolster).

Like the upper-force limit, the transition impulse for the small female injury assessment criteria was also developed by scaling midsize male data. For impulse, the scaling factor was 0.580. This factor was derived as described in the Appendix, using the same dimensional analysis based scaling techniques described by Mertz et al. (2003). Scaling the transition impulse also requires scaling the method used to calculate impulse. For the KTH injury assessment criteria for the Hybrid III midsize male, impulse is calculated by integrating the femur force history from the start of knee loading to the time that force last exceeds 4.05 kN. For the small-female ATD, impulse is calculated by integrating the femur force history from the start of knee loading to the time that force last exceeds 2.75 kN, which is equal to 4.05 kN multiplied by the 0.679 femur force scaling factor reported by Mertz et al. (2003).

Table 6 lists the small female injury assessment criteria for levels of KTH injury risk ranging from 3% to 75%. Transition impulse and the lower-force limit for the 3% and 5% injury assessment reference boundaries do not apply with this ATD since the upper-force limit is less than the lower-force limit and therefore applies to all femur force histories. These injury assessment reference boundaries individually assess whether a particular Hybrid III small female femur force history is associated with a risk of injury greater than a specified value. Alternatively, these boundaries can be used together, as described above, to assess the maximum possible risk of hip injury and the risk of knee/distal femur injury associated with a particular femur force history.

Table 6. Injury Assessment Criteria Associated with Risk of KTH Injury from 3% to 75% for Hybrid III Small-Female ATD.

Risk (%)	Lower-force limit (kN)	Transition impulse (Ns)	Upper-force limit (kN)
3	3.65*	NA*	3.37
5	3.82*	NA*	3.86
10	4.13	70.6	4.66
15	4.33	74.1	5.22
20	4.49	77.0	5.67
25	4.65	79.5	6.06
30	4.79	81.9	6.41
35	4.91	84.4	6.74
40	5.05	86.6	7.04
45	5.18	88.9	7.34
50	5.33	91.2	7.62
75	6.09	104.8	9.14

*Not applicable because the upper and lower-force limits are equal.

DISCUSSION

The injury assessment reference boundaries listed in Table 5 were computed such that, under the assumptions of the model, all combinations of peak Hybrid III femur force and impulse that are associated with a risk of KTH injury that is greater than a specified percentage will be above the boundary. However, some combinations of peak femur force and impulse that are associated with risks of injury that are less than the value associated with the boundary can fall above the boundary. In other words, each boundary represents a test with approximately 100% sensitivity but less than 100% specificity for peak forces between the upper and lower-force limits. For peak femur forces that are less than the lower-force limit or greater than the upper-force limit, the injury assessment reference boundary will accurately predict injury risk, subject to the limitations discussed below.

Because they were developed using one-dimensional lumped parameter models, the injury assessment reference boundaries listed in Tables 5 and 6 are limited in several ways. First, the models and the IARVs only apply to symmetric knee loading. The farther a knee-loading condition deviates from applying similar forces to both knees, the less applicable these IARVs will be. This is because asymmetric knee loading has the potential to increase the amount mass behind the hip on the side to which higher force is being applied. This will increase the percentage of force applied to the knee transmitted to the hip and thereby increase the risk of hip injury in a manner that is not accounted for by the lower force limits described in this paper. As a result, the new injury assessment criteria described in this paper will under predict hip-injury risk for asymmetric knee loading. However, this limitation is not important for frontal crash testing in FMVSS 208 and NCAP, where loading is primarily symmetric.

In addition, because the injury assessment reference boundaries were developed using one-dimensional models, they cannot predict two-dimensional phenomena, such as femur bending, which is thought to be the primary mechanism of femoral shaft fracture in frontal crashes (Viano and Stalnaker, 1980). However, since most femur bending in frontal crashes is produced by axial compression (which is assessed by the injury reference boundaries), the failure of the injury assessment reference boundaries to account for femur bending may not be a major limitation.

The models also do not account for the effects of lower-extremity muscle tension due to occupant braking and/or bracing on KTH injuries. Based on the results of recent FE modeling, muscle activation reduces the percentage of force applied to the human knee that is transmitted to the hip by increasing the coupling of muscle mass distal to the hip (Chang, 2009). As a result, with muscle activation, the ratio of peak force at the Hybrid III femur load cell to peak force at the cadaver hip used to establish the lower force limit of the new IARVs will be greater, and the ATD femur forces associated with the lower bound will also be greater.

The injury assessment reference boundaries listed in Tables 5 and 6 are all associated with a single hip posture, which is considered typical of a midsize male at the time of peak knee-bolster loading. Variations from this posture will affect hip-injury tolerance, and will therefore shift the lower force limit and the transition impulse, but will have no effect on the upper force limit associated with knee/distal-femur fracture, which is posture independent.

The injury assessment reference boundaries developed in this study are based on limiting the risks of hip and knee/distal-femur injuries to the same risk levels. However, hip injuries are generally considered more costly to society, more difficult to treat, and more disabling than knee or distal femur injuries (Read et al. 2002). Therefore, in the future, it may be appropriate to calculate the new injury assessment criteria using lower risks of hip injury than the risks of knee/distal-femur injury.

The new KTH injury assessment criterion developed in this study were tested to ensure that they appropriately identify loading conditions that are associated with risks of KTH injury greater than specified levels. Further evaluation of the new injury criterion is described in a companion paper (Kirk and Kuppa 2009), which applies the injury assessment reference boundaries to Hybrid III femur forces measured in NHTSA and IIHS crash tests, and compares the predicted levels of injury risk to those observed in similar real-world crashes investigated in the National Automotive Sampling Systems (NASS).

Developing KTH injury assessment criteria for ATDs would be greatly simplified if the Hybrid III family of dummies produced similar knee impact forces and transmitted similar amounts of force to the hip as the humans that they are designed to represent. With improved ATD biofidelity, the risks of KTH injury could be assessed by applying peak forces measured by ATD femur and acetabular load cells to existing injury risk curves for the femur and hip, respectively. However, with current ATDs, the modeling approach described in this paper is needed to accurately interpret ATD femur forces with respect to human injury risk.

CONCLUSIONS

A one-dimensional lumped-parameter model of the midsize-male Hybrid III ATD has been developed and validated. Simulations with this model and the previously described lumped-parameter model of the midsized male cadaver were performed to explore the relationship between forces in the Hybrid III KTH complex and forces in the human KTH complex. Results of these simulations indicate that the relationships between peak forces measured by the Hybrid III femur load cell and peak forces in the cadaver KTH complex vary with the force-deflection characteristics of the knee bolster. Since knee bolster characteristics in different vehicles vary, it is not possible to develop a singular relationship between peak forces measured by the Hybrid III femur load cell and the risks of injury to the human KTH complex.

For this reason, a new injury assessment criteria for the KTH was developed that uses peak Hybrid III femur force and the impulse of Hybrid III femur force to define the smallest possible femur force histories that are associated with a given probability of KTH injury. The use of impulse allows the new injury assessment criteria to identify the high-rate, short-duration loading associated with knee/distal-femur fractures and the lower-rate, longer-duration loading conditions associated with hip fractures.

ACKNOWLEDGEMENTS

This research was sponsored by the National Highway Traffic Safety Administration, U.S. Department of Transportation under contract DTNH22-05-H-01020.

REFERENCES

Chang, C.Y. (2009). The effects of muscle forces on the predicted risk of knee-thigh-hip injury in frontal crashes. Ph.D. Dissertation. The University of Michigan, Ann Arbor, MI

Chang, C.Y. Rupp, J.D., Schneider, L.W., and Kikuchi, N. (2008). Development of a Finite Element Model to Study the Effects of Muscle Forces on Knee-Thigh-Hip Injuries in Frontal Crashes. Stapp Car Crash Journal 52.

Donnelly, B.R. and Roberts, D.P. (1987). Comparison of cadaver and Hybrid III dummy response to axial impacts of the femur. Proceedings of the Thirty-First Stapp Car Crash Conference, Paper No. 872204, pp. 105-116. Society of Automotive Engineers, Warrendale, PA.

Kirk K. and Kuppa, S. (2009). Application and Evaluation of a Novel KTH Injury Criterion for the Hybrid III Dummy in Frontal Crash Test Environments. Paper #09-0196. Proceedings of the 21st International Technical Conference on the Enhances Safety of Vehicles. National Highway Traffic Safety Association, Washington DC.

Kuppa, S., Wang, J., Haffner, M., and Eppinger, R. (2001). Lower extremity injuries and associated injury criteria. Proceedings of the 17th International Technical Conference on the Enhanced Safety of Vehicles, Paper No. 457. National Highway Traffic Safety Association, Washington, DC.

Kuppa, S. and Fessahaie, O. (2003). An overview of knee-thigh-hip injuries in frontal crashes in the United States. Proceedings of the 18th International Technical Conference on Experimental Safety Vehicles. National Highway Traffic Safety Association, Washington DC.

Masson and Cavallero (2003). Comparison between Hybrid III Dummy and Cadaver knee response in frontal impact. Proceedings of the 2003 International Conference on the Biomechanics of Impact, pp 359-360. IRCOBI, Bron, France.

Read, K. M., Burgess, A. R., Dischinger, P. C., Kufera, J. A., Kerns, T. J., Ho, S. M., and Burch, C. (2002). Psychosocial and physical factors associated with lower extremity injury. Proceedings of the 46th Annual Conference of the Association for the Advancement of Automotive Medicine, pp. 289-303. Association for the Advancement of Automotive Medicine. Des Plaines, IL

Rupp, J.D., Reed M.P., Jeffreys, T.J., and Schneider L.W (2003a). Effects of hip posture on the frontal impact tolerance of the human hip joint. Stapp Car Crash Journal 47: 21-33.

Rupp, J.D., Reed, M.P., Madura, N.H., Kuppa, S., and Schneider L.W. (2003b) Comparison of knee/femur force-deflection response of the Thor, Hybrid III, and human cadaver to dynamic frontal-impact knee loading. Proceedings of the 18th International Conference of Experimental Safety Vehicles. National Highway Traffic Safety Administration, Washington DC.

Rupp, J.D. (2006). Biomechanics of hip fractures in frontal motor-vehicle crashes. Ph.D. Dissertation. The University of Michigan, Ann Arbor, MI.

Rupp J.D., Reed, M.P., Madura, N.H., Miller, C.S., Kuppa, S.M., and Schneider L.W. (2005). Comparison of the inertial response of the THOR-NT, Hybrid III, and unembalmed cadaver to simulated knee-to-knee-bolster impacts. Proceedings of the 19th International Technical Conference on the Enhanced Safety of Vehicles, Paper 05-0086. National Highway Traffic Safety Administration, Washington, DC.

Rupp, J.D., Miller, C.S., Madura, N.H., Reed, M.P., and Schneider L.W. (2007) Characterization of knee impacts in frontal crashes. Proceedings of the 20th International Technical Conference on the Enhanced Safety of Vehicles. Paper 07-0345. National Highway Traffic Safety Administration, Washington DC.

Rupp, J.D., Miller, C.S., Madura, N.H., Reed, M.P., Klinich, K.D., and Schneider L.W. (2008a). Characterization of Knee-Thigh-Hip Response in Frontal Impacts Using Biomechanical Testing and Computational Simulation. Stapp Car Crash Journal 52

Rupp, J.D. and Flannagan C.A. (2009). Development of New Injury Risk Curves for the Knee/Distal and Hip for Use in Frontal Impact. Report # UMTRI-2009-08, University of Michigan Transportation Research Institute, Ann Arbor, MI.

Society of Automotive Engineers Dummy Testing Equipment Subcommittee (1998). User's manual for the midsize Hybrid III test dummy, Engineering Aid 23. Society of Automotive Engineers, Warrendale, PA.

Viano, D.C. and Stalnaker, R.L. (1980). Mechanisms of femoral fracture. Journal of Biomechanics 13: 701-715.

APPENDIX: DERIVATION OF IMPULSE SCALING FACTOR

Since the units of impulse are Ns, the scale factor for impulse, λ_I, must equal the scale factor for force, λ_F, multiplied by the scale factor for time, λ_{Time}, as shown in Equation A1. The scale factor for force is defined by Equation A2 (Mertz et al. 2003). The scale factor for time was derived by recognizing that the units of force are kg m/s^2 and that as a result, the scale factor for force must equal the scale factor for mass, λ_m, multiplied by the scale factor for width/height, λ_x, divided by the square of the scale factor for time (Equation A3). Since this quantity is equal to the scale factor for force (λ_x^2), it follows that the scale factor for time is defined by Equation A4. Substituting Equation A4 into Equation A1 gives the formula scale factor for impulse that is listed in Equation A5. Applying the values for λ_F, λ_m, and λ_x reported by Mertz et al., which are 0.679, 0.601, and 0.824, respectively, to Equation A5 gives a scale factor for impulse of 0.580.

$$\lambda_I = \lambda_F * \lambda_{Time} \qquad [A1]$$

From Mertz et al. (2003), $\lambda_F = \lambda_x^2$ [A2]

Since the units of force are kg m /s^2,

$$\lambda_F = \lambda_m * \lambda_x / \lambda_{Time}^{\ 2} = \lambda_x^2 \qquad [A3]$$

$$\lambda_{Time} = [\lambda_m / \lambda_x]^{0.5} \qquad [A4]$$

$$\lambda_I = \lambda_F * [\lambda_m / \lambda_x]^{0.5} \qquad [A5]$$

APPLICATION AND EVALUATION OF A NOVEL KTH INJURY CRITERION FOR THE HYBRID III DUMMY IN FRONTAL CRASH TEST ENVIRONMENTS

Kristin Kirk
Shashi Kuppa
National Highway Traffic Safety Administration
United States of America
Paper Number 09-0196

ABSTRACT

This paper evaluates a recently published comprehensive knee-thigh-hip (KTH) injury criterion through its application to the Hybrid III 50th percentile male (HIII-50M) and 5th percentile female (HIII-5F) dummies in frontal crash tests along with a comparison with real world KTH injury risk in frontal crashes. This criterion, developed by Rupp et al. (2009) (Rupp-KTH criterion), determines risk of injury to the hip, femur, and knee using the peak compressive femur force and impulse.

Femur load cell data from various frontal crash tests were analyzed using the Rupp-KTH criterion. The risk of KTH injuries as calculated with this criterion in the various crash conditions was compared to that observed in real world frontal crashes using the National Automotive Sampling System-Crashworthiness Data Systems (NASS-CDS) data files. The relative proportion of knee, thigh, and hip injuries predicted by the Rupp-KTH criterion was also compared to that observed in real world crashes.

The Rupp-KTH criterion predicts an overall KTH injury risk reflective of real world risk with unbelted Hybrid III dummies, but under-predicts real world injury risk for belted dummies. The proportion of hip injuries among all KTH injuries is predicted reasonably well for unbelted occupants and under-predicted for belted occupants. Dummy interaction with the knee bolster in different restraint conditions likely affects the level of agreement between predicted and observed injury risk.

This study applied injury criteria to Hybrid III dummy responses in specific crash conditions and seating configurations. Injury risk prediction may be improved with other dummy designs or crash environments.

INTRODUCTION

With the increasing use of safety belts and the availability of air bags, more occupants survive serious crashes. However, many people involved in frontal crashes sustain disabling lower extremity injuries (Kuppa et al., 2003). Though lower extremity injuries are not typically life threatening, the physical and psychosocial consequences of lower extremity injuries are often long lasting (Read et al., 2002). Lower extremity injuries require comparatively longer periods of hospitalization and recovery than injuries to other body regions (Read et al., 2004).

Using NASS-CDS data files, Kuppa et al. (2003) concluded that the lower extremity is the most frequently injured body region in frontal crashes accounting for 36% of all AIS 2+ injuries. Approximately half of lower extremity injuries are to the knee-thigh-hip (KTH) complex and the other half are below the knee. A detailed analysis of KTH injuries indicated that 46 percent of all KTH injuries are to the hip. The relatively high frequency of hip/pelvis injuries is of particular concern because hip injuries are generally more difficult to treat than injuries to the either the knee or the thigh.

NHTSA funded a research program to better understand the mechanism of KTH injuries in frontal crashes and to determine the fracture tolerance of the hip relative to that of the knee and thigh for knee impact conditions that are representative of those resulting from frontal impacts of late-model air bag/knee-restraint-equipped vehicles. Results of this program showed that the hip is the weakest part of the KTH complex under these loading conditions and that hip flexion and adduction from a standardized automotive seating posture significantly reduce hip fracture tolerance (Rupp, 2002, 2003a).

NHTSA then funded research to better assess the relationship between cadaveric testing and the Hybrid III dummy responses in crash tests. The research indicated that the knee/femur complex of the Hybrid III dummy is 2 to 16 times stiffer than that of the human (Rupp, 2003b). In addition, knee impact forces in cadavers were significantly lower than those in the Hybrid III dummy under similar impact conditions (Rupp, 2005). Therefore, in order to assess KTH injury risk using the Hybrid III dummy, the forces measured by the Hybrid III femur load cell need to be transformed to represent equivalent forces in a human KTH complex under similar impact conditions.

As part of the NHTSA-funded program, Rupp et al. (2008) conducted symmetric axial knee impacts to human cadavers representing the range of knee impact conditions observed in frontal crashes of recent vehicle models. This test data was used to develop and validate a one-dimensional lumped parameter model of the human midsize-male KTH complex. A similar one-dimensional lumped parameter model was also developed of the Hybrid III dummy KTH complex (Rupp et al., 2009). The simulations with the human model indicated that for long duration impacts (axial knee impact with energy absorbing knee bolster), the risk of hip injury is higher than the risk of knee or distal femur injury while for short duration axial knee impacts (impact with hard rigid surface), the risk of knee/distal femur injury is higher. The cadaver and Hybrid III dummy models were exercised in different knee impact loading conditions (Rupp et al., 2009) to develop a relationship between the measured Hybrid III femur force time history and the risk of hip injury.

This paper applies the KTH injury risk formulations developed by Rupp et al. (2009) for the Hybrid III 50th percentile male dummy (HIII-50M) and the Hybrid III 5th percentile female dummy (HIII-5F) in different frontal crash test modes. Risks predicted by the new formulation are compared to the injury risk observed in real world frontal crashes of comparable crash modes.

Development of KTH Injury Risk Curves for the Hybrid III Dummy

Rupp et al. (2009) has developed a new KTH injury criterion for the Hybrid III dummy that uses both peak compressive femur force, which is measured along the long axis of the femur, and impulse of the force to calculate the risk of injury to the knee, thigh, and hip. This method takes into account both the magnitude and duration of the load to the KTH complex. As discussed in Rupp et al. (2009), the revised injury assessment reference boundaries have an upper force limit that is based on limiting peak Hybrid III femur force so that it does not exceed the force associated with a specified risk of AIS 2+ knee/distal femur fracture, while the lower force limit and the impulse limit are set to correspond to a specified risk of AIS 3+ hip injury. An illustration of the criterion is shown in Figure 1.

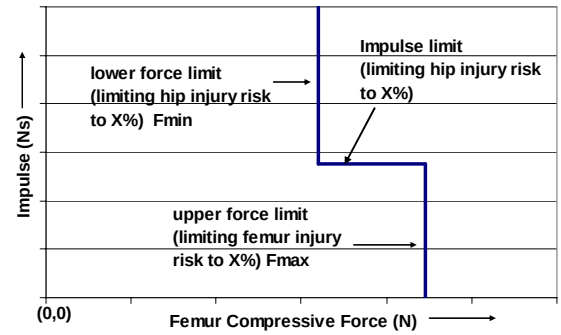

Figure 1. Layout of injury assessment reference boundary represented by the peak compressive femur force and the associated impulse for a specified level of KTH injury risk.

Table 1 lists the HIII-50M lower force limit, the impulse limit, and the upper force limit reported in Rupp et al. (2009) that is associated with injury assessment reference boundaries for 3%, 5%, 10%, 15%, 20%, 25%, 30%, 35%, 40%, 45%, 50%, and 75% risk at a hip posture that is 30˚ flexed and 15˚ abducted (i.e., the typical posture at the time of peak femur force in a FMVSS No. 208 or NCAP test) (Rupp, 2003b). Table 2 lists the lower force limit, impulse limit, and upper force limit as measured in the HIII-5F dummy for risks of KTH injury from 3-75 percent. In Table 1 for 3% risk and in Table 2 for 3 and 5% risk, impulse limits are not provided because the lower force limit is greater than or approximately equal to the upper force limit. In this situation, the impulse limit for hip injury does not apply.

Table 1.
Injury Assessment Reference Boundaries Associated with Risk of KTH Injury from 3% to 75% for the HIII-50M Dummy (Rupp et al., 2009)

Risk %	Lower force limit Fmin	Impulse Limit	Upper Force Limit Fmax
	(kN)	(Ns)	(kN)
3	4.97		4.97
5	5.22	113.5	5.69
10	5.63	121.8	6.87
15	5.92	127.7	7.69
20	6.16	132.7	8.35
25	6.38	137.1	8.92
30	6.59	141.3	9.44
35	6.79	145.5	9.92
40	6.98	149.4	10.37
45	7.18	153.3	10.8
50	7.35	157.2	11.23
75	8.4	180.7	13.45

Table 2.
Injury Assessment Reference Boundaries Associated with Risk of KTH Injury from 3% to 75% for the HIII-5F Dummy (Rupp et al., 2009)

Risk %	Lower force limit Fmin	Impulse Limit	Upper Force Limit Fmax
	(kN)	(Ns)	(kN)
3	3.65		3.37
5	3.82		3.86
10	4.13	70.6	4.66
15	4.33	74.1	5.22
20	4.49	77	5.67
25	4.65	79.5	6.06
30	4.79	81.9	6.41
35	4.91	84.4	6.74
40	5.05	86.6	7.04
45	5.18	88.9	7.34
50	5.33	91.2	7.62
75	6.09	104.8	9.14

The Rupp et al. (2009) KTH injury criterion involves determination of the overall risk of KTH injury by calculating and comparing the risks of injury to the hip and femur in any given test. To do this, it was necessary to develop injury risk curves that could be used to determine the risk of femur or hip injury at any measured force or impulse. The risk of femur injury uses a 2-parameter Weibull as the underlying distribution and assumes that the applied knee force on the cadaver is equivalent to the compressive force measured by the femur load cell in the Hybrid III dummy under similar impact conditions (Rupp et al., 2009). The resulting injury risk curves for the HIII-50M and the HIII-5F are shown in Figure 2 and Equations 1a and 1b.

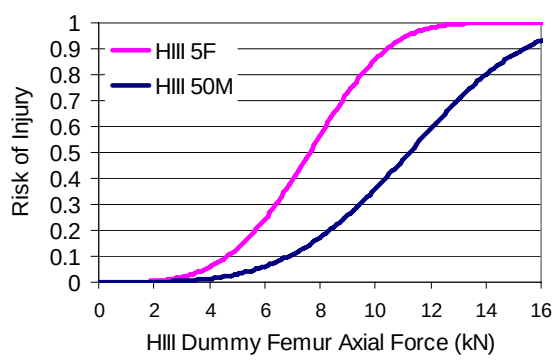

Figure 2. Risk of distal femur / knee injury as a function of peak compressive femur force measured by the HIII-50M and HIII-5F femur load cells.

$HIII-50M$:

$$P(distalfemur/kneeinjury) = 1 - e^{-a} \qquad (1a.)$$

where

$$a = e^{\frac{\ln(F)-2.514}{0.2611}}$$

$HIII-5F$:

$$P(distalfemur/kneeinjury) = 1 - e^{-b} \qquad (1b.)$$

where

$$b = e^{\frac{\ln(F)-2.127}{0.2611}}$$

Where F is the peak compressive force in kN measured in the HIII-50M and HIII-5F dummy femurs.

The risk of hip injury derived from cadaver test data (Rupp et al., 2009) as a function of force at the hip, subject stature, hip flexion, and abduction angle is presented in Equation 2a. For an occupant stature of 178 cm (corresponding to the size of a HIII-50M dummy), seated in normal driving posture (hip flexion =30 degrees and hip abduction=15 degrees), the corresponding hip injury risk is as shown in Equation 2b. Similarly, the hip injury risk for occupant stature of 150 cm, corresponding to the size of a HIII-5F dummy, in normal driving posture is presented in Equation 2c.

$$Risk(hip\ injury) = \Phi\left[\frac{\ln(F)-(-0.2141+0.0114*s)-\ln(1-(f-a)/100)}{0.1991}\right] \qquad (2a.)$$

50th *percentile male* :

$$Risk(hip\ injury) = \Phi\left[\frac{\ln(F)-1.6526}{0.1991}\right] \qquad (2b.)$$

5th *percentile female* :

$$Risk(hip\ injury) = \Phi\left[\frac{\ln(F)-1.3334}{0.1991}\right] \qquad (2c.)$$

Where:
Φ is the cumulative normal distribution;
s is occupant stature, in cm;
f is hip flexion angle, in degrees;
a is hip abduction angle, in degrees; and
F is the peak hip force, in kN.

The hip injury risk curve applicable to the Hybrid III dummy femur force measure was derived by fitting a lognormal distribution to the data in the second column in Table 1. This equation is the same as that presented in Equation 2b for a normally seated 50th percentile male occupant with the force scaled by

0.7126 (Equation 3a and Figure 3). This scale factor represents the transformation of the measured compressive femur force in the HIII-50M dummy to the equivalent hip force in the cadaver in simulations of knee impacts by force limiting knee bolsters. According to Rupp et al. (2009), the risk of injury using the force in the second column in Table 2 was developed by scaling the force in Equation 2c for a 5th percentile normally seated female occupant by 0.7143 (=1/1.4: factor to scale the force at the HIII 5F femur load cell to equivalent force at the cadaver acetabulum in simulation of knee impacts with force limiting knee bolsters). The resulting hip injury risk curve using the force measured at the HIII-5F femur load cell is presented in Equation 3b and Figure 3.

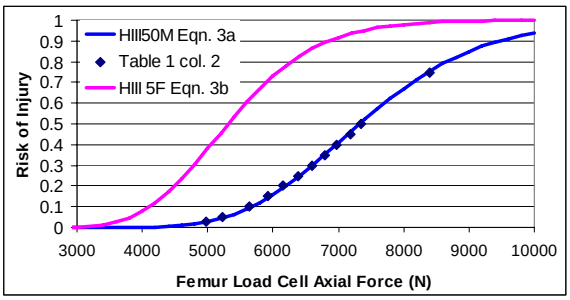

Figure 3. Risk of hip injury as a function of peak compressive femur force in the HIII-50M and HIII-5F dummies.

$HIII-50M$:

$$P_{hip} = \Phi\left(\frac{\ln(0.7126F) - 1.6526}{0.1991}\right) \qquad (3a.)$$

$HIII-5F$:

$$P_{hip} = \Phi\left(\frac{\ln(0.7143F) - 1.3334}{0.1991}\right) \qquad (3b.)$$

Where:
Φ is the cumulative normal distribution; and
F is the compressive force measured on the dummy in kN.

The risk curve for hip injury as a function of impulse of the femur force was obtained by fitting a logistic distribution to the data in column 3 of Table 1. The risk of hip injury for the HIII-50M dummy impulse of the compressive femur force is shown in Figure 4 and Equation 4a. According to Rupp et al. (2009), the risk of hip injury as a function of compressive femur force impulse of the HIII-5F dummy was obtained by scaling the impulse in Equation 4a by a factor of 0.58 as shown in Equation 4b.

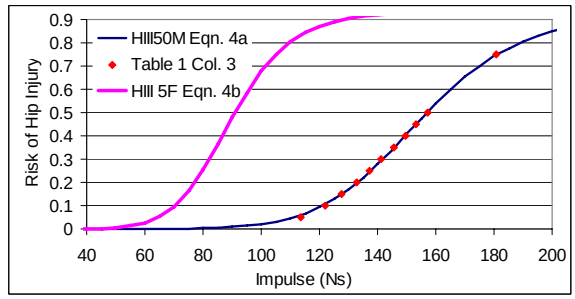

Figure 4. Risk of hip injury as a function of the impulse of the compressive femur force in the HIII-50M and HIII-5F dummies.

$HIII-50M$:

$$P_{hip} = \frac{0.9386}{1+\left(\frac{impulse}{154.5037}\right)^{-8.7288}} \qquad (4a.)$$

$HIII-5F$:

$$P_{hip} = \frac{0.9386}{1+\left(\frac{0.58 * impulse}{154.5037}\right)^{-8.7288}} \qquad (4b.)$$

Where *impulse* is the impulse of the compressive femur force measured on the dummy in Newtons.Seconds.

METHODS

Investigation of KTH Injuries in NASS-CDS

The risk and proportion of KTH injuries in real world crashes were investigated by analyzing the NASS-CDS data files for years 1993-2007 and vehicle model years (MY) 1991-2008 using a similar methodology as that presented by Kuppa et al. (2003). Frontal crashes were defined as those with impact direction between 10-2 o'clock with general area of damage in front and forward of the A-pillar. Frontal crashes were further classified into three categories representing a full frontal rigid barrier crash test (FFB), a left offset and a right offset deformable barrier crash test (LOV and ROV) as defined by Stucki et al. (1998) using impact direction, type of object contacted (fixed or vehicle), general area of damage, and the location of maximum crush. Only vehicles not involved in a rollover, and driver and front passenger occupants with an air bag available at their seating position were included. Only outboard front seat occupants (driver and right front passenger) who were at least 15 years of age and were not ejected were included in the analysis. Cases were aggregated by frontal crash mode, vehicle

model year, occupant stature, seating position (i.e., driver or passenger), restraint status, and crash DeltaV. Injury risks were calculated for multiple body regions with the lower extremities divided into the KTH complex and below knee. Additionally, KTH injuries were examined in further detail to determine the proportion of KTH injuries to the knee, thigh, and hip for various crash, occupant, or restraint types and crash DeltaVs using the knee, thigh, and hip injury categories defined by Kuppa et al. (2003).

Application of the KTH Injury Criteria to Determine KTH Injury Risk in Frontal Crash Environments

50th Percentile Male Data: Femur force-time data were extracted from frontal NCAP, FMVSS No. 208, IIHS frontal offset, and vehicle-to-vehicle frontal and offset tests for the HIII-50M. NCAP femur data were taken from tests conducted on belted HIII-50M driver-side dummies in MY 1995-2008 vehicles in 56 km/h (35 mph) frontal crash tests. The FMVSS No. 208 tests were full frontal barrier tests conducted on MY 2002-2007 vehicles at 40 and 48 km/h (25 and 30 mph), with unbelted HIII-50M dummies. Frontal offset tests from IIHS include MY 1995-2003 vehicles tested with 64.4 km/h (40 mph) closing speed. The HIII-50M driver was belted in these tests. Finally, a series of 50% left offset and collinear vehicle-to-vehicle tests conducted as part of NHTSA's compatibility research was included (Summers and Prasad, 2005). In this series, bullet vehicles impacted the stationary struck vehicle (a 2004 Honda Accord) such that the DeltaV of the struck vehicle was 56 km/h. Femur data from this test series were taken from the belted HIII-50M dummy driver with Thor-Lx/HIIIr in the struck vehicle. For the NCAP, FMVSS No. 208, NHTSA offset, and vehicle-to-vehicle crash tests, the dummies were positioned according to dummy placement specified in FMVSS No. 208. For the IIHS offset tests, the dummies were positioned according to IIHS offset barrier crash test protocol Version IX with the driver seat in the midtrack full-down position. All data are available on the NHTSA vehicle database at http://www-nrd.nhtsa.dot.gov/database/nrd-11/veh_db.html.

5th Percentile Female Data: Femur force-time data for the HIII-5F were taken from unbelted FMVSS No. 208 tests of MY 2003-2008 vehicles in full frontal barrier crash tests at 40 km/h (with the exception of one test at 32 km/h (20 mph)). Femur data were also collected from NHTSA research tests using the HIII-5F in full frontal, belted environments at 40, 48, and 56 km/h. Finally, femur data were collected from HIII-5F drivers in three 40% left offset frontal tests of MY 2002 and 2004 vehicles at 40 km/h. All tests were conducted with the HIII-5F positioned as specified for the HIII-5F in FMVSS No. 208. All data are available on the NHTSA vehicle database at http://www-nrd.nhtsa.dot.gov/database/nrd-11/veh_db.html.

Femur Force, Impulse, and Risk Calculation: Peak left and right compressive femur forces for each test were obtained after processing the femur force time histories with SAE CFC 600. The impulse of each force was then calculated by integrating the filtered femur force time history from Tzero, the time that force last equals zero prior to the peak compressive force, to the time after the peak force when the compressive force first equals 4050 N for the HIII-50M or 2750 N for the HIII-5F (Figure 5). These are the compressive forces in the Hybrid III dummies that correspond to the minimum force required for KTH injury in cadavers. If the peak compressive femur force is less than 4050 N (or 2750 N for the HIII-5F), the integral is taken from Tzero to the time of the peak force (Fmax).

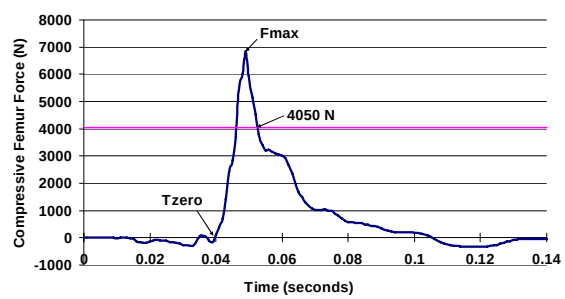

Figure 5. Impulse integration limits for the HIII-50M.

The peak compressive force and impulse values were then used in Equations 1, 3, and 4 to calculate the risks of injury to the femur and hip. A femur force time history with peak force levels lower than Fmin of Figure 1 has a hip injury risk less than X% regardless of the level of impulse. On the other hand, a short duration femur force time history with peak femur force greater than Fmin in Figure 1 has a hip injury risk less than X% only if the impulse is less than the impulse limit associated with X% injury risk. Therefore, the overall risk of hip injury (P_{hip}) is determined by the lower of the risks due to force and impulse, calculated using Equations 3 and 4. As a result, short duration femur force spikes (high peak compressive femur force with low impulse) and low force level-long duration time histories will have relatively low risk of hip injury. The overall risk of KTH (P_{KTH}) injury due to axial, compressive loading of the femur was determined as the greater of the risk to the hip (P_{hip}) and to the distal femur/knee (P_{knee})

from Equation 1. In other words,

P_{KTH}=Maximum(Minimum($P_{hip\text{-}Eqn.\ 3}$, $P_{hip\text{-}Eqn.\ 4}$), $P_{knee\text{-}Eqn\ 1}$)

This process of determining overall risk is illustrated using Figure 6 and Table 3. The 25 and 35 percent risk of KTH injury lines along with points A, B, C, and D representing four peak compressive femur force and impulse combinations for the HIII-50M dummy are shown in Figure 6. Table 3 presents the hip, femur/knee, and the overall KTH injury risk for each of the 4 combinations of force and impulse. Point A (high force and low impulse) lies on the 35 percent risk boundary associated with femur/knee injury risk. Though the peak femur force is high for Point A, the risk of hip injury is low because of the low impulse level. Point B represents a relatively high force-short duration force time history. Though the peak femur force of Point B is associated with a 62 percent hip injury risk, the impulse of Point B is only associated with a 25 percent injury risk. Point C represents a relatively low force-long duration time history. Though the hip injury risk from impulse is 74 percent, the femur force level of Point C is only associated with a 35 percent risk of injury. Point D provides another example of a low force, long duration time history. Although the hip risk due to impulse is fairly high (54%), the overall risk is determined by the risk of hip injury due to femur force, which is 30%.

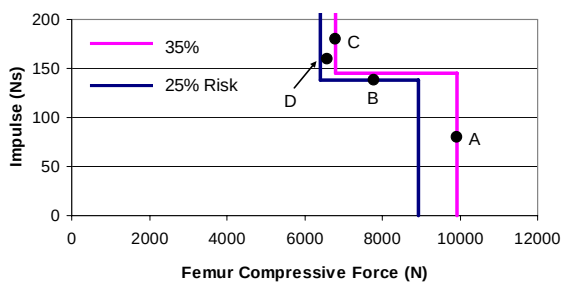

Figure 6. Peak compressive femur force versus impulse plot for the HIII-50M dummy to illustrate the process of determining KTH injury risk. Points A, B, C, and D represent four compressive femur force and impulse combinations of the HIII-50M dummy.

Table 3.
Risk of Injury to the KTH Complex using Equations 1, 3, and 4.

	A	B	C	D
Compress. Femur Fz (N)	9920	7800	6800	6585
Impulse (Ns)	80	138	180	160
Hip Injury Risk Eqn. 3	0.94	0.62	0.35	0.30
Hip Injury risk Eqn. 4	0.00	0.25	0.74	0.54
Hip Injury Risk (Min. risk of rows 4 and 5)	0.00	0.25	0.35	0.30
Femur/knee Injury Risk	0.35	0.16	0.10	0.09
Overall KTH risk (Max of rows 6 and 7)	0.35	0.25	0.35	0.30
What is injured?	femur/knee	hip	hip	hip

RESULTS

NASS Analysis of KTH Injuries

Compared to other injuries, lower extremities (KTH + below knee combined) continue to have the highest risk of all body regions of AIS 2+ injuries to front seat occupants in frontal crashes of air bag equipped vehicles (Figure 7).

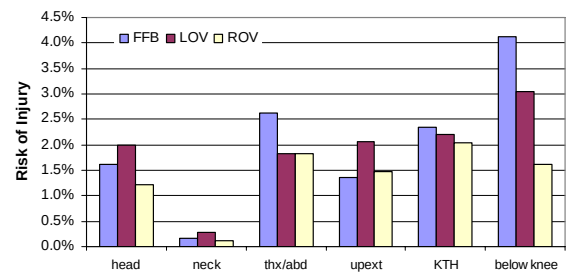

Figure 7. Risk of AIS 2+ injury by body region, for driver and front seat passenger in air bag equipped vehicles in different frontal crash modes (FFB= crashes representative of full frontal rigid barrier crashes; LOV, ROV= crashes representative of left and right offset deformable barrier crashes) (NASS-CDS 1993-2007).

Risk of KTH injury for belted occupants is 1.5-2%, while for unbelted occupants this risk is 4-7.6%. The risk for unbelted occupants was higher than that for belted occupants in each crash mode. The risk of KTH injury is higher in full frontal rigid barrier type crashes than in the left and right offset crash modes for unbelted occupants while there is not much difference in KTH injury risk in the three crash modes for belted front seat occupants (Figure 8).

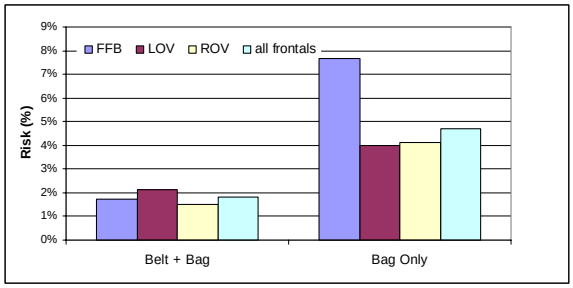

Figure 8. Risk of AIS 2+ KTH injury in belted and unbelted drivers and passengers in frontal crashes (NASS-CDS 1993-2007).

The proportion of knee, thigh, and hip injuries to drivers and passengers in all frontal crashes are similar for belted as for unbelted occupants. Additionally, knee injuries occur with somewhat greater frequency than hip injuries (Figure 9).

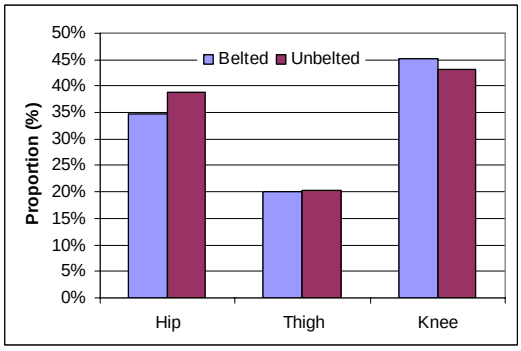

Figure 9. Proportion of knee, thigh, hip injuries among front seat occupants by restraint status (NASS-CDS 1993-2007).

Agency crash tests are conducted with both 50th percentile male and 5th percentile female-sized dummies. Because of this, NASS-CDS data files were examined using occupant stature categories according to Samaha et al. (2001) that correspond to the occupant heights representative of the HIII-5F dummy (143-162 cm) and HIII-50M dummy (163-182 cm). Since many occupant heights are listed as "unknown" in NASS-CDS, the number of observations for this category (i.e., occupant height) is much smaller than that for other categories.

The belted and unbelted front seat occupants, represented by the HIII-5F dummy size (5F) had somewhat greater risk of AIS 2+ KTH injury than those represented by the HIII-50M dummy (50M) as shown in Figure 10. The proportion of knee, thigh, and hip injuries were essentially equal in the belted 5F group while the proportion of thigh injuries were lower than hip and knee injuries in the belted 50M group. The greatest proportion of KTH injuries in the unbelted 5F and 50M groups was to the hip, although the 5F group had a nearly equivalent proportion of thigh injuries (Figure 11).

Figure 10. Risk of AIS 2+ KTH injury for belted front seat occupants in frontal crashes for small female and average male height occupants (NASS-CDS 1993-2007).

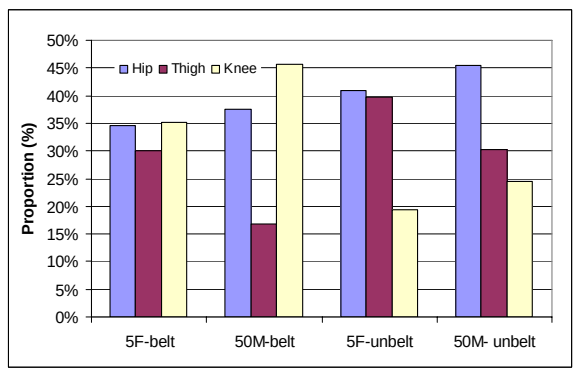

Figure 11. Proportion of KTH injuries in belted and unbelted occupants by occupant stature (NASS-CDS 1993-2007).

In addition to crash mode, restraint, and occupant size, risk of injury by vehicle model year was also examined. For belted occupants, risk of AIS 2+ KTH injury remained relatively constant between MY 1991-2000, then decreased slightly in MY 2001-2008 vehicles (Figure 12). The proportion of thigh injuries relative to all KTH injuries remained at approximately 20% for all model years, while the proportion of hip injuries decreased from 40% to 20% and the proportion of knee injuries increased from 40% to 60% from 1991-1995 MY vehicles to 2001-2008 MY vehicles (Figure 13).

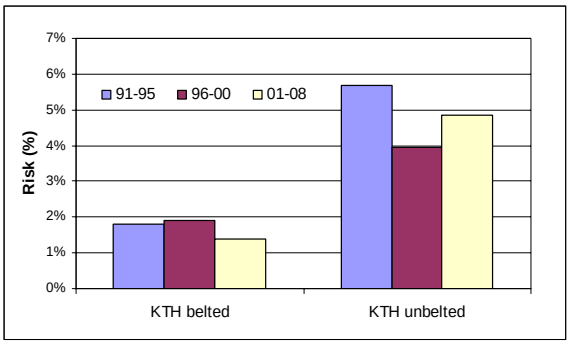

Figure 12. Risk of KTH injury by model year for belted and unbelted front seat occupants (NASS-CDS 1993-2007).

The risk of AIS 2+ KTH injury is higher among unbelted occupants than belted occupants for all three categories of vehicle model years. Additionally, hip injuries are dominant for unbelted occupants, while knee injuries are dominant for belted occupants (Figure 13). In unbelted occupants, the proportion of hip injuries increased from earlier to more recent vehicle model years, while in belted occupants it decreased in more recent model years. Knee injuries in unbelted occupants remained relatively constant from 91-95 to current model year vehicles.

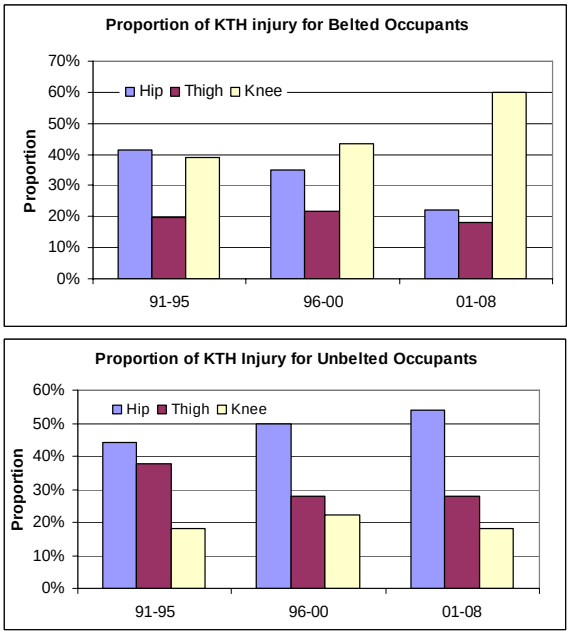

Figure 13. Proportion of AIS 2+ KTH injury by model year for belted and unbelted front seat occupants in air bag equipped vehicles (NASS-CDS 1993-2007).

To obtain real world injury risk at crash severities similar to that of the various crash tests, the NASS-CDS data files were further parsed by the crash DeltaV. For belted occupants, frontal crashes of DeltaV ranging 48-70 km/h were considered, and for unbelted occupants, frontal crashes of DeltaV ranging 35-60 km/h were considered. For simplicity, these results will be referred to as "high severity" belted and unbelted frontal crash results, to distinguish them from the results derived from crashes of all DeltaVs.

Risk of KTH injury for belted drivers in high severity frontal crashes ranged from 10% for right offset crashes to 27% for left offset crashes, and had a 20% risk for full frontal crashes. The risk of KTH injury for unbelted drivers in high severity crashes ranged from 18 to 20 percent. With the exception of unbelted passengers, the risk of KTH injury is higher for the driver in left offset crashes than in right offset crashes, and higher for the passenger in right offset crashes than left offset crashes (Figure 14). This finding is consistent with the expectation that occupants closer to the impact site are at a higher risk of injury than occupants farther away from the impact site.

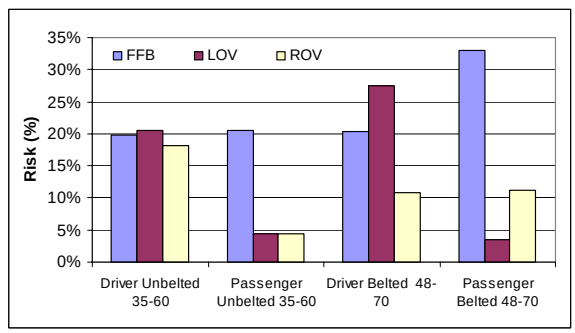

Figure 14. Risk of AIS 2+ KTH injury in high severity unbelted and belted frontal crashes (NASS-CDS 1993-2007).

Hip injuries account for a large proportion of KTH injuries in high severity unbelted and belted frontal crashes. Hip injuries account for 32 to 41% of AIS 2+ KTH injuries in these high severity belted frontal crashes and 45 to 51% of KTH injuries in unbelted frontal crashes. In both belted and unbelted occupants in high severity crashes, when looking at all frontal crash modes combined, hip injuries were most common, followed by thigh, then knee injuries. This trend was also seen in full frontal unbelted crashes. Full frontal belted crashes had nearly equal hip and thigh injuries, and somewhat fewer knee injuries (Figure 15).

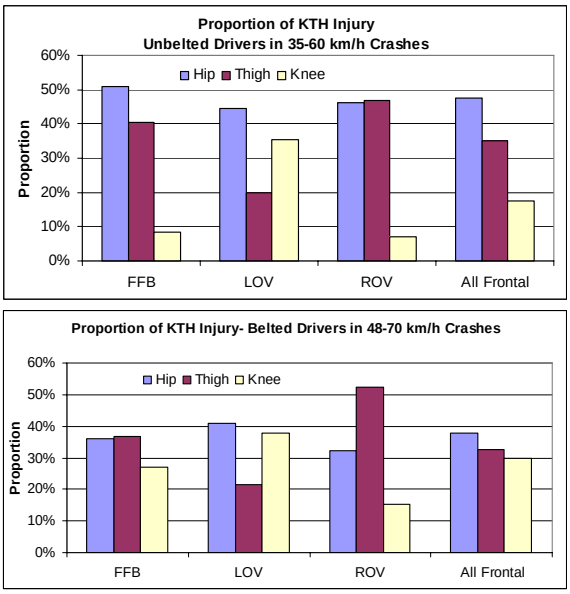

Figure 15. Proportion of KTH injuries for unbelted and belted drivers in high severity crashes (NASS-CDS 1993-2007).

Application of KTH Criterion to the 50th Percentile Male Dummy

As described previously, risk of KTH injury is defined by the maximum risk to the femur/knee or the hip. The risk of hip injury is determined by the minimum risk computed from Equations 3 and 4. For purposes of this discussion, when the hip injury risk is determined by Equation 3, it will be stated that the hip(force) has the greatest injury risk. For cases where the hip injury risk is determined by Equation 4, it will be stated that the hip(impulse) has the greatest injury risk. Equation 1 is used to determine the risk of distal femur and knee injuries and is noted as femur/knee.

NCAP Tests: The compressive femur forces and impulses for belted 50th percentile male dummies in 566 56 km/h NCAP tests of MY 1995-2008 vehicles are graphically presented in Figure 16. For reference, lines of 25% and 35% risk of KTH injury are also shown. These levels of injury risk were selected because these risk levels have been used in previous studies as injury threshold levels for lower extremity injuries (Kuppa et al., 2001). The force and impulse values from NCAP tests were input into Equations 1, 3, and 4 to calculate overall risk for the driver in each test; the risks are presented in Figure 17. The average calculated risk of KTH injury in 50th percentile male drivers in NCAP tests is 5.2%. By model year group, the average risk of MY 1995 vehicles is 7.49%; of MY 1996-2000 vehicles is 7.61%; and of MY 2001-2008 vehicles is 3.70%. This risk is quite low compared to the NASS risk for belted drivers in 48-70 km/h delta V frontal crashes of MY 1991-2008 vehicles, which was 20% as shown in Figure 14. However, the lower risk for more recent model year vehicles than previous model year vehicles is consistent with NASS results for all crash severities shown in Figure 12.

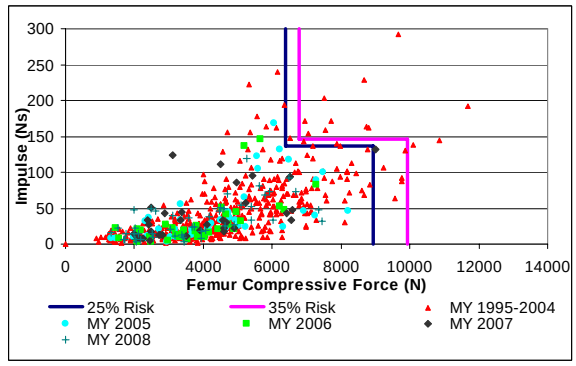

Figure 16. Peak compressive femur force and impulse in NCAP tests.

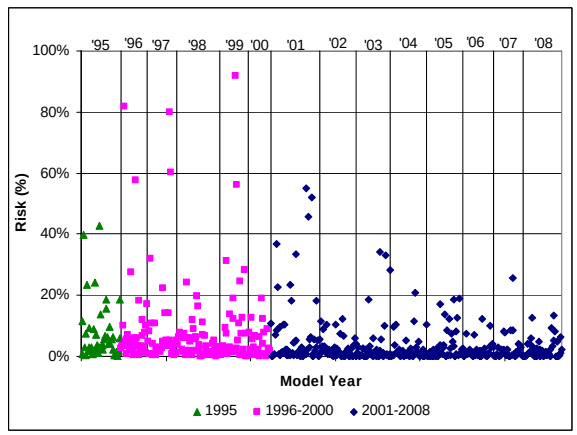

Figure 17. Calculated risk of KTH injury in the 50th percentile male in NCAP tests.

When the KTH criterion is applied to the HIII-50M in NCAP tests, risk of femur/knee injury dominates the risk of hip injury for nearly all tests. However, in most tests the risk is low. Only 21 out of 566 tests (3.71%) have an overall injury risk greater than 25%. Of these higher risk tests, risk of hip injury was greatest in MY 1995-1997 and 1999, while in 2001 and 2003, femur/knee injury risk was greatest. After 2003, only one test (in 2007, femur/knee dominant risk) failed the 25% injury risk criterion, with a risk of 25.8%. The dominant risks are presented by number of vehicles in Figure 18.

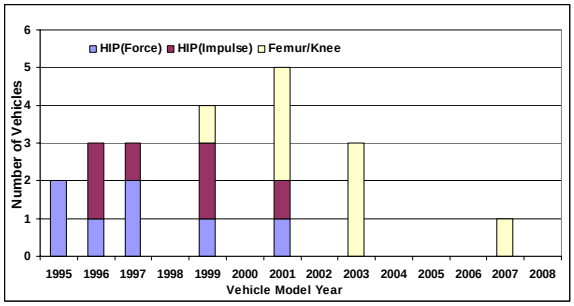

Figure 18. Dominant risk of injury for 50th percentile male driver when risk of KTH injury is at least 25%.

Although overall risk is underpredicted, the trend of increasing femur/knee injuries and decreasing hip injuries with model year is consistent with results from NASS-CDS shown in Figure 13. However, real world, high severity belted crashes show nearly equal proportions of hip and thigh+knee injuries (Figure 15), while NCAP test data indicates that among those with KTH risk greater than 25 percent, hip injury was predominant.

FMVSS No. 208 Unbelted Tests: The compressive femur force and impulse from 26 unbelted HIII-50M drivers and 26 passengers in 40-48 km/h full frontal FMVSS No. 208 tests are graphically presented in Figure 19. The average calculated risk of KTH injury in drivers and passengers of these MY 2002-2008 vehicles was 13.8%, where drivers had a risk of 11.3% and passengers had a risk of 16.3%. These risks are comparable to the real world risks of KTH injury in high severity unbelted crashes for drivers and passengers in MY 1991-2008 vehicles (about 20%), shown in Figure 14, particularly for passengers.

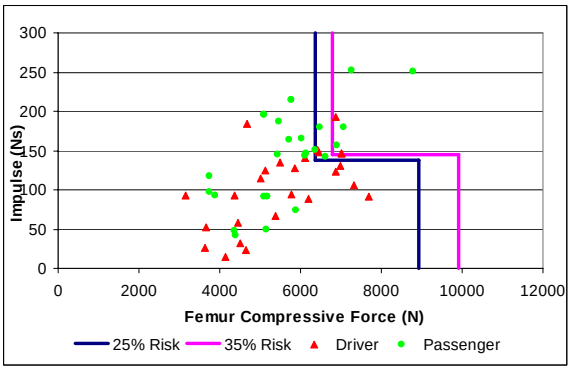

Figure 19. Peak compressive femur force and impulse in FMVSS No. 208 tests with the HIII-50M dummy.

In comparison to the NCAP tests for the same model years (Figure 18), there was a greater proportion of tests where hip injury risk was higher than femur/knee injury risk in the unbelted FMVSS No. 208 tests (Figure 20). This difference in proportion of hip injuries is consistent with the difference in proportions in the real world for unbelted high severity crashes compared to belted high severity crashes (Fig. 15), which show greater proportions of hip injuries in unbelted tests.

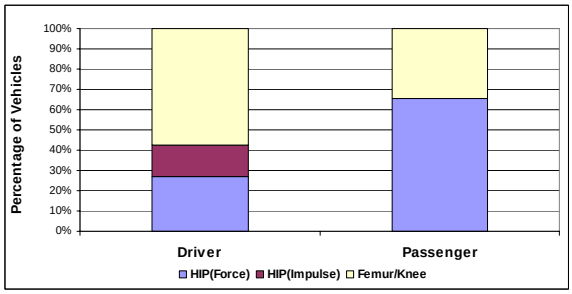

Figure 20. Dominant risk of injury, by percentage of vehicles, in unbelted 50th percentile male driver and passenger dummies in FMVSS No. 208 tests.

Of the 26 unbelted FMVSS No. 208 tests conducted with HIII-50M dummies, 5/26 drivers (19.2%) and 6/26 passengers (23.1%) had KTH injury risks above 25%. This percentage of occupants exceeding 25 percent injury risk is consistent with the real world risk of KTH injury to unbelted occupants (Figure 14). In these tests, hip(force) had the greatest risk of injury in most tests (see Figure 21). The greatest risk of injury being to the hip is in agreement with NASS data for unbelted drivers in high severity crashes, presented in Figure 15. However, the proportion of thigh+knee injury in the real world is underpredicted in these unbelted tests.

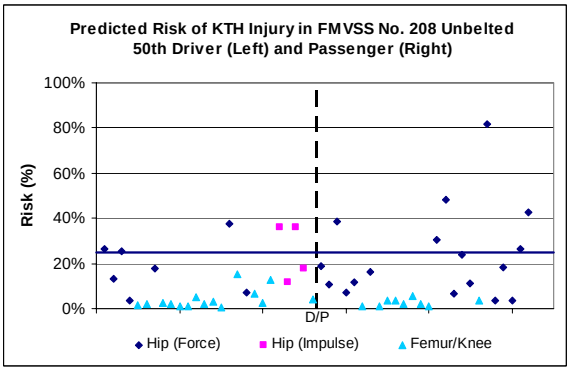

Figure 21. Dominant risk of injury in 50th percentile dummy driver (left) and passenger (right) in unbelted FMVSS No. 208 tests.

IIHS Frontal Offset Tests: Compressive femur force and impulse in 179 IIHS 40% left offset frontal crash tests are presented graphically in Figure 22. In these belted tests of HIII-50M drivers, risk of

injury to the femur/knee was found to be dominant. Like in the NCAP tests, the risk of injury was generally low (Figure 23), with an average risk of 6.93%. Note however, that the average risk in frontal offset tests is slightly higher than that in NCAP tests, just as belted left offset tests have slightly higher risk (27%) than belted frontal tests (20%) in NASS high speed belted crashes (Figure 14). In IIHS frontal offset tests, injury risk was lower in recent model years; the average injury risk for MY 2001-2003 was 3.93% compared to a risk of 14.7% for MY 1995 and 7.8% for MY 1996-2000. This decrease in risk with model year was also observed in belted NCAP tests. Among 179 frontal offset tests, only 15 (8.4%) had an overall injury risk greater than 25%. For these tests, hip(force) was the dominant injury risk, as seen in Figure 24. Hip injuries were also most prevalent in the real world crashes of this type and severity. However, the criterion does not predict the femur/knee injuries that also occur with significant proportions in the real world (Figure 15).

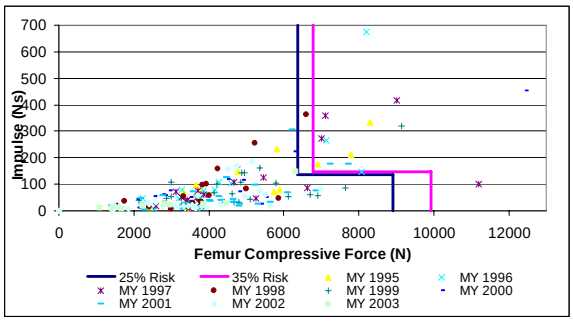

Figure 22. Peak compressive femur force and impulse in IIHS frontal offset tests with the HIII-50M dummy.

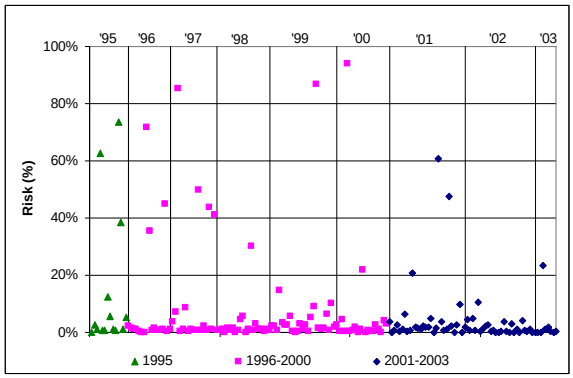

Figure 23. Predicted risk of KTH injury in IIHS frontal offset tests, by model year.

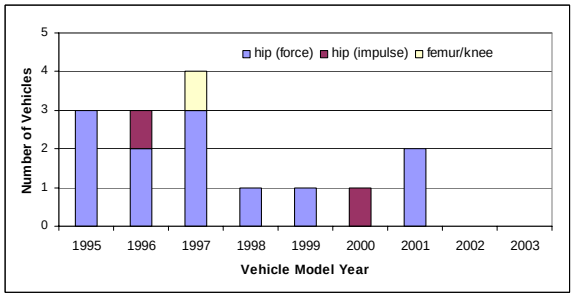

Figure 24. Dominant risk of KTH injury in IIHS frontal offset tests where risk is at least 25%.

<u>Vehicle-to-Vehicle Offset and Collinear Tests:</u> Compressive femur forces and impulses were generally low in the HIII-50M driver of a 2004 Honda Accord struck by various LTVs, as seen in Figure 25. The maximum overall risk was less than 3.6% for all nine tests, with the highest risk to the femur/knee. The extremely low risk of injury in vehicle-to-vehicle crash conditions is inconsistent with the risk of injury in high speed, belted frontal crashes in the real world, which is 20-27% as shown in Figure 14.

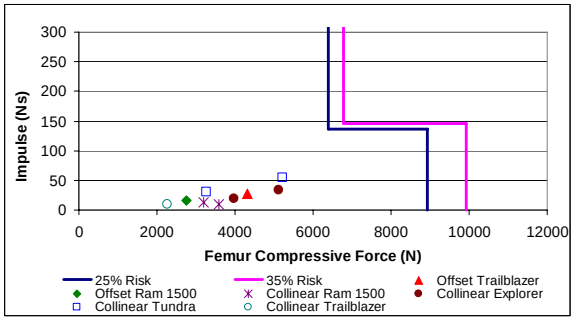

Figure 25. Peak compressive femur forces and impulses in HIII-50M driver of a 2004 Honda Accord struck by LTVs.

Application of the KTH Criterion to the 5th Percentile Female Dummy

<u>FMVSS No. 208 Unbelted Tests:</u> Compressive femur forces and impulses for 67 unbelted 5th percentile female driver and 66 passenger dummies in FMVSS No. 208 tests are presented graphically in Figure 26. There are a greater number of tests exceeding 25 or 35 percent risk of KTH injury in the passenger than the driver. The average risk of injury for the driver is 10.9% while the average risk for the passenger is 20.5%. The average risk overall is 15.7%. This is somewhat higher than the average risk for the HIII-50M in FMVSS No. 208 unbelted tests (13.8%). The HIII-5F having somewhat higher risk than the HIII-50M is consistent with the real

world data shown in Figure 10. Additionally, the passenger risk of 20.5% is in agreement with the real world injury risk for unbelted passenger occupants in high severity full frontal crashes (about 20%, as shown in Figure 14). However, the average risk for drivers is somewhat lower than the corresponding real world injury risk shown in Figure 14.

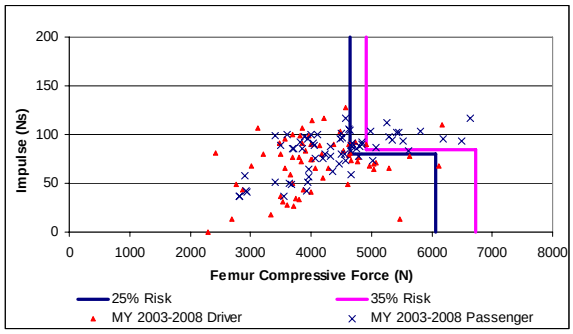

Figure 26. Peak compressive femur force and impulse in FMVSS No. 208 unbelted 5th percentile female frontal crash tests.

In this unbelted environment, the dominant risk of KTH injury was the femur/knee for the driver and the hip(force) for the passenger. For occupants with a calculated KTH injury risk of at least 25%, the dominant risk in five out of six tests for the driver was to the hip(force) (Figure 27). These six tests represent 9.1% of the number of tests conducted. In the passenger, 22 tests exceeded 25% risk of injury (33.3% of tests conducted), with the hip having the highest risk of injury for all tests. Hip(force) had the highest risk for 16 passenger tests, and hip(impulse) for six tests. The high risks of hip injury are in reasonable agreement with real world data, which shows high proportions of hip injuries (Figure 15). However, NASS data shows an almost equal proportion of thigh+knee injuries, which are not represented in the crash test data.

Compared to proportions of risks in the HIII-50M unbelted tests, the HIII-50M risks greater than 25% were all to the hip, while the HIII-5F had one risk greater than 25% to the femur/knee. Figure 11 shows that in the real world, unbelted occupants with height represented by the HIII-50M have a higher proportion of hip than thigh or knee injuries, compared to the 5F unbelted occupants with nearly equal proportions of hip and thigh injuries. Although NASS and the crash test data are in some agreement in this comparison, since the HIII-50M had no femur/knee risks greater than 25% and the HIII-5F had one, in general femur/knee injuries are underpredicted for both dummy sizes.

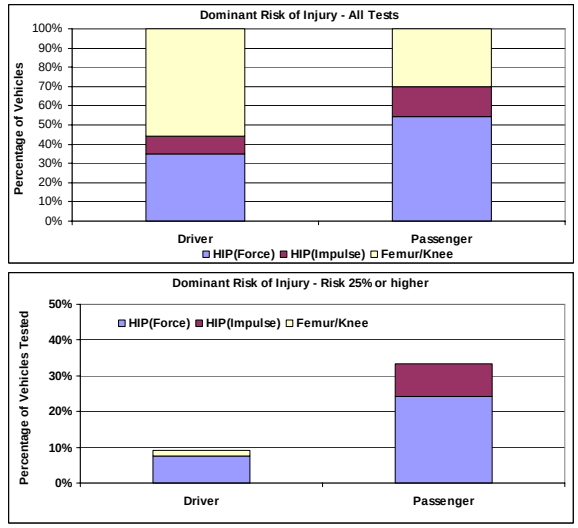

Figure 27. Dominant risk of injury in unbelted 5th percentile female frontal crash tests for all tests and for tests where risk is at least 25%.

Belted Frontal Research Tests: Only one out of 71 tests of the HIII-5F driver in a belted full frontal crash test environment had a calculated risk of KTH injury greater than 25%, as seen in Figure 28. Two other tests had risks close to 25%, but the majority of calculated risks were well below this level, with an average risk of 3.14%. Compared to real world risk for belted drivers in high severity full frontal crashes (20%), this risk is very low.

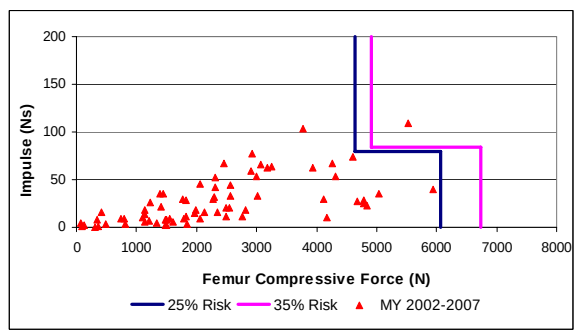

Figure 28. Peak compressive femur forces and impulses in belted frontal crash tests with 5th percentile female drivers.

97% of the drivers in this belted test have their greatest risk of injury to the femur/knee. However, in the one test with risk greater than 25%, the dominant risk was to the hip(force). Real world injuries occur in equal proportion to hip and thigh, with only somewhat smaller proportion to the knee (Figure 15). The predicted risks do not reflect the real world injuries for this crash condition.

Frontal Offset Tests: Three frontal offset tests at 40 km/h were conducted with belted 5th percentile

female dummies in the driver position. In all three tests, there was essentially zero risk of KTH injury (average calculated risk = 0.024%). This is a very small sample of crash tests, but the real world risk for high severity left frontal offset crashes is much higher at 27% (Figure 14). However, this real world risk may be elevated somewhat because it was determined from higher deltaV crashes (48-70 km/h) than were simulated in these crash tests.

DISCUSSION

The compressive femur forces and impulses in FMVSS No. 208 unbelted tests are noticeably greater than those in the belted NCAP tests (or belted research tests, for the 5th percentile female) even though the NCAP tests and many of the belted research tests were conducted at higher speeds than the FMVSS No. 208 tests. This is because the unbelted dummy in the FMVSS No. 208 test strokes the knee bolster to a greater extent than the belted dummy. Higher forces and impulses lead to higher average calculated risks in the unbelted tests than the belted tests. This observation is consistent with real world crash data, which shows higher risk for unbelted occupants than belted occupants.

The risk of KTH injury obtained from 48-64 km/h frontal crash tests with belted dummies underestimated the observed risk in corresponding real world crashes with belted occupants. This observation is similar to that reported by Saunders et al. (2004) where KTH injury risk obtained in frontal offset deformable barrier crash tests with belted dummies using the current FMVSS No. 208 femur injury criterion, was found to under-represent the corresponding real world injury risk. This underestimation of real world KTH injury risk using belted dummies may be related to the low levels of dummy knee-to-knee bolster interaction, as evidenced by the low femur force and impulse values in belted dummies compared to unbelted dummies in frontal crash tests.

Although KTH injury risk was underestimated in belted crash tests, in both NCAP and IIHS, the calculated risk was lower in recent model year vehicles than in older model year vehicles. This trend is consistent with NASS data, which showed a lower risk for belted occupants in MY 2001-2008. Decrease in risk could be attributed to improved restraints, such as pretensioners, that help to reduce the occupant's forward travel and engagement with the knee bolster or other vehicle structures. Improved restraints could have also played a part in the decrease in hip injuries with vehicle model year, a trend that was seen in both the crash test data and the real world data for belted occupants.

The frontal crash tests examined were collinear crashes where the dummy knees contacted the knee bolster with knee loading primarily along the femur longitudinal axis. However, many of the real world frontal crashes investigated were oblique impacts, which could result in varied occupant kinematics. The dummies representing two specific occupant statures were positioned in the crash tests using set procedures. However, occupant shape, size, weight, posture, and seating position relative to the passenger compartment are quite varied in the real world. As a result, the knee impacts in real world crashes may have been with surfaces other than the knee bolster and in various impact directions other than along the femur axis. Additionally, risk derived from the crash test "fleet" was not adjusted to account for the distribution of vehicle models in real world crashes. All these factors may have an affect on the comparison between the KTH injury risk estimated from the crash test data and that observed in the real world.

The Rupp KTH injury criterion applied to the Hybrid III dummy is able to discern the relative risk of hip and femur/knee injury for a given femur force time history using both the peak compressive femur force as well as the associated impulse of force. This additional information may aid in the design of knee bolsters where both peak dummy femur force and the impulse are used as optimization parameters to minimize the risk of KTH injury for belted and unbelted occupants.

In unbelted full frontal crashes, overall risk of KTH injury, as well as the occurrence of hip injuries, was reasonably well predicted by the KTH criterion. However, the thigh and knee injuries that occur in large proportions in the real world are not represented in these crash tests. This may be partly due to the fact that the femur/knee portion of the KTH injury criterion only addresses distal femur and knee injuries and does not account for injuries in the femur shaft that can occur due to bending. Therefore, KTH injuries in the real world that occur due to bending stress in the femur may not be fully accounted for with this criterion.

This KTH criterion was developed using human cadavers but could not be directly applied to the Hybrid III dummies due to differences in response between the dummies and cadaveric subjects to axial knee impacts (Rupp et al. 2003a, 2005) and because hip forces cannot be directly measured in the Hybrid III dummy. Therefore, a new KTH injury criterion formulation applicable to the Hybrid III dummies was developed by applying the cadaver KTH criterion to simulations using mathematical models of the cadavers and dummies under similar impact conditions (Rupp et al., 2009). However, this

formulation did not take into consideration differences in kinematics and interaction with the restraint environment between humans and dummies. Use of a dummy with KTH responses and knee restraint interaction similar to the human and with instrumentation to directly measure hip forces would allow direct application of the Rupp et al. (2009) KTH cadaver injury criterion to the dummy. This would eliminate any uncertainties that may arise from the additional step of developing injury risk formulations applicable to the dummy.

CONCLUSIONS

The KTH criterion developed by Rupp et al. (2009) was applied to various frontal crash tests using the HIII-50M and the HIII-5F femur data. Using this criterion, the risk of AIS 2+ KTH injury was underpredicted for belted occupants. However, injury risk predicted for unbelted occupants was reasonably close to the real world risk. Trends by model year (i.e. decreasing overall risk and risk of hip injury for belted occupants) are consistent between real world and crash test data, even though the risk level in belted crash tests is very low. For unbelted occupants, hip injuries are the dominant injury mode for both the real world and the crash tests. However, femur and knee injuries that occur in the real world are underpredicted in frontal crash tests with the HIII dummies.

REFERENCES

Kuppa, S., Wang, J., Haffner, M., Eppinger, R., "Lower Extremity Injuries and Associated Injury Criteria," 17th ESV Conference, Paper No. 457, 2001.

Kuppa S., and Fessahaie O. "An Overview of Knee-Thigh-Hip Injuries in Frontal Crashes in the United States," 18th ESV Conference, Paper No. 416. 2003.

Read, K., Burgess, A., Dischinger, P., Kufera, J., Kerns, T., Ho, S., Burch, C., "Psychosocial and physical factors associated with lower extremity injury," Proceedings of the 46th Annual Conference of the Association for the Advancement of Automotive Medicine, pp. 289-303, 2002.

Read, K., Dischinger, P., Kerns, T., Ho, S., Burgess, A., Burch, C., "Life-Altering Outcomes after Lower Extremity Injury Sustained in Motor Vehicle Crashes," Journal of Trauma, 57(4): 815-823.

Rupp, J., Reed, M., Kuppa, S., Wang, S., Goulet, J., Schneider, L., "The Tolerance of the Human Hip to Dynamic Knee Loading," Stapp Paper No. 2002-22-0011. 2002.

Rupp, J., Reed, M., Madura, N., Kuppa, S., Schneider, L., "Comparison of Knee/Femur Force-Deflection Response of the Thor, Hybrid III, and Human Cadaver to Dynamic Frontal Impact Knee Loading," 18th ESV Conference, Paper No. 160. 2003a.

Rupp, J., Reed, M., Jeffries, T., Schneider, L., "Effect of Hip Posture on the Frontal Impact Tolerance of the Human Hip Joint," Stapp Paper No. 2003-22-0002. 2003b.

Rupp, J., Reed, M., Madura, N., Kuppa, S., Schneider, L., "Comparison of the Inertial Response of the Thor-NT, Hybrid III, and Unembalmed Cadaver to Simulated Knee-to-Knee Bolster Impacts," 19th ESV Conference, Paper No. 05-0086. 2005.

Rupp, J., Miller, C., Reed, M., Madura, N., Klinich, K., Schneider, L., "Characterization of Knee-Thigh-Hip Response in Frontal Impacts Using Biomechanical Testing and Computational Simulations," Stapp Car Crash Journal, Vol. 52 (November, 2008), pp. 421-474.

Rupp, J., Reed, M., Miller, C., Madura, N., Klinich, K., Schneider, L., Kuppa, S., "Development of New Criteria for Assessing the Risk of KTH Injury in Frontal Impacts using Hybrid III Femur Force Measurements," 21st ESV Conference, 2009.

SAE J211: Society of Automotive Engineers, Recommended Practice J211/1 Part 1 – Electronic Instrumentation, Rev. March 1995.

Samaha, R., Elliott, D., "NHTSA Side Impact Research: Motivation for Upgraded Test Procedures," 18th ESV Conference, 2003.

Saunders, J.W., Kuppa, S., Prasad, A., "NHTSA's Frontal Offset Research Program," SAE No. 2004-01-1169, SAE International, SAE World Congress, 2004.

Summers, S., Prasad, A., "NHTSA's Recent Compatibility Test Program," 19th ESV Conference, 2005.

Stucki, L., Hollowell, W., Fessahaie, O., "Determination of Frontal Offset Test Conditions Based on Crash Data," 98-S1-O-02, 16th ESV Conference, 1998.

CHARACTERISTICS OF FATALITIES IN THE CIREN DATABASE

Peter G. Martin
Stephen Ridella
National Highway Traffic Safety Administration
U.S. Department of Transportation
Washington, D.C., USA

Patricia C. Dischinger
Gabriel E. Ryb
Cynthia Burch
Shiu Ho
National Study Center for Trauma & EMS
University of Maryland School of Medicine
Baltimore, Md., USA

Paper Number 09-0253

ABSTRACT

This paper examines whether CIREN fatal cases are representative of crash fatalities in terms of injury patterns and the time to death. To examine the association, CIREN fatalities are compared with those of all motor vehicle crashes. Comparison data sets are derived from FARS data and from records obtained from the Maryland Office of the Chief Medical Examiner. Differences in injury patterns between those who died early-on vs. those who died later are documented. The findings suggest that the CIREN dataset is representative of real-world fatalities in terms of the fraction of deaths occurring within thirty minutes of the crash; and that, as expected, occupants who die early-on in CIREN are observed to have more severe injuries than those who die later. Moreover, injuries among early-on deaths appear to have a slightly different distribution than among those who die later. Also, CIREN has a higher fraction of cases where occupants died after twenty-four hours than in the U.S. population. The results of this study will help to refine methods used to estimate mortality associated with particular injuries by assessing the completeness of injury records for fatal cases.

BACKGROUND

The National Highway Traffic Safety Administration (NHTSA) is responsible for reducing deaths, injuries, and economic losses resulting from motor vehicle crashes in the US. NHTSA's goal of reducing highway traffic fatalities is achieved by establishing safety priorities driven by real-world crash data.

Typically, a NHTSA plan of action focuses on an intervention aimed to mitigate injuries. It is accompanied by a benefits analysis in which costs and lives lost are computed for a given priority area. This involves the identification of a target population to which the benefit is directed. A target population consists of an occupant group sustaining injuries to a particular body region that are associated with high mortality and may be mitigated by a proposed intervention. Unit costs are first established by equating a cost to a given injury type, injury severity, and injured body part. These costs are then applied to a target population to compute benefits associated with interventions aimed at narrow ranges of injuries.

One of the difficulties in using crash data in this type of analysis is that the categorization of motorists by injury type and body region is not usually straightforward. As a result, a given crash victim is typically categorized by selecting the injury associated with the maximum severity score in accordance with the Abbreviated Injury Scale (MAIS). For each occupant injury record, however, there are frequently multiple injuries in multiple body regions. This makes it difficult to judge how likely it is that a life will be saved if a specific injury is mitigated. Nonetheless, it is reasoned that the cost associated with the MAIS injury is the approximate cost incurred by the victim. Thus, the costing methodology is an averaging process: it is understood that most victims suffer multiple injuries, and all injuries contribute to the overall cost. This methodology offers a reasonable means to account for injury costs.

<u>New injury accounting process</u>. A new injury accounting methodology was developed by Martin and Eppinger (ESV 2005) that takes into account multiple injuries. Estimates are made of costs and the number of fatalities attributable to specific types

of injuries. The procedure examines a crash victim's entire injury record in the process. Fatalities attributable to specific injuries are determined by considering the effect that a specific injury or set of injuries has on fatality risk. Attributable costs are estimated in a similar manner. The procedure estimates the risk to life that multiple injuries pose to crash victims. It also estimates the costs borne by and the number of fatalities attributable to specific types of injuries. For example, if one desires to estimate the number of lives saved if a particular injury is mitigated, it may be accomplished directly. This is much harder to accomplish in the context of an MAIS value which represents just one injury from a record of multiple injuries.

Ranking CIREN injuries via optimization. The injury accounting process is based on a ranking of AIS injury codes established using an optimization scheme (see Martin and Eppinger, 2003). Each seven-digit AIS code is placed into one of approximately 60 individual injury groups and each group is assigned a mortality constant ranging from zero to one. Mortality constants were previously derived from Crash Injury Research and Engineering Network (CIREN) data.

For each CIREN case, the mortality constants associated with each of the crash victim's injuries are determined by the overall dataset which makes use of a probability function that predicts mortality. For each case, deviance is computed by comparing the probability of fatality to the case fatality observed (0=nonfatal, 1=fatal). Optimization solvers are then used to assign mortality constants to each of the 60 codes such that the average deviance of all cases is minimized.

The accuracy of the ranking system, and hence, the fatality attribution process is contingent upon complete and accurate injury records in fatal cases. Crash victims entered into the CIREN database are selected based on patient admission into the Trauma Center, vehicle model year, injury severity, crash type, and occupant restraint condition. Also, CIREN enrollees (or next of kin) must consent to enrollment. CIREN is not sampled with the intention of providing a dataset that represents a U.S. population. Exceptions to the consent process are made for "dead on arrival". Nonetheless, CIREN fatalities may be under-represented by those who died at the scene and were never admitted to the trauma center.

Recent studies comparing CIREN data to the nationally representative National Automotive Sampling System – Crashworthiness Data System (CDS) sample have shown that the fatality rates are about the same. Flannagan and Rupp (2009) found that when CDS cases that met the CIREN criteria were compared to CIREN, the two datasets were quite similar in terms of the fatality rate. However, this study only considered the incidence of fatalities, and not the distribution of injuries. A similar study applied the Mahalanobis distance metric methodology to determine similarity between CIREN and CDS cases and found the mortality rate among occupants in the CIREN database to be much lower than those in the CDS (Stitzel et al, 2007). But this likely occurred because MAIS 2 cases (which are almost always non-fatal) were stricken from their CDS dataset.

OBJECTIVE

This paper examines whether CIREN fatal cases are representative of real-world fatalities in terms of injuries and the fraction of early-on deaths. It investigates the extent of any selection bias in CIREN for fatal cases by determining whether early-on fatalities are under-represented. It also investigates whether occupants who die early-on have different injuries than those who die later. Several other data sources are also examined to offer insights into the limitations associated with benefits analyses aimed at mitigating particular injuries and combinations of injuries.

DATA SOURCES

The following data sources were used in this study:

CIREN Database. The CIREN database is maintained by NHTSA as a means to examine injury causation in crashes. This database contains a sample of comprehensive medical records of severely injured occupants admitted to one of eight U.S. Level 1 trauma centers. It consists of 300-400 passenger car crashes per year and the database now includes information on approximately 4,000 drivers and passengers.

The injury ranking methodology described earlier was determined based on CIREN data of adults. For the analysis herein, the CIREN dataset was limited to adult fatalities only. The dataset includes the time-to-death from the crash and all injury information. Based on the findings of this study, the caveats and conditions upon which CIREN data may be used in such a ranking methodology shall be discussed.

Maryland Autopsy Reports – Autopsy reports generated by the Maryland Office of the Chief

Medical Examiner (OCME) are used to provide a dataset for comparison of fatalities with CIREN data. OCME cases for years 2000-2002 for all deaths of passenger car drivers are used. The OCME cases, which include about 900 deaths, represent an unbiased census of fatally injured occupants in Maryland. They include those that died at the scene of the crash early-on and those that died later after hospital treatment.

The autopsies are conducted by medical examiners trained in pathology. Every traffic fatality is accompanied by a police crash report and any related available records. Injuries are identified at the time of the autopsy from either a full investigation by the medical examiner or from a combination of an external investigation and existing medical records.

The cause of death is determined by the medical examiner based on the documented injuries. The time of death from the crash is determined from medical records, if the person is declared dead in the field by a medical doctor, or investigative techniques employed by the medical examiner.

OCME Variables. Injury information takes the form of text descriptions of the findings of a pathologist. OCME reports also include a listing of injuries identified in the examination. Each autopsy report is unique and the final listing of injuries abstracted.

Other variables that typically appear on an OCME report include age, date of birth, gender, vehicle make and model, crash date, crash time, seating location, seatbelt use, airbag use, rollover collision (y/n), alcohol/drug use, date of death, time of death, cause of death, and hospital treatment. Vehicle and crash information are taken from the police crash report; alcohol/drug use are taken from the OCME toxicology testing or hospital record; hospital treatment is determined from medical records.

Fatal Automotive Reporting System (FARS). The FARS – another crash data base maintained by NHTSA – is a census of all fatalities involving motor vehicles on public trafficways in the United States. FARS records only include fatalities occurring within 30 days of the crash. FARS also contains information on the time of death, but has limited injury information. FARS records for 2000-2002 were abstracted into a dataset that contained fatally injured passenger car drivers in the U.S. In order to compare directly with the OCME dataset, the FARS dataset was subdivided into a secondary dataset of crashes occurring in the state of Maryland. The FARS dataset is used to compare the time-to-death from the crash captured in the CIREN and OCME datasets.

METHODS

The first objective is carried out by investigating whether CIREN fatal cases are representative of real-world fatalities in terms of the fraction of early-on deaths. Fatality census counts provided by FARS are compared to CIREN cases. Since FARS is a census of all U.S. fatalities, it represents the baseline for the comparison.

The second objective involves investigating whether occupants who die early-on have different injuries than those who die later. A comparison of CIREN fatalities is carried out comparing the injuries sustained in those two categories of cases. Fatality data abstracted from the Maryland OCME files are compared in the same manner to provide an independent evaluation. The OCME's records constitute a census of all motor vehicle fatalities in Maryland.

Maryland OCME Data Abstraction. Injury data on fatalities were obtained by abstracting autopsy reports at the Office of the Chief Medical Examiner for the State of Maryland. While these reports are quite detailed, for this purpose a summary provided at the end of the report was utilized to abstract the injury descriptions. Given the fact that some of the data required for coding AIS scores, such as duration of loss of consciousness, are obviously not available, it was decided to code the injuries using the more anatomic-based ICD-9 codes.

In applying ICD-9 codes to OCME injury descriptions, severity levels were estimated to be 'moderate' if there was no further qualifying information. These codes were then 'translated' to AIS scores using software that was developed for that purpose. Maximum AIS scores (MAIS) were then determined, based on the highest AIS score for a given individual. For example, if the autopsy report reported 'spleen laceration', in the absence of further detail it was translated to a Grade III spleen laceration.

Therefore, in order to provide consistency in coding, ICD-9 codes were selected to represent the injuries described on the narratives. Those codes were then entered into a software program, ICD-9 MAP (Johns Hopkins, 1997) that converted the ICD-9 codes into AIS codes.

OCME reports from which a detailed set of injury codes could not be abstracted were excluded from the dataset. An example of a case where the OCME file was not coded is where the final list of injuries consisted of the words "brain injuries" or "multiple injuries." Without the full report containing specific observations, these cases were not able to be coded and were excluded.

CIREN and OCME Case Categorization. The CIREN and OCME datasets were broken down by time-to-death from the crash for comparison with the FARS dataset. "Early-on" deaths are defined as those occurring within thirty minutes of the crash. About 95% of early-on fatalities in the CIREN dataset died at the scene of the crash. The remainder died in transport or were pronounced dead soon after arrival to a hospital. "Later" deaths include all others. Furthermore, the CIREN and OCME datasets were examined case-by-case to determine the most severe injury.

Reduced CIREN and OCME Datasets. To judge whether CIREN data is appropriate for establishing mortality constants in accordance with the optimization methodology without bias, the respective CIREN and OCME datasets were reduced to non-deterministic cases. In other words, cases where a non-survivable injury was present were not included in the dataset. Such injuries include all those having an AIS code with a severity score of 6, and a few with a score of 5. These injuries have been observed to always result in a fatality and have an associated mortality constant that results in an estimate of probability of fatality of 100%. All codes with an AIS severity score of 2 were also removed since most have little influence on fatality probability.

RESULTS

OCME Abstracts. Table 1 shows the number of OCME autopsy reports for the period 2000 to 2002. There were a total of 1,044 crash reports involving a fatality, of which 732 (70%) provided abstractable injury information that was fully coded. For reference, Maryland fatalities recorded in FARS are provided to corroborate the OCME crash reports. The slightly higher incidence appearing in the OCME dataset reflects additional OCME cases where the crash may have occurred on a non-public trafficway or where the occupant died over 30 days after the crash.

The OCME and FARS datasets are very similar, which is expected given that FARS statistics are derived in part from the OCME files. The comparison is shown for reference to demonstrate that the autopsy extracts are an accurate representation of all Maryland fatalities and are unbiased by the inclusion criteria.

Time-to-Death Comparison. Table 2 shows the distribution of time intervals between the crash and death for the OCME dataset, the CIREN dataset, and in FARS. Early-on deaths (i.e., those that occurred within thirty minutes of the crash) in CIREN occurred in about the same proportion as in the FARS census data. These represent mostly cases where occupants died before being admitted to a treatment facility.

In comparing the Maryland OCME autopsy data with FARS, it is seen that most of the OCME records that could not be abstracted were early-on deaths where time to death was less than 30 minutes (39% vs. 50%). And among those who died later, Table 2 indicates that CIREN is over-represented by those who survived longer.

Table 1. OCME 2000 to 2002 Driver Fatalities
(Age 16 and over, excluding motorcycle and moped riders)

Year	Md. Fatalities in FARS	OCME Crash Reports	OCME Autopsy Extracts		OCME Autopsy Extracts With Injury Data	
			N	% of Crash Reports	N	% of Crash Reports
2000	297	325	286	88	264	81
2001	352	360	330	92	315	88
2002	349	359	208	58	153	43
Total	998	1,044	824	79	732	70

Table 2. Fatality Counts in OCME, CIREN, and FARS Datasets by time to death from crash.

Time from Crash to Death	CIREN (N=404) %	OCME w/ Injury Data (N=676) %	Md. Fatalities in FARS, (N=935) %	FARS Entire U.S. (N=66,160) %
0 – 30 Minutes	45	39	50	48
31-60 Minutes	9	19	14	15
1 to 2 Hours	6	17	15	17
2 to 24 Hours	15	14	9	10
1 to 5 days	10	5	7	5
6 to 30 days	15	4	6	5
31+ days	-	2	-	

*There are 56 OCME and 63 FARS cases with missing time to death.

Injury Severity Comparison – Full Datasets. Figure 1 and Figure 2 show the distribution of injuries among various body regions for the OCME and CIREN datasets. Each bar represents the percentage of cases in which the injury is present. For example, 148 of the 181 "Died early-on" cases (82%) included a thoracic organ injury of which 47 (32%) had a severity score of AIS 6. Among the 148 cases, the average thoracic organ injury MAIS was 4.8 (typically there were multiple thoracic organ injuries per case). Other injury categories such as deep brain, burns, lumbar spine, knee, and eyes and ears all appeared in less than 8% of deaths and are not shown in Figure 1 and 2.

It is apparent from Figure 1 and Figure 2 that early-on fatalities are generally associated with injuries having a higher threat to life. This is reflected in the higher average AIS scores and the greater number of cases containing unsurvivable injuries.

As expected, the CIREN injury scores are consistently higher than those abstracted from the Maryland OCME reports. As described earlier, the data extraction process, including the use of ICD-9 MAP software, tends to result in conservatively coded injuries. Therefore, the two datasets are only compared for within-dataset trends and not as a case/control comparison.

Figures 1 and 2 also reveal how the frequencies of injuries differ within body regions for early-on deaths vs. those who died later. The biggest differences are seen in the CIREN dataset (Fig. 1) where thorax organ injuries, brain injuries (non diffuse), skull fractures, and cervical spine injuries all occur more often in early-on deaths. Diffuse axonal injuries (DAI), including "Loss of Consciousness" injuries of severity AIS 3+ are notable exceptions. In the OCME dataset, the relative evenness of the bars in Fig. 2 indicates that the fractions of all injuries are about the same.

Injury Severity Comparison – Reduced Datasets. As explained earlier, the optimization routine to determine injury rankings operates on a reduced dataset in which all fatal cases having unsurvivable injuries have been removed. For both the reduced CIREN and OCME datasets, there are only five categories of injuries that occur in more than 15% of deaths. Furthermore, they are the same five categories. Referring to Fig. 3, they are: 1. Thoracic organ injuries; 2. Rib/Sternum; 3. Cortical brain, SDH, SAH; 4; Skull fractures (vault or base); 5. Abdominal organ injuries.

In terms of the frequencies of deaths occurring early vs. later, the reduced OCME and CIREN datasets show similar trends as the full datasets. As shown in Fig. 3, the CIREN frequency bars for early vs. later are more aligned than in the full set.

The overall MAIS scores of both CIREN and OCME reduced datasets are understandably lower than the full dataset. And in CIREN in particular, the severity scores of early-on deaths vs. those who died later begin to converge. This is also understandable given the high fraction (almost half) of early-on deaths that have been removed from the reduced dataset due to the presence of an unsurvivable injury.

The biggest change in going from the full to reduced datasets occurs with OCME rib/sternum injuries. Due to the removal of a high number of AIS 2 codes, their frequency is markedly decreased in the reduced set.

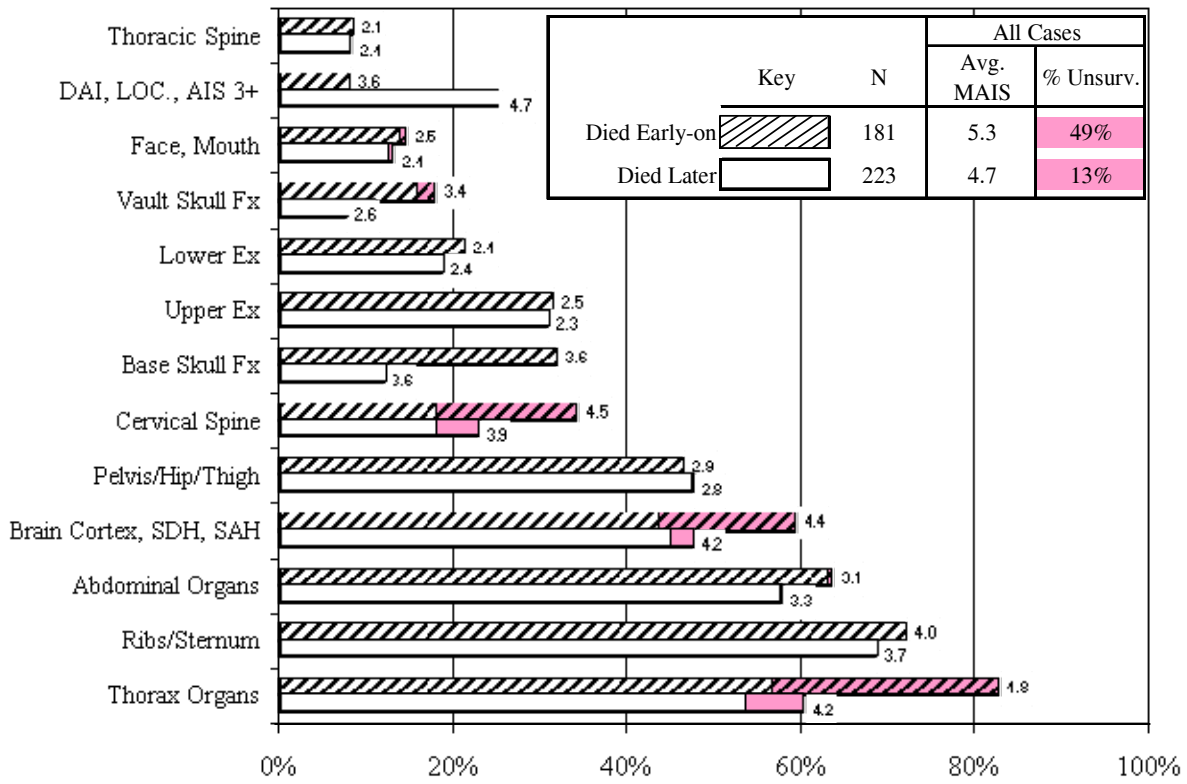

Figure 1. Full CIREN Dataset Comparison. Injury make-up of CIREN dataset by time-to-death. Colored areas represents cases where unsurvivable injuries were present.

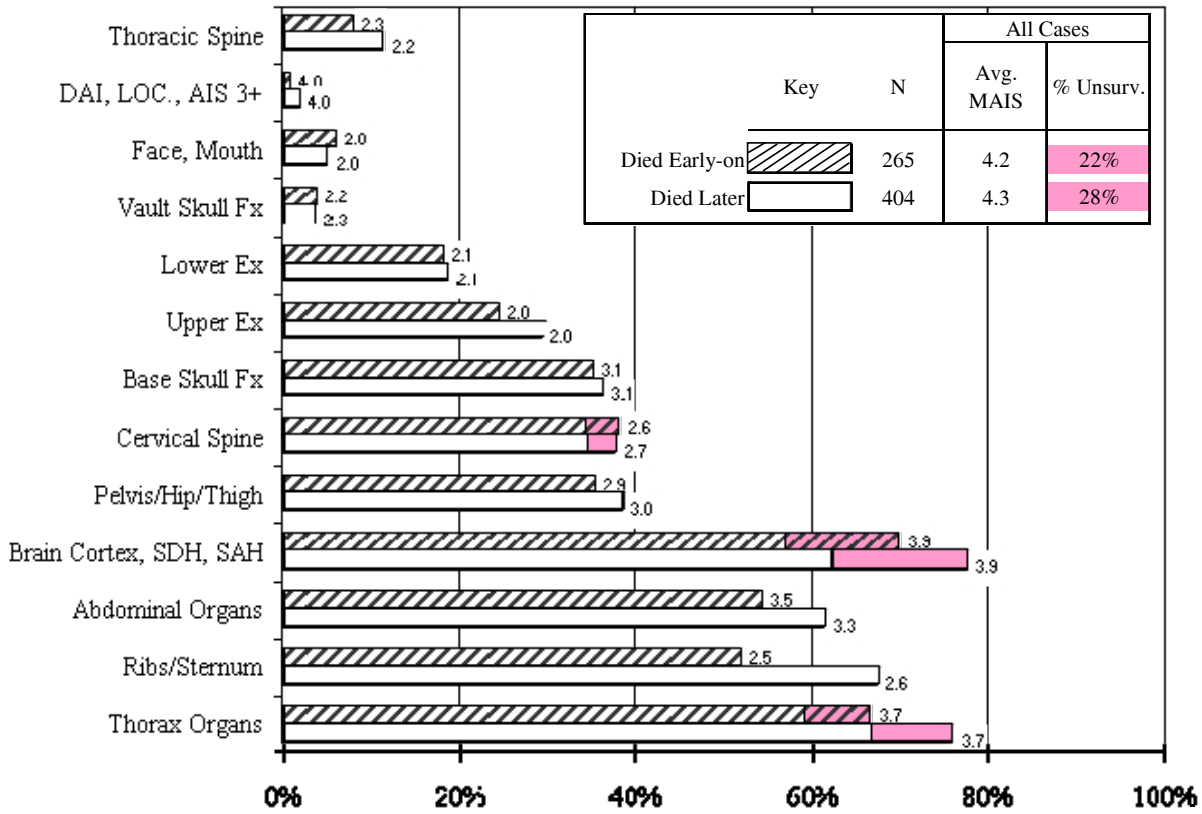

Figure 2. Full OCME Dataset Comparison. Injury make-up of OCME dataset by time-to-death. Colored areas represents cases where unsurvivable injuries were present.

Key	CIREN N	CIREN Avg. MAIS	OCME N	OCME Avg. MAIS
Died Early-on	93	4.6	207	3.7
Died Later	195	4.5	301	3.8

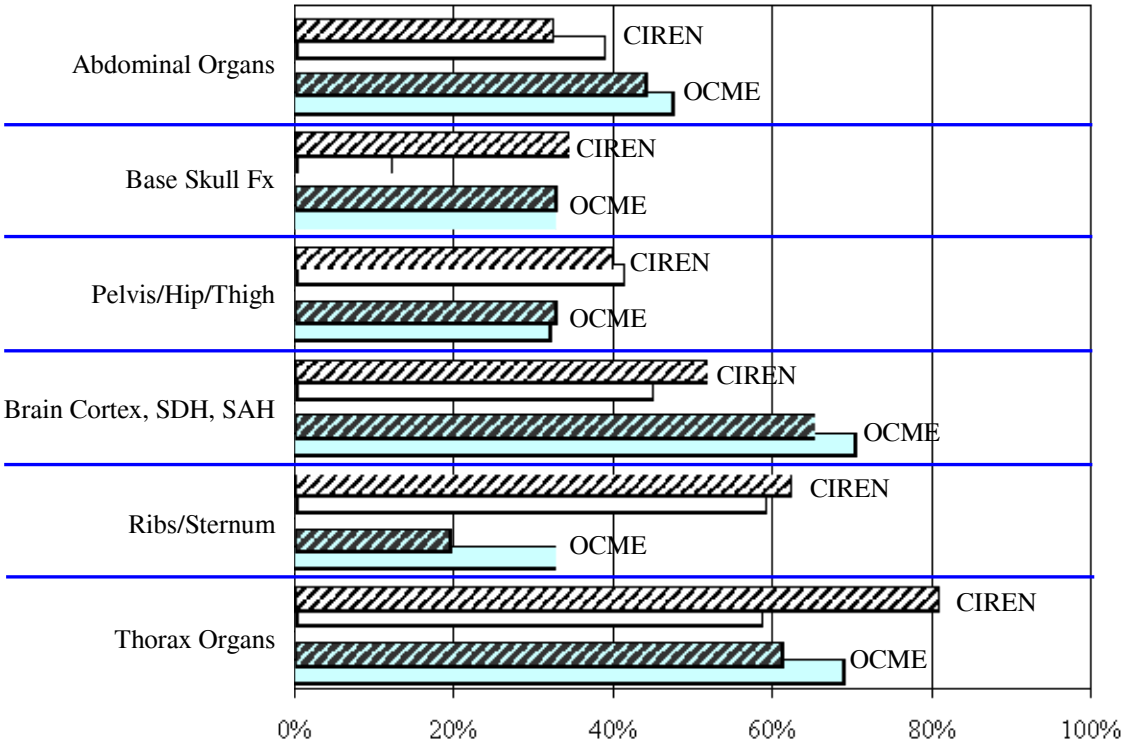

Figure 3. Reduced Dataset Comparison. Injury make-up of CIREN and OCME datasets by time-to-death.

DISCUSSION

Objective 1 – Fraction of early-on deaths in CIREN. In comparison with the FARS and OCME datasets, the CIREN dataset appears to have a similar fraction of early-on deaths. But among those who died later, CIREN contains a greater proportion of those who died several days later (versus died within 24 hours).

This over-representation of deaths after the first day may be explained partly by the contributions of patients transferred from other hospitals. Typically, patients at Level 2 trauma centers that require specialized care (i.e. management of complex spinal and orthopedic injuries) are transferred to Level 1 trauma centers after they become physiologically stable. Since they arrive in a stable condition to the CIREN center, they are unlikely to die within the first 24 hours. Hence, the inclusion of transfers is likely to over-represent those that die after 24 hours.

Also, CIREN's patient recruitment process, in which consent for admitted patients is required, makes it difficult to enroll patients who are admitted and die within two hours (i.e., prevailing events take priority over the enrollment protocol.)

Objective 2 – Differences in injuries for early-on deaths. A within-dataset comparison of CIREN data vs. OCME data shows the two datasets to be slightly at odds over whether early-on injuries are much different than injuries of those who died later (Figs. 1 and 2). As seen earlier, the CIREN dataset indicates that thoracic injuries, skull fractures, and cervical spine injuries appear more often in early-on deaths. The CIREN dataset also shows, as expected, that early-on deaths more often have injuries that are

unsurvivable than in those who die later (49% vs. 13%). In the OCME dataset, unsurvivables are about the same in both (18% vs. 20%). This latter finding within the OCME may be an artifact of the data abstraction process (see below).

Data Origin - OCME vs. CIREN. The differences in injury make-up between the CIREN and OCME datasets prompt further discussion. For early-on deaths in particular, one would expect CIREN and OCME to be very similar. On-scene deaths in CIREN (which include the majority of early-on deaths) represent cases in which occupants receive no hospital treatment. It follows that CIREN early-on deaths should be just like any other early-on deaths, suggesting that the make-up of injuries sustained in CIREN early-on deaths should not differ from those in all Maryland early-on deaths.

Nonetheless, the make-up of injuries in the OCME and CIREN early-on deaths do differ. In the OCME dataset, there is little difference in the MAIS levels per injury (Fig. 2) between early-on vs. later deaths. But this is uncharacteristic, as it seems reasonable to believe that early-on deaths should have more severe injuries than those who died later.

The abstraction process used to code OCME reports probably played a roll in the uncharacteristic data. As stated earlier, those with less information on the injury list appear to be biased by time-to-death. In the OCME dataset, 23% of early-on deaths contain three or fewer AIS 2+ codes on the injury record, compared to 4% in died later cases. On the other hand, only 11% of CIREN cases - for both early-on and later deaths – have three or fewer injuries coded.

The injury severity discrepancy between OCME and CIREN is also related to the process of abstracting injury codes. Often, injury lists are not detailed enough to ascertain injury severity level. The practice of assuming a "moderate" severity level when coding cases has the general affect of undercoding injuries, as many are probably "major" or "complex" injuries with corresponding scores of AIS 4 or 5 given that they occurred in a victim that died. On the other hand, CIREN medical records are coded by AIS directly, resulting in more accurate coding.

The CIREN and OCME are relatively consistent in the frequency of the various injury categories (i.e., the descriptions listed in Figs. 1 and 2). The largest discrepancy is with the greater incidence of brain injuries (non-DAI) in the OCME data. This may be related to the CIREN enrollment criteria, which may under-sample crash scenarios where brain injuries may be particularly prominent, such as crashes involving unbelted occupants and crashes involving vehicles without frontal airbags. This merits further investigation. (The other big difference is with DAI/Level of Consciousness injuries, which will be discussed later.)

Notwithstanding the differences discussed above, the content of predominant injuries (i.e., those occurring in over 50% of deaths) is still fairly similar: thoracic organ injuries, rib injuries, brain injuries (non-DAI), and abdominal injuries.

Maryland vs. U.S Population. Given that trauma care and crash response time in Maryland is very good, the injuries sustained by victims of fatal crashes may vary in other parts of the U.S. The OCME's records constitute a census of all motor vehicle fatalities in Maryland (about 450 per year). However, not all records were retained for this analysis.

Table 3. Characteristics of Fatally Injured Drivers, 2000-2002.

	FARS Entire U.S. (N=66,160) %	FARS Md Only (N=998) %
Male	71	71
Mean Age	42	43
Taken to hospital	41	56
Seat Belt Used	36	53
Rollover Crash	31	18
Ejection	27	19

Table 3 compares the FARS dataset between fatalities occurring in Maryland and those occurring in the United States at large for the years 2000-2002. Maryland fatalities are shown to be aligned with the U.S. population in terms of occupant age, sex, and time-to-death. Although Maryland had a higher percentage of fatally injured drivers taken to the hospital, this may not necessarily reflect more treatable (and less severe) injuries among Maryland deaths. Maryland has been shown to have a very well coordinated trauma system that gets patients to the hospitals efficiently. In fact, the FARS dataset indicates that some drivers who died within 30 minutes – classified as "early-on" deaths herein – were actually brought to the hospital.

In addition, Maryland has one of the highest driver belt use rates in the country (Glassbrenner, 2004). Table 3 also shows that rollover crashes occur less

often in Maryland. These two factors contribute to fewer occupant ejections, and ejections generally produce more severe injuries than other crash modes. This merits further study since the degree to which injuries differ among deaths of those who are belted vs. unbelted and ejected vs. non-ejected was not investigated herein.

Implications for determining mortality rankings. The methodology described in the Introduction to rank injuries provides a relative comparison of the threat-to-life posed by various injuries. As stated earlier, the accuracy of the rankings (and hence, the fatality attribution process) is contingent upon complete and accurate injury records in fatal cases. The effects of biased and incomplete injury records directly affect the rankings.

Prior to this study, the authors were concerned that many CIREN crash victims who die at the scene might have incomplete injury records. The concern was that medical records might be lacking for those who never made it to a hospital, and only a few, easy-to-observe, low-threat injuries would be reported. It would have meant that rankings of injuries undetected in early-on deaths would be too low because the injuries would have been detected (and reported) in a disproportionate share of nonfatal cases. However, the results reported herein have tempered this concern.

The findings of this study do highlight another concern regarding the category of brain injuries that are coded by level of consciousness or as diffuse axonal injuries (DAI, LOC of AIS 3+ in Figs. 1 and 2). According to the AIS coding manual, a level of consciousness code is only applied in the absence of an anatomical description of a brain injury, or when the LOC severity level is greater than the anatomical severity level. And it is never applied to fatalities that occur within 24 hours. Diffuse axonal injuries, observable only from radiographs, are rarely reported in early-on deaths. This coding convention is clearly evident in Figs. 1 and 2.

Similarly, any other injury categories or severity levels that are difficult to observe positively in an autopsy (such as codes which can only be applied if a certain amount of blood loss is observed) may not be coded as heavily in early-on deaths. The end effect on the mortality ranking process is for such injury categories to be ranked relatively low.

Implications for General Studies Biased or miscoded fatal data affects any benefits analysis, such as that described in the Introduction, where a fatally injured occupant is characterized by a single injury. Thus all benefits are directed to the prevention of that injury. Though fatalities are relatively low in number compared to survivors, they have high associated costs. Thus, the underlying data should be correct.

Other limitations. While not examined at this time, the overall fraction of fatal cases within CIREN has been shown to be representative of the U.S. population for crashes that meet the CIREN enrollment criteria for crash type, vehicle model, and injury severity. The use of the methodology is limited to this criteria. However, these cases are generally the ones NHTSA priorities are focused upon.

Future effort: Imputation. As mentioned earlier, certain injury categories may have deflated threat-to-life rankings due in part to the AIS coding convention and the ability to observe certain injuries at autopsy. Given the logistics involved with the disposition of early-on fatalities, there may be no practical way to observe such injuries. A solution may be to impute codes in early-on deaths.

Methods to impute missing data within NHTSA's databases have been developed for certain variables. For example, Rubin et al (1998) describes a method to impute blood alcohol levels that are missing from fatality crash data. It may be possible to develop a method to impute injuries in early-on fatality records using the other variables within the dataset.

CONCLUSIONS

The purpose of this study is to investigate the extent of any selection bias in CIREN for fatal cases. The primary goal is to help refine methods to estimate mortality associated with particular injuries and combinations of injuries. In pursuit of that goal, the following observations were made.

1. The CIREN dataset appears to be representative of crash fatalities in terms of the fraction of early-on deaths. However, CIREN also appears to have a higher fraction of cases where occupants died after twenty-four hours than in the U.S. population.

2. Occupants who die early-on appear to have different injuries than those who die later. Those who died at the scene tend to have more unsurvivable injuries. It follows that they have more severe injuries in terms of MAIS and their probability of fatality. Early-on deaths also tend to have a higher frequency of brain injuries, skull fractures, thorax organ injuries, and cervical spine injuries.

3. The CIREN dataset also appears to be representative of crash fatalities in terms of the frequency of injuries in early-on vs. later deaths, but this could not be confirmed by comparison with the OCME dataset. This issue should be investigated in the future. Also, brain injuries appear to be under-represented within CIREN deaths.

4. When considering a reduced dataset in which all cases with unsurvivable injuries have been removed, a dataset derived from CIREN is similar to that of the OCME in terms of the frequency of the most predominant categories of injuries and the fraction of early-on deaths. However, CIREN cases tend to be more serious.

5. Implications for injury costs/benefits analyses suggest that benefits could be misplaced if injury records of fatalities are not complete.

ACKNOWLEDGEMENT

The OCME autopsy reports, which are confidential, were obtained by the National Study Center for Trauma & EMS, University of Maryland School of Medicine under agreement with the CODES project. The project has been approved by the University IRB, and meets all requirements for HIPAA. This work was funded by NHTSA under Cooperative Agreement number DTNH22-05-H-01001.

REFERENCES

Association for the Advancement of Automotive Medicine (1998), The Abbreviated Injury Scale, 1990 Revision, Update 98. Des Plaines ILAssociation for the Advancement of Automotive Medicine.

Flannagan CA, Rupp, JD (2009), Evaluation of the Use of NASS-CDS in Categorical Analysis of CIREN Data, Accident Analysis and Prevention (in press).

Glassbrenner, D (2004), Safety Belt Use in 2003 – Use Rates in the States and Territories, Technical Report No. DOT HS 809 713, Dept. of Transportation (US), National Highway Traffic Safety Administration.

ICDMAP-90 Software User's Guide (1997), Johns Hopkins University, Tri-Analytics, 1997.

Martin PG, Eppinger RH (2003), Ranking of NASS injury codes by survivability, 47th Annual Proceedings, Association for the Advancement of Automotive Medicine, Des Plaines IL, October 2003.

Martin PG, Eppinger RH (2005), A method to attribute fatalities and costs to specific injuries, ESV Conference, Paper No. 05-0220, 2005.

National Highway Traffic Safety Administration (2000), National Automotive Sampling System – Crashworthiness Data System, Users Manual. Dept. of Transportation (US), National Highway Traffic Safety Administration.

Stitzel JD, Kilgo P, Schmotzer B, Gabler HC, Meredith W (2007). A population-based comparison of CIREN and NASS cases using similarity scoring, Association for the Advancement of Automotive Medicine, 51st Annual Conference, October 2007.

RECONSTRUCTION OF A REAL WORLD CRASH INVOLVING A CHILD USING HYBRID III 10-YEAR OLD AND 5TH PERCENTILE ADULT FEMALE ATDS

Joseph Ash
Jeff Crandall
Dan Parent
University of Virginia
Center for Applied Biomechanics
United States of America
Chris Sherwood
Insurance Institute for Highway Safety
United States of America
Kristy B. Arbogast
Children's Hospital of Philadelphia
United States of America
Paper 09-0365

ABSTRACT

Validation data for child anthropomorphic test devices (ATDs) are scarce, making it difficult to assess their biofidelity. The goal of this study was to use previously collected real-world data involving a frontal crash with a child occupant to assess the biofidelity of current child dummies. The 9-year old child's anthropometry placed him between the size of the Hybrid III 10-year old and 5th-percentile Adult Female (AF5) dummies. Though injuries on the child indicated that he was properly belted, there were contact points on the vehicle interior and the exact position of the child before the accident could not be definitively determined from the crash investigation. Sled tests with identical seat belts and bench seat were conducted with the HIII-10 year old (n=9) and AF5 (n=6) in various seating configurations to explore the possible posture of the child before the accident. The tests were designed to reproduce the predicted Delta-V of 51 km/h with a smaller subset of the tests performed at 59 km/h to assess the implications of a higher speed on occupant contacts. Video analysis was performed to determine trajectories of the dummy head, chest, pelvis, and extremities. Despite the variation in speed, neither dummy was able to achieve the maximum head excursion necessary to make contact with the dash board. The results suggest that the dummies may underestimate the magnitude of excursion experienced by the child involved in the actual crash. To further investigate this finding, a sensitivity study was carried out using MADYMO Hybrid III 5th percentile female model. In addition to making use of existing data to further the investigation of child dummies, this study examines the biofidelity of two dummies used in child response approximation.

INTRODUCTION

The design of safety equipment for children relies on accurate biomechanical information about their response in crashes. Given the paucity of validation data for child ATDs used in the development and evaluation of safety equipment, efforts must be made to use all available sources. The source of additional data examined in this study is the reconstruction of an automobile crash involving a child. Information about the characteristics of the crash will be used to attempt to recreate the outcome of the crash in laboratory conditions. In the actual crash, the child appeared to be correctly belted in a three point belt when the vehicle had a severe frontal crash with a tree. It is likely that the child was leaning in some fashion to the left in an attempt to help steer the vehicle due to the fact that the driver had lost consciousness while driving. This hypothesis stems from the fact that the child had a head contact closer to the centerline of the vehicle.

This case was chosen for reconstruction because the child seemed to be belted properly (lung contusions, chest contusions, right clavicle fracture all consistent with good shoulder belt placement), did not show signs of submarining (no abdominal injuries, presence of contusions from lap belt low on pelvis), and had a definitive head contact in the vehicle (severe head injury and definite head loading marks on dash). The only criteria which were not ideal were that the child had some degree of non-optimal initial positioning leading to the head contacting the dash approximately 40 cm left of his centerline seating position.

METHODS

Real World Crash

The case was drawn from the Partners for Child Passenger Safety (PCPS) Crash Investigation database. The PCPS Crash Investigation database, from a collaboration between Children's Hospital of Philadelphia and State Farm Insurance Companies, consists of crashes involving child passengers reported to a US auto-insurance company and selected for detailed crash investigation.

The case vehicle was a 1998 Chevrolet W/T 1500 pick-up truck. The W/T stands for "work truck" and indicates the trim level of the vehicle. The work truck is the most basic model of the 1500 series. The work truck trim level differs in several ways from the other trim packages offered in the 1998 model year selection of 1500 series truck with one of the most important differences being the vinyl bench seat as opposed to a cloth bench or cloth captain's chairs that were offered in other levels. The vehicle was also equipped with an after-market seat covering resembling a cotton blanket. The vehicle had cargo in the bed of the truck that increased the overall mass of the vehicle by 159 kg which included the following: camping equipment, 3 bicycles, and tents. With cargo and occupants included the total mass of the vehicle was 2141 kg.

The vehicle was traveling on a tortuous, wooded road when the driver, an adult male, lost consciousness, veered off the road and struck a tree. The driver was restrained with a three point belt and airbag while the child passenger, a 9-year old male, was only restrained with a three point belt. The passenger airbag had been turned off due to the age of the child according to current recommendations. Based on the crash reconstruction, the vehicle had a Delta V of 51.4 km/h and an impact speed of 55.6 km/h. The vehicle made impact with the tree near the centerline of the vehicle causing the crash to be a directly frontal crash with no rotation. The principal direction of force was approximately 360 degrees and the maximum crush depth was 78.4 cm located 7 cm right of the vehicle center line. The child showed injury signs consistent with belt loading on his pelvis and right shoulder indicating proper belt use. The vehicle interior contact locations suggested that the child was out of position at the time of the crash. It was speculated that the child was attempting to either assist the driver or steer the vehicle before the tree impact occurred.

The injuries to the child were severe and caused the child to remain deeply comatose for 12 days after the accident. His head impact was attributed to contact with the displaced vent cover. Heavy scuffing and residual epidermis deposits were found on the vent cover located on the dashboard near the centerline of the vehicle (Figure 1).

Figure 1. Interior of vehicle with contact locations identified.

The case occupant's severe head injuries consisted of a cerebral edema (AIS-3), left medial temporal/posterior basal gangliar hemorrhagic contusions (AIS-5), a diffuse subarachnoid hemorrhage and a diffuse axonal injury with a white matter injury (AIS-5). He also sustained soft tissue ecchymosis areas above each eye (AIS-1). The proper use of belts was determined by injuries sustained to the child's torso and pelvis. His lower torso loaded the lap belt webbing which resulted in ecchymotic lesions over his pelvis (AIS-1). His interaction with the shoulder belt webbing resulted in a right chest contusion (AIS-1), a complete fracture through the mid-shaft of the right clavicle (AIS-2) and a right lung contusion (AIS-3) with residual atelectases. Though other injuries occurred, these injuries were the most pertinent to crash reconstruction and the severity of the crash.

Crash Reconstruction

The child's anthropometry placed him between the size, stature and approximated seated height, of the Hybrid III 10 year old and Hybrid III 5th percentile female dummies (Table 1). Both dummies were tested, and due to the relatively small differences between the child and each dummy size, no scaling was performed on the dummy injury metrics or kinematic trajectories.

Table 1.
Anthropometric data for 9-year old involved in crash

Measurement	Unit	Value
Shoulder to Hip	cm	41
Elbow to Beginning of Hand	cm	20
Hip to knee	cm	37
Knee to ankle	cm	33
Seat to Shoulder	cm	50
Bottom of Neck to Top of Head	cm	20
Head Circumference	cm	51
Neck Length	cm	5
Chest Circumference	cm	76
Height	cm	145
Weight	kg	34
Percentile based on Height	%	95
Percentile based on Weight	%	85

The sled tests were conducted using the UVA sled system (Via Systems Model 713). The test fixture, or "buck," utilized in this test series consisted of the front bench seat of a 1998 Chevrolet 1500 W/T with correct anchorage locations for the vehicle seatbelts. The anchorage locations were determined from measurements of a similar vehicle using a portable measurement device (Platinum FARO Arm, FARO Technologies Inc.). The seat-adjustment mechanism was removed to make it more durable for repeated testing, and both the seat pan and seat back were rigidly fixed to the buck. One test was conducted with the standard seat fixture to determine the effect of rigidizing the seat.

The tests were recorded using three high-speed (1000 frames/s) digital video imagers. The color imagers (Redlake HG-TH) were positioned to provide a perpendicular view from each side of the sled track, and an overhead view. These imagers were used to capture complete video records of the entire deceleration phase of the test event. Numerous photo targets were placed on the occupant and vehicle buck. Photos documenting both pre- and post-test conditions were taken with a digital still camera.

Sled deceleration and restraint belt loads were recorded for all of the tests. The ATD was instrumented to record accelerations, forces, and moments. Triaxial accelerometers were mounted at the head center of gravity (CG), at the chest CG, and at the pelvis CG. Load cells were located at the upper neck, lower neck, and lumbar spine and captured F_x, F_y, F_z, M_x, and M_y forces and moments. Load cells were also located at the left and right iliac spines, capturing F_x and M_y data. Chest displacement was also measured. Appendix C contains complete instrument descriptions.

Electronic data was acquired at 10,000 samples/sec using TRAQ-P, a DSP Technology Transient Acquisition and Processing System. The data was collected using IMPAX (DSP Technology) a PC-based data acquisition program. Data associated with a time domain from the beginning of the test event (T_0) until 150 ms after T_0 were selected for post-processing. Raw force and acceleration data were processed by subtracting small initial offset values, filtering to SAE J211-prescribed filter classes, and calculating resultants and injury criteria parameters.

Several parameters were included in the test matrix. The original case analysis predicted a Delta-V of 51 km/h, and the majority of the sled tests were performed at this speed. A subset of test conditions was repeated at 59 km/h to test the effect of speed. One final test was also performed in which the vehicle bench seat was tested without the rigidized base which was used for every other test. Replacing the seat support system with a rigid component is common in sled tests to create a more consistent, durable testing environment. For this final test, however, the original seat support system was installed.

The most important parameter varied, however, was the initial position of the dummy. The baseline tests positioned the dummies as specified by FMVSS 213, except for modifications suggested by Reed (2006) (Figure 2 and Figure 3).

Figure 2. View of baseline ATD positioning in reconstruction tests with Hybrid III 10-year old.

Figure 3. Oblique view of baseline ATD positioning in reconstruction tests with Hybrid III 10-year old.

The dummy was calibrated prior to the baseline testing, and all joints were adjusted to the relevant specification (1 g). For the Hybrid III 10-year old the lumbar joint was adjusted to a zero degree angle (most upright), while the adjustable neck was located in the 8 degree position. In addition, a 20 mm pad was placed behind the pelvis so that the dummy more accurately matched the sitting position of real children (Reed, 2006). To attempt to account for the unknown position of the child before the crash began, each dummy was moved in a variety of possible postures that the child could have been in before the crash. One position, "Torso," was based on the possibility that the child was leaning forward (sitting more upright) without moving his lower body (Figure 4).

The dummy was also positioned to simulate the situation in which the child may have been slouched significantly forward (possibly sleeping) and then sat straight up. For this condition "Body," the entire dummy was translated forward, which provided a good comparison with the baseline tests with no significant change in dummy orientation (Figure 5).

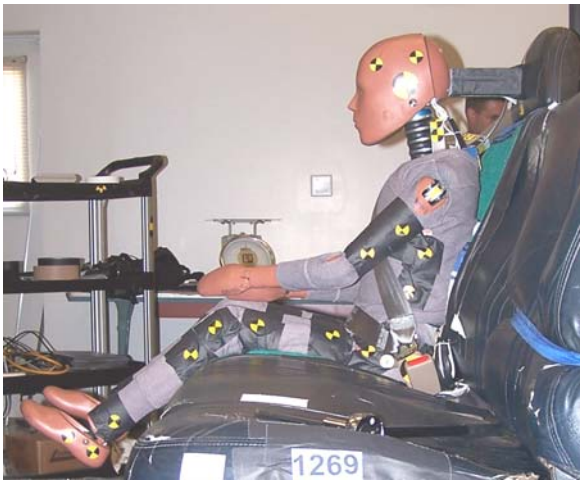

Figure 4. View of "Torso" adjusted position of ATD in reconstruction test with Hybrid III 10-year old.

Figure 5. View of "Body" adjusted position of ATD in reconstruction test with Hybrid III 10-year old.

Since there was strong evidence that the child had moved to the left prior to the crash, possibly while shaking the driver or attempting to steer the truck, the next dummy position, "Lean," involved leaning the dummy to the left with no other rotation along the Z axis, although there was some forward movement of the upper body (Figure 6).

Figure 6. View of "Lean" adjusted position of ATD in reconstruction test with Hybrid III 10-yeal old.

Finally, the most extreme position, "Lean-Rotate," involved both leaning the dummy to the left and rotating the dummy to the left along the Z axis (Figure 7 and Figure 8).

Figure 7. Frontal view of "Lean-Rotate" adjusted position of ATD in reconstruction test with Hybrid III 10-yeal old.

Figure 8. Side view of "Lean-Rotate" adjusted position of ATD in reconstruction test with Hybrid III 10-yeal old.

Both of the ATDs were tested in each of the adjusted positions with the Hybrid III 10-year old tested at the higher speed as well. The 5th percentile female was not tested at the higher speed but was tested with the standard, non-rigidized, seat support (Table 2).

Table 2.
Test matrix for reconstruction tests involving the Hybrid III 10-year old and 5th percentile female ATDs

9-Year Old Real World Reconstruction Tests		
	HIII 10yo	**AF5**
Baseline	X	X
Baseline, higher speed	X	
Baseline, non-rigidized seat		X
Torso leaning forward ("Torso")	X	
Whole body shifted forward ("Body")	X	X
Whole body shifted forward ("Body"), higher speed	X	
Leaning left ("Lean")	X	X
Leaning left/whole body rotated ("Lean-Rotate")	X	X
Leaning left/whole body rotated ("Lean-Rotate"), higher speed	X	

For use in the sled testing, a crash pulse was developed that represented the unknown crash pulse of the case vehicle. Using Insurance Institute for

Highway Safety (IIHS) event data recorder (ERD) pulse information for totally frontal pole crashes it was found that the velocity-time curves were similar between crashes with an 80 ms duration for several crash events. The shape of the known velocity-time curves was used along with the 80 ms duration to develop the crash pulse that would be used in our test series (Figure 9).

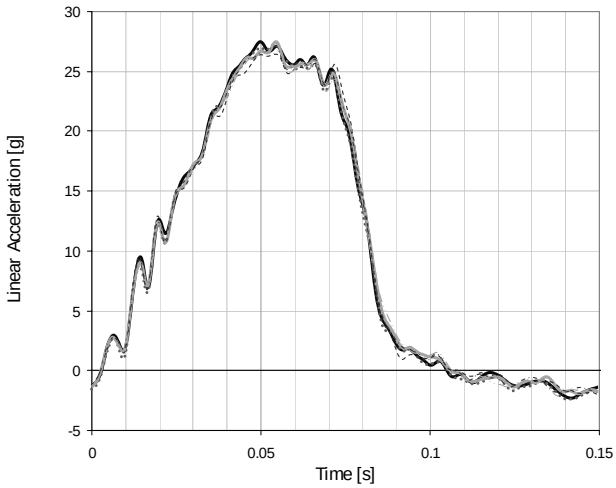

Figure 9. Example crash pulse from reconstruction tests developed from ERD pulse information involving totally frontal pole crashes.

Video Analysis

Markers for post test video analysis were placed on the ATDs. The markers were placed on tape that was directly attached to the outer skin of the dummy. Holes were cut in the clothing covering the ATDs to allow for direct attachment of the tape markers to dummy skin. This direct attachment was done to prevent any introduction of error in the video analysis from marker movement during testing. A coordinate system was established for the kinematics of the ATDs with the origin at the junction of the top surface of the seat cushion and the rear surface of the backrest.

Sensitivity Study

In order to assess the sensitivity of subject response to various conditions, a series of computer simulations were conducted using the MADYMO 6.4.1 solver (MADYMO, 2008).

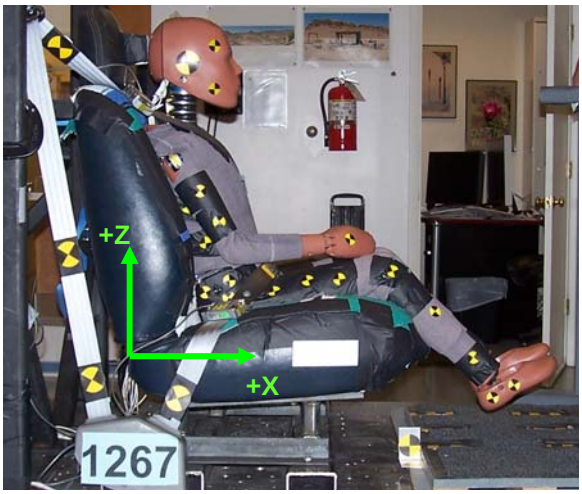

Figure 10. Origin of coordinate system for ATD kinematics.

A baseline simulation mirroring the initial sled test of the Hybrid III 5th percentile small female test dummy (Figure 11) was refined to within 10% of the measured response for shoulder belt tension, head excursion, head acceleration, chest acceleration, and chest deflection. Before conducting a parameter sensitivity study, the MADYMO model of the Hybrid III 5th percentile female was modified to include joint in the thoracic spine, similar to a previous study using the Hybrid III six-year-old test dummy (Sherwood, 2003). However, instead of a revolute joint, a free joint was added with restraints in all six degrees of freedom: longitudinal shear, lateral shear, tension/compression, flexion/extension, lateral bending, and torsion. The baseline restraint functions for each of these degrees of freedom were set to be twice as stiff as those of the modified Hybrid III six-year-old dummy, though the initial magnitude was not expected to influence the parameter sensitivity study.

A total of nineteen parameters were included in the parameter sensitivity study (Table 3). The first eighteen parameters represent a scale factor applied to the force or moment component of the force-deflection or moment-rotation restraint characteristics of the lumbar spine, thoracic spine, and the neck. Changes to the neck joint restraints are applied to each of the five neck joints. The final parameter describes the orientation of the subject about the longitudinal axis of the vehicle, expressed in radians.

Figure 11. Comparison of the MADYMO simulation (top) to the physical sled test of a Hybrid III 5th percentile female dummy.

Table 3.
List and description of variables included in the MADYMO Hybrid III 5th percentile female parameter sensitivity study.

Category	Description	Component	Minimum Value	Maximum Value
Neck	Longitudinal Shear	FX	0.01	1.5
	Lateral Shear	FY	0.01	1.5
	Tension/Compression	FZ	0.01	1.5
	Lateral Bending	MX	0.01	1.5
	Flexion/Extension	MY	0.01	1.5
	Torsion	MZ	0.01	1.5
Thoracic Spine	Longitudinal Shear	FX	0.01	1.5
	Lateral Shear	FY	0.01	1.5
	Tension/Compression	FZ	0.01	1.5
	Lateral Bending	MX	0.01	1.5
	Flexion/Extension	MY	0.01	1.5
	Torsion	MZ	0.01	1.5
Lumbar Spine	Longitudinal Shear	FX	0.01	1.5
	Lateral Shear	FY	0.01	1.5
	Tension/Compression	FZ	0.01	1.5
	Lateral Bending	MX	0.01	1.5
	Flexion/Extension	MY	0.01	1.5
	Torsion	MZ	0.01	1.5
Orientation	Lateral Leaning	RX	0.0 radians	0.25 radians

Using these nineteen parameters, 5,000 designs were constructed using a randomizing algorithm that results in a uniform distribution of each variable between its minimum and maximum values. If computational errors occurred during simulation of any of the designs, the design was removed from this initial population. Such errors occurred when the chosen parameters resulted in model instability, which can occur when low restraint forces allow unrealistically high relative velocities between rigid bodies.

The output from each design was the forward head excursion, measured as the difference between the initial position of the center of gravity (CG) of the head and the forward-most position of the head CG at any point in the simulation.

This calculation assumed that the distance between the CG and the anterior portion of the head was similar to the distance between the CG and the superior portion of the head, either of which could impact the instrument panel of a vehicle in a frontal collision.

RESULTS

Video analysis

The trajectories of the head CG, shoulder, and knee joints were measured. Based on pre-test measurements, the location of the H-Point was determined based on a distal thigh marker location and the angle of the femur, which was recorded during ATD placement. Thus, the data presented are those of the actual H-Point location, except for tests involving "Lean" and "Lean-Rotate" when the out of plane positioning of the dummy eliminated the use of this procedure. In these tests, the approximate position of the H-Point was estimated during the video analysis digitization process. Figures presented are from tests where the ATD was translated forward in the seat or leaning forward (Figure 12 - Figure 18) where out of plane motion is not substantially present.

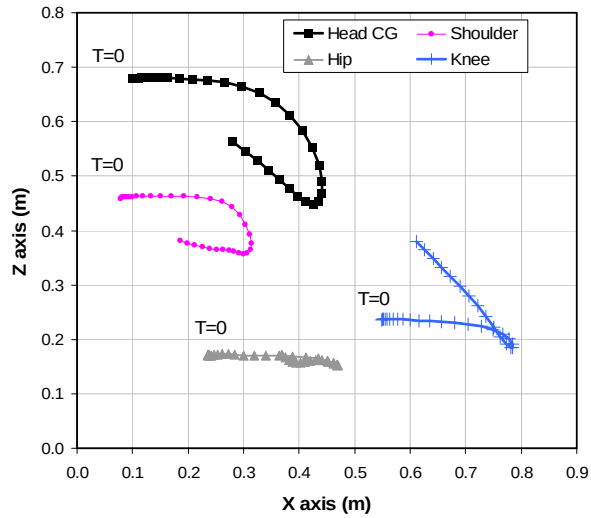

Figure 12: Kinematic trajectory for a low speed baseline test involving the Hybrid III-10 year old (Test #1267).

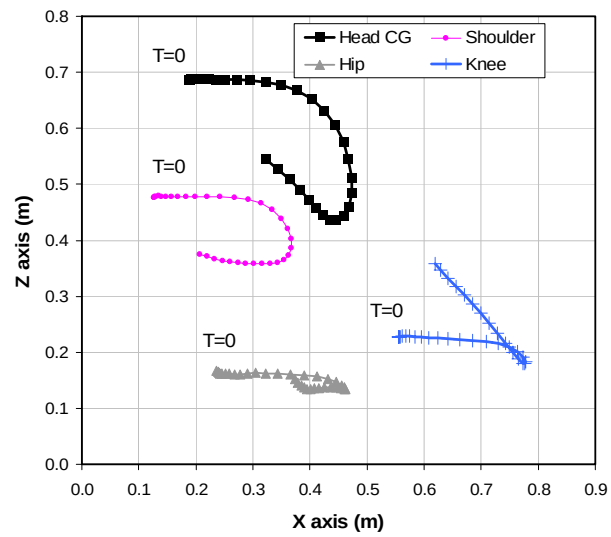

Figure 13: Kinematic trajectory for a low speed "Torso" positioned test involving the Hybrid III-10 year old (Test #1269).

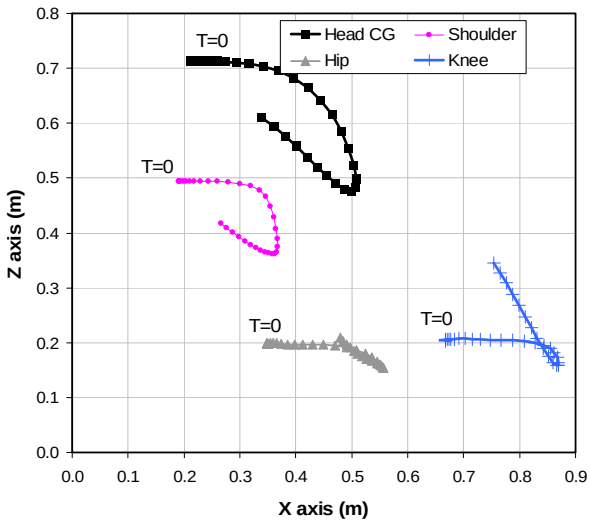

Figure 14. Kinematic trajectory for a low speed "Body" positioned test involving the Hybrid III-10 year old (Test #1270).

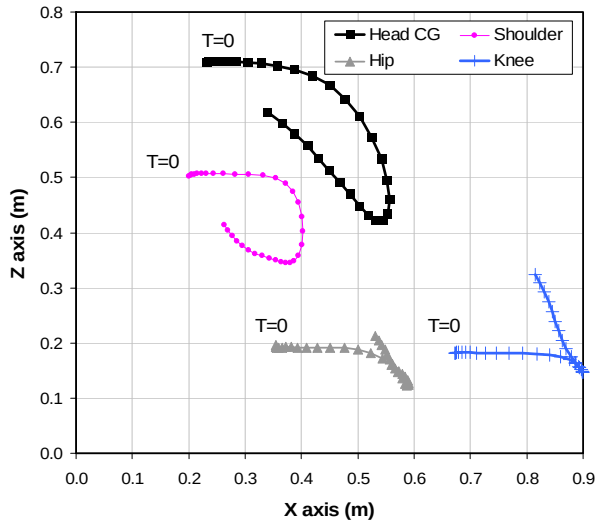

Figure 16. Kinematic trajectory for a high speed "Body" positioned test involving the Hybrid III-10 year old (Test #1274).

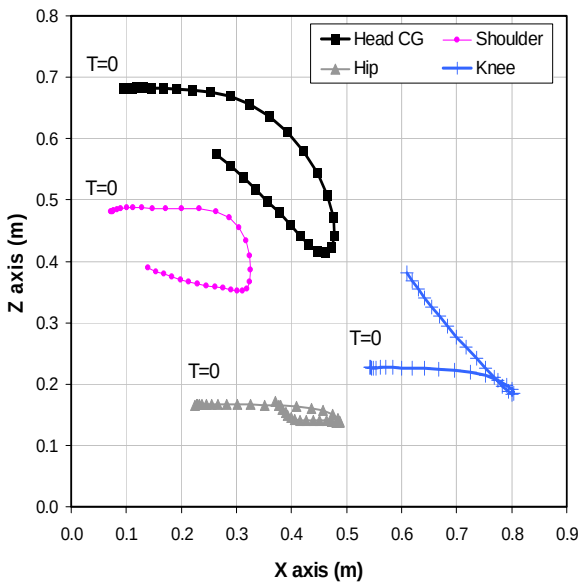

Figure 15. Kinematic trajectory for a high speed baseline test involving the Hybrid III-10 year old (Test #1273).

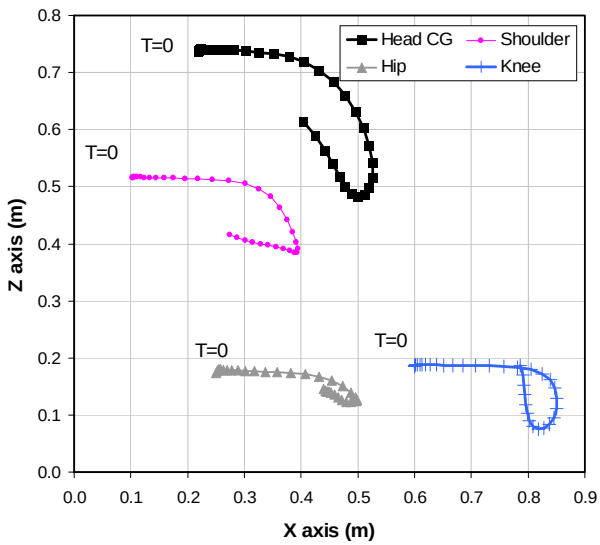

Figure 17. Kinematic trajectory for a low speed baseline test involving the 5th percentile female ATD (Test #1278).

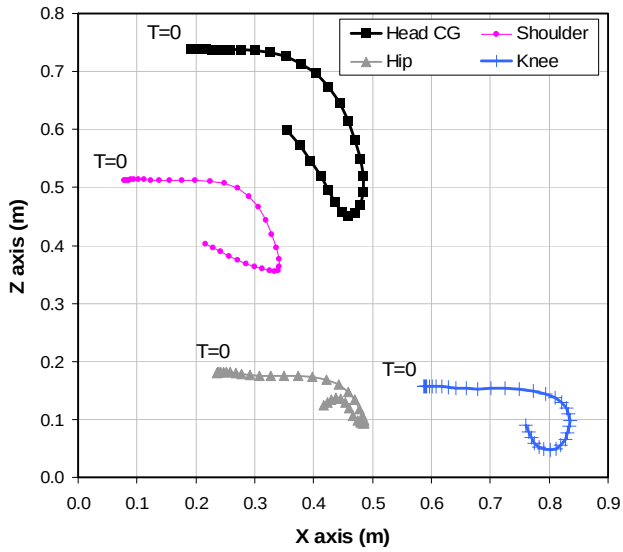

Figure 18. Kinematic trajectory for a low speed baseline test involving the 5th percentile female ATD with original (non-rigid) seat support (Test #1282).

The low speed and high speed tests under the same positioning conditions produce similar kinematic trajectories with a slightly larger head excursion value (Figure 12 vs Figure 15 and Figure 14 vs Figure 16). The effect of making the seat base rigid may cause the dummy excursion values to be overestimated. When the seat base was allowed to deform during the test, the head excursion value was reduced by 3.5 cm (Figure 18 compared to Figure 17).

In order for the ATDs to achieve a head excursion value that would cause contact with the vent on the vehicle's dashboard, the front of head excursion would need to exceed 71.3 cm in the kinematic trajectory reference frame (Figure 10). The front of head excursion value was digitized during video analysis in order to determine the forward-most point on the ATD's head (Figure 19). No excursions reached the 71.3 threshold.

Figure 19. Front of head excursion point and head CG point found during video analysis.

Table 4.
Peak Front of Head excursion data (data in cm)

	Low Speed		High Speed
	HIII 10yo	AF5	HIII 10yo
Baseline	55.4	61.0	59.1
Baseline non-rigid		57.5	
Torso	58.3		
Body	62.1	69.4	66.5
Lean	62.4	67.6	
Lean-Rotate	62.4	69.1	64.9
Truck head contact point	**71.3**	**71.3**	**71.3**

Sensitivity Study

Head excursions ranged from 24.4 to 59.6 centimeters (parameters that result in each of these conditions are listed in Table 5).

Table 5.
Parameter values that result in the lowest and highest head excursions.

Category	Component	Min. Head Excursion	Max. Head Excursion
Neck	FX	0.0116	0.9924
	FY	1.3663	0.5468
	FZ	0.1090	1.0072
	MX	1.2378	1.1990
	MY	0.9023	1.1581
	MZ	0.2820	0.8485
Thoracic Spine	FX	0.4934	0.2083
	FY	0.9801	0.1921
	FZ	0.5836	0.3922
	MX	0.9444	1.3581
	MY	0.7079	1.4102
	MZ	0.8138	0.9837
Lumbar Spine	FX	0.9353	0.8258
	FY	1.0499	0.4395
	FZ	1.2172	0.8479
	MX	0.5496	1.4118
	MY	0.7383	0.1920
	MZ	0.6336	0.9876
Orientation	RX	0.0034 rad	0.2175 rad

Table 6.
Results of an ANOVA comparing the means of head excursion between groups of values for each variable.

Category	**Component**	**F-statistic**	**P-value**
Neck	FX	19.56	<0.000001
	FY	9.48	<0.000001
	FZ	21.92	<0.000001
	MX	5.36	2.68E-04
	MY	7.36	6.71E-06
	MZ	5.76	1.29E-04
Thoracic Spine	FX	1.01	4.00E-01
	FY	6.52	3.18E-05
	FZ	3.51	7.25E-03
	MX	12.09	<0.000001
	MY	2.45	4.44E-02
	MZ	4.54	1.18E-03
Lumbar Spine	FX	8.69	<0.000001
	FY	2.16	7.08E-02
	FZ	7.21	8.93E-06
	MX	8.31	1.15E-06
	MY	3.08	1.52E-02
	MZ	6.74	2.14E-05
Orientation	RX	445.82	<0.000001

For each of the nineteen variables, an analysis of variance (ANOVA) was carried out to determine whether changes in that variable resulted in changes in head excursion. To begin this process, the head excursion values for the design population were divided into five bins based on the value of the respective variable. The ANOVA was conducted to determine whether the differences in the means of the five bins were statistically significant ($p<0.05$), which indicates that the model prediction of head excursion was sensitive to changes in the respective variable.

All but two of the nineteen parameters had a significant effect on the head excursion. The two parameters which do not affect head excursion were thoracic spine longitudinal shear (FX) stiffness and lumbar spine lateral shear (FY) stiffness. For the remaining parameters, the variance between the bins was much larger than the variance within each bin, indicating that the head excursion changed with changes in the parameter values (Table 6). The strongest trend occurred with changes the orientation of the subject in the seat, which showed an increasing trend (Figure 20). There was also a strong influence of the model prediction of head excursion with changes in longitudinal shear stiffness and tension/compression stiffness of the neck, as well as lateral rotation stiffness of the thoracic spine.

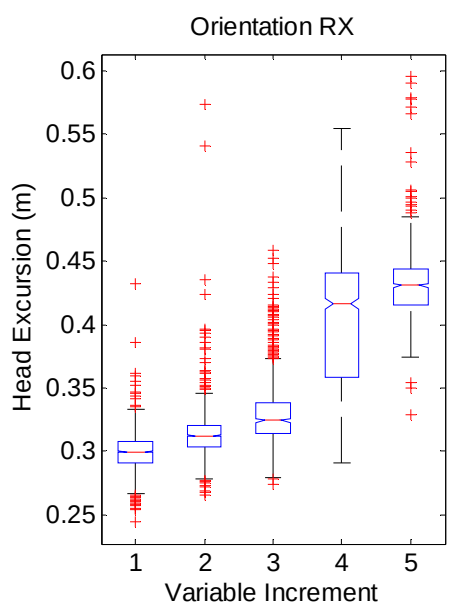

Figure 20. Median (red), 5% range (notch), and inter-quartile range (blue box) of head excursion for five increments of initial longitudinal orientation of the subject on the seat.

The sensitivity study determined an absolute difference in the head excursion between the beginning of the test and the point of maximum excursion. This excursion values can be compared to the excursion values from the ATD tests by using the initial offset in the baseline 5th percentile female test (Figure 17). This initial offset can be used because the positioning used in the MADYMO simulations before any lateral adjustments matched this test. Once the lateral adjustments were incorporated the initial X value of the head CG would still match the baseline position value since only lateral movement was included. The initial offset in the X direction of the baseline 5th percentile female was 21.8 centimeters. This offset then caused the simulation maximum excursion values to range from 56.2 to 81.4 centimeters in the kinematic trajectory coordinate system. The maximum value of the simulation maximum excursion value exceeded the truck head contact point value, indicating that the adjusted 5th percentile female from the simulations would be capable of striking the vent of the vehicle's dashboard.

DISCUSSION

The results suggest that the child dummies likely underestimate the excursion amounts experienced by the child involved in the actual crash. There were many complex factors involved in the analysis of this data, and the results do not lend themselves to definitive conclusions. There were some results, however, which are promising, and this data should be considered to be a single component of a large study of the response of pediatric ATDs.

The overall kinematic motions of the dummy were consistent and similar among all tests. Even when rotated or leaning to the left, the shoulder belt maintained its position on the chest, which is likely occurred in the actual crash as evidenced by the clavicle fracture. Despite very different initial positions, the measured forward head excursion values fell in a very narrow range. This might suggest that given any reasonable seating position, the total excursion value is relatively consistent when measured with the dummy.

This parameter sensitivity study suggested that even with spinal stiffness changes to the existing Hybrid III 5th percentile female test dummy, the head excursion necessary for a subject of similar size to impact the instrument panel was not possible without changes to the initial position of the subject from the standard seating position. However, head excursion did increase with the addition of a joint in thoracic spine of the dummy model, though the main influence of thoracic spine stiffness on head excursion occurred with changes to its lateral bending stiffness. This suggests that the dummy is more sensitive to the load path of the shoulder belt when additional degrees of freedom are introduced in the spine, as increased head excursion occurs as the dummy rotates around the axis of the shoulder belt. Adjustments to rigid spine of 5th percentile adult female yielding larger excursion values also agrees with other studies that have examined the role of the rigid spine in ATD kinematics (Sherwood, 2003 and Ash, 2009)

LIMITATIONS

A limitation of this study was the limited number of tests conducted at each position of the dummy. Additionally, though several positions were tested in an attempt to account for the unknown position of the child before the crash, the various positions were not a comprehensive examination of all possible positions. Though it would have been impractical to have each test performed on a standard, non-rigid seat, the introduction of the rigidized seat likely affected the response of the ATDs. There are also errors inherently introduced during the video analysis.

CONCLUSIONS

This study found that under the reconstructed conditions of the crash using ATDs of similar size compared with the child involved in the crash, the maximum head excursion needed to have head strike on the dash was not achievable with the current dummies. It was found that if adjustments were made to the neck, thoracic spine and lumbar spine of the 5th percentile female ATD model in MADYMO simulations, the excursion value needed for head strike was achievable.

ACKNOWLEDGMENTS

We would like to thank NHTSA for their support of the dummy tests although the opinions expressed in this paper are solely those of the authors. Additionally, we would like to thank Shashi Kuppa, Steve Ridella, and Erik Takhounts for their technical guidance.

REFERENCES

Ash, J., Sherwood, Abdelilah, Y., C., Crandall, J., Parent, D., Kallieris, D (2009). Comparison of Anthropomorphic Test Dummies with a Pediatric Cadaver Restrained by a Three-Point Belt in Frontal Sled Tests. 21st International Technical Conference

on the Enhanced Safety of Vehicles (ESV). Stuttgart, Germany

MADYMO 6.4.1, TNO Automotive Safety Solutions, 2008.

National Highway Traffic Safety Administration (NHTSA). (2000) U.S. DOT/NHTSA - Report - Hybrid III 5th Percentile Small Adult Female Crash Test Dummy - Drawings. Document NHTSA-2000-6940-16.

National Highway Traffic Safety Administration (NHTSA). (2005) US DOT/NHTSA - HIII-10C drawing package. Document NHTSA-2005-21247-4.

Reed, M. P., Schneider, L. W., Klinich, K. D., Manary, M. A., Ebert-Hamilton, S. M. Improved positioning procedures for 6YO and 10YO ATDs based on child occupant postures. Paper SAE 2006-22-0014. Stapp Car Crash Journal, Vol 50, Nov. 2006, pp. 337-388. Society of Automotive Engineers, Warrendale, PA.

SAE (2003) SAE J211/1 Instrumentation for Impact Test. Part 1. Electronic Instrumentation. Society of Automotive Engineers, Warrendale, PA, 2003.

Sherwood, C.P., Shaw, C.G., Van Rooij, L., Crandall, J.R., Orzechowski, K.M., Eichelberger, M.R., and Kallieris, D. Prediction of cervical spine injury risk for the 6-year-old child in frontal crashes. Traffic Injury Prevention, 4-3: 206–213, September 2003.

COMPARISON OF DYNAMIC RESPONSES OF THE THOR-NT AND HYBRID III IN OFFSET FRONTAL CRASH TEST

Masayuki Yaguchi
Koshiro Ono
Japan Automobile Research Institute
Mitsutoshi Masuda
Takatomo Watamori
Takeshi Seshita
Tatsuya Hibino
Japan Automobile Manufacturers Association
Japan
Paper Number 09-0268

ABSTRACT

A 64 km/h offset frontal crash test was conducted with the THOR-NT and Hybrid III to investigate the responses of both dummies under a crash situation that includes both deformation and rotational behavior of a vehicle.

Though the dummies were installed in the driver seat according to the ECE R94 positioning procedure, their postures were slightly different. The head and heels of the THOR-NT were positioned rearward. Similarly, the shoulders and knees were positioned forward compared to the Hybrid-III. Therefore, it is expected that these differences will affect the responses of both dummies.

During the tests, both dummies showed similar kinematics, except for the rotation about Z-axis of the head, and the contact situation to the instrument panel of the arms.

For the injury measures, the chest acceleration of the THOR-NT showed sharp inclination at 100 ms to 120 ms, presumed to be caused by the contact between the arms and instrument panel. The initial time history curve of the lap belt force was approximately the same between both dummies; however, the maximum force of the THOR-NT was less than half of the Hybrid III. For this difference, it was strongly presumed that more kinetic energy was absorbed by the knee bolster for the THOR-NT since its longer femur shortened the initial clearance between the knee and knee bolster. In addition, it was also presumed that the difference of the flesh characteristics around the iliac wing between both dummies affected the results.

The injury measures of both dummies were compared to the injury criteria specified in FMVSS 208 and ECE R94. As for the results, almost equivalent values between the two dummies were observed.

Moreover, as reference, the additional injury measures in the THOR-NT are shown in this paper.

INTRODUCTION

In 1976, the Hybrid III mid-sized male, instrumented test dummy was first released [1]. Subsequently, the Hybrid III has been adopted in the current regulations for frontal impact tests in many countries. The National Highway Traffic Safety Administration (NHTSA) of the U.S. acknowledged the need for improved biofidelity and measurement capabilities of the Hybrid III, consistent with the advancement of vehicle safety devices. Moreover, NHTSA announced plans to develop an advanced crash test dummy with improved biofidelity under frontal impact conditions with expanded injury assessment capabilities [2]. In 1992, the initial advanced ATD known as "Trauma Assessment Device - 50th percentile male (TAD-50M)" was developed by a NHTSA-sponsored consortium of universities and industrial partners [3]. The principal objectives were to review the anthropometry and dynamic biofidelic responses subject to more contemporary occupant seat positionings and restraint systems. In 1994, NHTSA initiated an aggressive effort to integrate existing advanced ATD components. Then, in 1996, the "Test Device for Human Occupant Restraint (THOR)" prototype was introduced [4]. Research organizations in several countries conducted experiments to improve this prototype dummy, leading to the introduction of the THOR-Alpha in 2001 [5]. In 2005, NHTSA released the THOR-NT (New Technology), which was a modified and improved version of the THOR-Alpha [6]. Currently, to improve the THOR-NT further, the discussion regarding the improvement for each body region and the certification and positioning procedures is in progress in SAE THOR Evaluation Task Force Group.

JAMA (Japan Automobile Manufacturers Association) /JARI (Japan Automobile Research Institute) has so far

performed the research activities for contributing to development and improvement of the THOR [7][8][9]. As part of the research activities, in order to investigate the responses of the THOR-NT and Hybrid III under a crash situation that includes both deformation and rotational behavior of a vehicle, authors conducted 64 km/h offset frontal crash tests (ODB tests), and compared the results between the dummies.

64 km/h ODB Tests with the THOR-NT and the Hybrid III

Test Condition

Figure 1 shows the collision configuration of the ODB test. The tests were conducted with 40 % overlap of the vehicle width against the deformable barrier at a impact speed of 64 km/h.

The test vehicles were a compact hatchback type passenger car with 5 doors. The test weights of the two vehicles were both 1090 kg. As shown in Figure 2, the front door of the driver's side was replaced by the steel bar in order to analyze the whole-body behavior of the dummy.

In each of the two ODB tests, the THOR-NT or the Hybrid-III was set on only the driver's seat. The seat positions were subject to the ECE R94 procedure. For the restraint devices, an airbag and a seatbelt with pretensioner and with force-limiter were used.

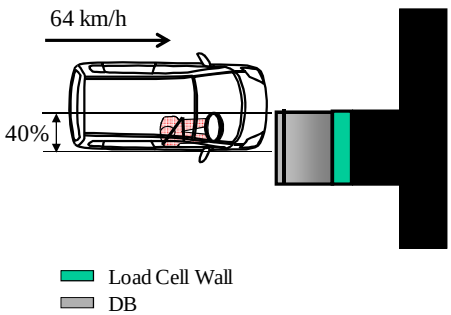

Figure 1. Collision Configuration of the ODB Test

Figure 2. Appearances of the Door Frame of the Driver's Seat Side

Measurements

During the ODB tests, the electrical measurements (e.g. acceleration) of the dummy and vehicle and the optical measurements using a high-speed digital video camera were done. In both pre-test and post-test, the deformation of the test vehicle was measured with the three-dimension measurement device.

For the electrical measurements, the accelerations, deflections and forces of the dummy were measured, and the accelerations at the engine block and the lower of B-pillar of the test vehicle were measured. These data were recorded by a data acquisition system mounted in the luggage room of the test vehicle, and they were filtered compliantly to SAE J211. The detail information of the instrumentations of the THOR-NT and Hybrid III is shown in Appendix.

For the optical measurements, a high-speed video camera was used to take the behaviors of the dummy and vehicle during the impact. The behavior of the dummy was observed as follows: The motions of the marks attached to some parts on the dummy were recorded by the video camera, then these were converted into the numerical movements using the video analyzer.

In both the pre-test and post-test, the some coordinate values on the vehicle were measured with the three-dimension measurement device, and the vehicle deformation amounts were calculated from the pre- and post-data. Note: the coordinate system of the vehicle was defined as follows: An origin point was on the trunk lid striker; the X-axis was the fore-aft direction; Y-axis was the lateral direction; and the Z-axis was the vertical direction.

Dummy Positioning

The THOR-NT and the Hybrid III were respectively set in the vehicle in accordance with the positioning procedure described in the ECE R94. Table 1 indicates the X and Z coordinate values of the head, shoulder, hip point (H.P.), knee and heel of the dummies respectively. Figure 3

compares the positions of each component of the dummies in the X-Z coordinate system.

When the H.P. of each dummy was set at the approximately same positions in the fore-aft direction (X-axis), the head and heels of the THOR-NT were positioned rearward, and its shoulders and knees were positioned forward, compared with those of the Hybrid III. In the vertical direction (Z-axis), the H.P., head, shoulders and knees of the THOR-NT were positioned above, compared with those of the Hybrid III. It was presumed that the knees of the THOR-NT were positioned more forward and upward than those of the Hybrid III, because the legs of the THOR-NT are longer than those of the Hybrid III.

Table 1. Coordinate Values of Each Component of the THOR-NT and the Hybrid III

	THOR		HYIII	
	X	Z	X	Z
Head	−77.6	448.6	−107.0	424.1
Shoulder	−78.0	189.9	−50.5	147.1
H.P.	−228.5	−223.5	−227.1	−233.7
Knee	−631.2	−91.1	−600.7	−118.3
Heel	−876.4	−563.5	−898.0	−560.2

Origin: Door Striker Bolt Unit: mm

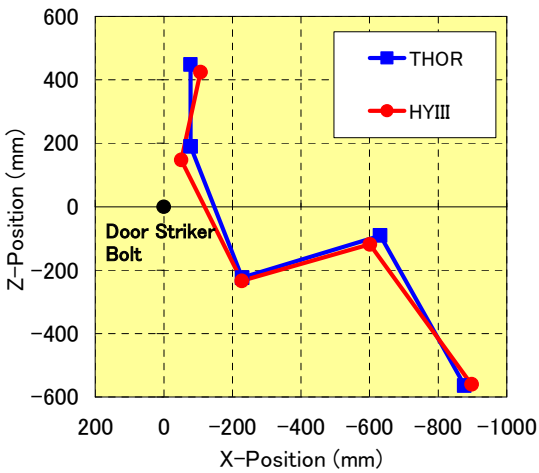

Figure 3. Comparison of Positionings of the THOR-NT and the Hybrid III

Test Results

(1) Vehicle Acceleration

Figure 4 indicates the comparison of the vehicle accelerations in the 64 km/h ODB tests. The acceleration responses between the test vehicles with the THOR-NT and Hybrid III were approximately similar.

(2) Vehicle Deformation

Figure 5 indicates the appearance of the vehicle deformation after the tests. The vehicle deformations in the two tests was similar each other.

(3) Vehicle Behavior

As shown in Figure 6, the behaviors of two vehicles during the impact were similar. The vehicles moved almost straightly until 80 ms, then these began to rotate greatly after 120 ms.

(4) Kinematics of the Dummies

In Figure 7 and Figure 8, the behaviors of the THOR-NT and Hybrid III were compared based on the track of each body part from the impact to just before the vehicle started rotating (120ms). It seems that the forward displacements of each body part of the dummies reached to the maximum at about 120 ms, and these behaviors were approximately similar, except for the rotation about Z-axis of the head, and the contact situation to the instrument panel of the arms. However, the maximum displacements relative to the initial positions of each body part between the dummies were different as shown in Table 2. With regard to the fore-aft direction, the head of the THOR-NT moved forward 28 mm than that of the Hybrid III, and the shoulder of the THOR-NT moved forward 12 mm than that of the Hybrid III. Oppositely, the H.P., knee, and ankle of the Hybrid III moved forward 19 mm, 13 mm, and 24 mm respectively than those of the THOR-NT. With regard to the vertical direction, the head and ankle of the Hybrid III moved downward 31 mm and 17 mm respectively than those of the THOR-NT. The shoulder of the THOR-NT moved downward than that of the Hybrid III, while the knee of the Hybrid III moved upward than that of the THOR-NT. The displacements of the H.P. were approximately same between the two dummies.

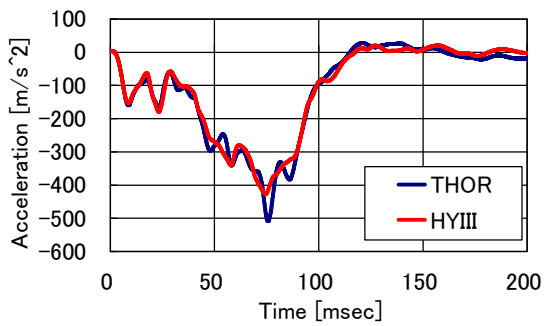

Figure 4. Vehicle Accelerations in 64 km/h ODB Tests

Figure 5. Appearance of the Vehicle Deformations in the Post-Tests

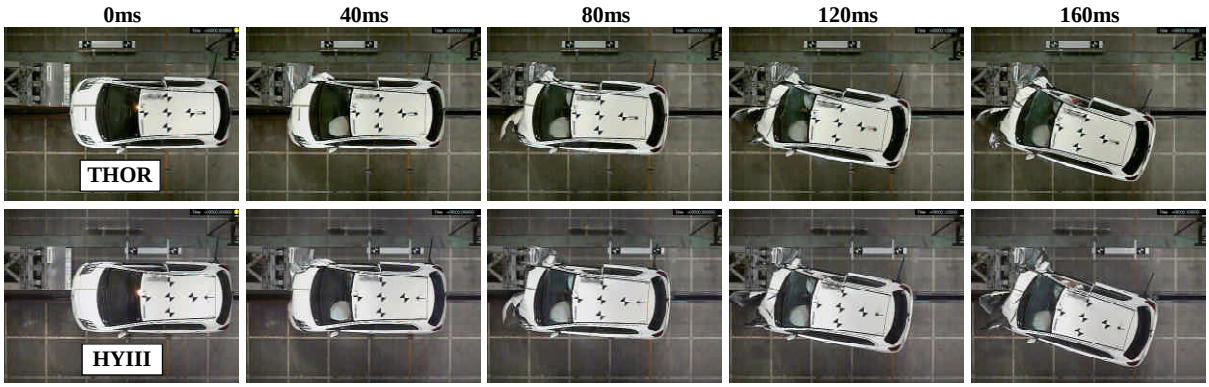

Figure 6. Vehicle Behavior During the Impact

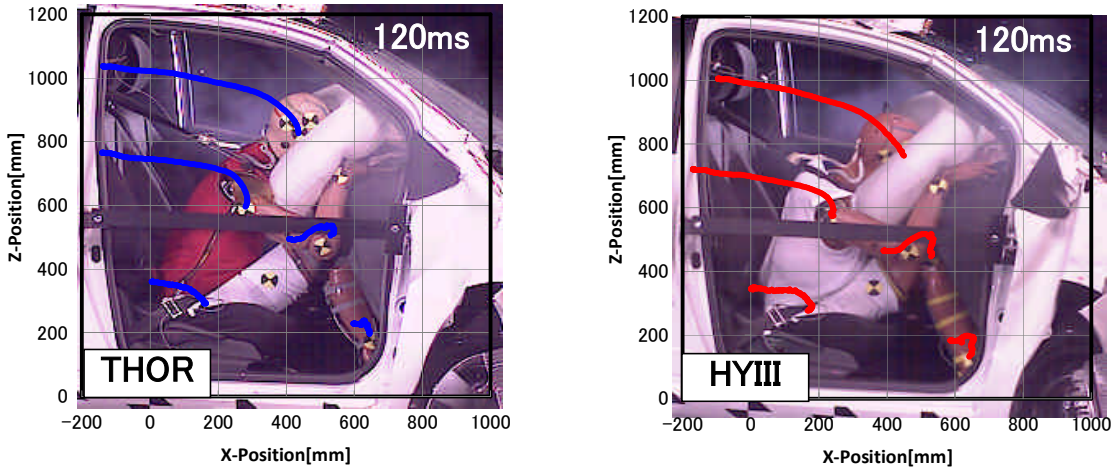

Figure 7. Track of Each Body Part of the Dummies

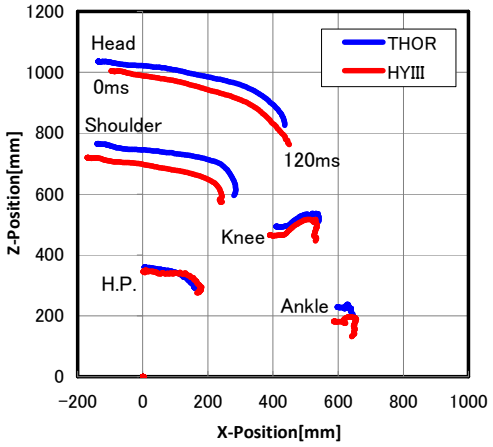

Figure 8. Comparison of the Track of Each Body Part of the Dummies (0 ms to 120 ms)

Table 2. Difference in the Maximum Displacement of Each Body Part of the Dummies

	THOR		HYIII		Difference between THOR and HYIII	
	X	Z	X	Z	X	Z
Head CG	570	−211	542	−242	28	31
Shoulder	423	−170	411	−147	12	−23
H.P.	156	−69	175	−70	−19	1
Knee	129	44	142	52	−13	−8
Ankle	43	−34	67	−51	−24	17

X−axis : Forward +, Rearward −
Z−axis : Upward +, Downward −
Unit : mm

(5) Dynamic Responses of the Dummies

Figure 9 indicates the head acceleration responses of the THOR-NT and Hybrid III. Although the initial time history curve of acceleration and the duration time were similar between the dummies, the responses of both dummies were different at the time (around 100 ms) when the peak accelerations occurred; namely, the peak acceleration of the THOR-NT was higher than that of the Hybrid III.

Figure 10 indicates the chest acceleration responses of the dummies. The initial time history curve of the acceleration, the values of the peak acceleration, and the duration time were similar in both the dummies. The acceleration responses were similar in both the dummies until about 70 ms, however, at about 70 ms to 100 ms, the acceleration of the Hybrid III was slightly higher than that of the THOR-NT.

Figure 11 indicates the pelvis acceleration responses of the dummies. The acceleration responses were similar in both dummies until about 40 ms. However, the responses from about 40 ms to the peak acceleration were different in both dummies, thus, the peak acceleration of the Hybrid III was higher than that of the THOR-NT.

Figure 12 and Figure 13 indicates Fz (axial force) and My (flexion and extension moment around the Y-axis) responses of the upper neck of the THOR-NT and Hybrid III. For the Fz, both the THOR-NT and the Hybrid III began to generate the tension forces at about 25 ms and reached the maximum forces at about 90 ms. For the My, on the whole, the occurring situations on moment were similar in both dummies; however, the timings of the peak flexion and extension of the Hybrid III were earlier than those of the THOR-NT.

Figure 14 indicates the thoracic deflection responses (fore-aft direction) of the THOR-NT where measured at four points (upper right, upper left, lower right, and lower left) on the thorax. Figure 15 indicates the thoracic deflection responses (fore-aft direction) of the Hybrid III where measured at one point (center) on the thorax. The deflection values on the lower left of the THOR-NT and the center of the Hybrid III were approximately same, and the deflection appearance was similar. However, the upper right of the THOR-NT indicated smaller deflection than the Hybrid III, and returned to the deflection around zero at about 120 ms. Furthermore, the deflection on the lower right of the THOR-NT was small, but generated in the opposite direction to the deflections on the other three points.

Figure 16 indicates the relative location between the seatbelt and the four measurement points of the THOR-NT thorax. The upper and lower measurement points on the left side of the thorax were approximately lapped over the seatbelt, and the point on the upper right was close to the seatbelt. Therefore, the three measurement points deflected in the compressive direction by loading of the seatbelt. On the other hand, the measurement point on the lower right was far position where it did not lap over the seatbelt. Due to this, it was presumed that the lower right of the thorax deflected in the tensile direction because the whole left side and the upper right of the thorax were distorted by the pressure of the seatbelt.

Figure 17 indicates the deflection response of the upper abdomen of the THOR-NT, and Figure 18 shows the deflection responses of its lower abdomen. The deflection of the upper abdomen was measured by the string potentiometer, while the right and left deflections of the lower abdomen were measured by the DGSP unit with

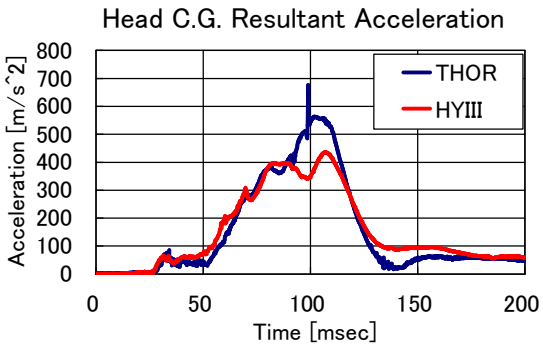

Figure 9. Head Acceleration

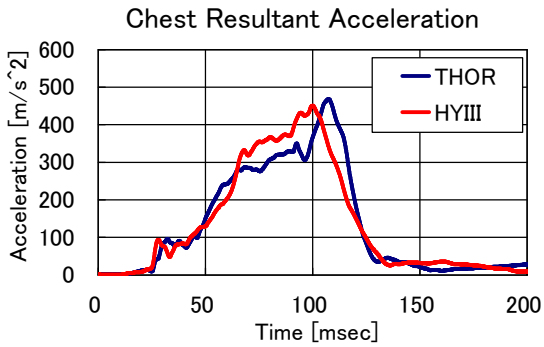

Figure 10. Chest Acceleration

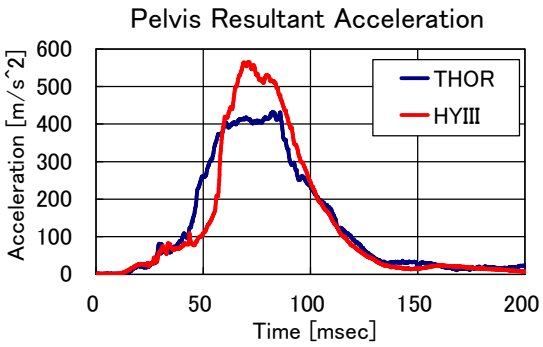

Figure 11. Pelvis Acceleration

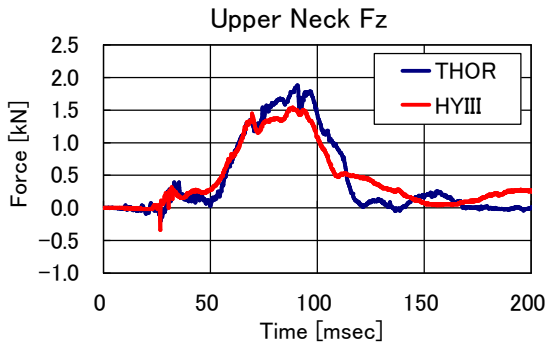

Figure 12. Upper Neck Axial Force

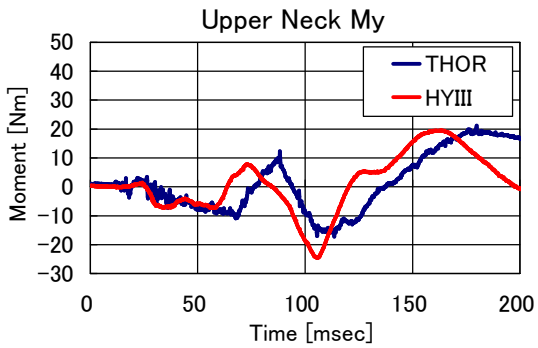

Figure 13. Upper Neck Moment (around Y-Axis)

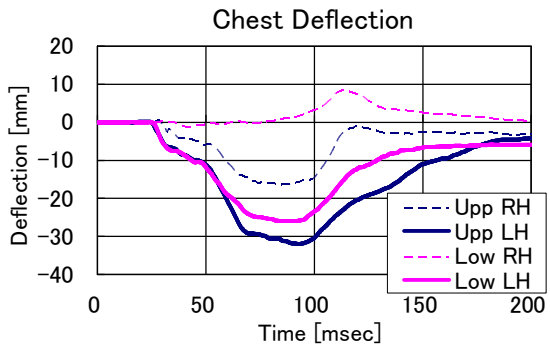

Figure 14. Thoracic Deflection of the THOR-NT (Upper Right, Upper Left, Lower Right, Lower Left)

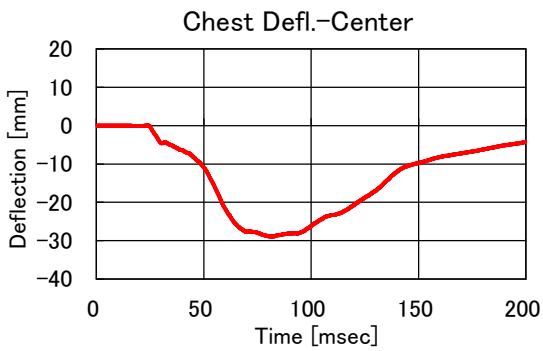

Figure 15. Thoracic Deflection of the Hybrid III (Center)

Figure 16. Relative Location between the Thoracic Measurement Points (UR, UL, LR, LL) and the Seatbelt

a linear potentiometer for measuring the fore-aft displacement and with two rotatory potentiometers for measuring the yaw and pitch angles. The abdominal deflection of the Hybrid III was not measured because it had not a sensor to measure the deflection. Therefore, only the results of the THOR-NT are stated herein. The deflection of the upper abdomen was smaller than that of the lower abdomen. The deflection of the upper abdomen reached the maximum value (10 mm) at about 90 ms and decreased to about 2 mm at about 120 ms. On the other hand, the right and left deflections of the lower abdomen exhibited a gentle decrease after reaching to the maximum deflection; the right side maintained the deflection of about 40 mm, and the left side was about 25 mm at 200 ms.

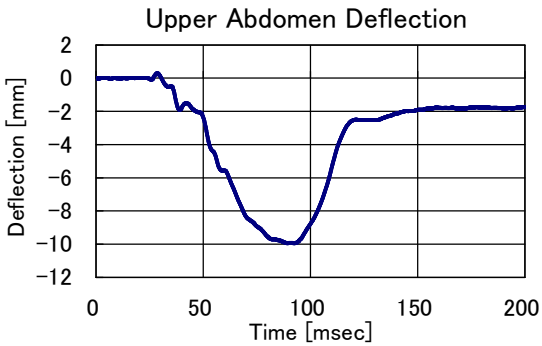

Figure 17. Upper Abdomen Deflection of the THOR-NT

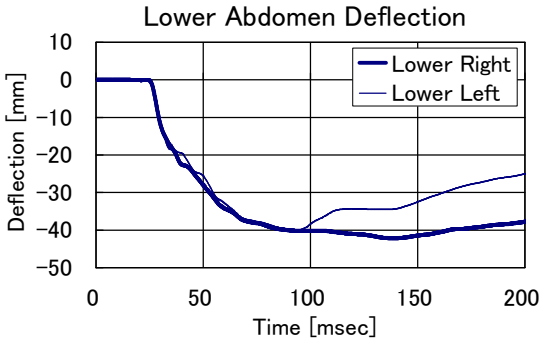

Figure 18. Lower Abdomen Deflection of the THOR-NT (Right and Left)

Figure 19 and Figure 20 indicates the axial force responses of the right and left femurs of the THOR-NT and Hybrid III. For the left femur, both the THOR-NT and the Hybrid III began to respond at about 40 ms. However, while the THOR-NT remained showing the compressive force from the occurrence and reached the maximum compressive force, the Hybrid III shifted to compressive force after showing the tensile force once, and then reached the maximum compressive force. The time of the maximum compressive force of the THOR-NT was slightly earlier than that of the Hybrid III, and the maximum force value of the THOR-NT was larger than that of the Hybrid III. For the right femur, also, the difference in the initial force response between the THOR-NT and the Hybrid III was observed. Although the time of the maximum compressive force of the Hybrid III was slightly earlier than that of the THOR-NT, the maximum forces of both the dummies were approximately the same.

Figure 21 to Figure 24 indicates the axial force responses of the tibia (upper right, upper left, lower right, and lower left) of the THOR-NT and Hybrid III. For the right tibia, the maximum force of the upper tibia was similar between the THOR-NT and Hybrid III. The maximum forces of the lower tibia were slightly different between the THOR-NT and Hybrid III, but the dummies exhibited similar responses. For the left tibia, the maximum axial forces of the upper and lower of the Hybrid III were larger than that of the THOR-NT, but the force responses were similar between the dummies.

Figure 25 to Figure 28 shows the time-series data of the Tibia Index (upper right, upper left, lower right, and lower left) of the THOR-NT and Hybrid III. For the upper side of the right tibia, the value of the Hybrid III increased until about 45 ms, whereas that of the THOR-NT decreased at 30 ms to 40 ms. In addition, the value of the THOR-NT increased at 40 ms to 55 ms and reached the maximum, while the value of the Hybrid III increased again after decreased at 40 ms and 70 ms and reached the maximum at about 80 ms. For the lower side of the right tibia, while

the THOR-NT showed two local peaks before the maximum at about 80 ms, the Hybrid III did not show any local peaks before the maximum at about 80 ms. As a result, the difference of the values between the dummies was large at about 55 ms. For the upper side of the left tibia, the time of the maximum value was approximately same between the dummies. For the lower side of the left tibia, the response until reached the maximum value was different; the time of the maximum value of the THOR-NT was earlier than that of the Hybrid III.

(6) Force Responses of the Seatbelt

Figure 29 shows the force responses of the shoulder belt of the dummies, and Figure 30 shows those of the lap belt. For the shoulder belt, the occurrence situations and amplitudes of the force were approximately the same between the dummies, whereas, for the lap belt, large difference of the force was observed between the dummies. The initial time history curve of the force was approximately the same (about 20 ms) between the dummies, however, the maximum force of the THOR-NT (3.1 kN) was less value than a half, compared to that of the Hybrid III (6.8 kN).

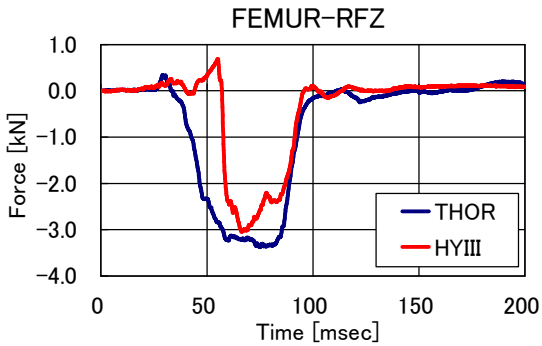

Figure 19. Axial Force of the Right Femur

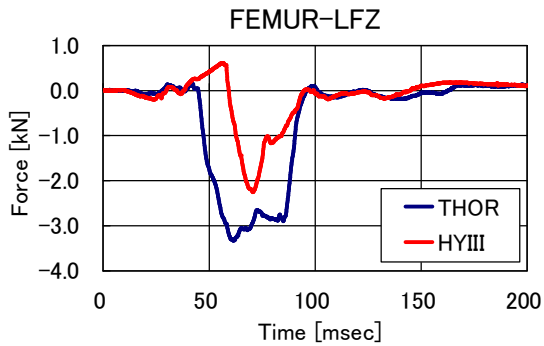

Figure 20. Axial Force of the Left Femur

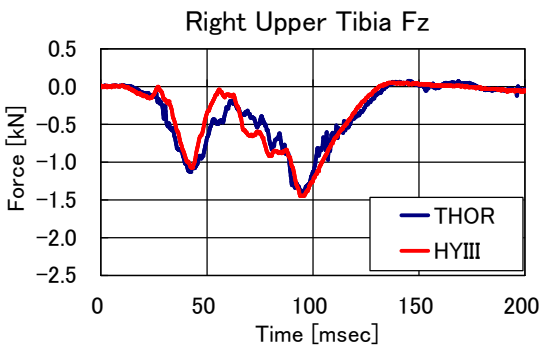

Figure 21. Axial Force of the Right Upper Tibia

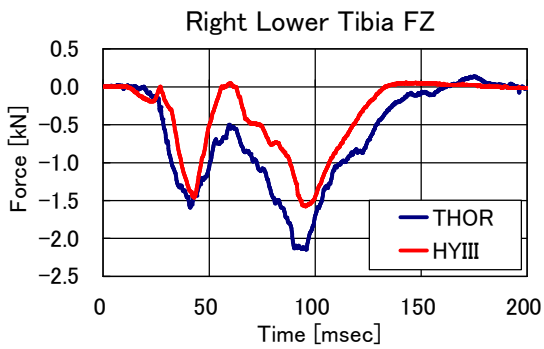

Figure 22. Axial Force of the Right Lower Tibia

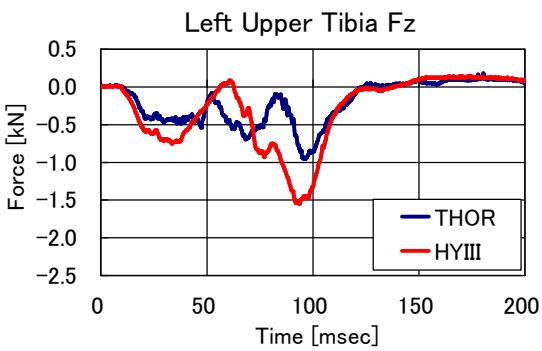

Figure 23. Axial Force of the Left Upper Tibia

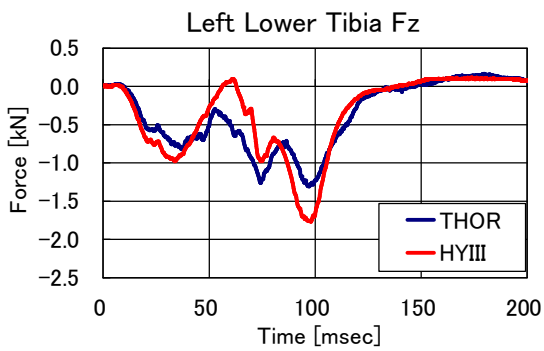

Figure 24. Axial Force of the Left Lower Tibia

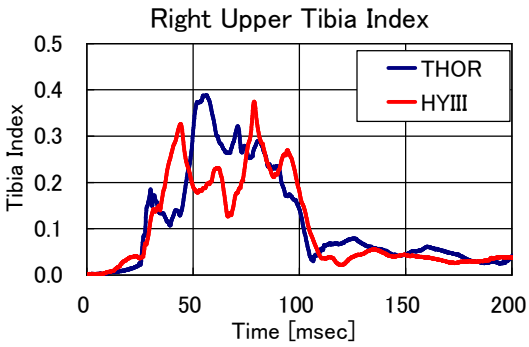

Figure 25. Tibia Index of the Right Upper Tibia

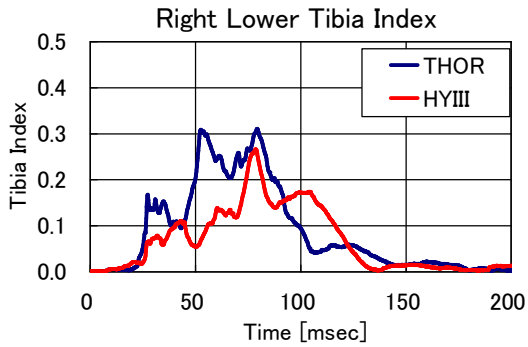

Figure 26. Tibia Index of the Right Lower Tibia

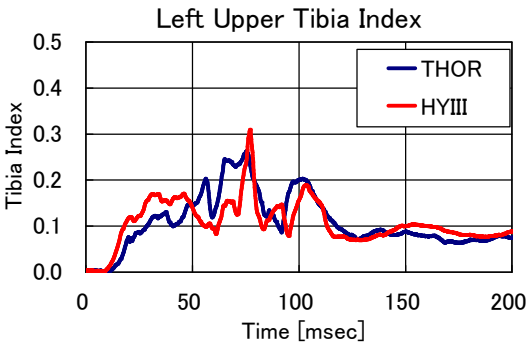

Figure 27. Tibia Index of the Left Upper Tibia

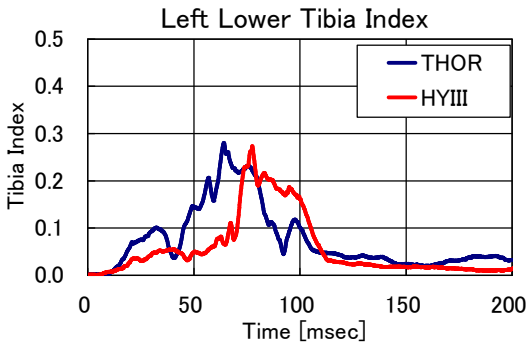

Figure 28. Tibia Index of the Left Lower Tibia

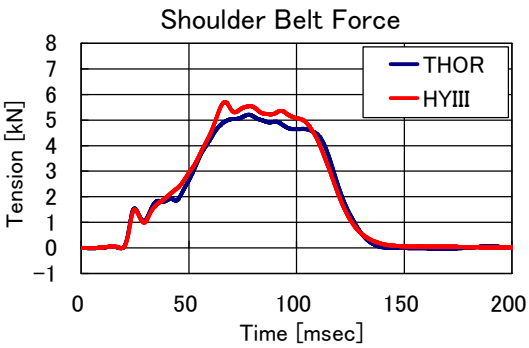

Figure 29. Shoulder Belt Force

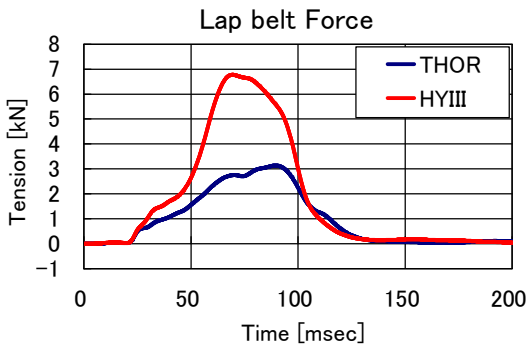

Figure 30. Lap Belt Force

(7) Injury Measurements

Table 3 indicates the injury measures of each component of the THOR-NT and Hybrid III. Furthermore, Figure 31 shows the ratios of the injury measures of the dummies to the injury criteria regulated in the ECE R94 and FMVSS208.

With regard to HIC 36 ms, HIC 15 ms, and head 3 ms G, the differences of the ratios of the measurements to the injury criteria between the dummies were larger than other injury measures; the injury values of the THOR-NT were larger than those of the Hybrid III. Secondly, with regard to the tension force and extension moment of the neck and the compressive force of the left femur, the differences of the results between the dummies were large; the neck tension force and femur force of the THOR-NT was larger than that of the Hybrid III, whereas the neck extension moment of the Hybrid III was larger than that of the THOR-NT. Other injury measures were approximately the same between the dummies. All injury measures of both dummies were less than the injury criteria. The chest G of both dummies and the head G of the THOR-NT showed relatively larger ratio against the injury criteria, comparing to the other injury measures.

On the other hand, as reference, the additional injury measures for the abdomen, knee-thigh-hip (KTH) and tibia in the THOR-NT are shown in Table 4.

Table 3. Injury Measures of the THOR-NT and the Hybrid III

		Injury Criteria	THOR	HYIII
Head	HIC 36ms	1000	549.0	351.2
	HIC 15ms	700	339.4	158.4
	3ms clip (G)	80	56.97	43.84
Upper Neck	Shear Force (Fx+) (kN)	3.1	0.320	0.170
	Tension Force (Fz+) (kN)	3.3	1.881	1.542
	Compression Force (Fz-) (kN)	4.0	0.197	0.337
	Extension Moment around Y-axis (My-) (Nm)	57	17.22	24.60
	Nij	1.0	0.350	0.305
Chest	Deflection (Upper Right) (mm)	50	-16.33	-
	Deflection (Upper Left) (mm)		-32.00	-
	Deflection (Lower Right) (mm)		8.34	-
	Deflection (Lower Left) (mm)		-25.94	-
	Deflection (Center) (mm)		-	-28.91
	Viscous Criterion (Upper Right) (m/s)	1.0	-0.053	-
	Viscous Criterion (Upper Left) (m/s)		-0.178	-
	Viscous Criterion (Lower Right) (m/s)		0.030	-
	Viscous Criterion (Lower Left) (m/s)		-0.093	-
	Viscous Criterion (Center) (m/s)		-	-0.149
	3ms clip (G)	60	46.78	44.57
Femur	Right Femur Axial Force (Compression) (kN)	10	3.38	3.05
	Left Femur Axial Force (Compression) (kN)		3.33	2.25
Knee	Right Tibia to Femur Translation (mm)	15	2.47	0.01
	Left Tibia to Femur Translation (mm)		0.16	0.75
Tibia	Right Upper Axial Force (kN)	8	1.44	1.45
	Right Lower Axial Force (kN)		2.15	1.58
	Left Upper Axial Force (kN)		0.95	1.55
	Left Lower Axial Force (kN)		1.31	1.77
	Right Upper Tibia Index	1.3	0.39	0.37
	Right Lower Tibia Index		0.31	0.27
	Left Upper Tibia Index		0.26	0.31
	Left Lower Tibia Index		0.28	0.27

For calculation of the upper rib VC of THOR-NT; Deformation Constant at #3 Rib: 219 mm, Scaling Factor: 1.3
For calculation of the lower rib VC of THOR-NT; Deformation Constant at #6 Rib: 234 mm, Scaling Factor: 1.3

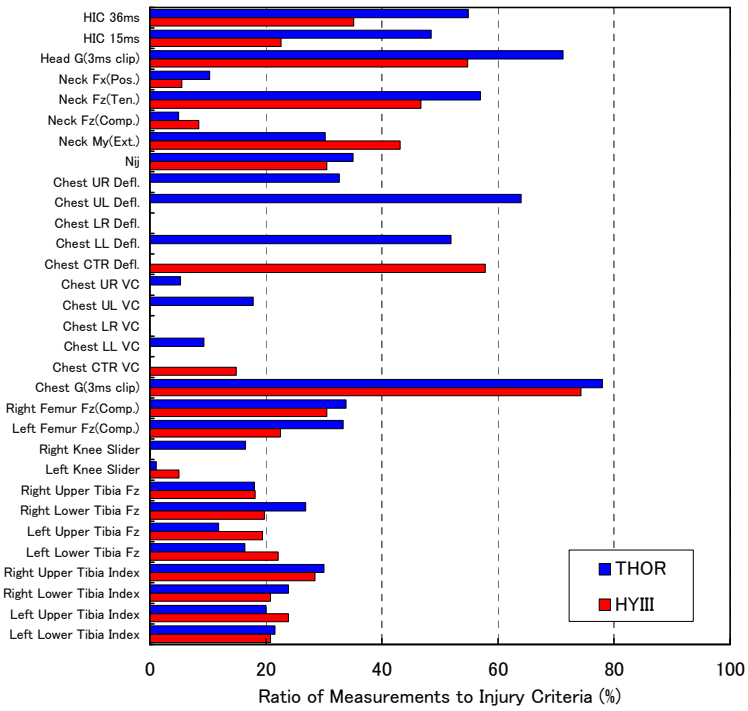

Figure 31. Ratio of the Injury Measures of the Dummies to the Injury Criteria in the Frontal Impact Regulations

Table 4. Injury Measures of the THOR-NT Except the Injury Criteria in the Frontal Impact Regulations

		THOR
Abdomen	Deflection (Upper) (mm)	9.93
	Deflection (Lower Right) (mm)	42.14
	Deflection (Lower Left) (mm)	40.02
	Viscous Criterion (Upper) (m/s)	0.012
	Viscous Criterion (Lower Right) (m/s)	0.141
	Viscous Criterion (Lower Left) (m/s)	0.169
Knee-Thigh-Hip (KTH)	Acetabulum Force with Neutral Posture (Right) (kN)	1.46
	Acetabulum Force with Neutral Posture (Left) (kN)	0.25
	Femur Bending Moment (Right) (Nm)	108.1
	Femur Bending Moment (Left) (Nm)	94.3
Tibia	Rivised Tibia Index (Right Upper)	0.39
	Rivised Tibia Index (Right Lower)	0.37
	Rivised Tibia Index (Left Upper)	0.28
	Rivised Tibia Index (Left Lower)	0.30
	Proximal Tibia Axial Force (Right) (N)	1437.7
	Proximal Tibia Axial Force (Left) (N)	955.0
	Distal Tibia Axial Force (Right) (N)	2147.8
	Distal Tibia Axial Force (Left) (N)	1306.5
	Ankle Dorsiflexion Angle (Right) (deg)	20.96
	Ankle Dorsiflexion Angle (Left) (deg)	20.39
	Ankle Inversion Angle (Right) (deg)	7.15
	Ankle Eversion Angle (Right) (deg)	6.66
	Ankle Inversion Angle (Left) (deg)	17.72
	Ankle Eversion Angle (Left) (deg)	21.16

For calculation of the upper and lower abdomen VC of THOR-NT;
Deformation Constant: 250 mm
(Supposed the abdominal depth of the THOR-NT equals that of the Hybrid III.)
Scaling Factor: 1.3

DISCUSSION

Differences in the Kinematics and Responses of the Dummies

(1) Differences in the Kinematics and Response of the Head

The face of the Hybrid III was positioning approximately forward at the early contact with the airbag, whereas the face of the THOR-NT was positioning downward (Figure 32). Furthermore, the head of the Hybrid III was rotating about Z-axis during the contact with the airbag by yaw of the vehicle, while the head of the THOR-NT was little rotating. For these differences in the kinematics of the flexion and twist of the head-neck, it was presumed that the difference in the structure and characteristics of the neck caused the different kinematics, but that the act on the head-neck of the resistant force from the airbag might have differed. The difference in the kinematics based on the different structure and characteristics of the neck might have affected the difference in the head response.

The head-neck of the THOR-NT flexed than that of the Hybrid III at near 100 ms. It was presumed that since the Z-axis sensitivity of the THOR-NT's head was near the fore-aft direction, the Z-axis acceleration of the THOR-NT was higher than that of the Hybrid III. On the other hand, the X-axis acceleration of the Hybrid III was smaller than that of the THOR-NT.

The Hybrid III generated the Y-axis acceleration because the head was rotating about Z-axis at near 120 ms. However, the THOR-NT was low Y-axis acceleration due to little rotating. With regard to the difference of the twist behaviors of the head-neck about Z-axis, it was presumed because of the differences in the structure and characteristics between both dummies.

(2) Differences in the Responses of the Thorax, Pelvis and Lap Belt

As shown in Figure 33, the chest acceleration response of the dummies differed. In the section of the mark 1, as for the relative position between the thorax and the steering wheel, and the thorax contact situation with the airbag, the difference between the dummies was not observed. Therefore, it was presumed that the difference in the acceleration in the section of the mark 1 was different in the transmissive force from the pelvis in the internal of the dummy. The pelvis acceleration of the Hybrid III was higher than that of the THOR-NT. It was presumed that the difference in the pelvis acceleration was caused by the different contact situation of the knees, due to the different leg length between the dummies, and caused the difference in the thorax acceleration because this difference was transmitted to the thorax as the transmissive force in the internal of the dummy. Furthermore, it was presumed that the event that the arms came in contact with the instrument panel affected the occurrence situation of the acceleration in the section of the mark 2.

As shown in Figure 30, for the lap belt, large difference of

the force was observed between the dummies. Herein, it states the consideration why the lap belt force of the THOR-NT was lower than that of the Hybrid III.

Figure 34 shows the lap belt force relative to the pelvis stroke of the dummies, and the femur force (total of the right and left) relative to the pelvis stroke. Moreover, Table 5 shows the cause of the difference in the lap belt force relative to the pelvis stroke between the dummies. Herein, the pelvis stroke was calculated according to Equation 1.

The difference of the lap belt force between the dummies began to appear until the pelvis stroke of the dummies reached to 39 mm. This difference is presumed because the characteristics of the lower abdomen of the THOR-NT is softer than that of the Hybrid III [8].

The difference of the lap belt force between the dummies became larger until the pelvis stroke of the dummies reached to 39 mm to 114 mm; this cause was presumed as follows: The characteristics of the lower abdomen of the dummies differ. In addition, the restricted timing of the motion of the legs was different. Because the THOR-NT has longer upper legs than the Hybrid III, the initial clearance between the knees and instrument panel for the THOR-NT was shorter than Hybrid III. Due to this, the timing when the legs of the THOR-NT contacted to the instrument panel was earlier than the Hybrid III. The THOR-NT began to generate the femur force from about 39 mm of the pelvis stroke (the legs contacted to the instrument panel), while the Hybrid III began to generate the femur force from about 114 mm. Based on this difference, the load to the lap belt of the THOR-NT was reduced, and its lap belt force became lower, compared to the Hybrid III.

The lap belt force of the THOR-NT was lower than that of the Hybrid III after 114 mm in the pelvis stroke; this cause was presumed as follows: In addition to the consideration explained above, it was presumed that the difference in the femur force affected the lap belt force. The femur force of the THOR-NT after 114 mm in the pelvis stroke was larger than the Hybrid III. The THOR-NT was earlier than the Hybrid III with regard to the timing when the legs contacted to the instrument panel, and the legs of the THOR-NT deeply intruded into the instrument panel.

Furthermore, it states the factor of the difference in the resultant pelvis acceleration in the tri-axis of the dummies shown in Figure 11 and Figure 33.

Figure 35 shows the resultant pelvis acceleration in the X and Z-axis relative to the pelvis stroke of the dummies, and the calculated pelvis acceleration relative to the pelvis stroke. The calculated pelvis acceleration means the acceleration calculated from the lap belt force and femur force (Equation 2).

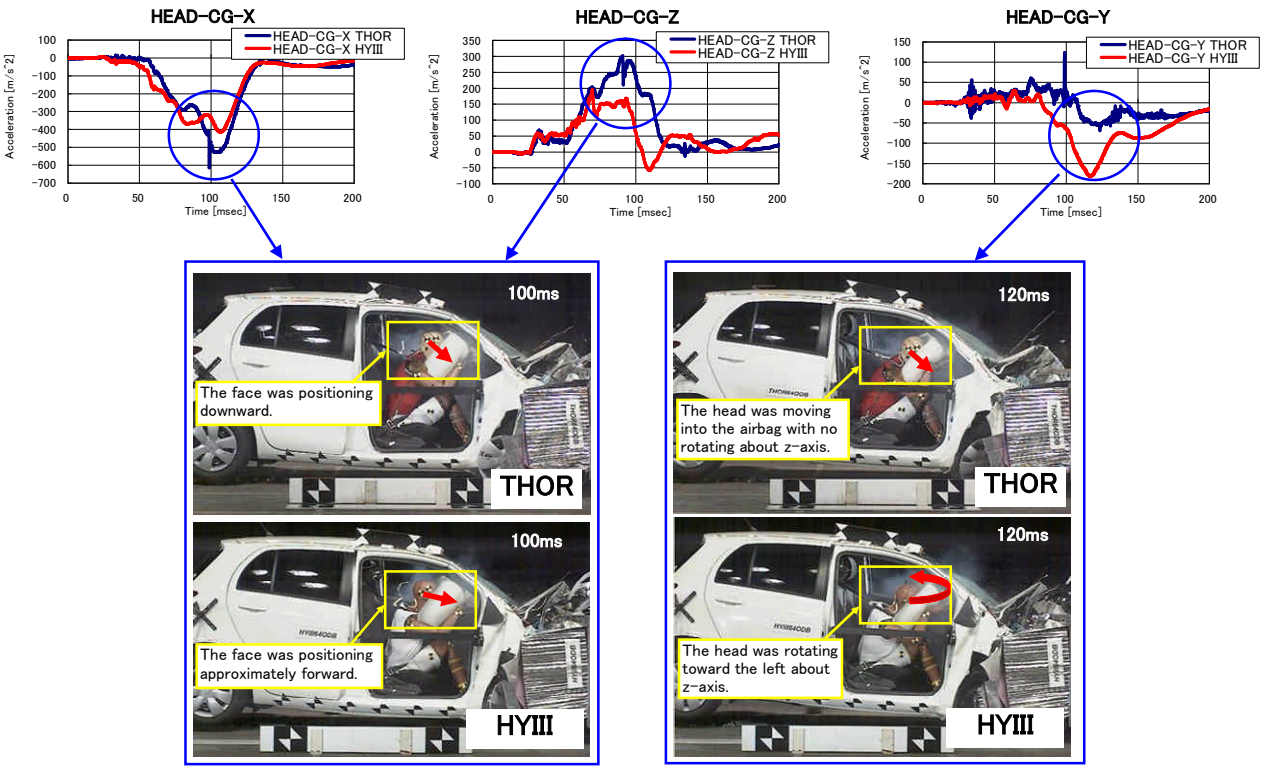

Figure 32. Differences in the Kinematics and Response of the Head

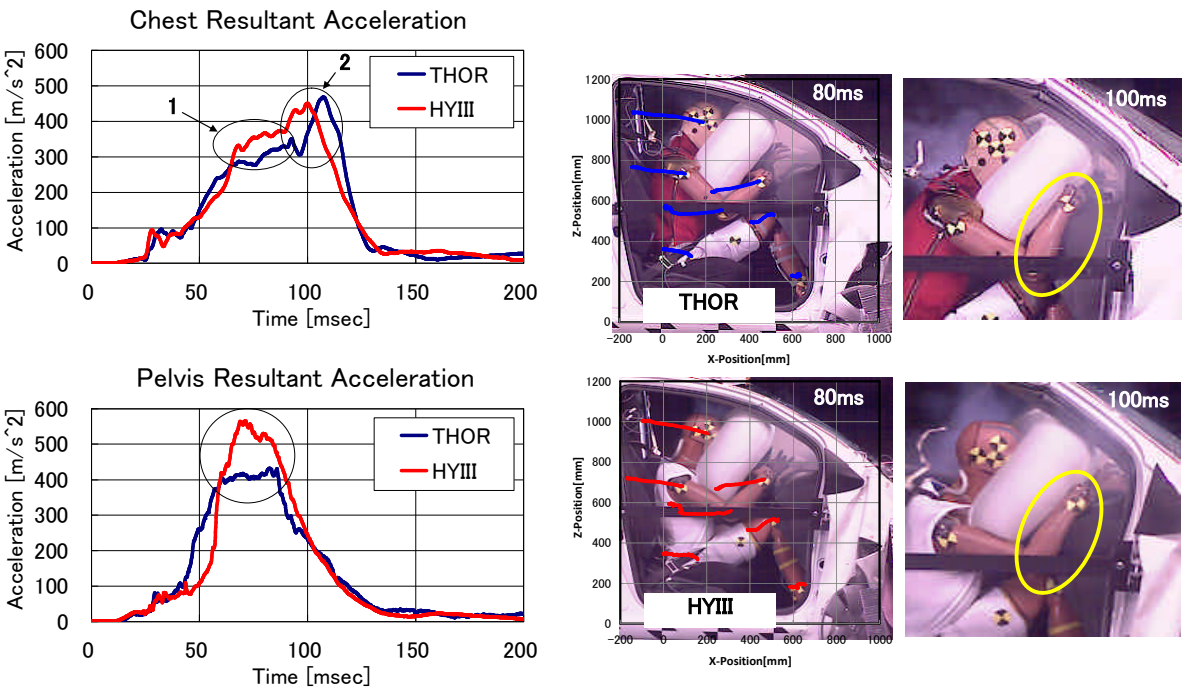

Figure 33. Differences in the Kinematics and Response of the Thorax and Pelvis

The resultant pelvis acceleration in the X and Z-axis and the calculated pelvis acceleration was almost the same. Therefore, it was presumed that two factors of the lap belt force and femur force affected the difference in the resultant pelvis acceleration between the dummies. The cause that the lap belt force and femur force differed between the dummies is as stated above. Therefore, it was presumed that the following factors affected the difference in the resultant pelvis acceleration in the tri-axis of the dummies; i) the lower abdomen of the THOR-NT is softer than the Hybrid III, and ii) the THOR-NT was earlier than the Hybrid III with regard to the timing when the legs contacted to the instrument panel because the THOR-NT has longer upper legs than the Hybrid III.

Equation 1:

$$Pelvis\ Stroke = \iint (a_{Pelvis} - a_{Vehicle})dt$$

where

a_{Pelvis} : *Resultant Pelvis Acc. in the X and Z – Axis*

$a_{Vehicle}$: *Vehicle Acc. in the X – Axis*

Equation 2:

$$Calculated\ Pelvis\ Acceleration = \frac{[Lap\ Belt\ Force + Femur\ Force\ (Total\ of\ the\ Right\ and\ Left)]}{Pelvis\ Mass}$$

where

Pelvis Mass is 22 kg for both THOR – NT and Hybrid III

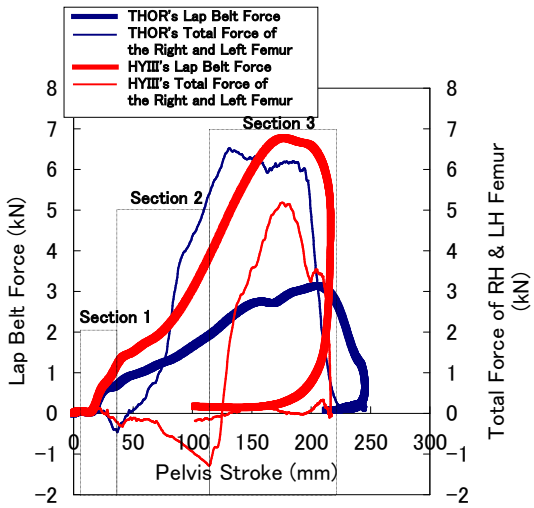

Figure 34. Lap Belt Force and Femur Force vs Pelvis Stroke

Table 5. Cause of the Difference in the Lap Belt Force Relative to the Pelvis Stroke Between the Dummies.

Pelvis Stroke		Factor for affecting the difference in the lap belt force
Section 1	To 39 mm	Difference in the characteristics of the lower abdomen
Section 2	39 mm to 114 mm	↑ + Difference in the timing when the legas contacted to the instrument panel
Section 3	After 114 mm	↑ + Difference in the femur force

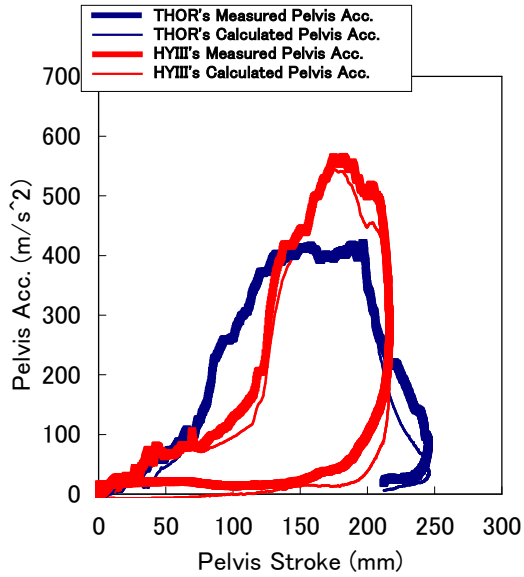

Figure 35. Resultant Pelvis Acceleration in the X and Z-axis and Calculated Pelvis Acceleration vs Pelvis Stroke

CONCLUSIONS

A 64 km/h offset frontal crash test was conducted with the THOR-NT and Hybrid III to investigate the responses of both dummies under a crash situation that includes both deformation and rotational behavior of a vehicle.

Although the THOR-NT and the Hybrid III were respectively installed in the driver seat in accordance with the ECE R94 positioning procedure, their postures were slightly different. The knees of the THOR-NT were positioned more forward and upward than those of the Hybrid III, because the THOR-NT has longer legs than the Hybrid III.

The THOR-NT and Hybrid III showed similar kinematics during the tests, except for the rotation about Z-axis of the head, and the contact situation to the instrument panel of the arms.

It was presumed that the difference in kinematics between both dummies affected the differences in the head, chest, and pelvis acceleration responses of the dummies. The difference in the head acceleration was affected by the different kinematics of the flexion and twist of the head-neck of the dummies caused by the differences in both structure and characteristics of the neck. The difference in the chest acceleration was affected by the differences in the transmissive force from the pelvis in the internal of the dummy, and the contact situation between the arms and the instrument panel. The difference in the pelvis acceleration was affected by the differences in the lap belt force and femur force between both dummies.

With regard to the differences in the lap belt force between the dummies, it was presumed that was because of the following factors; i) the lower abdomen of the THOR-NT is softer than the Hybrid III, and ii) the difference in the femur force between the dummies (The THOR-NT was earlier than the Hybrid III with regard to the timing when the legs contacted to the instrument panel because the THOR-NT has longer upper legs than the Hybrid III).

The injury measures showed almost equivalent values between the dummies, and all injury measures were less than the injury criteria specified in FMVSS 208 and ECE R94.

ACKNOWLEDGMENTS

The authors would like to express their gratitude to NHTSA for leasing THOR-NT dummy, used for this study.

REFERENCES

[1] Foster J.K., Kortge J.O. and Wolanin M.J. "Hybrid III- A Biomechanically-Based Crash Test Dummy." Proceedings of the 21st STAPP Car Crash Conference, 1977

[2] Backaitis S. and Haffner M. "Development of the NHTSA Advanced Dummy for the Occupant Protection Standard Upgrade." 7th International Technical Conference on the Enhanced Safety of Vehicles, 1979

[3] Schneider L.W., Ricci L.L., Salloum M.J., Beebe M.S., King A.I., Rouhana S.W., Neathery R.F. "Design and Development of an Advanced ATD Thorax System for Frontal Crash Environments, Volume 1: Primary Concept Development." U.S. Department of Transportation, DOT-HS-808-138, June, 1992

[4] Rangarajan N., White R., Shams T., Beach D., Fullerton J., Haffner M.P., Eppinger R.E., Pritz H., Rhule D., Dalmotas D., Fournier E. "Design and Performance of the THOR Advanced Frontal Crash Test Dummy Thorax and Abdomen Assemblies." Proceedings of the 16th International Technical Conference on the Enhanced Safety of Vehicles, 1998

[5] Haffner M., Eppinger R., Rangarajan N., Shams T., Artis M., Beach D. "Foundations and Elements of the NHTSA THOR Alpha ATD Design." Proceedings of the 17th International Technical Conference on the Enhanced Safety of Vehicles, 2001
[6] Shams T., Rangarajan N., McDonald J., Wang Y., Platten G., Spade C., Pope P., Haffner M. "Development of THOR-NT: Enhancement of THOR Alpha-the NHTSA Advanced Frontal Dummy." Proceedings of the 19th International Technical Conference on the Enhanced Safety of Vehicles, 2005
[7] Onda K., Matsuoka F., Ono K., Kubota M., Martin P., Zhao Y. "Differences in the Dynamic Responses of the THOR-NT and THOR-FT dummies." SAE Paper No. 2006-01-0676, Society of Automotive Engineers, 2006
[8] Yaguchi M., Ono K. and Masuda M. "Biofidelic Responses of the THOR-NT and Hybrid III Based on Component Tests." SAE Paper No. 2008-01-0520, Society of Automotive Engineers, 2008
[9] Masuda M., Yaguchi M. and Ono K. "Repeatability and Sensitivity to Seat-Position of THOR-NT and Hybrid III Based on HYGE Sled Tests." Proceedings of IRCOBI, 2008

APPENDIX

Table A-1. Instrumentations of theTHOR-NT and Hybrid III

		# of channels	
		THOR-NT	Hybrid III
Head	Head accelerometer array	9	9
Neck	Upper neck six-axis load cell	6	6
	Lower neck six-axis load cell	6	-
	Neck compression load cells (front and right)	2	-
	Head rotation potentiometer	1	-
Chest	CRUX chest rotary potentiometers	12	-
	Chest displacement potentiometer (normalized)	-	1
	Chest accelerometer triax	3	3
	Mid sternum uniaxial accelerometer	1	-
Abdomen	Upper abdomen string potentiometer	1	-
	Lower abdominal DGSP transducers (left and right)	6	-
	Upper abdomen uniaxial accelerometer	1	-
Spine	Spine T1 accelerometer triax	3	-
	T12 five-axis load cell	5	-
	Lumbar spine three-axis load cell	-	3
	Spine T12 accelerometer triax	3	-
Pelvis	Acetabular three-axis load cells (left and right)	6	-
	Iliac load cells (left and right)	2	-
	Pelvis accelerometer triax	3	3
Femur	Femur six-axis load cells (left and right)	12	-
	Femur single-axis load cells (left and right)	-	2
Knee	Knee slider potentiometers (left and right)	2	2
	Knee clevis, inside load cells (left and right)	-	2
	Knee clevis, outside load cells (left and right)	-	2
Tibia	Upper tibia five-axis load cells (left and right)	10	-
	Lower tibia five-axis load cells (left and right)	10	-
	Upper tibia four-axis load cells (left and right)	-	8
	Lower tibia four-axis load cells (left and right)	-	8
	Tibia x-axis uniaxial accelerometers (left and right)	2	-
	Tibia y-axis uniaxial accelerometers (left and right)	2	-
Ankle	Ankle rotary potentiometers (left and right)	6	-
Foot	Foot accelerometer triaxes (left and right)	6	-
Total		120	49

IMPROVEMENT OF DUMMY POSITIONING AND VEHICLE PARTS DURING A CRASH THROUGH THE INTEGRATION AND FILTERING OF INERTIAL SENSORS

Andrés Aparicio
José Manuel Barrios
Eva Palacios
Arturo Dávila
Jaime López
IDIADA Automotive Technology SA (1)
Spain
Paper Number 09-0372

ABSTRACT

The objective of this paper is to discuss the potential capabilities of inertial sensors for point tracking and the presentation of a new tool which is able to place vehicle and dummy parts in 3D during a crash. This tool can help in the understanding of crash dynamics and optimize restraint system integration as well as CAE correlation.

This paper analyses the uses given to inertial sensors in crash applications, describes the errors obtained and proposes methods to correct them. The use of accelerometer-only based and accelerometer and gyroscope-based platforms is discussed. Recommendations for placement, filtering and calculation methods are given. A tool able to track in 3D the trajectory of a point is presented and the limitations found are commented.

The sled tests carried out to obtain relevant information are presented. Possible applications in current tests and probable new tests exploiting the capabilities of the new tool are suggested.

INTRODUCTION

Accelerometers are the most commonly utilized sensors for crash applications in the automotive industry today. They are installed in order to obtain acceleration, relative speeds and displacement, thus providing invaluable information to aid in the calculation of the most important injury parameters. The specification of their response characteristics is pre-defined and the operation and signal filtering is described by the testing protocols.

Another type of sensor used in crash testing is the gyroscope, although the use of this instrument is not that widely spread in crash testing. The precision data provided by the new damped gyroscope generations is enabling their use in a broader variety of applications. Despite the exceptional performance that these inertial sensors could have, their capabilities are not fully exploited. If errors are minimized and an additional degree of accuracy in the use and calculation is given, they may be used to precisely track the position of any part they are installed and referenced to. Gyroscopes add an important value: they can measure rotation, which can be used as an input to correctly project the signals.

Tracking a moving object's position in time is a big issue, found in a wide variety of applications, including the military, industrial and medical. Nevertheless, and up to date, the most used methodology is 2D tracking of the parts, which only allows tracking of simple movements. In addition to that, tracking requires a huge set up, which is not always possible during a crash: calibrated optics, targets always visible and fixed reference points on the same plane and close to the visual range of the camera. Films obtained by high speed cameras are not capable of providing enough information about dummy parts that stay behind the vehicle's chassis. It is also impossible to determine with precision the amount of intrusion of certain parts of the dummy, such as the head or chest against the airbag, as they are obscured on contact, losing any visual reference available.

METHODOLOGY

The fore mentioned problem can be solved efficiently with an inertial measuring system and its related methodology, consisting of three accelerometers (measuring linear acceleration) and three gyroscopes (measuring angular velocity) orthogonally placed in the dummy and the vehicle. Thanks to this data flow, the required mathematical calculations and the development of special software, we are now able to trace the movement of the dummy with respect to the vehicle.

Euler's Rotational Theorem

According to Euler's Rotational Theorem, any rotation or group of successive rotations may be expressed as one rotation around a single direction or main rotational axle. In this manner, every rotation or group of rotations, found in a three-dimensional space can be specified through the equivalent rotation axle defined by vectors with

three parameters. Generally, these three parameters are called rotational degrees of freedom.

These angles constitute a group of three angular coordinates used to specify the orientation of a reference system of orthogonal axles, generally mobile, respect to another reference system of orthogonal axis, but in this case, fixed.

They are based in describing the way to achieve the final position from the initial one with three rotations, called yaw, pitch and roll. They must be given and calculated in that order, since the final result depends on the order of application.

Coordinate Systems

For this project, three different coordinate systems have been chosen:

- A fixed global system.
- A system referenced to the vehicle.
- A system with origin in the C.G. of head, chest and pelvis of the dummy.

Six parameters describe the location and orientation of a mobile segment relative to the reference segment: three translations (X, Y, Z) and three rotations (yaw, pitch, roll) in the reference point.

Rotations:

- Yaw – rotation around X axis
- Pitch – rotation around Y axis
- Roll – rotation around Z axis

Translations:

- Longitudinal (X) – Direction of the vehicle.
- Lateral (Y) – In direction of Y axis of the vehicle.
- Vertical – In direction of the Z axis of the vehicle.

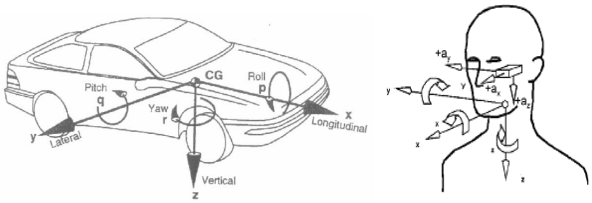

Figure 1. Coordinate Systems.

Calculation Sequence

In figure 2 we find the calculation sequence developed in this project, designed specifically to measure the dummy's global kinematics during a frontal crash. From this methodology, special software was programmed for *Diadem 10.1*, capable of calculating automatically the necessary operations.

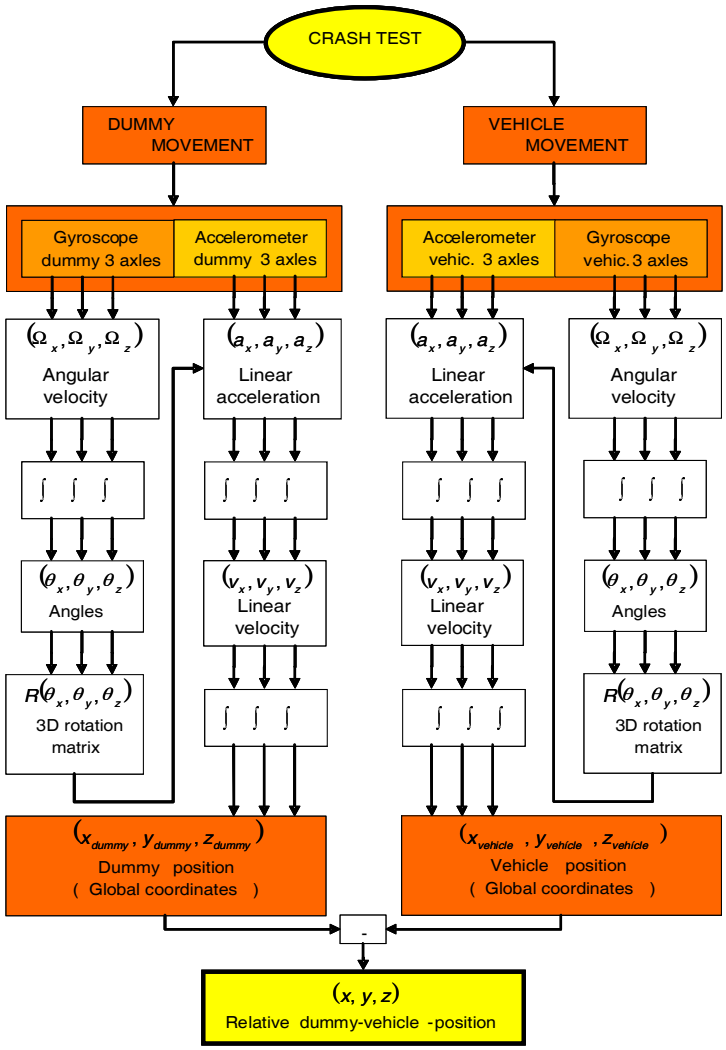

Figure 2. Calculation sequence.

First, the different angular components for the dummy (given by the corresponding three-axial gyroscope) are integrated with respect to time, obtaining the Euler angles. From these angles, a rotational 3D matrix is generated, from the local to the global system, which will be directly multiplied by the different acceleration components (obtained from the accelerometers located in the C.G. of each of the dummy's parts). As a result, a matrix with the acceleration components given as global coordinates is obtained.

By integrating the matrix components, the linear velocity is obtained and after a second integration the dummy's position with respect to the origin in global coordinates is calculated.

Parallel to this activities, the analogous calculus for the vehicle will be made (accelerometers and gyros located in the car) and will finally be subtracted from the dummy's position, giving then the relative dummy position respecting the vehicle.

Frontal Crash Analysis for 2D Modelling

Data from a frontal crash test were used during the first displacement analysis. The crash had a frontal configuration (Frontal impact 40% ODB 64 km/h), with a 40% offset, impacting on the left side of the car (left hand drive car). Crash speed was designated at $64^{\pm 1}$ km/h, having a real impact speed of 63.68 km/h. The available 2D methodology was used to analyze its deficiencies. In this phase of the project, dummy kinematics were studied with the 2D macro (rotation in Y, accelerations in X and Z axes).

In the next figure, two instants of the frontal crash are presented with a superposed X-Z graph (for the driver) obtained via the 2D methodology. Good results are obtained until the 125th millisecond, when the trajectory graph falls abruptly, due to car rotation (not considered in 2D methodology) and some other factors (integration in time).

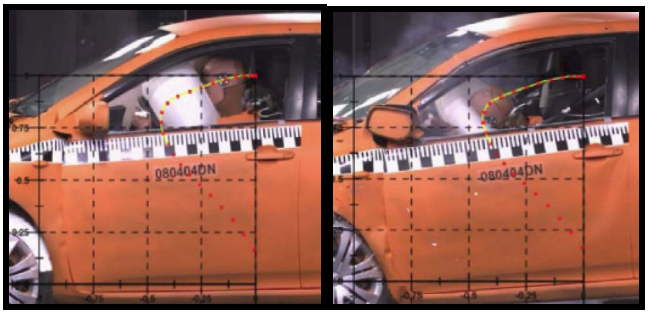

Figure 3. 2D kinematics.

Car Reference Selection

The graph in figure 4 reflects the importance of wisely choosing the X acceleration reference point in the car. Until now, the B pillar driver's side had been the reference point for calculations made for dummies both in the driver and passenger side. Nevertheless, this study demonstrates that the ideal place for reference is the B pillar on the side closest to the dummy whose kinematical data are to be analyzed.

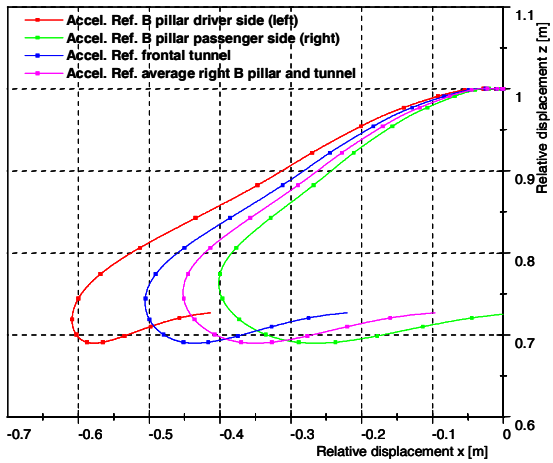

Figure 4. Relative head displacements of the dummy for different vehicle parts.

We can observe the results from the relative head displacement study in a car during a frontal crash test, taking as an acceleration reference for the car, different parts where accelerometers have been installed. There are accelerometers located in: B pillar opposite side (red line), B pillar dummy side (green line), frontal tunnel (blue line) and arithmetical average between frontal tunnel and B pillar dummy side (pink line).

After superposing the lines with the static measurement (figure 5) of the dummy's contour (passenger side), seat and dashboard; before (blue contour) and after (red contour) the crash, we prove that the B pillar closest to the dummy should be the X reference point in the car.

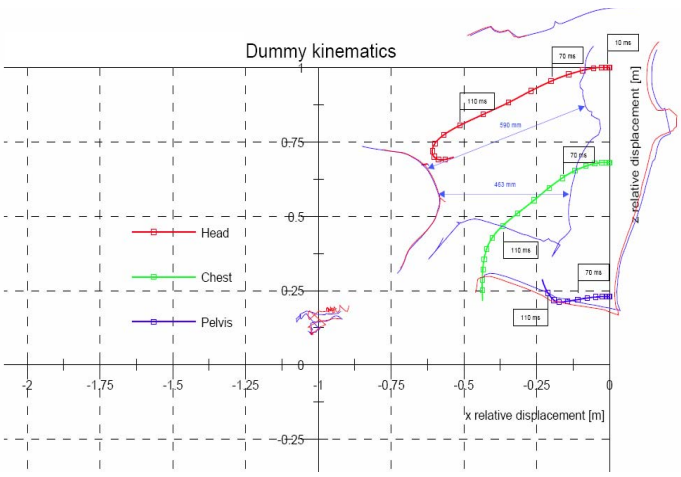

Figure 5. 2D head, chest and pelvis kinematics superposed to the static measurement.

SLED TEST WITH DUMMY ROTATION

Objective

The objective of this test was to determine the precision of the followed 3D methodology. Due to the fact that frontal crash tests are not completely linear, as they include a slight dummy and vehicle rotation, the established method is to be validated using a sled test adapted to the purpose.

After evaluating a series of alternative tests, a rotation in the dummy was forced by putting the seat with a 30º angle with respect to the longitudinal forward direction, as shown in the next figure.

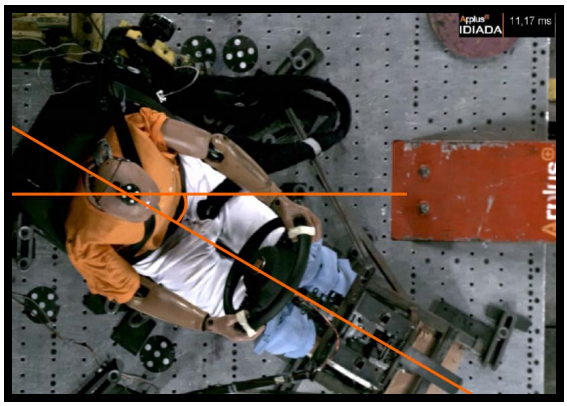

Figure 6. Dummy and seat placement for sled test.

Dummy Instrumentation

In the next figure, the final dummy instrumentation can be observed inside the head, chest and pelvis (accelerometers and three-axial gyroscope IES 3103-3600).

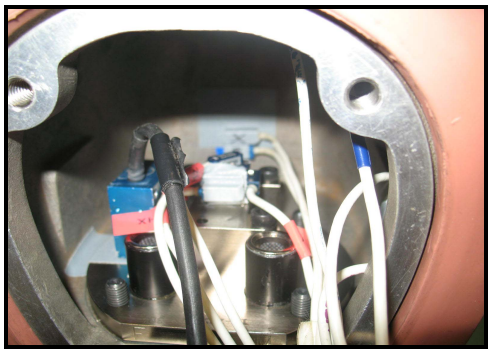

a) Accelerometers

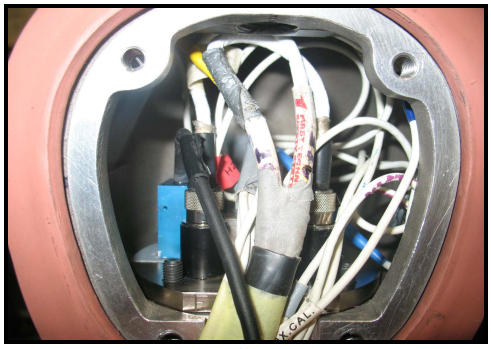

b)Head Gyroscope

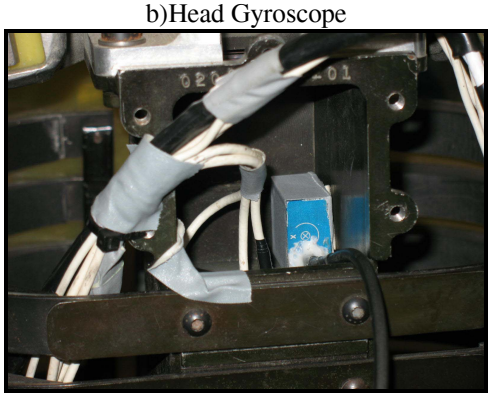

c) Chest Gyroscope

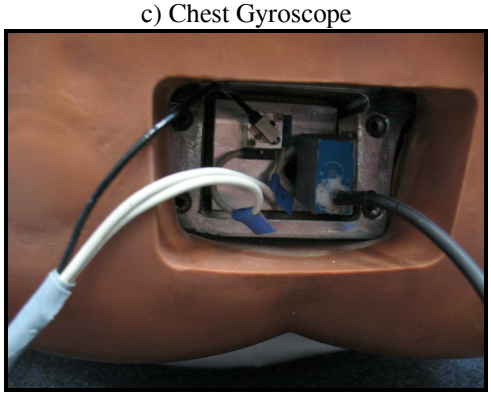

d) Pelvis Gyroscope

Figure 7. Dummy instrumentation.

Test Results

<u>Visual Tracking vs. Calculated Trajectory</u> – To estimate the exactitude and liability of the methodology developed during the course of this study, the calculated position graphs have been superimposed (on the same scale) to the films captured during the test. In figure 8, the calculated projections (a) X-Z and (b) X-Y of the head path (red lines) can be seen, superposed in a picture taken in the instant of greatest X displacement of the head (t= 90ms.).

From the available videos, (a) left side camera and (b) top view camera, an estimation of the real C.G of the head is made (green lines) during the entire duration of the test. Note that, due to the nature of the test and equipment, it is very difficult to make a visual tracking of the chest and pelvis.

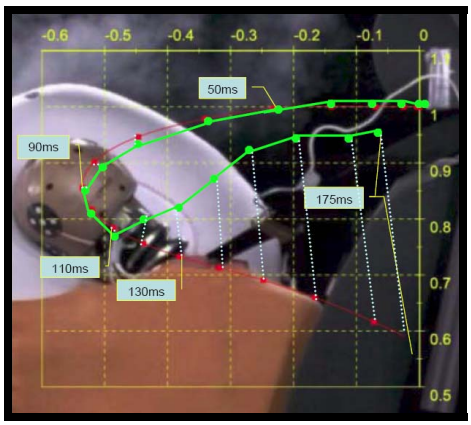

a) Left View (X-Z)

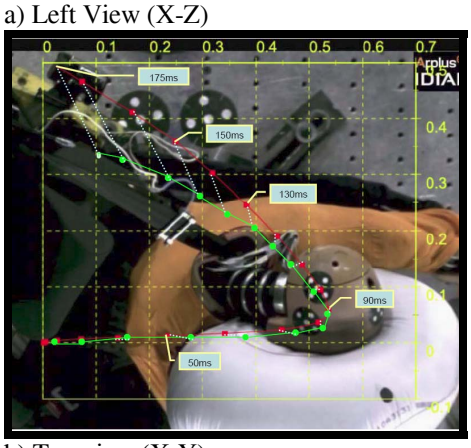

b) Top view (X-Y)

Figure 8. Head path comparison (red line: real path; green line: calculated).

Shown next is a chart that shows all the data obtained, including the estimated error (ε_X, $\varepsilon_{X'}$,ε_Y, ε_Z) from the video analysis. Up to the 120th ms, the methodology would give a position error of less than 15% in all cases, which, although improvable, is considered satisfactory. In fact, as shown in the chart, up to the 120th ms the average of all errors taken every 10 ms is in all cases, less than 7%.

Table 1.
Estimated error

	HEAD										
	Calculated movement			Real movement				Error			
t (s)	x	y	z	x	x'	y	z	ε_x (%)	$\varepsilon_{x'}$ (%)	ε_y (%)	ε_z (%)
0,000	0,000	0,000	1,000	0,000	0,000	0,000	1,000	0,000	0,000	0,000	0,000
0,010	0,004	0,002	1,000	0,004	0,004	0,002	1,001	7,036	7,036	2,050	0,087
0,020	0,026	0,004	1,000	0,025	0,030	0,004	1,001	2,494	14,589	0,395	0,083
0,030	0,071	0,006	1,000	0,071	0,078	0,006	1,001	0,062	9,031	6,560	0,074
0,040	0,140	0,009	1,001	0,160	0,140	0,010	1,001	12,197	0,346	7,059	0,027
0,050	0,233	0,013	0,997	0,274	0,225	0,012	0,997	14,959	3,675	5,672	0,035
0,060	0,341	0,018	0,979	0,375	0,340	0,018	0,970	9,062	0,299	0,432	0,921
0,070	0,447	0,025	0,946	0,466	0,449	0,022	0,930	3,970	0,442	13,499	1,756
0,080	0,517	0,038	0,902	0,521	0,509	0,033	0,887	0,818	1,520	14,534	1,639
0,090	0,536	0,060	0,856	0,535	0,535	0,055	0,852	0,135	0,135	9,435	0,457
0,100	0,521	0,095	0,817	0,510	0,521	0,095	0,810	2,105	0,051	0,154	0,923
0,110	0,487	0,140	0,785	0,460	0,486	0,140	0,765	5,786	0,045	0,130	2,588
0,120	0,439	0,191	0,756	0,430	0,439	0,170	0,800	2,047	0,046	12,297	5,450
0,130	0,382	0,246	0,733	0,395	0,381	0,210	0,820	3,347	0,204	17,129	10,601
0,140	0,319	0,303	0,713	0,340	0,320	0,225	0,870	6,323	0,468	34,702	18,080
0,150	0,249	0,359	0,691	0,290	0,270	0,260	0,930	14,306	7,959	38,111	25,717
0,160	0,167	0,412	0,660	0,233	0,199	0,290	0,948	28,337	15,882	41,960	30,366
0,170	0,073	0,465	0,617	0,150	0,120	0,325	0,948	51,417	39,272	43,211	34,958
0,175	0,023	0,494	0,590	0,109	0,070	0,338	0,955	78,788	66,969	46,200	38,200

Displacement in X is considered valid until the 150th ms, as the error is still underneath the 15% mark.

2D vs. 3D Comparison

The results obtained through the 3D methodology developed in this project and the results that would have been obtained following the original 2D methodology (considering only angular velocity in Y and accelerations in X and Z) were compared. As presented in figure 9, after the 80th ms, 2D simplification (green lines) would not have been valid, as the tendency lines fall abruptly.

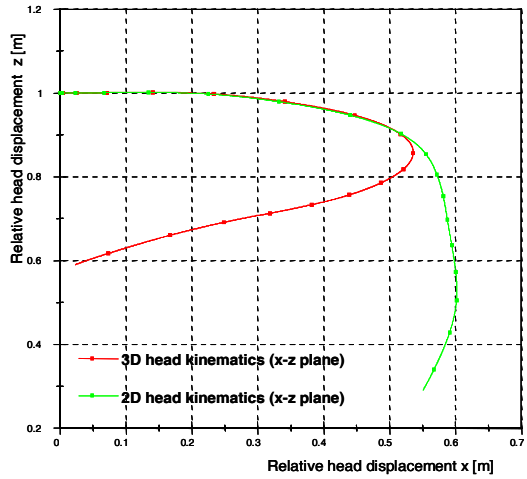

a) X-Z

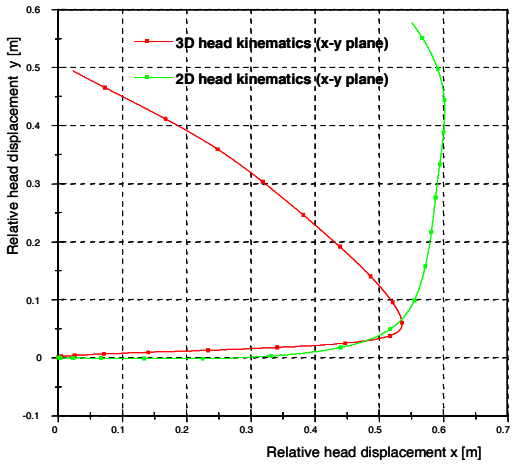

b) X-Y

Figure 9. Head trajectory from 2D methodology.

It is worth mentioning that the advantages of the 3D methodology reside in the fact that it allows the representation of the trajectory of the different parts of the dummy in a 3D space, not just in the bi-dimensional projections. In figure 10 we can appreciate the 3D representation of the global

dummy kinematics during the 30º test, for the head (red line), chest (green line) and pelvis (blue line).

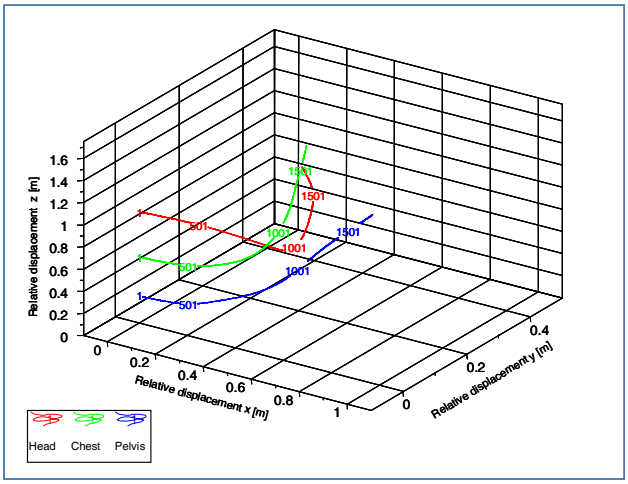

Figure 10. Global Dummy Kinematics.

The test concluded at a mere 49,59 km/h against the sled decelerators from the planned 50 ± 1 km/h. The angle was 30º from the centreline and the airbag was triggered at 17 ms.

ALTERNATIVE SOLUTIONS

There are a number of alternative solutions to obtain these data during crash testing. For this project, the tests included a 2D analysis, which used data obtained from accelerometers and gyroscopes. These accelerometers were installed in the B pillars, the central tunnel and the arithmetical average between the tunnel and B pillar. A gyroscope was used to measure rotation around the Y axis.

For the proposed 3D test, a setup of 3 accelerometers and 3 tri-axial gyroscopes were used. The recalled information was analyzed and good results were obtained.

One of the proposed alternative methods, instead of making use of tri-axial accelerometers and gyroscopes, is to use 2 tri-axial accelerometers in the same test. This setup has to be orthogonal, so that no axles end up aligned in the same plane as another one. This assures the consecution of 6 different acceleration pulses, each one in a specific direction, using (Equation 1) for solution.

$$\mathbf{a}(P_s) = \mathbf{a}(O_s) + \boldsymbol{\alpha}^s \wedge \overline{\mathbf{OP}} + \left|\boldsymbol{\Omega}^s \wedge \left(\boldsymbol{\Omega}^s \wedge \overline{\mathbf{OP}}\right)\right. \quad (1).$$

Using this procedure, any combination of points would be enough to solve the problem, as in the end, there are 6 unknowns: 3 $\boldsymbol{\Omega}$ and 3 $\boldsymbol{\Omega}'$ (derivatives), having a total of three equations.

Until now, a triple tri-axial accelerometer setup has been tested and the $\boldsymbol{\Omega}$ and its derivative have been calculated via iterative methods. This setup faces a number of problems, such as convergence, sensitivity to signal filtering, etc. Every time iteration is made, an approximate result is obtained and when deriving, some signal noise is generated. This noise is the cause that the convergence is low for the system.

In 1975, Padgaonkar et al. developed a new method using nine accelerometers placed on a mount, which has the form of a rectangular Cartesian coordinate system. There were two accelerometers at the end of each axis, normal to that axis, and three at the origin. Having this 3-2-2-2 arrangement, the equations become algebraic, thus eliminating the need for integration.

People at Robert A. Denton, Inc. have created a female dummy head that allows an array of up to 15 accelerometers. This head, the one of a Hybrid III 5th percentile female, has been developed using the 9-accelerometer model, accounting now for top, front, left, rear and a C.G. mount inside the device.

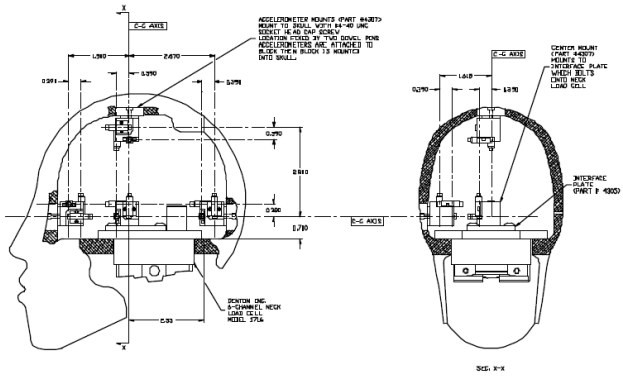

Figure 11. Robert A. Denton's dummy head array.

Padgaonkar et al. (1975) showed that this 3-2-2-2 scheme presents a significant advantage over the six accelerometer scheme in that the calculation of angular acceleration at any time point is independent of previous measurements, avoiding the possibility of errors accumulating over time.

The 3-2-2-2 array concept has been widely used and there has been considerable work done to develop techniques for the compensation and calibration of the array.

Some other techniques for measuring rigid body acceleration have been developed. These include measuring the angular velocity directly, using magneto-hydrodynamic sensors and an array of nine accelerometers divided in three tri-axial groups. However, these improved techniques are

more costly and require more data acquisition channels.

Whichever the case may be, it is difficult to obtain reliable data. Unreliable data is obtained because of:

- Accelerometer integration errors.
- Accelerometer alignment.
- The systems (as a whole) are used to find peak accelerations, not rotation.
- We look for trajectory, so the error accumulates and shows the wrong data (second derivates and much iteration).

CONCLUSIONS

The initial tests conducted using 2D and 3D models have shown an important improvement in movement tracking and trajectory calculation. Nevertheless, more testing and model improvements need to be made. An important part of the future steps is the trial of 1 tri-axial accelerometer plus 3 pairs of 2 single axle accelerometers setup. This setup will serve as a comparison array to aid the other tests in selecting the most precise testing setup.

Signal managing is another issue, as noise generated through integration and iteration may create large errors that may lead to incorrect data management and use. These errors must be quantified and corrected, so as to have the knowledge on how integration and sensor positioning have an influence on the result.

The general purpose of these tests is to obtain a reliable and robust methodology and equipment that leads to a better understanding and modelling of passenger behaviour during an accident. All the tests and their respective results must develop into a precise, yet practical instrument system for dummy monitoring.

REFERENCES

[1] Palacios Bazán, Eva María. 2008. "Desarrollo de una Metodología que Permita Determinar la Cinemática Global de Dummy durante el Ensayo de Choque Frontal".

[2] Padgaonkar, A.J., Krieger, K.W. and King, A.I. 1975. "Measurement of angular acceleration of a rigid body using linear accelerometers", Journal of Applied Mechanics, 552-556

[3] Robert A. Denton, Inc. 2002. "Model 4263 Small Female Head Accelerometer Array".

[4] Anderson, Robert .W. G. 2000. "A study on the biomechanics of axonal injury".

OBJECTIVE RATING OF SIGNALS USING TEST AND SIMULATION RESPONSES

Christian Gehre
PDB – Partnership for Dummy Technology and Biomechanics
Germany
Heinrich Gades
VOLKSWAGEN AG
Germany
Philipp Wernicke
BMW Group
Germany
Paper Number 09-0407

ABSTRACT

Today the numerical simulation is an inherent process of the development of the passive safety of vehicles. Robust and predictable computational models are the base of successful application of numerical simulations. The evaluation of the level of correlation of those models to the real world needs objective and reliable rating methods. In the past this rating was either done by engineering judgment or by analysing single peaks or zero-crossings of response curves in comparision with test data. Nowadays, it is common agreement that for an objective rating the complete curve data have to be taken into account.

In this paper, a new method is presented that provides an objective evaluation of whole response curves coming from test and simulation. The method combines two independent sub-methods, a corridor rating and a cross-correlation rating. The corridor rating evaluates the fitting of a response curve into user-defined or automatically calculated corridors. The cross-correlation method evaluates phase shift, shape and area below curves. It was found that the use of both of these two sub-methods is essential because the disadvantages of each sub-method are compensated by the other method. Both methods were implemented into a tool called CORA – correlation and analysis. The philosophy of this tool is to separate engineer's knowledge from the algorithms. External parameters to adjust the algorithms are representing this knowledge. So it is possible to tune the evaluation to the specific needs of the application.

The rating method was successfully used in a project on the improvement of Hybrid III 50th dummy models. It was possible to distinguish qualitatively and quantitatively between different releases of the model. In summary, the development of this rating method is a step forward to get an objective quality criterion of computational models.

In a next step the robustness of the rating will be analysed by varying the external parameters. Furthermore, the tool will also be used to analyse and evaluate results of physical tests.

INTRODUCTION

The analysis and comparison of signals coming from test and simulation is one of the major tasks of engineers working in vehicle safety business. A standardised method with reasonable scores is required to obtain an objective rating of the correlation of signals. So the requirements to a supplier regarding the level of validation of a computational model could be described more precisely in the future. The first step to an overall evaluation of the level of validation is the development of a metrics to compare a set of signals.

The evaluation of the correlation of two or more signals is not only relevant for the automotive industry. Hence, there are few rating tools on the market and even more published in the literature. For instance, the international standard ISO/TR9790 [1] uses a corridor method to compare cadaver and dummy responses for the biofidelity assessment of side impact dummies.

Each of the existing tools and algorithms has pros and cons but none seems to be both universal and adjustable to specific applications. Therefore, a new approach was developed to fulfil these requirements.

APPROACH

The existing rating algorithms suffer mainly from two reasons. Firstly, most of the algorithms are at least semi-universal but the settings, assumptions and simplifications made for implementation into software tools restrict the versatil-

ity. Secondly, many of the known algorithms are not robust enough to provide a reliable and applicable rating for good correlation as well as for poor correlation.

The new approach CORA avoids these issues. At first, the algorithms were consequently separated from the knowledge. Almost every parameter can be adjusted by the user. So it is possible to tune the algorithm to specific applications. Furthermore, completely different rating algorithms are integrated into the tool. Disadvantages of each algorithm are compensated by another algorithm. The user can decide about use and weighting of the different methods.

METHODS OF EVALUATION

CORA uses two different methods to calculate and assess the correlation of signals. While the corridor method calculates the deviation between the curves with the help of user-definied or automatically generated corridors, the cross correlation method analyses specific curve characteristics via parameters like phase shift or shape of the signals. The rating results ranges from "0" (no correlation) to "1" (perfect match).

The influence of the methods on the global rating is adjusted by user-defined weighting factors. Figure 1 shows the structure of the rating scheme in principle.

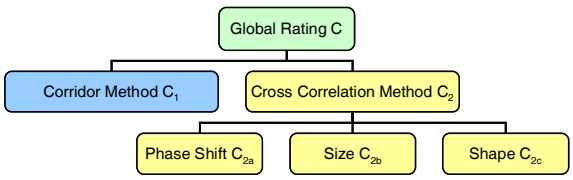

Figure 1. Interaction of the sub-methods.

The equations (1), (2) and (3) are showing the calculation of the global rating of a signal by using weighting factors for each sub-method.

$$C = w_1 \cdot C_1 + w_2 \cdot C_2 \qquad (1).$$

$$C_2 = w_{2a} \cdot C_{2a} + w_{2b} \cdot C_{2b} + w_{2c} \cdot C_{2c} \qquad (2).$$

$$1 = \sum w_i \qquad (3).$$

Other algorithms are analysing the global peak and the timing of peak. These parameters are captured by the metrics of CORA indirectly and can be controlled by a reduction of the corridor width around the peak. The direct implementation of these features into CORA is not intended, because it would somehow overrate the evaluation of signal parts. It is emphasised that the focus of CORA is on the assessment of the overall correlation of signals and not on the evaluation of single characteristics.

Filtering of the signals is a crucial point of almost every method. Noisy signals are difficult to analyse. Especially mathematical methods like the cross correlation method may fail to calculate the right level of correlation. Therefore, the user has to filter the signals prior the start of the rating tool.

Corridor method

The corridor method calculates the deviation between two signals by means of corridor fitting.

At first the mean curve of the references signals, usually coming from tests, is calculated. Two corridors, the inner and the outer corridor, are defined along the mean curve. If the evaluated curve is within the inner bounds, a score of "1" is given. The assessment declines from "1" to "0" between the bounds of inner and outer corridor. This transition is user-defined. Usually it is linear, quadratic or cubical. The three different rating zones are shown in Figure 2.

The compliance with the corridors is calculated for each time step. The final rating of a signal is the average of all single time step ratings.

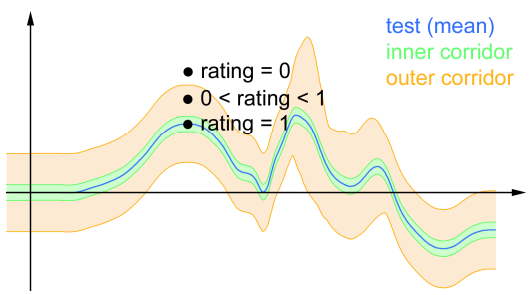

Figure 2. Corridor method using corridors of constant width.

The philosophy is to use a narrow inner corridor and a wide outer corridor. It limits the number of "1" ratings to only good correlations and gives the opportunity to distinguish between poor and fair correlations. If the outer corridor is too narrow, too many curves of a fair or moderate correlation would get the same poor rating of "0" like signals of almost no correlation with the reference. The width of the corridors can be adjusted in order to reflect the specific signal characteristic.

One of the advantages of the corridor method is the simplicity and the clearness of the algorithm.

It reflects criteria which are used intuitively in engineering judgement. Especially the rating results are easy to understand because the method rates the hits of the rating zones. The simplicity is at the same time the disadvantage of the method. In case of little curve coincidence it may lead to an inadequate rating. As shown in Figure 12, the simulation curve scores 0.431 (corridor rating only) without any correlation to the reference signal. The scores are gathered by hitting the inner and the outer corridor arbitrarily. Therefore, a second method is required to counterbalance this disadvantage. Typically, the corridor method gives realistic results above ratings of approximately 0.5.

Different approaches to define the width of the corridors are implemented. The most common option is the use of constant corridor widths (Figure 2). Typically a share of the global absolute maximum is used as width.

The width can also be calculated by using the root mean square deviation (sigma). Sigma is added to baseline corridors of constant width. So it is possible to consider the scatter of the reference signals. If the balance between constant baseline width and variable sigma term is inadequate, the corridors could become either very small or large (Figure 3). The signals shown in Figure 2 and Figure 3 used the same data to calculate the corridors.

Finally, it is also possible to integrate user-defined corridors.

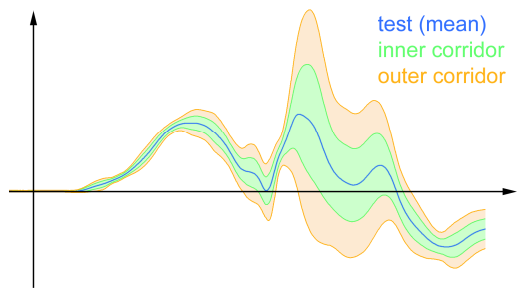

Figure 3. Corridor method using sigma-based corridor width.

Cross correlation method

The cross correlation method avoids the disadvantages of the corridor method by analysing the characteristics of signals. Three sub-methods with individual weightings factors are implemented. Similar to the corridor method, the mean curve of the reference signals is taken as base for the evaluation.

Firstly, the time shift of a signal to its reference is analysed (Figure 4). The maximum range of shifting is limited to avoid confusions of the algorithms in case of sinus-like signals. The size and progression of a signal is evaluated after adjustment of the phase error.

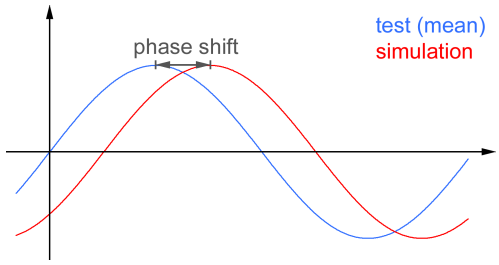

Figure 4. Evaluation of the phase shift.

Secondly, the size of the signals is analysed by comparing the area below the two curves globally. It is a helpful evaluation but is not sufficient to evaluate the real level of correlation. For instance, the area below a signal with high and narrow peak could be identical to the area of a curve with low but wide peak. The size method would evaluate this example with "1" although the shape of the signals is completely different.

Thirdly, the progression of the signal is calculated by means of the cross correlation function. This rating can be considered as a quantitative assessment of the shape of a signal.

The transition between ratings from "1" to "0" can be adjusted in all three sub-methods. Usually it is either linear or quadratic. Higher degrees are possible.

Compared to the corridor method, the cross correlation algorithms evaluate the level of correlation analytically. This kind of analysis is quite complex. Hence, the acceptance by users might be less than of the corridor method. The split of the cross correlation rating into three less complex sub-ratings improves the clearness and acceptance.

As shown in Figure 11, the cross correlation method is sensitive to noisy signals. The rating could be wrong if the noise interferes significantly the correct analysis of a signal.

Interval of evaluation

Most of the tools available on the market are analysing whole curves. The recording time of crash signals and simulation runs is typically slightly longer than required. So it would not be correct to simply use the whole signal for correlation analysis. Non-relevant parts of a signal may improve or worsen the rating. To avoid this, the response curve has to be cut properly before starting the rating. Figure 5 shows exemplarily the problem. The score of the

signal improves from 0.611 to 0.822 (approx. +35%) in this example when extending the interval of evaluation from the red tagged area to the whole curve, tagged in yellow. The differences may increase further if there are oscillations or peaks in the non-relevant parts of the signal.

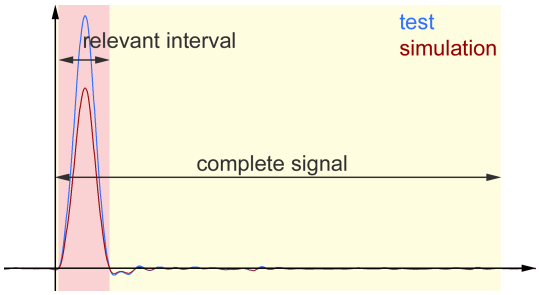

Figure 5. Interval of evaluation.

Therefore, it is essential to restrict the interval of evaluation to the relevant part of a signal. Two options are implemented. Firstly, the user can define this interval for every signal manually and secondly, the software calculates this interval for each signal individually.

To define the start of the interval, the analysis starts from the first recorded value of the mean reference signal by forward scanning of the signal along the timeline. If the signal exceeds a pre-defined threshold, the start of the interval of evaluation is set. There are additional parameters available to modify the starting point slightly. This mechanism is very reliable.

Very similar to that, the signal is scanned backwards along the timeline to define the end of the interval of evaluation. The end is set if the signal falls below a given threshold.

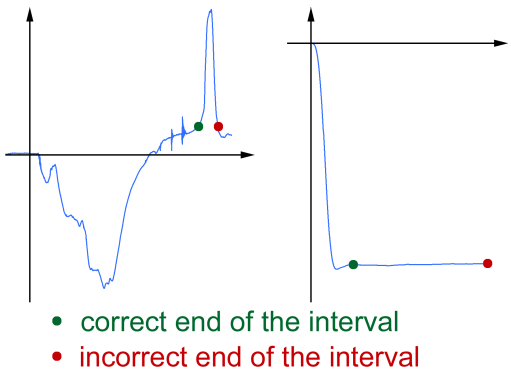

Figure 6. Critical signals for automatically definition of the interval of evaluation.

Unfortunately, this mechanism does not work properly for all types of response curves. Signals which end at an almost constant high level (e.g. delta-v curves) or with a secondary impact (e.g. peak of a rebound) are not treated in the right way (Figure 6).

Therefore, an additional method is introduced to handle signal endings of delta-v-like curves. At first, the end of the interval is defined by using the standard mechanism. Afterwards, a narrow corridor is defined for the remaining curve. The new end of the interval is set to that point when the signal leaves the corridor. This mechanism works fairly well but needs to be improved. This corridor is not linked to the corridors of the corridor method.

The second type of crucial signals cannot be treated right for the moment. The user has to set the end of interval of evaluation manually to exclude secondary impacts from the rating.

APPLICATION

CORA is a command line tool for several computer platforms that realises the developed approaches. It is solely a demonstrator of the proposed algorithms. There is no intension to use CORA commercially. A description of the methods used as well as the software itself will be available to the research community.

Program flow

Figure 7 shows the flow of the rating process in principle. At first the reference data set (input data 1) is defined. The data can be obtained from test or simulation. If more than one curve per channel is defined, the software calculates a mean curve because the rating algorithms are only able to compare and assess two signals.

Afterwards, the interval of evaluation is defined by using the information provided with the parameter set.

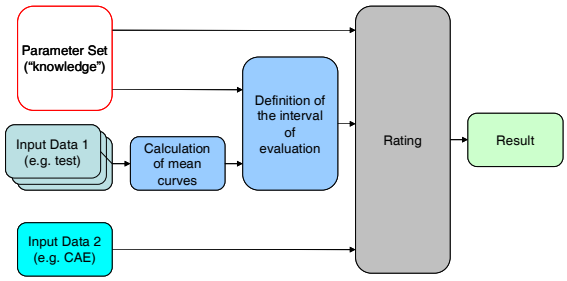

Figure 7. Process of preparation and evaluation of the data.

In a next step, the software imports the second data set which has to be compared with the reference data. The information of setting up the rating algorithms is taken again from the parameter file. Additionally, the validity of the interval of evaluation is checked. If the recording

time of input data 2 is shorter, the interval is adjusted automatically.

The results of the rating are stored in several formats. A plain text file contains a brief summary of the rating. All control parameters, weighting factors, calculated parameters (e.g. interval of evaluation) as well as the rating results are included in this file. It can be processed by other software like spreadsheet programs. Furthermore, a detailed HTML report is provided with graphs of the signals. The calculated mean curves and corridors are also exported. They can be processed by any CAE postprocessor.

Hierarchy of the data

CORA provides not only a rating of a single pair of curves. The rating of signals can also be extended to sub-ratings (sub-load case) and global ratings. All sub-load cases are merged to a load case rating. Finally, the rating of the load cases is combined to the global rating (Figure 8).

This four level structure was mainly introduced to cover the requirements of the ISO/TR9790 biofidelity rating. The sub-load cases contain all biofidelity tests of a body region such as head, neck or plevis. The combination of all load cases (body regions) is the total biofidelity rating of a dummy. Each signal, sub-load case as well as load case has individual weighting factors. So the influence of unimportant signals or tests on the rating of the higher level can be reduced.

The intruduced hierachy is also applicable for any other application.

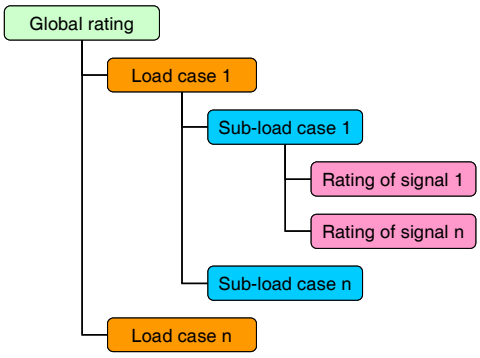

Figure 8. Hierachy of the data.

Biofidelity rating according ISO/TR9790

The biofidelity rating according the ISO standard was implemented in the latest version of the tool. A pre-defined template of the control parameter set is provided with the software to simplify the rating process. The user has to define the source of the test data only. All biofidelity corridors and weighting factors are already provided with the template.

Examples

The pros and cons of the described rating method are explained in the following examples.

Figure 9 shows the chest deflection of a Hybrid III 50th dummy and of two different models of it. Simulation 2 correlates better with the test curve. The corridor rating is 0.648 and the cross correlation rating is 0.681 (total rating of 0.665). The response of simulation 1 has got a corridor rating of 0.400 and a cross correlation rating of 0.507 (total rating of 0.454). All results correspond with subjective expectations on the rating.

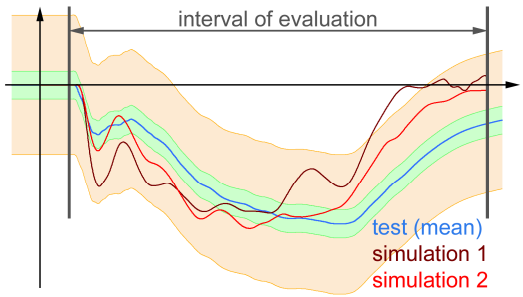

Figure 9. Evaluation of chest deflection, constant corridor width.

The same signals are shown in Figure 10. Solely the calculation of the corridors was changed. Inner and outer corridors are using the standard deviation to calculate the corridor width. Furthermore, the width of the corridors is significantly reduced. The rating using the corridor method drops from 0.648 to 0.251 (simulation 1) and from 0.400 to 0.168 (simulation 2). The cross correlation rating remains unchanged.

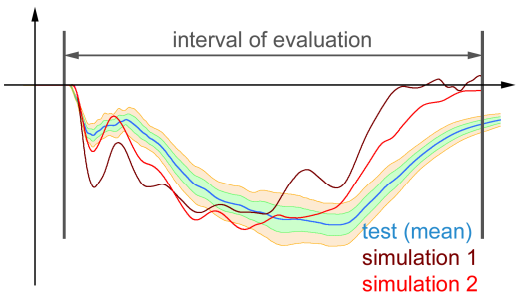

Figure 10. Evaluation of chest deflection, variable corridor width.

This scoring does not reflect subjective expectations of users. Due to the improper adjustment of the outer corridor, which is actually too narrow, the signals are very often outside of this corridor and obtain scores of “0”.

Furthermore, the absolute difference between both signals is reduced and the rating does not reflect the real level of correlation to the reference signal.

Another example demonstrates the influence of filtering on the rating. Figure 11 shows the neck tension force of a Hybrid III 50th dummy in a frontal test. The signals simulation 1 and simulation 2 are taken from the same simulation run but using different filter classes.

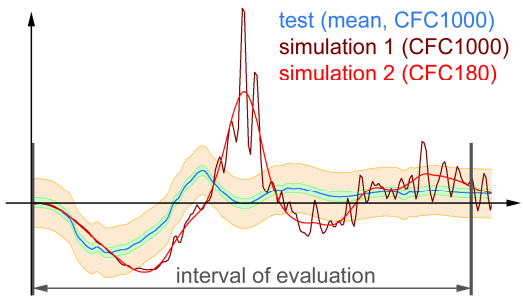

Figure 11. Evaluation of neck tension forces, influence of filtering on the rating.

The corridor rating is not sensitive to the applied filter class in this example. The difference of the rating is less than 0.005 (relative change of approx. 2%). Compared to that, the sub-ratings of the cross correlation method improve up to 0.07 (relative change of 14%) if the signal is filtered with CFC180. The algorithms of the cross correlation method are sensitive to noise. The spikes makes it is difficult to identify the right phase shift and progression.

The total rating of the simulation improves from 0.366 (simulation 1) to 0.389 (simulation 2) by using CFC180 instead of CFC1000. However, ratings should not be improved by applying higher filter classes. If there are noisy signals in the computational model, the cause of the noise should be fixed first.

The last example points out the limitations of rating methods. Figure 12 shows the knee displacement (knee slider) of a Hybrid III 50th measured in a frontal sled test without knee contact. The signal is caused by the inertia of the knee slider only. The maximum displacement is less than 2 mm. So the signal might not be relevant when evaluating a model in this specific load case.

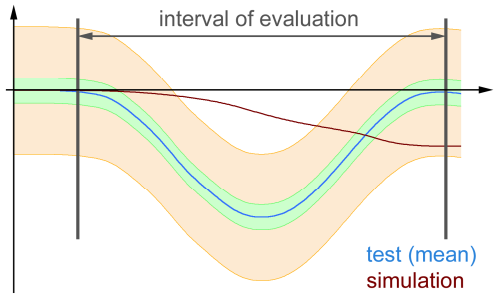

Figure 12. Evaluation of knee slider, limitations of the rating.

The total rating of the simulation curve is 0.391 (0.431 corridor method, 0.351 cross correlation method). This rating does not correlate to any subjective rating of users because there is no correlation between test and simulation. The rating of the previous example (Figure 11) is similar but the correlation between test and simulation is clearly better.

The disproportion is not necessarily a problem of the applied rating methods and their control parameters. The user has to define weighting factors for each channel. So the rating of the knee slider signal (Figure 12) might be acceptable if the influence on the global rating is smaller than that of the neck force (Figure 11). The definition of those weighting factors cannot be handled with a rating tool automatically.

LIMITATIONS

The development of the tool and the methods is not completed yet. The current version offers the opportunity to compare and evaluate signals coming from any source and groups single ratings to combined ratings. It is a first step to the objective rating of computational models.

Limitations of the algorithms

The introduced mechanism to define the interval of evaluation needs to be improved. There are certain types of signals that treated not correctly. So the user has to ensure manually that the right interval is defined. Otherwise the rating would not meet the expectations.

Furthermore, the algorithms are not able to handle signals with hysteresis. So it is impossible to evaluate force-deflection characteristics. The user has to evaluate the time history signals of force and deflection separately.

Classification of the rating

One of the uncertainties of the approach is the global meaning of the calculated scores. In case of using the same parameter set it is possible to distinguish between different variants of a model. Most of the results correlate with the subjective rating of users.

Changes of the parameter set do not change the ranking totally. The distances between models may vary and also the ranking of very similar signals may change. However, it is impossible to get the best rating for the worst model and the other way round just by modifying the control parameters.

The global meaning of the score has to be clarified in the future. There is a reference needed to be able to assign 0.6, 0.8 or any other score to a certain level of validation.

Evaluation of models

The tool offers the opportunity to evaluate whole models including different load cases and signals. Every signal and load case can be assigned with specific weighting factors. However, some general decision must be made before starting this global rating. At first, relevant load cases for the evaluation of a model have to be selected and prioritised. Afterwards, weighting factors for every signal of the load cases must be defined. This has to be done by the user. The CORA tool is not able to do this or to recommend baseline settings. Furthermore, the user has to adjust the control parameters of the algorithms. Only these settings can be derived from previous evaluations.

The difficulties of the selection and right weighting of load cases and signals are exemplarily explained on a dummy model.

Usually, there are extensive databases of certification tests available. The validation of many dummy models started with these data. It is assumend that the performance of the computational model in these tests is very well. A rating tool would probably calculate high scores.

However, a dummy model is typically used in vehicle environments. The load paths as well as the load levels may differ significantly to the conditions of certification tests. It is not guaranteed that the performance of the model in vehicle load cases is similar to that in certification tests. Therefore, the scoring in certification tests is probably not relevant in vehicle tests.

A global rating of a model must include all relevant loading conditions including the right balance between them (weighting factors).

The selection and evaluation of the right signals of a load case is sensitive too. There are important and less important signals measured with a dummy. Especially the handling of secondary axes has to be considered (e.g. transverse acceleration in a frontal crash). Firstly, these axes could be treated like the main axes. Acceptable deviation would become then a disproportional influence on the final rating. Secondly, they could also be ignored by using small weighting factors but then any problem with one of these axes would probably not be noticed in the global rating. Thus, there is an optional mechanism in the CORA tool that offers a special treatment of secondary axes. The main parameters, such as width of the corridors are taken from the main axis. So the rating of secondary axes is more tolerant but relevant deviations are reflected in the global rating.

However, more investigation is needed to extend the rating of single signals to a global rating of computational models.

SUMMARY

A new approach of the evaluation of the correlation of signals coming from test or simulation was developed. The algorithms and its control parameters are separated. That offers the opportunity to adjust the rating scheme to specific needs of each application and the requirements of users.

In total four methods are implemented to counterbalance the disadvantages of each submethod. The influence of each method on the global rating can be influenced by control parameters.

Besides these features, there is an algorithm implemented that calculates the interval of evaluation automatically. It ensures that only the relevant parts of a signal are considered for the rating. All introduced automatisms can be switched off and replaced by user-defined settings.

The latest feature of CORA is the integration of the biofidelity rating of side impact dummies according ISO/TR9790.

The development of the software is not completed yet. More investigation is needed to define a valid and robust parameter set. This set could become the baseline or starting parameter set. Additionally, more investigation is needed to improve the implemented automatisms like the calculation of the interval of evaluations.

The software and the description of the methods used will be available for the research community. The most likely option is the publication as freeware.

OUTLOOK

As mentioned above the development is not completed yet. It is intended to use this approach as part of the evaluation of computational models in the future.

Furthermore, the work of ISO TC22 SC10/12 Working Group 4 is supported. This group is working on international standards to evaluate the correlation of response curves with the focus on the comparison of test and simulation.

REFERENCES

[1] International Organization for Standardization. Technical Report 9790; Road Vehicles; Anthropomorphic side impact dummy – lateral impact response requirements to assess the biofidelity of the dummy; Geneva; 1999.

STUDY OF VEHICLE DYNAMICS AND OCCUPANT RESPONSE IN SIDE IMPACT CRASH TESTS

Brock Watson
Duane Cronin
Brett Campbell
University of Waterloo
Canada
Paper Number 09-0016

ABSTRACT

Side impact crash is a leading cause of fatalities on the roadways of the industrialized world. In the mid 1990's NHTSA implemented a new car assessment program testing the lateral crashworthiness of vehicles entering the market with a moving deformable barrier. Previous work has been done in an attempt to distill these tests into finite element simulations using specific vehicle test results; however there has not been a comprehensive study attempting to develop a model that includes a large number of tests to evaluate trends in vehicle kinematics and how they affect the occupants coupled with finite element simulations. To this end, a study of side NCAP tests was performed on all sedans based on the test results reported in the NHTSA Vehicle Crash Test Database since the introduction of the 2005 model year. This data was used to evaluate typical motion of the target vehicle during a regulatory crash test, and the corresponding occupant response. This sample consisted of new models entering the market and nameplates with major redesigns with a sample size of 72 vehicles. From these tests a series of velocity profiles were developed including time versus average velocity plots for vehicle center of gravity, door sill, driver's seat and driver door. These parameters have been shown to be important in occupant response and injury. There was significant variability in the response at several accelerometer locations. It was also found that rotation of the vehicle did not become significant until after 100 ms, after the maximum injury was predicted by the dummy. A parametric finite element analysis was performed using the both the USSID and ES-2re models to study the response of a restrained occupant during a typical crash test. These simulations showed that the velocity of the intruding door had a large effect on the thoracic injury predicted by the side impact dummy models.

INTRODUCTION

The response of vehicle occupants to side impacts has been a major focus of study for automotive safety experts for a number of years. Between 1994 and 1997 the United States government phased in a dynamic side impact compliance test to the Federal Motor Vehicles Safety Standards (FMVSS) to ensure all vehicles sold provided adequate safety performance in side impact [Kahane 2007]. Following the introduction of FMVSS 214, a side impact test was introduced to the New Car Assessment Program (NCAP) with the intention of providing safety information to consumers. Of the 22,716 vehicles involved in fatal crashes in the United Sates in 2007, 24.5% had the vehicles side as the initial point of impact, while 26.6% of injurious collisions had the lateral portion of the vehicle as the initial point of impact [NHTSA 2008a]. In research conducted prior to new side impact testing legislation to be introduced, NHTSA found that in side impacts chest injury accounted for 38% of fatalities and 59% of injuries, face and head injuries accounted for 40% of fatalities and 13% of injuries, and abdominal impact led to 8% of fatalities and 7% of injuries [NHTSA 2004].

During NHTSA's Side NCAP test, a moving deformable barrier (MDB) impacts the driver's side of a stationary target vehicle. The front of the MDB is fitted with a honeycomb structure to simulate the front bumper and crumple zone of an impacting vehicle. The wheels of the 1368 kg barrier are crabbed (turned slightly) 27° in an attempt to simulate relative motion between the target vehicle and the MDB. The nominal forward velocity of the barrier is 61 km/h. In the current version of this test, two DOT-SIDs (Side Impact Dummies) are placed in the vehicle on the struck side to measure the impact loads on driver and rear driver's-side passenger. These dummies are instrumented with accelerometers on the dummies upper rib (analogous to the 4th human rib), the lower rib (analogous to the 8th human rib), the lower spine (analogous to the T12 vertebra of a human), the head and the pelvis, along with load cells in the neck. There are 18 locations where accelerometers are mounted on the vehicle to record the response of the vehicle during the impact. Of these 18 locations, 5 on the vehicle door are considered optional [NHTSA 1997] and are often excluded. The Thoracic Injury Criteria (TTI) [Eppinger 1984, Morgan 1986] is the only injury criteria used in the current NCAP test, however if the

Head Injury Criteria (HIC) [Versace 1971] value is excessively high, the vehicle is flagged with a safety concern warning [Safercar.gov 2009]. For model year 2011 [NHTSA 2008c], the dummy used in this test will change to the ES-2re and rib deflection, HIC36, abdominal force and pelvic force will be used to measure the probability of injury to the dummy. This new testing procedure is part of the new NCAP program which will involve measuring the overall safety of a new vehicle by combining a frontal crash test, a side MDB test, a side pole impact test and a rollover test into on metric [NHTSA 2008d].

METHODS

The focus of this study was to investigate NCAP side impact test data and use this data as input conditions for a finite element model of a simplified sled, with a model seat, door and safety belt system. The explicit finite element solver LS-Dyna [LSTC 2007] Version 971 Revision 3.1 was used for all simulations. The desired outcome of this study was to assess the potential for injury on a USSID and ES-2re finite element model, both of which were developed by DYNAmore GmbH and supplied by FTSS [Franz 2002, Franz 2004, Schuster 2004]. The ultimate goal of this study was to understand the difference, if any, in severity of injury predicted by the ES-2re and the USSID finite element models. This work was essentially split into two parts, the first consisting of surveying crash test information from the NHTSA Vehicle Crash Database and the second consisting of using a side impact sled model [Campbell, 2008] with the crash test information to evaluate side impact response in typical crash scenarios. These two methods are outlined below.

NHTSA Database Information

To obtain the vehicle response information required in this study the NHTSA Vehicle Crash Test Database [NHTSA Vehicle Crash Test Database 2008] was surveyed. Of interest in this work were the vehicle and occupant responses in more recent crash tests using the USSID, so only data between model years 2005 and 2009 were studied. Additionally, to reduce any issues arising from a mismatch between the barrier and vehicle door, only 4 door sedans were studied. This meant that a total of 72 vehicles were considered. These vehicles were primarily vehicles which were new to the American marketplace (either new nameplates or cars previously available only in foreign markets), vehicles with major redesigns, or vehicles with the addition of new safety features (such as the inclusion of side airbags). Unfortunately, for all but 12 of the vehicles in the sample set, the door mounted accelerometers were not fitted. This means that the door intrusion velocity was captured during only these 12 tests. These 12 vehicles were all from model year 2005, so an understanding of door intrusion is somewhat limited for newer vehicle designs.

In addition to studying the velocity profiles of the vehicle accelerometers, the front seat dummy response was recorded for each test. This included the Thoracic Trauma Index, the dummy pelvic acceleration, and the Head Injury Criterion. Additionally, the offset between the dummy's arm and the vehicle door (AD distance), and the maximum door crush distance after testing were reviewed to identify trends.

The accelerometer data published in the NHTSA Vehicle Crash Test Database generally begins 20 ms prior to the MDB contacting the door of the target vehicle and lasts for 200-300 ms after the initial impact. The maximum thoracic response, as predicted by TTI, typically occurs in the first 50 ms after the MDB contacts the door. Therefore this study focused on occupant response during the first 100 ms after impact.

The data was filtered following the guidelines laid out in SAE J-211 [SAE 2003]. The velocity of the vehicle was found from each accelerometer by numerically integrating the acceleration trace. The time histories were then subsampled so that all of the traces had a sampling rate of exactly 1000 Hz. From this sub sampled data, 'average' velocity histories were determined using the mean value at each point within the velocity history, along with curves representing one standard deviation above and below the mean.

Initial evaluation of the data suggested that vehicle rotation during impact may be important. To study the rotation of the target vehicles, a simple kinematic analysis was performed. Based on the reported Cartesian position of the vehicle accelerometers, vehicle rotational acceleration was calculated using Equation 1.

$$\alpha = \frac{\Delta_{Rear_y}(a_{CG} - a_{Front}) + \Delta_{Front_y}(a_{Rear} - a_{CG})}{\Delta_{Front_y} \cdot \Delta_{Rear_x} - \Delta_{Rear_y} \cdot \Delta_{Front_x}} \qquad (1).$$

Where 'Δ' refers to the distance between the front and rear right side sill accelerometers and the CG accelerometer location prior to testing in the x and y directions, and 'a' refers to the lateral acceleration at each time step for the front and rear right side sill and center of gravity accelerometers. It is important to

note that this equation assumes that the accelerometers remain in fixed positions relative to each other and there is no local rotation of any accelerometer during the impact, thus these accelerometers were assumed to be moving as a rigid body. The right (non-struck) side sill and CG accelerometers were used to calculate this rotational acceleration since no damage is seen surrounding these positions (unlike the struck vehicle side). There were several tests where this method could not be used due to erroneous data from crash testing (when accelerometer channels failed, for example).

These rotational acceleration traces were then numerically integrated twice to determine the vehicle rotation as a function of time.

Finite Element Model Description

The sled model used in this study (Figure 1) was validated under side impact conditions [Campbell 2008] and included a seat, restraint system and intruding deformable door. The seat of the model consisted of a pair of rigid uprights which were prescribed the velocity of the driver's under-seat accelerometer. These uprights were connected to a deformable seat pan which was modeled using an elastic-plastic material model, as was the seatback. On top of these two surfaces a simplified seat was laid. The material properties for the seat foam were taken from a series of polymeric split Hopkinson pressure bar tests at elevated strain rates [Campbell 2007]. The three restraint system anchorage points for the safety harness were prescribed the velocity of the right front sills from the crash test data. This location was chosen because the CG location from several vehicles included in this study exhibited prominent peaks very early in the velocity time history which meant that at for this portion the method used to calculate the average time history provided a poor representation of most vehicles motion due to the amount of scatter. For this reason the time history of the right side front sill which exhibited very little scatter was used as the input condition for the floor and anchorage points of the simulations. The left sill was not used to represent the motion of the vehicle due to the deformation in this region which would have biased the input. An intruding door was created by using a simplified cross section of the Ford Taurus model provided in the Finite Element Model Archive by the National Crash Analysis Center [NCAC 2009]. The door was modeled as 1.5 mm sheet steel backing with a 3 mm thick plastic door panel, using the elastic-plastic material properties provided with the model. The ends of both the door panel and the metal back were boxed to increase the stiffness of the door. The door was placed so that the front face of the arm rest was at a distance of 800 mm from the centerline of the seat for all simulations. The backside face of the door was prescribed the velocity of the upper centerline accelerometer. The model was tested against NHTSA crash test 3522 of the Ford Taurus, which was used in developing the new version of FMVSS 214, and also an NCAP test of the Ford Five-Hundred to compare the simulated occupant thoracic injury to the tested values. For the Taurus test case The ES-2re dummy used in testing had a maximum rib deflection of 34.5 mm while the simulation predicted a maximum deflection of 31.9 mm. The NCAP test of the Five-Hundred produced a TTI score of 48 G while the model predicted a TTI of 30 G.

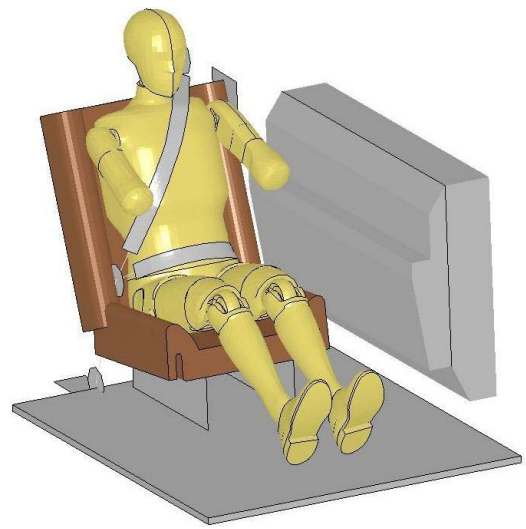

Figure 1. ES-2re Model in Sled

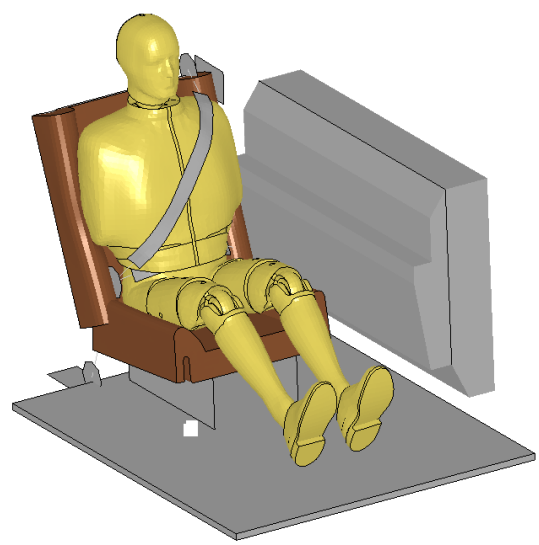

Figure 2. USSID Model in Sled

Response was measured using both the USSID model and the ES-2re model [Franz 2002, Franz 2004, Schuster 2004] as shown in Figures 1 and 2. Prior to the impact simulation the dummies and were sunk into the seat to ensure the stress equalized in the seat foam material. This was done by creating a rigid shell of the occupant and prescribing a displacement such that the occupant's position was at a reasonable position within the seat. A seat belt system was then modeled ensuring that the position of the anchorage points and slip rings were within the positions specific by SAE J383 [SAE 1995]. A pretensioner was used on the seat belt which drew in 100 mm of the seat belt in the first 30 ms of the simulation. An image of the ES-2re model in the sled is shown in Figure 1 while the USSID in the sled model is shown in Figure 2.

The baseline test case was performed first with the average velocities for the door, seat and floor. The door and seat velocities were then varied to plus or minus one standard deviation above or below the mean. Table 1 shows the door and seat velocity combinations simulated.

Table 1: Simulation Input Test Matrix

Simulation	Occupant Model	Door Velocity	Seat Velocity
1	ES-2re	Average	Average
2	USSID	Average	Average
3	ES-2re	+1SD	+1SD
4	USSID	+1SD	+1SD
5	ES-2re	-1 SD	-1 SD
6	USSID	-1 SD	-1 SD
7	ES-2re	+1SD	-1 SD
8	USSID	+1SD	-1 SD
9	ES-2re	-1 SD	+1SD
10	USSID	-1 SD	+1SD

Response was evaluated using risk curves developed by Kuppa et al. [2003] to quantify the injury predicted by both the USSID and ES-2re. These curves were developed from a series of cadaver sled impact tests as well as sled tests with the ES-2re. A logistic regression analysis was then performed to assess the probability of AIS 3 or greater and AIS 4 or greater injury as a function of TTI and maximum rib intrusion. The equations are of the form shown in Equation 2.

$$Probability\ of\ injury = \frac{1}{1+e^{a-b*criteria\ value}} \qquad (2).$$

The coefficients 'a' and 'b' are shown in Table 2 for both AIS 3+ and AIS 4+ injuries for TTI and rib deflection.

The coefficients in Table 2 for rib deflection were based on results from several sled tests performed by Kuppa et al. on ES-2re dummies and were correlated to the cadaveric tests performed, while the coefficients for TTI were found by curve fitting equation 2 to the risk curves provided for the TTI kernel, which ignores the age of the cadaveric subject. Because of this method for obtaining these coefficients there may be some error in the prediction of injury of the USSID.

Table 2: Injury Coefficients [Kuppa 2003]

Injury criteria	AIS	a	b
Chest Deflection [mm]	3+	2.0975	0.0482
	4+	3.4335	0.0482
TTI [G]	3+	6.0027	0.0736
	4+	5.8981	0.0517

RESULTS

NHTSA Database

Figure 3 through Figure 5 show the results of the survey of the NHTSA database which were used as input parameters during finite element modeling (driver's seat track lateral velocity, right front sill lateral velocity, and the upper centerline door lateral velocity). Each velocity history shows the average curve, as well as the upper corridor, lower corridor, and a curve representing the average value plus and minus one standard deviation. When there was an obvious error in the accelerometers recording (such as dislodging), the trace was excluded from the average and standard deviation calculation.

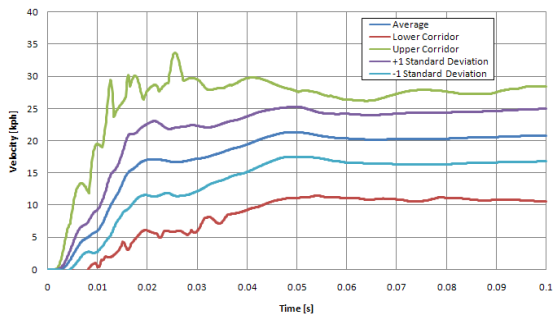

Figure 3. Right Seat Track Lateral Velocity History

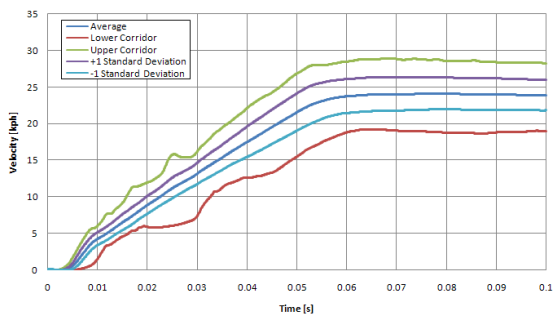

Figure 4. Right Front Sill Lateral Velocity History

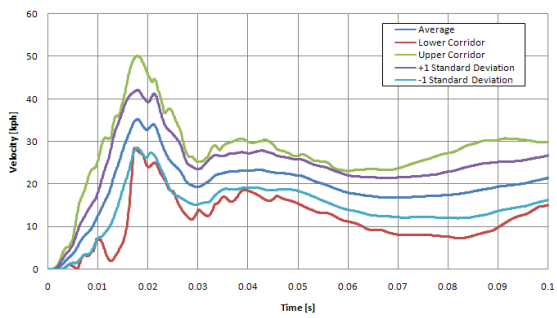

Figure 5. Upper Centerline Door Lateral Velocity History

Figure 6 depicts the calculated average rotation of the vehicle plotted along with the average spinal and rib accelerations of the occupant. This illustrates the small rotation of the vehicle prior to peak injury being predicted and justifies why vehicle rotation was not included in finite element modeling.

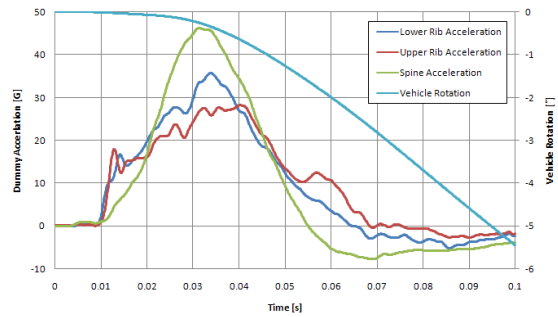

Figure 6. Rotation and Occupant Response Time History

Finite Element Model

Table 3 shows the predicted thoracic response for the simulations performed along with the load conditions. It is important to note that the USSID has only one element with which to measure rib deflections (at the middle rib) while the ES-2re has three. Additionally TTI is not a standard injury criterion for the ES-2re and likewise, maximum rib deflection is not a standard measure of injury for the SID and these values are provided only for comparison. The risk of injury is also shown in this table.

Table 3: Simulation Results

Sim #	Max Rib Deflection [mm]	TTI [G]	Probability of AIS 3+ Injury [%]	Probability of AIS 4+ Injury [%]
1	42.44	48.40	48.70	19.97
2	30.50	40.78	4.74	2.21
3	53.21	53.89	61.48	29.55
4	37.32	55.28	12.63	4.56
5	17.40	26.06	22.11	6.95
6	15.99	26.96	1.77	1.09
7	45.68	73.29	52.60	22.58
8	38.76	57.46	14.50	5.08
9	13.06	39.67	18.73	5.71
10	22.98	28.00	1.90	1.15

Figure 7 and Figure 8 depict the thoracic injury criteria results graphically with simulations with the same inputs grouped together.

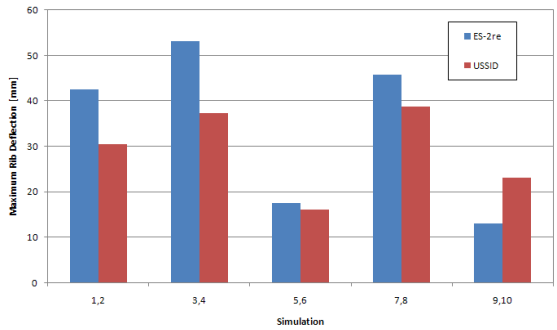

Figure 7. Maximum Rib Deflection Simulation Results

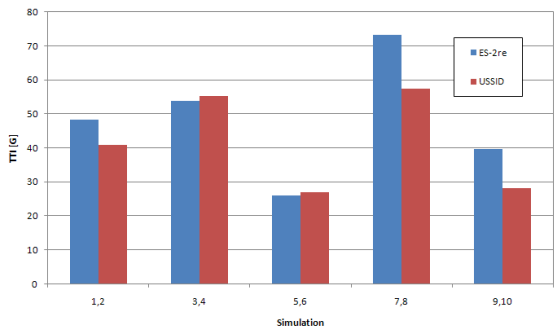

Figure 8. TTI Simulation Results

DISCUSSION

NHTSA Database

The various velocity-time histories determined from the database are in good agreement with the existing literature, including the pronounced peak observed in the door velocity history. This is often attributed to the outer skin of the door collapsing. Once the barrier reaches the outer structure of the door (the A and B pillars) the door velocity decreases and equalizes with the pillar velocity. When these structures collapse the velocity of the door again increases [Payne 1997]. It has also been suggested that as the door begins to collapse, the velocity is elevated until the first peak at which time the interior door contacts the occupant, slowing the door velocity until the occupant is pushed away, at which time the velocity increases again [Chan 1998].

One significant issue to consider with respect to the database is the effect of side airbags on occupant response. A further review of the vehicles tested by NHTSA during the time period of interest for this study showed that there was a significant increase in side airbag installation over the time in which the study has focused. A number of the vehicles in the early part of the data set either were not equipped with side airbags or they were optional equipment for that vehicle. For cases where they were optional equipment, the LINCAP test was often performed twice on the vehicle model; once on a vehicle with side airbags, and once on a vehicle without side airbags. Of the 72 vehicle included in this survey, the average TTI score of the 60 vehicles with at least one side airbag was 53 g while the 12 without side airs scored an average of 74.5 g. The majority of the vehicles without side airbags were from the 2005 and 2006 model years. A search of all cars (sedans, coupes and wagons) tested over the same time period (a total of 119 tests) showed that this phenomena was not limited to sedans. Figure 9 shows that as the average number of side airbags per vehicle for the driver have steadily increased over the past 5 years, the average TTI score has decreased. This finding was highlighted in a NHTSA report [Kahane 2007] which concluded that the large drop in TTI since the inception of the FMVSS 214 regulatory test, upon which the LINCAP test is based, is due in large part to the inclusion of side airbags on an ever increasing number of vehicle models.

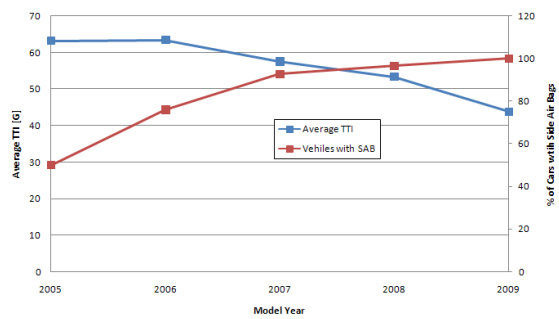

Figure 9. Side Airbag Installation and TTI in Cars between 2005 and 2009

Finite Element Model

The first and most obvious observation that can be made from the simulation results is that there are significant differences in the probabilities of injury predicted by the ES-2re model and the USSID model. This shows that the assumption of cadaveric injury data to develop risk curves for use with the USSID requires further investigation.

As expected the simulations with increased door intrusion speed (Simulations 3, 4, 7 and 8) showed the highest probability of injury for both dummies. The cases with elevated seat and door velocity predicted the highest injury to the ES-2re model, while the USSID predicted the case with higher differential velocities between the seat and door (higher door velocity and lower seat velocity) would

be more injurious. In general, the simulations with the elevated door velocity predicted higher injury than this with lower door velocity. This would indicate that reducing the door velocity would, in general, reduce injury. Interestingly the baseline case, based on average response, also showed an elevated injury potential for the ES-2re.

The maximum rib deflections were consistently higher for the ES-2re model than for the USSID. This is likely due primarily to the lack of a lower rib potentiometer on the USSID. In the simulations performed on the ES-2re the lower rib exhibited the most deflection due to the shape of the door panel. The armrest was at the same height as the position of the lower rib of the dummy leading to contact between the arm rest and the lower rib. The vertical position of the arm rest relative to the occupant may significantly affect injury response.

In addition to the position of the displacement potentiometer on both models and it relation to the position of the arm rest, the rib deflection curves themselves show quite different behaviors. Figure 10 shows the rib deflections of both the USSID and ES-2re models for Simulations 1 and 2. This figure illustrates that the middle rib of the USSID does not rebound in the same manner as the ribs of the ES-2re, but stays in a compressed state much longer. This behavior is seen in all load cases and was also seen in early work on the USSID and EuroSID when Bendjellal et al. [1988] performed several drop tests on both dummies, though in this work the reasons for this difference were not discussed. This figure also shows the degree to which the deformation of the lower rib differs from the upper two ribs on the ES-2re model, though the other load cases do not show this difference to the degree seen here.

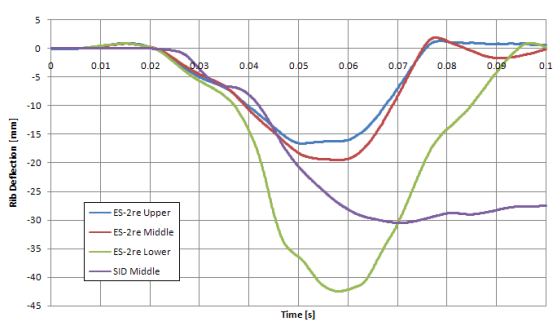

Figure 10. Typical Rib Deflection

In the new NCAP test, the actual risk curve that will be used is shown in Equation 3. This risk curve was developed by reanalyzing the data used by Kuppa et al. to develop the risk curves shown previously and assumes that the AIS 4+ risk curve found during the reanalysis should be used as an AIS 3+ curve.

$$P(AIS3 =) = \frac{1}{1 + e^{5.3895 - 0.0919 * max.rib.deflection}} \quad (3).$$

If the data for predicted the rib compression of the ES-2re model is reanalyzed using this risk curve the predicted results of AIS 3+ injury are shown in Table 4, along with those calculated using the TTI output of the USSID.

Table 4: Comparison of Prediction of Injury Based on NCAP Risk Curve

Sim #	NCAP Probability of AIS 3+ Injury [%]	SID Probability of AIS 3+ Injury [%]
1,2	18.40	4.74
3,4	37.77	12.63
5,6	2.21	1.77
7,8	23.29	14.50
9,10	1.49	1.90

Using this metric to predict risk of injury shows that the ES-2re results are considerably closer to those predicted by the USSID, though the ES-2re still predicts a higher likelihood of injury in most cases. These results show the importance of selecting a proper risk curve when comparing different injury criteria.

The values of TTI predicted by the models suggest that this response of the two dummies to the same load conditions is actually quite close for a number of load cases. This is despite a significant difference in the thoracic anatomy of both models. Indeed one of the concerns when the USSID was introduced was that the effective mass of the ribs on the USSID was too high when compared to EuroSID and the human body [Viano 1987].

CONCLUSIONS

In this study a review of side crash tests of four- door sedans tested by the NCAP program between model year 2005 and 2009 was completed. A series of average velocity profiles revealed that there was a good level of continuity of vehicle response throughout the majority of the tests. Maximum injury to the occupant was shown to occur roughly 35 ms after the movable deformable barrier impacted the target vehicle. The door velocity profiles were

limited in number and only available for the older vehicles in the sample set, thus the understanding of the kinematics of these components is somewhat limited. The average rotation of the vehicles in this dataset was found to be less than 2° prior to maximum injury prediction and was therefore not considered in the modeling aspect of this study.

The results of the survey of the NHTSA crash test database were used as inputs for a simplified side impact scenario, with finite element models of both the USSID and the ES-2re. A door model was prescribed velocity using data from the upper door accelerometer; while a simplified seat model was prescribed the seat track velocity found in the database review. The thoracic injury criteria used by each dummy model were compared using risk curves developed by Kuppa et al. These results, while not directly comparable between dummy models show the same general trends. The maximum injury prediction occurred with the greatest velocities as expected; however the dummy models differed in that the USSID predicted the greatest chance for injury when the differential velocity between the seat and door was the greatest, while the ES-2re predicted the highest probability of injury in the case of the largest velocity of both the door and seat. Future work will involve the inclusion of side airbags to the model, improved seat and door geometry, as well as studying the injury imparted to out of position occupants.

ACKNOWLEDGMENTS

The authors would like to express their appreciation to General Motors of Canada Limited and the Premier's Research Excellence Award for funding this work. The authors would also like to acknowledge First Technology Safety Systems and DYNAmore GmbH for the use of their dummy models in this work and the National Crash Analysis Center for the use of their crash data.

REFERENCES

Bendjellal, F., Tarriere, C., Brun-Cassan, F., Foret-Bruno, J., Callibot, P, Gillet, D. (1988) 'Comparative Evaluation of the Biofidelity of EuroSID and SID Side Impact Dummies' SAE 881717

Campbell, B.M. (2008) 'A Numerical Side Impact Model to Predict Thoracic Injury in Lateral Impact Scenarios', MASc Thesis, University of Waterloo, Waterloo, Ontario, Canada

Campbell, B.M., Cronin, D.S., Salisbury, C.P. (2007) 'High Rate Characterization of Automotive Seat Foams,' Society of Experimental Mechanics Conference, Springfield, MA

Chan, H., Hackney, J.R., Morgan, R.M., Smith, H.E. (1998) 'An analysis of NCAP Side Impact Crash Data' 16th International Technical Conference on the Enhanced Safety of Vehicles Proceedings, Paper 98-S11-O-12

Eppinger, R., Marcus, J., Morgan, R. (1984) 'Development of Dummy and Injury Index for NHTSA's Thoracic Side Impact Protection Research Program', SAE 840885

Franz, U. and Graf, O. (2004) 'Accurate and Detailed LS-DYNA FE Models of the US- and EUROSID: A Review of the German FAT Project', 6th International LS-DYNA Users Conference Proceedings

Franz, U., Schmid, W., Schuster, P. (2002) 'Observations During Validation of Side Impact Dummy Models – Consequences for the Development of the FAT ES2 Model', Nordic LS-DYNA Users' Conference 2002

Kahane, C.J. (2007) 'An Evaluation of Side Impact Protection - FMVSS 214 TTI(d) Improvements and Side Air Bags', DOT HS 810 748

Kuppa, S., Eppinger, R.H., McKoy, F., Nguyen, T., Pintar, F.A., Yoganandan, N. (2003)' Development of Side Impat Thoracic Injury Criteria and Their Application to the Modified ES-2 with Rib Extensions (ES-2re)' Stapp Car Crash Journal Vol. 47, SAE 2003-22-0010

Livermore Software Technology Corporation (LSTC) (2007) 'LS-Dyna Keyword Users Manual'

Morgan, R.M., Marcus, J.H., Eppinger, R.H. (1986) 'Side Impact - The Biofidelity of NHTSA's Proposed ATD and Efficacy of TTI', SAE 861877

National Crash Analysis Center (2009) 'Finite Element Model Archive' http://www.ncac.gwu.edu/vml/models.html

National Highway Traffic Safety Administration (1997) 'Laboratory Test Procedure for New Car Assessment Testing Side Impact Testing', Docket No. NHTSA-1998-3835, Document 0001

National Highway Traffic Safety Administration (2004) 'Federal Motor Vehicle Safety Standards;

Side Impact Protection; Side Impact Phase-In Reporting Requirements; Proposed Rule, Federal Register, Part IV, Department of Transportation 49 CFR Parts 571 and 598', Docket No. NHTSA-2004-17694, Document 0003

National Highway Traffic Safety Administration (2008a) 'Traffic Safety Facts 2006 (Early Edition)', DOT HS 811 002

National Highway Traffic Safety Administration (2008b) 'Revision to the New Car Assessment Program', Docket No. NHTSA-2006-26555, Document 0114

National Highway Traffic Safety Administration (2008c) 'Revision to the New Car Assessment Program', Docket No. NHTSA-2006-26555, Document 0116

National Highway Traffic Safety Administration (2008d) 'Revision to the New Car Assessment Program', Docket No. NHTSA-2006-26555, Document 0115

NHTSA Biomechanics Test Database (2009) http://www.nrd.nhtsa.dot.gov/database/aspx/biodb/querytesttable.aspx

NHTSA Vehicle Crash Test Database (2009) http://www-nrd.nhtsa.dot.gov/database/veh/veh.htm

Payne, A.R., Mohacsi, R., Allan-Stubbs, B. (1997) 'The Effects of Variability in Vehicle Structure and Occupant Position on Side Impact Dummy Response Using the MIRA M-SIS Side Impact Technique', SAE International Congress and Exhibition 1997, SAE 970571

Safercar.gov, NHTSA (2009) 'NCAP FAQs' http://www.safercar.gov

Schuster, P., Franz, U., Stahlschmidt, S., Pleshberger, M., Eichberger, A. (2004), 'Comparison of ES-2re with ES-2 and USSID Dummy – Consideration for ES-2re model in FMVSS Tests' LS-DYNA Forum 2004 Proceedings

Society of Automotive Engineers (SAE) (1995) 'SAE J383 - Motor Vehicle Seat Belt Anchorages--Design Recommendations'

Society of Automotive Engineers (SAE) (2003) 'SAE J211-1 - Instrumentation for Impact - Test Part 1 – Electronic Instrumentation'

Versace, J. (1971) 'A review of the severity index', Proceedings of the 15th Stapp Conference, SAE 710881

Viano, D.C. (1987) 'Evaluation of the SID Dummy and TTI Injury Criterion for Side Impact Testing' SAE 872208

DEVELOPMENT OF A MOTORCYCLE RIDER MODEL WITH FOCUS ON HEAD AND NECK BIOFIDELITY, RECURRING TO LINE ELEMENT MUSCLE MODELS AND FEEDBACK CONTROL

Filipe Fraga
Lex van Rooij
TNO Automotive – Integrated Safety
Riender Happee
BioMechanical Engineering, Faculty of Mechanical Engineering, Delft University of Technology
Jac Wismans
SafeTeq
The Netherlands
Ioannis Symeonidis
Steffen Peldschus
Institute of Legal Medicine, Ludwig Maximilian University, Munich
Germany
Paper Number 09-0244

ABSTRACT

Despite continuing improvements in vehicle safety, motorcyclist casualties are estimated between 13% and 17% of road fatalities. Looking at the last two ESV conferences for a tentative measure of the research effort that is geared towards motorcycle safety, oral/written papers referring to two-wheelers averaged 6%/3% of each group. This tendency is also identifiable in the clearly lagging development of experimental techniques and computational models for the study of crash scenarios involving PTWs. This *status quo* prompts further developments of PTW-specific design tools to stem from existing occupant (and pedestrian) tools, rather than already available motorcycle-specific solutions.

This paper aims at filling some of that gap by proposing developments in computational models for motorcyclists alongside real-world trials. The paper concludes that a MADYMO human body model, equipped with PID-controlled neck muscles, reasonably maintains its biofidelic erect posture in sample scenarios, under the assumption that riders attempt to maintain their head upright. Preliminary results yield activation levels of up to 50 and 55% during severe (± 1,7G and 0,8G) longitudinal and lateral loading scenarios, respectively.

Preliminary volunteer trials (N=8) were conducted to provide initial validation in the event of braking. Although not yet complete, the analysis suggests that the resulting head kinematics for an average aware volunteer is compatible with the simulated response.

This development focuses R&D efforts on preventing injuries to the head-neck-complex, the body's most vulnerable region, by providing biofidelic postures and reactions to developers of personal protective equipment and advanced occupant/rider restraint systems. It also allows the evaluation of a motorcycle active safety system's impact on human response, which directly influences the consequences of the potential subsequent pre-crash or crash event. Finally, it represents a first step towards fully active human models, which will provide life-like pre-crash behaviour to e.g. OEMs, equipment and barrier manufacturers, and policy makers.

INTRODUCTION AND BACKGROUND

When one specifically takes into account Europe's 8.5+ million motorcycles (mopeds excluded) and the estimated 5000 annual motorcyclist casualties [COST 327, 2001] (corresponding to somewhere between 1/6 and 1/8 of total road fatalities yearly), it is still not clear that the corresponding research effort and budget are allocated in proportion with PTW (Powered Two-Wheeled) vehicles' relevance within the road safety context. This can be unmistakably identified in the less-than-ideal development of human body models for the study of crash scenarios involving PTWs, regardless of the former's type: animal and PMHS trials have been almost unheard of, the appropriate ATD designed in the '90s (the "Motorcyclist ATD") does not reflect the latest biomechanical thinking mirrored in some car-specific modern alternatives (and also lacks multiple body sizes) [MATD ISO], and specifically-designed and validated computational models are generally limited as researchers have focused strongly on the occupants' and pedestrians' perspectives. The fact that the MATD achieved limited acceptance in the industry also lessened its effectiveness as a tool for the sharing of knowledge and solutions between PTW and car safety work. This context prompts the further development of PTW-specific design tools to stem from existing occupant (and/or pedestrian)

models, rather than already available (and hence less developed) motorcycle-specific solutions or the models developed specifically for automotive applications. That is indeed the chief objective here. PTW accident scenarios are far more dependent on their pre-crash dynamics (herein called "trajectories") than their four-wheeled counterparts, and thus the relevant human body modelling approaches are limited to those which are compatible with relatively long simulated timeframes (at least a couple of seconds). Also, because the posture and movement of PTW occupants DOES significantly influence the global system's behaviour (PTW+riders), the modelling approach must allow relatively broad magnitudes of movement and interaction of the simulated human body in relation to its environment (at least, the motorcycle). Jointly considered, these two points imply that the implemented solution needs to be truly "dynamical", i.e. designed to simulate a complex sequence of events corresponding to the whole scenario under study, rather than focusing on any specific event with extensive detail.

Towards biofidelic active human models

As researchers develop methodologies and tools to understand driving-related injury, both known statistics on the subject [IRCOBI Future Research 2006] and the knowledge of human anatomy and physiology points to the head-neck complex (HNC) as a priority in terms of which regions to model and what dynamics are of crucial understanding.
From the perspective of computational simulations, it has been clearly demonstrated over the past decade that the contribution of actively controlled human muscular action in automotive safety situations can not be neglected. Van der Horst resorted to computational modelling in MADYMO to define realistic lines of action and insertion points for the cervical region's multi-segment muscles [vd HORST 1997 and 2002]. It was thus possible to analyse the effects of muscular activation as the resulting force was exerted along a complex path surrounding the vertebrae, and hence study the former's influence on the HNC's global kinematic behaviour. Some authors even argue that muscle activation is unequivocally important and fundamentally changes the behaviour of an otherwise unrealistically passive model, based on an approach which also provides the moments of inertia and the forces produced by the cervical musculature [Brelin-Fornari 1998]. More recently, Lopik and Acar developed a model of the human HNC in visualNASTRAN 4D and used MatLab's Simulink to control the corresponding muscles. Rear impact scenarios then suggested that the influence of muscle activation in an unaware occupant's kinematics was small, but nevertheless the authors concluded that the forces recorded on the neck's soft tissues (and presumably the injury potential) were considerably influenced by the activation of the muscles [van Lopik 2004]. Even more recent work has demonstrated that neck muscle contraction stabilizes the head and neck during whiplash and reduces soft tissue deformation in aware impact situations [Stemper 2006].
From the experimental perspective, on the other hand, studies regarding HNC muscular responses are usually related to out-of-position automobile occupants. In one approach, the authors recurred to ElectroMyoGraphy (EMG) and subjected human volunteers to mild whiplash-like rear and lateral impacts while their torso and head were flexed out of the normal stance inside an automobile [Kumar 2004 and 2005]. The measured signals pointed towards a set of muscles which seem to be of primary relevance in the body's attempt to stabilize its posture and avoid injuries.

SCOPE AND OBJECTIVES

Whether one focuses on automobile occupants or motorcycle riders, it is consensual to state that severe decelerations ("high-G") will cause more destructive structural injuries than low- and medium-G scenarios. Given the apparent reflexive time delays and intrinsic limitations of active muscle force, muscular action is obviously much more relevant in low- and medium-G scenarios than it is in high-G, and thus only for impact will human response be completely passive. Therefore, the widely available passive human body models (of either the actual human body or ATDs) CAN accurately emulate human response under impact conditions, if necessary with stiffened joints. However, potentially perilous low-G scenarios may still arise (for instance) when an occupant swerves abruptly between two steering directions and his head is projected from one side to the other in a short amount of time, or in the event of a rollover.
The development of advanced crash-avoidance systems and impact restraint mechanisms depends on sensing and acting upon the pre-crash reactions of the human body. Throughout a potentially hazardous event, both the vehicle (with its safety systems) and the external environment will interact in real time with the human-in-the-loop, so their influence on the latter, and the human's reactions, may in turn impact the way the situation unfolds.
For motorcyclists specifically, it was already discussed how actively-controlled muscular action considerably influences the outcome of virtually all hazardous road situations, since the dynamics of motorcycle-specific scenarios are even more

dependent on the actions and posture of the rider (both at the level of pre-crash and actual crash) than their automobile counterparts.
Also, when it comes to low-G or pre-crash simulations, the time lapses involved are significantly larger and any chosen models for an alert driver/rider should exhibit some degree of muscular activation and the ability to react and adapt to the ongoing events in real time. Consequentially, any passive model displays a clear disadvantage in terms of its dynamic biofidelity, and truly dynamical models of the actual human body are unmistakably required.
Because of its particular relevance in this issue, recent research has focused on the HNC, establishing where the quest for active muscles and posture should receive the most effort. Naturally, as with all simulation-based approaches, any proposed advances will require motorcycle-specific validation trials, probably using EMG to identify the relevant muscles.
In conclusion, active human body models permit the study of how posture and movement influence the simulated response, and eventually the injury potential, in scenarios typically addressed within the vehicle safety field. For that end, they require the implementation of muscle models (for instance of the Hill type) and a dynamic mechanism to control their voluntary and/or involuntary activation. All but the last of these requirements are nowadays fulfilled with MADYMO's facet human body model with a detailed head and neck [vd HORST 2002].

AN ACTIVE HUMAN MODEL FOR PTWS

If it is to be effective as a design tool for research and industry alike, the desired end product must build on a validated and widely accepted model for the system being studied, and thus the chosen basis was Van der Horst's detailed multibody head and neck as integrated with the MADYMO facet human body model [vd HORST 2002, MADYMO HBM Manual]. It consists of a rigid head and vertebrae, (non)linear viscoelastic discs, frictionless facet joints, nonlinear viscoelastic ligaments and segmented contractile muscles which follow the curvature of the neck, thus allowing realistic lines of action. Literature data provided the mechanical properties of the tissues involved, and the model is capable of outputting their local loads and deformation. A more extensive description does not fit within the scope or focus of this paper, except for a specific note regarding the muscle modelling itself. Van der Horst resorted to MADYMO's implementation of the Hill-type muscle model: it comprises a "contractile element" (CE), which describes the actively generated contractive force, and a passive "parallel element" (PE), which describes the elastic force arising from the elongation of the muscle tissue. Total force is therefore the sum of these two contributions, which are described extensively in [vd Horst 2002]. Some representations of the Hill-type muscle model also include another passive elastic element in *series* with the CE, meant to introduce a spring-like "delay" when the CE is producing force, but in MADYMO that contribution is built into the latter.
Specifically on the contractile element's behaviour, its contribution to the total force depends on an "activation state" which describes the normalized activation level of the muscle and adopts values between 0 (rest state) and 1 (maximum activation). It is precisely this parameter that will become the control variable in order to attain the desired posture or movement of the HNC.
In total, the van der Horst HNC model comprises 16 muscle pairs divided in 68 muscle segment pairs. Their activation signals were initially arranged in three groups: flexors, extensors, and the single-member sternocleidomastoids. In order to isolate the muscles with relevant contribution to lateral (roll) motion, each individual muscle pair was activated on one side to analyse the head's response. This procedure led to a new set of muscle groups, each with a relatively clear biomechanical function:

"Pure" flexors: longus coli, hyoids, longus capitis

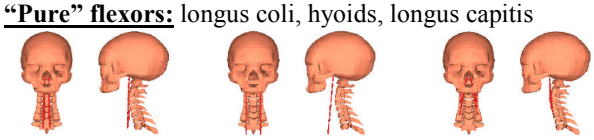

"Pure" extensors: semispinalis cervicis, longissimus capitis, multifidus cervicis

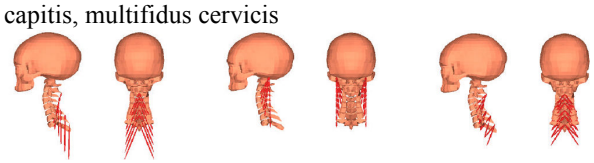

Rollers with secondary flexion function: scalenus anterior, scalenus medius, scalenus posterior

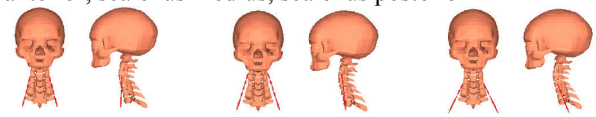

Rollers with secondary extension function: trapezius, levator scapulae, longissimus cervicis

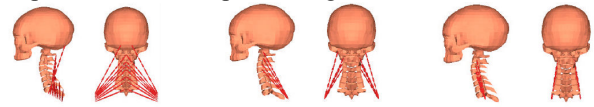

Yaw with secondary extension function: splenius capitis, splenius cervicis (above), sternocleidomastoid, semispinalis capitis (below)

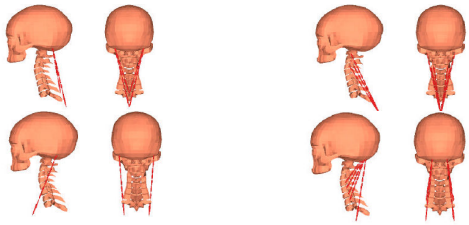

Figure 1. HNC muscle groups divided in flexors, extensors, rollers, and yaw.

A feedback approach to muscle activation control

As discussed before, at least one recent human body model possesses most of the features required to begin the work at hand. What is lacking is a method of controlling muscle activation so that a certain target posture or movement is dynamically displayed. A computational control system (or control loop) is commonly defined as encompassing the computational model (in this case, the human body's HNC), various sorts of sensors, one or more controllers, and various actuators (applying for instance forces, torques or displacements) which in this case are implemented as line element muscles. Within linear control systems, the ones that include some sensing of the results they are trying to achieve are making use of feedback and so can, to some extent, adapt to dynamically varying circumstances. This feedback control method was chosen amidst the classes available to design an active system. The *rationale* for this choice is fairly straightforward: no other method allows such tuneable and swift design. Furthermore, feedback control's ease of implementation is unrivalled directly through MADYMO or resorting to a coupling with Matlab/Simulink.
For the activation of the muscles, one needs to characterize the dynamic behaviour of the physical system so that the control loop's features can be properly designed. The first step would be the definition of what exactly are the relevant control parameters. The following picture illustrates the very first thoughts on the subject:

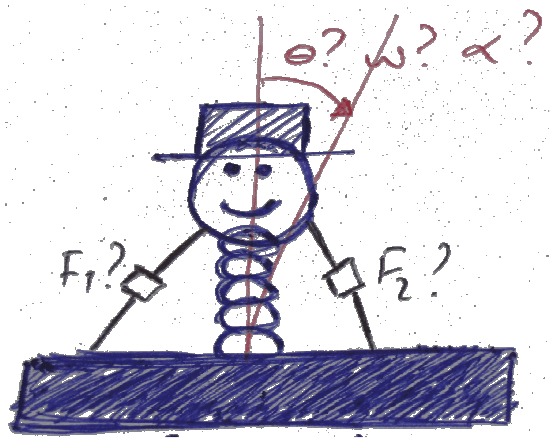

Figure 2. First sketch of what would eventually become the model's HNC control variables.

The following steps led to a deeper analysis but the burgeoning idea was retained, and the next section describes how the angular displacements between the head and the reference space became control inputs. Actually, in any feedback controlled system, both the relevant input and reference signals must be specified as numerical functions of time (and eventually other parameters). In this case, the direct modeling method was used: the fundamental features of the system (the human body's HNC) were analyzed as to their physical principals and desired behaviour, and appropriate control variables were identified. Considering that the model's range of movement was conceived to emulate human biomechanics, the articulation and the kinematics of the HNC joints and bodies should be reasonable proxies for their human counterparts. These are described below:

Neck Pitch – anteroposterior flexion and extension of the HNC, occurring in the sagital plane. This movement is not a unitary one, as it is permitted by the composition of small movements between adjacent cervical vertebrae with the help of the intervertebral discs. The downwards pitch is considered the positive direction for this displacement.

Neck Roll – the lateral abduction (away from the body's longitudinal axis) and adduction (towards the axis) equivalent of the Neck Pitch, occurring in the frontal plane. The rightwards roll is considered the positive direction for this displacement.

Head Yaw – the head's rotation about the neck's vertical axis. In actual fact, the head and the atlas rotate together on top of the axis (the second cervical vertebra) using the axis's dens (a tooth-shaped

process) as a pivot. The leftwards yaw is considered the positive direction for this displacement.

It was decided that Head Yaw should be residual at all times, not because of humans being unable to perform the equivalent movement (which is clearly untrue) but because of modelling difficulties associated with the individual control of the model's facial orientation while the muscles are balancing the other two degrees of freedom (pitch and roll). Near forward-looking orientation was achieved for all attempted simulations as a direct consequence of the active control of the head's roll and pitch, because muscle tension intrinsically stabilizes the neck.

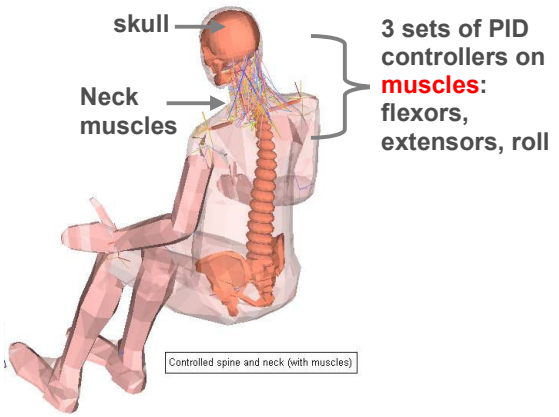

Figure 3. MADYMO facet human body model with detailed neck and optimised muscle groups.

The relevant movements can be sensed by the human vestibular apparatus and as such their equivalents should be sensed in a similar manner to render controller inputs. The corresponding analogues are presented shortly. It must however be said that the chosen methodology consists of an approximation, for the sensed parameters (angular deviations) bare resemblances to the biological system but are still not actual counterparts to it – in fact, the vestibular apparatus senses angular accelerations and is also able to "predict" the dynamic loading to some extent. This is one of the reasons why the authors believe the control method will require a different approach in the near future, as the validation progresses to more demanding scenarios.
As for the control references, maintaining overall head verticality (*i.e.*, keeping the head's longitudinal axis orthogonal to the ground) was the chosen criterion. This idea's stems were twofold: knowledge of the biological semicircular canals' arrangement, which suggest that the postural control mechanisms work at their best in said position, and the notion that the cortical processing of visual perceptions is strongly dependent upon the horizontal reference provided by the horizon. It is nevertheless debatable whether this criterion is valid regardless of one's role on a motorcycle or inside an automobile. That is, not only is the verticality approach an approximation in itself, but it could also be reasonably expectable that a distracted and/or relaxed rider/occupant (unwary to the perception acuteness necessary for the safety of the driving process) will allow significantly broader HNC displacements even if at the expense of visual and postural references.
The output signals are of arguably trivial choice: since an active system requires some sort of actuation applied to appropriate joints or bodies in order for the system to follow a reference, the controller outputs need to be fed to such actuators. As aforementioned, in this case line element muscles embraced that role: they present realistic force points of application and direction vectors, and as such their combined effects influence the whole system. This design decision thus correlates with accepted biomechanical evidence: the body's muscles apply contractive forces to the bones in order to generate torques and thus rotations of the same bones about the body's joints.

Implementing a controlled head-neck-complex

The chosen control approach implies that the true spatial status of the head-neck complex – how "vertical" it is at any given moment, regardless of its position in relation to the thorax – must be known at all times. That said, two sensors were implemented to provide the absolute (spatial) pitch and roll of the head. This formulation allows for the measurement of the head's deviation from verticality in any chosen direction and throughout the simulation, which would be untrue if joint angular displacement sensors had been used with the same purpose (since these would yield relative pitch and roll). In fact, experiments with low level random perturbations illustrated the importance of vestibular feedback in neck stabilization [Guiton 1986, Kesher 2000/2003] and the combined visual and vestibular feedback can be assumed to register head orientation in space as well as rotational velocity and acceleration.
The signals from the sensors are sent to PID controllers, which at every moment attempt to determine the "error correcting" signal: the one which nullifies the difference between the sensor and a reference signal supplied by the user (which represents the abovementioned "vertical" head position). The outputs from the PIDs are then sent to the muscles, specifying the activation state that is necessary to maintain the desired position (in this case, the head's verticality) against external stimulation – the trajectory-induced inertial forces. Naturally, each of the previously defined "pitch"

muscle groups (flexors and extensors) requires its own PID and associated parameters because the corresponding muscles and model geometry are not symmetrical at all. The completely symmetrical "roll" muscle groups, though, are activated on the left or right side depending on whether the difference between sensed and reference angles is respectively positive or negative, allowing the use of a single (rectified) PID. This leads to 3 separate PID controllers and control parameters for the HNC.

Tuning of the control parameters – Due to the absence of pre-existing biomechanical data, the control parameters were determined with the Ziegler-Nichols method, educated guesses, and trial-and-error, taking into account these notions:

Table 1.
Expected effect of increasing control parameter

Parameter	Rise Time	Overshoot	Settling Time	Steady-state Error
P	Decrease	Increase	Small Change	Decrease
I	Decrease	Increase	Increase	Eliminate
D	Small Change	Decrease	Decrease	Small Change

Neural delay and the activation dynamics time constants have so far been ignored in this study.
The controller output, which is the muscle activation state necessary to combat the angular deviation from the reference, is expressed in arbitrary units and sent to the corresponding muscle after normalization.
An early set of control parameters (obtained through Ziegler-Nichols) yielded a very satisfactory and credible HNC behaviour in most situations, but sudden shifts in the input trajectory led to non-physiological reaction times between the reversion of the previous trend and the adequate response to the next, along with occasional resonant oscillatory results. Trial-and-error was then used to fine tune the parameters until the response was adequate.

Human body model on APROSYS motorcycle

MADYMO allows complex models to be "driven" by means of supplying the positions and angular motions that they should follow over time. As a result, one can observe the model's reactions (both in terms of animations and the time evolution of several key parameters, like the angles between the neck and several spatial references) when it follows any trajectory which is considered relevant to understand the HNC's behaviour. The "dynamical" nature of the target scenarios requires a trajectory (as opposed to the traditionally used impact acceleration pulses) that can be fed to a proxy for a motorcycle which the human model is "riding", so this motion will be completely prescribed for the model to follow. This approach will ensure that the human model's posture and external loading profile is consistent with real (or at least plausible) road situations, which naturally include gravity in all simulations. For simplicity, and also because it was not the focus of this work, no detailed description of the motorcycle's "banking" when cornering was developed, so its motion involves just the three planar degrees of freedom. The chosen model was developed within [APROSYS], representing a "touring-style" vehicle that can be considered typical of one of the most common classes of PTWs in Europe.
The MADYMO facet/multibody human model [Lange et al 2005] was adopted in conjunction with the MADYMO detailed neck model [vd Horst 2002] as the basis for the work described in this paper.
To ensure that the rider followed the motorcycle, "point restraints" were implemented between the wrists and handlebar, the feet and feet rest, and pelvis and motorcycle seat. These restraints apply supportive forces (between the corresponding bodies) which increase quickly with distance (up to 30 kN for 10 cm), so the human body model is adequately secured to its "surroundings" which is what is actually being driven with the trajectory. Finally, the HBM spine joints were locked to ensure the torso stayed upright, focusing the analysis on the HNC.

Figure 4. MADYMO human body model positioned on APROSYS motorcycle.

DYNAMICAL SCENARIOS

Having devised an actively controlled computational model of the human HNC (along with the rest of the still passive human body and motorcycle), the system should be put to the test under simple conditions so that relevant outputs can be obtained and analysed in the quest for biofidelity. Two simple trials were thus conceived to assess whether or not the model was reacting adequately, one for longitudinal accelerations and the other for lateral (roll) ones. In these straightforward examples, the rotation in the sagital plane (linear sled test) and in the frontal plane (circular test) can be studied separately. In both test cases, for each time step chosen for the multibody calculations, MADYMO requires a global (i.e., referenced to the reference space) XX and YY position (the motorcycle follows planar trajectories) as well as an angular heading so that it moves along the desired trajectory. Computing these (XX, YY) pairs is trivial and will not be described here.

Simulated linear sled test

The first test is a softer version of the rocket sled ridden by Colonel John Paul Stapp. In addition to being a somewhat historic experiment, it is a simple trial that may be reproduced in real life albeit if only with very high performing vehicles. In this test, the modelled motorcycle is accelerated from naught to about 180 km/h at 1.7G for three seconds, then it retains its speed for two seconds before finally braking for three more seconds at a constant 1.7G (Figures 5-8). This sort of acceleration is attainable with top sport motorcycles (so-called "superbikes"), while the braking deceleration is limited to very special roads cars or racing cars. The global scenario is therefore a sequence of intensive conditions, illustrating how demanding the non-impact settings this work is aiming for can be. During the course of the test, the vehicle travels about 240m.

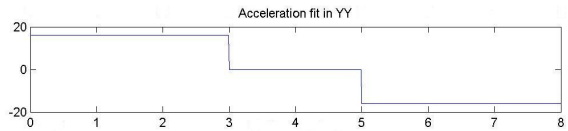

Figure 5. Acceleration felt during the sled test ((m.s-2) vs. time (s)).

Figure 6. Screenshots from the linear sled acceleration test, corresponding to accelerating, constant speed and decelerating (left to right).

The three stages of this experiment are very distinguishable when one analyses the model's behaviour. Three screenshots were taken at key moments of the simulation (previous figure) to help visualize and understand the simulated response. They all allow the observation of the hands of the model: because only the wrist is restrained to the handles, the hands themselves display their inertial response by pointing back, down and to the front as the motorcycle accelerates, cruises and then brakes.

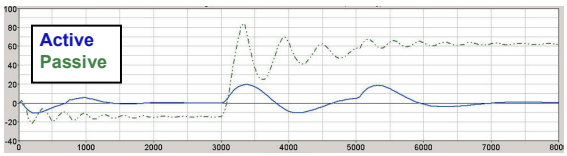

Figure 7. Active and passive HNC pitch angle for the sled test (degrees vs. time (ms)).

Figure 8. Muscle activation curves for the sled test (activation fraction vs. time (ms)).

As shown in Figure 7, the passive HNC extends about 15 deg backwards while accelerating, flexes about 70-80 degrees forward during cruising, and stabilizes at a 60 degree flexed posture while braking. The results from this 8 second long trial suggest that, based on the limited data available, the active HNC's response can be judged to be biofidelic while enduring significant longitudinal accelerations: the HNC never tilts more than roughly 20º from verticality under either positive or negative acceleration. The distribution of intervertebral rotations through the neck is quite homogeneous. The flexor muscle group (of which the *longus colli* is an example), exhibits very moderate activation (15 to 25%) only during the first phase as it is enough to maintain the desired posture. For the second phase a *Semispinalis Cervicis* was chosen to represent the "extensor" muscle group. The extensors' initial response displays some overshoot but eventually the signal stabilizes within the 2 seconds of the "constant speed" phase, at roughly 15% of the full activation potential. The next overshoot, from the onset of braking, is dealt with less smoothly (activation peaks at 55%) but the extensor muscles reach equilibrium with the external stimulation at 50% after 2 seconds. Owing in part to the locked spinal joints, T1 rotation never exceeds 10 deg in this simulation, which implies that the results actually relate to head and

neck stabilisation and are not compounded by spinal motion below T1. The maximum displacements occur with the 2 deceleration "initiations": forward acceleration stops at 3.0 sec and the head is pushed forward as a result of inertia, and later (5 sec) the actual braking again propels the head (and indeed the whole body, to a lesser extent) forward.
The reaction time needed to counteract all of the accelerations and nullify the angle never exceeds one second, even though the two instances mentioned above are very demanding.
All the lateral roll outputs are null throughout, as they should be since there is no lateral acceleration.

Simulated uniform circular motion test

The second experiment consists of a uniform circular motion that gives rise to a constant lateral acceleration, much like the centrifuge used to test the maximum g-force that a fighter pilot can withstand. The simulation is carried out with a lateral acceleration of 0.8G over a 5m radius circular trajectory for the same eight seconds, which corresponds to an angular velocity of about 1,26 rad.s-1. These acceleration values are attainable in most everyday cars, but might actually not be easy to reproduce in a motorcycle – at least without tilting it laterally. This motorcycle-specific "limitation" is immaterial to the work being developed on the model's HNC, and more realistic motorcycle trajectories are needed.

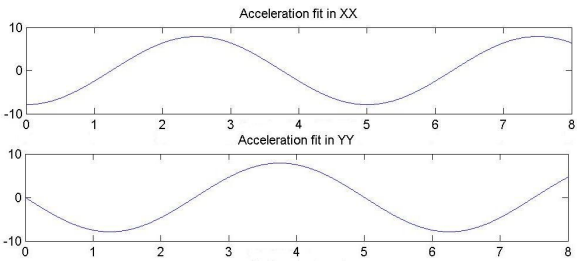

Figure 9. Constant lateral acceleration XX and YY (global) projection vs. time (s).

In this figure one may observe the projected acceleration patterns used to simulate the uniform circular motion in MADYMO. Since lateral acceleration is constant, its projections in the (global) XX and YY axis are sinusoidal and their phase difference 90º, which should be expected for such a movement. The model responded as follows:

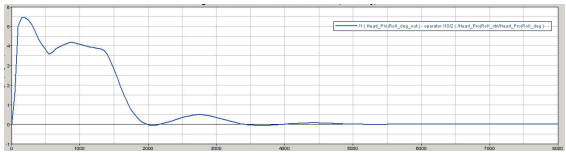

Figure 10. Active HNC roll angle for the circle test (degrees vs. time (ms)).

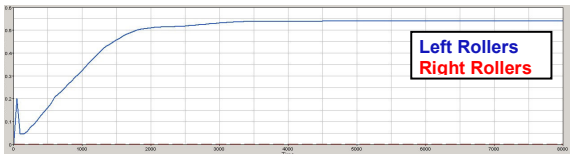

Figure 11. Muscle activation curves for the circle test (activation fraction vs. time (ms)).

The passive HNC presents a trivial response: the roll angle shoots to its maximum value of 30 degrees and remains there throughout the simulation. It was not included in the graphic to facilitate readability and avoid representation issues due to disparate scaling. The trajectory provided here is far more homogeneous than in the previous case: the longitudinal and lateral accelerations are null and constant, respectively. Consequentially, the active HNC needed only to counteract the outward-propelling centrifugal acceleration (~ 0.8 G) and within little more than two seconds it had endured the maximum angular displacement (< 6º), forced a very slight inward overshoot, and attained dynamic equilibrium with the centrifugal force at 0º. The previous figure shows that the left "roller" muscle group (of which the *trapezius* is an example) displays a quick activation spike to 20% in the first quarter of a second while the controller stabilized the HNC against the external stimulation (which pushed the head to the right). The activation state then rose steadily over the next 2 seconds, and once the control response was in steady-state 55% of this muscle group's activation potential was eventually required to counter the constant lateral acceleration. As expected, the right *trapezius* (and the other "right" rollers) did not display any noticeable activation.

EXPERIMENTAL BRAKING SLED TRIAL

In order to preliminarily validate the model response for a typical riding scenario, volunteer trials were conducted using an inverted braking sled setup [Symeonidis et al 2008]. Eight volunteers participated in the experiment. Steady-state decelerations of 0,2G and 0,4G were employed in two modes: "aware" (the volunteer triggered the sled motion) and "unaware" (the sled was launched by the researcher, unbeknownst to the volunteer). The riders' kinematics and muscle activation patterns

were captured with an optoelectronic motion capture system and electromyography equipment.
The corresponding analysis is still not complete and will be adequately published in the near future, but in order to include some initial insight for this paper, one set of data was chosen for visualization. The selected case was the 0,4G aware run of a volunteer with average ("middle of the corridor") responses. Perhaps because of these factors, the resulting HNC kinematics was trivial: very slight oscillation of the head around verticality, never exceeding 2 degrees. Using the acceleration data measured at the sled, the model presented in this paper was subjected to the same trial and yielded the following response, in which the deviation reaches a maximum of 6 degrees.

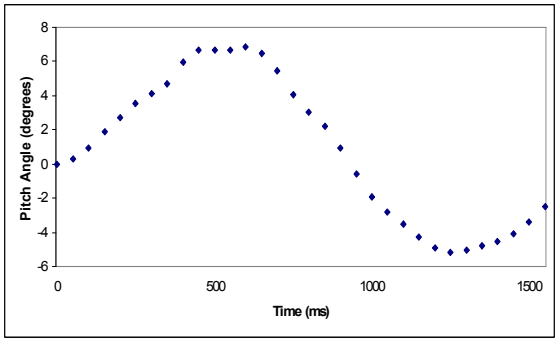

Figure 12. Active HNC pitch angle for the inverted braking sled trial (degrees vs. time (ms)).

Although further analyses will still be developed, it seems that the simulated HNC kinematics may be compatible with the response of this aware volunteer.

CONCLUSIONS

This paper allows for one foremost conclusion: a computational model of a human body, equipped with a feedback-controlled HNC, does seem to reasonably maintain its target erect posture in simple, one-degree-of-freedom loading scenarios. A very preliminary comparison with an experimental sled braking study seems to confirm that same conclusion. The authors acknowledge, however, that unlike a real human subject this model is not able to predict future events, which would be especially relevant in a test with changing trends like the first one, and so the proposed computational solution is (at least at this stage) simply reactive. Some sort of prediction or learning may become possible in the future, since the authors believe a new control paradigm is required (e.g. neural networks) and will attempt to implement. Even so, the outputs presented so far suggest that the active HNC is able to mimic expected human reactions in an acceptably biofidelic manner, at least if one assumes riders attempt to maintain their head upright at all times. In fact, a rider's (or driver's) priority would probably not be his comfort but rather his ability to maintain kinematic stability between his visual senses and the vehicle's behaviour, thus emphasizing the need for an adequate posture. A vehicle's passenger, however, will probably not forcefully maintain his head's verticality but instead minimise effort or possibly balance several strategies. This conclusion mainly draws upon the reactions (and other selected outputs) provided by such an active model, both at "pitch" and "roll" levels, when it went through a preliminary analysis in a couple of scenarios. Time-dependent position data was used to build those scenarios, devising a general procedure that can be applied to more elaborate situations.
The controlled HNC assembly was itself the outcome of applying active control methodologies to a multibody model that was augmented to comprise a facet human body model and a touring motorcycle that was propelled along the chosen trajectories. Sensors and muscles groups were thus selected, tested, and adequately implemented in the model.

ACKNOWLEDGEMENTS

The first and third authors would like to specifically thank the European Commission (EC) 6th Framework Programme for the support provided through the Marie Curie project MYMOSA (MRTN-CT-2006-035965) on motorcycle and motorcyclists' safety.

REFERENCES

[1] COST 327, "Motorcycle Safety Helmets", Final Report of the Action, European Communities, Belgium, 2001.

[2] ISO 13232-3:2005: Motorcycles, "Test and analysis procedures for research evaluation of rider crash protective devices fitted to motorcycles – Part 3: Motorcyclist anthropometric impact dummy (MATD)".

[3] International Research Council on the Biomechanics of Impact (IRCOBI), "Future Research Directions in Injury Biomechanics and Passive Safety Research", Technical report, Bron, France, 2006.

[4] van der Horst, M., Thunnissen, J., Happee, R., van Haaster, R., Wismans, J., "The influence of muscle activity on head-neck response during impact", Proceedings of the 41st Stapp Car Crash Conference Society of Automotive Engineers (paper 973346), 1997.

[5] van der Horst, M., "Human head neck response in frontal, lateral and rear end impact loading – modeling and validation", PhD Thesis, Eindhoven University of Technology, ISBN 90-386-2843-9, 2002.

[6] Brelin-Fornari, J., Arabyan, A., Deng, Y.-C., “Use of active muscles in a model of the human head and neck”, Proceedings of the 42nd Stapp Car Crash Conference Society of Automotive Engineers, 1998.

[7] van Lopik, D., Acar, M., “A computational model of the human head and neck system for the analysis of whiplash motion”, International Journal of Crashworthiness 9(5), 465–473, 2004.

[8] Stemper, B.D., Yoganandan, N., Pintar, F.A., “Occupant awareness affects whiplash biomechanics”, Journal of Biomechanics 39(S1), S147, 2006.

[9] Kumar, S. et al, “Cervical muscle response to trunk flexion in whiplash-type right lateral impacts”, International Journal of Crashworthiness 10(1), 2005.

[10] Kumar, S. et al, “The effect of occupant position in volunteers subjected to whiplash-type rear impacts”, International Journal of Crashworthiness 9(6), 2004.

[11] Yu, H. et al, “Head-neck finite element model of the crash test dummy THOR”, International Journal of Crashworthiness 9(2), 2004.

[12] Barton, P. M., Hayes, K. C. , “Neck flexor muscle strength, efficiency, and relaxation times in normal subjects and in subjects with unilateral neck pain and headache", Arch. Phys. Med. Rehabil., 77(7):680-7, 1996.

[13] Ono, K. et al, “Cervical vertebral motions and biomechanical responses to direct loading of human head”, Traffic Inj. Prev., 4(2):141-52, 2003.

[14] Coakwell, M. R. et al, “High-risk head and neck movements at high G and interventions to reduce associated neck injury”, Aviation Space Environ. Med., 75(1):68-80, 2004.

[15] Kettler, A. et al, “In vitro acceleration study on human cadaveric cervical spine specimens”, Spine, 29(21):2404-9, 2004.

[16] Guitton, D. et al, “Visual, vestibular and voluntary contributions to human head stabilization”, Exp. Brain Res. 64(1):59-69, 1986.

[17] Keshner, E.A., “Modulating active stiffness affects head stabilizing strategies in young and elderly adults during trunk rotations in the vertical plane”, Gait and Posture 11, 1-11, 2000.

[18] Keshner, E.A., “Head-Trunk Coordination During Linear Anterior-Posterior Translations”, Journal of Neurophysiology 89, 1891-1901, 2003.

[19] Lange R. de, Rooij L. van, Mooi H., Wismans J., “Objective Biofidelity Rating of a Numerical Human Occupant Model in Frontal to Lateral Impact”, STAPP Car Crash Journal, Vol. 49, 457-479, 2005.

[20] Hedenstierna, S., Halldin, P., “How does a three-dimensional continuum muscle model affect the kinematics and muscle strains of a finite element neck model compared to a discrete muscle model in rear-end, frontal, and lateral impacts”, Spine 33(8):E236-45, 2008.

[21] Gugler, J., Steffan, H., “Improvement of rollover safety for passenger vehicles”. ROLLOVER Project - Final report, EC 5th Framework Program, 2006.

[22] Oakley, C., “Roadmap of future automotive passive safety technology development”. Technical report, APSN—European Vehicle Passive Safety Net., 2004.

[23] TNO Automotive Safety Solutions, “MADYMO Human Models Manual, version 6.3.2.”, Delft, The Netherlands, 2006.

[24] Dickman, D., “Vestibular system primer”, Washington University School of Medicine, 2001.

[25] Lee, S., “Anatomy of the Vestibular System”, University of North Carolina, 2006.

[26] Almeida, J., Fraga, F., Silva, M. T., Silva-Carvalho, L., “Feedback control of the head–neck complex for nonimpact scenarios using multibody dynamics”, Journal of Multibody System Dynamics, Springer, 2009 (in press).

[27] www.aprosys.com

[28] Symeonidis I., Kavadarli G., Peldschus S., Schuller E., Fraga F., van Rooij L., “Laboratory set-up for the analysis of motorcyclists' behaviour during deceleration”, in Conference Proceedings of The 6th Int. Forum of Automotive Traffic Safety (INFATS), Xiamen, China, 2008.

CREATING REPRESENTATIVE CURVES FROM MULTIPLE TIME HISTORIES OF VEHICLE, ATD AND BIOMECHANICS TESTS

Guy S. Nusholtz
Timothy P. Hsu
Yibing Shi
Sadegh Babaii Kochekseraii
Manuel Alejandro Gracián Luna
Chrysler LLC
USA
Paper Number 09-0249

ABSTRACT

When test responses from specimens such as Post-Mortem Human Surrogates (PMHS), anthropomorphic test devices (ATD) or vehicle crash events are "perfectly repeatable," the response in terms of transducer time histories is similar and the output from any one of the tests can be used to represent any other test. However, if there is test-to-test variability, the underlying fundamental response as obtained by the transducer time history is not determined by a single test and methods are needed that can use multiple tests to reduce the inherent error. This paper will explore, using different transducer time histories from PMHS, ATD and vehicle tests, the effect of signal alignment and signal "shape" on the results from signal addition. New procedures for transducer time history alignment and signal addition will be introduced and discussed, and different methods of obtaining the underlying response will be evaluated.

INTRODUCTION

If measurements subject to random variation about some nominal or "true" value, there is potential to better understand the nominal performance with repeated measurements. For data sets in which each measurement is a single scalar value and multiple measurements are independent, the central mean theorem implies that the mean should be a better estimate of the true value of the measurement than any of the individual measurements. Comparisons of two or more different measurement data sets can be accomplished by comparing the means. However, it is not clear that this approach is valid for comparisons of different sets of finite duration time history measurement, such as: acceleration, force or displacement time history obtained from a human surrogate test or the load time history from a barrier load cell array in a vehicle crash.

Although addition of scalar data is straightforward, the addition of finite time histories is not; for example, defining the numerical procedures such as alignment, individual or accumulative durations, and magnitude of the time histories, to name a few, is subject to interpretation and different definitions could result in different end points. Consequently, there exist a large number of possible methods of signal addition resulting in no unique "best" average signal. Nonetheless, there have been several attempts to combine time history signals to obtain an "average" or "representative" time history [1,2,3,4].

This paper presents two different methods for obtaining a representative time history or "representative curve" (RC) of finite duration time history signals: The first (Procedure A) considers both the shape and magnitude of the time history and the resulting representative signal is constructed by weighing each of the signals by its magnitude; the second (Procedure B) considers only the shape of the signal and the resulting representative signal is constructed by weighing each of the signals equally. In both procedures the signals are shifted to minimize the difference between them and they are then combined. Using the same signals these two procedures can produce different RCs depending on the nature of the signals used in the construction.

Signal Alignment and Representative Curve (RC) Generation

In many cases, signals from a test series taken under the same test conditions do not duplicate well. Many techniques are available to build a RC out of the group. Very often, alignment is necessary to position the signals in time to obtain meaningful results. Figures 1-3 show the different means resulted from the same signals with different alignment schemes. The shapes and curves are different. The magnitude may also be different.

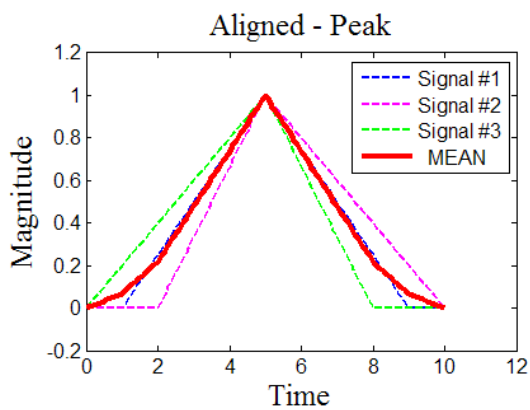

Figure 1 - Mean with Signals Aligned at Peak

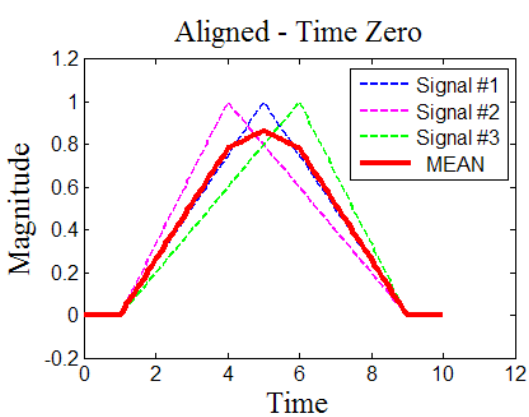

Figure 2 - Mean with Signals Aligned at Time Zero

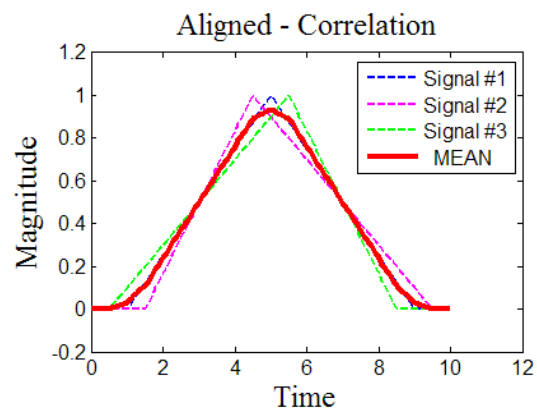

Figure 3 - Mean with Signals Aligned based on Maximum Cross-Correlation

Creating an RC by aligning the time histories so that they can be added is not always trivial. In many cases, adding the signals, after they have been aligned, will distort the "underlying response" and reduce the value of the resulting average: the representative curve is not representative of the curves used to construct it. The key question as to the usefulness of the information in the RC is whether the differences in the signals are dominated by random variations or due to deterministic changes. If they are deterministic, then the RC may be an artifact of the process used and not representative of the underlying response. This question will not be answered in this paper. Instead it will be assumed that there is a fundamental basis to attribute the variation to randomness.

If the variations can be attributed to randomness then statistically speaking, the standard deviation of all the signals can be obtained, and minimizing the covariance or maximizing the correlation will give the best results for alignment. The correlations at the aligned state can be used as an assessment of the quality of the agreement between the signals with emphasis on the “phasing” component of the agreement. It may be supplemented by a measure similar to variance, but normalized at each time step by the mean value of the signals (the coefficient of variation) to give another evaluation of the

agreement that emphasizes more on the "magnitude" component of the agreement.

On the other hand, if the difference among the signals is determined to be dominated by deterministic changes among tests, then the above approach does not address the nature of the problem. In this case, the goal would be to identify a master curve that entails the response characteristics of the system, and different curves are then to be "scaled" back to this master curve. An example of this is the acceleration response curves of crash tests of the same vehicle under different velocities, where a second order differential equation can be utilized to model the behavior and "scale" the set of signals. In more general cases, the task will essentially be a system identification problem to define the fundamental characteristics of the system.

What criteria should be used to align signals and to judge the quality of created RCs needs to be decided first. For alignment, commonly used tools are: "eyeballing," "time zero," minimum variance, and maximum correlation. When digital data are absent and correlations are low, especially with old data (non-digital) and different lab facilities, eyeballing presents itself to be the preferred choice. Time zero has the advantage of aligning the event in time, an example being vehicle crash signals in which distinct time zero information is available. However, in many cases, due to vehicle build variation and other confounding factors, the first mode frequencies are often quite different causing the overlaid signals to be inconsistent with the time integrals (as required by conservation of momentum). The variance and the correlation approach, on the other hand, often yield similar time shifts. The starting times do not always line up; however, aligning in many cases ensures a consistent RC.

The following presents two statistical, correlation based methods that build upon the work incorporated into ISO9790 [1] and the Maltese methods [3]. One notable difference is that the current methods do not generate acceptance corridors. Instead they examine and compare the magnitude, shape, and phase of the curves to determine the level of similarity.

Procedure A (Maximal Correlation and Normalization) - Methodology and Characteristics

"Phase," "shape," and "magnitude" are three concepts that have been defined and used in previous studies [4]. Procedure A uses these to establish an RC from multiple time histories which are assumed to have independent random phase, shape, and magnitude variations.

Phase Alignment

With a set of n time history responses $R_i(t)$ ($i=1, 2, ..., n$) for phase alignment, since absolute time is immaterial, without loss of generality, the time for the first response is picked as the absolute time. There are then only $n-1$ time shifts to be found per some requirement. These are denoted as h_i ($i=2, 3, ..., n$).

The coefficient of correlation is used as a measure of the phase agreement between a pair of similar signals,

$$c_{ij} = c_{ij}(h_i, h_j),$$

where $h_1=0$. It is noted that $c_{ij}=1$, when $i=j$.

At this point, a measure is needed that collectively gauges the quality of the matrix $[c_{ij}]$. The most straightforward summary measure would be the sum of all its elements. Based on this, the following normalized alignment measure C is constructed:

$$C(h_2, h_3, ..., h_n) = \frac{1}{n(n-1)}\left(\left(\sum_{i=1}^{n}\sum_{j=1}^{n} c_{ij}(h_i, h_j)\right) - n\right).$$

Note that $-1 \le C \le 1$. (Since the sign of c_{ij} is significant, the above uses the actual value instead of the absolute value or the square of c_{ij}).

The measure C is a gauge of the quality of the collection of the time shifts. It is a function of the $n-1$ shifts. Maximizing C with respect to these shifts will determine the optimal collective phase agreement. In this study, the unconstrained nonlinear optimization routine in Matlab® was used with minor modifications to avoid local trapping associated with discrete signals.

Shape Extraction

For each of the n phase-shifted responses $X_i(t)=R_i(t-h_i)$, its normalized response is defined to be,

$$x_i = \frac{X_i}{\|X_i\|},$$

where $\|X_i\|$ is a norm defined as

$$\|X_i\| = \sqrt{\int X_i^{\,2} dt}\,.$$

The integration is used here for ease of expression, and it is to be interpreted as summation if the time histories are treated as discrete signals. The integral, as all others throughout this paper, has limits of (-∞, +∞). All time histories here are assumed to be bounded (i.e., the norm exists). This condition is automatically satisfied by impact test signals which start and end at zero magnitude.

The following time history *y* is defined as the shape representation of the set of time histories:

$$y = \frac{\frac{\sum x_i}{n}}{\left\|\frac{\sum x_i}{n}\right\|} = \frac{\sum x_i}{\|\sum x_i\|}.$$

In other words, *y* is the normalized version of the average of the normalized responses. The average of its correlation with each of the original signals is found as:

$$p = \frac{1}{n}\sum p_i = \frac{1}{n}\sum \int x_i y dt = \int \frac{\sum x_i}{n} y dt = \left\|\frac{\sum x_i}{n}\right\|,$$

which is the norm of the average of the signals.

p is named the "shape similarity factor" of the original set of signals, as it reflects the overall shape similarity quality based on all the signals.

A special property of *p* is:

$$p = \left\|\frac{\sum x_i}{n}\right\| = \frac{1}{n}\sqrt{\int \left(\sum x_i\right)^2 dt} \le \frac{1}{n}\sum \int x_i^{\,2} dt = \frac{1}{n}\sum 1 = 1,$$

or, $0 \le p \le 1$. The inequality in the above relationship is based on the Minkowski's inequality which basically says that the norm of the sum is no more than the sum of the norms; and the last equality in the expression is because x_i is already normalized.

Magnitude Scaling

The normalized optimal shape *y* established above needs to be scaled back to the physical measurement space to carry an appropriate magnitude. Given that each signal has a magnitude factor, assuming it is randomly distributed, then its sample average is an unbiased estimate of the mean of the magnitude. Therefore, the final representative curve is:

$$Y = \left(\frac{1}{n}\sum \|X_i\|\right) y = \left(\frac{1}{n}\sum \|X_i\|\right) \frac{\sum x_i}{\left\|\sum x_i\right\|}.$$

Procedure B (Mean-To-Mean Approach) - Methodology and Characteristics

The Mean-To-Mean (MTM) methodology is based on a number of available statistical and numerical analysis methods. The major ones are the normalized cross correlation assessment known as cross correlation coefficient of a pair of signals [5]. An approach using an iterative improvement of solution of non-linear equations is also implemented in the procedure (Appendix A).

For the set of signals to be aligned using the cross correlation coefficient, two signals in the group that are most correlated are identified. The pair is aligned using maximum cross correlation process and its sample means calculated. The mean is grouped with the rest in the signal set again replacing the two most correlated signals. All the signal subsets associated with that group pair should be shifted based on the alignment of the pair. This process continues until all signals in the set are aligned using the same procedure.

Additional optimization steps are incorporated in the MTM algorithm, including a prescreening process to identify signal pairs with mutual maximal cross correlation coefficients (CCC). The process is as follows: for a signal set with n signals, CCCs between each signal and another signal in the set are calculated. For each signal, there will be n-1 CCCs. The maximal CCC for each signal is identified. The maximal CCCs for all signals are listed according to their values, from maximum to minimum. Signal pairs with mutual maximal CCC are taken out and put in separate groups. This is a way of identifying the signals with the most influence early in the alignment process and at the same time reducing the effects of any individual signals on the overall performance of the alignment process.

A numerical procedure is generated based on this algorithm. The key element in this algorithm is to evaluate only two signals at a time.

To explain the methodology, an example is shown here with 6 signals: A, B, C, D, E and F.

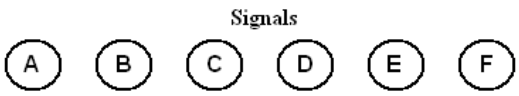

Figure 4 – Time Domain Signals

First, the cross correlation coefficients are obtained with respect to each other in order to identify the pair of signals with the highest cross correlation coefficient. The pair is aligned based on the maximal CCC.

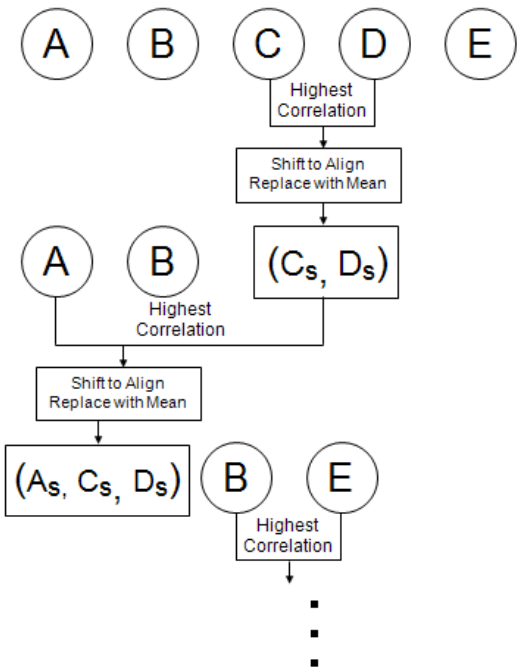

Figure 5 - Procedures for Signal Alignment

Suppose that signals C and D have the highest cross correlation coefficient. They are aligned based on time lag of the maximum cross correlation and their mean obtained as follows:

$$Mean = \frac{C_s + D_s}{2}$$

where C_S and D_S are the shifted signals of C and D. The mean, Mean, then replaces C_S and D_S in the subsequent analysis. The whole process is repeated until a final mean is obtained.

$$Mean = \frac{A_s + B_s + C_s + D_s + E_s + F_s}{2}$$

Further improvement of the final mean or the representative curve is achieved with additional iterations of the process as follows,

- Obtain initial solution
- Repeat the alignment process
- Subtract the error from the solution
- Obtain the improved solution
- Repeat until convergence achieved

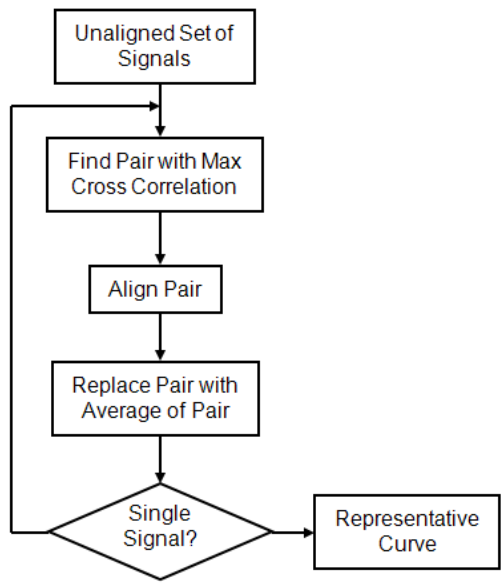

Figure 6 – Flowchart for Signal Alignment

Examples

The methods discussed have application limitations. A variety of data sets, taken from NHTSA' database, has been selected to provide some examples of its range of applicability. The specific units used in the graphs and tables shown are purposely left out, they are for illustrative purposes only and not for direct comparison to real test events. Time is plotted as steps depending on the sampling rate used and cannot be directly related to real time.

PMHS Tests:

PMHS tests are used to characterize the response of the human body to impact. Similar tests carried out on different PHMSs in different labs can result in signals with marked contrasts, creating a challenge to aggregate such contrasting signals and obtain a unique representative signal for the set.

Figure 7 shows the original PMHS data that serve as a base for both methodologies. Figures 8-10 show the results from Method A, Method B and their comparison. Table 1 shows the time shifts (in number of time steps) using the alignment schemes of Method A and Method B.

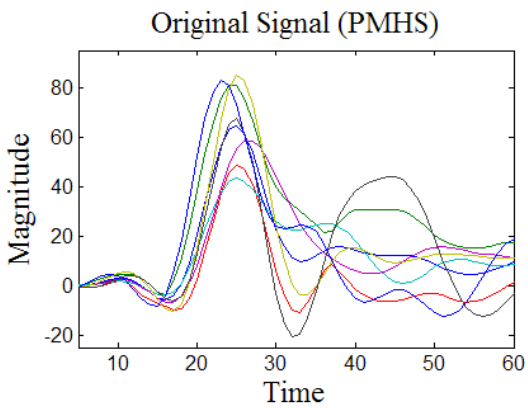

Figure 7 - Original PMHS Signals

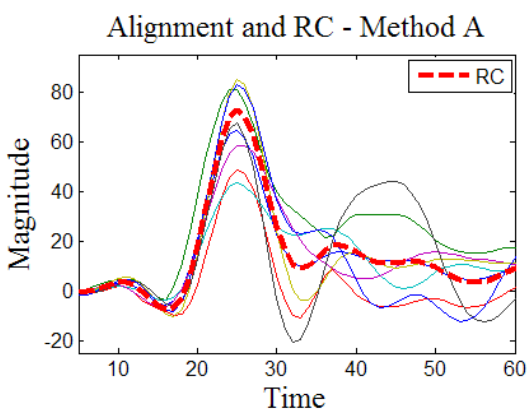

Figure 8 - PMHS Signals Processed (Method A)

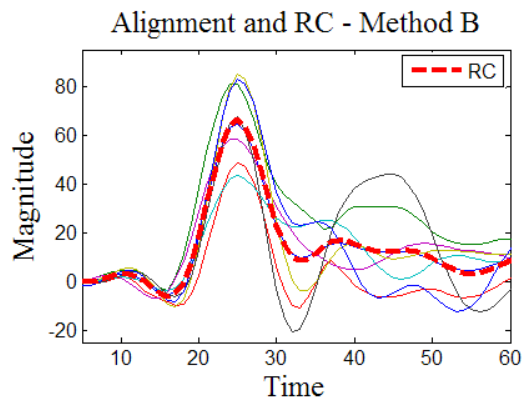

Figure 9 - PMHS Signals Processed (Method B)

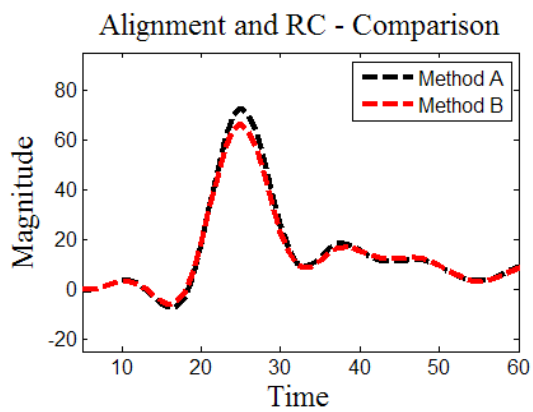

Figure 10 - PMHS Signals Processed (Overlay)

Signal ID	Method A	Method B	Difference (A vs. B)
1	-98	-98	0
2	-98	-98	0
3	-98	-98	0
4	-98	-98	0
5	-99	-100	-1
6	-98	-98	0
7	-98	-98	0
8	-96	-96	0

Table 1 - Time Shifts Comparison (PMHS)

Vehicle Crash (NCAP) Tests:

Vehicles available in NHTSA crash database [6] are classified into compacts cars, sedans, SUVs, minivans and trucks. Frontal rigid barrier forces

from NCAP tests were downloaded from the database and summed over the total number of cells in the rigid barrier to obtain the total force of impact for each test. Method A and Method B are used to align and extract a representative curve for the set. Figures 11-14 and Table 2 show the results from the study.

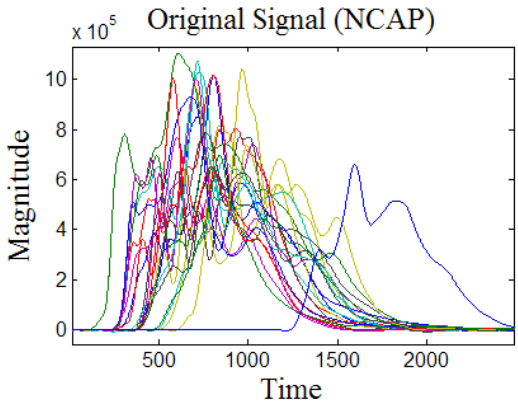

Figure 11 - Original NCAP Signals

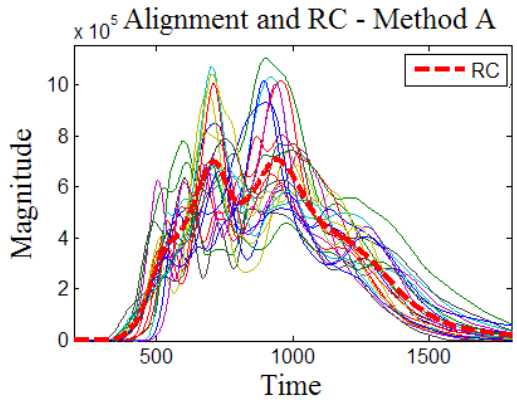

Figure 12 - NCAP Signals Processed (Method A)

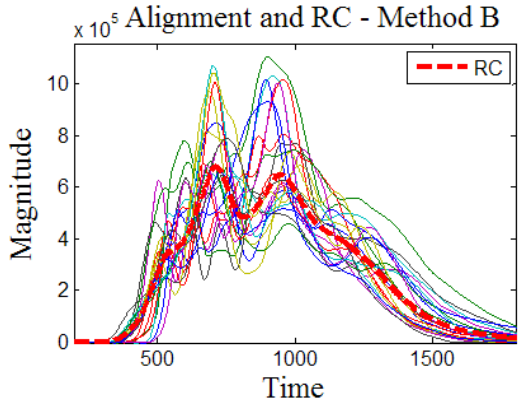

Figure 13 - NCAP Signals Processed (Method B)

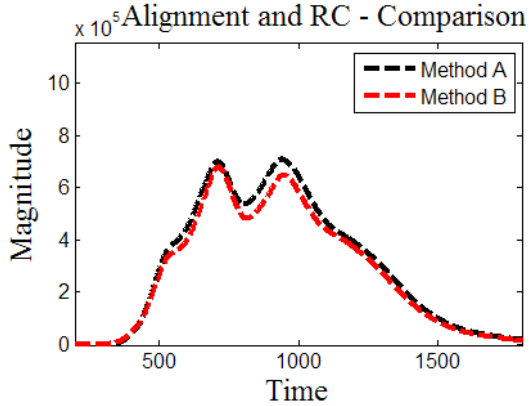

Figure 14 - NCAP Signals Processed (Overlay)

Signal ID	Method A	Method B	Difference (A vs. B)
1	867	867	0
2	1161	1166	5
3	898	898	0
4	1062	1064	2
5	873	872	-1
6	711	708	-3
7	867	869	2
8	957	965	8
9	993	996	3
10	1019	1022	3
11	718	717	-1
12	1000	1000	0
13	853	848	-5
14	805	804	-1
15	1089	1098	9
16	725	722	-3
17	999	997	-2
18	856	852	-4
19	1097	1097	0
20	607	604	-3
21	859	860	1
22	1	0	-1

Table 2 - Time Shifts Comparison (NCAP)

CONCLUSIONS

Two signal alignment methods are presented and used to analyze different types of time domain data. One scheme aligns the signals based on the cross correlation coefficients and normalizes the signals to form a representative curve (RC). The other aligns the signals based on cross correlations and then averages the signals.

The methods are aimed at minimizing the differences between the resultant RC and the signals used to generate the RC. Assuming that the variations from test to test for the transducer time histories are the result of randomness and not deterministic, these methods may be useful for obtaining the underlying response characteristic. The representative curve obtained from these methods may be used for different types of analysis such as determining the biofidelity metrics for ATD design, comparing different ATD responses under similar impact conditions and analysis of different vehicle crash characteristics.

REFERENCES

[1] ISO/TR9790. (1999) Road Vehicles Anthropomorphic Side Impact Dummy - Lateral Impact Response Requirements to Assess the Bio-fidelity of the Dummy. International Standards Organization, American National Standards Institute, NY, NY

[2] Hsu, T. P, Nusholtz, G. S. (2005) Considerations of Bio-fidelity Corridors for Lateral Impacts, SAE Technical Paper Series 2005-01-0308, April 11, 2005.

[3] Maltese, M. R.; Eppinger, R. H.; Rhule, H. H.; Donnelly, B. R.; Pintar, F. A.; Yoganandan, N. (2002) Response corridors of human surrogates in lateral impacts. National Highway Traffic Safety Administration, Washington, D.C./ Wisconsin Medical College, Milwaukee/ Veterans Affairs Medical Center, Milwaukee, Wisc. 31 p. Stapp Car Crash Journal, Vol. 46, Nov. 2002, p. 321-351.

[4] Xu, L.; Agaram, V.; Rouhana, S.; Hultman, R. W.; Kostyniuk, G.W.; McCleary, J.; Mertz, H.; Nusholtz, G.S.; and Scherer, R.. (2000) Repeatability Evaluation of the Pre-Prototype NHTSA Advanced Dummy Compared to the Hybrid III, SAE Technical Paper Series 2000-01-0165, March 6-9, 2000

[5] Ifeachor, E. C.; and Jervis B. W. (1993), Digital Signal Processing: A Practical Approach, Addison-Wesley.

[6] http://www-nrd.nhtsa.dot.gov/database/aspx/vehdb/queryvehicle.aspx
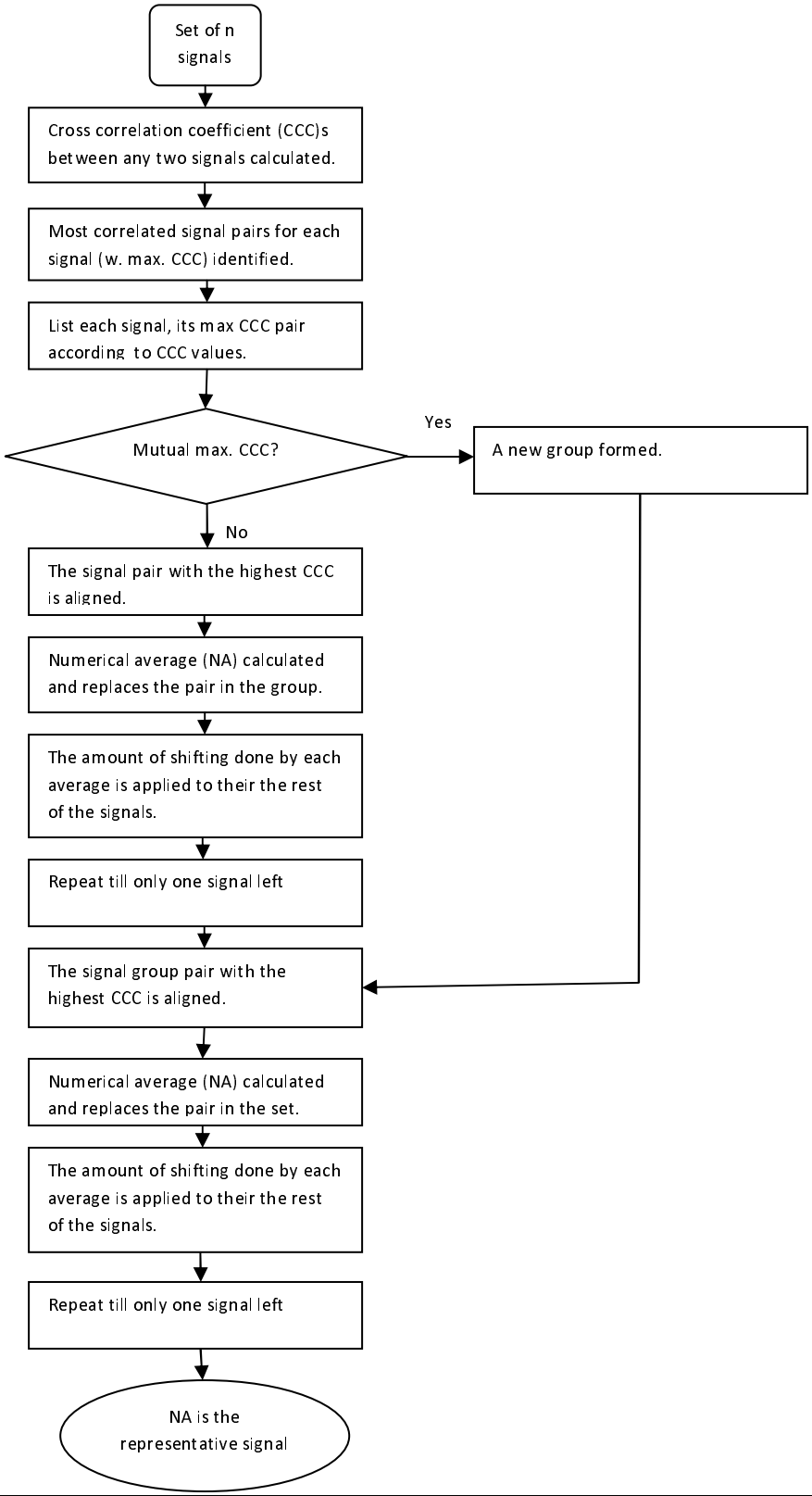
Appendix A: MTM Flowchart